

# AIRCRAFT AND ROTORCRAFT SYSTEM IDENTIFICATION

## Engineering Methods with Flight Test Examples

Mark B. Tischler  
Robert K. Remple



AMERICAN INSTITUTE OF  
AERONAUTICS AND ASTRONAUTICS

**AIAA EDUCATION SERIES**  
JOSEPH A. SCHETZ  
EDITOR-IN-CHIEF

# **Aircraft and Rotorcraft System Identification**

**Engineering Methods with  
Flight-Test Examples**

This page intentionally left blank

# Aircraft and Rotorcraft System Identification

## Engineering Methods with Flight-Test Examples

**Mark B. Tischler**  
**Flight Control Group Leader**  
**Senior Scientist**  
U.S. Army Aeroflightdynamics Directorate  
Ames Research Center  
Moffett Field, California

**Robert K. Remple**  
**Senior Technical Writer**  
University of California, Santa Cruz  
Ames Research Center  
Moffett Field, California



### EDUCATION SERIES

Joseph A. Schetz  
Series Editor-in-Chief  
Virginia Polytechnic Institute and State University  
Blacksburg, Virginia

Published by  
American Institute of Aeronautics and Astronautics, Inc.  
1801 Alexander Bell Drive, Reston, VA 20191-4344

American Institute of Aeronautics and Astronautics, Inc., Reston, Virginia

1 2 3 4 5

**Library of Congress Cataloging-in-Publication Data on file.**

Copyright © 2006 by the American Institute of Aeronautics and Astronautics, Inc. All rights reserved. Printed in the United States of America. No part of this publication may be reproduced, distributed, or transmitted, in any form or by any means, or stored in a database or retrieval system, without the prior written permission of the publisher.

Data and information appearing in this book are for informational purposes only. AIAA is not responsible for any injury or damage resulting from use or reliance, nor does AIAA warrant that use or reliance will be free from privately owned rights.

## Table of Contents

<b>List of Figures</b> .....	<b>xi</b>
<b>List of Tables</b> .....	<b>xix</b>
<b>Nomenclature</b> .....	<b>xxiii</b>
<b>Acronyms</b> .....	<b>xxix</b>
<b>Preface</b> .....	<b>xxxi</b>
<b>Chapter 1. Introduction and Brief History of System Identification in the Frequency Domain</b> .....	<b>1</b>
1.1    Basic Concepts of System Identification of Aircraft and Rotorcraft .....	1
1.2    Relationship Between Simulation and System Identification .....	6
1.3    Special Challenges of Rotorcraft System Identification .....	8
1.4    More About the Role of Nonparametric vs Parametric Models in Flight-Vehicle System Identification .....	9
1.5    Frequency-Response Identification Method Is Well Suited to Flight-Vehicle Development .....	12
1.6    Role and Limitations of Flight-Mechanics Models Determined with the System-Identification Method .....	17
1.7    Brief History of the Development of Frequency-Domain Methods for Aircraft and Rotorcraft System Identification .....	18
1.8    Organization of this Book .....	20
Problems .....	22
<b>Chapter 2. Frequency-Response Method for System Identification</b> .....	<b>25</b>
2.1    Road Map of Frequency-Response Method for System Identification .....	25
2.2    Key Features of the Frequency-Response Method for Flight-Vehicle System Identification .....	29
2.3    Frequency-Response Identification Method Applied to the XV-15 Tilt-Rotor Aircraft .....	35
2.4    Examples of CIFER® Applications .....	51
Problems .....	53
<b>Chapter 3. Description of Example Cases</b> .....	<b>55</b>
3.1    Pendulum Example Problem .....	55
3.2    XV-15 Tilt-Rotor Aircraft .....	58

3.3	XV-15 Dynamic Characteristics in Hover .....	58
3.4	Measurements for Closed-Loop Hover Flight Testing .....	60
3.5	XV-15 Test Case Database for Hover .....	62
3.6	XV-15 Dynamic Characteristics in Cruise .....	64
3.7	Measurements for Open-Loop Cruise Flight Testing .....	64
3.8	XV-15 Test Case Database for Cruise .....	65
	Problems .....	67
<b>Chapter 4. Overview of CIFER® Software .....</b>		<b>69</b>
4.1	Basic Characteristics of the CIFER® Software .....	69
4.2	Dataflow Through CIFER® .....	71
4.3	CIFER® Menu .....	73
4.4	CIFER® User Interface .....	73
4.5	Examples of CIFER® Utilities .....	78
4.6	Interfaces with Other Tools .....	79
	Problems .....	81
<b>Chapter 5. Collection of Time-History Data .....</b>		<b>83</b>
5.1	Overview of Data Requirements for System Identification (Time Domain and Frequency Domain) .....	83
5.2	Optimal Input Design .....	85
5.3	Recommended Pilot Inputs for the Frequency-Response Identification Method .....	86
5.4	Instrumentation Requirements .....	88
5.5	Overview of Piloted Frequency Sweeps .....	90
5.6	Detailed Design of Frequency-Sweep Inputs .....	92
5.7	Flight-Testing Considerations .....	94
5.8	Open-Loop vs Closed-Loop Testing for Bare-Airframe Identification .....	95
5.9	Piloted Frequency Sweeps: What IS and What IS NOT Important .....	97
5.10	Summary of Key Points in Piloted Frequency-Sweep Technique .....	100
5.11	Computer-Generated Sweeps .....	102
5.12	Frequency-Response Identification from Other Types of Inputs .....	112
	Problems .....	117
<b>Chapter 6. Data Consistency and Reconstruction .....</b>		<b>119</b>
6.1	Modeling Measurement Errors in Flight-Test Data .....	119
6.2	Simple Methods for Data Consistency and State Reconstruction .....	129
	Problems .....	143

<b>Chapter 7. Single-Input / Single-Output Frequency-Response Identification Theory</b> .....	<b>145</b>
7.1 Definition of Frequency Response .....	146
7.2 Relating the Fourier Transform of the Time Signals to the Frequency Response $H(f)$ .....	147
7.3 Simple Example of Frequency-Response Interpretation .....	149
7.4 General Observations .....	152
7.5 Calculating the Fourier Transform and Spectral Functions .....	152
7.6 Interpreting Spectral Functions .....	158
7.7 Frequency-Response Calculation .....	159
7.8 Coherence Function .....	165
7.9 Random Error in the Frequency-Response Estimate .....	167
7.10 Window Size Selection and Tradeoffs .....	169
7.11 Frequency-Response Identification in CIFER® Using FRESPID .....	175
7.12 Summary of Guidelines for Frequency-Response Identification .....	177
7.13 Pendulum Example .....	177
7.14 Applications and Examples Problems .....	178
	203
<b>Chapter 8. Bare-Airframe Identification from Data with Feedback Regulation Active</b> .....	<b>209</b>
8.1 Limiting Conditions in Closed-Loop Identification .....	209
8.2 Quantification of Bias Errors .....	211
8.3 Bias Errors Defined .....	213
8.4 Numerical Study of Identification Results Obtained Under Closed-Loop Conditions .....	215
8.5 Flight-Test Implications .....	224
8.6 Identification of Unstable Inverted Pendulum Dynamics .....	225
8.7 Conclusions .....	226
	226
<b>Chapter 9. Multi-Input Identification Techniques</b> .....	<b>229</b>
9.1 Multi-Input Terminology .....	229
9.2 Need for Multiple-Input Identification Technique .....	230
9.3 Simple Two-Input Example .....	231
9.4 Conditioned Spectral Quantities .....	237
9.5 Example of a Two-Input Identification Solution Using the XV-15 Flight Data .....	239
9.6 General MIMO Solution .....	245
9.7 High Control Correlation .....	248
9.8 Multiple-Input Identification in CIFER® Using MISOSA .....	249

9.9	Example of MISO Solution for a Hovering Helicopter .....	250
9.10	MIMO Identification Using a Multi-Input Maneuver .....	254
9.11	Determination of Broken-Loop Response for MIMO Control System .....	256
	Problems .....	257
<b>Chapter 10. Composite Windowing .....</b>		<b>259</b>
10.1	Background .....	259
10.2	Composite-Window Approach .....	260
10.3	Choice of Window Sizes .....	263
10.4	Composite-Window Calculations in CIFER® using COMPOSITE .....	263
10.5	Composite-Window Results for Pendulum Example .....	263
10.6	COMPOSITE Windowing in Single-Input and Multi-Input Analyses .....	266
10.7	Composite-Windowing Results for XV-15 Closed-Loop SISO Identification in Hover $p/\delta_{\text{lat}}$ .....	268
10.8	Composite-Windowing Results for Bo-105 Helicopter MIMO Identification .....	271
10.9	Composite Results for Structural System Identification .....	273
10.10	Composite Windowing in Spectral Analysis of Time-History Signals .....	274
10.11	Summary .....	275
	Problems .....	275
<b>Chapter 11. Transfer-Function Modeling .....</b>		<b>277</b>
11.1	Motivations for Transfer-Function Modeling .....	277
11.2	Transfer-Function Modeling Identification Method .....	278
11.3	Model Structure Selection .....	281
11.4	SISO Transfer-Function Identification in CIFER® Using NAVFIT .....	284
11.5	Pendulum Example .....	285
11.6	Handling-Qualities Applications .....	286
11.7	Flight-Mechanics Characterization Studies .....	298
11.8	Flight-Dynamics Models for Control System Design .....	307
11.9	Aeroelastic Model Identification .....	310
11.10	Subsystem Component Modeling .....	314
11.11	Summary and a Look Ahead .....	317
	Problems .....	317
<b>Chapter 12. State-Space Model Identification—Basic Concepts .....</b>		<b>321</b>
12.1	Background .....	322
12.2	MIMO State-Space Model Identification Using the Frequency-Response Method .....	323

12.3	Accuracy Analysis .....	330
12.4	Key Features of the Frequency-Response Method for State-Space Model Identification .....	340
12.5	State-Space Model Structure .....	342
12.6	State-Space Model Identification in CIFER® Using DERIVID .....	347
12.7	Pendulum Example .....	348
12.8	Identification of a XV-15 Closed-Loop State-Space Model .....	350
12.9	Structural System Identification .....	353
	Problems .....	357
<b>Chapter 13. State-Space Model Identification:</b>		
	<b>Physical Model Structures .....</b>	<b>359</b>
13.1	Background .....	360
13.2	Buildup Approach to Developing the Appropriate Physical Model Structure .....	362
13.3	Equations of Motion for Flight Vehicles .....	362
13.4	Model Formulation in a State-Space Structure .....	366
13.5	Frequency-Response Database and Frequency Ranges .....	371
13.6	Checking the Initial Model Setup .....	377
13.7	Model Identification and Structure Reduction .....	378
13.8	Identification of Three-DOF Lateral/Directional Model for XV-15 in Cruise .....	379
13.9	Identification of Three-DOF Lateral/Directional Model for XV-15 in Hover .....	394
13.10	Accurate Determination of Stability and Control Derivatives from Nonlinear Simulation Using System Identification .....	402
13.11	Identification of a Three-DOF Longitudinal Model of a Fixed-Wing UAV .....	406
13.12	System Identification of a six-DOF MIMO Model of a Lightweight Manned Helicopter .....	413
	Problems .....	430
<b>Chapter 14. Time-Domain Verification of Identification Models .....</b> <b>433</b>		
14.1	Motivation for Time-Domain Verification .....	433
14.2	Time-Domain Verification Method .....	434
14.3	Estimating the Constant Bias and Reference Shift .....	436
14.4	Correlation Problem .....	439
14.5	Data Conditioning for Time-Domain Verification .....	440
14.6	Time-Domain Verification in CIFER® Using VERIFY .....	440
14.7	Closed-Loop Transfer-Function Model Verification for XV-15 .....	441
14.8	Bare-Airframe Model Verification for Cruise (XV-15) .....	442
14.9	Bare-Airframe Model Verification for Hover (XV-15) .....	447
	Problems .....	449

<b>Chapter 15. Higher-Order Modeling of Coupled Rotor/Fuselage Dynamics .....</b>	<b>451</b>
15.1    Background and Literature on Identification of Extended Helicopter Models .....	451
15.2    Hybrid Model Formulation .....	452
15.3    Hybrid Model Identification of SH-2G Helicopter .....	464
15.4    Lead-Lag Dynamics Identification for S-92 Helicopter Problems .....	490
<b>Appendix A: Summary of Suggested Guidelines .....</b>	<b>495</b>
<b>References .....</b>	<b>499</b>
<b>Index .....</b>	<b>515</b>
<b>Supporting Materials .....</b>	<b>525</b>

## List of Figures

Fig. 1.1	Aircraft as an input-output system . . . . .	2
Fig. 1.2	Helicopter as an input-output system . . . . .	2
Fig. 1.3	Typical frequency-sweep input . . . . .	3
Fig. 1.4	Typical doublet input . . . . .	3
Fig. 1.5	Typical Bode plot and transfer-function model . . . . .	4
Fig. 1.6	Simulation vs system identification . . . . .	8
Fig. 1.7	Roles of system identification in the flight-vehicle development process (Ref. 9) . . . . .	13
Fig. 1.8	Flowchart of frequency-response method for system identification . . . . .	14
Fig. 2.1	Flowchart of frequency-response method for system identification . . . . .	26
Fig. 2.2	XV-15 tilt-rotor aircraft in hover configuration (NASA photo) . . . . .	36
Fig. 2.3	XV-15 tilt-rotor aircraft in cruise configuration (NASA photo) . . . . .	36
Fig. 2.4	Two lateral-stick frequency sweeps in cruise . . . . .	37
Fig. 2.5	Roll-response comparison of flight vs simulation . . . . .	38
Fig. 2.6	Roll-response transfer-function model identification (XV-15, cruise) . . . . .	40
Fig. 2.7	Location of roll-rate transfer-function parameters in the s-plane . . . . .	41
Fig. 2.8	Frequency responses for XV-15 in cruise . . . . .	43
Fig. 2.8	Frequency responses for XV-15 in cruise (continued) . . . . .	44
Fig. 2.9	Verification of identified model for XV-15 in cruise (aileron input) . . . . .	46
Fig. 2.10	Verification of identified model for XV-15 in cruise (pedal input) . . . . .	47
Fig. 2.11	Frequency responses for XV-15 in hover . . . . .	49
Fig. 2.11	Frequency responses for XV-15 in hover (continued) . . . . .	50
Fig. 2.12	Verification of identified model for XV-15 in hover . . . . .	52
Fig. P2.3	Example Bode plot of roll-rate response . . . . .	54
Fig. 3.1	Pendulum example case . . . . .	56
Fig. 3.2	Block diagram realization of pendulum dynamics . . . . .	57
Fig. 3.3	XV-15 in hover (helicopter configuration) (NASA photo) . . . . .	59
Fig. 3.4	XV-15 in cruise (fixed-wing configuration) (NASA photo) . . . . .	59

Fig. 3.5	Roll and yaw control of XV-15 in hover . . . . .	60
Fig. 3.6	Measurements for closed-loop hover flight testing . . . . .	61
Fig. 3.7	Roll and yaw control of XV-15 in cruise . . . . .	65
Fig. 3.8	Measurements for open-loop cruise flight testing . . . . .	65
Fig. 4.1	Software and database components used in CIFER® . . . . .	70
Fig. 4.2	Software components of CIFER® . . . . .	73
Fig. 4.3	CIFER® menu of programs and utilities. . . . .	74
Fig. 4.4	Example of CIFER® screen: screen 1 of FRESPID . . . . .	76
Fig. 4.5	Example of CIFER® screen: screen 2 of FRESPID . . . . .	77
Fig. 4.6	Utility 93: configuration summary . . . . .	78
Fig. 4.7	Utility 19: plot frequency responses . . . . .	79
Fig. 4.8	Example frequency-response plots generated by utility 19 . . . . .	80
Fig. 4.9	Example TeX report generated by CIFER® results utility . . . . .	81
Fig. 5.1	Typical frequency-sweep input . . . . .	87
Fig. 5.2	Typical doublet input . . . . .	88
Fig. 5.3	Frequency-sweep input for handling-qualities testing (Bell 214ST, hover) . . . . .	91
Fig. 5.4	Roll-rate response: Bell 214ST during hover sweeps . . . . .	92
Fig. 5.5	Schematic of helicopter pitch SCAS . . . . .	95
Fig. 5.6	Degradation of bare-airframe identification with SCAS-on flight testing . . . . .	96
Fig. 5.7	Simultaneous actuation of multiple aerodynamic control effectors . . . . .	97
Fig. 5.8	ADOCS Demonstrator . . . . .	101
Fig. 5.9	Piloted frequency-sweep flight testing of the ADOCS Demonstrator . . . . .	101
Fig. 5.10	Frequency progression for typical automated sweep [Eq. (5.17)] . . . . .	103
Fig. 5.11	Typical automated frequency-sweep input [Eq. (5.17)] . . . . .	104
Fig. 5.12	Feedback loops to maintain reference condition during simulation model testing . . . . .	106
Fig. 5.13	Simulation inputs for lateral frequency sweep including off-axis white-noise inputs . . . . .	107
Fig. 5.14	Automated excitation signal for rotor test . . . . .	109
Fig. 5.15	Sikorsky bearingless main rotor (SBMR) test in the NASA Ames 40 × 80-ft subsonic wind tunnel . . . . .	109
Fig. 5.16	Sample time-history data from frequency-sweep wind-tunnel tests (SBMR) . . . . .	110
Fig. 5.17	Autospectrum of swashplate pitch input (SBMR) . . . . .	111
Fig. 5.18	Pathfinder in flight over Hawaii (NASA photo by Nick Galante) . . . . .	111
Fig. 5.19	Automated frequency sweep for Solar Pathfinder . . . . .	112
Fig. 5.20	Lateral frequency-sweep flight tests (UH-60A, hover) . . . . .	113
Fig. 5.21	Lateral-stick doublet flight tests (UH-60A, hover) . . . . .	113

Fig. 5.22	Comparison of on-axis identification results from sweep and doublet maneuvers (UH-60A, hover) . . . . .	114
Fig. 5.23	Comparison of off-axis identification results from sweep and doublet maneuvers (UH-60A, hover) . . . . .	116
Fig. 6.1	Deterministic measurement errors . . . . .	121
Fig. 6.2	Random measurement errors . . . . .	122
Fig. 6.3	Body-axis coordinate system . . . . .	123
Fig. 6.4	Comparison of flight data and reconstructed responses for the Bo-105 (80 kn) . . . . .	125
Fig. 6.5	Lateral velocity response identification using flight vs reconstructed data. . . . .	126
Fig. 6.6	Effect of excitation on lateral velocity scale factor . . . . .	127
Fig. 6.7	Effect of linking on scale factor and bias determination . . . . .	128
Fig. 6.8	Roll-axis error model . . . . .	130
Fig. 6.9	Roll-response consistency check for Bo-105 (80 kn). . . . .	132
Fig. 6.10	Instrumentation system elements for handling-qualities flight testing . . . . .	133
Fig. 6.11	Kinematic consistency check for the Shadow <sup>TM</sup> 200 fixed-wing UAV . . . . .	137
Fig. 6.12	Reconstructed lateral velocity response for XV-15 in hover . . . . .	138
Fig. 6.13	Detection of faulty data (AH-64) . . . . .	140
Fig. 6.14	System representation of gearing and linkage dynamics . . . . .	141
Fig. 6.15	Yaw control rigging identification for the XV-15. . . . .	142
Fig. 7.1	Bode plot for one-DOF system. . . . .	150
Fig. 7.2	Overlapped windowing of flight data (adapted from Bendat and Piersol <sup>106</sup> ). . . . .	155
Fig. 7.3	Spectral density functions for SCAS-on roll sweep (XV-15, hover) . . . . .	159
Fig. 7.4	Measurement noise at the input and output . . . . .	160
Fig. 7.5	Roll-rate response to lateral stick: SCAS on (XV-15, hover) . . . . .	162
Fig. 7.6	Secondary inputs in single-input/single-output identification. . . . .	166
Fig. 7.7	Coherence function for roll-rate response identification: SCAS-on (XV-15, hover) . . . . .	167
Fig. 7.8	Random-error function for roll-rate response identification: SCAS on (XV-15, hover) . . . . .	169
Fig. 7.9	Structural system identification of test stand using three window sizes . . . . .	174
Fig. 7.10	Flowchart of computational procedures performed by the FRESPID program. . . . .	176
Fig. 7.11	Pendulum example identification . . . . .	179

Fig. 7.12	Comparison between identified and ideal frequency responses (pendulum) . . . . .	180
Fig. 7.13	AH-64 vertical vibration autospectrum (130 kn) . . . . .	181
Fig. 7.14	Block diagram for pilot-in-the-loop analysis . . . . .	182
Fig. 7.15	Pilot control activity: simulation vs flight (UH-60, hover) . . . . .	184
Fig. 7.16	OH-58D pitch response in hover (SCAS-off) . . . . .	185
Fig. 7.17	Least-squares determination of phase delay . . . . .	186
Fig. 7.18	OH-58D SCAS-off hover comparison with ADS-33E . . . . .	187
Fig. 7.19	Comparison of six-DOF perturbation and nonlinear simulation models (AH-64, hover) . . . . .	189
Fig. 7.20	XV-15 error functions (cruise) and proposed level D simulation fidelity criteria . . . . .	191
Fig. 7.21	Comparison of flight and simulation directional responses for solar Pathfinder . . . . .	192
Fig. 7.22	Block diagram for stability-margin test . . . . .	193
Fig. 7.23	Stability-margin determination for a large helicopter . . . . .	194
Fig. 7.24	Real-time CIFER® interface . . . . .	195
Fig. 7.25	Simplified schematic of roll-axis modernized control system (UH-60 MCLAWS) . . . . .	197
Fig. 7.26	Command model comparison for roll axis (UH-60 MCLAWS) . . . . .	198
Fig. 7.27	Roll-rate SAS compensation comparison (UH-60 MCLAWS) . . . . .	199
Fig. 7.28	Roll broken-loop response comparison (UH-60 MCLAWS) . . . . .	201
Fig. 7.29	Roll closed-loop response comparison (UH-60 MCLAWS) . . . . .	202
Fig. P7.14	Diagram showing insertion of input measurement noise, output measurement noise, and process noise . . . . .	204
Fig. P7.20	Signals for control system validation and design . . . . .	206
Fig. 8.1	Single degree-of-freedom closed-loop roll-response model . . . . .	210
Fig. 8.2	Analysis model of closed-loop identification . . . . .	212
Fig. 8.3	Verification of closed-loop response ( $K = 3.0$ , no noise) . . . . .	216
Fig. 8.4	Identification of unstable bare airframe ( $K = 3.0$ , no noise) . . . . .	217
Fig. 8.5	Verification of closed-loop response ( $K = 6.5$ , no noise) . . . . .	218
Fig. 8.6	Identification of bare airframe ( $K = 6.5$ , no noise) . . . . .	219
Fig. 8.7	Effect of low noise ratios on bare-airframe identification ( $K = 3.0$ ) . . . . .	220
Fig. 8.8	Effect of high noise ratios on bare-airframe identification ( $K = 3.0$ ) . . . . .	222
Fig. 8.9	Bias errors in identification of model parameters ( $K, a$ ) . . . . .	223
Fig. 8.10	Comparison between identified and ideal responses for (unstable) inverted pendulum . . . . .	225

Fig. P8.5	Process noise for unstable pendulum problem .....	227
Fig. P8.7	Process noise reflected to output .....	227
Fig. P8.9	Pendulum broken-loop exercise .....	228
Fig. 9.1	Schematic model of roll-rate response to rudder and aileron inputs .....	232
Fig. 9.2	Rudder and aileron control inputs during directional sweep (XV-15, cruise) .....	240
Fig. 9.3	Cross-control coherence (XV-15, cruise) .....	241
Fig. 9.4	Rudder input autospectrum: SISO vs MISO (XV-15, cruise) .....	241
Fig. 9.5	Roll-rate output autospectrum: SISO vs MISO (XV-15, cruise) .....	242
Fig. 9.6	Rudder-to-roll-rate cross spectrum: SISO vs MISO (XV-15, cruise) .....	242
Fig. 9.7	Off-axis frequency-response identification: SISO vs MISO (XV-15, cruise) .....	243
Fig. 9.8	Partial coherence for aileron inputs (XV-15, cruise) .....	244
Fig. 9.9	Multiple coherence (XV-15, cruise) .....	244
Fig. 9.10	On-axis frequency response and coherence: SISO vs MISO (XV-15, cruise) .....	245
Fig. 9.11	MISO identification of roll-rate response for SH-2G (four inputs) .....	251
Fig. 9.12	Partial coherences for secondary inputs and multiple coherence .....	252
Fig. 9.13	Comparison of MISO and SISO solutions for on-axis roll-rate response .....	253
Fig. 9.14	Comparison of MISO and SISO solutions for off-axis pitch-rate response .....	254
Fig. 9.15	Multi-input maneuver .....	255
Fig. 9.16	Determination of broken-loop pitch response for MIMO control system .....	256
Fig. 10.1	Fundamental tradeoff in window-size selection .....	260
Fig. 10.2	Identification results for pendulum example using three window sizes .....	264
Fig. 10.3	Comparison of composite and nominal (15-s) window for pendulum .....	265
Fig. 10.4	COMPOSITE windowing in single-input analyses .....	266
Fig. 10.5	COMPOSITE windowing in multi-input analysis .....	267
Fig. 10.6	Closed-loop roll-rate response for 40-s and 10-s windows (XV-15, hover) .....	269
Fig. 10.7	Composite closed-loop roll-rate response using five spectral windows (XV-15, hover) .....	270
Fig. 10.8	Coherence functions for three different window sizes (Bo-105 helicopter) .....	271

Fig. 10.9	Frequency response and coherence for composite window result (Bo-105 helicopter) . . . . .	272
Fig. 10.10	Structural system identification using composite windowing . . . . .	273
Fig. 10.11	Composite-window result for spectral analysis . . . . .	274
Fig. 11.1	Comparison of identified transfer-function model and frequency-response data for stable pendulum . . . . .	286
Fig. 11.2	ADOCS pitch-rate response and transfer-function model (hover) . . . . .	288
Fig. 11.3	Analysis of ADOCS handling qualities based on equivalent system data (from Ref. 154) . . . . .	290
Fig. 11.4	Effect of equivalent time delay on handling qualities (from Ref. 155) . . . . .	291
Fig. 11.5	ADOCS transfer-function model verification (hover) . . . . .	292
Fig. 11.6	Roll-rate and sideslip transfer-function models (XV-15, cruise) . . . . .	295
Fig. 11.7	Error functions for transfer-function models (XV-15, cruise) . . . . .	296
Fig. 11.8	Block diagram representation of rotor-body coupling . . . . .	301
Fig. 11.9	Root locus of rotor-body coupling with increasing rotor-flap stiffness (following Heffley et al. <sup>21</sup> ) . . . . .	302
Fig. 11.10	Cascade model of rotor-body response applicable to small flap stiffness . . . . .	303
Fig. 11.11	Comparison of coupled rotor-body and quasi-steady model structures for the UH-1 helicopter . . . . .	304
Fig. 11.12	OH-58D helicopter . . . . .	306
Fig. 11.13	Roll-response transfer-function models (OH-58D, hover) . . . . .	307
Fig. 11.14	Helicopter roll-attitude response model (Bo-105, hover) . . . . .	309
Fig. 11.15	Root-locus varying roll-rate gain (Bo-105, 80 kn) . . . . .	310
Fig. 11.16	Frequency-sweep input and wing-bending strain-gauge response (XV-15, 180 kn) . . . . .	311
Fig. 11.17	Aeroelastic transfer-function model (XV-15, 180 kn) . . . . .	313
Fig. 11.18	Symmetric wing beam mode (XV-15, 180 kn) . . . . .	314
Fig. 11.19	AFCS actuator model identification . . . . .	316
Fig. 11.20	Simulation model of actuator . . . . .	316
Fig. 12.1	Frequency-response results for stable pendulum identification . . . . .	349
Fig. 12.2	Closed-loop roll-response identification (XV-15, hover) . . . . .	351
Fig. 12.3	NASA V/STOL system research aircraft (VSRA) (NASA photo) . . . . .	353
Fig. 12.4	Aeroelastic response identification (VSRA, 120 kn) . . . . .	354
Fig. 12.5	Root locus for roll-rate feedback to aileron (VSRA, 120 kn) . . . . .	357
Fig. 13.1	Identification model structure for cruise (XV-15) . . . . .	381

Fig. 13.2	Identification model structure for cruise (XV-15) . . . . .	381
Fig. 13.3	GTR simulation and final identification models for cruise (XV-15) . . . . .	387
Fig. 13.3	GTR simulation and final identification model for cruise (XV-15) (continued) . . . . .	388
Fig. 13.3	GTR simulation and final identification model for cruise (XV-15) (continued) . . . . .	389
Fig. 13.3	GTR simulation and final identification model for cruise (XV-15) (continued) . . . . .	390
Fig. 13.4	Yaw-equation time vector for Dutch-roll mode . . . . .	393
Fig. 13.5	Identification model structure for hover (XV-15) . . . . .	395
Fig. 13.6	Identification model structure for hover (XV-15) . . . . .	396
Fig. 13.7	GTR simulation and final identification model for hover (XV-15) . . . . .	399
Fig. 13.7	GTR simulation and final identification model for hover (XV-15) (continued) . . . . .	400
Fig. 13.7	GTR simulation and final identification model for hover (XV-15) (continued) . . . . .	401
Fig. 13.8	Frequency-response comparison of STOVL perturbation and identification models (from Engelland et al <sup>194</sup> ) . . . . .	404
Fig. 13.9	Time-response comparison of STOVL perturbation and identification models (from Engelland et al <sup>194</sup> ) . . . . .	405
Fig. 13.10	Shadow <sup>TM</sup> 200 fixed-wing UAV (U.S. Army photo) . . . . .	407
Fig. 13.11	Identification of Shadow <sup>TM</sup> 200 UAV longitudinal dynamics . . . . .	408
Fig. 13.11	Identification of Shadow <sup>TM</sup> 200 UAV longitudinal dynamics (continued) . . . . .	409
Fig. 13.11	Identification of Shadow <sup>TM</sup> 200 UAV longitudinal model (continued) . . . . .	410
Fig. 13.12	Time-response verification of Shadow <sup>TM</sup> 200 UAV model for elevator input . . . . .	411
Fig. 13.13	Time-response verification of Shadow <sup>TM</sup> 200 UAV model for engine RPM input . . . . .	412
Fig. 13.14	Fire Scout P2 demonstrator—a variant of the Schweitzer 333 (Northrop Grumman photo) . . . . .	414
Fig. 13.15	Vertical acceleration response to collective in hover (Fire Scout P2) . . . . .	416
Fig. 13.16	Identification of lateral speed damping for hover (Fire Scout P2) . . . . .	418
Fig. 13.17	Identification of six-DOF helicopter model in hover (Fire Scout P2) . . . . .	424
Fig. 13.17	Identification of six-DOF helicopter model in hover (Fire Scout P2) (continued) . . . . .	425

Fig. 13.17	Identification of six-DOF helicopter model in hover (Fire Scout P2) (continued) . . . . .	426
Fig. 13.18	Time-response verification for longitudinal stick doublet (Fire Scout P2, hover) . . . . .	428
Fig. 13.19	Component contributions to overall pitch response . . . . .	429
Fig. 14.1	Lateral step input for closed-loop model verification (XV-15, hover) . . . . .	441
Fig. 14.2	Control inputs for roll-response verification (XV-15, cruise) . . . . .	443
Fig. 14.3	Roll-response verification of bare-airframe model (XV-15, cruise) . . . . .	444
Fig. 14.4	Control inputs for yaw-response verification (XV-15, cruise) . . . . .	445
Fig. 14.5	Yaw-response verification of bare-airframe model (XV-15, cruise) . . . . .	446
Fig. 14.6	Control inputs for roll-response verification (XV-15, hover) . . . . .	447
Fig. 14.7	Verification of bare-airframe model (XV-15, hover) . . . . .	448
Fig. 15.1	Rotor tip-path-plane degrees of freedom . . . . .	454
Fig. 15.2	Rotor lead-lag degrees of freedom . . . . .	458
Fig. 15.3	U.S. Navy version of the SH-2G (Kaman Aerospace Corporation photo) . . . . .	465
Fig. 15.4	Identification and simulation models for hover (SH-2G) . . . . .	470
Fig. 15.4	Identification and simulation models for hover (SH-2G) (continued) . . . . .	471
Fig. 15.4	Identification and simulation models for hover (SH-2G) (continued) . . . . .	472
Fig. 15.5	Time-response verification of identified model for hover (SH-2G) . . . . .	484
Fig. 15.5	Time-response verification of identified model for hover (SH-2G) (continued) . . . . .	485
Fig. 15.6	Time-response verification of identified model for 60 kn (SH-2G) . . . . .	486
Fig. 15.6	Time-response verification of identified model for 60 kn (SH-2G) (continued) . . . . .	487
Fig. 15.7	Time-response verification of identified model for 100 kn (SH-2G) . . . . .	488
Fig. 15.7	Time-response verification of identified model for 100 kn (SH-2G) (continued) . . . . .	489
Fig. 15.8	Hybrid model identification including lead-lag dynamics (S-92, hover) . . . . .	490

## List of Tables

Table 1.1	Models of fixed-wing aircraft dynamics .....	6
Table 1.2	Models of rotary-wing aircraft dynamics .....	7
Table 1.3	Nonparametric vs parametric models .....	10
Table 1.4	Comparison of frequency-response and time-response methods .....	15
Table 1.4	Comparison of frequency-response and time-response methods (continued) .....	16
Table 2.1	<i>F</i> -matrix identification for XV-15 in cruise .....	45
Table 2.2	<i>G</i> -matrix identification for XV-15 in cruise .....	45
Table 2.3	<i>F</i> -matrix identification for XV-15 in hover .....	51
Table 2.4	<i>G</i> -matrix identification for XV-15 in hover .....	51
Table 3.1	XV-15 hover test case (database #1) .....	63
Table 3.3	System characteristics for databases #1 and #2 .....	64
Table 3.2	SCAS configurations for hover maneuvers (database #1) .....	64
Table 3.4	XV-15 cruise test case (database #2) .....	66
Table 3.5	SCAS configurations for cruise maneuvers (database #2) .....	67
Table 4.1	Mapping between the components of Fig. 4.1 and chapters in this book .....	72
Table 4.2	Frequency-response analysis utilities .....	74
Table 4.3	Program parameter utilities .....	75
Table 4.4	Results utilities .....	75
Table 4.5	Database and setup utilities .....	75
Table 4.6	Navigating between CIFER® screens using the F keys .....	76
Table 6.1	Effect of correcting for instrumentation system dynamics .....	135
Table 7.1	AH-64 vibration analysis (130 kn) .....	181
Table 7.2	Handling-qualities characteristics for the OH-58D pitch response in hover (SCAS-off) .....	186
Table 7.3	MIL-F-9490D gain-and-phase margin requirements (dB, deg) (from Ref. 88) .....	194
Table 7.4	Stability-margin results for a large helicopter .....	195
Table 9.1	Lateral-sweep-data analysis (cruise) .....	249
Table 9.2	Pedal-sweep-data analysis (cruise) .....	250
Table 10.1	Lateral-sweep-data analysis (cruise) .....	267
Table 10.2	Pedal-sweep data analysis (cruise) .....	268

Table 11.1	Evaluation of XV-15 lateral-directional handling qualities in cruise . . . . .	297
Table 12.1	Comparison of identification and parameter scatter results (XV-15, hover) . . . . .	335
Table 12.2	Comparison of key identification and parameter scatter results (Bo-105, 80 kn) . . . . .	335
Table 12.3	Identification results for stable pendulum example . . . . .	350
Table 12.4	Eigenvalues for identified stable pendulum model . . . . .	350
Table 12.5	Closed-loop roll identification results for initial model structure (XV-15, hover) . . . . .	352
Table 12.6	Confidence ellipsoids for closed-loop response identification (XV-15, hover) . . . . .	352
Table 12.7	Closed-loop roll identification results for reduced model structure (XV-15, hover) . . . . .	352
Table 12.8	Eigenvalues of final closed-loop model identification (XV-15, hover) . . . . .	353
Table 12.9	Aeroelastic response identification (VSRA, 120 kn) . . . . .	356
Table 13.1	Example of frequency-response table (Fire Scout P2 demonstrator, hover) . . . . .	372
Table 13.2	Dropped derivatives for hover example (Fire Scout P2 demonstrator) . . . . .	376
Table 13.3	Frequency-response ranges for cruise (XV-15) . . . . .	380
Table 13.4	Initial identification results for cruise (XV-15) . . . . .	383
Table 13.5	Cost functions for cruise model identification (XV-15) . . . . .	384
Table 13.6	Intermediate model (V170M2) for cruise (XV-15) . . . . .	384
Table 13.7	Final identified model and GTR simulation for cruise (XV-15) . . . . .	385
Table 13.8	Confidence ellipsoid for parameter $Y_p$ with largest Cramér–Rao bound (V170M3) . . . . .	385
Table 13.9	Cost functions for identification and GTR simulation models (XV-15, cruise) . . . . .	386
Table 13.10	Eigenvalues of identified cruise model (XV-15): Eigenvalues ( $\lambda_i$ ) of $[M_{\text{inverse}}][F]$ . . . . .	391
Table 13.11	Scaled eigenvectors for cruise model (XV-15) . . . . .	392
Table 13.12	Frequency-response ranges for hover (XV-15) . . . . .	394
Table 13.13	Cost functions for identification and GTR simulation models (XV-15, hover) . . . . .	396
Table 13.14	Final identified model and GTR simulation for hover (XV-15) . . . . .	397
Table 13.15	Eigenvalues of identified hover model (XV-15): Eigenvalues ( $\lambda_i$ ) of $[M_{\text{inverse}}][F]$ . . . . .	402
Table 13.16	Comparison of STOVL perturbation derivatives and identification results (from Engelland et al <sup>194</sup> ) . . . . .	403

Table 13.17	Identification results for three-DOF longitudinal model of Shadow™ 200 UAV . . . . .	413
Table 13.18	Transfer-function costs . . . . .	413
Table 13.19	Identification results for six-DOF helicopter model in hover (Fire Scout P2): F-matrix . . . . .	421
Table 13.20	Identification results for six-DOF helicopter model in hover (Fire Scout P2) . . . . .	422
Table 13.21	Cost functions for six-DOF helicopter model in hover (Fire Scout P2): Transfer-function costs . . . . .	423
Table 14.1	Roll-response verification results for closed-loop model (XV-15, hover) . . . . .	442
Table 14.2	Verification results for bare-airframe model (XV-15 cruise) . . . . .	445
Table 14.3	Roll-response verification results for closed-loop model (XV-15, hover) . . . . .	449
Table 15.1	Hybrid model identification results (SH-2G, hover) . . . . .	467
Table 15.1	Hybrid model identification results (SH-2G, hover) (continued) . . . . .	468
Table 15.2	Hybrid model identification cost functions (SH-2G, hover) . . . . .	469
Table 15.3	Eigenvalues for identified hybrid model (SH-2G, hover): Eigenvalues ( $\lambda_i$ ) of $[M_{\text{inverse}}][F]$ . . . . .	473
Table 15.4	Simulation and (equivalent six-DOF) identification parameters (SH-2G, hover) . . . . .	477
Table 15.4	Simulation and (equivalent six-DOF) identification parameters (SH-2G, hover) (continued) . . . . .	478
Table 15.5	Simulation and identification model cost functions (SH-2G, hover) . . . . .	479
Table 15.6	Identification results for three flight conditions (SH-2G) . . . . .	480
Table 15.6	Identification results for three flight conditions (SH-2G) (continued) . . . . .	481
Table 15.7	Identification cost functions (SH-2G) . . . . .	482
Table P15.6	Trim data . . . . .	492
Table A.1	Suggested guidelines . . . . .	495

This page intentionally left blank

## Nomenclature

<b><math>A, B, C, D</math></b>	= state-space representation (standard form)
$A \circ B$	= Schur product of matrices (element-by-element multiplication): $A \circ B \equiv [a_{ij}b_{ij}]$
$a$	= lift-curve slope
$a_x, a_y, a_z$	= accelerometer components along the body axes (longitudinal, lateral, vertical)
$B_e$	= frequency resolution ( $B_e \equiv \Delta f$ )
$B_r$	= half-power bandwidth
$b$	= with subscript, a bias error parameter (e.g., $b_\phi$ ≡ bias error in $\phi$ )
$C_T$	= thrust coefficient
$C_\varepsilon$	= constant to account for spectral window overlap
$C_0$	= Carpenter–Fridovich inflow constant
$CR_i$	= Cramér–Rao bound of the $i$ th identified parameter ( $\theta_i$ ) of the converged solution ( $\Theta_0$ )
$c$	= rotor-blade chord
$D$	= matrix of gradients $\partial \mathbf{y}_e / \partial \Theta$ , where $\mathbf{y}_e = \mathbf{y}_{\text{data}} - \mathbf{y}$
$d^B/dt$	= time derivative in an Eulerian (body-fixed) frame of reference
$d^I/dt$	= time derivative in an inertial frame of reference
$\text{dec\_span}$	= decade span, defined as $\text{dec\_span} = \log(\omega_{\max}/\omega_{\min})$ to characterize the fraction of a decade for which acceptable data are available
$e$	= offset of the rotor-blade flapping hinge from the center of rotation of the rotor shaft
$\mathbf{F}$	= external force vector
$f$	= frequency, Hz
$f_{\min}, f_{\max}$	= theoretical minimum/maximum frequency that can be identified
$f_r$	= resonance peak frequency
$f_s$	= sampling rate (frequency), defined as $1/\Delta t$
$G_{xx}, G_{yy}, G_{xy}$	= input autospectrum, output autospectrum, and cross spectrum
$G_{\delta_r p \cdot \delta_a}$	= example of conditioned spectrum: cross spectrum between rudder input $\delta_r$ and roll response $p$ , conditioned to remove effects of partially correlated aileron input $\delta_a$
$\mathcal{H}$	= Hessian matrix for the cost function $J$
$\hat{H}_1(f), \hat{H}_2(f)$	= unbiased frequency-response estimate when noise is present only at output, unbiased frequency-response estimate when noise is present only at input
$H(f)$	= frequency-response function
$H(s)$	= transfer function
$h_r$	= height of the rotor hub above the fuselage center of gravity
$\mathbf{I}$	= identity matrix

<b><math>I</math></b>	= inertia tensor
$I_b$	= moment of inertia of the rotor blade about the flapping axis
$I_i$	= insensitivity of the $i$ th identified parameter $\Theta_i$ of the converged solution $\Theta_0$
$I_{xx}, I_{yy}, I_{zz}$	= roll, pitch, yaw moments of inertia
$I_{xz}$	= product of inertia
$J$	= cost function for frequency-response error
$J_{\text{rms}}$	= cost function for time-response error
$K_\beta$	= rotor-blade flapping spring
$L$	= number of time-history points in a spectral window
$L, M, N$	= external moments about the aircraft center of gravity (roll, pitch, and yaw)
$L'_i$	= primed roll derivative, defined by $L'_i = [L_i + (I_{xz}/I_{xx})N_i]/[1 - I_{xz}^2/(I_{xx}I_{zz})] \text{ for } i = u, v, w, p, q, r, \delta_a, \delta_e, \delta_r, \delta_t$
$L_p$	= example of stability derivative; $L_p \equiv (1/I_{xx})(\partial L/\partial p)$
$L_{\beta_{1s}}$	= rotor flap-stiffness constant
$L_{\delta_a}$	= example of control derivative; $L_{\delta_a} \equiv (1/I_{xx})(\partial L/\partial \delta_a)$
$M, F, G, H_0, H_1$	= generalized equation-of-motion matrices (CIFER® form)
$M_x$	= test stand rolling moment
$M_\beta$	= first mass moment of rotor blade
$N$	= number of discrete frequency points in identified spectrum
$N$	= vehicle scale ratio
$N'_i$	= primed yaw derivative, defined by $N'_i = [N_i + (I_{xz}/I_{zz})L_i]/[1 - I_{xz}^2/(I_{xx}I_{zz})] \text{ for } i = u, v, w, p, q, r, \delta_a, \delta_e, \delta_r, \delta_t$
$n$	= noise at output accounting for both process and output measurement noise
$n$	= number of states in a multiple-input/multiple-output (MIMO) linear time-invariant system
$n_b$	= number of rotor blades
$n_c$	= number of control inputs
$n_d$	= number of independent time-history averages
$n_o$	= number of response outputs
$n_p$	= number of identification parameters
$n_{\text{TF}}$	= number of transfer functions included in the identification
$n_t$	= number of time-history points in the verification data record
$n_w$	= number of windows
$n_\omega$	= number of frequency points included in the identification cost function
$P, p$	= total value and perturbation value (in this case fuselage roll rate)
$p, q, r$	= fuselage angular rates (roll rate, + right wing down; pitch rate, + nose up; yaw rate, + nose right)
$p/\delta_a$	= example of a frequency-response pair; roll-rate response $p$ to aileron input $\delta_a$

$\frac{p}{\delta_a}(s)$	= example of a transfer function; roll-rate response $p$ to aileron input $\delta_a$
$p/\delta_r \cdot \delta_a$	= example of a conditioned frequency response: the single-input/single-output (SISO) solution for $p/\delta_r$ , conditioned to eliminate the linear effects of partially correlated aileron input $\delta_a$
$R$	= rotor radius
$S(\omega)$	= signal-to-noise ratio
$s$	= Laplace variable
$T$	= time constant
$T_F$	= total length of concatenated records
$T_{\min}, T_{\max}$	= minimum and maximum period of interest
$T_{\text{rec}}$	= length of a flight-test record
$T_{\text{win}}$	= time duration or “width” of a spectral window
TIC	= Theil inequality coefficient
$T(s)$	= frequency-response of SISO transfer-function model
$\mathbf{T}(s)$	= MIMO frequency-response matrix of identification model
$t_{\text{double}}$	= time to double (the amplitude)
$\mathbf{U}(s), \mathbf{Y}(s)$	= Laplace transform of the input and output vectors ( $\mathbf{u}$ and $\mathbf{y}$ )
$\mathbf{u}$	= control input vector consisting of $n_c$ control inputs $u_1, u_2, \dots, u_{n_c}$
$u, v, w$	= input measurement noise, output measurement noise, and process noise
$u, v, w$	= velocity components (longitudinal, + forward; lateral, + right; vertical, + down)
$\mathbf{W}$	= diagonal weighting matrix consisting of the weighting parameters $W_g$ , $W_p$ , and $W_\gamma$ in the cost function calculation
$W_g, W_p, W_\gamma$	= identification weighting for magnitude, phase, and coherence functions
$X, Y, Z$	= external forces on the aircraft center of gravity (longitudinal, lateral, vertical)
$X(f), Y(f)$	= Fourier coefficients of input [ $x(t)$ ] and output [ $y(t)$ ]
$\mathbf{X}(s), \mathbf{Y}(s)$	= Laplace transform of the input and output vectors ( $\mathbf{x}$ , $\mathbf{y}$ , respectively)
$\mathbf{x}$	= state vector consisting of $n$ states $x_1, x_2, \dots, x_n$
$x_a, y_a, z_a$	= offsets of the accelerometer package relative to the center of gravity
$\dot{x}_b$	= constant acceleration bias vector (also <b>bias</b> )
$x_{\text{nb}}, y_{\text{nb}}, z_{\text{nb}}$	= offsets of nose boom location relative to the center of gravity
$x(t), y(t)$	= system input (excitation) and output time signals
$\mathbf{y}$	= measurement (or output) vector consisting of $n_o$ available measurement signals $y_1, y_2, \dots, y_{n_o}$
$\mathbf{y}_{\text{ref}}$	= constant reference-shift vector (also <b>yref</b> )
$\alpha$	= angle of attack
$\alpha_n(f)$	= noise-to-signal (PSD) ratio for the input
$\beta$	= angle of sideslip
$\beta_n(f)$	= noise-to-signal ratio (PSD) for the output
$\beta_0, \beta_{1c}, \beta_{1s}$	= rotor flap angles for coning, longitudinal, lateral tip path plane coordinates (+ up; + flap down to left; + flap up over rear)

$\gamma^*$	= lock number and effective (reduced) Lock number
$\gamma_{x_i y \cdot (n_c - 1)}$	= partial coherence for frequency response ( $y/x_i$ ) with the effects of remaining ( $n_c - 1$ ) controls removed
$\gamma_{xy}^2$	= coherence function between input $x$ and output $y$
$\gamma_{\delta_r \delta_a \cdot p}^2$	= multiple coherence showing contribution of multiple controls ( $\delta_r$ and $\delta_a$ in this case) to a single output ( $p$ in this case)
$\Delta$	= variation or perturbation
$\Delta f$	= frequency resolution
$\Delta J_{\text{ave}}$	= jump in the reconverged average cost function
$\delta$	= control input
$\delta_a, \delta_e, \delta_r, \delta_t$	= control inputs for fixed-wing aircraft (roll, pitch, yaw, and throttle controls)
$\delta_{a_{\text{UC}}}, \delta_{a_{\text{c}}}$	= components of the secondary aileron input that are uncorrelated correlated (uc) and correlated (c) with the primary input
$\delta'_{\text{col}}$	= lagged collective control to account for engine dynamics
$\delta_{\text{excitation}}$	= computer generated sweep input, enriched with white noise
$\delta_{\text{lat}}, \delta_{\text{lon}}, \delta_{\text{ped}}, \delta_{\text{col}}$	= control inputs for rotorcraft (roll, pitch, yaw, and vertical control)
$\delta_{\text{rpm}}$	= control input for engine rpm
$\delta_{\text{sweep}}$	= computer-generated frequency-sweep input
$\epsilon$	= vector of magnitude and phase errors for the identified model
$\epsilon_b$	= bias error in frequency-response estimate
$\epsilon_r$	= random error in frequency-response estimate
$\epsilon_{\text{sim}}(f)$	= simulation error response function: $\epsilon_{\text{sim}}(f) \equiv H_{\text{sim}}(f)/H_{\text{flight}}(f)$
$\zeta$	= damping ratio for second-order system
$\zeta_o, \zeta_{1c}, \zeta_{1s}$	= rotor lead-lag angles for collective, cosine, sine degrees of freedom (+ all blades deflect clockwise; + blades deflect to left side; + blades deflect to aft of helicopter)
$[\zeta, \omega_n]$	= shorthand notation for $[s^2 + 2\zeta\omega_n s + \omega_n^2]$ , a second-order factor of a transfer function
$\Theta$	= identification vector $\Theta = [\theta_1 \ \theta_2 \ \dots \ \theta_{n_p}]$ , consisting of all of the parameters to be identified in the model matrices $M$ , $F$ , $G$ , $\tau$
$\bar{\Theta}_{\text{CR}_i}$	= scaled confidence ellipsoid vector associated with a specific Cramér–Rao bound $\text{CR}_i$
$\theta, \phi, \psi$	= fuselage attitudes (pitch, + nose up; roll, + right wing down; yaw, + nose right)
$\theta_e$	= error between the current pitch of the aircraft $\theta$ and the commanded pitch $\theta_c$
$\theta_i$	= identification parameters
$\theta_0, \theta_{1c}, \theta_{1s}$	= rotor swashplate deflection angles (collective, cosine, sine)
$\lambda$	= with subscript, a scale factor error parameter (e.g., $\lambda_\phi$ ≡ scale factor error in $\phi$ )

$\lambda$	= eigenvalue
$\lambda_n$	= output noise-to-excitation (PSD) ratio
$\rho$	= atmospheric density
$\rho_{ij}$	= correlation coefficient between the two identified parameters $\theta_i$ and $\theta_j$ of the converged solution $\Theta_0$
$\sigma$	= rotor solidity
$\sigma$	= rms value
$\sigma_n$	= rms noise level
$\tau$	= time delay
$\tau_e$	= engine time constant
$\tau_{eq}$	= equivalent time delay
$\tau_f$	= rotor flap time constant
$\tau_p$	= phase delay
$v$	= rotor inflow velocity
$\bar{v}_0$	= trim inflow ratio
$v_\zeta$	= rotor lead-lag natural frequency in the rotating frame normalized by the rotor rotational speed $\Omega$
$\Phi_{2\omega_{180}}$	= phase value at twice frequency of $-180$ deg phase lag
$\varphi$	= phase shift
$\Omega$	= rotor rotation speed, rad/s (U.S. convention is counter-clockwise as viewed from above)
$\omega$	= frequency, rad/s
$\omega$	= angular velocity vector of the body-fixed axis system
$\omega_{BW}$	= bandwidth frequency (handling-qualities definition)
$\omega_c$	= crossover frequency
$\omega_{co}$	= pilot operating frequency or cutoff frequency
$\omega_f$	= filter cutoff frequency (also referred to as the filter bandwidth)
$\omega_{\min}, \omega_{\max}$	= minimum and maximum frequency of interest (and of excitation)
$\omega_{Nyq}$	= nyquist frequency
$\omega_n$	= undamped natural frequency for second-order system
$\omega_s$	= sample rate
$\omega_{180}$	= frequency at which the phase of the attitude response is $-180$ deg
$(1/T)$	= shorthand notation for $(s + 1/T)$ , a first-order factor of a transfer function
$  $	= magnitude, dB
$\angle$	= phase, deg

### Subscripts

ave	= average value
CF	= crossfeed (piloted or via control system)
c	= composite window value
cg	= value at center of gravity
data	= flight data value
dB	= magnitude of a complex function expressed in decibels (e.g., $H_{dB} = 20 \log_{10} H(j\omega) $ ); power variables are expressed in “power decibels” [e.g., $G_{xx_{dB}}(f) = 10 \log_{10}G_{xx}(f)$ ]
deg	= argument of a complex function expressed in degrees
dr	= Dutch roll mode

## xxviii

e	= estimated, or corrected, value of a flight measurement
effective	= effective (or quasi-steady derivative) value
err	= error value
$f_r, f_a, f_c$	= rotor flapping modes (regressing, advancing, coning)
$ll_r, ll_a, ll_c$	= rotor lead-lag modes (regressing, advancing, collective)
m	= flight measurement
max	= maximum value
min	= minimum value
mod	= model value
mx	= mixer input value
nb	= measurement made at the nose boom
$R, I$	= real/imaginary parts of a complex number
r	= roll mode
s	= spiral mode
tot	= total value
0	= trim value, converged value

*Superscripts and Overmarks*

$T$	= the transpose of a matrix
$\hat{}$	= complex conjugate value
$\bar{}$	= weighted average
$\bar{\cdot}$	= normalized value
$\wedge$	= smooth spectral estimate
$\sim$	= rough spectral estimate

## Acronyms

ACAH	= attitude command, attitude hold
ADOCS	= Advanced Digital Optical Control System
AFCS	= Automatic Flight Control System
AFDD	= U.S. Army Aeroflightdynamics Directorate (Ames Research Center)
AGARD	= Advisory Group for Aerospace Research and Development
AIAA	= American Institute of Aeronautics and Astronautics
ARI	= aileron-to-rudder interconnect
ASE	= aeroservoelastic, also automatic stabilization equipment (SH-2G)
CIFER®	= Comprehensive Identification from Frequency Responses software package
COMPOSITE	= CIFER® program that combines multiple spectral windows to achieve a final frequency response
CONDUIT®	= Control Designer's Unified Interface software package
CZT	= chirp z-transform
DERIVID	= CIFER® program used to identify a state-space model structure that best fits the MIMO frequency-response database
DFT	= discrete Fourier transform
DLR	= Deutsche Forshungsanstalt für Luft- und Raumfahrt (until 1989: DFVLR)
DOF	= degree(s) of freedom
FCS	= Flight control system
FFT	= fast Fourier transform
FRESPID	= CIFER® program that calculates SISO frequency responses using a chirp z-transform (an advanced FFT)
GENHEL	= Sikorsky general helicopter flight dynamics simulation program
GTR	= generic tilt-rotor simulation
HQR	= Cooper–Harper handling-qualities rating
IMU	= inertial measurement unit
LOES	= lower-order equivalent system
LTI	= linear time invariant
MCLAWS	= modernized control laws
MIL-STD-nnnn	= military requirements standard
MIMO	= multiple-input/multiple-output
MISO	= multiple-input/single-output
MISOSA	= CIFER® program that determines frequency responses when multiple inputs are present
MUAD	= maximum unnoticeable added dynamics
NASA	= National Aeronautics and Space Administration (US)

XXX

NAVFIT	= CIFER® program used to identify a pole-zero transfer-function model
PIO	= pilot-induced oscillations
PM	= phase margin
PSD	= power spectral density
RASCAL	= Rotorcraft Aircrew Systems Concepts Airborne Laboratory, a JUH-60 Black Hawk helicopter with digital fly-by-wire control system (operated by AFDD)
rms	= root mean square
rpm	= revolutions per minute
SAS	= stability augmentation system
SBMR	= Sikorsky bearingless main rotor
SCAS	= stability and control augmentation system
SISO	= single-input/single-output
SMACK	= smoothing from aircraft kinematics program, used to check the time-history data prior to identification
STOVL	= Short take-off/vertical landing aircraft
TIC	= Theil inequality coefficient
TM	= real-time telemetry
UAV	= unmanned air vehicle
VERIFY	= CIFER® program (state-space model verification) used to check the time-domain predictive accuracy of an identified model
VMS	= vertical motion simulator
VSRA	= V/STOL (vertical/short takeoff and landing) system research aircraft
XV-15	= tilt-rotor demonstrator aircraft

## Preface

Aircraft system identification is a highly versatile procedure for rapidly and efficiently extracting accurate dynamic models of an aircraft from the measured response to specific control inputs. Models might be desired to characterize the aircraft dynamics as a whole or to characterize an aircraft subsystem, such as an actuator, rotor system, or the engine. Key applications of aircraft system-identification results include piloted simulation models, comparison of wind-tunnel vs flight measurements, validation and improvement of physics-based simulation models, flight-control system development and validation, and handling-qualities specification compliance testing.

As indicated by the title, this book addresses the system identification of both *aircraft* and *rotorcraft*, focusing on *engineering methods* and *flight-test examples*. Specialized testing and data-analysis methods, as well as considerable physical insight, are required to obtain models that are accurate and reasonable in terms of the underlying physics. This book presents the *frequency-response method* for system identification as developed by the leading author and his colleagues from the U.S. Army Aeroflightdynamics Directorate (AFDD) and NASA at Ames Research Center over the past more than 20 years, drawing on practical experience from many and varied individual flight projects cited in the reference list. The analysis methods are embodied in the software package *Comprehensive Identification from Frequency Responses* (CIFER<sup>®</sup>), also developed at Ames Research Center (and distributed commercially). System-identification projects have ranged from small (9-in. diam) ducted-fan unmanned air vehicles (UAVs) to large (100-ft wing span) solar-powered UAVs, including a wide range of manned fixed-wing aircraft and rotary-wing aircraft (*rotorcraft*) configurations. There have also been many applications involving the extraction of subsystem models from wind-tunnel data (e.g., rotor system response) and bench-test data (e.g., actuators and other flight control components). Examples are given in the overview of Sec. 2.4 and throughout the book.

The identification of dynamics models of flight vehicles from flight-test data is made difficult by many factors, as explained in this book. These are associated with the limitations of the flight-data measurement system, test inputs, signal-to-noise ratio, and test record length. The determination of rotorcraft response models is perhaps the most challenging application of system identification. These vehicles have a wide range of possible configurations—from small ducted fans to tilt-rotor aircraft, single and tandem helicopters, and helicopter/sling-load configurations. Many rotorcraft exhibit a high-order dynamic response because of the tightly coupled dynamics of the fuselage/rotor/inflow/engine, so that typical lower-order approximations of fixed-wing aircraft responses often do not apply. Inputs in one axis generally produce responses of comparable magnitude in all axes—referred to as *cross coupling*—in which case the fixed-wing assumption of decoupled longitudinal and lateral/directional responses is no longer valid.

Additional complicating factors in the case of rotorcraft are the typically very low signal-to-noise ratios for near-hovering flight maneuvers, unstable pitch and roll dynamics, and high levels of noise in the measurements (e.g., caused by vibration and atmospheric disturbances). System-identification techniques and typical results for rotorcraft are emphasized in this book and presented throughout for comparison with the fixed-wing examples.

Many excellent books are available that cover the theory of system identification with some general applications and example results. The analysis methods and software tools are often demonstrated with simple examples commonly drawn from lower-order systems and numerical simulations. In most cases, a new analyst has little guidance on the important practical aspects of instrumentation, flight-testing methods, flight-data conditioning, model structure determination, and model validation. For the difficult and highly specialized problem of aircraft and rotorcraft system identification from flight-test data, it is most certainly true that the “devil is in the details.” System identification of flight vehicles has long had the reputation of being “more art than science.” This is caused in large part by the uncertainty in how to properly set the many “knobs” in the analysis in order to obtain a satisfactory model from real flight-test data. Despite the immense power of system identification to help rapidly solve dynamics and controls problems, expertise tends to be concentrated at only a handful of research centers worldwide.

This book presents validated methods and guidelines for the specialized application of aircraft and rotorcraft system identification. The frequency-response method developed at Ames Research Center (and embodied in the CIFER® analysis tool) provides a robust and systematic approach that is highly effective in addressing the difficult problems of flight-vehicle system identification from flight-test data. Engineering methods and flight-test results are demonstrated herein with a wide range of flight examples worked on at the Ames Research Center, including UAVs, aircraft, rotorcraft, and vehicles subsystems. Throughout the book—and summarized in an appendix—are many specific guidelines for flight vehicle testing, data analysis, modeling, and interpretation of results. This book emphasizes the importance of physical insight in model development and interpretation. Many specialized identification techniques that allow a significant improvement in the quality of the results are discussed in the book. These methods and much of the practical guidance are embodied in CIFER®, which is used to obtain all of the results presented herein. A student version of the software and user’s manual is available with this book via the AIAA Web site. The student version provides all of the functionality of the professional version (<http://uarc.ucsc.edu/flight-control/cifer>) but only allows the identification of models of limited complexity (two control inputs, four dynamics states), which is sufficient for the student exercises that follow each chapter. Also included is access to the flight-test data for the XV-15 tilt-rotor aircraft and simulated data for a typical helicopter as needed to complete the student exercises.

This book grew out of a short course on aircraft and rotorcraft system identification taught by the leading author for several years. The book addresses the entire process from instrumentation and flight testing to model determination and validation. The emphasis is placed on the fundamental principles, engineering methods, and interpretation of the flight-test results, with ample citations of more

in-depth theoretical treatments. Two detailed case studies are tracked throughout the identification process in order to address the specific problems of aircraft and rotorcraft. Many additional examples are included in each chapter to illustrate the wide-ranging roles of system identification, including the analysis of flight mechanics, automatic control, vibration, structural analysis, handling qualities, and simulation. This book is intended for use in an advanced undergraduate or graduate level course on system identification. The exercises give the student hands-on experience with a wide range of aircraft and rotorcraft applications using flight-test and simulation data. The material herein assumes some familiarity with basic concepts of aeronautics, Laplace transforms, flight dynamics, and classical control, as presented at a typical undergraduate level.

The main concepts of system identification and a historical overview are presented in Chapter 1. A schematic diagram (*road map*) of the frequency-response method and typical flight-test results for aircraft and rotorcraft are presented in Chapter 2. The succeeding chapters trace the steps of the roadmap from flight-test planning and instrumentation to data checking, appropriate choice of model structure, and then the central topics of model identification and verification. Each chapter presents the theory, engineering methods, practical guidelines for application, examples, and flight-test results for the particular step in the road map. A section of each chapter discusses the implementation of the methods in the CIFER® software, but the methods and guidelines in the book are meant to be useful independently from this tool, and they can also be implemented in other software tools, such as MATLAB®.

The basic methods and results are first illustrated using a numerical simulation of an inverted pendulum to provide a simple example with known (theoretical) dynamic response results. Most of the examples in the book, however, are based on flight-test results because it is the authors' experience that many methods and guidelines which work well using simulated data break down for real flight-test applications. Flight-test results for the XV-15 tilt-rotor aircraft are used to illustrate the methods in each chapter, thereby providing a consistent example from the start to the finish of the system-identification road map. The results for the XV-15 in forward flight illustrate typical results for an aircraft configuration, whereas the results for the same vehicle in hovering flight illustrate typical results for a helicopter configuration. Many additional flight-test examples—including those of the solar Pathfinder, the Fire Scout P2 demonstrator (based on the Schweizer 333 helicopter), the Shadow™ 200 fixed-wing UAV, and the SH-2G helicopter—demonstrate the utility of system-identification methods for a broad scope of dynamics and control applications.

The material in Chapters 1–11 covers basic identification concepts, instrumentation and flight testing, frequency-response identification for multi-input/multi-output and closed-loop systems, and transfer-function modeling. This material is at a technical level that is suitable for a one-semester course for undergraduate students. These methods and many example applications also cover the needs for system identification by many practicing engineers. Chapters 12–14 present the advanced topics of state-space model identification and verification for aircraft and rotorcraft. Chapter 15 discusses the identification of higher-order models for helicopters; these models are needed to accurately characterize more agile manned rotorcraft configurations and, especially, for small UAV helicopters.

The complete book is suitable for a more advanced undergraduate or graduate level course in system identification and as a resource for practicing engineers and researchers. There are extensive problem sets to be worked at the end of each chapter that give the reader (and student) hands-on experience with the system-identification methods and interpretation of the results. These are based on the numerical simulation of the inverted pendulum, XV-15 flight-test data, and simulated flight data for a typical helicopter (provided via the AIAA website). A solutions manual is also available by contacting the publisher.

A frequency-response perspective is at the center of the system-identification approach presented herein and embodied in the CIFER® software. The genesis for this was based on a wonderful period spent by the leading author at Systems Technology, Inc., from 1980–1982. Aircraft and rotorcraft system identification has been a passion and focus of this author since coming to the AFDD in 1983. The AFDD laboratory, part of the U.S. Army Aviation Missile Research Development and Engineering Center (AMRDEC), has provided an ideal environment to pursue and apply this technology to a wide range of projects, both at the Ames Research Center and in cooperative efforts with U.S. and international industry and research colleagues. The support and encouragement of the AFDD Director, Andrew W. Kerr, and the Chief of the AFDD Flight Control and Cockpit Integration Branch, Barry R. Lakinsmith, has made possible the long-term pursuit of this research topic. Their support and encouragement for writing this book is also greatly appreciated. The CIFER® software has been developed and supported over the years thanks to the outstanding effort and dedication of Joseph G.M. Leung, Mavis G. Cauffman, Gary L. Villere, Lawrence E. Pierce, Dexter L. Hermstad, and Paul S. Salchak. A special thanks go to my father, Morris Tischler, for his lifelong encouragement and for being my greatest fan.

The second author came to the subject matter of this book from a very different direction. The experience gained while teaching mathematics to undergraduate and graduate students provided invaluable insights into how to explain difficult subjects to students with varying levels of education. His work at Ames Research Center over a period of more than 26 years on a wide variety of projects produced an eclectic background that was well suited to the task of helping to distill the technical knowledge and experience of the leading author into a book that would convey the concepts to as wide an audience as possible, both students and established engineers. A key role for this author was to be the “reality check” on whether the information was written in a manner that would be clear and understandable to the target audience.

The ideas and results presented herein draw heavily on many research collaborations over the years. Thanks go foremost to the many AFDD and NASA colleagues that have worked with the leading author and whose results are presented and referenced throughout this book. Especially important international research collaborations were with Juergen Kaletka (DLR) under the U.S./FRG Memorandum of Understanding (MOU) and with the AGARD Flight Mechanics Panel Working Group 18 and Lecture Series 178 on Rotorcraft System Identification (under the outstanding leadership of Peter G. Hamel). In addition, many photos and results presented herein reflect long and successful research collaborations with numerous companies and research organizations in the United States and internationally.

Special thanks go to several individuals for their help in the development of this text. Howard C. ("Pat") Curtiss, Jr., spent many hours reviewing the draft and providing a wealth of feedback and perspective. The leading author has benefited from a career-long close working relationship with Pat, who has been a wonderful colleague and mentor. A careful and detailed review was also provided by M. Hossein Mansur, a close colleague and friend. The suggestions of Jeffery A. Schroeder in the early stage of the book were very valuable. Many excellent contributions to the exercise sections were made by Christina M. Ivler, who also authored the instructor's solution manual. Thanks go to Thomas J. Esposito for his care in preparing all of the final graphics material. Special thanks go to Jeffery A. Lusardi and Colin R. Theodore for their help in proofing the final galleys. Thanks again from both of us to everyone that helped and encouraged us in this project.

The second author expresses deep gratitude to a number of people who were critical to his successful participation in writing this book. Management support from the University of California at Santa Cruz and Ames Research Center, especially Bassam Musaffar and Larry Hogle, created ideal conditions for working on the book while balancing the scheduling demands of other important projects. A special thanks goes to Mark Tischler for the invitation to collaborate in writing the book and for being an outstanding mentor, a stimulating colleague, and a good friend. Finally, the second author wishes to thank his wife, Evelyn Brown Remple, and their son, Jonathan Remple, for the support, encouragement, and understanding that he received from them while working on this book. They both tolerated with good spirits the long hours of work and the stacks of papers that sometimes intruded on the family's time and space.

**Mark B. Tischler**  
**Robert K. Remple**  
December 2005

This page intentionally left blank

# Introduction and Brief History of System Identification in the Frequency Domain

This chapter presents both a general introduction to system identification and a brief history of the development of frequency-domain-based methods. The following topics will be covered in this chapter: 1) basic terminology and concepts of system identification of aircraft and rotorcraft, 2) special challenges of rotorcraft system identification, 3) role of nonparametric vs parametric models, 4) how system identification supports the aircraft development process, 5) comparison of frequency-response vs time-response methods, 6) brief history of the development of frequency-domain methods for aircraft and rotorcraft system identification, and 7) organization of this book.

## 1.1 Basic Concepts of System Identification of Aircraft and Rotorcraft

This section introduces the basic terminology and concepts of system identification (as highlighted in italics), with special emphasis on aircraft and rotorcraft applications. An aircraft can be considered as an input-output system, as shown in Fig. 1.1. The vehicle dynamics are excited by the *control inputs*, which in the current case are the conventional aerodynamic surfaces: aileron  $\delta_a$  for roll control, elevator  $\delta_e$  for pitch control, rudder  $\delta_r$  for yaw control, and throttle  $\delta_t$  for speed control. We can record the aircraft *dynamic response* to the control inputs in numerical form using an onboard measurement system. Typical flight-vehicle measurements for flight dynamics consideration are shown in the figure: translational velocities, angular velocities, attitudes, linear accelerometers, and aerodynamic angles. Additional measurements could include the engine response, wing strain, and aircraft position.

A *dynamic model* relates the control inputs to the vehicle dynamic response. This model can be as simple as a graph of the input-to-output response or as complex as a set of differential equations of motion. Dynamic models are needed for many applications, including analysis of aircraft stability and control, pilot simulations, flight-control design, and analysis of aircraft handling characteristics (*handling qualities*).

An analogous illustration of the input-output process for a helicopter is shown in Fig. 1.2. Now the inputs are the controls for the main rotor and tail rotor: lateral cyclic  $\delta_{lat}$  for roll control, longitudinal cyclic  $\delta_{lon}$  for pitch control, pedal  $\delta_{ped}$  to command tail rotor collective for yaw control, and collective pitch  $\delta_{col}$  for vertical speed control. The output signals listed for flight dynamics considerations are the same as in the aircraft case, although aerodynamic angle measurement is not used at low-speed (and hover). Again, additional measurements that might be available include rotor-blade deflections, main rotor shaft rpm, and structural strains.

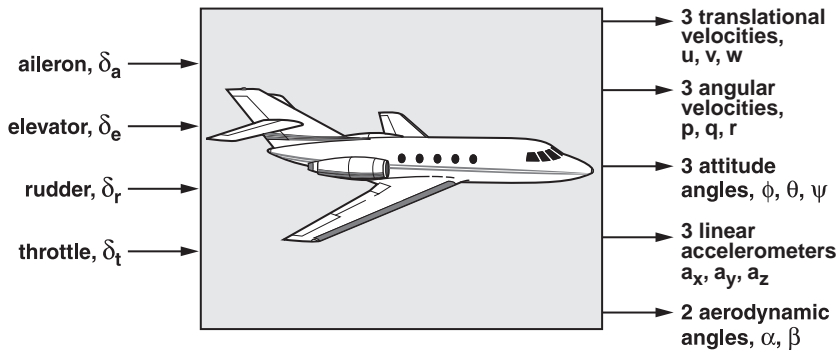


Fig. 1.1 Aircraft as an input-output system.

Aircraft *system identification* is a highly versatile procedure for rapidly and efficiently extracting accurate dynamic models of the aircraft from the measured response to specific control inputs. Models might be desired to characterize the aircraft system as a whole (e.g., as shown in Figs. 1.1 and 1.2) or to characterize an aircraft subsystem, such as an actuator or the engine. So at its most simple definition, system identification is a process that provides a model that best characterizes (in some least-squares sense) the measured responses to controls. Specialized flight-test maneuvers are used to *excite* the dynamics of concern for a particular application, such as the study of flight dynamics and control (low frequencies of interest) or structural stability (higher frequencies of interest). Typical excitations for system-identification purposes are *frequency sweeps* (Fig. 1.3) and *doublets* (Fig. 1.4).

### 1.1.1 Frequency-Response Model

A *frequency response* is a data curve identified from the flight-test data that displays the ratio of the response (e.g., roll rate) per unit of control input (e.g., aileron) as a function of control input frequency. The frequency response is obtained using the *fast Fourier transform* and associated *windowing* techniques. We are concerned with both the output/input amplitude ratio and the phase shift. An

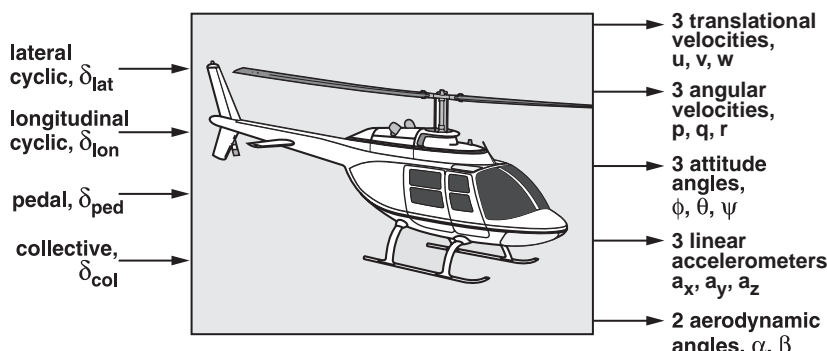


Fig. 1.2 Helicopter as an input-output system.

## INTRODUCTION AND BRIEF HISTORY

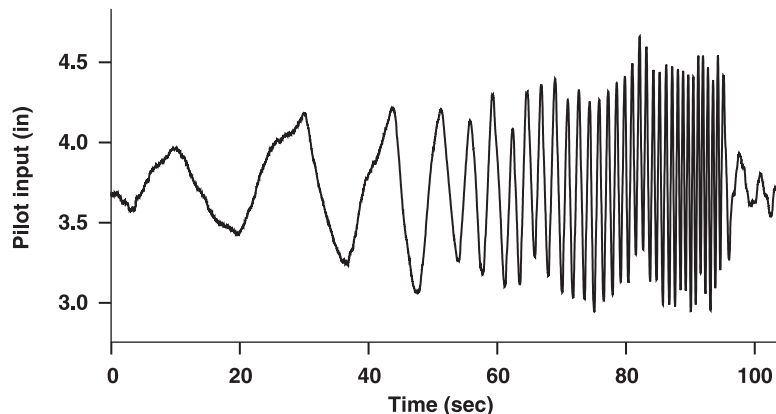


Fig. 1.3 Typical frequency-sweep input.

effective format, used exclusively herein for presenting identification results in the frequency domain, is the *Bode plot* of the frequency-response function  $H$ , which displays log-magnitude ( $20 \log_{10}|H|$ , dB) and phase ( $\angle H$ , deg) vs log-frequency ( $\omega$ , rad/s herein) on a semilog scale. A typical example is the Bode plot for aircraft sideslip response to rudder  $\beta/\delta_r$  obtained from flight-test data shown in the solid curve of Fig. 1.5. The bottom plot is the associated *coherence* function  $\gamma_{xy}^2$ , which is an excellent indicator of the frequency-response accuracy. A coherence value greater than 0.6 ( $\gamma_{xy}^2 \geq 0.6$ ), which in this example is true for all but the highest frequencies, indicates an accurate frequency-response identification result.

A frequency-response data curve that characterizes a single-input/single-output (SISO) subsystem such as an actuator can easily be obtained from the measurement data of the excitation (electrical input) and response (actuator displacement).

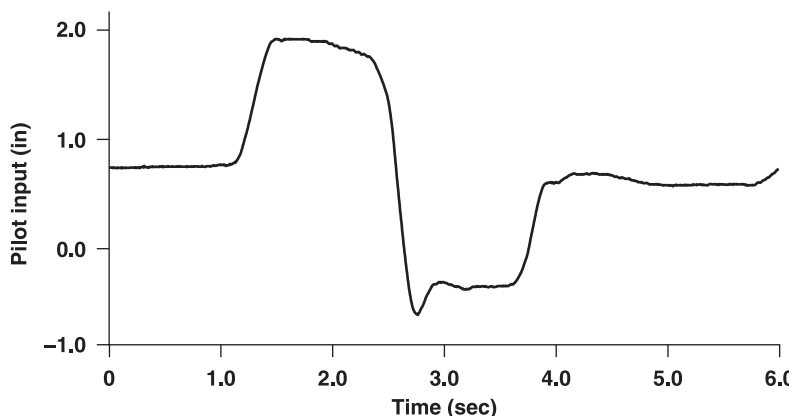


Fig. 1.4 Typical doublet input.

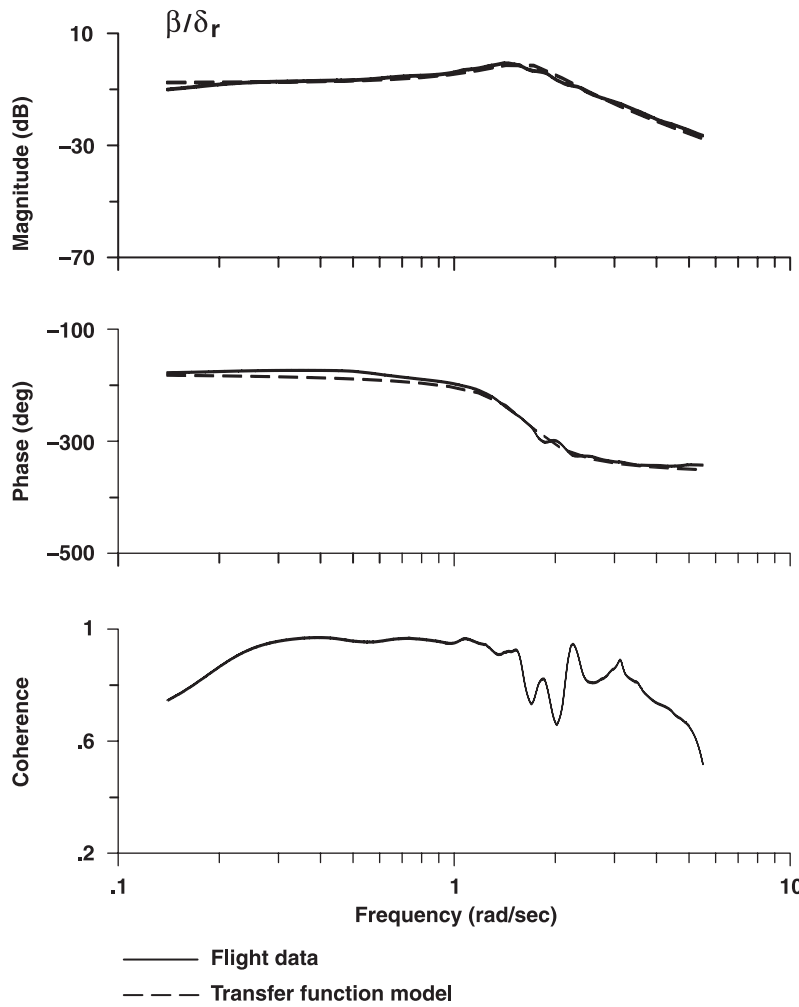


Fig. 1.5 Typical Bode plot and transfer-function model.

However, flight tests of aircraft and helicopters usually involve multiple inputs and multiple outputs (also denoted as multi-input/multi-output, or *MIMO*), and special *conditioning* techniques are required to obtain a *MIMO* frequency-response matrix that characterizes the overall dynamic system response. The frequency-response data fully characterize the dynamics of the complete input-to-output system. In the terminology of system identification, the frequency-response data curve constitutes a *nonparametric model*<sup>1,2</sup> because it characterizes the input-to-output process at a large number of data points (i.e., discrete frequencies). For this type of model, there is no need for a set of model parameters, such as the coefficients of the differential equations of motion.

### 1.1.2 Transfer-Function Model

With some additional effort, we can extract a closed-form equation that is a good representation (i.e., an accurate curve fit) of the frequency-response data. One such example is a transfer-function model

$$T(s) = \frac{(b_0 s^m + b_1 s^{m-1} + \dots + b_m) e^{-\tau_{eq}s}}{(s^n + a_1 s^{n-1} + \dots + a_n)} \quad (1.1)$$

where the system identification determines the values of the numerator coefficients ( $b_0, b_1, \dots, b_m$ ) and denominator coefficients ( $a_1, \dots, a_n$ ). An example of a transfer-function representation for the frequency-response  $\beta/\delta_r$  is shown in the dashed curve of Fig. 1.5. The transfer function is one type of *parametric model*<sup>1,2</sup> because it is composed of a limited set of characteristic quantities, or *parameters*—in this case the numerator and denominator coefficients of the transfer function.

### 1.1.3 State-Space Model

The ultimate product of a more intensive system-identification effort can be a parametric model composed of the complete differential equations of motion that characterize the MIMO behavior of a fixed-wing or rotary-wing aircraft. The linear equations of motion for small perturbations about a trim flight condition are represented in state-space form as

$$\dot{x} = Ax + Bu(t - \tau) \quad (1.2)$$

where the control vector  $u$  is composed of the control-surface deflections (inputs) of Figs. 1.1 or 1.2, and the vector of aircraft states  $x$  is composed of the response quantities (speeds, angular rates, and attitude angles). The time-delay vector  $\tau$  allows a separate time-delay value for each control axis as a lumped representation of the higher-order dynamics (e.g., actuators, linkages, etc.) that are not explicitly included in the state-space model. Typically, the set of available flight-test measurements  $y$  is composed of a subset of the states;  $y$  can also include combinations of the states, such as the angles of attack and sideslip as measured by a nose boom sensor. The measurement vector can also include additional quantities, such as the accelerometers shown in (Fig. 1.1), which respond directly to control inputs. The general form of the measurement vector can therefore be written as

$$y = Cx + Du(t - \tau) \quad (1.3)$$

System identification determines the values of the matrices  $A, B, C, D$  and the vector  $\tau$  that define the state-space model.

The level of complexity of the state-space model required to characterize the aircraft response depends on the vehicle configuration and intended application of the model result. Tables 1.1 and 1.2 show that models can range from three degrees of freedom (DOF) for a typical fixed-wing configuration to 13 DOF for an agile rotorcraft

Table 1.1 Models of fixed-wing aircraft dynamics

Model	DOF	Assumptions	Applications/examples in book (*)
Fully-coupled rigid body	Six DOF: Three translations (longitudinal, lateral, vertical) Three rotations (pitch, roll, yaw)	Vehicle is treated as a single rigid-body (fuselage/wing/tail) Significant coupling among all degrees-of-freedom	Asymmetric trim flight condition Asymmetric configuration (e.g., yawed wing)
Decoupled longitudinal	Three DOF: Two translations (longitudinal, vertical) One rotation (pitch)	Vehicle is treated as a single rigid-body (fuselage/wing/tail) Longitudinal and lateral-directional degrees-of-freedom have little or no coupling	Most conventional fixed-wing aircraft XV-15 cruise flight* Pathfinder UAV* Shadow™ 200
Decoupled lateral directional	Three DOF: One translation (lateral) Two rotations (roll, yaw)	Aircraft has planar symmetry Symmetric trim flight condition	fixed-wing UAV* STOVL*

configuration. The tables summarize the key applications of the various levels of model complexity and specific examples presented in this book. These models are explained in greater detail in the context of various examples throughout this book.

## 1.2 Relationship Between Simulation and System Identification

In contrast to system-identification-based modeling, the simulation-based approach to aircraft modeling involves adopting many a priori assumptions about the vehicle characteristics. The model is typically built up from aerodynamic, inertial and structural characterizations of the aircraft's individual component elements, such as the wing, tail, fuselage, rotor, etc. A simple approach to aerodynamic modeling can be based on first principles such as finite-wing theory or from empirical data of similar aircraft components using DATCOM (Data Compendium).<sup>3</sup> More complex aerodynamic models might make use of wind-tunnel data or computational-fluid-dynamics (CFD) calculations. Estimates of the mass and inertia properties of the aircraft components can involve coarse approximations or accurate CAD/CAM drawings. More complex structural models may be based on NASTRAN calculations. A mathematical model is thus built up in modular fashion. When incorporated into a simulation, the model is expected to predict the aircraft dynamic response that results from given control inputs.

This physics-based modeling approach can be very labor intensive, requiring the estimation or measurement of the aerodynamic, inertial, and structural properties of the many elements of the aircraft, but certainly it is a significant advantage

## INTRODUCTION AND BRIEF HISTORY

Table 1.2 Models of rotary-wing aircraft dynamics

Model	DOF	Assumptions	Applications/examples in book (*)
Hybrid fully coupled	13 DOF: Coupled fuselage/ regressive-flap dynamics (eight DOF) Coupled coning- inflow dynamics (two DOF) Lead-lag dynamics (two DOF) Engine torque response (one DOF)	Short-term regressive flap/coning/inflow dynamics are modeled using first-principles physics equations. Lead-lag modeled in canonical form Advancing rotor flap/lag modes are beyond frequency of interest. Low-frequency rotor response is captured using quasi-steady derivatives.	Applicable to all rotorcraft Required for configurations with high flap stiffness (i.e., low roll inertia and/or large flap hinge-offsets) Bo-105* UH-60* OH-58D* SH-2G* S-92*
Quasi steady	Six DOF: Three translations (longitudinal, lateral, vertical) Three rotations (pitch, roll, yaw)	Transient rotor dynamics are modeled as equivalent time delays. Rotor steady-state response is modeled as equivalent quasi- steady fuselage derivatives.	Applicable to helicopters with small effective flap stiffness Fire Scout P2 demonstrator* UH-1H*
Quasi-steady longitudinal	Three DOF: Two translations (longitudinal, vertical) One rotation (pitch)	Transient rotor dynamics are modeled as equivalent time delays Rotor steady-state response is modeled as equivalent quasi-steady fuselage derivatives.	Tilt-rotor configuration: V-22 XV-15 hover*
Quasi-steady lateral directional	Three DOF: One translation (lateral) Two rotations (roll, yaw) Rotor dynamics are treated as uncoupled from the fuselage.	Longitudinal and lateral- directional degrees of freedom are not coupled. Aircraft has planar symmetry.	Tandem-rotor configuration: CH-47

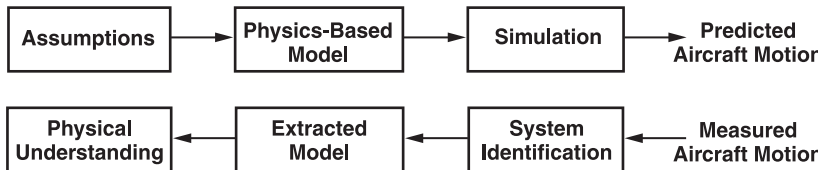


Fig. 1.6 Simulation vs system identification.

that this can be done before the aircraft has been built. In some cases the agreement between the predicted and measured dynamic behavior is unsatisfactory, at least initially, before “tuning,” because of the accumulated uncertainties and modeling simplifications. The approach is less suitable for small unmanned air vehicles (UAVs), which often have unique designs that are not similar to any existing database.

System identification and simulation modeling can be seen as inverse procedures, as shown in Fig. 1.6. In system identification the aircraft response is measured, and a dynamic model is extracted from the data, the reverse of developing a simulation. This extracted model can be compared directly with the simulation model, thereby providing greatly increased physical understanding about the nature of the characteristics of the physical systems that are being modeled. One role of system identification is to quantify where the actual and predicted motions do not match and to provide information on proper tuning for improved prediction accuracy. In that respect the two procedures, one forward and one inverse, are highly complimentary.

Key applications of system-identification results include piloted simulation models, comparison of wind-tunnel vs flight measurements, validation and improvement of physics-based simulation models, flight-control system development and validation, and handling-qualities specification compliance testing. For example, the U.S. Army’s modern specification for the handling qualities of rotorcraft (ADS33E Ref. 4) requires the use of system-identification procedures to extract parameters such as bandwidth and phase delay directly from flight-test frequency-response data. Handling-qualities criteria acceptance testing for U.S. fixed-wing aircraft (MIL-STD-1797 Ref. 5) involves using system identification to extract transfer-function models, also referred to as *equivalent system models*, from flight-test frequency responses. System-identification procedures and example results of handling-qualities and flight-control analyses of rotorcraft and fixed-wing aircraft are presented extensively in this book.

### 1.3 Special Challenges of Rotorcraft System Identification

There are special problems and challenges in system identification from rotorcraft flight data as compared to data from fixed-wing aircraft. Rotorcraft data generally exhibit a reduced signal-to-noise ratio in the measurement data, especially for low-speed and hovering flight regimes. In such regimes, the commanded vehicle motions (signal) are often the same order of magnitude as the noise contributions to the measurements arising from vibrations (rotor, engine,

and drive train), fuselage structural response, and unsteady air mass (inflow) passing through the rotor.

Further complications for rotorcraft applications arise from the high-order nature of the vehicle dynamics as compared to a fixed-wing aircraft. The rotorcraft cannot generally be considered as a single rigid body (i.e., fuselage/wing/tail) and must be modeled as a coupled multibody dynamics system. There is strong coupling between the dynamics of the rotor blades and the dynamics of the air flow passing through the rotor (*inflow*) with those of the fuselage, control system, and engine, so that as many as 13 degrees of freedom (or even more) are often necessary to model the dynamic response accurately. The planar symmetry of a fixed-wing aircraft also leads to considerable simplification of system-identification model structures, decoupling into a three-DOF model for the longitudinal dynamics and a separate three-DOF model for lateral/directional dynamic characteristics. Such simplifying assumptions are generally not possible with single-rotor helicopters, and the fully coupled lateral/longitudinal dynamic system must be taken into account in order to extract a model that is accurate for predicting the responses to control inputs. The various assumptions for fixed-wing aircraft and rotorcraft lead to the range of state-space models as summarized in Tables 1.1 and 1.2.

A last and very important characteristic of both rotorcraft and many modern and high-performance fixed-wing aircraft is that these vehicles generally exhibit dynamically unstable response characteristics. This is reflected by important eigenvalues of the short-term response in the right half-plane. As a result, the flight tests have to be completed with feedback by the pilot or with the automatic flight-control system active (*closed-loop testing*) to keep the responses within a reasonable range of amplitudes. As will be discussed later, this aspect can impact the suitability of the identification methodology selected: time domain vs frequency domain.

The AGARD Flight Mechanics Panel Working Group 18, under the able leadership of Peter G. Hamel (DLR), researched and developed system-identification methods suitable for the rotorcraft. The product of this effort was the comprehensive report AR 280 (Hamel<sup>10</sup>) that covers international activities, flight-test and identification techniques, detailed results, and key applications. There is a wealth of useful information in this report for further study on rotorcraft applications of system identification.

## 1.4 More About the Role of Nonparametric vs Parametric Models in Flight-Vehicle System Identification

As we introduced in Sec. 1.1, there are two types of models to consider when discussing system identification: nonparametric and parametric models. This section describes the key roles for each type of model and some important distinctions, as summarized in Table 1.3.

In the case of nonparametric models, we are concerned with characterizing only the measured input-to-output behavior of the aircraft dynamics, not the nature of the aircraft equations of motion. Examples of nonparametric modeling are impulse responses (time domain) and frequency responses (frequency domain), which are both derived directly from the test data. In either case no assumptions are required about the structure of the dynamic model.

Table 1.3 Nonparametric vs parametric models

Characteristic	Nonparametric models	Parametric models
Examples	Include impulse responses (time domain) and frequency responses (frequency domain)	Include transfer-function and state-space models (time and frequency domain)
SISO systems	Fully characterized by the frequency-response curve	Fully characterized by the transfer-function model
MIMO coupled systems	Fully characterized by the frequency-response matrix	Fully characterized by the state-space model
A priori assumptions	Nonparametric models are based on measured input-to-output behavior of the aircraft dynamics. No other a priori assumptions about the model are required.	Parametric models require a priori assumptions about the model, such as its order, degree of coupling, structure of the equations of motion, and initial estimates of key parameters.
Frequency-response method of system identification	Starts by identifying a non-parametric model (a frequency response or a matrix of frequency responses)	Uses the information obtained from the nonparametric models as the basis for identifying parametric models (either a transfer-function model or a state-space model)
Applications include	Handling-qualities analysis in terms of the bandwidth and phase-delay parameters Pilot-in-the-loop analysis Stability margin determination Classical control system design Validation and tuning of physics-based simulation models.	For transfer function (SISO): Short-term response to control inputs (e.g., roll-rate response to aileron input) Obtaining information about the stability, transient behavior, and key time constants of a system Control system synthesis based on root-locus techniques applied to bare-airframe response Handling-qualities analysis using equivalent system models of the closed-loop response of an aircraft to piloted inputs with the AFCS active
		For state-space model (MIMO): Determination of simulation models for piloted simulation MIMO control system design Comparison of wind-tunnel vs flight values of stability/control derivatives Direct determination of correction factors for tuning physics-based simulation models

In contrast, parametric modeling requires that certain assumptions must be made, including the following:

- 1) What model order is necessary to capture the key dynamics?
- 2) How highly coupled are the dynamics degrees of freedom?
- 3) What is the proper structure of the equations of motion?
- 4) What are good initial guesses for identification parameters?

For new or unconventional aircraft configurations, there might not be a good basis for making these modeling assumptions at the start of system identification. But once a model structure is known, what remains is to determine the values of the unknown coefficients in the model equations. Here the general problem of system identification reduces to the more restricted problem of *parameter estimation*.<sup>6</sup>

Nonparametric system-identification modeling provides excellent insight into the key aspects of the aircraft dynamics before moving on to the more complex parametric modeling stage. For example, the nonparametric results can be used to great benefit in selecting the appropriate order of the transfer-function and/or state-space models. The frequency-response identification method presented in this book is an integrated two-stage process of nonparametric followed by parametric modeling.

There are many applications based solely on the frequency-response characterizations, including handling-qualities analysis in terms of the bandwidth and time-delay parameters, pilot-in-the-loop analysis, stability margin determination, classical control system design, and validation and tuning of physics-based simulation models. For these and many other applications, the nonparametric model is often sufficient.

The parametric modeling stage generally involves a more intensive effort, with added focus on the physical understanding of the system being modeled to ensure that the appropriate model structure is adopted. Parametric modeling in the frequency domain can take two forms: transfer-function and state-space models. The simplest form uses transfer functions, which are the pole-zero representations of individual SISO frequency-response pairs. For example, simple low-order transfer functions can often be used in fixed-wing applications to accurately model the short-term response to control inputs (e.g., roll-rate response to aileron). These transfer-function models provide the key dynamic modes and control sensitivities. Transfer-function models of the *bare-airframe response* can be used directly for control system synthesis based on root-locus techniques, whereas equivalent system models of the *closed-loop response* with the automatic flight-control system (AFCS) active are widely used for handling-qualities analyses.

In some applications, it might be necessary to proceed to the ultimate identification step of extracting a state-space description in terms of identified stability and control derivatives. An example of a *stability derivative*  $L_p$  is the rolling moment caused by roll rate, normalized by the roll moment of inertia [ $L_p \equiv (1/I_{xx})(\partial L/\partial p)$ ]. The units of this angular response derivative are  $(\text{rad/s}^2)/(\text{rad/s}) = \text{s}^{-1}$ , which is the response inverse time constant  $1/T$ . An example of a *control derivative* ( $L_{\delta_a}$ ) is the rolling moment caused by aileron deflection, normalized by the roll moment of inertia [ $L_{\delta_a} \equiv (1/I_{xx})(\partial L/\partial \delta_a)$ ]. This has units of  $(\text{rad/s}^2)/\text{deg-ail}$ , which is the initial angular acceleration response per deg of aileron deflection. System identification can also provide a *physical model* given in terms of basic vehicle mechanical

and aerodynamic quantities such as spring constants or the aerodynamic lift-curve slope that appear in the physical equations of motion of the aircraft. State-space model determination is the most sophisticated and labor intensive of the modeling techniques, and much of the CIFER® system-identification facility is designed to support this step. Applications requiring identification of state-space models include the determination of simulation models for piloted simulations, MIMO control system design, the comparison of wind-tunnel vs flight values of stability and control derivatives, and the direct determination of correction factors for tuning physics-based simulation models.

A tradeoff exists for model complexity vs model variability.<sup>2</sup> Retaining extraneous parameters in a model can incrementally reduce the fitting error, but result in a higher variability of the estimated parameters. Further, models that are *over-parameterized* or *overmodeled* can result in a model with poorer predictive capability.<sup>7</sup> This tradeoff reflects the general principle of *parsimony*,<sup>8</sup> for which we quote a good definition given by Klein and Morelli<sup>6</sup>: “Given two models fitted to the same data with nearly equal residual variances (i.e., errors), choose the model with the fewest parameters.” Considerable emphasis is given in this book to systematic methods of model structure reduction that achieve this goal.

## 1.5 Frequency-Response Identification Method Is Well Suited to Flight-Vehicle Development

System identification is a key technology for modern fly-by-wire flight-vehicle development and integration. Frequency-response-based methods in particular provide a unified flow of information regarding system performance around the entire life cycle from specification and design through development and flight test, as seen in Fig. 1.7.

This theme is addressed at length by Tischler,<sup>9</sup> with examples based on many flight- and ground-based applications. Specific roles are shown in the highlighted boxes at each step in the cycle, including the definition of system requirements, specification and analysis of handling qualities, evaluation of proposed control-law concepts, validation and improvement of complex simulation models, validation of subsystem components and development facilities, and flight-test optimization of control laws. A similar road map for the application of system-identification methods to rotorcraft development was previously proposed by Schrage (Ref. 10, Section 3.1). Examples of system-identification applications in recent international manned flight-vehicle programs are described in Tischler’s volume on aircraft flight control.<sup>11</sup> System-identification techniques have proven highly effective in supporting UAV development for a wide range of vehicle sizes and configurations, including the important role for modeling and flight-control development when schedules are highly compressed, as is often the case for smaller-sized vehicles. When significant modifications to vehicle inertia characteristics and configuration are made on an almost daily basis, physics-based modeling become impractical. Instead, a quick frequency-sweep test and system identification can rapidly provide the needed dynamic models for flight mechanics characterization and control law tuning. This is discussed in a survey paper by Theodore et al.,<sup>12</sup> which covers UAV experience at the Ames Research Center during the period 1995–2003.

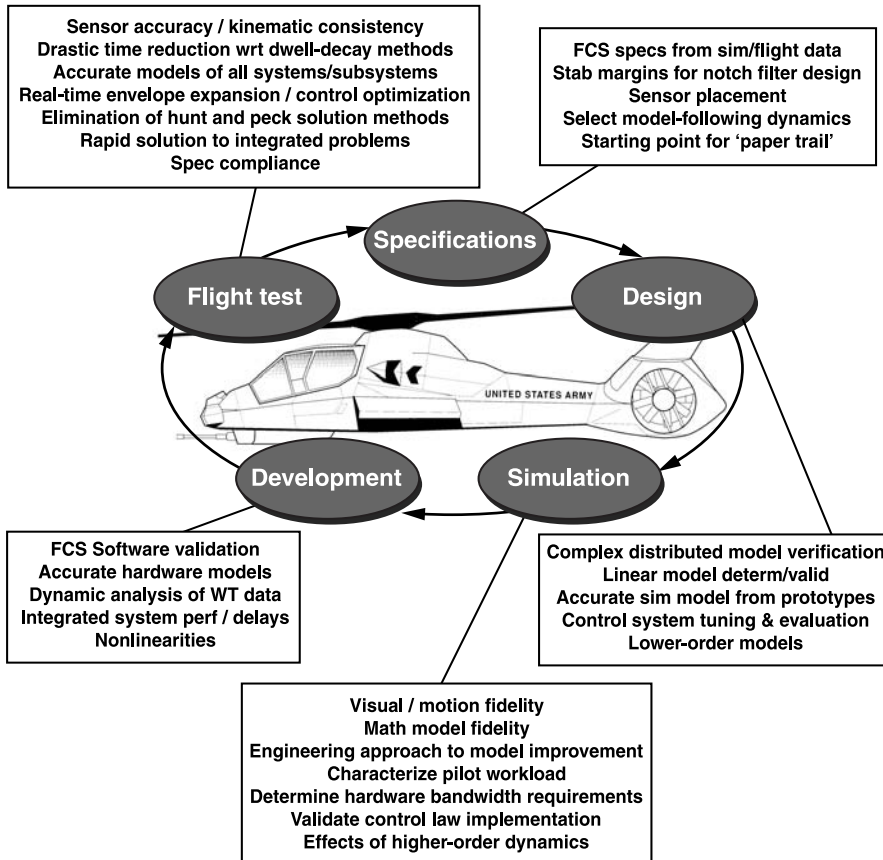


Fig. 1.7 Roles of system identification in the flight-vehicle development process (Ref. 9).

This book presents a frequency-response-based approach illustrated in Fig. 1.8. As discussed in the detailed presentation of the approach (Chapter 2), there are fundamental aspects of the frequency-response identification method that make it especially well suited for system identification of aircraft and rotorcraft dynamics models from flight-test data. Although many system-identification methods can be shown to produce satisfactory results using simulation (i.e., synthesized) data or test data from simple second-order systems, they often prove unreliable when applied to real flight data of aircraft and rotorcraft. The frequency-response identification method was developed and refined in numerous applications to aircraft and rotorcraft flight data, as illustrated in the many examples and references in this book.

Differences between the frequency-response and time-response methods that are especially significant for aircraft and rotorcraft applications are summarized in Table 1.4. Similarities between the methods are as follows: good results

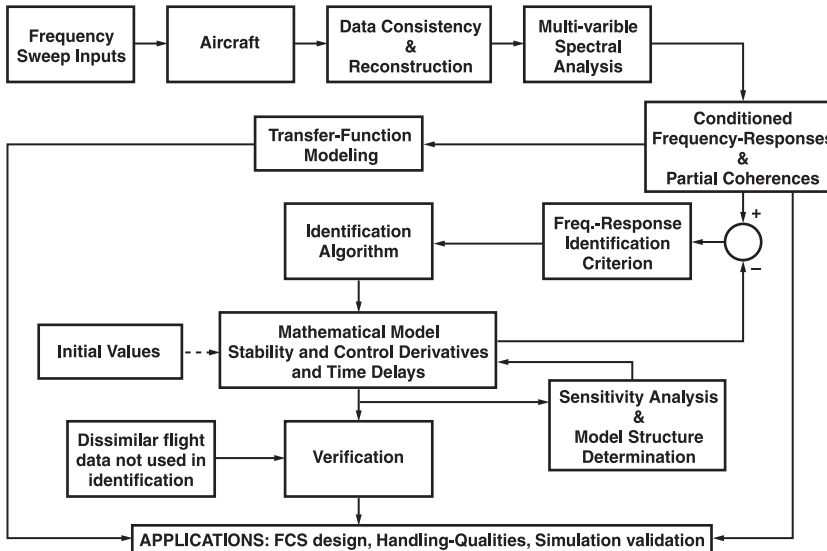


Fig. 1.8 Flowchart of frequency-response method for system identification.

depend on satisfactory excitation of key dynamic modes; multiple inputs must not be fully correlated; identification of parametric models—transfer-function models (SISO) and state-space models (MIMO); and models are ultimately verified in the time domain. These aspects are discussed in more detail in Sec. 2.2 and throughout the book. Comparative studies of time- and frequency-domain methods were conducted under a U.S./German memorandum of understanding (MOU) using flight-test data from the XV-15 tilt-rotor aircraft<sup>13</sup> and the Bo-105 helicopter.<sup>14</sup>

The frequency-response identification method is particularly well suited to support the development and validation of flight-vehicle dynamic systems. The direct comparison between flight-test frequency responses and those from simulation models provides an excellent means of model validation and update for the system components (e.g., actuators, sensors, airframe, flight-control software) as well as the end-to-end behavior. Feedback stability and noise amplification properties are determined from the broken-loop frequency response and characterized by metrics such as crossover frequency and associated gain-and-phase margins. Command tracking performance is determined from the closed-loop frequency response and characterized by metrics such as bandwidth, time delay, and equivalent-system eigenvalues. The system-identification approach presented in this book allows the direct and rapid (including real-time) identification of these frequency responses and metrics without the need to first identify a parametric (state-space) model structure, as is required when applying time-domain methods. Careful tracking of the broken-loop and end-to-end closed-loop frequency-response behavior, from the preliminary design studies through detailed design and simulation and into the flight test, provides an important “paper trail” for

## INTRODUCTION AND BRIEF HISTORY

15

Table 1.4 Comparison of frequency-response and time-response methods

Characteristic	Frequency-response methods	Time-response methods
Method for linear and nonlinear models	Frequency-response methods provide a linearized characterization of system dynamics. For nonlinear systems, this produces a describing function model.	Time-response methods can be used to obtain linear or nonlinear models.
Initial data	Consist of frequency responses (derived from time-history data)	Consist of time-history data
How models are identified	By matching predicted frequency responses against measured frequency responses	By matching predicted time histories against measured time histories
Starting the method	Frequency-domain methods start by calculating frequency responses, getting some preliminary information about the model structure, and then (if necessary) identifying a more detailed and accurate parametric model structure.	Time-domain methods must start by assuming or otherwise identifying the parametric model structure.
Noise	Bias effects of noise in response measurements and process noise are eliminated from the analysis.	Noise models must be identified. If the presence of noise is ignored (either output error or equation error formulation), it will introduce biases in the identification results.
Independent measure provided	Coherence function provides a direct and independent measure of system excitation, data quality, and system response linearity.	No independent metric to assess system excitation and linearity.
Responses	Response pairs are fit only in the frequency range over which the data are accurate.	Fit over the same time (and frequency) ranges
Time delays	Direct and precise identification of time delays caused by linear phase shift with frequency	Not identified directly
Bias or reference shifts	No biases or reference shifts to be identified	Must be identified and can be correlated with aerodynamics parameters

(Continued)

Table 1.4 (continued)

Characteristic	Frequency-response methods	Time-response methods
Number of points	Small number of points are included in iterative identification criterion, which improves computational efficiency.	Large number of points are included in iterative identification criterion (e.g., factor of 30 increase).
Algorithms or equations used	Identification algorithms are very efficient because frequency responses are determined algebraically from updated parameters.	Equations of motion must be numerically integrated in time for each iterative update in the parameters.
Unstable systems	Good results are obtained with unstable systems (e.g., rotorcraft, high-performance fighter aircraft).	Special techniques for application to unstable systems can degrade the quality of the results.
Typical input	Frequency sweep (broadband input) involving longer flight-test records than multistep inputs	Multistep (e.g., doublets, 3-2-1-1) involving shorter record lengths
Parameter accuracy bounds	Accurate estimates	Very optimistic estimates (factor of 5–10)

documenting system performance and solving problems that might appear in the later phases of development.

The availability of comprehensive and reliable computational tools has substantially enhanced the acceptability of frequency-domain techniques in the flight-control and flight-test communities. Benefits derived from applying these techniques include the reduction of flight-test time required for control-system optimization and handling-qualities evaluation, especially for complex control-law architectures, as well as improvements in the final system performance. Frequency-domain methods offer a transparent understanding of component and end-to-end response characteristics that can be critical in solving system integration problems encountered in flight test.

The Army/NASA Rotorcraft Division (Ames Research Center) jointly developed the Comprehensive Identification from Frequency Responses (CIFER®; Ref. 15) integrated facility for system identification based on the frequency-response approach of Fig. 1.8. This tool is composed of six core analysis programs built around a sophisticated database, along with a set of user utilities to provide a highly interactive, graphics-oriented environment for dynamics studies. The foundation of the CIFER® approach is the high-quality extraction of a complete MIMO set of nonparametric input-to-output frequency responses. These responses fully characterize the coupled characteristics of the system without a priori assumptions. Advanced chirp z-transform (CZT) (Chapter 7), multi-input

conditioning (Chapter 9), and composite window techniques (Chapter 10), developed and exercised with over 20 years worth of flight project applications, provide significant improvements in frequency-response quality relative to standard fast Fourier transforms (FFTs). Sophisticated nonlinear search algorithms are used to extract parametric models of varying complexity from this MIMO frequency-response database that are used in simulation, handling-qualities, and flight-control studies.

The key features of the CIFER® tool are as follows: 1) identification algorithms that have been extensively applied and proven on many flight projects; 2) implementation of frequency-response identification in a step-by-step sequence of core programs; 3) checks of user inputs against key guidelines (as summarized in Appendix A); 4) chirp z-transform and composite window optimization for high-quality frequency-response identification; 5) multi-input frequency-response solution; 6) highly flexible and interactive definition of identification model structures; 7) fully automated weighting-function selection based on frequency-response accuracy; 8) reliable parameter accuracy metrics; 9) integrated procedure for identification and model-structure determination; 10) time-domain verification of models, including identification of offsets and biases; and 11) a suite of specialized utilities that support many of the applications just mentioned, which is uniquely suited to the difficult problems associated with flight-test data analysis.

CIFER® is the first such integrated package for the end-to-end frequency-response identification method, and it has proven to be a very effective tool for the difficult problems of rotorcraft system identification. CIFER® has seen wide use for a range of fixed-wing, rotary-wing, and UAV programs.

## 1.6 Role and Limitations of Flight-Mechanics Models Determined with the System-Identification Method

Physics-based simulation models provide the first estimates of vehicle response prior to first flight. Developing a simulation model entails a comprehensive effort to determine the many geometric, aerodynamic, and mechanical parameters required for the input deck. As demonstrated herein and in many other validation studies (e.g., Ref. 10, 16, and 17), key physical parameters (such as inertias) or physical effects (such as cross coupling or rotor/fuselage aerodynamic interaction) are poorly known. Thus, for example, even after the completion of an expensive blade-element-type modeling effort for a helicopter simulation, there ensues an intensive “validation effort” to bring the simulation closer to flight. The accurate determination of flight-control parameters and the rapid solution of complex flight-control interactions on modern aircraft demand a degree of model precision that can quickly (and perhaps only) be achieved using system identification (e.g., Refs. 17–20) in the early flight-test stage. System-identification results can then be used to update the physics-based simulation models (as in Tischler et al.<sup>17</sup>).

The compressed development schedule of UAV compared to manned aircraft (e.g., 6–12 months rather than 5–10 years) and unusual configurations often preclude the physics-based modeling approach; as a consequence, flight-control development can depend entirely on system-identification models obtained from dedicated flight tests at the start of the program, as was the case in the development

of the Northrop-Grumman vertical takeoff UAV (VTUAV) demonstrator<sup>19</sup> and other recent UAV projects.<sup>12</sup>

An often-cited deficiency of the system-identification approach is that the identified parameters reflect the “lumped” contributions of numerous physical mechanisms. For a rotorcraft application, the identified rotor flap stiffness  $L_{\beta_{1s}}$  has key contributions as a result of hinge offset, rotor hub height above the c.g., and roll inertia. The identified stability derivative parameters such as  $X_u$  or  $M_u$  reflect even more numerous and offsetting contributions. This lumping of aerodynamics and dynamics contributions in a single effective parameter often makes it difficult to track down the individual physical contributions as a means to improve the fidelity of physics-based simulation models. However, as far as the pilot or the flight-control system is concerned, the dynamic response characteristics depend solely on these lumped parameters, such as the dependency of response bandwidth and other handling-qualities metrics on the rotor flap stiffness  $L_{\beta_{1s}}$  (Ref. 21). Pilot opinion of the dynamic response is largely a function of the *crossover characteristics*, which emphasize the importance of input-to-output frequency-response accuracy rather than the individual contributions of modular elements of the aircraft.

Another concern often raised in conjunction with system identification is the range of variations in flight condition over which the models are accurate. The frequency-response identification method produces a *describing function* that is a linear model which best models the nonlinear responses. The aircraft and rotorcraft results presented herein show that these identified models accurately predict the response for fairly large aircraft motions (e.g., as large as 30 deg/s in roll) and thus are not small-perturbation models in the classical sense. Therefore, models identified at a limited number of conditions with a common model structure might be sufficient to characterize the dynamic variations for flight-control design and allow interpolation for continuous flight simulation and control system gain scheduling at intermediate speeds. This approach to simulation model determination has been used widely in the fixed-wing community.<sup>22</sup> Ultimately, the integration of physics-based simulation modeling and system-identification-based model extraction will yield the high-fidelity full-flight envelope predictions needed for flight control and handling-qualities applications.<sup>23</sup>

## 1.7 Brief History of the Development of Frequency-Domain Methods for Aircraft and Rotorcraft System Identification

This section summarizes key milestones in the development of frequency-domain methods for aircraft and rotorcraft system identification. An excellent and in-depth historical survey that covers the development of both time- and frequency-domain methods of flight-vehicle system identification was published by Hamel and Jategaonkar.<sup>24</sup>

The earliest reported research in frequency-response identification of aircraft dynamics from flight-test data was conducted at the Cornell Aeronautical Laboratory beginning in 1945 (summarized in Milliken<sup>25</sup>). Steady-state sine-wave inputs were used to (laboriously) extract the frequency responses of the North American B-25J fixed-wing aircraft. Lower-order transfer-function models were then derived from a least-squares fit of the frequency responses displayed on a

## INTRODUCTION AND BRIEF HISTORY

19

polar plot. Fourier transform methods were subsequently developed<sup>25,26</sup> to allow frequency-response identification from shorter-duration discrete maneuver data, such as those obtained from step and pulse inputs. These techniques were applied in flight research activities at the Air Force Flight Test Center (Edwards Air Force Base) during the 1950s (see Schofield et al.<sup>27</sup> for a list of references). Various methods for determining frequency responses and transfer functions from aircraft flight-test data were also developed in the same time period at the NASA Langley Research Center.<sup>28</sup> These methods included steady sine waves, Fourier analysis, and a mechanical rolling sphere harmonic analyzer. Donegan et al.<sup>29</sup> used a fitting method to extract aircraft lateral-directional stability derivatives from the identified frequency responses. Early experience with helicopter frequency-response identification was reported by Kaufman and Peress,<sup>30</sup> who used a constant frequency flight-test method to (laboriously) obtain frequency responses of the S-55 helicopter. Schultz<sup>31</sup> mentions the use of the rolling sphere harmonic analyzer to extract frequency responses from transient-response flight data of the XH03S-2 helicopter. The helicopter stability derivatives for longitudinal motion were then determined from these frequency responses using fitting methods. As pointed out by Schofield et al.,<sup>27</sup> all of the early efforts in frequency-response identification suffered from the lack of large-scale computing power. The development of the FFT algorithms in the 1960s and the significantly improved computing capabilities of this period led to much greater interest and success in frequency-response identification.

Marchand and Koehler,<sup>32</sup> of the Institute for Flight Mechanics (DFVLR, now DLR) in Braunschweig, Federal Republic of Germany, developed an equation-error method for state-space model identification from frequency-transformed data. Flight data were obtained with prescribed multistep control inputs known as the “3-2-1-1” excitation, developed by the DFVLR and now widely used, in a key outgrowth of research in optimal input design. Klein,<sup>33</sup> from the George Washington University Joint Institute for Advancement of Flight Sciences at the NASA Langley Research Center, formalized a frequency-domain-based maximum-likelihood (ML) method for aircraft parameter identification. The frequency-domain ML method was further developed by Marchand and Fu<sup>34</sup> at the DLR and applied in many flight-vehicle programs, including the X-31 fixed-wing<sup>35</sup> and the Bo-105 helicopter.<sup>36,37</sup> Rotorcraft identification in the frequency domain using equation-error and output-error methods has also been a dedicated focus in the United Kingdom,<sup>38,39</sup> including unique flight-test applications to autogyros.<sup>40</sup> Morelli, a colleague of Klein at the NASA Langley Research Center, advanced equation-error/output-error methods in the frequency domain and compared his lower-order system identification results on the Tu-144LL with those of CIFER® (Ref. 41). Morelli has also developed methods for optimal input design and recursive methods for online frequency-response determination and parameter estimation.<sup>6</sup>

A comprehensive tool for multivariable frequency-response (matrix) identification and analysis (frequency-response analysis, or FRA) was developed by Twisdale and Ashurst<sup>42</sup> of the Air Force Flight Test Center at Edwards Air Force Base. One key feature of the FRA identification approach was the incorporation of the ordinary, partial, and multiple coherence function calculations, which provide important measures of spectral estimation accuracy for multi-input excitations (see Chapter 9). Twisdale’s flight-testing approach, system identification from tracking

(SIFT), achieved frequency-response identification from handling-qualities evaluations of air-to-air tracking and flight refueling. Frequency-response identification from flight data obtained with the prescribed *frequency-sweep* input was pioneered by Systems Technology, Inc. (STI) for applications that included research aircraft,<sup>43</sup> manned-powered aircraft,<sup>44</sup> and simulators.<sup>45</sup> The STI frequency-sweep testing technique was a simplification of an earlier flight-test method by Hall,<sup>46</sup> which used a metronome-like paced command (via earphones) to signal the pilot to reverse the control input with variable duration square waves. STI also developed specialized packages for frequency-response identification (Frequency Domain Analysis Routine, FREDA; Magdaleno<sup>47</sup>) and for extracting parametric state-space models by simultaneously fitting several frequency-response data curves (Multiple-Response Fitting Program, MFP; DiMarco and Magdaleno<sup>48</sup>). Advancements in lower-order transfer-function modeling were also made by Hodgkinson et al.,<sup>49</sup> Bischoff and Palmer,<sup>50</sup> and Mitchell and Hoh<sup>51</sup> in support of the development of an updated handling-qualities specification for military fixed-wing aircraft.<sup>52</sup>

Tischler of the U.S. Army Aeroflightdynamics Directorate (Ames Research Center) was the first to extensively identify frequency-response and transfer-function models of rotorcraft from flight tests using frequency-sweep inputs. The initial applications were to the XV-15 tilt-rotor aircraft<sup>53</sup> and the Bell 214ST helicopter.<sup>54</sup> Tischler and Cauffman<sup>15</sup> developed CIFER® (Comprehensive Identification from Frequency Responses), an integrated facility for system identification using a frequency-response method that embodies several key innovations. Significant improvements in frequency-response identification accuracy were achieved with the chirp z-transform and a numerical optimization procedure that combines the results of individual spectral window calculations. The use of a robust secant-pattern search algorithm, rather than a gradient search method, allows the extraction of complex models of up to 100 unknown parameters, simultaneously matching up to 80 multi-input/multi-output frequency responses, with constraints among the identification parameters easily included. Another unique innovation in CIFER® is the integration of coherence function information and theoretical-accuracy metrics into a powerful unified approach for parametric model-structure determination and identification.

## 1.8 Organization of this Book

The frequency-response method for system identification flowchart in Fig. 1.8 is also the road map for the organization of the remainder of this book. Each block in Fig. 1.8 is covered sequentially by one or more chapters and is also supported by a specific function in CIFER®. At the end of each chapter is an exercise set intended to give the students hands-on experience with a wide range of applications of the techniques covered therein. The flight-test and simulation data for aircraft and rotorcraft configurations needed for these exercises can be downloaded from the publisher's website along with a student version of CIFER®.

Chapter 2 explains in detail the frequency-response method for system identification, which is the focus of this book, and is implemented in CIFER®. Typical results of the frequency-response identification method as obtained for the XV-15 tilt-rotor aircraft are presented for hover and cruise flight conditions.

The system-identification methods presented throughout this book make use of three case study examples, which are introduced in Chapter 3. The first case study is of a simple inverted pendulum, and it provides a convenient demonstration of the system-identification methods, accuracy, and interpretation of the results for a known set of dynamics. The main case studies of system identification of flight vehicles are based on flight-test data for the XV-15 tilt-rotor aircraft in hover and cruise conditions. The hover results are typical of rotorcraft applications, whereas the cruise results are typical of fixed-wing aircraft applications. The XV-15 presents a useful case study, using a single vehicle, to illustrate key aspects of aircraft and rotorcraft system identification as presented in this book. Many other examples, drawn from the leading author's system identification experience with a broad range of flight-test, bench-test, simulation, and wind-tunnel programs, are also presented throughout the book.

Chapter 4 serves as an introduction to the CIFER® software, which is used throughout the book to develop and illustrate the example results. The material in this chapter is not intended to be a user's manual. A student version of the CIFER® software and a primer are available without charge via the AIAA website or by contacting the leading author. Chapter 5 focuses on the first step in the system identification process of Fig. 1.8: the collection of a well-suited time-history database. The ultimate quality of the identification results is highly dependent on 1) properly designed and executed flight tests of the aircraft being studied and 2) properly selected and well-documented characteristics of the instrumentation system. Regardless of how much care is taken in instrumentation and flight testing, there will often exist kinematic inconsistencies between independent measurements of dynamically related variables. Chapter 6 covers typical sources of data inconsistencies and presents both sophisticated and simple methods for isolating and correcting for such errors. The basic concepts of single-input/single-output (SISO) frequency-response identification theory are presented in Chapter 7. The importance of windowing and the tradeoff associated with window length selection is discussed at length. An understanding of these concepts is an important prerequisite to the success of the system identification process.

Chapter 8 addresses the identification of bare-airframe dynamics from flight-test data with feedback regulation active. The greatest concern here is that the stability and control augmentation system (SCAS) feedback introduces correlation between the output noise and the bare-airframe excitation signal. Depending on the noise-to-signal ratio, this correlation can cause significant bias errors in the frequency-response estimate. Chapter 9 discusses the identification of MIMO systems from flight-test records where there is excitation from more than one control surface (input) and coupling between the multiple inputs and outputs. In this case the use of SISO identification methods can result in considerable errors in the frequency-response identification results. Instead, the MIMO frequency-response matrix must be determined. The composite window technique presented in Chapter 10 combines the frequency-response results obtained with various window sizes into a single, MIMO frequency-response matrix of exceptional quality and dynamic range. This optimization-based technique is unique to the CIFER® identification procedure. The need for manual optimization of window size and the compromise involved in selecting a single window

size are drawbacks of other frequency-domain methods, drawbacks that are overcome by CIFER®.

Chapter 11 discusses the determination of transfer-function representations, which are input-to-output descriptions of the dynamic system. For many applications these rather simple transfer-function models are found to be quite sufficient, including handling-qualities analysis, actuator and other subsystem models, aeroelastic mode determination, and models for root-locus-based control system design. Even if the ultimate goal is the determination of a fully coupled state-space representation, the transfer-function models are a useful intermediate step in that they provide information on the fundamental dynamic characteristics and good estimates of key parameter values.

Direct identification of state-space models is covered in two chapters (Chapters 12 and 13). Chapter 12 presents the basic concepts, the implementation method in CIFER®, and applications to canonical representation of SISO systems. Chapter 13 extends the discussion to the identification of physical structure representations of MIMO systems. An important assessment of the model fidelity, robustness, and the limitations of the linear model is provided by evaluating the predictive capability in the time domain for test inputs, such as steps or doublets, which are dissimilar from those used in the identification. In this last step in the system-identification procedure, covered in Chapter 14, the model parameters are held fixed, and only the flight data offsets and biases are determined. Then the predicted response of the model is compared with the flight data.

To improve their maneuverability, modern helicopters often feature designs with higher flap stiffness, achieved with increased equivalent hinge offset (including hingeless and bearingless rotors) and/or low fuselage moments of inertia. An accurate characterization of the dynamic response requires an extended model structure that explicitly includes the states of the rotor. Chapter 15 presents the hybrid model structure that is applicable for a range of flap stiffness values and is suitable across the flight envelope. Flight-test results for the SH-2G helicopter show that the hybrid model provides an excellent characterization of the coupled rotor/fuselage dynamics and is a suitable common model structure for the entire flight envelope. The formulation and methods presented in this final chapter provide a general template for helicopter system identification. The student problems at the end of this chapter use simulated test data for a typical helicopter and give the student experience with the most challenging aspects of state-space model formulation and identification.

## Problems

### *System-identification concepts*

- 1.1** How could system-identification techniques be used to improve a simulation model?
- 1.2** Provide some examples of dynamic subsystems on an aircraft that could be identified with system identification.
- 1.3** What types of measuring devices could be used to measure the inputs and outputs for system identification of an aircraft?

*Nonparametric vs parametric models*

**1.4** What is a nonparametric model? What is a parametric model? Give an example of a situation for which each model type would be appropriately used.

**1.5** What types of information about system dynamics (i.e., types of metrics) can be determined from parametric models? From nonparametric models?

**1.6** How could a nonparametric frequency-response model be used to assess the validity of a simulation model? How is this different than comparing the two responses in the time domain?

This page intentionally left blank

## 2

## Frequency-Response Method for System Identification

This chapter presents a general overview of the frequency-response method for system identification, which is the focus of this book and is implemented in CIFER®. We also present results of the frequency-response method obtained for the XV-15 tilt-rotor aircraft, which, depending on its configuration, has flight dynamics behavior typical of fixed-wing or rotary-wing aircraft. The following topics will be covered in this chapter: 1) basic components of the frequency-response method for aircraft system identification; 2) key features of the frequency-response approach; and 3) overview of the frequency-response method applied to the XV-15, including results for hover and cruise flight configurations.

### 2.1 Road Map of Frequency-Response Method for System Identification

The overall road map for system identification using the frequency-response method, illustrated by the flowchart in Fig. 2.1, is the basis for much of the organization of this book. Each of the elements of the flowchart will be briefly described in this section, with the individual block names referenced in italics within parenthesis.

The frequency-response method for system identification was developed to accurately characterize the dynamic response behavior of fixed-wing aircraft and rotorcraft from flight data. The models are intended for use in a wide range of applications (*Applications*), including control system design, handling-qualities analysis, and the determination and validation of simulation math models. The method uses dynamic response time-history test data (e.g., from flight, piloted simulation, bench tests) generated from pilot- or computer-generated inputs, such as sweeps or other inputs with good spectral content (*Frequency Sweep Inputs*). These inputs excite the system vehicle dynamics (*Aircraft*), which could be an aircraft or any other physical system or subsystem (e.g., actuators, filters) of interest.

After conducting the aircraft tests and collecting measurement data, the next step is to check that the database is internally consistent and, to the extent possible, free of spurious noise (*Data Consistency & Reconstruction*) before actually starting the identification process *per se*. The effects of known scale-factor errors in the measurement system (a type of *deterministic error*) should be removed from the data. For example, if there is a scale-factor error in a rate gyro measurement of aircraft roll-rate response, this will show up as a scale-factor error in aerodynamic roll-control sensitivity  $L_{\delta_a}$ . Other sources of deterministic errors that can be introduced by the data system and should be corrected prior to system identification include time skews, inconsistencies in units and sign conventions, and biases. These will all introduce bias errors in the identified model parameters,

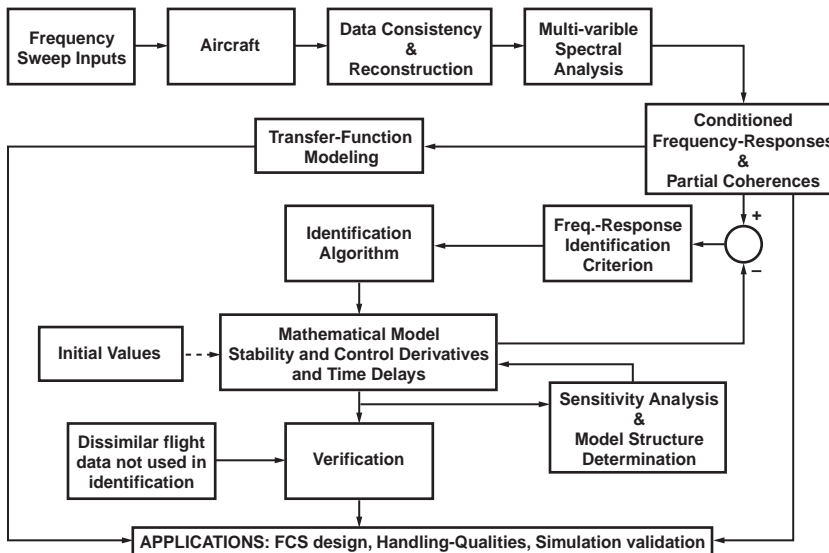


Fig. 2.1 Flowchart of frequency-response method for system identification.

and later it will be impossible to tell that the seemingly incorrect or physically unexpected results were in fact caused by a corruption or inconsistency introduced by the measurement system.

Random or *nondeterministic* errors, such as dropouts and spikes, should also be removed prior to identification. If there are dropouts, estimates should be made using state reconstruction methods of what the signal values should be during the time of the dropout, based on redundant measurement sources. Obvious data spikes should also be removed at this time using a wild-point removal algorithm. Untreated dropouts and spikes show up as uncorrelated high-frequency noise and degrade the overall accuracy of the identified model.

These various data issues are well understood by the instrumentation engineers, but they are often ignored by the “users” of the data and must be addressed. Before proceeding with the system identification, it is crucial to stop and perform a sanity check on the data to ensure that the various signals in the data are kinematically consistent. For example, the integral of angular-rate measurements should be consistent with Euler roll-angle measurements, the integral of acceleration measurements should be consistent with the speed measurements, and so forth. A small amount of effort at this early stage will save countless hours trying to understand otherwise “mysterious” identification results later.

The next step is to perform a multivariable spectral analysis of the data (*Multivariable Spectral Analysis*). This analysis, which is a multi-input/single-output (MISO) generalization of the simple SISO FFT, is necessary for most aircraft system-identification applications because real flight-test data inevitably involve multiple, partially correlated control inputs during a single excitation maneuver. Repeating this process for each of the aircraft outputs yields a MIMO frequency-response database. The MIMO frequency-response

## FREQUENCY-RESPONSE METHOD FOR SYSTEM IDENTIFICATION 27

matrix constitutes a *nonparametric model* of the aircraft response because it fully characterizes the input-to-output behavior without the need for defining a model structure or determining model parameters. As shown in Fig. 2.1, these nonparametric modeling results support many direct applications (*Applications*), including the design and analysis of flight control systems, stability margin determination, piloted handling-qualities analysis, and the validation and improvement of simulation models.

The frequency response is a *linear* model of the input-to-output process under examination. The parametric models extracted later to fit these responses are also linearized representations. When the dynamics contain nonlinear behavior, the frequency-response function as extracted using the Fourier transform is the *describing function*, which is the linear model that best characterizes the nonlinear behavior of the system.<sup>55</sup> Although there might often be significant localized nonlinear characteristics in some of the aircraft subsystems (e.g., local airfoil stall, mechanical linkage hysteresis, or even an actuator that reaches a transient limit), the input-to-output dynamic response can almost always be well modeled using linear models or describing function concepts. This is largely because the inertial (i.e.,  $k/s^2$ ) response of a system truncates the higher-harmonic remnants associated with the nonlinearities in the local forcing functions (Sec. 7.7.4). The overall flight dynamics response of aircraft and rotorcraft can also most often be well characterized by these linearized describing function models as well. Systems design and analysis methods that use the products of system identification are also almost entirely based on linear modeling concepts (e.g., transfer functions, state-space design and analysis, root locus, handling qualities). Finally, the subsystems and overall aircraft behavior are designed to provided a mostly linear input-to-output response that minimizes the potential for undesirable limit cycles and provides for optimum piloted handling.<sup>56</sup> When true nonlinear models are required, system identification must be completed in the time domain.<sup>6</sup> An example is the identification of aerodynamics models for stall and spin regimes, where the derivatives can follow a highly nonlinear function of angle of attack, sideslip, and products of states and controls. Nonlinear model structure selection and validation has not been widely studied.

As described in later chapters, two key features of the spectral analysis described herein, and implemented in CIFER®, are the chirp z-transform and composite window optimization. The chirp z-transform is an advanced and flexible FFT algorithm that provides an accurate frequency response over the frequency range of interest. Spectral windowing is a process by which the time-history data are segmented, and the frequency response is determined for each segment or *window*. By averaging the frequency responses from individual window segments, the effect of noise is reduced significantly. In composite windowing, repeated frequency-response determinations are carried out with varying window lengths, and these results are then combined using a numerical optimization procedure into a single result. Together, the chirp z-transform and composite window optimization methods produce a frequency-response database of exceptionally high accuracy and resolution over a broad dynamic range for real flight-test data. An important byproduct of this analysis is the coherence function, which provides key information about the frequency-response accuracy (*Conditioned Frequency Responses & Partial Coherences*).

All of the data analysis setup options and results are stored in the database for rapid processing of batch cases, and the database is supported by CIFER® with a variety of tools for plotting, searching, analyzing, and bookkeeping. Without this integrated database, it would be easy to become overwhelmed by the large quantity of spectral data generated for real-world applications. Flight-test studies typically involve large numbers of inputs, outputs, flight conditions, aircraft configurations, and spectral processing options, which together can result in hundreds or even thousands of individual frequency responses.

When *parametric models* are required, transfer-function modeling is a rapid and logical next step in the system-identification procedure (*Transfer-Function Modeling*). The values of the transfer-function gain, pole locations, and zero locations are determined numerically to provide a best match (in a least-squares sense) to the frequency-response data. Transfer-function models are often sufficient end-products of system identification for many applications (*Applications*). Classical procedures for synthesizing flight-control systems track the movement of the transfer-function eigenvalues using root-locus plots. A large body of literature on piloted handling-qualities analyses is based on simple (i.e., first- or second-order) representations of the aircraft dynamic response, referred to as *lower-order equivalent systems* (LOES). Many (perhaps most) applications of system-identification methods in the aircraft dynamics and control field involve frequency-response identification followed by transfer-function modeling as a final product.

The next step, if desired, involves the extraction of state-space or physical model structures. These model structures are formulated directly from the linearized first-order differential equations of motion as derived from Newton's Second Law. State-space and physical model identification can be much more involved than transfer-function identification and requires significantly more insight into the dynamics of the system being modeled. Much of material in this book and the capabilities of CIFER® address state-space model identification. The overall goal of this step is to determine a set of linear first-order differential equations constituting a model (*Mathematical Model*) whose frequency responses match the measured MIMO frequency-response data. The accuracy of this identified math model is quantified in terms of the weighted sum of the magnitude and phase errors (*Frequency-Response Identification Criterion*). Initial guesses for the model parameters can be obtained from the transfer-function identification results, from a priori estimates based on first principles, or from rapid equation-error regression methods.<sup>6,10</sup> A powerful and highly robust secant optimization algorithm (*Identification Algorithm*) is used to tune the identification parameters in the model structure (e.g., stability and control derivatives, time constants, time delays) to minimize the identification cost function and thereby drive the model responses to the best match of the flight-test responses. The optimization stops when a minimum cost function value is reached that provides the best choice of identification parameters for the assumed model structure.

At this stage in the process, we have achieved a state-space model that best matches the MIMO frequency-response database. But there are still a number of important issues to consider before the model can be considered to adequately characterize the physics of the aircraft dynamics (*Sensitivity Analysis & Model Structure Determination*). For example, if the model structure selected contains too many identification parameters for the aircraft dynamics or available

## FREQUENCY-RESPONSE METHOD FOR SYSTEM IDENTIFICATION 29

measurements, there will be redundant parameters in the model that trade off one against the other. Thus the model might match the input-to-output frequency-response data very well, but the individual identification parameters might not have any real physical meaning. Model structure determination finds the model that matches the test data with minimum model redundancy. The basis for this step is a sensitivity analysis to determine the accuracy and correlation of the parameters that have been identified. This can show, for example, that certain parameters are known accurately and should be retained in the model, whereas others have to be discarded because it is impossible to determine or isolate their values caused by parameter correlation. Model structure determination, sensitivity analysis, and model reconvergence constitute an iterative loop that refines the structure of the model to ensure that it is both physically appropriate and accurate to within specified error bounds.

With the completion of the model *identification* in the frequency domain, it is necessary to *verify* that the model has good predictive capability and robustness to input shape in the time domain (*Verification*). For this, we would like to see an accurate and direct comparison of predicted and measured time responses to measured control inputs that are completely different in character from those used in the identification (*Dissimilar flight data not used in identification*). For example, if flight-test data from frequency-sweep inputs were used for the identification, then data from step or multistep inputs might be used for verification. Evaluating the predictive accuracy for various input amplitudes is useful for assessing the acceptability of the identified *linear* model. Once the model has been verified, it can be used in the various applications shown (*Applications*).

## 2.2 Key Features of the Frequency-Response Method for Flight-Vehicle System Identification

There are eight important features of the frequency-response identification method that make it especially well suited to system identification of flight-vehicle dynamics from flight-test data: 1) unbiased frequency-response estimates when flight data contain process and output measurement noise; 2) access to the coherence function as an unbiased measure of nonparametric identification accuracy and system response linearity; 3) the wealth of knowledge concerning appropriate model structure provided by the nonparametric identification results; 4) frequency ranges selected individually for each input/output pair to include only accurate data; 5) direct and accurate identification of time delays; 6) elimination of biases and reference shifts as identification parameters; 7) significant improvement in computational efficiency; and 8) identification of systems with unstable dynamics. Each of these features will now be described in detail.

*Unbiased frequency-response estimates when flight data contain process and output measurement noise:* As described in more detail in Chapter 7, the frequency-response estimate is determined from the ratio of the input autospectrum estimate  $\hat{G}_{xx}$  to the cross-spectrum estimate  $\hat{G}_{xy}$  at each discrete frequency  $f$ :

$$\text{Frequency-response estimate} = \hat{H}(f) = \frac{\hat{G}_{xy}(f)}{\hat{G}_{xx}(f)} \quad (2.1)$$

This specific choice of spectral ratios eliminates potential biases in the frequency-response calculation caused by process noise (e.g., turbulence) and output measurement noise (e.g., sensor electrical noise)—subject to the assumption that the noise is uncorrelated with the prescribed excitation inputs, which is usually the case. This drops the requirement to identify a noise model structure and associated parameters, a necessary step when using time-domain maximum-likelihood identification methods. Alternatively, a common simplification adopted in time-domain identification studies is to assume that the process noise is not important (*output-error method*) or that the measurement noise is not important (*equation-error method*), as discussed by Hamel.<sup>10</sup> In situations involving reduced signal-to-noise content in the test data, which is often the case for real flight data, ignoring the noise will introduce biases in the identified parameters. By using the frequency-response calculation of Eq. (2.1), the bias effects of the noise will drop out, thus greatly reducing the number of identification parameters without compromising identification accuracy. Also, with the effects of noise eliminated, the parameter error bounds are determined with much greater accuracy. Still, the presence of these noise sources introduces random scatter in the identification results and degrades the accuracy of the identified parameters.

*Access to the coherence function as an unbiased measure of nonparametric identification accuracy and linearity:* The coherence function estimate

$$\text{coherence} = \hat{\gamma}_{xy}^2(f) = \frac{|\hat{G}_{xy}(f)|^2}{|\hat{G}_{xx}(f)||\hat{G}_{yy}(f)|} \quad (2.2)$$

is obtained directly from the measurements. [The estimate symbol  $\hat{\cdot}$  and the dependency on discrete frequency ( $f$ ) are generally dropped for notational convenience, but are implied throughout.] The coherence provides a key measure of the frequency-response accuracy as a function of frequency, without any dependency on parametric model structures (as is the case for the innovations metric in the time-domain methods). It indicates whether the system has been satisfactorily excited across the entire frequency ranges of interest and shows whether the system being modeled is well characterized as a linear process in this frequency range. Coherence data can be evaluated in real time from the telemetry stream to determine the level and effect of noise in the instrumentation system, the adequacy of the flight-testing inputs in exciting dynamics of interest, and the influence of atmospheric disturbances. During the parametric system identification step, the coherence function determines the appropriate frequency range for model fitting and is used effectively to weight the data to emphasize the frequency-response points that have higher accuracy. The availability of the coherence function is one of the primary advantages of the frequency-response identification method.

*The wealth of knowledge concerning appropriate model structure provided by the nonparametric identification results:* The frequency-response data provide a nonparametric model, exposing many key aspects of the vehicle dynamics without requiring that a parametric (transfer-function or state-space) model first be identified. The frequency responses expose the estimates of control derivatives, key dynamic modes, degree of stability, order of system response, presence of time delays, and degree of coupling. This information provides important insight

## FREQUENCY-RESPONSE METHOD FOR SYSTEM IDENTIFICATION 31

into vehicle dynamics needed for the selection of an appropriate parametric (e.g., state-space) model structure. Using the method explained in Sec. 13.5.3, the state-space model structure can be significantly simplified when a particular frequency response exhibits no significant input-to-output energy transfer (as indicated by very low coherence over the entire frequency range). Model structure selection and reduction are perhaps the most important and difficult aspects of system identification for aircraft and rotorcraft, especially so for unique configurations (such as UAVs).

*Frequency ranges selected individually for each input/output pair to include only accurate data:* In system identification, state-space models that best fit the multi-input/multi-output flight-test database are determined. For the frequency-response method, this database is composed of the pair-wise (input/output) frequency responses and associated coherence functions. The frequency ranges for the identification criterion are selected individually for each input/output pair according to the range of good coherence. For example, the velocity responses (e.g.,  $u/\delta_e$ ) will generally be most accurate (good coherence) at low frequencies (0.1–1 rad/s) in the frequency range of the phugoid response and be much less accurate (unacceptable coherence) at higher frequencies. On the other hand, the angular-rate responses (e.g.,  $q/\delta_e$ ) will often exhibit good coherence over a broad frequency (0.1–10 rad/s), which includes both phugoid and short-period responses. The frequency points included in the identification criterion are then selected linearly across the logarithmic scale of the appropriate frequency range for each response pair. By including only the most accurate data, a more reliable model is obtained. In time-domain methods, the identification criterion includes all responses over the same time (and equivalent frequency) ranges.

*Direct and accurate identification of time delays:* Time delays and equivalent time delays are commonly found in various components of a flight vehicle, and their accurate determination is crucially important, both for achieving overall model parameter accuracy and as a key aspect of handling-qualities and flight-control applications. There are “pure” digital delays associated with flight control and flight-data processing. Frequently, there are many sources of high-order/high-frequency dynamics (e.g, the dynamics of linkages/hydraulics, control system and instrumentation filters, and the rotor/inflow dynamic system in the case of rotorcraft) that yield phase lags in the frequency range of interest and contribute to the “equivalent delay.” In the frequency-response identification method, these important time delays are identified directly and very accurately owing to the linear relationship between the time delay  $\tau$  and frequency-response phase shift with frequency  $\omega$  (rad/s):

$$\varphi = -\tau\omega \text{ rad} \quad (2.3)$$

Because the identification cost function is based on the weighted sum of the magnitude and phase error, the cost function is a linear function of the time delay and can thus be identified very accurately. (This is not true in the time-domain identification cost function.) In fact, an accurate estimate of time delay can be made directly from the identified frequency-response plots; this is a key aspect of handling-qualities analysis for rotorcraft.

*Elimination of biases and reference shifts as identification parameters:* This important feature of the frequency-response identification method (and frequency-domain methods in general) results from eliminating the need to determine many biases and measurement offsets in the real flight data, as is necessary in time-domain identification methods. To see why this is so, we consider the identification of state-space models.

The model to be identified is represented as a set of first-order linear differential equations of motion representing the transient response from trim of the state vector  $\mathbf{x}$  to control input  $\mathbf{u}$ :

$$\dot{\mathbf{x}} = \mathbf{Ax} + \mathbf{Bu}(t - \boldsymbol{\tau}) + \mathbf{bias} \quad (2.4)$$

In these equations, the unknowns of interest for system identification are the elements of  $\mathbf{A}$  (stability derivatives),  $\mathbf{B}$  (control derivatives), and  $\boldsymbol{\tau}$  (equivalent time delays). The time-delay vector is a lumped model of the high-order dynamics not explicitly included in the state-space model. We must also include a vector of constant unknown biases (**bias**) in Eq. (2.4) to accommodate unmeasurable inputs (e.g., turbulence), initial conditions in the dynamic states, biases in the assumed values of trim-control inputs, and errors in the model structure, all of which are prevalent in applications of system identification to real flight data. Regardless of their physical sources, the biases drive the aircraft through the equations of motion, and their effects on model matching error can become very difficult to distinguish from the elements of  $\mathbf{A}$  and  $\mathbf{B}$ .

Generally, not all of the state variables can be measured, and so we define a measurement vector  $\mathbf{y}$ ,

$$\mathbf{y} = \mathbf{Cx} + \mathbf{Du}(t - \boldsymbol{\tau}) + \mathbf{yref} \quad (2.5)$$

to relate the measured quantities in terms of the states and controls. The equation includes the vector of constants **yref**, associated with the steady-state offsets that are often present in the measurement devices, such as rate gyros (that measure angular rates) and accelerometers (which measure specific aerodynamic forces). For example, there is a  $-1g$  (up) trim bias in the vertical-acceleration measurement for a level flight condition. The elements of  $\mathbf{C}$  and  $\mathbf{D}$  are usually known from kinematics or are repeated values of the same stability and control derivatives contained in  $\mathbf{A}$  and  $\mathbf{B}$  (for the accelerometer measurements). In the time-domain output-error identification method, the elements of  $\mathbf{A}$ ,  $\mathbf{B}$ ,  $\boldsymbol{\tau}$ , **bias**, and **yref** are adjusted, and the equations of motion are time integrated until the error between the model output  $\mathbf{y}$  and the flight-data measurements is minimized. The state-space model parameters of interest are contained in  $\mathbf{A}$ ,  $\mathbf{B}$ , and  $\boldsymbol{\tau}$ . The elements of **bias** and **yref** are referred to as *nuisance parameters*<sup>6</sup> because they complicate the time-domain identification process and they must be included, even though they are later discarded.

In the frequency-response identification method, the error function between the measured and model frequency responses is minimized. The MIMO frequency-response matrix of the identified model for control-surface inputs is obtained by

taking the Laplace transform of Eqs. (2.4) and (2.5), yielding

$$\mathbf{T}(s) = (\mathbf{C}[s\mathbf{I} - \mathbf{A}]^{-1}\mathbf{B} + \mathbf{D})e^{-\mathbf{\tau}s} \quad (2.6)$$

The frequency-response matrix isolates the forced response to control inputs, so that the influence of initial conditions, biases, and offsets drops out of the problem. Now the solution of the identification problem using the frequency-response identification method involves tuning only the elements of  $\mathbf{A}$ ,  $\mathbf{B}$ , and  $\mathbf{\tau}$  over a specified frequency range of interest ( $s = j\omega$ ;  $\omega = \omega_{\min}$  to  $\omega_{\max}$ ) until the error between the model and flight-data frequency responses is minimized.

Let us now examine the resulting number of unknowns in a typical identification of the flight dynamics. If we choose to neglect the transient response of the rotor (in the case of helicopters), the flight dynamics of the aircraft are composed of six degrees of freedom (three angular and three linear). As described in detail in Sec. 13.4, the formulation of the equations of motion in state-space form results in eight states, four control inputs, and generally nine measurements. When the air-vehicle configuration has symmetrical geometric and response properties, as in the case of fixed-wing aircraft, the equations can be separated into two decoupled sets of three-DOF systems. This is not the case for single rotor helicopters, which must consider the six-DOF system as fully coupled. The dynamic parameters of interest in the identification are the aerodynamic stability and control derivatives (36 contained in the  $\mathbf{A}$  matrix and 24 contained in the  $\mathbf{B}$  matrix for the coupled six-DOF case) and the four time-delay parameters (contained in the  $\mathbf{\tau}$  matrix), for a total of 64 unknowns.

In time-domain identification methods we also need to identify eight bias terms, one for each state in Eq. (2.4). In addition, the multiple records of flight data need to be linked together, one record for a maneuver in each of the four control axes, to form a single database that ensures identifiability. This adds nine output reference shifts for each time-history record, for a total of 36 additional terms ( $\mathbf{yref}$ ) to be identified. In all, there are 44 extraneous bias and reference-shift terms that can be highly correlated with the identification parameters of interest, thereby making the identification analysis much more difficult. As the order of the dynamic system being modeled increases—as happens, for example, in the case of rotorcraft—the time-domain algorithms become significantly burdened by these extra nuisance parameters that must be identified, and the frequency-response identification method becomes increasingly attractive and much more widely used.

*Significant improvement in computational efficiency:* An identification criterion  $J$  is a single parameter that characterizes the error between the flight data and the identified model. In frequency-domain methods, it is based on the squared errors between the frequency-response functions obtained from the model and the flight data. In time-domain methods, it is based on the squared errors between the time histories of the model predictions and the flight data. The identification algorithm varies the identification parameters to minimize the value of the identification criterion. In the frequency domain, the cost function is an algebraic function of the identification parameters, so that each iterative update is computationally very fast. In contrast, the time-domain cost function requires the

integration of the equations of motion, so that each iterative update is computationally intensive. This difference in computational efficiency is increased greatly as a result of the difference in the number of points included in the two identification criteria, as will be discussed next.

It is instructive to compare in detail the number of data points to be included in the identification criteria  $J$  for frequency-domain vs time-domain methods applied to the same aircraft. Consider the case discussed earlier of identifying a six-DOF state-space model for a rotorcraft. The flight-test data might typically be composed of four distinct maneuvers—one 50-s maneuver for each of the four control inputs (roll, pitch, yaw, and heave). There are typically nine response variables of interest (three angular rates, three velocities, and three accelerometers). These four inputs and nine outputs result in 36 frequency-response pairs to be considered in the frequency-response identification method. The identification criterion includes both magnitude and phase errors at each of (typically) 20 discrete frequency values, for a total of  $36 \cdot 20 \cdot 2 = 1440$  data points to be included in the cost function. The analogous time-domain cost function works directly with the four flight-data records. For a typical data rate of 50 samples/s (50 Hz) and the same nine outputs, the time-domain cost function will be composed of  $50 \cdot 50 \cdot 9 \cdot 4 = 90,000$  data points as part of the identification of the stability and control derivatives (and extraneous biases and offsets). This amounts to a considerable increase in the computational complexity as compared to the frequency-response method.

It is important to remember that we must process just as many flight-data points whether the analysis is carried out in the time domain or in the frequency domain. The difference is that in the frequency-domain methods the conversion from time-history flight data to frequency-response data is done as a batch (noniterative) calculation using FFT methods and is not linked to the identification of the stability and control derivatives. The same 90,000 points are processed using FFT techniques to extract the MIMO frequency-response database. But from that point on, the iterative identification of the parametric model is based only on the 1440 points in the frequency-domain cost function, a reduction factor of about 60 compared to the time-domain analysis, which will require the iterative processing of the original 90,000 data points.

This difference in computational burden can be quite significant when a high sample rate is needed, such as for higher-order systems (e.g., rotorcraft) or for aircraft model identifications that include widely spaced structural modes, and it gives a considerable advantage to the frequency-response identification method (as also pointed out by Raisinghani and Goel<sup>57</sup>).

The example presented herein is based on the assumption that the same input signal is used for time-domain and frequency-domain identification methods. The 3-2-1-1 multistep input, commonly adopted for time-domain identification, is typically about half the duration of a frequency sweep, used for frequency-domain identification methods. This can be seen in the AGARD flight-test database for the Bo-105 helicopter identification.<sup>10</sup> Thus the actual reduction in the number of points is probably closer to about 30.

*Identification of systems with unstable dynamics:* Modern fixed-wing aircraft, especially high-performance aircraft, are typically designed with neutrally stable

## FREQUENCY-RESPONSE METHOD FOR SYSTEM IDENTIFICATION 35

or unstable bare-airframe characteristics for improved agility and reduced trim drag. The bare-airframe characteristics of rotorcraft are unstable as a result of the vehicle configuration. The identification of the bare airframe must be capable of working with the unstable characteristics associated with the vehicle response to control-surface deflections.

The frequency-response identification method, and frequency-domain-based identification methods in general, are especially well suited to the identification of systems with unstable dynamics. Because the model matching is conducted entirely in the frequency domain, we avoid the need to conduct time-history integrations during the identification process. An unstable dynamic mode shows up simply as a *phase increase* at the relevant mode, as compared to a phase decrease for stable modes. By contrast, the time-domain identification methods involve forward time integration of the trial model response to the measured inputs. Because there will always be some modeling or measurement errors present, right half-plane eigenvalues will cause the time integration of the model to diverge rapidly from the flight-test responses, and the identification process will break down. This weakness of time-domain system identification can be overcome by mapping the model and the data through a stabilizing transformation,<sup>58</sup> but only at the expense of reduced accuracy in the identification of the unstable modes. As a result, frequency-domain methods are widely used for system identification of flight vehicles with unstable dynamic characteristics—such as rotorcraft and high-performance fighter aircraft. The flight-testing procedure must include some stabilization from the pilot or the stability augmentation system in order to provide flight-test data with bounded inputs and outputs as is required (Sec. 7.2). But the identification of the bare-airframe characteristics uses the control surface inputs (rather than the piloted inputs) together with the corresponding vehicle responses.

### 2.3 Frequency-Response Identification Method Applied to the XV-15 Tilt-Rotor Aircraft

So far this chapter has presented a general overview of the frequency-response identification method and typical applications to fixed-wing and rotary-wing aircraft dynamics and control. We now turn our attention to the specific example of the system identification of XV-15 tilt-rotor aircraft dynamics, which has been studied extensively with CIFER® and is used throughout the book to illustrate the key steps in the frequency-response identification method (Fig. 2.1). The following summary of XV-15 identification for hover and cruise gives the reader a sense of the typical identification results and achievable accuracy, with the analysis details examined in the following chapters of this book.

The XV-15 tilt-rotor aircraft can be operated over a broad speed range from hover to 300 km by tilting the prop-rotor nacelle from 90 deg (prop rotation axis vertical) to 0 deg (prop rotation axis horizontal). In its hover configuration, shown in Fig. 2.2, the XV-15 tilt rotor has many of the key flight dynamics properties of a hovering helicopter and vertical/standard takeoff and landing (V/STOL) aircraft, albeit without the strong degree of dynamic coupling seen with single-rotor helicopters. Figure 2.3 shows the aircraft in a forward flight or cruise configuration in which it has many of the key characteristics of a typical fixed-wing aircraft.



Fig. 2.2 XV-15 tilt-rotor aircraft in hover configuration (NASA photo).

### 2.3.1 XV-15 Frequency-Sweep Data: $V = 170 \text{ kn}$

As an illustration of the first two blocks in Fig. 2.1 (*Frequency Sweep Inputs and Aircraft*), the basic input used for identification of the XV-15 in cruise is a frequency sweep. Figure 2.4 shows flight-test data recorded at an indicated air-speed of 170 kn. The first plot shows the pilot lateral input  $\delta_{\text{lat}}$  and the second the roll-rate response  $p$ .

There are some basic dos and don'ts that will be discussed later regarding how this frequency-sweep maneuver should be executed for best identification results,



Fig. 2.3 XV-15 tilt-rotor aircraft in cruise configuration (NASA photo).

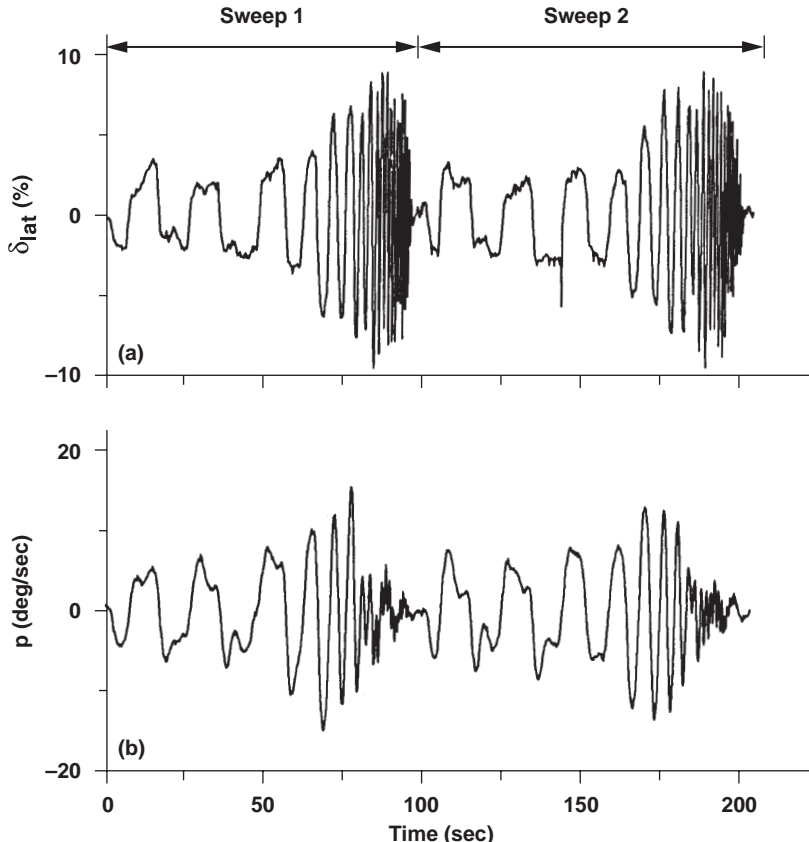


Fig. 2.4 Two lateral-stick frequency sweeps in cruise.

but it should be clear that in order to get a good identification the dynamics must be excited well. Figure 2.4 shows two pilot sweeps that have been concatenated (linked) together along with the roll-rate response. The graphs show that the flight-test method produced a sizeable excitation, as can be seen by the actual response of the aircraft, with roll-angle variations of up to  $\pm 15$  deg/s. This ensures that the identified model will be accurate for typical maneuvering flight involving large excursions, as shown later in Figs. 2.9 and 2.10, and will not be limited to small (perturbation) inputs.

### 2.3.2 *Simulation Model Validation*

As shown in the block labeled *Applications* in Fig. 2.1, the validation of a simulation model is one of the applications that can be performed directly from the nonparametric (frequency-response) results. Figure 2.5 shows the roll-rate response  $p$  to aileron input  $\delta_a$  in hover. The ailerons are actuated by the same

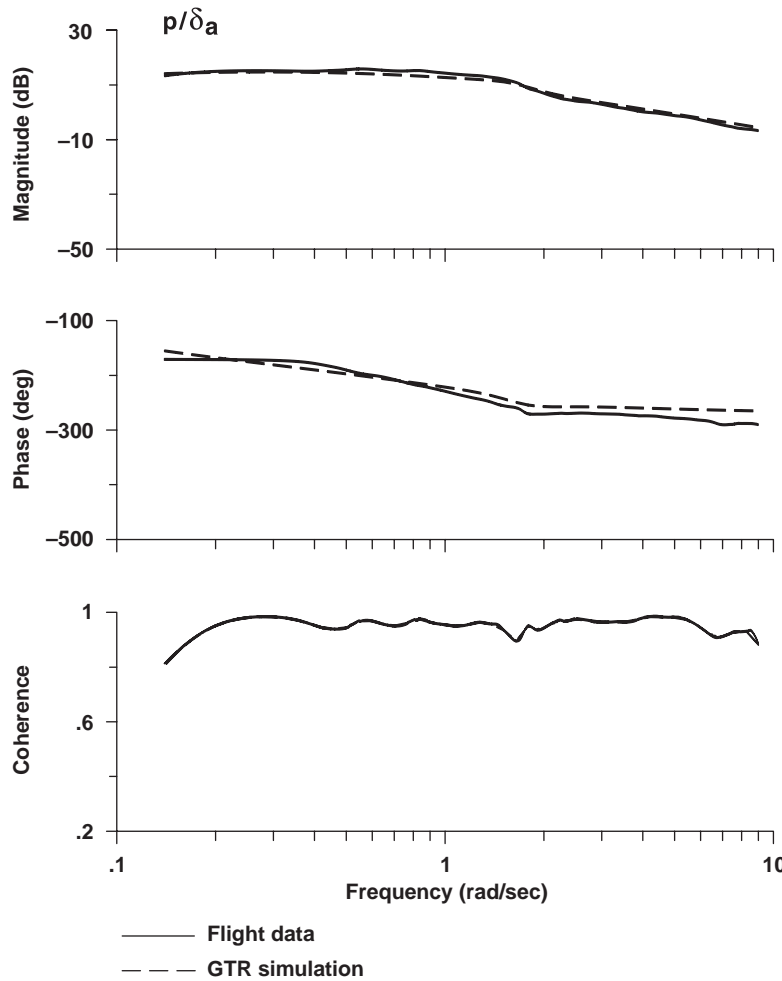


Fig. 2.5 Roll-response comparison of flight vs simulation.

signal as the differential rotor collective, the latter being the source of roll control in hover. Therefore, the aileron measurement provides a consistent measurement of roll-control input for the entire flight envelope from hover through forward flight. The solid lines in the first two subplots (Fig. 2.5) present the aircraft frequency-response  $p/\delta_a$  in magnitude and phase vs frequency derived from the block labeled *Conditioned Frequency Responses & Partial Coherences* in Fig. 2.1. The third subplot (Fig. 2.5) shows the coherence function  $\gamma_{xy}^2$ , which is a good indicator of the accuracy of the identified response. When the coherence exceeds ( $\gamma_{xy}^2 \geq 0.6$ ), the response is considered accurate (low scatter). This is also seen in the very smooth frequency response over a wide range of frequencies.

## FREQUENCY-RESPONSE METHOD FOR SYSTEM IDENTIFICATION 39

The dotted lines in Fig. 2.5 show the results of a detailed physics-based simulation model, namely, the generic tilt-rotor (GTR) simulation, a math model developed by Bell Helicopter. The cruise flight condition results of Fig. 2.5 show that the GTR math model matches the flight-test data very well. In general, the match between an aircraft math model and the flight-test data might not be this close. The GTR math model, however, is very detailed and uses many aerodynamic force and moment look-up tables obtained from full-scale XV-15 wind-tunnel test data. Figure 2.5 provides a clear indication that the GTR model is very accurate. The (small) magnitude and phase errors can be quantified in terms of allowable “mismatch” tolerances to demonstrate satisfactory frequency-domain simulation validity.

### 2.3.3 Transfer-Function Model Identification

Next, we will consider the transfer-function model identification (*Transfer-Function Modeling* in Fig. 2.1) of the roll-rate response in cruise for handling qualities or flight-control applications. The flight response of Fig. 2.5 is repeated in the solid line of Fig. 2.6.

Recall that a transfer-function model is one of the two types of parametric models discussed in Sec. 1.4, and so it is necessary to assume an identification model structure. For example, we can choose to assume that the lateral-directional response of a fixed-wing test aircraft in cruise flight exhibits the classical flight-dynamics modes of response. The lateral-directional transfer functions will have a common denominator, containing the spiral, Dutch-roll, and roll-subsidence modes. The numerator dynamics are distinct for each input-to-output pair, and they will each include an aerodynamic control derivative, zeros, and a time delay.<sup>59</sup>

In our cruise-flight example, the preceding assumptions lead to the following transfer-function model for roll-rate response to aileron:

$$\frac{p}{\delta_a}(s) = \frac{L_{\delta_a} s [\zeta_\phi, \omega_\phi] e^{-\tau_\phi s}}{(1/T_s)(1/T_r)[\zeta_{dr}, \omega_{dr}]} \quad (2.7)$$

where we have adopted the shorthand notation for factors of the transfer-functions:

$$\left(\frac{1}{T}\right) \Rightarrow \left(s + \frac{1}{T}\right); \quad [\zeta, \omega_n] \Rightarrow [s^2 + 2\zeta\omega_n s + \omega_n^2] \quad (2.8)$$

The model parameters that best characterize the XV-15 flight-data response for cruise are determined using CIFER® (as described in Sec. 11.6.2):

$$\frac{p}{\delta_a}(s) = \frac{-4.60s[0.278, 1.93]}{(0.0912)(1.00)[0.237, 1.67]} e^{-0.0533s} \text{ deg/s/deg-ail} \quad (2.9)$$

This identified transfer-function model is plotted in the dashed line of Fig. 2.6 and is seen to match the flight-test data very well.

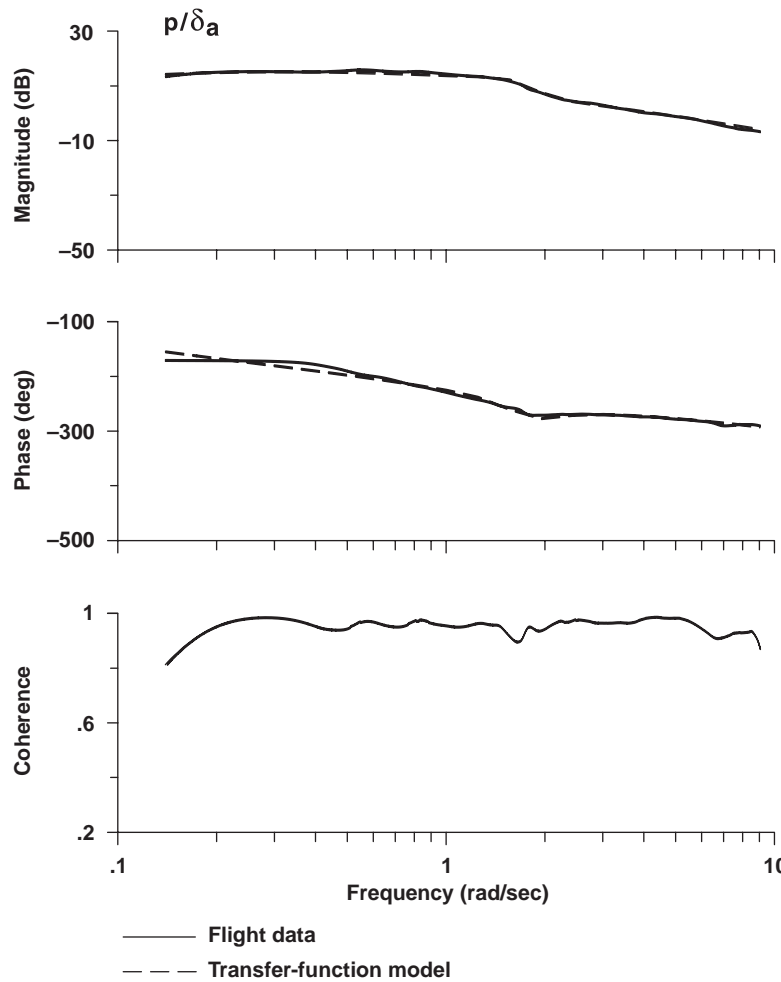


Fig. 2.6 Roll-response transfer-function model identification (XV-15, cruise).

The extracted parameters provide important information about the aircraft dynamics characteristics. First of all, the time delay is small ( $\tau = 0.053$  s) and is associated mostly with the control linkage dynamics in the system. There is a stable low-frequency spiral mode (nearly at the origin), which is characterized by a very long period response in roll and sideslip. The roll convergence mode, with a frequency of 1 rad/s, dominates the on-axis roll response to aileron inputs. Finally, we see that the lightly damped Dutch-roll mode ( $\zeta_{dr} = 0.24$ ,  $\omega_{dr} = 1.7$  rad/s) is nearly cancelled by a nearby zero, and therefore does not contribute significantly to the roll response to aileron inputs. All of this information about the dynamic characteristics of the system is contained in the identified transfer function.

### 2.3.4 Handling-Qualities Specifications

Handling-qualities analysis and handling-qualities specification compliance testing for fixed-wing aircraft (e.g., Ref. 5) are based heavily on the results of transfer-function system identification modeling. Consider Fig. 2.7, which shows the s-plane location of roll-rate transfer-function parameters of Eq. (2.9), corresponding to the XV-15 cruise response for roll  $p/\delta_a$ . The boundary for minimum roll mode ( $1/T_r$ ) shown in this chart is an example of the fixed-wing specification for satisfactory (i.e., level 1) handling; the location of the corresponding pole shows that the criterion has been met. The amount of separation between the  $[\zeta_{dr}, \omega_{dr}]$  pole and the  $[\zeta_\phi, \omega_\phi]$  zero is specified to limit the level of roll-yaw coupling in the Dutch-roll response. Finally, there are bounds on the minimum damping of the low-frequency spiral mode ( $1/T_s$ ).

### 2.3.5 Stability and Control Derivative Model Identification in Cruise

Transfer-function model identification provides a parametric description of the input-to-output behavior in terms of poles and zeros, which characterize the dynamic modes of motion and responses to controls. These methods are best suited to SISO system modeling and become cumbersome for systems with higher levels of coupling. Further, there are many applications that require a complete model of the system in terms of the differential equations of motion as represented in state-space form. The coefficients of the differential equations

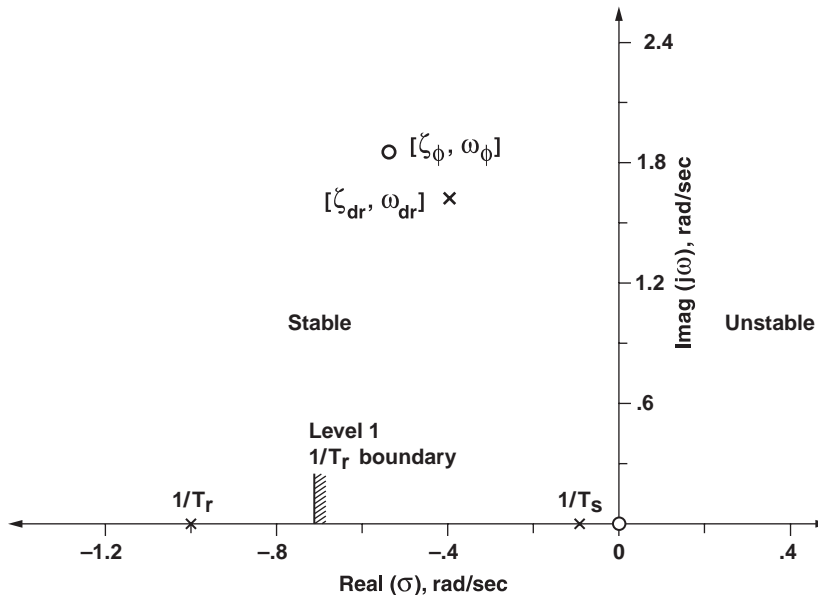


Fig. 2.7 Location of roll-rate transfer-function parameters in the s-plane.

(elements of the state-space matrices) are the stability and control derivatives to be identified. This section will present an overview of the results for stability and control identification (*Mathematical Model...* in Fig. 2.1) of the XV-15 in a cruise flight condition of  $V = 170$  kn (true airspeed).

Incorporating a mass matrix  $\mathbf{M}$  in the conventional state-space representation of Eqs. (2.4) and (2.5) adds greater flexibility in the defining the identification model structure:

$$\dot{\mathbf{Mx}} = \mathbf{Fx} + \mathbf{Gu}(t - \tau) + \mathbf{bias} \quad (2.10)$$

The measurement output equation is

$$\mathbf{y} = \mathbf{Hx} + \mathbf{Ju}(t - \tau) + \mathbf{yref} \quad (2.11)$$

The stability and control parameters, contained in the  $\mathbf{M}$ ,  $\mathbf{F}$ ,  $\mathbf{G}$ , and  $\tau$  matrices of the state equation, are identified by simultaneously matching the eight frequency-response pairs. For the cruise condition, the inputs are aileron  $\delta_a$  and rudder  $\delta_r$ . The outputs are roll rate  $p$ , yaw rate  $r$ , lateral accelerometer  $a_y$ , and sideslip angle  $\beta$ . Four of the response pairs ( $p/\delta_a$ ,  $a_y/\delta_a$ ,  $p/\delta_r$ ,  $\beta/\delta_r$ ) are shown in the magnitude and phase plots of Figs. 2.8. In each graph, the flight-test data are indicated by solid lines, and the response obtained from the identified stability and control derivative model is indicated by the dashed lines.

In forward flight, the flight database for system identification is typically of higher quality than for a hovering condition. This is because of the combination of generally larger inputs in cruise and reduced gust response—resulting in a high signal-to-noise ratio, and therefore high values of coherence as seen in Fig. 2.8. High levels of coherence reflect low random error (i.e., low scatter), consistent with the smooth identified frequency responses seen in the plots.

Table 2.1 shows the parameters of the  $\mathbf{F}$  matrix, the *stability derivatives*, such as the key parameters of lateral dihedral  $L_v$ , roll damping  $L_p$ , and yaw damping  $N_r$ , all of which have typical values for fixed-wing aircraft. Shown in Table 2.2 are the parameters of the  $\mathbf{G}$  matrix, the *control derivatives*, such as roll control  $L_{\delta_a}$  and yaw control  $N_{\delta_r}$ . We also note that the identified value of the roll control derivative

$$L_{\delta_a} = -0.07775 \text{ rad/s}^2/\text{deg-ail} = -4.455 \text{ deg/s}^2/\text{deg-ail} \quad (2.12)$$

nearly matches the high frequency (acceleration response) gain of the roll-rate response transfer-function model identified in Eq. (2.9), as expected.

As will be discussed in Chapter 12, the Cramér–Rao bound, given in the last column in the table, is a reliable measure of parameter accuracy for the frequency-response identification method. In general, if the flight-test data are reasonably good (i.e., light turbulence, good excitation, kinematically consistent data), it is possible to identify most parameters to within a 10–20% accuracy, as in this case, which we consider quite acceptable.

## FREQUENCY-RESPONSE METHOD FOR SYSTEM IDENTIFICATION 43

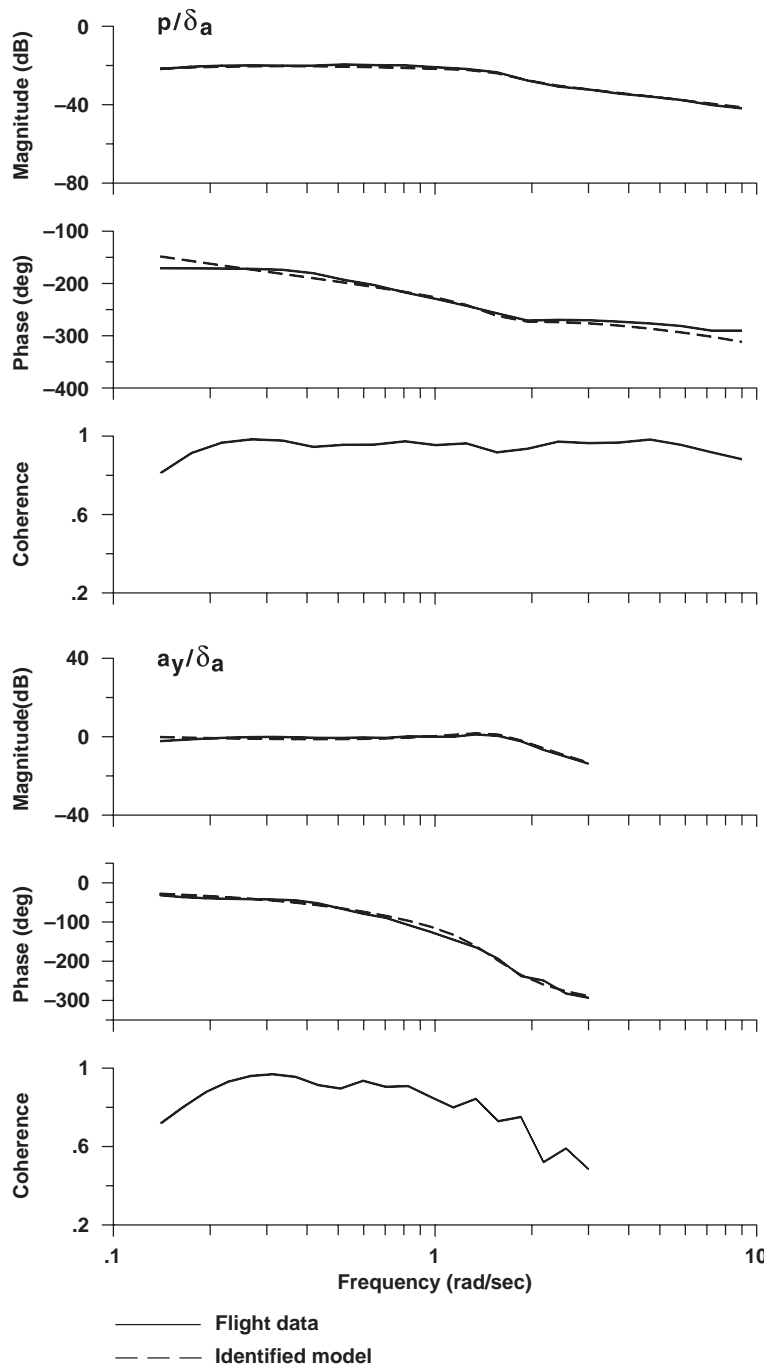


Fig. 2.8 Frequency responses for XV-15 in cruise.

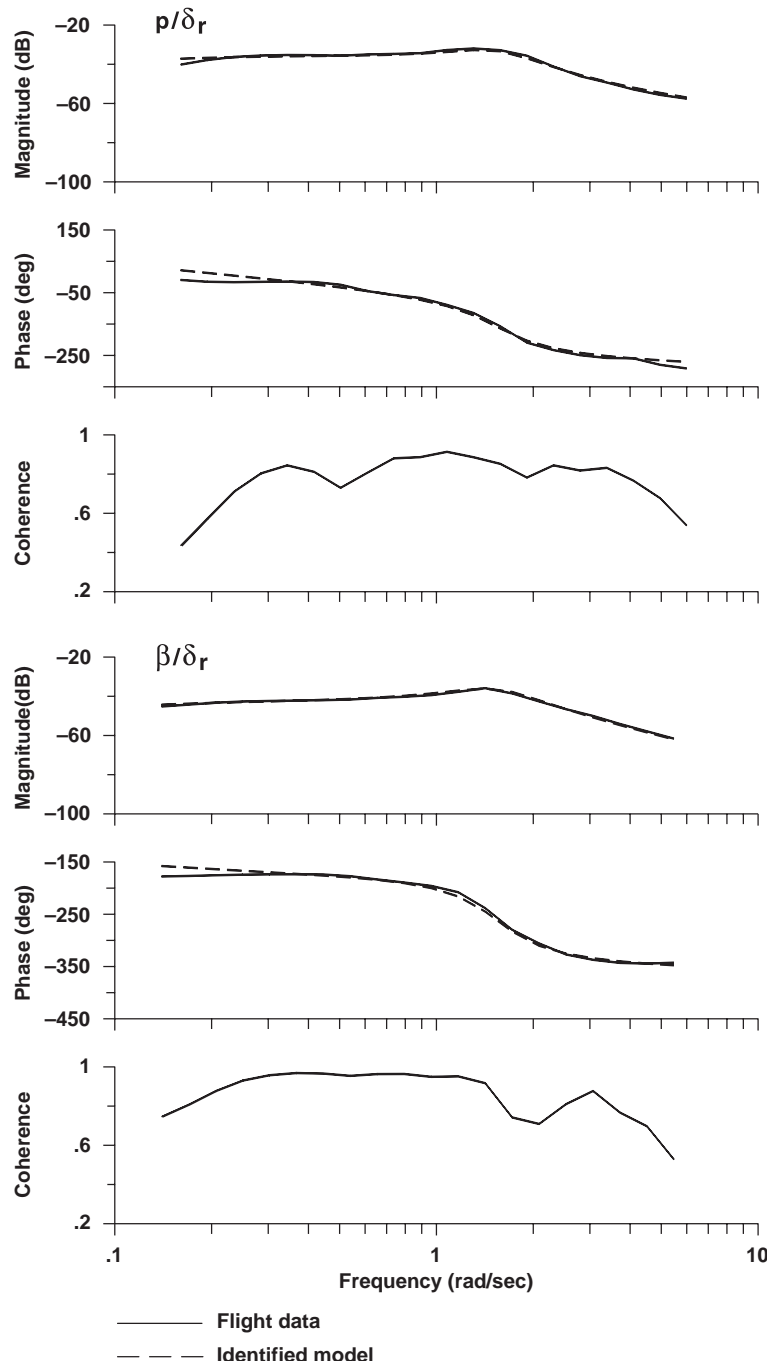


Fig. 2.8 Frequency responses for XV-15 in cruise (continued).

**Table 2.1** *F-matrix identification for XV-15 in cruise<sup>a</sup>*

Derivative	Parameter value	Cramér–Rao, %
$Y_v$	–0.2797	3.64
$Y_p$	–1.984	31.32
$Y_r$	16.44	9.65
$L_v$	–8.119E-03	4.23
$L_p$	–0.6780	6.03
$L_r$	0.000 <sup>b</sup>	—
$N_v$	7.240E-03	2.85
$N_p$	–0.2308	7.57
$N_r$	–0.9759	5.05

<sup>a</sup>All results in English units.

<sup>b</sup>Eliminated during model structure determination.

**Table 2.2** *G-matrix identification for XV-15 in cruise<sup>a</sup>*

Derivative or symbol	Parameter value	Cramér–Rao, %
$Y_{\delta_a}$	0.000 <sup>b</sup>	—
$Y_{\delta_r}$	–0.2173	8.35
$L_{\delta_a}$	–0.07775	4.27
$L_{\delta_r}$	–7.024E-03	10.09
$N_{\delta_a}$	–0.02166	4.66
$N_{\delta_r}$	0.02213	3.14
<i>Time delays</i>		
$\tau_a$	0.08920	11.84
$\tau_r$	0.03276	25.10

<sup>a</sup>Control deflections in degrees.

<sup>b</sup>Eliminated during model structure determination.

### 2.3.6 Time-Domain Verification of Cruise Model

Next we demonstrate the time-domain verification of the identified state-space model for cruise (*Verification* in Fig. 2.1). The verification is conducted with cruise flight data not used in any way in the identification process (*Dissimilar flight data not used in identification* in Fig. 2.1). Recall that frequency sweeps were used (Fig. 2.4) in the model identification process. It is also important to remember that the model is already identified, and no adjustments are made at this step to any of the parameters of  $\mathbf{M}$ ,  $\mathbf{F}$ ,  $\mathbf{G}$ , and  $\boldsymbol{\tau}$ . A simple least-squares algorithm (Sec. 14.3) first determines the needed constant biases and reference shifts in Eqs. (2.10) and (2.11), and then the model is driven open loop and compared to the flight-test data.

The verification for a step input in roll is shown in Fig. 2.9. The measured responses to this input, namely, roll rate  $p$ , yaw rate  $r$ , lateral acceleration  $a_y$ , sideslip  $\beta$ , and roll angle  $\phi$ , are shown by the solid line. Next, the same step input

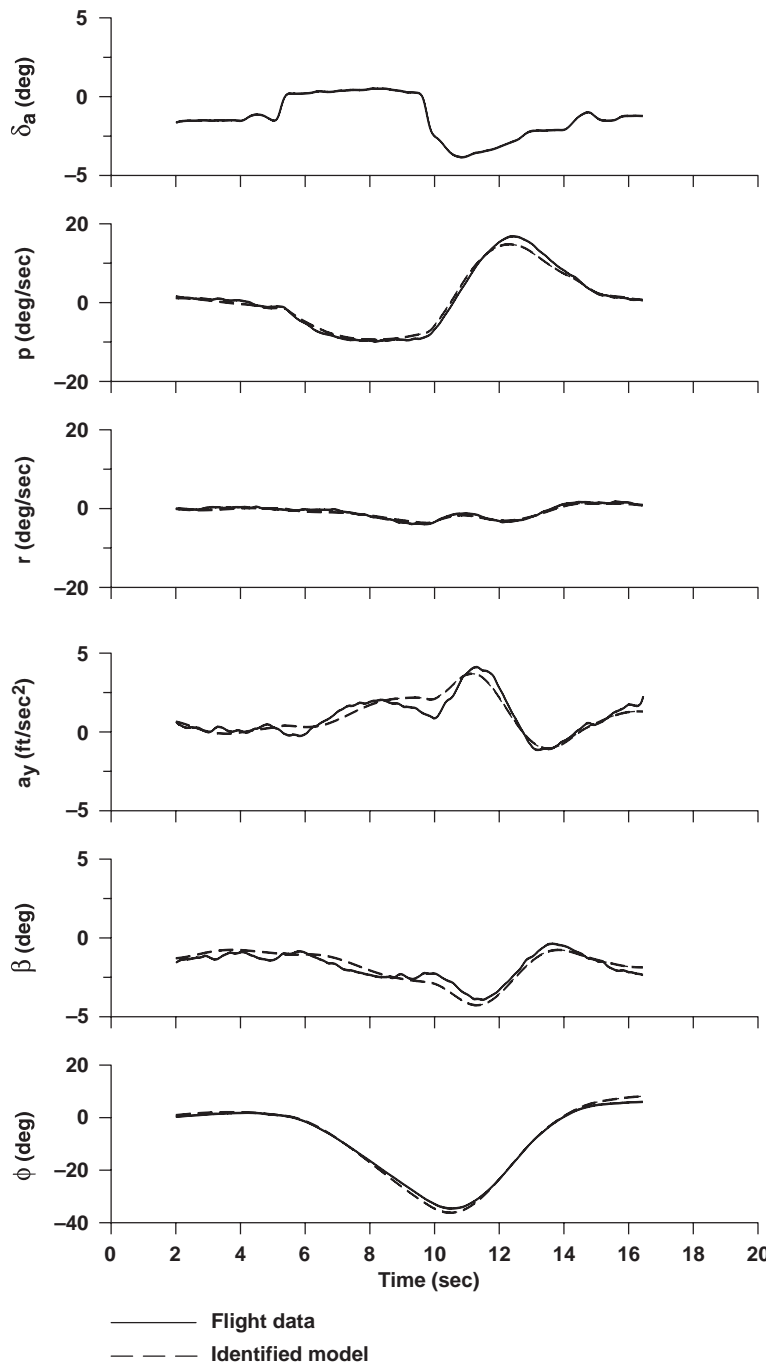


Fig. 2.9 Verification of identified model for XV-15 in cruise (aileron input).

## FREQUENCY-RESPONSE METHOD FOR SYSTEM IDENTIFICATION 47

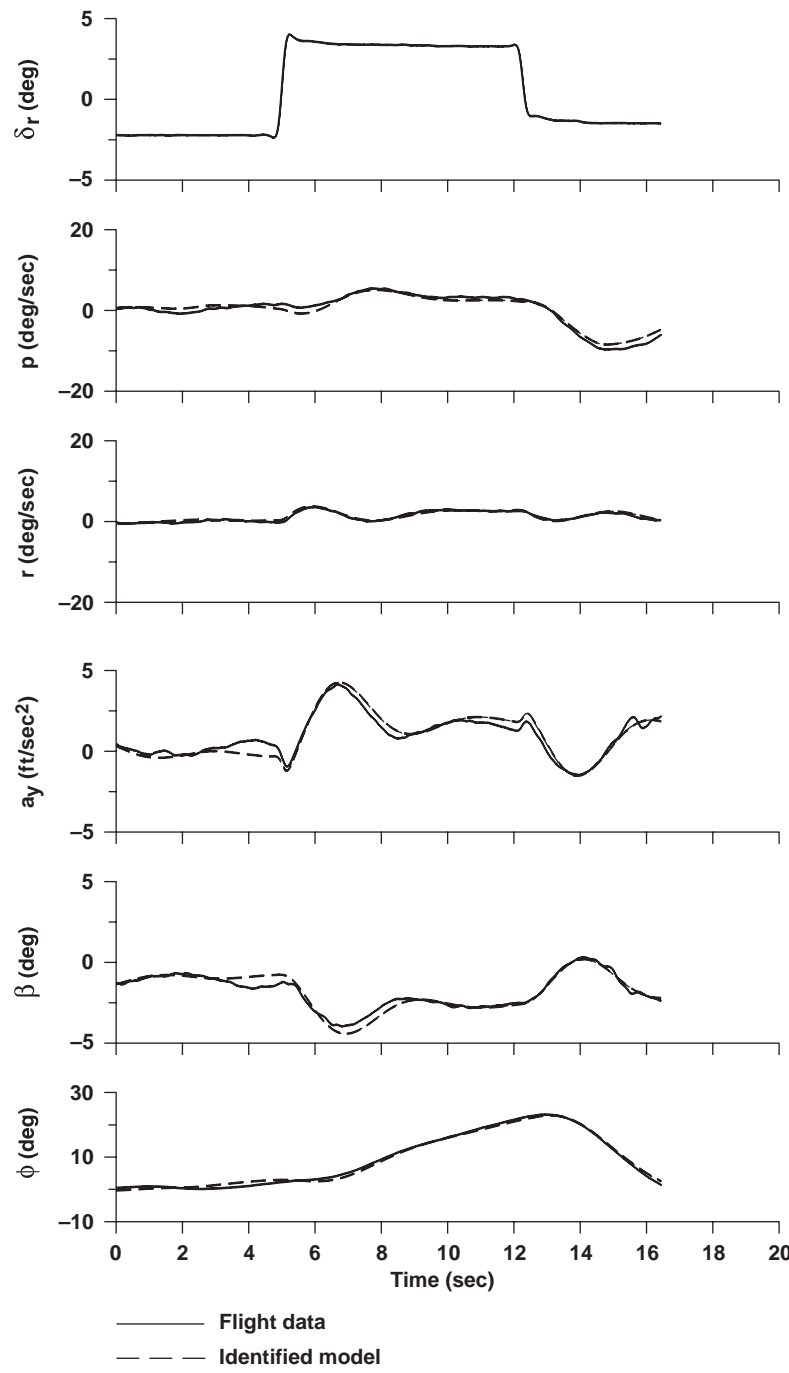


Fig. 2.10 Verification of identified model for XV-15 in cruise (pedal input).

is used to drive the extracted state-space model; the output generated by the model is the dashed line of the figures. The analogous verification for a yaw input is shown in Fig. 2.10. The results show that the model achieves excellent time-response predictions for step inputs in aileron and rudder. Both on-axis and coupling responses to each input are predicted very well.

Note that the roll-angle variations for the verification response are as large as 30–40 deg, which again underscores the fact that the validity of the model identified using the frequency-response method is *not restricted to small-perturbation motions*. Indeed, the extracted frequency response and the associated state-space models constitute linearized describing functions, or optimal linear models, of the nonlinear systems. Clearly, a 40-deg roll-angle transient is not generally considered to be within the linear response range, and yet the prediction is excellent.

### 2.3.7 Stability and Control Derivative Model Identification and Verification in Hover

A state-space model was also identified from the XV-15 flight data for the hover condition, as is shown in Fig. 2.11. The responses shown are the roll attitude response to aileron input ( $\phi/\delta_a$ ), lateral velocity response to aileron input ( $v/\delta_a$ ), yaw-rate response to aileron input ( $r/\delta_a$ ), and yaw-rate response to rudder input ( $r/\delta_r$ ). For hovering and low-speed flight, the sideslip vane reading  $\beta$  is not meaningful, and instead we use the lateral velocity  $v$  that is reconstructed from the lateral accelerometer  $a_y$  and roll angle  $\phi$  measurements (Sec. 6.2.3).

In hovering flight, the flight database for system identification is typically of poorer quality than for cruise flight. The reduced coherence and larger random error is evident in the “jaggedness” seen in some of the responses of Fig. 2.11. This is caused by the reduced signal-to-noise ratio that is typical for hovering flight tests as compared to the cruise condition. The resulting identified models are therefore generally less accurate for hover than for cruise (compare Figs. 2.8 and 2.11).

As before, in each graph the flight-test data are shown with the solid line. Because the identification is based on the control-surface inputs, we obtain the XV-15 SCAS-off response in hover, so that the data reflect the bare-airframe response characteristics. The dashed lines in the graphs represent the corresponding frequency responses obtained from the identified state-space model. The results show a generally good comparison between the flight-test data and the model in all of the degrees of freedom.

Tables 2.3 and 2.4 show the identified stability and control derivatives and associated parameter accuracies in the hover condition. As in the cruise case, most of the parameters are seen to be accurate to within 10–20%, which is in the desired range, except for the derivative  $N_p$ .

The time-domain accuracy of the identified MIMO model is checked as before using a doublet input in  $\delta_a$  and  $\delta_r$ , as shown in Fig. 2.12. The measured responses in the hover case are roll angle, roll rate, yaw rate, and lateral acceleration, as shown in the figure. As usual, the flight-test data are displayed as a solid line, and the model prediction as a dashed line.

Again, as in cruise, the responses are large, with roll angles approaching 20 deg, well beyond what we might consider as small perturbation, and yet the

## FREQUENCY-RESPONSE METHOD FOR SYSTEM IDENTIFICATION 49

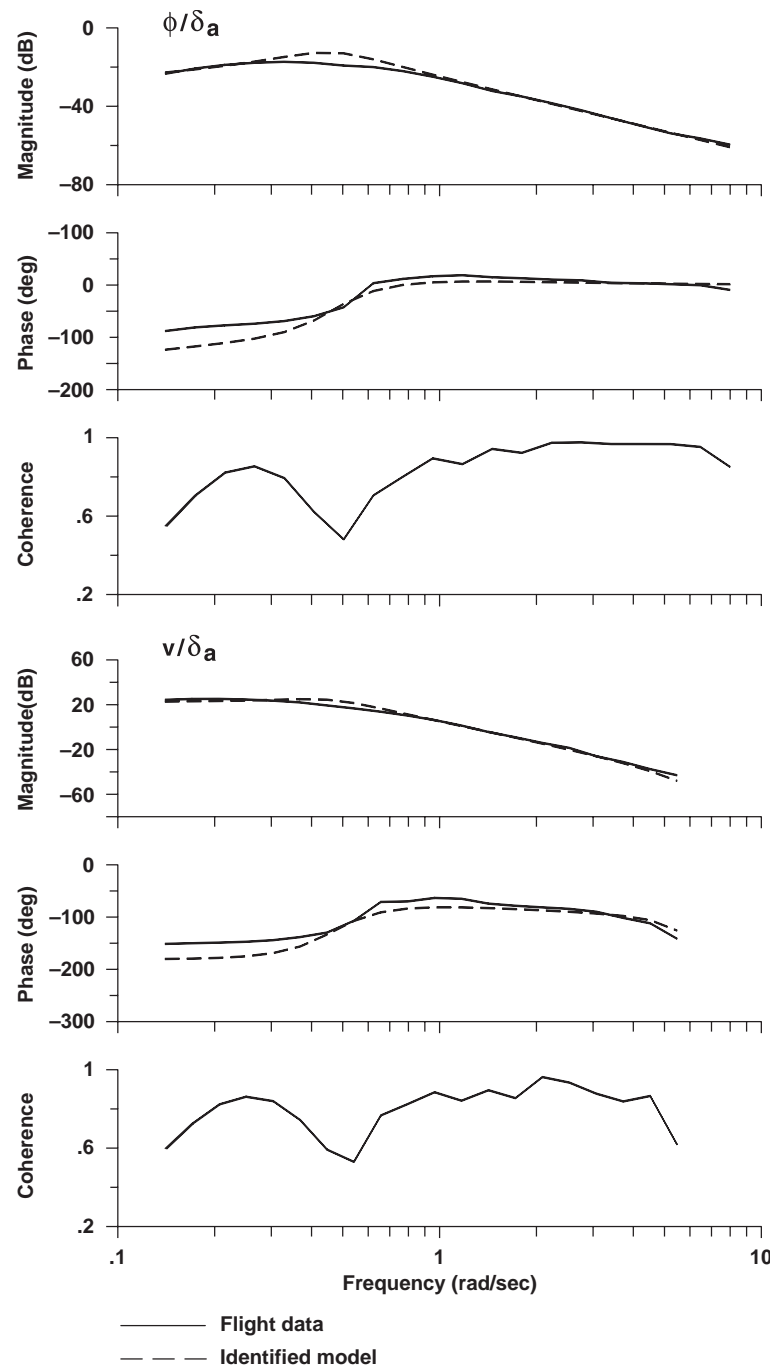


Fig. 2.11 Frequency responses for XV-15 in hover.

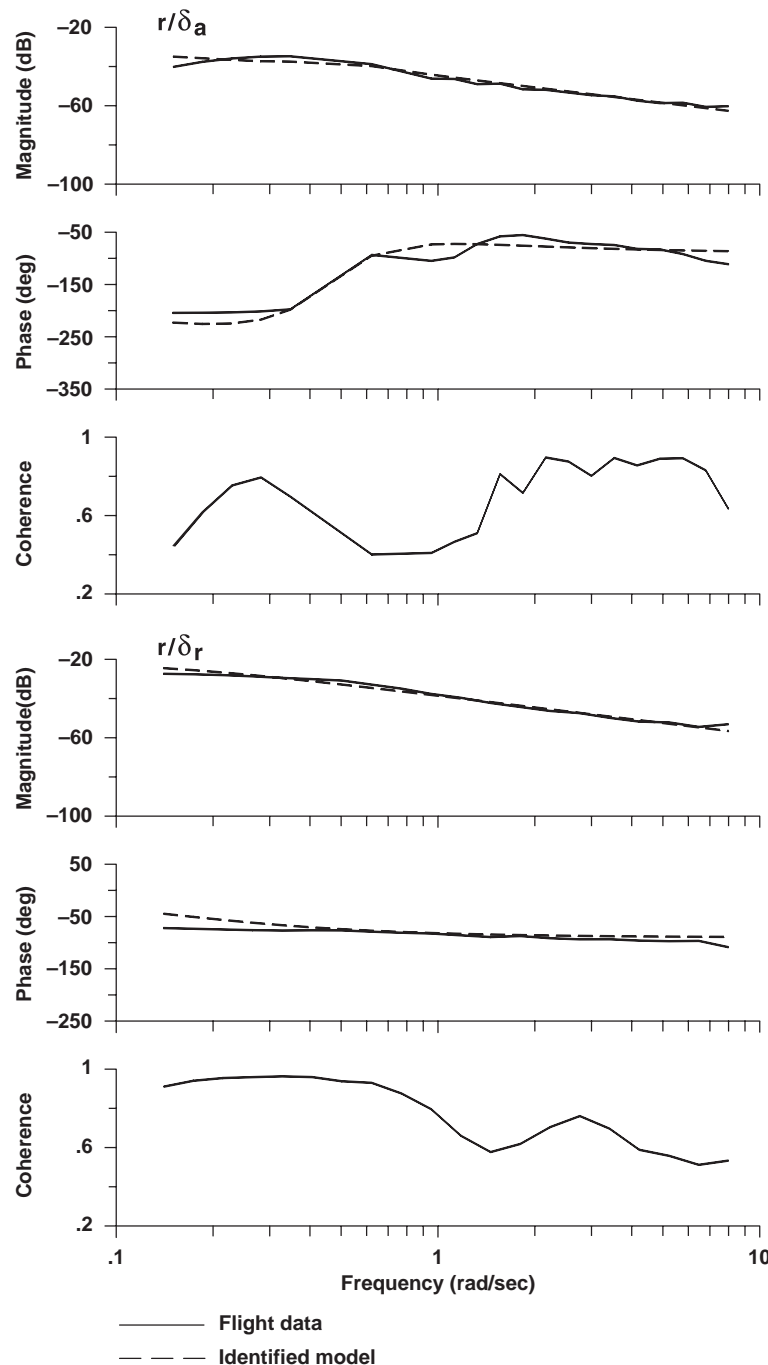


Fig. 2.11 Frequency responses for XV-15 in hover (continued).

## FREQUENCY-RESPONSE METHOD FOR SYSTEM IDENTIFICATION 51

 Table 2.3 *F*-matrix identification for XV-15 in hover<sup>a</sup>

Derivative	Parameter value	Cramér–Rao, %
$Y_v$	–0.09755	6.65
$Y_p$	–1.489	12.78
$Y_r$	0.000 <sup>b</sup>	—
$L_v$	–4.374E-03	5.38
$L_p$	–0.2365	15.41
$L_r$	0.000 <sup>b</sup>	—
$N_v$	7.152E-04	7.67
$N_p$	0.03862	29.86
$N_r$	–0.1416	13.17

<sup>a</sup>All results in English units.

<sup>b</sup>Eliminated during model structure determination.

 Table 2.4 *G*-matrix identification for XV-15 in hover<sup>a</sup>

Derivative or symbol	Parameter value	Cramér–Rao, %
$Y_{\delta_a}$	–0.04523	5.83
$Y_{\delta_r}$	0.000 <sup>b</sup>	—
$L_{\delta_a}$	–0.05777	2.41
$L_{\delta_r}$	0.000 <sup>b</sup>	—
$N_{\delta_a}$	5.910E-03	5.13
$N_{\delta_r}$	0.01187	4.58
<i>Time delays</i>		
$\tau_a$	0.000 <sup>b</sup>	—
$\tau_r$	0.000 <sup>b</sup>	—

<sup>a</sup>Control deflections in degrees.

<sup>b</sup>Eliminated during model structure determination.

response prediction is quite good. All of the key dynamics characteristics, including the control response coupling, are well captured by the identified linear model. In general, we would expect the model to be accurate for the range of motions that were experienced during the identification maneuvers—roughly  $\pm 20$  deg in attitude,  $\pm 20$  deg/s in attitude rate, and  $\pm 20$  kn in airspeed.

## 2.4 Examples of CIFER® Applications

This chapter has presented a brief overview of the frequency-response identification method and some typical flight dynamics results as obtained by using CIFER®. There is a very broad range of documented applications of CIFER®, including over 30 flight-test projects by the Flight Control Technology Group (Army Aeroflightdynamics Directorate) at Ames Research Center starting from

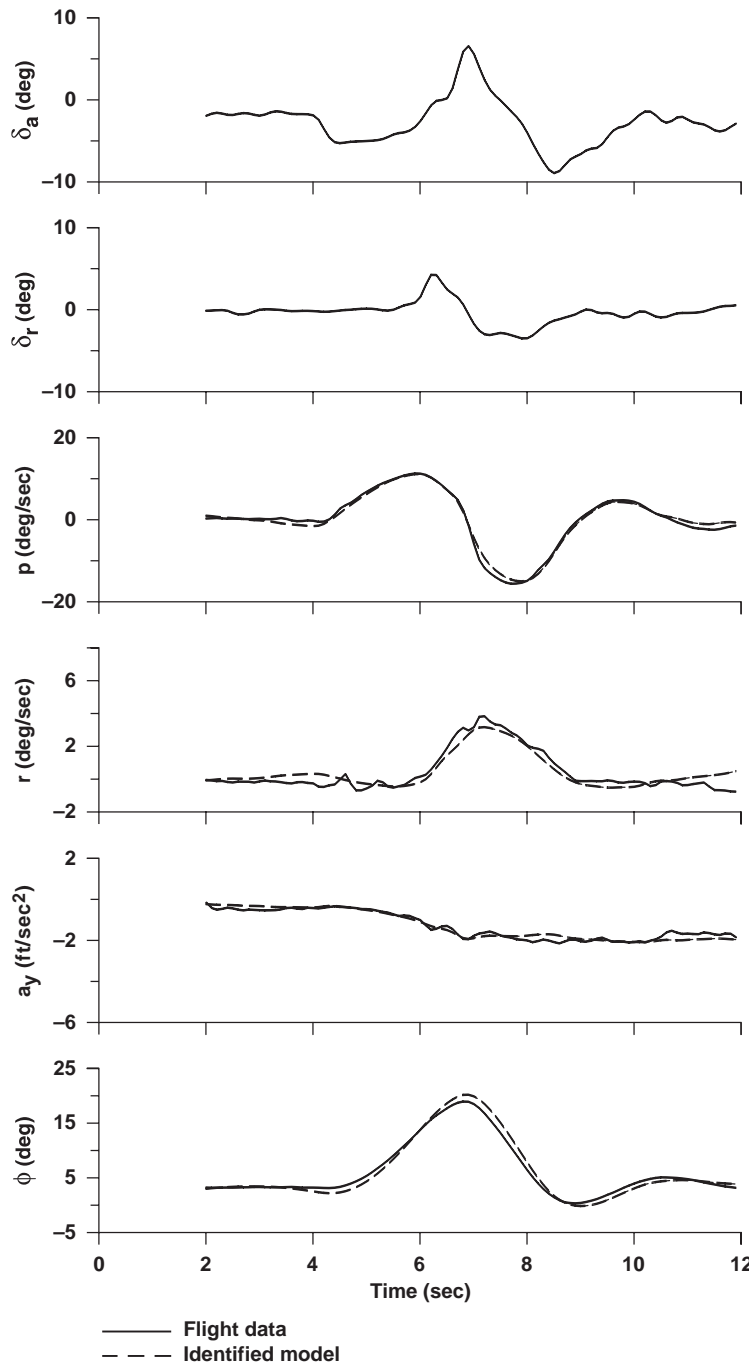


Fig. 2.12 Verification of identified model for XV-15 in hover.

## FREQUENCY-RESPONSE METHOD FOR SYSTEM IDENTIFICATION 53

the initial development of this tool in 1987. Documented CIFER® applications in the United States include the following:

- 1) Fixed-wing (manned) aircraft: Navion, B-2, TIFS, Tu-144LL, A/STOVL, VSRA (fly-by-wire Harrier), and Boeing JSF demonstrator;
- 2) Rotorcraft (manned): CH-47, XV-15, ADOCS, RASCAL, MD900, MH53J, B214ST, B205, Schweitzer 333, UH-60, V-22, OH58D, AH-64, Bo-105, RAH-66, SH-2G, S-92, CH-47, and helicopter/sling-load configurations;
- 3) Unmanned air vehicle (UAV): Shadow™ 200, Solar Pathfinder, Kmax-BURRO, R50, RMAX, iStar, and OAV (ducted-fan configurations); and
- 4) General dynamic systems-identification applications: actuator dynamics, structural modes, flutter margins, mixer/linkage systems, rotor system dynamics in wind-tunnel tests, and simulators (including the motion and visual systems of the Ames Vertical Motion Simulator).

## Problems

### *Review of second-order systems*

**2.1a** Overlay Bode plots (using MATLAB® or another suitable tool) for second-order systems with  $\omega_n = 1$  rad/s and  $-1 < \zeta < 1$  at intervals of 0.25.

**2.1b** Overlay Bode plots (using MATLAB® or another suitable tool) for second-order systems with  $\zeta = 0.3$  and  $0.5 < \omega_n < 5$  rad/s at intervals of 0.5 rad/s.

**2.2a** Overlay step responses for the transfer functions in **Problem 2.1a** for  $0 < \zeta < 1$  at intervals of 0.25 (using MATLAB® or another suitable tool). Discuss the relationships between the time domain and frequency domain for these responses. Calculate percent overshoot, peak time, and settling time for each case using known analytical expressions.

**2.2b** Overlay step responses for the transfer functions in **Problem 2.1b** for  $0.5 < \omega_n < 4.5$  rad/s at intervals of 1.0 rad/s (using MATLAB® or another suitable tool). Discuss the relationships between the time-domain and frequency-domain characteristics for these responses. Calculate percent overshoot, peak time, and settling time for each case using known analytical expressions.

### *Transfer-function identification concepts*

**2.3a** Given the Bode plot for  $p/\delta_a$  shown in Fig. P2.3, what is the steady-state response (rad/s/deg-ail)?

**2.3b** Fit a first-order transfer function to the Bode plot in **Problem 2.3a** by using asymptote approximation.

**2.4** If the Bode plot in **Problem 2.3a** represents  $p/\delta_a$ , what are  $L_p$  and  $L_{\delta_a}$ ? [Hint: Use the first-order approximation  $p/\delta_a = L_{\delta_a}/(s - L_p)$ ].

**2.5** What is the short-term roll-rate response (per degree of aileron) of Eq. (2.9) for frequencies between 1 and 1.67 rad/s? What is the initial roll acceleration for Eq. (2.9)?

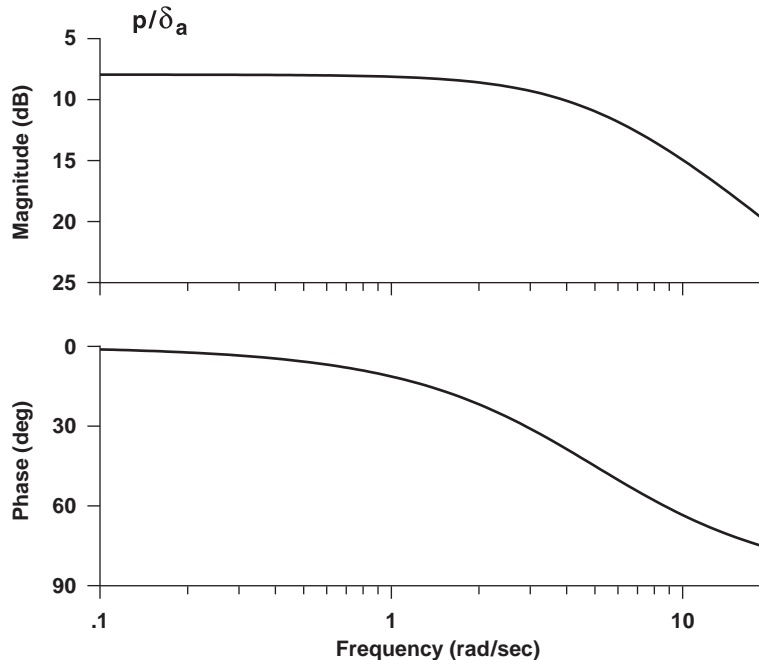


Fig. P2.3 Example Bode plot of roll-rate response.

**2.6** Propose a simple transfer-function model of Eq. (2.9) for frequencies between 0.1 and 10 rad/s.

*State-space model review*

**2.7** Given the state-space representation in the following equation for the simplified longitudinal dynamics of the A4-D,<sup>56</sup> determine the transfer function  $q/\delta_e$ , and generate the corresponding Bode plot (with MATLAB<sup>®</sup> or another suitable tool).

$$\begin{bmatrix} \dot{u} \\ \dot{w} \\ \dot{q} \\ \dot{\theta} \end{bmatrix} = \begin{bmatrix} -0.01558 & -0.00379 & 0 & -32.2 \\ -0.1442 & -0.873 & 446.194 & 0 \\ -0.000441 & -0.01972 & -0.988 & 0 \\ 0 & 0 & 1 & 0 \end{bmatrix} \begin{bmatrix} u \\ w \\ q \\ \theta \end{bmatrix} + \begin{bmatrix} 0 \\ -0.7105 \\ -0.2012 \\ 0 \end{bmatrix} \begin{bmatrix} \delta_e \end{bmatrix} \quad (\text{P2.13})$$

**2.8** Discuss the natural modes associated with the longitudinal dynamics of the A4-D from **Problem 2.7**.

## 3

## Description of Example Cases

A basic understanding of the dynamic characteristics and available flight-data measurements for the aircraft under study is necessary as a starting point for system-identification studies. The system-identification analyst should be asking throughout, “Do the identified models make physical sense based on the known vehicle characteristics?”

The system-identification methods presented throughout this book make use of three example cases. We start with a simple example involving the simulation (using SIMULINK) of a simple inverted pendulum, stabilized with attitude and rate feedbacks. This example demonstrates the accuracy and interpretation of the methods and tools for known dynamic characteristics and perfect measurements. The basic inverted pendulum exhibits an aperiodic, unstable behavior, while the closed-loop system exhibits well-damped, second-order dynamics. This example is useful to demonstrate the ability to extract unstable bare-airframe characteristics from closed-loop data.

Two key examples that are developed as case studies throughout this book are based on flight-test data for the XV-15 tilt-rotor aircraft for hover and cruise conditions. We have specifically chosen to illustrate most of the system-identification methods and results using real flight data. Although identification studies based on synthesized data from simulations are useful for illustrating basic concepts, such studies do not expose the practical problems of aircraft system-identification applications for real-world flight data. The effects of measurement/process noise, multiple inputs, input correlation, piloting technique, high-order modes, and nonlinearities can present considerable challenges. Many of these factors are present in the XV-15 flight data, thereby allowing the demonstration and discussion of the methods and guidelines presented in this book for a realistic application. The reader should refer back to this overview of the example cases to ensure that the models extracted via system identification reflect the key dynamic characteristics of each configuration.

The following topics are covered in this chapter: 1) pendulum example problem description, 2) key aspects of XV-15 flight dynamic characteristics in hover and cruise, 3) review of XV-15 measurement signals, and 4) XV-15 hover and cruise flight databases.

### 3.1 Pendulum Example Problem

The simple inverted pendulum problem depicted in Fig. 3.1 provides a convenient example of system-identification methods and tools for a known set of dynamics. The dynamics of the bare inverted pendulum (without the spring and damper feedbacks) are characterized by two aperiodic modes at equal spacing from the origin—one stable and one unstable ( $s_{1,2} = \pm\sqrt{g/l}$ ). By including a

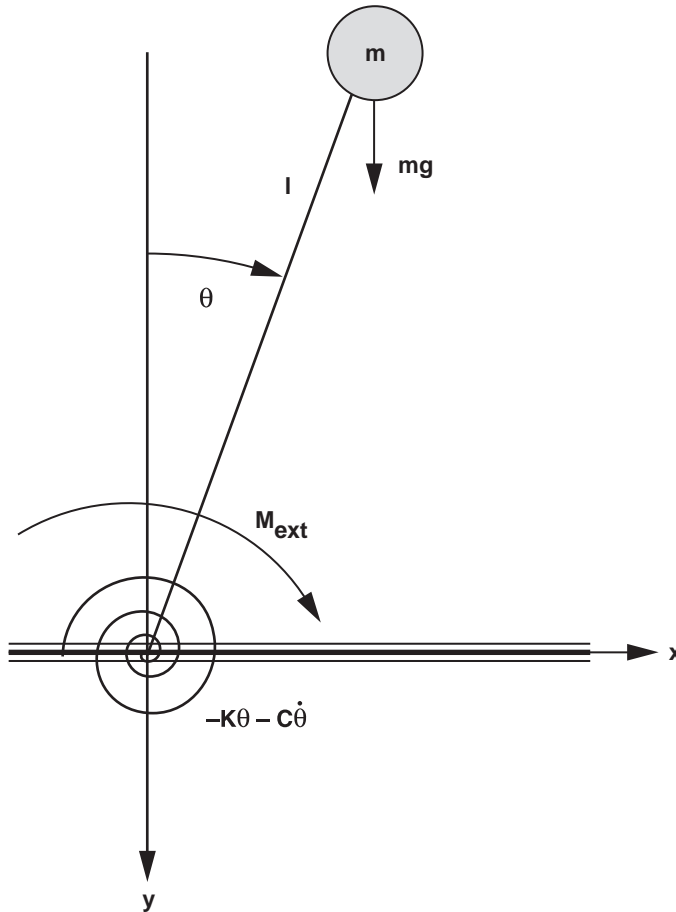


Fig. 3.1 Pendulum example case.

spring moment feedback ( $-K\theta$ ) and a damper moment feedback ( $-C\dot{\theta}$ ), the closed-loop dynamic characteristics can be stabilized. For small angular displacements the response to external moment inputs  $M_{ext}$  is linear and corresponds to a standard, simple spring-mass-damper system. For larger angular displacements, the nonlinear gravity term becomes more important.

The governing equation for the inverted pendulum is obtained by applying Newton's Second Law. The time rate of change of the angular momentum about the pivot point is equal to the sum of the external moments about the pivot point:

$$I\ddot{\theta} = \Sigma M \quad (3.1)$$

$$ml^2\ddot{\theta} = mgl \sin \theta - K\theta - C\dot{\theta} + M_{ext} \quad (3.2)$$

## DESCRIPTION OF EXAMPLE CASES

57

Dividing through by the inertia ( $ml^2$ ),

$$\ddot{\theta} = \frac{g}{l} \sin \theta - \bar{K}\theta - \bar{C}\dot{\theta} + \bar{M}_{\text{ext}} \quad (3.3)$$

where we have defined

$$\bar{K} = \frac{K}{ml^2}, \quad \bar{C} = \frac{C}{ml^2}, \quad \bar{M}_{\text{ext}} = \frac{M_{\text{ext}}}{ml^2} \quad (3.4)$$

The nonlinear dynamics are simulated using the feedback architecture of Fig. 3.2. The stabilized pendulum response is characterized by the closed-loop transfer-function  $\theta/\bar{M}_{\text{ext}}$ .

The linearized form (about the  $\theta = 0$  reference condition) results in the transfer-function model

$$\frac{\theta}{\bar{M}_{\text{ext}}} = \frac{1}{s^2 + \bar{C}s + \left(\bar{K} - \frac{g}{l}\right)} \text{ rad/(rad/s}^2\text{)} \quad (3.5)$$

For an example case to be used in this book, we take

$$\bar{K} = 15.25, \quad \bar{C} = 2.10, \quad l = 5.15 \text{ ft}, \quad g = 32.174 \text{ ft/s}^2 \quad (3.6)$$

This results in a transfer function from Eq. (3.5) of

$$\frac{\theta}{\bar{M}_{\text{ext}}} = \frac{1}{[0.35, 3.0]} \text{ rad/(rad/s}^2\text{)} \quad (3.7)$$

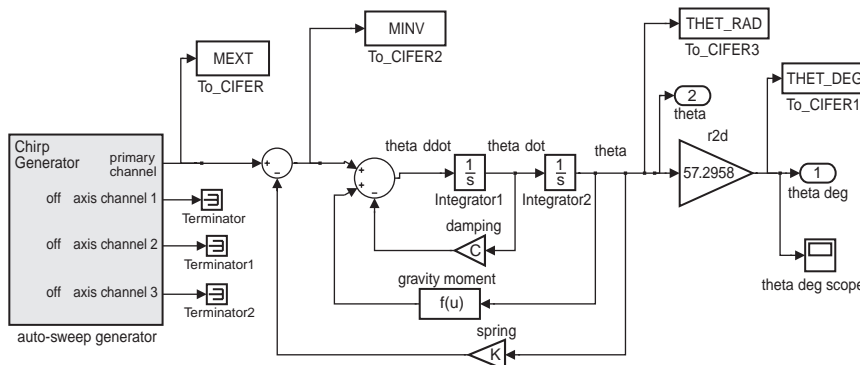


Fig. 3.2 Block diagram realization of pendulum dynamics.

where we recall that the shorthand notation  $[\zeta, \omega_n]$  in Eq. (3.7) implies  $[s^2 + 2\zeta\omega_n s + \omega_n^2]$ , with  $\zeta$  = damping ratio and  $\omega_n$  = undamped natural frequency (rad/s). So this is a lightly damped ( $\zeta = 0.35$ ) second-order system with a natural frequency of  $\omega_n = 3$  rad/s.

Some examples in this book illustrate the extraction of the unstable inverted pendulum dynamics that result when only rate damping feedback is included, as characterized by  $\theta/\bar{M}_{\text{inv}}$  of Fig. 3.2. The associated analytical result for this case is obtained from Eq. (3.5) by setting  $\bar{K} = 0$ :

$$\frac{\theta}{\bar{M}_{\text{inv}}} = \frac{1}{(-1.66)(3.76)} \quad \text{rad/(rad/s}^2\text{)} \quad (3.8)$$

This equation displays two real poles, one unstable and one stable. The extraction of these unstable dynamics is achieved from the simulation data for the stable closed-loop system (with both attitude and rate feedbacks active) using the measurement of  $\bar{M}_{\text{inv}}$ .

### 3.2 XV-15 Tilt-Rotor Aircraft

Many of the lab exercises and illustrative examples that are presented throughout the remainder of this text are based on lateral-directional data from dedicated system-identification flight tests of the XV-15 tilt-rotor aircraft.<sup>60,61</sup> The XV-15 presents a useful case study for illustrating key aspects of system identification for aircraft and helicopters using a single vehicle. In a hover configuration, the XV-15 exhibits helicopter-like dynamics, without the high level of dynamic coupling and complexity of a single-rotor helicopter. The key roll-damping derivative  $L_p$  in hover has a value about an order of magnitude smaller than is typical for conventional helicopters. This is caused by the large roll inertia of the tilt rotor, associated with the wing-tip mounted engine nacelles. In a cruise configuration, the XV-15 exhibits classical fixed-wing dynamic modal characteristics, but once again at reduced frequencies, as a result of the large relative inertias. By using the tilt-rotor aircraft, capable of both hovering (rotor borne) and cruise flight (wing borne), we can highlight the differences in analysis techniques and dynamic characteristics as they relate to conventional aircraft vs rotorcraft. Detailed engineering information on the XV-15 tilt-rotor aircraft is available in the aircraft familiarization document.<sup>62</sup>

The hover flight-test condition (Fig. 3.3) corresponds to zero flight speed, out-of-ground effect, 90-deg nacelle angle, and a gross weight of 13,000 lb. This hover data set will also be referred to in some of the tables in this book as database #1. The data for the XV-15 forward-flight condition (Fig. 3.4) are an indicated speed of 170 kn (corresponding to a true airspeed of 182 kn), altitude of 2500 ft, zero nacelle angle, and the same gross weight of 13,000 lb. This cruise data set will also be referred to as database #2.

### 3.3 XV-15 Dynamic Characteristics in Hover

As shown in Fig. 3.5, roll control in hover is achieved via differential rotor thrust, that is, increasing the thrust on one rotor and decreasing it on the other.

## DESCRIPTION OF EXAMPLE CASES

59



Fig. 3.3 XV-15 in hover (helicopter configuration) (NASA photo).

Yaw control in hover is achieved by tipping the plane of one rotor forward and the other one backward via cyclic rotor pitch. Pilot inputs are made via conventional centerstick and pedals.

In the XV-15, the lateral-directional dynamics are well decoupled from the longitudinal dynamics, caused primarily by the side-by-side prop-rotor configuration, so that database #1 contains only lateral-directional measurement signals. Also, the rotor transient flapping response is not a significant aspect of the flight dynamics and can be treated as an actuator-type delay. These characteristics



Fig. 3.4 XV-15 in cruise (fixed-wing configuration) (NASA photo).

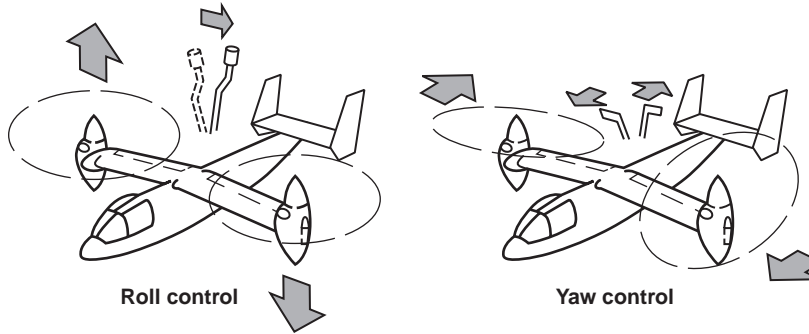


Fig. 3.5 Roll and yaw control of XV-15 in hover.

allow a significant simplification of the system-identification model's structure as compared to a conventional single-rotor helicopter. One unique aspect of the XV-15 dynamics is the strong roll/yaw coupling in hover. This is associated with the torque split for differential rotor thrust used in roll control.

With the stability and control augmentation system (SCAS) disengaged (also referred to as "SCAS-off"), the roll dynamics of the bare airframe are dominated by a low-frequency unstable phugoid-type mode, as is the case for hovering helicopters. The unstable lateral mode for the XV-15 in hover has an associated time-to-double amplitude of  $t_{\text{double}} = 4.4$  s. Furthermore, the yaw damping in hover is essentially negligible because the tilt-rotor configuration has no tail-rotor unit. (The tail rotor is the primary source of hover yaw damping on a conventional helicopter.) Finally, the bare-airframe response exhibits very small time delays in roll and yaw control because the input measurements are at the control surfaces, thus excluding the actuator dynamics, as will be seen in the next section. When the SCAS is engaged (also referred to as "SCAS-on"), the closed-loop XV-15 hover dynamics are well damped, and the aircraft exhibits good handling-qualities characteristics. The roll response is now dominated by the closed-loop time constant  $T = 1/(\zeta\omega_n) = 0.27$  s.

### 3.4 Measurements for Closed-Loop Hover Flight Testing

The measurement signals for the flight test in hover are indicated in Fig. 3.6. All variables refer to total measured quantities. The tests were completed with the SCAS engaged. Pilot inputs are via the lateral stick  $\delta_{\text{lat}}$  for roll control and pedals  $\delta_{\text{ped}}$  for yaw control. In hover, these pilot inputs command differential rotor collective (roll) and differential longitudinal flapping (yaw). At the same time that the inputs drive the rotor system, they also actuate the conventional aerosurfaces (aileron  $\delta_a$  and rudder  $\delta_r$ ) via a mechanical mixing box, which can be considered as a simple matrix of gains. Clearly, although the aileron and rudder aerosurfaces do not produce control moments in hover, they provide an (indirect) measurement of the commanded inputs to the rotor. So the airframe control inputs can be calibrated in terms of the motions of these surfaces rather than the rotor controls.

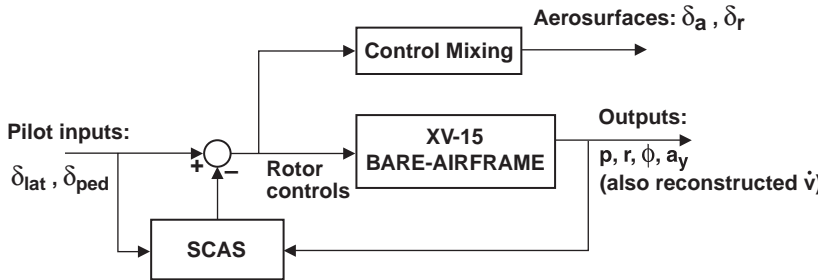


Fig. 3.6 Measurements for closed-loop hover flight testing.

This is useful because the available test-flight database does not include the rotor controls. Also, the use of the aerosurface measurements provides a consistent measure for control inputs for both hover and forward-flight conditions. The identified hover model will therefore have control derivatives scaled to units of aerosurface deflection [e.g.,  $(\text{rad/s}^2)/(\text{deg-aileron})$ ], rather than scaled to differential rotor swashplate collective deflection.

The outputs shown in Fig. 3.6 are the flight dynamics measurements of the aircraft lateral-directional response in terms of roll rate  $p$ , roll angle  $\phi$ , yaw rate  $r$ , and lateral accelerometer (i.e., specific aerodynamic force  $a_y$ ). A final output of interest is the lateral body-axis acceleration  $\dot{v}$ , which is obtained by state reconstruction using CIFER® (Sec. 6.2). The SCAS (Fig. 3.6) combines pilot stick inputs and aircraft response measurements to generate rotor commands for maneuvering and stabilization.

Piloted handling qualities and closed-loop simulation are concerned solely with the vehicle response to piloted control inputs, as characterized by the overall transfer function of SCAS-on response to pilot stick inputs. Here we use the pilot stick measurements as the inputs and vehicle responses as the outputs, and we can ignore the internal aspects of the SCAS feedback and bare-airframe aerodynamics. This approach allows the rapid identification of a rather simple, but accurate, closed-loop lower-order equivalent system model of the SCAS-on flight dynamics, which is sufficient for many applications.

When we seek to specifically model the bare-airframe response, then the measurements of the rotor controls (Fig. 3.6) are now the inputs of concern, not the pilot stick deflections. Even when the flight tests are conducted with the SCAS-on, the bare-airframe system can be identified directly, provided we have a measurement of the bare-airframe inputs. In this case we use the aerosurfaces (e.g.,  $\delta_a$  and  $\delta_r$ ) rather than the pilot inputs ( $\delta_{\text{lat}}$  and  $\delta_{\text{ped}}$ ) as inputs into the system-identification procedure. The extracted model is exactly the same result that would be obtained from SCAS-off flight tests. Finally, flight (or ground) data measurements of the response of the aerosurfaces to pilot control inputs with the SCAS-off allows the determination of the control mixing block (Fig. 3.6). Once this is done, it is possible to express the bare-airframe control derivatives in units of equivalent pilot stick inputs.

### 3.5 XV-15 Test Case Database for Hover

Table 3.1 presents a listing of parameters contained in the hover database (database #1). For each parameter, the table lists the flight-test instrumentation channel name (column 1), engineering name (column 2), engineering symbol (column 3), sign convention (column 4), and the units of measurement (column 5). Again, all variables refer to total measured quantities. When working with the database, it is important to pay close attention to the sign conventions and the units for the parameters to avoid errors. For example,  $\phi$  is provided in degrees, but it will have to be converted to radians for state-space model identification. Similarly,  $a_y$ , provided in  $g$ , will be converted to  $\text{ft/s}^2$ . If the proper units are not used in the analysis of the data, scale factors will appear in the state-space derivatives, and these errors can be difficult to isolate later.

As shown in Table 3.1, data events 882, 883, and 884 refer to lateral frequency-sweep maneuvers. Note that event 882 is a poor quality run that should not be used for basic results, but it is included in the database to provide the reader with an example of how to detect the presence of bad data using the methods described in Chapter 6. Events 889, 890, and 891 refer to directional sweep maneuvers. Asterisks are used to indicate that data for a given channel are present for a particular event. These six events provide all of the data needed to identify both a closed-loop model and a lateral-directional bare-airframe state-space model for hover. Event 743 is a roll step input to be used in the model verification process (i.e., dissimilar data).

The hover trim conditions [subscript ( )<sub>0</sub>] are

Pitch and roll angles:

$$\Theta_0 = \Phi_0 = 0 \text{ deg} \quad (3.9)$$

Body-axis velocities:

$$U_0 = W_0 = 0 \quad (3.10)$$

Table 3.2 shows the configuration of the SCAS for the flight-test maneuvers. For example, the lateral sweeps were conducted with both the roll SCAS-on and the yaw SCAS-on. As discussed in Sec. 3.4, the availability of aerosurface measurements make it possible to extract the bare-airframe response for these various SCAS configurations.

Additional important information concerning the flight-data measurement system is presented in Table 3.3. Based on these measurement system characteristics, we see that the frequency content of the identification database will not exceed 20 Hz. However, because the test pilots were instructed to terminate the sweep inputs at about 1.5 Hz to avoid structural excitation, we would not expect useful information content for frequencies above 2 Hz or so. This is suitable for determining flight dynamics models for application to piloted simulation, handling qualities, and flight control, but the database does not have the information content at higher frequencies needed for detailed models of rotor transient dynamics (beyond an equivalent time-delay representation).

Table 3.1 XV-15 hover test case (database #1)

**Table 3.2 SCAS configurations for hover maneuvers (database #1)**

Maneuver	Roll SCAS	Yaw SCAS
Lateral sweeps	ON	ON
Directional sweeps	ON	OFF
Roll step	OFF	ON

### 3.6 XV-15 Dynamic Characteristics in Cruise

Database #2 contains the flight-test data for the XV-15 in the 170-kn (indicated airspeed) cruise condition. For cruise flight, the ailerons and rudder are the source of the aerodynamics control moments, and the rotor controls are disabled (see Fig. 3.7). The pilot commands roll via the lateral stick, which moves the aileron surfaces, producing roll moments. Yaw control is commanded via the pedals, which moves the rudder, producing yaw moments.

As was the case with the XV-15 in hover, the lateral-directional dynamics are well decoupled from the longitudinal dynamics, and we will consider only the lateral-directional dynamics in the examples and lab exercises of this book. The tilt rotor in cruise exhibits the classical fixed-wing flight dynamics modes. There is a stable, aperiodic roll mode, with a time constant of  $T_r \approx 1$  s, a lightly damped Dutch-roll mode ( $\zeta_{dr} = 0.24$ ,  $\omega_{dr} = 1.7$  rad/s), and a stable spiral mode with a time constant of  $T_s \approx 10$  s.

In forward flight the XV-15 exhibits favorable (or *proverse*) aileron-to-yaw coupling ( $N_{\delta_a}/L_{\delta_a} > 0$ ). This means that when the pilot commands a right-roll input the aircraft will also yaw nose right into the turn. This tilt-rotor response is the opposite of the adverse coupling, resulting from differential aileron drag that is common to most fixed-wing aircraft. The XV-15 also has a significant amount of sideslip-roll coupling caused by a stable dihedral effect ( $L_v < 0$ ). As a result, a positive sideslip deviation (i.e., wind from the right side) will cause the aircraft to roll to the left (negative). Finally, the time delays for both roll and yaw are very small, on the order of  $\tau \approx 0.05$  s, which reflects the small effects of the rotor control linkage dynamics or hysteresis.

### 3.7 Measurements for Open-Loop Cruise Flight Testing

The block diagram for the cruise condition (Fig. 3.8) is very simple because these flight tests were conducted entirely SCAS-off. The pilot inputs ( $\delta_{lat}$  and  $\delta_{ped}$ ) are processed through the control mixing to produce differential aileron

**Table 3.3 System characteristics for databases #1 and #2**

System characteristics	Value
Sample rate	250 Hz
Filtering	50 Hz matched input/output anti-aliasing
Measurement system bandwidth	20 Hz

## DESCRIPTION OF EXAMPLE CASES

65

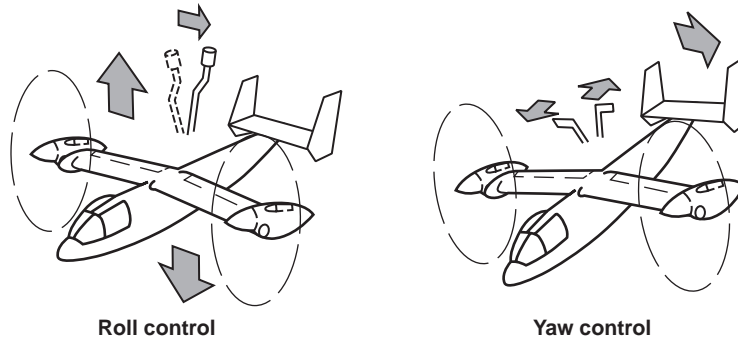


Fig. 3.7 Roll and yaw control of XV-15 in cruise.

deflections  $\delta_a$  and rudder deflections  $\delta_r$ , respectively. These aerosurface deflections generate the aerodynamics roll and yaw moments that drive the bare-airframe response. The outputs of interest for lateral-directional flight dynamics are sideslip angle at the center of gravity  $\beta_{cg}$ , roll rate  $p$ , yaw rate  $r$ , and lateral accelerometer  $a_y$ . Note that sideslip is actually measured by a wind angle vane at the boom  $\beta_{nb}$ . The sideslip angle at the center of gravity is obtained by

$$(\beta_{cg})_{deg} = (\beta_{nb})_{deg} - (0.06)(r)_{deg/s} \quad (3.11)$$

System identification based on pilot stick measurements yields bare-airframe control derivatives in units of percent pilot stick, with the (small) influence of the pilot stick linkage dynamics and control mixing included (Fig. 3.8). Identification based on the aerosurface measurements yields control derivatives in terms of aileron and rudder deflection in degrees, excluding the control linkage dynamics. Finally, the mixer/linkage dynamics can be isolated using pilot stick measurements as inputs and aerosurface deflections as outputs.

### 3.8 XV-15 Test Case Database for Cruise

Table 3.4 presents a listing of parameters contained in the cruise database (database #2). Again, all variables refer to total measured quantities. Events 799 and 800 refer to lateral (roll) frequency-sweep maneuvers, and events 801 and 802 refer to directional (yaw) maneuvers. Events 795 and 798 refer to step input data for roll and yaw, respectively, and are used for model verification.

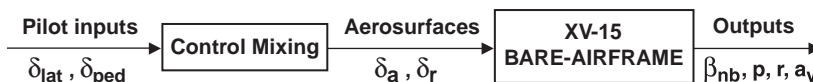


Fig. 3.8 Measurements for open-loop cruise flight testing.

Table 3.4 XV-15 cruise test case (database #2)

Channels	Engineering name	Engineering symbol	Sign convention	Unit	Flight 169 time history					
					Lateral sweep maneuvers		Dir sweep maneuvers		Roll step maneuvers	
					Event 799	Event 800	Event 801	Event 802	Event 795	Event 798
A300	C.G. lateral vibration	$a_y$	+: right accel	g	*	*	*	*	*	*
D009	Roll attitude - cabin	$\phi$	+: roll right	deg						
D022	Lateral stick position	$\delta_{lat}$	+: roll right	%	*	*	*	*	*	*
D024	Pedal position	$\delta_{ped}$	+: yaw right	%	*	*	*	*	*	*
D284	Rudder position	$\delta_r$	+: yaw right	deg	*	*	*	*	*	*
D645	Right wing aileron position	$\delta_a$	+: roll left	deg	*	*	*	*	*	*
	Roll rate - cabin	$p$	(negative $p$ )							
V012	Yaw rate - cabin	$r$	+: roll right	deg/s	*	*	*	*	*	*
V014	Sideslip angle at nose boom vane	$\beta_{nb}$	+: yaw right	deg/s	*	*	*	*	*	*
D007			+: wind from right	deg	*	*	*	*	*	*

**Table 3.5 SCAS configurations for cruise maneuvers (database #2)**

Maneuver	Roll SCAS	Yaw SCAS
Lateral sweeps	OFF	OFF
Directional sweeps	OFF	OFF
Roll step	OFF	OFF
Yaw step	OFF	OFF

The trim conditions [subscript ( )<sub>0</sub>] based on the true airspeed and trim attitude are as follows:

Flight velocity:

$$(V_{\text{tot}})_0 = 307.7 \text{ ft/s} \quad (3.12)$$

Pitch angle:

$$\Theta_0 = 4.57 \text{ deg} \quad (3.13)$$

The resulting body-axis velocity components are as follows:

Longitudinal velocity:

$$U_0 = 306.7 \text{ ft/s} \quad (3.14)$$

Vertical velocity:

$$W_0 = 24.5 \text{ ft/s} \quad (3.15)$$

Table 3.5 shows that the SCAS is off in all channels for all maneuvers, as mentioned earlier. The sample rate, filtering, and measurement system bandwidth values are the same as for the hover condition (see Table 3.3).

## Problems

### *Inverted pendulum model*

**3.1** Develop a simulation model (using SIMULINK or another suitable tool) to represent the nonlinear dynamics of the pendulum example of Sec. 3.1.

**3.2** Compare the time responses of the nonlinear model [Eq. (3.3)] and linear transfer-function model [Eq. (3.7)] for a small step input ( $\bar{M}_{\text{ext}} = 0.7 \text{ rad/s}^2$ ). Repeat for a larger step input ( $\bar{M}_{\text{ext}} = 3.5 \text{ rad/s}^2$ ). For what size input and associated maximum angular displacement  $\theta$  does the steady-state error exceed 5%?

**3.3** Derive the linearized pendulum equation from Eq. (3.3), resulting in Eq. (3.5). Why does this break down for large inputs?

**3.4** Analytically determine the response to initial conditions  $\theta(0) = 5$  deg and  $\dot{M}_{\text{ext}} = 0$  rad/s<sup>2</sup>. Does this response match simulation?

**3.5** Introduce a deadband of  $\pm 0.004$  rad into the spring. Compare the response (time domain) of the pendulum to a small external moment (0.8 rad/s<sup>2</sup>) with and without the deadband. Based on the comparison, what can you say about using a linear model to approximate a system that has localized nonlinear elements?

*Measurements for system identification with SCAS engaged*

**3.6** What inputs and outputs should be measured in order to identify a closed-loop longitudinal model of a fixed-wing aircraft with the SCAS engaged?

**3.7** What inputs and outputs should be measured in order to identify a bare-airframe longitudinal model of a fixed-wing aircraft when the SCAS is engaged?

*XV-15 test case database*

**3.8** Use FREPSID to save the XV-15 conditioned time histories (for all nine signals) of the concatenated hover lateral sweeps (events 883, 884) to an ASCII file. (Hint: this option is on FRESPID page 7.) Do not use the filtering option within FRESPID. Then load the time histories into MATLAB® or another suitable plotting program.

**3.9** Plot the concatenated time history for each measured signal (nine total). Is the response in the linear range?

**3.10** Which signals from **Problem 3.9** are noisy? In general, do the input or the output signals contain more noise using the rms utility? Estimate the noise-to-signal ratio  $\beta_n$  for the roll-rate output signal. Note that  $\beta_n \approx (\sigma_{\text{noise}}/\sigma_{\text{signal}})^2$ , where  $\sigma$  represents rms. Assume that noise constitutes all frequency content above 15 rad/sec and use 300 rad/sec as the maximum frequency in your analysis.

## 4

## Overview of CIFER® Software

The goal of this chapter is to help the reader develop a basic understanding of CIFER® software. This material does not serve as a user's manual. The student version of CIFER® and a user's primer is available without charge via the AIAA website or by contacting the leading author. Information on the professional version of CIFER® is available from the Web site <http://uarc.ucsc.edu/flight-control/cifer> or by contacting the leading author. The following topics are covered in this chapter: 1) overview of the structure of CIFER® software, 2) user interface, 3) frequency-response naming conventions, and 4) support utilities. Key attention is paid to explaining the relationship between the structure of CIFER® and the various components in the system identification flowchart of Fig. 2.1.

### 4.1 Basic Characteristics of the CIFER® Software

At the highest level, CIFER® is an integrated set of system-identification programs and utilities linked to relational databases. Figure 4.1 shows the six core CIFER® programs that carry out the basic computations of the frequency-response identification method of Fig. 2.1. These programs are for conditioning the data and performing FFTs (FRESPID), multi-input conditioning (MISOSA), window combination (COMPOSITE), transfer-function model identification (NAVFIT), state-space model identification (DERIVID), and verification (VERIFY). In conjunction with these programs, there is a comprehensive set of utilities that perform many types of related and useful tasks, such as searching/deleting/compressing elements of the database, creating plots, receiving input from and sending output to other common engineering software, and generating reports.

Data storage, organization, and retrieval within an integrated database management system is an important requirement for large-scale system identification and is a distinguishing aspect of CIFER®. CIFER® has utilities to allow direct links to many standard databasing formats (e.g., MATLAB®, Excel®, and ASCII tab delimited) as well as to a user's external flight-test database, without requiring the user to convert the data format prior to processing. Furthermore, the many frequency responses generated during the course of the system-identification procedure are stored and cataloged in the CIFER® database. The database entry contains all of the information on how the frequency response was determined (e.g., flight records, sampling, filtering, spectral windows). This database is available to all of the CIFER® programs and utilities, many of which in turn generate additional frequency-response and parametric modeling results that are then written back into the database. As a consequence, the database grows as the user progresses through the steps of the identification process, but it is easily managed with the many database utilities integral to the CIFER® software. In addition, the

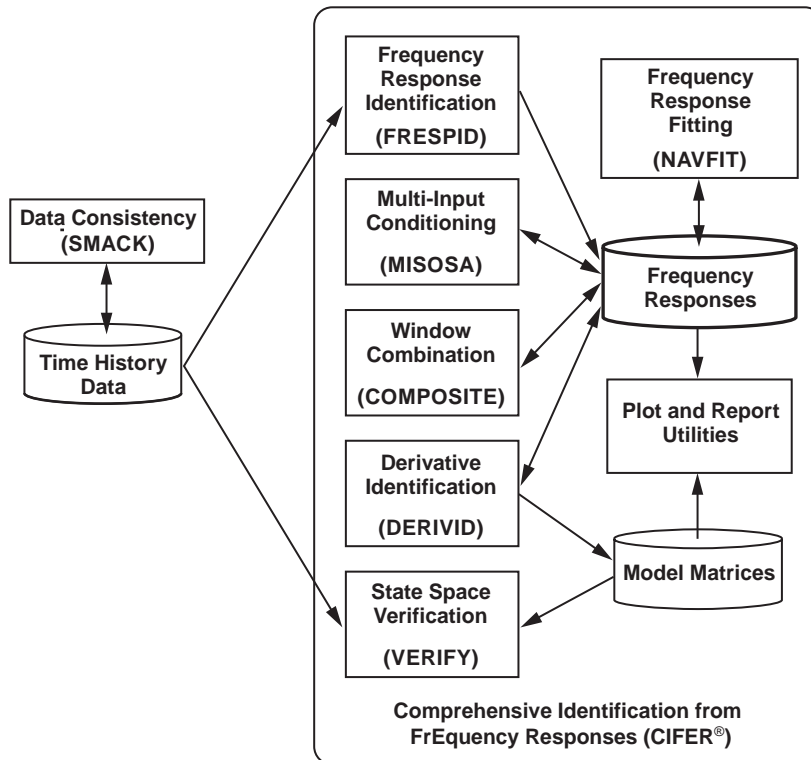


Fig. 4.1 Software and database components used in CIFER®.

database can be shared by multiple users of CIFER®, and multiple databases can be combined and compressed.

The parameter selections for the core calculations are entered interactively via a graphical user interface (GUI). For example, in order to run FRESPID, which is the first program used in the identification process, the data channel names must be specified, along with information about the flight numbers and events to be used, how each event should be included in the analysis, and whether correction factors (e.g., units, signs) should be applied. Additional choices include deciding what window sizes should be used in the FFT and whether to create a combined channel that is the arithmetic combination of other flight measurement channels. Also at the GUI level, the software checks the user inputs against the many suggested data-processing guidelines that are presented throughout this book. [An example of such a guideline is Eq. (7.61); the label *Guideline*: is used in this text to highlight these guidelines]. Finally, the GUI prepares a batch command file for the actual batch job calculations and stores the user's selections as *case names* in the CIFER® database for future retrieval. The ability to retrieve current or prior cases produces a setup process that, to a large extent, is greatly streamlined because the initial setup information used to start up the first program can be saved and then reused with the other programs.

The CIFER® GUI itself is a sequence of graphical screens that displays the needed information in a linear and intuitive sequence that follows the system-identification methods presented herein. The user can quickly input or edit the parameters as needed. The screens are presented as a series of easily navigated interactive forms. The user can step forward, backward, or jump back and forth among the screens in the programs. This method of user-interface navigation is standardized throughout the core programs, so that once the user is comfortable with the look, feel, and the mechanics of using the screens, the experience will be similar for all of the programs in CIFER®.

FRESPID, MISOSA, COMPOSITE, and DERIVID, the most computationally intensive programs in CIFER®, are run by first setting up the problem in the problem definition database and then sending off the computations for batch processing. Any errors or other significant events that occur during the batch computations are recorded in a log file. It is important to check the log file because it is possible for a job to complete successfully even though there might be computational warnings or errors.

By the time a number of the CIFER® programs and utilities have been run as part of a particular project, the amount of data and the number of generated files can be daunting. The situation becomes even more challenging if the tools are being applied to more than one project. Fortunately, CIFER® allows the user to set up multiple sets of projects in such a way that it is easy to specify which project is the active one (i.e., the one that is to be used when executing the programs and utilities in CIFER®) and which database the software will read from and write to and use for generating plots. In general, CIFER® assists the user with the multitude of bookkeeping chores necessary to deal with all of this complexity in an organized and correct manner.

Finally, CIFER® is quite flexible in terms of the definition and size of the problems it can handle. For example, the problem can have up to 10 control inputs, 20 outputs, five spectral windows, 40 states, 80 simultaneous frequency-response matches, and 100 unknown state-space identification parameters. Furthermore, it is possible to specify whether the identification parameters are free or fixed and whether there are arithmetic constraints between them (see Sec. 13.4.6).

CIFER® is available for the range of common operating systems: UNIX, LINUX, and WINDOWS. The reader should check the website (<http://uarc.ucsc.edu/flight-control/cifer>) for more information on the software and computer requirements.

## 4.2 Dataflow Through CIFER®

Figure 4.1 presents a picture of the various software and database components of CIFER®. The left side of the diagram illustrates that time-history data enters the system at two different points. The first set of time-history data is processed into frequency responses at the start of the CIFER® procedures. At the end of the procedure, a second set of time-history data, from inputs dissimilar to those used for the identification, is used to verify the identified model.

Within CIFER®, there are three programs that are run sequentially to generate the MIMO frequency-response database. Starting with the time-history data, FRESPID calculates SISO frequency responses for a range of spectral windows

using a chirp z-transform (an advanced FFT). These results are written into the frequency-response database. Next, MISOSA reads in the SISO data from the frequency-response database and conditions these responses for the effects of multiple, partially correlated controls that might have been present in the same maneuver record. Again, the results are written back out to the database. Lastly, COMPOSITE performs optimization across the multiple spectral windows to achieve a final frequency-response database with excellent resolution, broad bandwidth, and low random error.

Two programs support parametric model identification. NAVFIT is used to a identify a pole-zero transfer-function model that best fits a selected SISO frequency response. DERIVID is used to identify a completely generic state-space model structure [ $M$ ,  $F$ ,  $G$ , and  $\tau$  of Eqs. (2.10) and (2.11)] that best fits the MIMO frequency-response database. Various DERIVID utilities are available to generate the many plots and tables associated with the state-space model identification results. Finally, VERIFY is used to check the identified model's time-domain response based on time-history data from maneuvers dissimilar to those used for the identification. Again, various utilities are available to document the verification results.

The smoothing from aircraft kinematics (SMACK) program shown in Fig. 4.1 is not actually part of the CIFER® software package; it is used to preprocess the time-history data prior to identification, as discussed in Chapter 6. For example, SMACK is used to interpolate the time-history channels to a common sample rate, start time, and end time, as required by CIFER®. The Kalman filter/smooth routines in SMACK are used to isolate measurement system biases and scale factors that will otherwise corrupt the identification. Finally, SMACK is also used for wild-point removal and data reconstruction before starting the CIFER® identification.

The software components of CIFER® shown in Fig. 4.1 are each covered in detail in later chapters in this book. The mapping between the components and the corresponding chapters is summarized in Table 4.1.

Another way to think about the software components of CIFER® is to map them onto the blocks in the system-identification block diagram, as in Fig. 4.2. The software components are shown in italics, with arrows pointing to the blocks in which they are used.

**Table 4.1** Mapping between the components of Fig. 4.1 and chapters in this book

Component	Function	Chapter
Time-history data	Input to FRESPID and SMACK	5
SMACK	Data consistency	6
FRESPID	Frequency-response identification	7
MISOSA	Multi-input conditioning	9
COMPOSITE	Window combination	10
NAVFIT	Transfer-function identification	11
DERIVID	State-space model identification	12, 13
VERIFY	State-space model verification	14

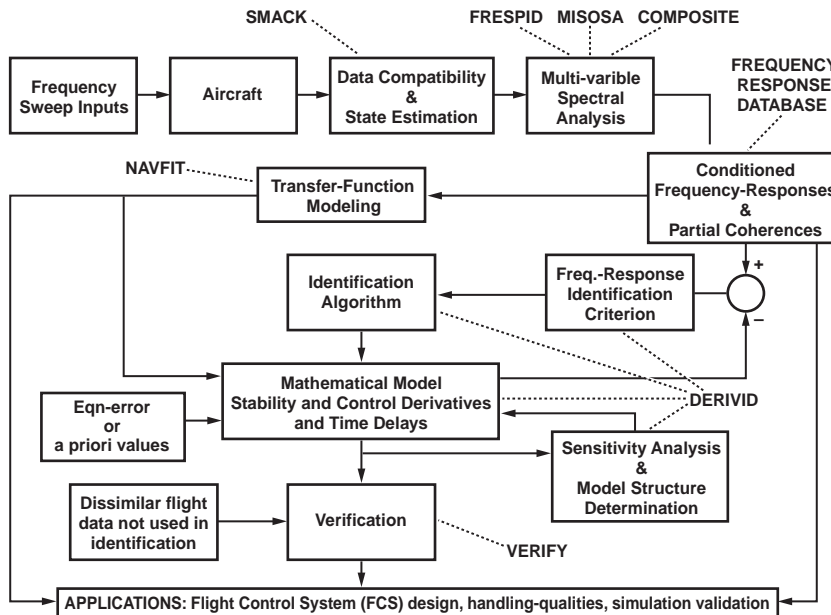


**Fig. 4.2** Software components of CIFER®

## 4.3 CIFER® Menu

Figure 4.3, the first screen displayed after typing **CIFER** at the computer, presents a menu listing all of the programs and utilities that are part of **CIFER®**. The core programs, numbered 1 through 6, are listed first: FRESPID, MISOSA, COMPOSITE, DERIVID, VERIFY, and NAVFIT.

The supporting utilities fall into several broad categories. The *frequency-response analysis utilities* (Table 4.2) support the frequency-response analyses performed by the main CIFER® programs. The *program parameter utilities* (Table 4.3) provide a variety of ways to interrogate or manipulate the frequency-response database. The *results utilities* (Table 4.4) allow the user to display the state-modeling results in either plot or tabular form. Finally, the *database and setup utilities* (Table 4.5) allow extensive manipulation of the database (searching, deleting, merging) and also support user selection of directory tree structures and various terminal/graphical emulation choices.

## 4.4 CIFER® User Interface

The CIFER® user interface consists of a sequence of screens that control the actions of the various programs and utilities. For example, Fig. 4.4 shows the first screen that appears when FRESPID is started. It is a very simple screen that allows the user to input a new case name to be used in the subsequent analysis or to retrieve a previous case stored in the database. Note that this screen is identified in the upper-right-hand corner with the label **FRESPID:1**, indicating that the screen

## Computational programs:

1 FRESPID	2 MISOSA	3 COMPOSITE
4 DERIVID	5 VERIFY	6 NAVFIT

## Frequency response analysis utilities:

7 RMS Util	8 Handling Qual & Stab Marg	9 Freq. Resp. Arith
------------	-----------------------------	---------------------

## Program Parameter Utilities:

14 Read ASCII Matrix File(s)
15 Read ASCII Response into the D/B
19 Plot Frequency Responses
20 Print Frequency Response Values

## Database and Setup Utilities:

10 Database Utilities...
91 User Interface & Graphics...
93 Configuration Summary

## Results Utilities:

31 Plot DERIVID Results
32 Plot VERIFY Results
33 Tabular DERIVID Reports
34 Tabular VERIFY Reports
35 Print DERIVID or VERIFY Results
36 Case Plotting Utility
37 DERIVID or VERIFY matrix reports
38 Eigenvalue Utility
39 DERIVID Parameter Dump

(Enter a number to select a program or utility. Enter <CR> when finished.)  
Input:

**Fig. 4.3** CIFER® menu of programs and utilities.

is the first screen of the FRESPID program. This convention is followed with the other main CIFER® programs as well.

Once the case name has been typed in, the user can navigate to other screens using the **F** keys of the keyboard. The use of the function keys **F1** through **F4** is summarized in Table 4.6. All of the CIFER® programs and utilities use this method of navigating between screens.

Following the current example a bit further, once the case name has been entered in the first FRESPID screen (Fig. 4.4), the user presses **F1** and moves on to the second screen (Fig. 4.5). The first field shows the case name **XVLATSWP** that was entered in the previous screen. The other fields allow the user to enter additional details about this case.

In this example, the user has chosen the control inputs to be **AIL** and **RUD** (i.e.,  $\delta_a$  and  $\delta_r$ ), and the outputs are **P**, **R**, **AY**, and **VDOT** (i.e.,  $p$ ,  $r$ ,  $a_y$ , and  $\dot{v}$ ), but in

**Table 4.2** Frequency-response analysis utilities

No.	Utility	Function
7	RMS util	Determines the rms value of a signal by integrating the autospectrum over a desired frequency range
8	Handling qual and stab marg	Computes handling-qualities and crossover characteristics
9	Freq. resp. arith	Computes a frequency response as the product, ratio, difference, or sum of two input responses

## OVERVIEW OF CIFER® SOFTWARE

75

Table 4.3 Program parameter utilities

No.	Utility	Function
14	Read ASCII matrix file(s)	Reads ASCII files containing $M$ , $F$ , $G$ , $H$ and $\tau$ matrices and stores them in case files for CIFER®
15	Read ASCII response into the D/B	Reads ASCII files containing frequency-response arrays and enters the data into the CIFER® frequency-response database
19	Plot frequency responses	Generates overlay plots of data for up to five frequency responses
20	Print frequency-response values	Prints all stored frequency-response values for a single response

Table 4.4 Results utilities

No.	Utility	Function
31	Plot DERIVID results	Generates overlay plots of up to five sets of DERIVID results
32	Plot VERIFY results	Generates overlay plots of up to five sets of VERIFY results
33	Tabular DERIVID reports	Generates tables comparing the results of up to five DERIVID cases
34	Tabular VERIFY reports	Generates tables comparing the results of up to five VERIFY cases
35	Print DERIVID or VERIFY results	Prints DERIVID or VERIFY results
36	Case plotting utility	Generates overlay plots of up to five arrays out of 14 available arrays (e.g., mag, pha, coh, gxx, etc.)
37	DERIVID or VERIFY matrix reports	Writes matrix values in LaTeX tabular format
38	Eigenvalue utility	A stand-alone version of the eigenvalue/eigenvector computations in DERIVID
39	DERIVID parameter dump	Generates an ASCII output file containing a summary of a DERIVID case

Table 4.5 Database and setup utilities

No.	Utility	Function
10	Database utilities...	Used to create, search, delete, copy, etc., various items in the database
91	User interface and graphics...	Set up keyboard mapping and terminal emulation preferences
93	Configuration summary	Shows current preferences

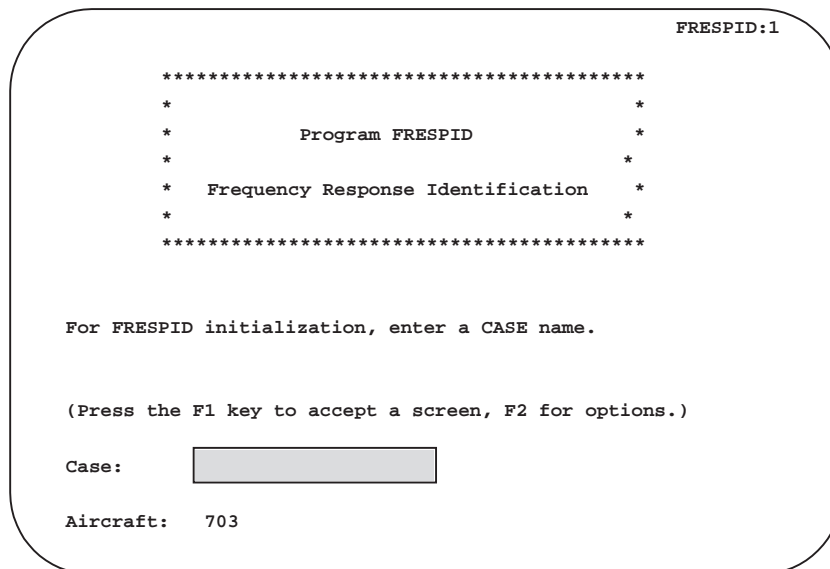


Fig. 4.4 Example of CIFER® screen: screen 1 of FRESPID.

general up to 10 different controls and 20 outputs can be named. Additional options include whether the channels are to be cross correlated, which is needed for MIMO frequency-response matrix identification, and whether the results of the frequency-response analysis should be saved in separate ASCII files in addition to the more compact CIFER® database. In the case shown in Fig. 4.5, the user has decided to work entirely within CIFER® (highly recommended).

Navigating around a screen with multiple input fields is accomplished in a consistent way in all of the CIFER® programs and utilities. The arrow keys will move the cursor to the left, right, up, or down. The tab key will move the cursor to the beginning of the next field. The carriage return key <CR> has the same effect as the down-arrow key. Wraparound is active, which means that if the cursor is, for example, already at the top of the screen, then pressing the up arrow will move the cursor to the bottom of the screen. When working in a complex screen of

Table 4.6 Navigating between CIFER® screens using the F keys

F key	Function
<b>F1</b>	Accepts the current screen and moves on to the next screen
<b>F2</b>	Opens a menu bar at the bottom of the screen that presents a number of navigation options: continue, backup, main, exit, and update; select option with the arrow keys and then press F1 to activate the selection
<b>F3</b>	Turns off prompting, allowing for “fast forwarding” through the screens
<b>F4</b>	Presents a prompt to enter which screen number to jump to

## OVERVIEW OF CIFER® SOFTWARE

77

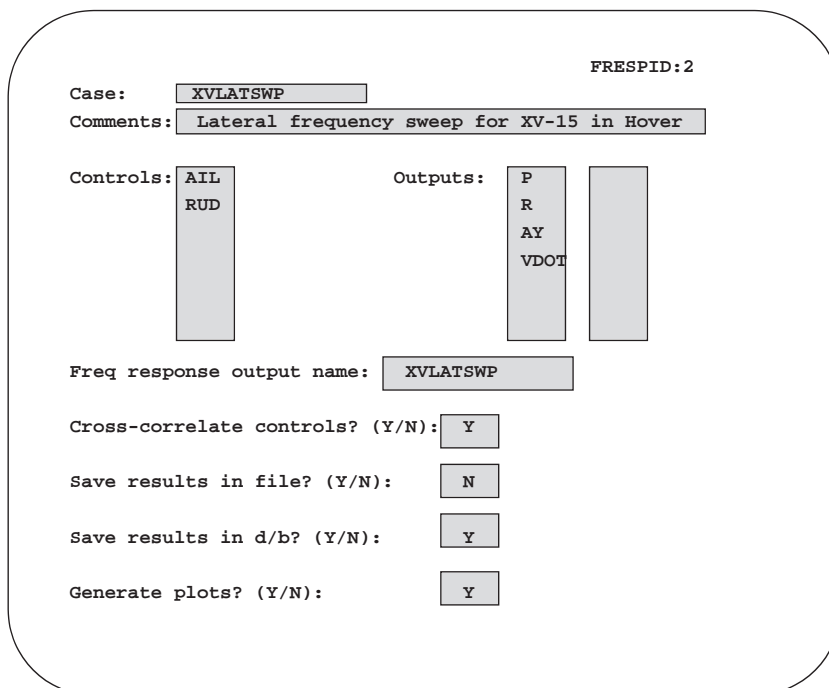


Fig. 4.5 Example of CIFER® screen: screen 2 of FRESPID.

arrays or tables, the software moves the cursor to the nearest editable field in the current row or column.

Throughout CIFER® there is a convention for naming frequency responses. The procedures for system identification involve generating, conditioning, fitting, and combining frequency responses, leading to a large number of related files, and so it is very important to follow a standard naming convention in order to keep track of all of the data and avoid confusion.

The standard CIFER® frequency-response name consists of five fields: casename\_pgm\_winds\_ctrl\_outc  
where

casename = user-defined case name (up to eight characters),  
pgm = source program (always three characters),  
winds = string indicating the window(s) used (five characters),  
ctrl = user-defined control name (up to four characters),  
outc = user-defined output name (up to four characters).

In our current example, a frequency response generated by FRESPID could have the following name: **XVLATSWP\_FRE\_0B000\_LAT\_P**.

The case name previously entered in screen 1 was **XVLATSWP**, so that appears in the first field of the frequency-response name. The data were produced by the

FRESPID program, and this is indicated in the second field by **FRE**. (A different abbreviation would be used for a different program, such as **MIS** for MISOSA, **COM** for COMPOSITE, **DER** for DERIVID, etc.) The windows field, **OB000**, indicates which window (**B** in this case) was used in calculating this frequency response in FRESPID), or which windows were combined in the case of COMPOSITE. (For example, **XVLATSWP\_COM\_ABC00\_LAT\_P** indicates the combination of the **A**, **B**, and **C** windows in COMPOSITE.) Finally, **LAT** and **P** are the control and output channels, respectively, used in this frequency response.

#### 4.5 Examples of CIFER® Utilities

The lists of utilities in Table 4.2–Table 4.5 give an indication of the broad range of the analysis, plotting, and database utilities available in CIFER®. A few of these utilities will be briefly discussed in this section to illustrate further their potential uses.

The screen for Utility 93, the “configuration summary” utility, is shown in Fig. 4.6. The fields on this screen show the current preferences that the user has set up for a particular project, such as the aircraft name, units used, terminal type, the location of the CIFER® database files, etc. Until these preferences are changed, these default values will be used every time the CIFER® software is run.

The first screen of utility 19, the “plot frequency responses” utility, is shown in Fig. 4.7. In this example, the frequency-response names that have been entered indicate that the user has decided to overlay three different frequency responses. The first response is COMPOSITE response for five windows (**A**, **B**, **C**, **D**, **E**) as obtained from the multi-input/single-output analysis of MISOSA. The second response is the multi-input/single-output result for spectral window (**A**), and the last response is for spectral window (**C**), two of the five windows making up the COMPOSITE response. In this case we have elected to plot only the magnitude, and no corrections are going to be made to the data (i.e., no corrections will be made to the

```
CIFER Configuration Summary

Active CIFUI      (Terminal setup ): mac_versaterm
Active CIFERTERM   (Terminal keymap): vt100
Keymap description (from TERMINFO ): (none defined)
Graphics setting      : versaterm

Active SIFDEF      (Aircraft.analysis): 703.default
CIFER database directory      : /u3/tischler/cifer/data/db

Units      : RAD
Plot directory      : /u3/tischler/cifernew/jobs/plots
Batch directory      : /u3/tischler/cifernew/jobs
Time history root directory      : /u3/tischler/cifer/data/th

TRENDS database      :
TRENDS tail id      :

Hit return to continue:
```

Fig. 4.6 Utility 93: configuration summary.

## OVERVIEW OF CIFER® SOFTWARE

79

```
*****
* Program QPLOT
* Frequency Response Overlay Utility
* Press F3 to exit.
* ^A or ^D to move to field beginning/end.
* ^G or ^L to move left/right one character.
* ^O/ESC (ESC/ESC on Solaris) toggles insert/overstrike.
*****
Which array?: 1,2,3      (1:mag, 2:phas, 3:coh, 4:GXX, 5:GYY, 6:GXY, 7:err,
                         8:pcoh2, 9:pcoh3, 10:pcoh4, 11:pcoh5, 12:pcoh6,
                         13:pcoh7, 14:pcoh8, 15:pcoh9, 16:mcoh)
Corrections?: 0,0,0,0,0  (For each array type enter 0 to skip, 1 to apply)
Freq Resp Names:          Gain   Ph Shift  Power
XVLATSWP_COM_ABCDE_AIL_P  1.00   0.00    0
XVLATSWP_MIS_A0000_AIL_P   1.00   0.00    0
XVLATSWP_MIS_00C00_AIL_P   1.00   0.00    0
                           1.00   0.00    0
                           1.00   0.00    0
                           1.00   0.00    0
Aircraft:     BOOK
Input from?: D          (F(file) or D(database))
```

Fig. 4.7 Utility 19: plot frequency responses.

gain, phase shift, or Laplace variable power shift  $s^n$ ). The data are retrieved from the CIFER® database.

The result is the plot shown in Fig. 4.8. As requested, magnitude, phase, and coherence functions are plotted against frequency, and the three curves represent the three different frequency responses that had been specified.

Finally, Fig. 4.9 shows an example of the tabular TeX output that can be generated by CIFER® utilities. In this case, the table of F matrix identification results from DERIVID was generated by utility 33, “tabular DERIVID reports.”

For more details on CIFER® software functionality, the reader is referred to the student version primer (available via the AIAA website and <http://uarc.ucsc.edu/flight-control/cifer>) and the detailed CIFER® user’s manual.<sup>63</sup>

## 4.6 Interfaces with Other Tools

Interfaces have been developed and are available to allow communication of data between CIFER® and several other tools. Key among these are MATLAB® and the control system analysis and optimization tool CONDUIT®.<sup>64</sup>

CIFER® can access time-history data for identification (FRESPID) and model verification, (VERIFY), which is stored a variety of formats, such as MATLAB®, UNC3, CIFER (binary), and TRENDS (NASA database). The user can also modify a simple stub subroutine (READMIS) to access data in any arbitrary format or from a native database.

Matrices and frequency responses stored in MATLAB® or ASCII text format can be read into the CIFER® database for processing, and all identification results can be dumped out in MATLAB®, Excel, and ASCII text formats.

Rupnik<sup>65</sup> developed a library of MATLAB® functions for the frequency-response determination modules (FRESPID, MISOSA, COMPOSITE) and many

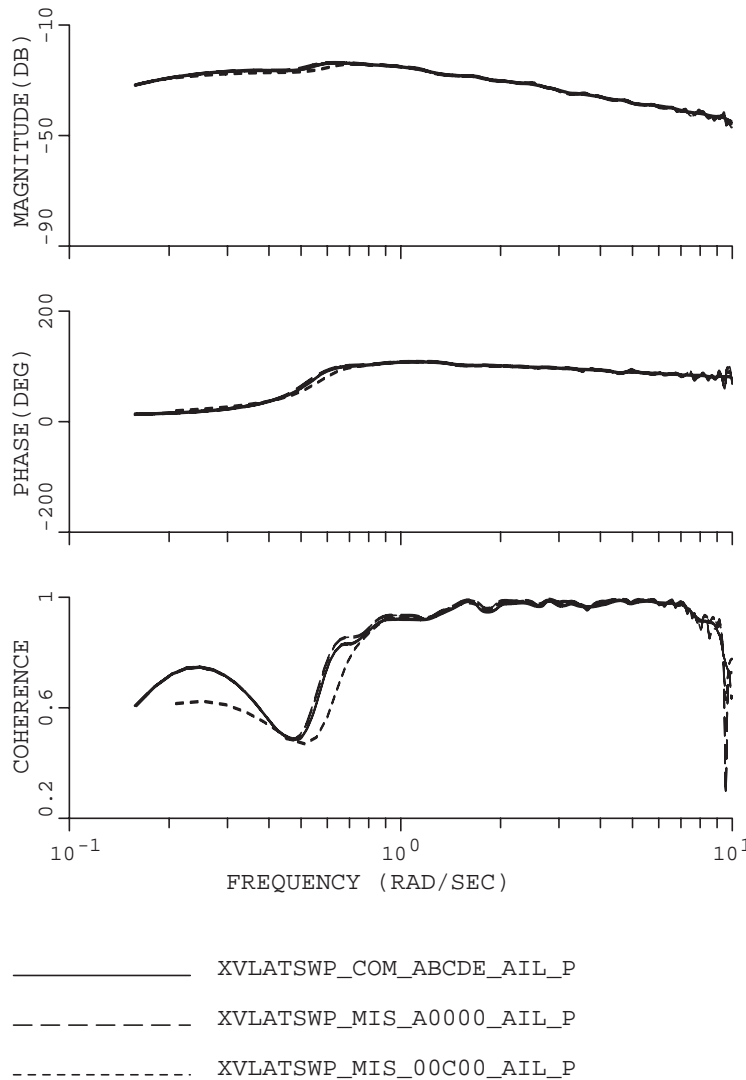


Fig. 4.8 Example frequency-response plots generated by utility 19.

of the associated utilities. The user creates a *template* case, for example, in FRESPID, using the standard CIFER® database. Thereafter, the CIFER® library can be called within standard MATLAB® scripts to automate system-identification processing. Rupnik also developed a prototype MATLAB® GUI that provides the user with a more modern browser-type interface, while preserving the same CIFER® screen organization and flow.

Case	Case ID
HOV174P2A	DROP XV

HOV174P2A			
Derivative	Param Value	C.R. (%)	Insens. (%)
$X_u$	-0.05614	16.34	7.597
$X_v$	0.000	.....	.....
$X_{b1c}$	33.70	2.463	0.5307
$Y_v$	-0.4004	5.862	1.171
$Y_p$	1.434	6.875	2.942
$Y_r$	1.721	19.50	2.139
$Z_w$	-0.06772	26.02	12.62
$L_u$	-0.02667	12.75	1.756
$L_v$	-0.08740	3.482	0.8052
$L_{b1s}$	-21.74	2.641	0.5267
$M_u$	-2.929E-03	24.37	2.546
$M_v$	-7.307E-03	20.74	2.848
$M_{b1c}$	-7.844	2.782	0.7036
$N_u$	-0.08040	16.54	1.730
$N_w$	-0.01930	24.72	3.100
$N_r$	-1.076	11.72	1.949
$S_{fbc}$	-0.4110	6.493	1.171
$C_{fbs}$	0.7526	7.598	1.548
$K_{the}$	0.08211	2.915	1.308
$N_{col}$	0.4051	14.42	2.608

Fig. 4.9 Example TeX report generated by CIFER® results utility.

Tischler et al.<sup>20</sup> have integrated CIFER® and the control system design tool CONDUIT®. The CONDUIT® tool can access directly the identified models and accuracy bounds from the CIFER® database to allow control-system optimization and robustness analysis, as described in the cited reference.

## Problems

### CIFER® installation, setup, and navigation

**4.1** Download the student version of CIFER® provided with this book via the AIAA website. Install the software for use with the LINUX operating system.

**4.2** Create a new “aircraft” (e.g., XV15), using utility 17, which sets up a database under this name for running the problems in this book.

**4.3** Setup the defaults (utility 11) to allow printing and access of time-history data from your computer.

**4.4** Check the configuration summary (utility 93) to be sure the defaults were set up satisfactorily.

*Reading and plotting utilities*

**4.5** Save the frequency, magnitude, and phase of the A4-D transfer-function  $q/\delta_e$  that you determined in **Problem 2.7** in ASCII format, using a frequency range of 0.1–10 rad/s. (Hint for MATLAB® users: use the “bode” function, then save in ASCII format using “dlmwrite”.) Then read in the frequency, magnitude, and phase into CIFER® using utility 15. Use the database utilities to determine that this response has been stored in the database. Then plot the response with utility 19.

**4.6** Make a hard copy of the figure plotted in **Problem 4.5**. (Hint: Use the “P” option within utility 19).

*Naming convention for frequency responses*

**4.7** Explain the meaning of the following case names:

- (a) XVLATSWP\_FRE\_A0000\_AIL\_R
- (b) XVLATSWP\_MIS\_0000E\_AIL\_R
- (c) XVLATSWP\_COM\_AB000\_AIL\_R

**4.8** Is XVLATSWP\_FRE\_ABCDE\_AIL\_R a valid case name?

# 5

## Collection of Time-History Data

This chapter will focus on the first step in the system-identification process of Fig. 2.1, which is the collection of a well-suited time-history database. The ultimate quality of the identification results is highly dependent on 1) properly designed and executed flight tests of the aircraft being studied and 2) properly selected and well-documented characteristics of the instrumentation system. The recommended input for frequency-domain identification is a frequency sweep because it provides a fairly uniform spectral excitation over the frequency range of interest for good frequency-response identification and is robust to uncertainties in a priori knowledge of the system dynamics.

The key points covered in this chapter include the following: 1) general aspects of data requirements for system identification, 2) instrumentation system requirements, 3) optimal inputs, 4) frequency-sweep input, 5) flight-testing considerations, and 6) computer-generated sweeps. Excellent resource material on flight-data collection for system identification is included in the publications by Hamel and Aiken,<sup>66</sup> Hamel,<sup>10</sup> Williams et al.,<sup>67</sup> and Klein and Morelli.<sup>6</sup>

### 5.1 Overview of Data Requirements for System Identification (Time Domain and Frequency Domain)

An overarching principle of system identification is that the flight-test records must include the information content of the dynamic characteristics that you wish to capture in the model. Succinctly stated, “For particular dynamic characteristics to be identified in the model, they must be apparent in the data.” Conversely, “If it’s in not in the data, don’t expect to be able to identify it in the model!” This basic principle impacts all aspects of flight-test preparation and conduct; critical among these are the selection of instrumentation, test inputs, and test conditions. This principle applies regardless of whether the identification is conducted in the time domain or the frequency domain, and although it seems obvious enough the principle is often ignored. Two key considerations determine much of the test preparations and conduct: frequency range of applicability for the identified model and dynamic coupling to be represented in the identified model. These terms and the implications for flight testing are considered in the following paragraphs.

#### 5.1.1 Frequency Range of Applicability

Each modeling result of system identification (i.e., a frequency response, a transfer-function model, or a state-space model) has associated with it a *frequency range of applicability*. Chen and Tischler<sup>68</sup> defined this to be the frequency range over which the identified model can be expected to be valid. This frequency range of applicability is a function both of 1) the range over which

the frequency response can be accurately identified (i.e., good coherence) and 2) the range over which the selected parametric model structure can accurately track the identified frequency responses. The intended application of the system-identification model determines the required frequency range of applicability. For example, the identification or validation of a flight-dynamics simulation model for piloted evaluation will typically require a frequency range of applicability of about 0.3–12 rad/s, while a model to be used in closed-loop flight-control applications must be accurate near the intended closed-loop bandwidth frequency. Subsystem models, such as models of the rotor flapping dynamics or actuator response, must be accurate near their respective natural frequency (e.g., the regressive flap mode  $\omega_f \equiv 14$  rad/s for a typical manned helicopter, as discussed in Sec. 15.2.1), but they can be less accurate at lower frequencies.

*Implications for piloted excitation inputs.* If certain dynamic modes within the frequency range of applicability are not well excited by the test inputs, then those modes will not appear in the data and therefore will not show up in the final identified model. In the terminology of the identification literature, the input signal must be *persistently exciting*, which roughly means that all of the modes (of interest) of a system are excited.<sup>1</sup> A piloted frequency sweep conducted for helicopter system identification is generally limited to a maximum frequency of a about 2–3 Hz (typical of handling qualities and flight dynamics testing). Natural spillover of excitation energy occurs as a result of the irregularities in the piloted inputs and for rotorcraft allows reliable identification of regressive rotor-flap/lag dynamics (up to about 3–4 Hz). Excitations of the high-frequency structural (and rotor) modes (e.g., up to 5 Hz and beyond) are commonly and best conducted using automated sweep inputs and can include real-time monitoring of structural loads (Sec. 5.11).

*Implications for record length.* Even when care has been taken to properly excite the aircraft, the data record lengths must be consistent with the modal periods of interest. As a general rule of thumb, an individual sweep record length should be at least two and ideally about four to five times the maximum dynamic period of interest [Eqs. (5.11) and (7.63)]. Although in theory an individual mode can be identified from a record length corresponding to a single period of the mode of interest, the practical issues of measurement noise, atmospheric turbulence, multiple closely spaced modes, and model structure uncertainty all drive the need for longer record lengths. For example, helicopters exhibit an unstable phugoid mode with a typical period of oscillation of about 20 s, corresponding to a phugoid mode frequency of  $f = 1/20 = 0.05$  Hz, or  $\omega_n = 0.314$  rad/s. For an accurate identification of the phugoid parameters from flight-test data, a data record length of about 80 s (= four phugoid periods) is desirable. This is a typical record length in frequency-sweep flight tests of aircraft and rotorcraft for the purpose of identifying a flight-mechanics model. On the other hand, the accurate identification of aircraft short-period dynamics for typical handling-qualities applications can be accomplished with much shorter records because the dynamic modes of interest are concentrated in the frequency range of 1–10 rad/s. This was demonstrated for the Tu-144LL aircraft using two frequency-domain methods (equation-error/output-error and CIFER<sup>®</sup>) with 20-s flight records.<sup>41</sup> Finally, if the primary interest is only for modeling the dynamics response at

higher frequencies, as would be the case for the identification of structural dynamics or control system linkages and actuator dynamics, then a sweep of only 5–10 s might be quite sufficient.

### 5.1.2 Dynamic Coupling

*Dynamic coupling*, also sometimes called *interaxis coupling*, is present when a control input intended to produce a response in one axis also results in responses in another axis. For example, the deflection of aileron produces a *primary* (also called *on-axis*) response in roll rate. But because of the dihedral effect, the aircraft will also respond in yaw, which is considered a *secondary* (also called *off-axis*) response.

Consider the implications of dynamic coupling on flight-test procedures. For example, the lateral/directional dynamics of a fixed-wing aircraft with the stability and control augmentation system disengaged (SCAS-off) will typically exhibit a lightly damped Dutch-roll motion that appears most clearly in the on-axis sideslip and yaw-rate responses to rudder inputs. However, the Dutch-roll mode is also present as a secondary coupling characteristic in the roll-rate response to aileron inputs. If a roll sweep test is conducted with a high-gain SCAS engaged, or the pilot acts to suppress all sideslip excursions using pedal inputs, all evidence of Dutch-roll coupling in the roll excitation data for aileron inputs will be eliminated. The resulting identified bare-airframe model will indicate that the yaw and roll dynamic motions are decoupled. Thus it is essential *not to mask or suppress* important aspects of the dynamics of concern. In this example, the SCAS can be disengaged in the yaw axis, and the pilot can be instructed to conduct the roll sweeps with “feet on the floor”—that is, with no pedal inputs, or with pulsed pedal inputs to bound yaw/sideslip excursions but that are not correlated with the primary (lateral stick) inputs.

If these important issues are not adequately addressed during flight-test planning, the flight-test data will not have sufficient information content to identify the characteristics of interest, and the overall quality of the system identification results will be severely compromised.

## 5.2 Optimal Input Design

Excitation inputs for system identification have been widely studied, and this has produced an extensive literature on optimal input design.<sup>10,69–72</sup> Optimal inputs are prescribed input forms designed to maximize information content (e.g., power spectral density) for minimum maneuver time or minimum peak response. There are limitations in the strict use of these optimal inputs because the input design process is based on a priori knowledge of the model structure and dynamic response characteristics. Although the model structure and dynamic modes might not be well known in advance, especially for unique UAV configurations or helicopters, rough guesses can provide a good initial estimate for the input design procedure, and this can be refined as the identification progresses. These optimal inputs are often excellent starting points for system-identification flight testing.

Multistep inputs, such as the “3-2-1-1” test input developed by the German DLR Research Laboratory,<sup>32,73</sup> maximize the power-spectral-density function

over a particular frequency range given an estimate of the model characteristics of interest. The 3-2-1-1 test signal and its variants have been highly successful in conjunction with time-domain system-identification applications such as the widely used maximum likelihood (ML) method. Researchers of the DLR (formerly the DFVLR) are world leaders in the ML identification of helicopters and fixed-wing aircraft using 3-2-1-1 type inputs and have published their work extensively.<sup>37,74,75</sup> Morelli (NASA Langley Research Center) has also contributed significantly to the flight-test validation of optimal input designs based on multisteps, with extensive applications to high-performance aircraft.<sup>71,72</sup>

Another optimal input well suited to frequency-domain identification methods is the Schroeder-phase signal. This is a multifrequency wave form composed of a large number of harmonics at equal frequency spacing. Young<sup>76,77</sup> presents a clear explanation of Schroeder-phased input and compares it with linear and log-rate frequency-sweep inputs, as well as the multistep input. This Schroeder-phase input design minimizes the peak excitation amplitude and results in a very flat power spectral density, characteristics that are ideal for frequency-domain identification methods. Young also demonstrates that the Schroeder-phase signal lessens the potential for frequency-response error because of transients effects. Further, Young shows that there is little difference in the accuracy of the frequency-response estimates as obtained from the log-rate sweep (also used herein, Sec. 5.11) vs the Schroeder-phased signal. Morelli<sup>78</sup> presents an optimal input design based on the Schroeder-phase signal that involves multiple control inputs for real-time parameters estimation in the frequency domain.

### 5.3 Recommended Pilot Inputs for the Frequency-Response Identification Method

Following the principles discussed earlier, the pilot maneuvers for system identification must be designed to suitably excite the aircraft modes that we wish to model. The piloted (or automated) frequency-sweep inputs presented in this chapter, and widely used by the leading author and many others, are not optimal *per se* (as are the inputs of Sec. 5.2), but they have proven to be an easy, safe, and reliable flight-test method for accurate and robust identification of fixed-wing and rotorcraft dynamics using the frequency-response method. Frequency-response identification of aircraft using piloted frequency-sweeps was pioneered by Systems Technology, Inc.,<sup>43</sup> in applications to fixed-wing aircraft. Tischler was the first to apply frequency-sweep testing methods to rotorcraft, with the identification of the XV-15 tilt rotor<sup>53</sup> and the B214-ST helicopter,<sup>54</sup> and subsequently to system-identification tests in more than 30 aircraft programs to date.

The *frequency sweep* refers to a class of control inputs that has a quasi-sinusoidal shape of increasing frequency. An example from flight tests for a UH-60 helicopter is shown in Fig. 5.1. The frequency-sweep input is particularly well suited for the frequency-response method for a number of reasons:

1) The excitation spectral content has a very uniform distribution (also called *power spectral density*) across the desired frequency range. Satisfactory spectral density over the frequency range of interest guarantees persistent excitation<sup>1</sup> and results in a consistent level of frequency-response coherence (accuracy) across the frequency range of interest. Thus, the frequency-sweep input yields an accurate

## COLLECTION OF TIME-HISTORY DATA

87

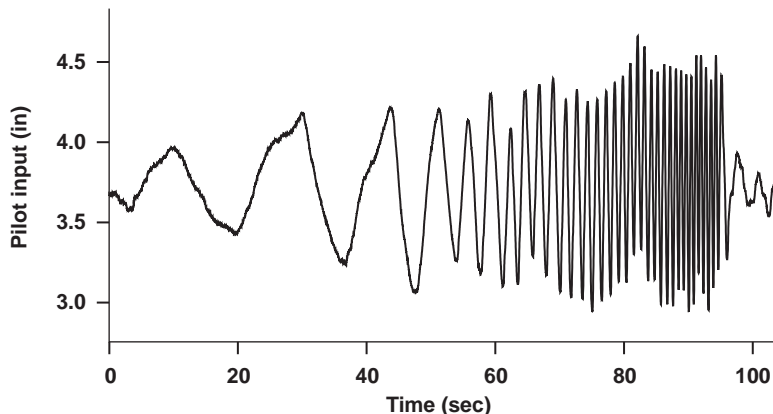


Fig. 5.1 Typical frequency-sweep input.

and reliable identification of model parameters, even when detailed a priori information of the dynamic modes is not available.

2) Response time histories are roughly symmetric. This means that the deviations in the inputs are generally equal (i.e., positive and negative) around the reference (trim). This symmetry is important both for maintaining the transients centered around the reference flight condition and for determining and subtracting out the nominal trim value of the input and output signals in the FFT analysis. In a well-executed piloted frequency sweep, the aircraft test will start in trim and end in trim, with the deviation in the inputs and outputs generally symmetric around the trim condition.

3) The frequency range of excitation is strictly controlled during the test. The frequency sweep test starts at a predefined minimum frequency and ends at a predefined maximum frequency. Both the minimum and maximum frequencies are easily monitored and reported to the test pilot in real time. Controlling the frequency range of the test in this way can be a quite important aspect of the safety of the flight-test procedure. For example, it might be undesirable to execute sharp step or multistep inputs that can “ring” lightly damped structural modes or that can overstress aircraft systems such as the transmission and drive train. The preferred sweep technique of slowly *increasing* the frequency and stopping at a predetermined maximum avoids these risks.

The frequency sweep is an ideal input for frequency-domain system *identification* of an accurate and complex state-space model. Frequency sweeps are generally less time efficient than the optimal inputs.<sup>6,10</sup> For example, record lengths for sweeps are about twice as long as the comparable 3-2-1-1 input, typically used for identifying the same aircraft using time-domain methods (see Hamel<sup>10</sup> for the Bo-105 system-identification program). The longer record lengths, needed for accurate broad-band conversion of the data from the time to the frequency responses, are sometimes cited as a drawback to using frequency-response methods for applications where only short “bursts” of data can be collected. This limitation can be overcome and good results obtained by concatenating several repeated

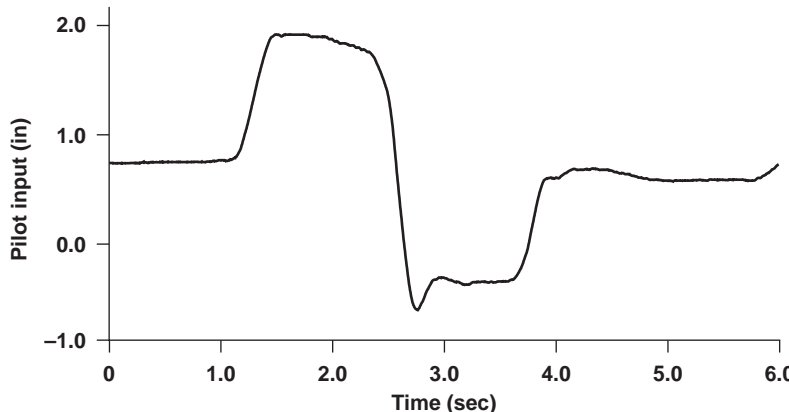


Fig. 5.2 Typical doublet input.

multistep inputs, as was demonstrated in an application to the Tu-144LL aircraft<sup>41</sup> and illustrated for a rotorcraft application in Sec. 5.12.

The goals for model verification are 1) to check the time-domain response predictions vs measured flight data to assess the importance of model mismatch in the identification process and 2) to ensure the robustness of the identified model for other input forms. The first goal can be achieved by using the same identification inputs for model verification (i.e., a frequency sweep for the frequency-response method). The second goal requires a flight-test input dissimilar from the identification maneuver. The recommended input for verification is a two-sided doublet, illustrated in Fig. 5.2. This is a common type of flight-test input, and it is a regular aspect of training for experimental test pilots. The fairly simple form of the doublet permits a good visualization of key aircraft dynamic characteristics and model performance. Further, the maneuver is characteristic of flight transients during typical maneuvering for which model fidelity is desired. The input is again roughly symmetric, which keeps the aircraft dynamics restricted to the range of transients over which the model is expected to be valid. Also, the doublet is different enough from a frequency sweep that it is a good check to ensure against overtuning of the model, wherein the model is accurate only for specific types of inputs.

#### 5.4 Instrumentation Requirements

For a given type of air vehicle, for example, a helicopter, the desired model to be obtained from system identification could range from a SISO frequency response (Bode plot) to a simple lower-order equivalent-system transfer-function model for handling-qualities analysis, a six-DOF quasi-steady stability and control derivative model, or a complete high-order state-space model that includes the physical equations of motion of the dynamics of the air mass, rotor, fuselage, actuators, and engine. The flight-test instrumentation requirements in each case are very different. In particular, the choice of model determines the input and output channels, associated filters, and sample rates that are needed. These various instrumentation characteristics must be determined and set up as part of the pre-flight-test preparations.

Input channels commonly required for flight mechanics model identification are pilot stick inputs and aerodynamic control surface deflections. Only the pilot stick inputs are needed if the application is limited to demonstrating handling-qualities specification compliance [e.g., MIL-STD-1797 (Ref. 5) for fixed-wing aircraft and ADS33E (Ref. 4) for rotorcraft], which is based on the end-to-end vehicle response to piloted inputs. On the other hand, system-identification modeling of the bare-airframe dynamics requires measurements of the aircraft aerodynamic control surfaces or at least the commands to the actuators.

The output channels needed to identify a six-DOF flight mechanics simulation model are as follows: air boom data [ $V, \alpha, \beta$ ] (or equivalently an inertial measurement unit [ $u, v, w$ ]) for nonhovering conditions; attitudes [ $\phi, \theta, \psi$ ]; angular rates [ $p, q, r$ ]; and linear accelerometers [ $a_x, a_y, a_z$ ]. Handling-qualities specification compliance applications can be achieved from measurements of only the angular rates and vertical acceleration. In contrast, all four types of the preceding outputs are needed to identify a six-DOF stability and control derivative model. Specialized identification studies might require measurement of the structural, engine, and rotor response parameters to determine models and interactions of these subsystems.

The selection of the appropriate data collection sample rate and data system filters flows directly from the frequency range of applicability of the identified model. We start by first considering signal processing filters, such as noise or anti-aliasing filters. *It is highly desirable that an identical filter be implemented on all input and output signals.* Consider the situation that arises if, for example, one filter is used on the roll-rate signal and a lower cutoff frequency filter is used on the pilot stick signal. The resulting models obtained from system identification will reflect an additional (spurious) high phase lead (rising phase curve) that will be reflected as biased identified parameter values in the aircraft dynamics equations. This spurious phase result is directly related to the difference between the filter cutoff frequencies, and it can be different for each input/output pair depending on the filters used for each channel. The phase error can be corrected in the frequency-response results as part of the analysis, but it is much easier and more precise to avoid this problem altogether by making sure ahead of time that the input and output filters match on all channels. Instrumentation engineers often select filter cutoff frequencies separately for each data channel as appropriate to that sensor's bandwidth. So, for example, potentiometer measurements of the pilot stick inputs might be typically filtered at lower frequencies (e.g., 5 Hz), angular rate gyro measurements at intermediate frequencies (e.g., 20 Hz), and linear accelerometers at higher frequencies (e.g., 50 Hz), unless the system-identification engineer specifies that all channels should be conditioned with the same filter.

As a good rule of thumb, it is recommended to select the filter cutoff frequency  $\omega_f$  (also referred to as the filter bandwidth) to be at least five times the desired maximum frequency of model applicability  $\omega_{\max}$ :

*Guideline:*

$$\omega_f \geq 5 \cdot \omega_{\max} \quad (5.1)$$

With the filter selected, we next choose a sample rate  $\omega_s$ , the same for all of the signals, with a value of at least another factor of five above the filter frequency:

*Guideline:*

$$\omega_s \geq 5 \cdot \omega_f \quad (5.2)$$

A typical six-DOF flight mechanics model for simulation and handling-qualities applications will require a frequency range of applicability that extends to  $\omega_{\max} = 12 \text{ rad/s} \approx 2 \text{ Hz}$ . Applying these rule-of-thumb formulas yields a filter frequency of  $\omega_f = 60 \text{ rad/s}$  and a data sample rate of  $f_s = 50 \text{ Hz}$ . These are common instrumentation characteristics for aircraft and helicopter flight testing. In the case of the XV-15 flight-test program, there was an interest in modeling structural modes up to frequencies of about 10 Hz, so that the filters were set at 50 Hz and the sample rate was 250 Hz, in accordance with the rules of thumb. The resulting factor of 25 between the sampling rate and the maximum frequency of interest [combine Eqs. (5.1) and (5.2)] is conservative in the sense that a somewhat smaller value could probably be used. In fact, theoretically the sample rate could be reduced to  $2\omega_{\max}$ , which puts the Nyquist frequency ( $\omega_{\text{Nyq}} \equiv 0.5\omega_s$ ) at the maximum frequency of interest. However, this low sample rate will not allow accurate identification near  $\omega_{\max}$  because of real-world sensor noise, atmospheric turbulence, and other effects. So the factor of 25 rule of thumb is still preferred whenever possible.

Obtaining an accurate model using system identification depends on the careful selection and documentation of instrumentation system filter characteristics and the sample rates for each signal. Even if the instrumentation system characteristics are not the optimum and do not match values recommended here, corrections can be made for this later on, but only if the exact values are known. A commonly faced problem is that once the flight-test instrumentation system is removed from the vehicle at the end of the test it becomes very difficult to reconstruct the exact characteristics for each input and output signal, and therefore there is a high risk of introducing spurious dynamics in the identified model. Other important factors not discussed herein are the range and resolution requirements for the sensors.<sup>6,10,67</sup>

## 5.5 Overview of Piloted Frequency Sweeps

Figure 5.3 shows an example of two piloted frequency sweeps that are well suited to system identification. Although they are shown as a single time history in the graph, the records were not collected as a continuous maneuver. The two runs are *concatenated* into a single (“linked maneuver”) record within CIFER®. These data were collected for basic handling-qualities (HQ) specification testing of a conventional single-rotor helicopter (Bell 214ST) in hover.<sup>54</sup> Note that the record starts and ends with the aircraft in a trim state. The pilot followed preflight briefing instructions to provide a trim record of 3 s before starting the maneuver, then perform the maneuver, and finally return to trim and remain there for 3 s before turning off the data recorder. Again, this record of the trim condition before and after the maneuver is important for the spectral analysis, which subtracts the trim state from the data.

The next point to observe in Fig. 5.3 is that the sweep starts with two low-frequency input cycles and then progresses smoothly to the mid and higher

## COLLECTION OF TIME-HISTORY DATA

91

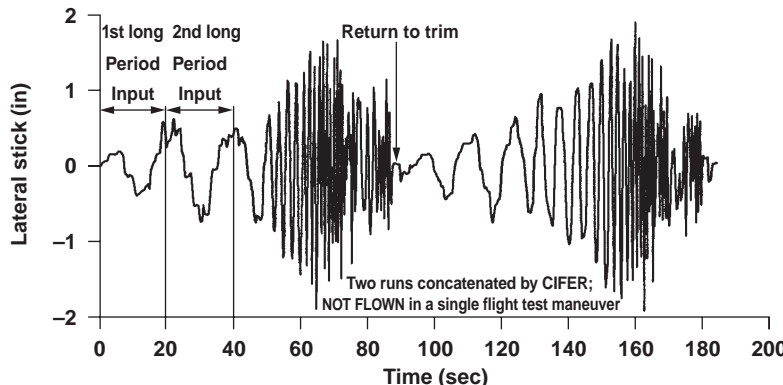


Fig. 5.3 Frequency-sweep input for handling-qualities testing (Bell 214ST, hover).

frequencies. In this example, the low frequency of interest in the frequency range of applicability was 0.05 Hz, which is equivalent to a maximum period of interest of  $T_{\max} = 1/0.05 = 20$  s. So the pilot was advised to execute two 20-s input cycles at the start of the maneuver. The low-frequency input is not a pure sine wave, and so this part of the sweep actually ensures good identification over a range of frequencies around 0.05 Hz. Then the pilot slowly increases the frequency of the input. The pilot has some discretion in how rapidly to increase the frequencies. In this example, the first sweep has fewer cycles at low frequency, more in the midrange, and fewer in the high frequencies, as compared to the second sweep. The exact nature of the increase in frequencies is not important; in fact, some irregularity in the input is actually beneficial because it improves the richness of the excitation power spectrum and thus improves the identification. Concatenating the signals ensures a rich spectral content.

The input amplitude also does not have to be exactly symmetric or constant, either. Sometimes the pilot can instinctively increase the input amplitude at midfrequencies and decrease it again at higher frequencies. The frequency-response identification method has been found to be very robust to such variations in piloting technique. What is important, however, is that 1) the maneuver starts and ends in trim, 2) there are two good low-frequency cycle inputs, 3) there is a regular and smooth increase in frequency, and 4) the aircraft oscillations are roughly symmetric about the trim condition.

Figure 5.4 illustrates the roll-rate response for the frequency-sweep input of Fig. 5.3. Aircraft responses for the frequency sweep are in the range of  $\pm 10$  deg in angular attitudes and  $\pm 10$  deg/s in angular rates, as can be seen in the figure. Responses of this typical magnitude are desirable because if the responses are too small the corresponding signal-to-noise ratio will be low and the identification quality will be degraded. If the amplitudes are too large, the aircraft will depart too much from the reference trim condition for the identified model to remain relevant and linear modeling assumptions to remain valid. The test pilot must be adequately briefed prior to the flight test as to the required amplitudes of the frequency-sweep maneuvers.

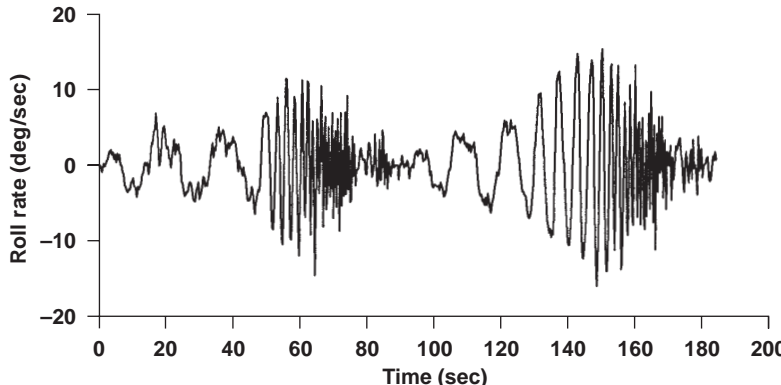


Fig. 5.4 Roll-rate response: Bell 214ST during hover sweeps.

## 5.6 Detailed Design of Frequency-Sweep Inputs

A key part of designing a frequency sweep is determining the needed minimum  $\omega_{\min}$  and maximum  $\omega_{\max}$  frequencies in the sweep required to ensure that the coherence and associated frequency-response accuracy will be acceptable over the frequency range of applicability of the model. As an example, for handling-qualities specification compliance applications, accurate frequency responses are needed over a range of frequencies of

$$0.5\omega_{\text{BW}} \leq \omega \leq 2.5\omega_{180} \quad (5.3)$$

where  $\omega_{\text{BW}}$  is the bandwidth frequency, which is defined in the handling-qualities community (e.g., Ref. 4) as the frequency at which the phase of the attitude response (e.g.,  $\phi/\delta_{\text{lat}}$ ) is  $-135$  deg. The parameter  $\omega_{180}$  is the frequency at which the phase of the attitude response is  $-180$  deg, or, in other words, exactly out of phase.

Estimates of the bandwidth and the  $-180$ -deg phase frequency can be obtained from analytical sources such as simulation models or basic flight mechanics calculations of the stability and control derivatives. Estimates of  $\omega_{\text{BW}}$  and  $\omega_{180}$  can also be obtained from step response time-history data, using the relationships between frequency-domain and time-domain response metrics for a second-order system (e.g., Ref. 79). Finally, a sample frequency sweep can be conducted in a flight test based on expected, typical, or conservative values of these parameters, and then the identification results can be used to refine the choice of frequency-sweep start and stop frequencies. As an example, a lower value for the expected bandwidth frequency for (SAS-off) rotorcraft is about  $1$  rad/s, and the  $-180$ -deg phase frequency is typically about  $6$  rad/s. The starting (i.e., minimum) frequency of the sweep is then selected as

$$\omega_{\min} = 0.5\omega_{\text{BW}} = 0.5 \cdot 1 = 0.5 \text{ rad/s} \quad (5.4)$$

## COLLECTION OF TIME-HISTORY DATA

93

corresponding to

$$f_{\min} = \frac{\omega_{\min}}{2\pi} = 0.08 \text{ Hz} \quad (5.5)$$

As will be discussed in Sec. 5.9, there should be two complete long-period inputs at the beginning of the sweep, corresponding to the minimum frequency:

$$T_{\max} = \frac{2\pi}{\omega_{\min}} \quad (5.6)$$

For our current example, because the minimum frequency of interest is 0.5 rad/s,

$$T_{\max} = \frac{2\pi}{0.5} \cong 12 \text{ s} \quad (5.7)$$

The ending (i.e., maximum) frequency of the sweep is thus

$$\omega_{\max} = 2.5\omega_{180} = 2.5 \cdot 6 = 15 \text{ rad/s} \quad (5.8)$$

corresponding to

$$f_{\max} = \frac{\omega_{\max}}{2\pi} = 2.4 \text{ Hz} \quad (5.9)$$

and

$$T_{\min} = \frac{1}{2.4} \cong 0.4 \text{ s} \quad (5.10)$$

System-identification flight tests to be conducted for the determination or validation of six-DOF simulation models intended for flight mechanics and piloted applications generally emphasize a frequency range that includes lower frequencies (0.3–12 rad/s). For flight-control design, the test frequencies typically cover the range of 1–20 rad/s, in order to provide the needed high-accuracy data from near the intended broken-loop crossover frequency  $\omega_c$  (at which the magnitude is 0 dB for determination of phase margin) to the –180-deg phase crossing (for determination of gain margin).

Experience for a wide range of flight dynamics and control applications has shown the total sweep record length  $T_{\text{rec}}$  should be about as follows:

*Guideline:*

$$T_{\text{rec}} \geq (4 \text{ to } 5)T_{\max} \quad (5.11)$$

Thus about 40% of the sweep maneuver is associated with the two low-frequency inputs (at  $f_{\min}$ ). The remaining time is used to complete the buildup to

the maximum frequency  $f_{\max}$  and to establish trim at the start and end of the record. For the handling-qualities and flight-mechanics modeling examples ( $T_{\max} = 12\text{--}20$  s), this guideline would mean an individual frequency-sweep record length of about  $T_{\text{rec}} = 60\text{--}90$  s, which is typical of frequency-sweep testing, as seen, for example, in the AGARD databases.<sup>10</sup>

Finally, the magnitude of the input is typically in the range of  $\pm 10\text{--}20\%$  of control inputs or  $\pm 0.5\text{--}1.0$  in. for a typical center stick. The resulting aircraft angular response is typically in the range of  $\pm 5\text{--}15$  deg (attitude variations),  $\pm 5\text{--}15$  deg/s (attitude rate variations), and  $\pm 5\text{--}10$  kn (velocity variations). This produces a time-history database for a system-identification model that is accurate for typical dynamic maneuvers during flight.

## 5.7 Flight-Testing Considerations

A detailed report was published by Williams et al.<sup>67</sup> covering the background of rotorcraft frequency-sweep testing, instrumentation requirements, and many important safety and testing aspects. Issues related to the safety of frequency-sweep flight testing are addressed by Tischler et al.<sup>80</sup> Some key flight-test considerations are as follows:

1) *Real-time telemetry (TM):* A real-time readout of telemetered aircraft attitudes, angular rates, airspeeds, and pilot inputs is desirable. This allows flight-test engineers and test directors to monitor the progress of the sweep test and critical aspects such as the start and cutoff frequencies, off-axis inputs, and the deviations from the trim condition. The data should be reviewed and pilot input technique critiqued after each sweep. Cockpit control position indicators visible to the test pilot are helpful if available, but not essential.

2) *Flight-test planning:* Allow approximately 1.0 h per flight condition, once the pilot has completed several practice runs. Three good sweeps and two doublets should be conducted in a particular control axis before the test proceeds to the next axis. The two best sweeps will generally be concatenated in the identification analysis. The doublet is executed with a sharp input in one direction until the maximum angular rate is achieved, followed by the same type of input in the opposite direction.

3) *Flight-test conditions:* For rotorcraft flight testing in hover, the steady winds should be 5 kn or less. For forward-flight tests of rotorcraft and fixed-wing aircraft, it is desirable to have no more than light turbulence (e.g.,  $\pm 5$  kn). If the winds or turbulence are too strong, there will be significant reduction in the signal-to-noise ratio and an associated degradation in the quality of the identification results.

4) *Flight-test conduct:* The copilot or a member of the flight-test team in the TM station should help coach the test pilot for proper timing of the sweep inputs. The copilot should use a simple stopwatch to count off every quarter-cycle for the two low-frequency periods  $\bar{T}_{1/4} \equiv \frac{1}{4}(T_{\max})$ . For the example case of Eq. (5.7), the copilot would call out “3, 6, 9, and 12,” thereby indicating to the pilot when the input should be at maximum (positive), center, maximum (negative), and back to center for the first low-frequency cycle. This count is repeated for the second low-frequency cycle, and then every 10 s thereafter until the end of the sweep. A flight-test engineer should monitor the sweep inputs based on the TM data stream and notify the pilot if excessive correlation of inputs is apparent and when

the maximum frequency has been achieved. In typical aircraft and rotorcraft frequency-sweep tests, the pilot is signaled with a call at “1 Hz” and “2 Hz knock-it-off.” The flight-test engineer should provide feedback and comments concerning the quality of the maneuver following each sweep.

## 5.8 Open-Loop vs Closed-Loop Testing for Bare-Airframe Identification

Data from SCAS-on flight tests (i.e., closed loop) *can be used* for bare-airframe identification as long as the control-surface deflections are measured. But, if possible, it is generally preferable to conduct the test with the SCAS off (open-loop) or with the SCAS gains reduced. The main reason is that the SCAS typically suppresses much of the low-frequency pilot inputs, leading to reduced signal-to-noise content in the data and a degradation in the identification accuracy at low frequencies.

Figure 5.5 is a schematic diagram for a helicopter pitch SCAS. The “control surface” in this case is the pitch-axis mixer input  $\delta_{\text{lon,}mx}$ , which commands a pitch response from the rotor system. Figure 5.6 presents coherence functions for the bare-airframe pitch-rate response identification of the AH-64 helicopter  $q/\delta_{\text{lon,}mx}$  in hover. In the case marked “open-loop test,” the flight tests were conducted with the SCAS disengaged, so that the bare-airframe input  $\delta_{\text{lon,}mx}$  and the piloted sweep input  $\delta_{\text{lon}}$  have the same excitation characteristics. In the second case (“closed-loop test”), the sweep tests were conducted with the SCAS on, but the bare-airframe response was again extracted using the mechanical control measurements  $\delta_{\text{lon,}mx}$  as inputs. At frequencies of about 0.6 rad/s and higher, the coherence levels are essentially the same, indicating equivalent identification accuracy for SCAS-off and SCAS-on tests. At the lower frequencies, the coherence drops more quickly (reduced identification accuracy) for the SCAS-on case because of the suppression of the low-frequency excitation. So even though the pilot executes a good sweep with satisfactory low-frequency excitation of the cockpit stick input  $\delta_{\text{lon}}$ , the SCAS feedback suppresses the low-frequency content of the bare-airframe input  $\delta_{\text{lon,}mx}$ , thereby degrading the coherence in this frequency range. This suppression of the low-frequency excitation is a common and often problematic occurrence for SCAS-on flight testing.

A second problem with bare-airframe identification from closed-loop test data is that the SCAS can induce significant correlation between the control inputs. As will be discussed in Chapter 9, this control correlation can significantly degrade the quality of off-axis response identification. A common and particularly difficult

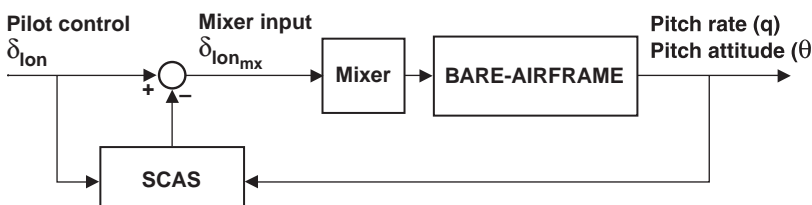


Fig. 5.5 Schematic of helicopter pitch SCAS.

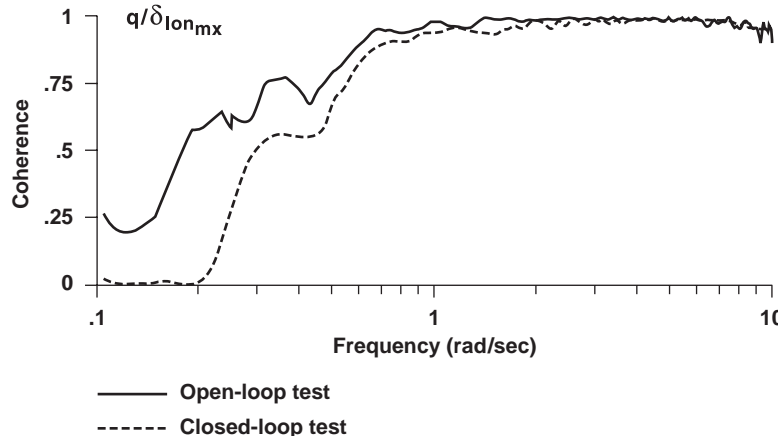


Fig. 5.6 Degradation of bare-airframe identification with SCAS-on flight testing.

circumstance arises for bare-airframe identification in fixed-wing applications if an aileron-to-rudder interconnect (ARI) is present in the control system.<sup>81</sup> The ARI is a mechanical or computer crossfeed that moves the rudder in direct relationship to aileron commands to achieve coordinated turns. This produces total correlation of the rudder and aileron surface movements for the aileron sweep and makes bare-airframe identification of the responses to aileron impossible (see Sec. 9.3.2, limiting condition # 1).

If flight testing is conducted with the SCAS engaged, special provisions must be made for the multiple aerodynamic surfaces to be independently actuated in order to achieve an identification of the aerodynamic control derivatives. For example, in the case of a typical high-performance aircraft configuration, there are typical control surfaces distributed along the wings and tail (or canard). A simple schematic of a notional pitch control system is depicted in Fig. 5.7. Pilot input  $\delta_{\text{pitch}}$  and measured pitch-rate response  $q$  are processed with the *flight control system* to determine an effective pitch input at the mixer  $\delta_{\text{pitch}_{\text{mx}}}$ . The pitch mixer distributes the input as a simultaneous (symmetric) actuation of multiple control surfaces ( $\delta_1, \delta_2, \dots$ ) based on a *control allocation* algorithm, as indicated in the figure. Pitch control surfaces might include canards, symmetric aileron deflection, and elevators. This renders the time histories of the control surfaces fully correlated. As a result, the individual bare-airframe control derivatives (e.g.,  $M_{\delta_1}$  and  $M_{\delta_2}$ ) cannot be reliably determined, even though the measurements of the individual surfaces  $\delta_1, \delta_2, \dots$  are available. Alternatively, a lumped pitch control derivative  $M_{\delta_{\text{pitch}_{\text{mx}}}}$  can be identified.

This control surface correlation problem was encountered in the initial identification studies on the X-31A experimental aircraft. In this project the moment commands were distributed to the various control surfaces resulting in nearly complete control correlation. The problem was overcome by repeating the flight tests with a special excitation system capable of actuating individually the aerodynamic control surfaces (e.g.,  $\delta_1$  alone) as discussed by Weiss et al.<sup>82</sup>

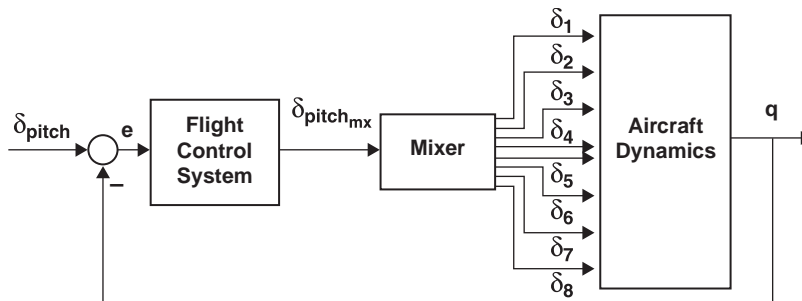


Fig. 5.7 Simultaneous actuation of multiple aerodynamic control effectors.

A final problem that can arise with bare-airframe identification from closed-loop test data is the potential for feedback of the disturbance response to the control input signals. In this case, some of the bare input excitation will be correlated with the disturbance response (e.g., turbulence) in addition to the primary response to the piloted (sweep) input. As will be discussed in detail in Chapter 8, this feedback correlation of noise results in a biased estimate of the bare-airframe response. The bias error can be minimized by ensuring a suitable ratio of sweep-to-disturbance input.

There are many situations when it is not practical or prudent to perform an open-loop test. For example, the bare-airframe dynamics might be too unstable or too highly coupled, leading to SCAS-off handling qualities that are not suitable for achieving good sweep inputs. If there is a high level of instability in a particular axis and if a “split-axis” SCAS configuration is possible, then the SCAS should be engaged only in those channels for which it is needed. Another useful technique is to reduce the feedback gains, if possible, thereby lessening the potential for control correlation and dynamic response suppression. In summary, open-loop testing is the preferred approach for bare-airframe system identification when the aircraft dynamics permit, but it is not mandatory.

## 5.9 Piloted Frequency Sweeps: What IS and What IS NOT Important

Test pilots and engineers are often trained in conventional flight-testing techniques (steps, pulses, controllability, etc.) and are often new to the concept of frequency-sweep testing. Sometimes it is not obvious as to what are the important aspects of frequency-sweep testing that translate into good frequency-domain identification results. The following short list of key dos and don’ts is based on the leading author’s experience with system-identification testing involving more than 30 aircraft programs to date.

The following points summarize **what IS important** in the conduct of piloted frequency-sweep tests:

- 1) Sweeps should start and end in trim, with 3 s of trim data contained in the test record. This is important for the determination of the trim values of the controls and responses as part of the subsequent spectral analysis.

2) After the initial trim period, execute two complete long-period inputs  $T_{\max}$ . This part of the maneuver is generally the most challenging because the aircraft will generally experience larger amplitude responses that might also be considerably out of phase with the pilot inputs. Good piloting technique is rapidly learned with some ground and flight practice prior to formal data collection. Timing indications, provided by a copilot or ground station engineer, can be very helpful for this part of the sweep (see item 6).

3) Maintain a smooth increasing progression in frequency, without rushing through the midfrequencies. Along with some coaching based on real-time telemetry, the pilot rapidly learns not to rush through the midfrequencies on the way to the higher frequency inputs.

4) Adjust the input to maintain the aircraft response transients to be roughly symmetric about the trim flight condition. For hover tests (rotorcraft and V/STOL), attitude and ground position provide good center references. In cruise condition tests (fixed wing and rotorcraft), roll attitude and aircraft airspeed provide good center references. Even if the input is symmetric, the aircraft response will not be symmetric because of atmospheric disturbances and off-axis inputs, causing the aircraft to tend to drift away from the reference condition. Configuration asymmetries or nonlinearities will also contribute to this drift. So, for example, the aircraft might start to drift slowly to the right during a roll sweep. The pilot should be advised to migrate the center point of the control input to the left during the sweep, so that the overall response is roughly symmetric about the reference flight condition. Pilots often use small pulse-type inputs to achieve the needed correction.

5) Nonswept controls are applied to “bound” the off-axis responses to be roughly symmetric with respect to the reference flight condition. This off-axis regulation should constitute a low-frequency or secondary task. For example, left uncorrected, a helicopter will develop significant yawing oscillations during a roll (lateral stick) sweep test. Although it is desirable to capture the coupling response of yaw caused by lateral stick inputs, large yawing motion is not desirable. Therefore some pulse-type off-axis inputs will be required to keep the yaw within reasonable bounds, say,  $\pm 10\text{--}20$  deg. However, *these secondary pedal inputs should not be highly correlated with the primary lateral stick sweep input*. Excessive correlation of secondary controls is generally avoided with clear preflight instructions and real-time feedback to the pilot during the conduct of the sweep. The pilot should be advised to concentrate on the primary sweep input; maintaining the response to be roughly symmetric about the reference condition should be treated as a secondary or low-frequency trim task. Another effective technique is for the copilot to take care of the needed off-axis corrections. This pulsing correction technique for maintaining the transients centered about the reference flight condition generally ensures that the secondary and primary inputs will not be highly correlated.

6) The flight-test engineer (in the aircraft or ground station) or copilot should provide timing indicators to the pilot to assist in the frequency-sweep tests. For example, suppose the long-period inputs for a lateral stick frequency sweep are selected as 16 s ( $T_{\max} = 16$ ) corresponding to a minimum frequency of  $\omega_{\min} = 0.39$  rad/s, typical for flight-mechanics applications. The flight-test engineer should call out “4, 8, 12, 16” to signal the pilot when the lateral stick position should be roughly at maximum right, center, maximum left, and center for the first long-period cycle. The flight test continues with “20, 24, 28, 32” for the

second long-period cycle. After this, the count to the pilot continues at every 10 s, “40, 50, ...,” until the end of the sweep, to help pace the pilot as to where the frequency progression is relative to the overall desired sweep record length  $T_{rec}$ .

7) Telemetry data are useful in monitoring the frequency progression and high-frequency cutoff point. Running the strip charts at a fast speed (e.g., 5 mm/s) allows the frequency of the stick inputs to be easily monitored in real time. Piloting technique to achieving a slow and steady buildup from the minimum to maximum frequencies benefits from some practice and coaching based on the TM data. Also, the pilot should be signaled as the maximum frequency is approached. For example, suppose that the high-frequency limit for the sweeps is selected as  $f_{max} = 2$  Hz. The flight-test engineer should signal the pilot with call-outs of “1 Hz,” “1.5 Hz,” and “2 Hz, knock it off” to ensure that maximum frequency is not exceeded. After the sweep is completed, the strip charts can be reviewed to ensure that the sweep was completed as desired (e.g., amplitudes, frequencies, centered about trim, etc.), and feedback can be given to the pilot before the next sweep is conducted.

The following points summarize **what IS NOT important** in the conduct of piloted frequency-sweep tests:

1) Constant input amplitude is not important. The pilot does not have to be concerned about maintaining constant input amplitude with changing frequency. The important consideration should be the frequency content of the input.

2) Exact sinusoidal input shape is not important and in fact is not desirable. Irregularity ensures a broader bandwidth of excitation, and nonrepeatability of the input wave form improves the overall information content when the repeat sweep records are concatenated (linked) in the analysis. The input does not have to be precisely defined or controlled by jigs or other techniques. The frequency-response identification method has been found to be very robust to considerable variations in input excitation.

3) Exact frequency progression is not important. Experiments have been performed using tones and lights and other means to help the pilot to track an exact frequency progression. Often the pilot is confused by these timing cues because the response of the aircraft will require nonsinusoidal (e.g., pulse type) input to maintain the aircraft generally centered about the reference flight condition. Frequency sweeps are best conducted without detailed external cues, beyond the general timing prompts discussed in Sec. 5.7 and in items 6 and 7 of the preceding subsection (i.e., “What IS important”).

4) Exact repeatability is not important and indeed is not desired. The pilot will naturally perform the sweep a little differently each time, thereby improving the information content of the linked records.

5) Increased input amplitudes at higher frequencies are not needed. As the higher-frequency inputs are reached, the aircraft response generally lessens (because of the  $k/s$  rigid-body rate-response behavior). The test pilot might feel it necessary to overcome this lack of perceived response by increasing the amplitude of the control inputs with increasing frequency. This is neither prudent nor required, and the pilots should be coached to avoid increasing amplitude inputs beyond the recommend limits of about  $\pm 10\text{--}20\%$ . Instead, they should allow the aircraft response to attenuate naturally with increasing frequency.

6) High-frequency inputs are not needed. The maximum frequency for piloted sweeps of aircraft and rotorcraft is typically limited to about 2 Hz, which results in

good identification models for flight mechanics and control applications. This cut-off frequency generally corresponds to the bandwidth for typical piloted and control system inputs during maneuvering flight. So by staying within these guidelines, aircraft loads during sweep tests typically do not exceed those expected for normal flight maneuvering and are usually much less than those encountered for typical controllability tests involving rapid control reversals. However, it is physically easy for a pilot to execute roll and pitch sweep inputs to frequencies as high as 4–5 Hz. Such high-frequency piloted inputs are neither necessary nor prudent and can lead to excessive structural loads on the aircraft. As already mentioned, the input frequency is easily monitored from telemetry of piloted control deflections. Frequency-sweep testing can be accomplished safely without telemetry, following some ground-based practice to sensitize the pilot to the issues around higher-frequency inputs and amplitudes. System-identification testing of high-frequency, lightly damped dynamics, such as flutter modes (fixed-wing aircraft) and rotor modes (helicopters), is a common and effective technique for modal determination, but it should be accomplished with computer-generated inputs and include provisions for automated sweep termination based on real-time monitoring of critical loads (Sec. 5.11).

## 5.10 Summary of Key Points in Piloted Frequency-Sweep Technique

The following points summarize the key considerations in the piloted frequency-sweep technique as discussed in the preceding sections:

- 1) The sweeps should start and end in a trim condition.
- 2) Nonswept controls should be applied as a secondary input to reduce large off-axis responses, but must not be excessively correlated with the primary input.
- 3) Large asymmetrical shifts in aircraft response should be countered by low-frequency shifts in the center control position.
- 4) The sweep technique should be practiced on the ground and in flight with timing cues provided by the copilot.
- 5) The required frequency range of the test should be determined in advance. The test engineer should monitor the input frequency and call “knock it off” when the maximum desired frequency is achieved.
- 6) All parties should be aware that pilots can easily generate large-amplitude inputs at frequencies of up to 5–6 Hz. This is generally not necessary and can be potentially damaging to the aircraft.

Modern aircraft employ high levels of command and feedback augmentation that greatly improve handling qualities and make the frequency-sweep testing easy to learn and very efficient to perform. An excellent example of this was the Advanced Digital Optical Control System Demonstrator (ADOCS), which incorporated a model-following control law and a sidestick controller in a UH-60A helicopter (Fig. 5.8). Piloted frequency-sweep testing and system-identification analyses using CIFER® were conducted to document the response characteristics and to compare handling-qualities characteristics with the (proposed at that time) ADS-33 design specifications.<sup>83</sup> Aircraft excitation, achieved via the side-stick controller, and the associated pitch-rate response are shown in Fig. 5.9. Real-time telemetry of pilot inputs and aircraft responses ensured that preestablished aircraft flight limits were not exceeded. A complete discussion of the ADOCS flight-test results is given by Tischler et al.<sup>84</sup>



Fig. 5.8 ADOCS Demonstrator.

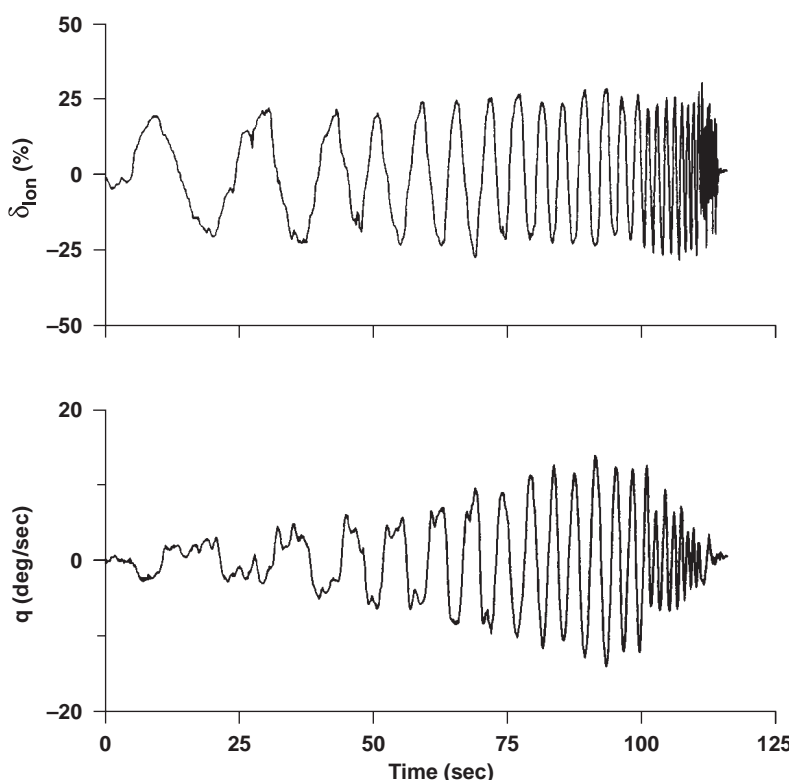


Fig. 5.9 Piloted frequency-sweep flight testing of the ADOCS Demonstrator.

### 5.11 Computer-Generated Sweeps

Computer-generated frequency-sweep inputs can be both effective and time efficient in many ground and flight applications, but they must be properly synthesized in order to obtain the desired frequency spectrum. The Schroeder-phase signal discussed earlier (Sec. 5.2) has shown promise for system-identification applications.<sup>77</sup> Tischler developed an automated frequency-sweep testing approach, using an exponential sweep and white noise, for the frequency-response identification of an off-line simulation model of the UH-60.<sup>85</sup> The exponentially increasing sweep frequency is used to ensure that more time is spent at the lower frequencies (longer characteristic periods) and less time at the higher frequencies (shorter characteristic periods). Young<sup>76</sup> and Young and Patton<sup>77</sup> also found that the logarithmic sweep was preferable to the linear sweep. They further concluded that the log-sweep and Schroeder-phase (optimal) inputs yielded comparable identification results for flight-dynamics applications.

At first glance, it would seem that the frequency sweep would simply be implemented as

$$\delta_{\text{sweep}} = A \sin(\omega t) \quad \text{with} \quad \omega = f(t) \quad (5.12)$$

A sweep generated using this algorithm will exhibit frequencies that increase much faster than the function  $\omega = f(t)$  because the product of  $\omega t$  in Eq. (5.12) is now actually time modulated  $f(t^n)$ . To solve this problem, the frequency-sweep component is generated by the equation

$$\delta_{\text{sweep}} = A \sin[\theta(t)] \quad (5.13)$$

where  $A$  is the sweep amplitude, typically 10% of the maximum deflection limits, and

$$\theta(t) \equiv \int_0^{T_{\text{rec}}} \omega(t) dt \quad (5.14)$$

The frequency progression is given by

$$\omega = \omega_{\text{min}} + K(\omega_{\text{max}} - \omega_{\text{min}}) \quad (5.15)$$

where

$$K = C_2[\exp(C_1 t / T_{\text{rec}}) - 1] \quad (5.16)$$

The values  $C_1 = 4.0$  and  $C_2 = 0.0187$  have been found to be suitable for a wide range of applications.

The general implementation of the automated sweep should include several additional features, such as trim duration, where zero input at beginning and end ensures a good steady-state condition; constant frequency of  $\omega_{\text{min}}$  for one full period, which ensures sufficient spectral content at the starting frequency before

starting the progression of Eq. (5.15); fade in and fade out, which avoids sharp inputs at the start and the end of sweep; and selectable notches, which attenuate magnitude, if desired, at known structural modes.

The values of the sweep parameters depend on the frequency range of interest and the units of the control input. Typical values for documenting aircraft flight dynamics are

$$T_{\text{rec}} = 90 \text{ s}, \quad A = 1.0, \quad \omega_{\text{min}} = 0.3 \text{ rad/s}, \quad \omega_{\text{max}} = 12.0 \text{ rad/s} \quad (5.17)$$

The frequency progression plotted in Fig. 5.10 starts with a 20-s period corresponding to the starting frequency (0.3 rad/s) and then progresses according to the exponential function [Eq. (5.16)]. The complete frequency-sweep input  $\delta_{\text{sweep}}$

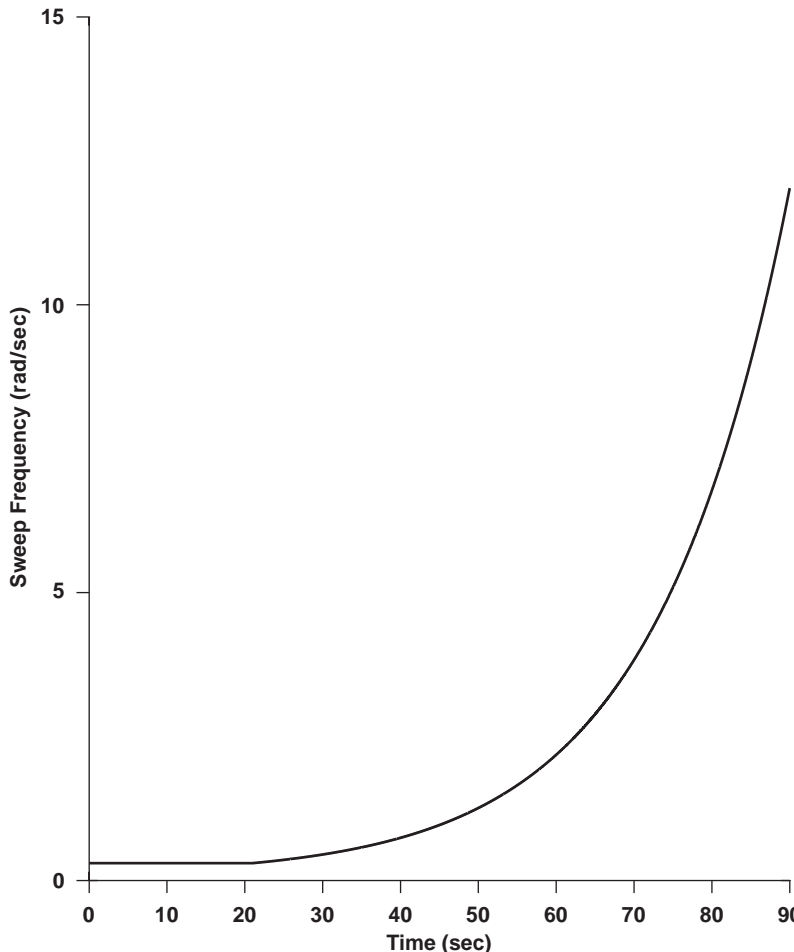


Fig. 5.10 Frequency progression for typical automated sweep [Eq. (5.17)].

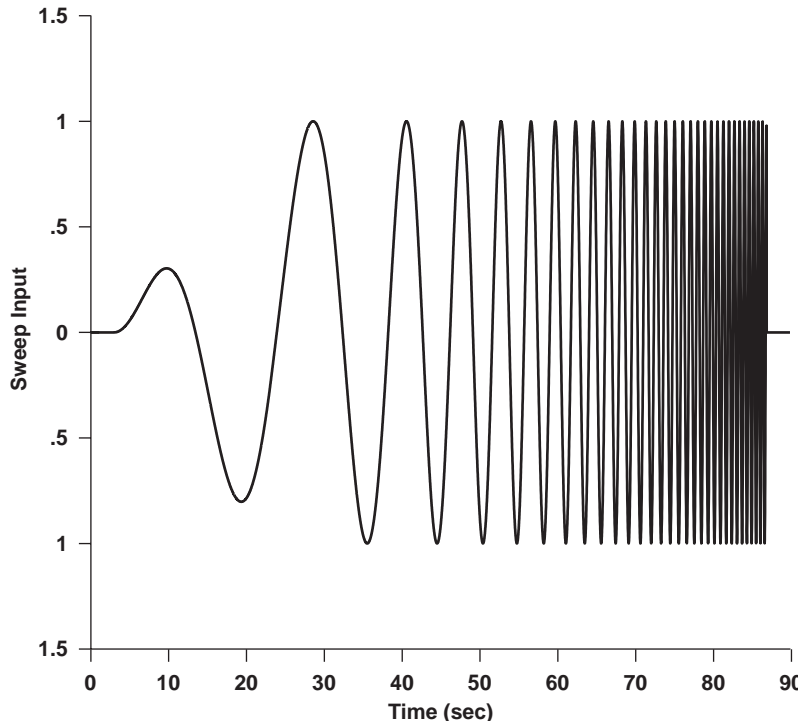


Fig. 5.11 Typical automated frequency-sweep input [Eq. (5.17)].

for this example [Eq. (5.17)] is plotted in Fig. 5.11; it includes the trim duration (3 s) and fade in during the initial starting frequency.

Computer-generated sine sweeps alone might sometimes not constitute an excitation signal with sufficient spectral richness because they will not have any of the irregularities in input shape that are evident in a pilot-generated sweep. So, if necessary, a band-limited white-noise component can be added to the sweep to enrich the spectral content:

$$\delta_{\text{excitation}} = \delta_{\text{sweep}} + \delta_{\text{white noise}} \quad (5.18)$$

A typical rms ( $1\sigma$ ) level of the noise signals is selected as

$$\delta_{\text{white noise}}: \sigma = 0.10A \quad (5.19)$$

The white-noise component should be processed with a low-pass filter ( $\omega_f = \omega_{\max}$ ) to suppress high-frequency content in the excitation.

This computer-generated input signal, which combines an exponential sweep and white noise, has proven highly effective for both flight- and ground-based testing purposes for a wide range of vehicles and subsystems (e.g., actuators). In flight-test and ground hardware applications, two repeat runs of the identical

sweep in Eq. (5.17) will allow an averaging out of the effect of random turbulence and provide a concatenated record length of  $T_F = 180$  s, which is ideal for typical flight-mechanics applications (e.g.,  $T_{\text{win}} = 36$  s,  $f_{\text{min}} = 0.028$  Hz, and  $n_d = 5$ ; see Sec. 7.10.1). For applications involving system-identification analysis of simulation math models, identical repeated inputs will yield identical responses and not contribute any averaging benefit. For these applications, two automated sweeps cases can be generated with different start and stop frequencies to provide the needed averaging effect and overall record length. An easier alternative for ground-based testing is a longer-duration single sweep of  $T_{\text{rec}} = 180$  s.

Automated data collection with computer-generated frequency sweeps has seen widespread use for both ground-based and flight-test applications. Examples of ground-based applications are bench testing of flight-control actuators and sensors, validation of feedback control algorithms in flight computers, wind-tunnel testing of rotor system dynamic response, extraction of linearized simulation models from complex nonlinear simulations, and testing of simulator motion and visual drive systems. Examples of flight-test applications of automated sweeps are stability margin testing, structural mode identification, rotor dynamics identification, and unmanned-air-vehicle (UAV) testing. Several interesting examples of automated frequency-sweep testing are presented in the next sections. A complete description of parameters included in the automated sweep implementation is given by Tischler et al.<sup>86</sup> for an application to a full-scale rotor test in the wind tunnel.

### 5.11.1 System-Identification Testing of Off-Line Simulation Models

Figure 5.12 shows a schematic diagram for extracting the *bare-airframe response* of an off-line (batch mode) simulation model of a helicopter.<sup>16</sup> The bare-airframe (i.e., aerosurface) inputs are the total (pilot + feedback) mechanical (mixer) inputs to the main rotor control for pitch  $\delta_{\text{lon}_{\text{mx}}}$ , roll  $\delta_{\text{lat}_{\text{mx}}}$ , heave  $\delta_{\text{col}_{\text{mx}}}$ , and the tail-rotor control  $\delta_{\text{ped}_{\text{mx}}}$  for yaw. The feedback loops in pitch, roll, and yaw are needed to ensure that the aircraft oscillations remain centered about the trim flight condition during the sweeps. Suppose the *bare-airframe* roll-rate response to pitch input ( $p/\delta_{\text{lat}_{\text{mx}}}$ ) is to be extracted from  $\delta_{\text{lat}_{\text{mx}}}$  (input) and  $p$  (output) data collected from a sweep of the lateral stick  $\delta_{\text{lat}}$ . When dynamic coupling (i.e., off-axis response) exists in the bare-airframe dynamics, the secondary response variables ( $q, r, w$ ) will be excited in a manner that is fully correlated with the primary control input  $\delta_{\text{lat}_{\text{mx}}}$ . The feedbacks of the pitch, roll, and yaw signals in the control system will result in a complete correlation of the associated aerosurface inputs ( $\delta_{\text{lon}_{\text{mx}}}, \delta_{\text{lat}_{\text{mx}}}, \delta_{\text{ped}_{\text{mx}}}$ ). As discussed in Chapter 9, this will cause the identification solution to become singular (breakdown).

To overcome this problem, distinct white-noise excitations (with different seeds) must be added into each of the off-axis pilot controls ( $\delta_{\text{lon}}$ ,  $\delta_{\text{ped}}$ , and  $\delta_{\text{col}}$ ) in order to ensure that the aerosurface deflections are not fully correlated by the feedback system. The rms ( $1\sigma$ ) level of the noise signals is selected in the range of

$$(\delta_{\text{white noise}})_{\text{off-axis}}: \sigma = (0.1 \text{ to } 0.5)A \quad (5.20)$$

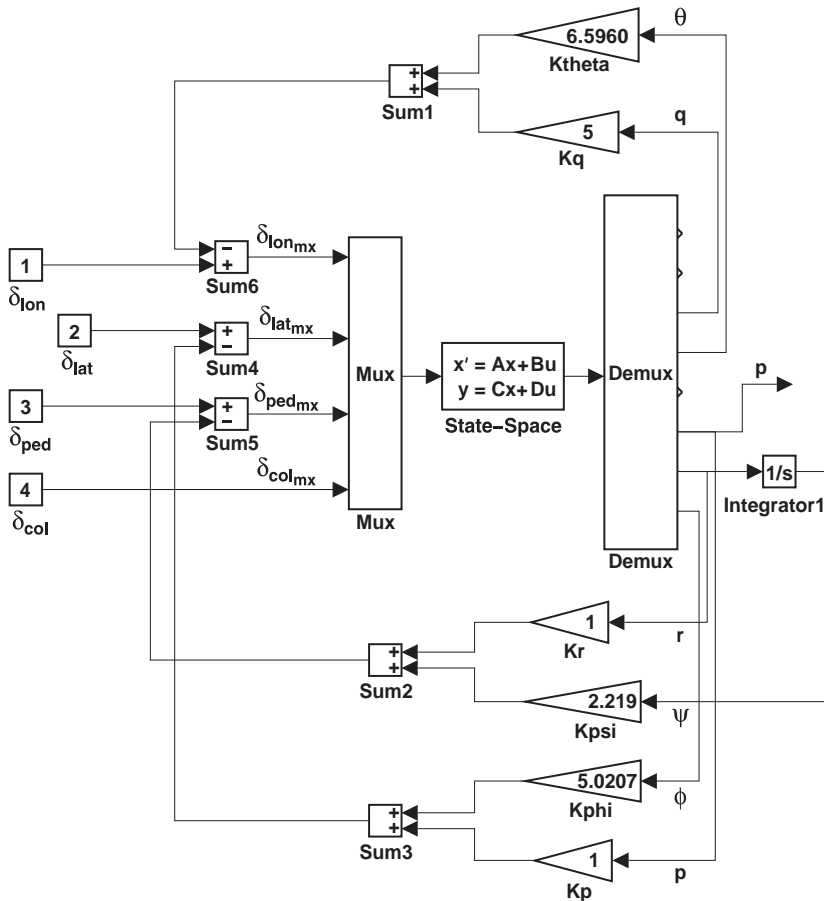


**Fig. 5.12** Feedback loops to maintain reference condition during simulation model testing.

where we recall that  $A$  is the amplitude of the on-axis sweep signal [Eq. (5.13)]. Figure 5.13 shows the input time histories ( $\delta_{\text{lat}}$ ,  $\delta_{\text{lon}}$ ,  $\delta_{\text{col}}$ ,  $\delta_{\text{ped}}$ ) for a lateral sweep case used to obtain the AH-64 bare-airframe response ( $p/\delta_{\text{lat}_{\text{mx}}}$ ) from simulation.

### 5.11.2 Structural-Response Determination

Automated frequency-sweep testing has also seen wide application to aircraft and rotorcraft to determine structural stability margins. A complete test program is generally a very time- and cost-intensive effort because of the many test conditions (e.g., flight speeds, aircraft loading, external store configuration) needed to demonstrate adequate margins over the expected flight envelope. These tests require a great deal of care because structural damping ratios can be as low as

## COLLECTION OF TIME-HISTORY DATA

107

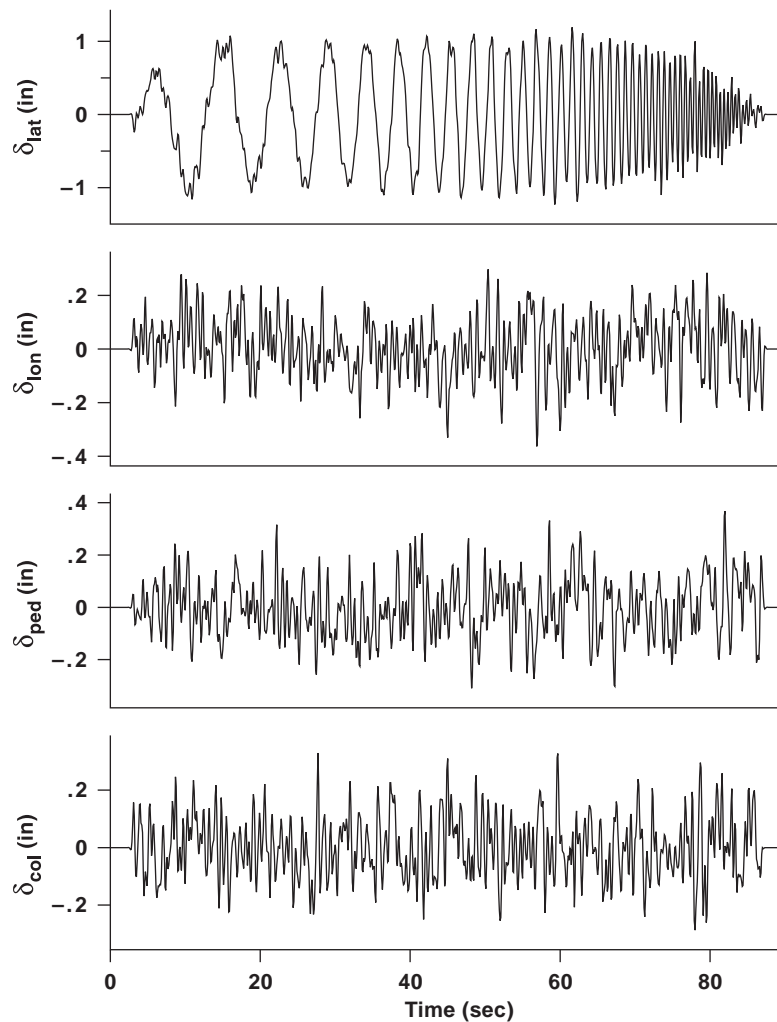


Fig. 5.13 Simulation inputs for lateral frequency sweep including off-axis white-noise inputs.

1 or 2% and the possibility of dynamic resonance and flutter (complete loss of structural damping) exists. Carefully tailored computer-generated inputs can be used that slowly build up the frequency, with notches to attenuate input amplitudes for particularly lightly damped modes and a rapid drop-off as the frequencies get higher. Key structural response parameters are monitored using strain gauges, with provisions for automatic termination of the test if the sensed loads or dynamic responses exceed safety limits. As discussed in detail in Sec. 7.10.4, the sweep record lengths for structural-response testing are also increased, as compared to the guideline of Eq. (5.11), to ensure that the modal characteristics are determined with sufficient accuracy.

Tilt-rotor aircraft can be susceptible to coupling of the engine nacelle/prop and rotor/wing, resulting in a phenomenon called whirl-mode instability. Acree and Tischler<sup>87</sup> used automated frequency-sweep testing and system identification to determine the characteristics of the key modes over the airspeed envelope and compared these results with analysis and other test techniques. Modern fixed-wing aircraft with high-bandwidth feedback flight-control systems are susceptible to a lightly damped dynamic coupling of the aerodynamics, flight control, and wing structure, referred to as aeroservoelastic coupling. An excellent discussion of aeroservoelastic testing and system-identification analysis is presented for the European Aircraft Program (EAP) and the Eurofighter by Caldwell.<sup>88,89</sup> In helicopters, the aeroservoelastic coupling of the lightly damped in-plane rotor response, fuselage roll mode, and the flight control can lead to a flutter-type response referred to as air resonance. Automatic frequency-sweep testing was conducted extensively in the development of the RAH-66A Comanche helicopter to determine aeroservoelastic stability margins, validate comprehensive math models, and develop feedback control methods for improving the damping of the air resonance modes. The automated inputs were introduced via the flight-test interface panel (FTIP) as described by Kothmann and Armburst,<sup>90</sup> and the analyses were conducted using CIFER®.

An extensive flight research effort was conducted at the NASA Dryden Flight Research Center to evaluate various testing and analysis methods for identifying the structural modes of a fixed-wing aircraft. This work, summarized by Brenner et al.,<sup>91</sup> used a specially modified F/A-18 aircraft. The frequency range of interest for these tests was 3–40 Hz. Identification results were compared for various sweep signals such as using logarithmic vs linear frequency progression and decreasing vs increasing frequency progression. The results show improved low-frequency excitation for logarithmic as compared to linear sweeps. Also, the analysis showed that there was no advantage to sweep records with greater than a 30-s duration for this structural-response application. Improved results were obtained when up to four repeated 30-s sweeps were conducted and concatenated in the analysis.

Figure 5.14 shows a generic example of the automated sweep signal capability that was developed for the wind-tunnel test of a full-scale helicopter rotor (Fig. 5.15), as described by Tischler.<sup>92</sup> Two notches were included to avoid excessively exciting some of the lightly damped structural modes. Note also the fade-in and fade-out function (indicated in Fig. 5.14) to avoid sharp inputs to the rotor that could have potentially excited lightly damped modes of the test stand. The excitation signal consisted of a sweep plus white noise, using Eqs. (5.18) and (5.20). Figure 5.16 shows the time-history data that was collected during this test. The rotor swashplate deflection  $\theta_{1c}$  is measured downstream of the actuator response, and it reflects some attenuation of the commanded sweep input at higher frequencies. The input autospectrum of the rotor swashplate  $G_{\theta_{1c}\theta_{1c}}$  shown in Fig. 5.17 reflects a uniform distribution of the computer excitation as defined herein, with the desired attenuation at the selected notches and a roll off at higher frequencies. Two key response variables shown in Fig. 5.16 are the test stand rolling moment  $M_x$  and rotor blade lead-lag deflections  $\zeta_{1c}$ . By tailoring the inputs carefully and monitoring the response so that no load limits were exceeded, the test was successfully and safely completed.

## COLLECTION OF TIME-HISTORY DATA

109

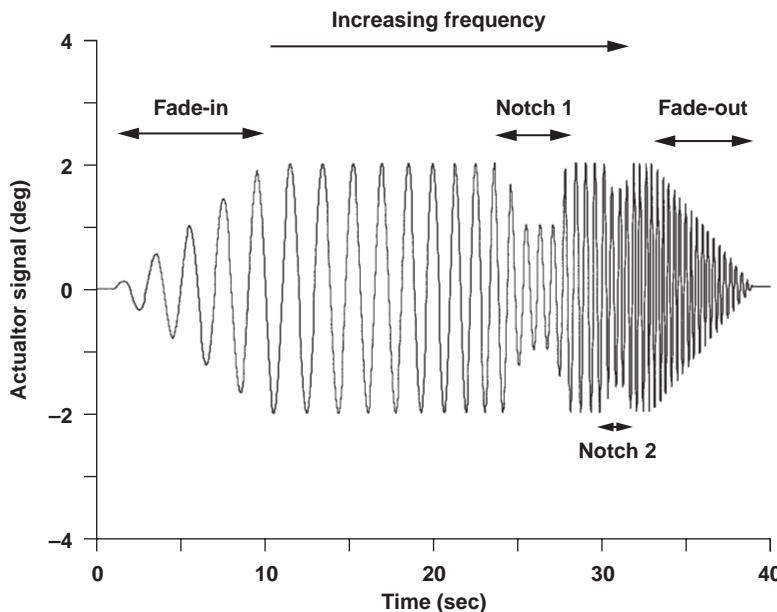


Fig. 5.14 Automated excitation signal for rotor test.



Fig. 5.15 Sikorsky bearingless main rotor (SBMR) test in the NASA Ames 40 x 80-ft subsonic wind tunnel.

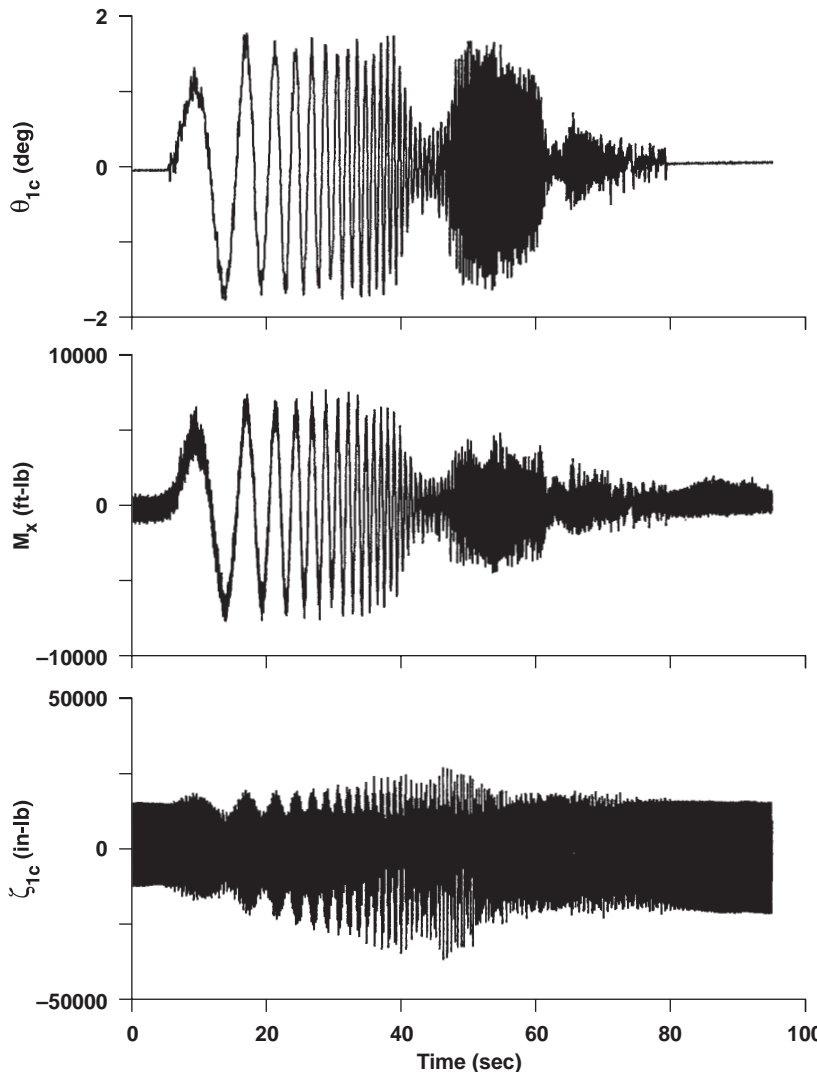


Fig. 5.16 Sample time-history data from frequency-sweep wind-tunnel tests (SBMR).

### 5.11.3 Unmanned Air Vehicles

Automated frequency-sweep testing has seen wide and successful application in support of UAV development. The highly unusual configurations of UAVs and the rapid configuration development and modification process means that there often are no available (or sufficiently accurate) physics-based simulation models. System identification has seen wide and highly successful utility for UAV development, supporting airframe dynamic model determination and control system validation and tuning.<sup>12</sup>

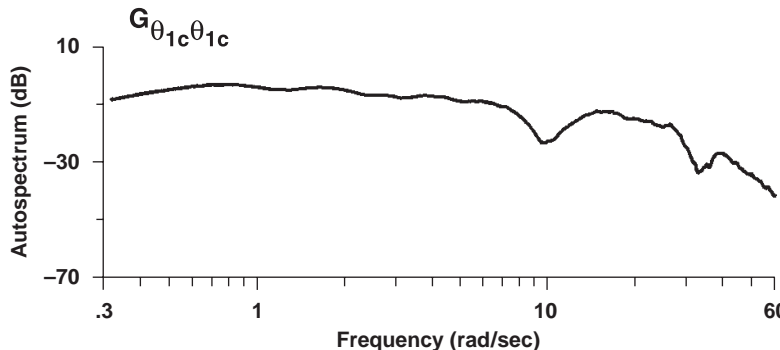


Fig. 5.17 Autospectrum of swashplate pitch input (SBMR).

One very interesting application of CIFER® was to the Pathfinder solar UAV aircraft<sup>93</sup> pictured in Fig. 5.18. A flight-data record for a typical automated sweep test is shown in Fig. 5.19. Sweeps conducted early in the flight-testing program were used for bare-airframe response identification and to optimize control system architecture and gain settings. During the high-altitude trials, which reached a record-breaking altitude of 71,500 ft, automated sweeps were conducted at every 10,000 ft of altitude during both ascent and descent to check the stability-margin sensitivity to the large changes in atmospheric density and temperature (which affected actuator performance) and to adjust the gain settings appropriately in real time.

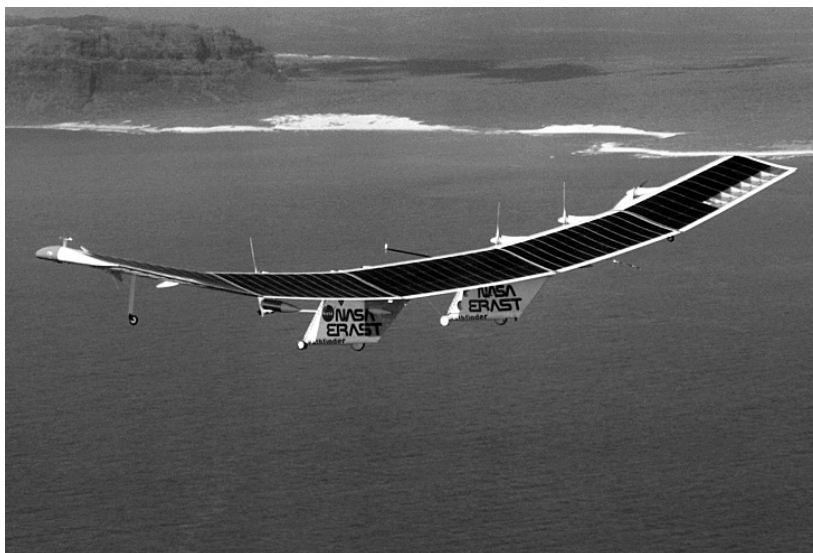


Fig. 5.18 Pathfinder in flight over Hawaii (NASA photo by Nick Galante).

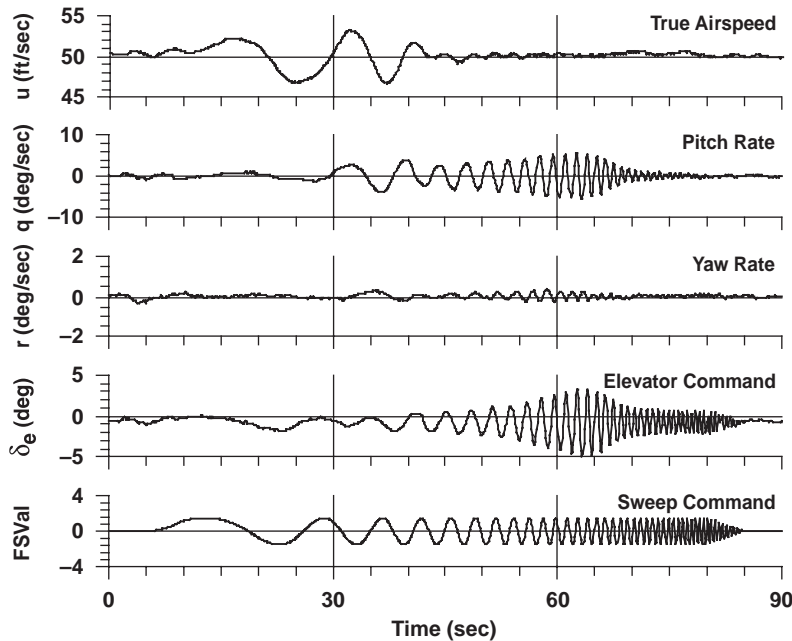


Fig. 5.19 Automated frequency sweep for Solar Pathfinder.

#### 5.11.4 *Important Issues for Automated Frequency-Sweep Testing*

Two important issues with computer-generated sweeps should be remembered:

- 1) Computer-generated symmetrical sweep inputs do not ensure symmetry in aircraft response. The SCAS or pilot can add the necessary trim inputs to keep the aircraft response centered near the reference flight condition.
- 2) Automated frequency-sweep tests for flight-dynamics identification can involve sizable response variations at low frequencies. Pilots generally do not like to "go for a ride" while the computer flies the sweep, especially for larger excitations. The pilot will generally allow larger excitations if they are executing the sweep input. Flight-test experience to date indicates that, for this reason, pilot-generated sweeps are preferable for handling-qualities tests of piloted vehicles.

#### 5.12 Frequency-Response Identification from Other Types of Inputs

Sometimes flight-test data available for system-identification studies are from maneuvers other than a frequency sweep. These can be dynamic maneuver data from flight tests not conducted specifically for frequency-domain identification purposes or from other commonly used identification inputs, such as steps, doubles, or time-optimal multisteps (e.g., 3-2-1-1 input). These flight data can be successfully used for the frequency-response method of system identification, but often with some (limited) loss in spectral content as compared to a frequency

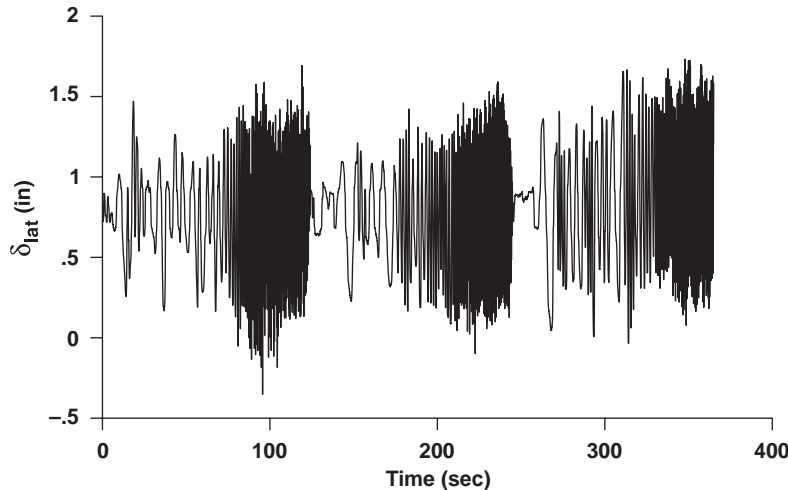


Fig. 5.20 Lateral frequency-sweep flight tests (UH-60A, hover).

sweep. This is demonstrated next using flight-test data from a UH-60A helicopter. Lateral-stick frequency sweeps and doublets were flown SCAS off in hover. The lateral-stick  $\delta_{\text{lat}}$  time histories for three repeat records for each type of maneuver are shown in Figs. 5.20 and 5.21. Notice that the doublet records are significantly shorter in duration than the sweep records.

Figure 5.22 compares the system-identification results of the on-axis roll-rate response ( $p/\delta_{\text{lat}}$ ) from the standard pilot sweeps (dashed lines) vs those from

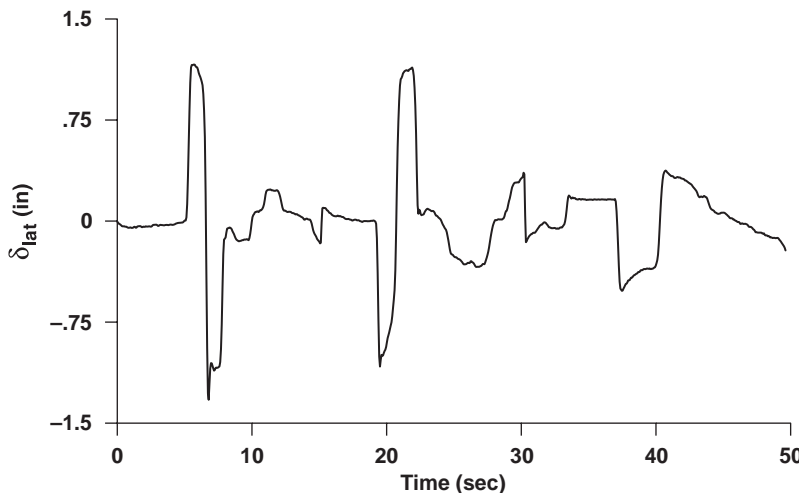


Fig. 5.21 Lateral-stick doublet flight tests (UH-60A, hover).

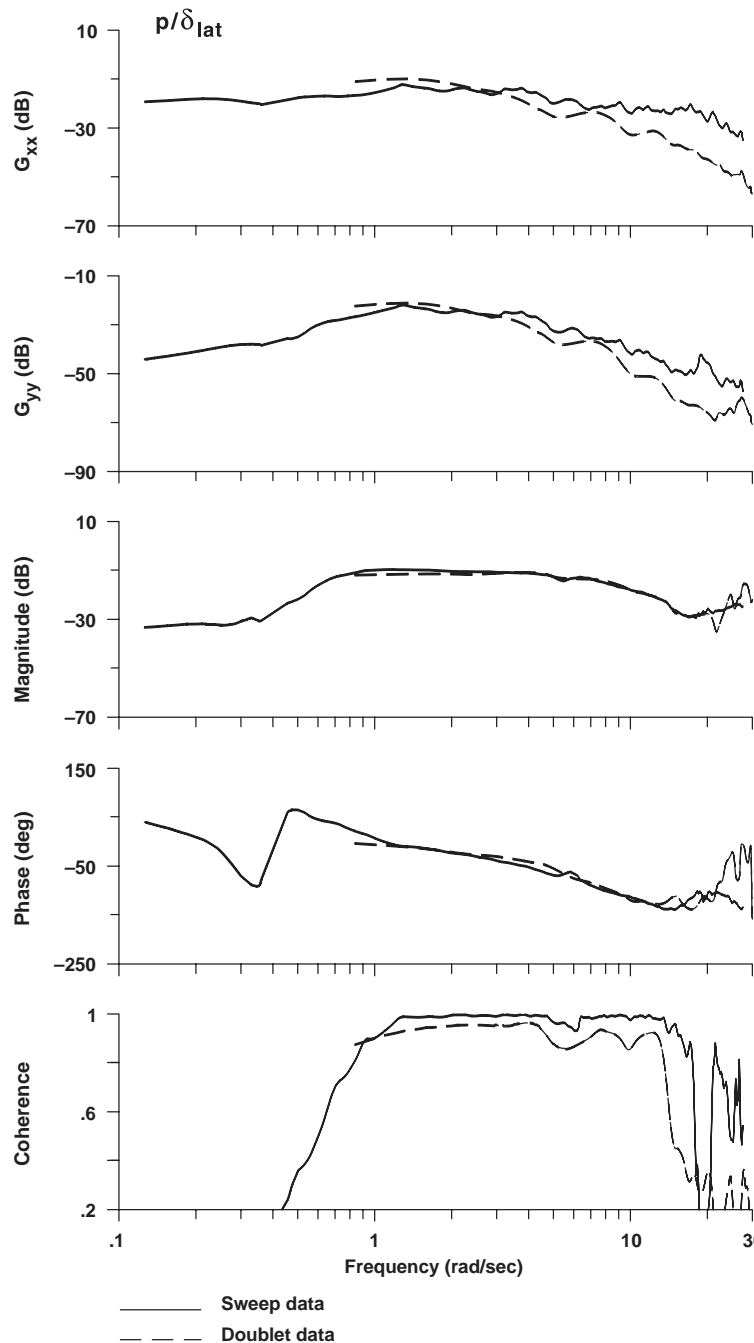


Fig. 5.22 Comparison of on-axis identification results from sweep and doublet maneuvers (UH-60A, hover).

linked-control doublet records (solid lines). The first two graphs show the input autospectrum  $G_{xx}$  and the output autospectrum  $G_{yy}$ , which are the frequency distributions of the excitation and response signal power. The next two graphs show the frequency-response ( $p/\delta_{lat}$ ) magnitude and phase. The last graph shows the coherence, which is a good indicator of identification accuracy. The identification results for the linked sweeps extend to very low frequency (0.13 rad/s) because of the long record lengths, as compared to the doublet data (identification starts at 0.8 rad/s). But in any case there is insufficient spectral content in the data to obtain good identification results from the sweeps at the lower frequencies (poor coherence at frequencies below 0.8 rad/s).

The input autospectrum for the sweep maneuver is quite uniform over a wide frequency range, indicating that the spectral content of the excitation is good over the frequency range of interest. The input autospectrum for the doublet data is slightly higher in the frequency range of 0.8–2.0 rad/s, and then falls off quite noticeably beyond 3.0 rad/s as compared to the sweep. The aircraft response (output) autospectrum also falls off more rapidly at high frequencies for the doublet input as compared to the sweep input, reflecting the differences in the excitation autospectrum.

The coherence values are high for both maneuvers over the wide frequency range of 0.8–12 rad/s, which indicates a common high degree of identification accuracy over this frequency range. The coherence drops for the doublet maneuver beyond 12 rad/s because of the greatly reduced input excitation. The frequency-response curves are essentially identical for the two types of maneuvers over the broad range of frequencies associated with the short-term response, with only minor differences in the phase response. Overall, the linked doublet maneuvers are seen to be equally effective as the frequency sweep for system identification of the *on-axis response* ( $p/\delta_{lat}$ ) using the frequency-response method.

The frequency-response identification results for the off-axis response ( $q/\delta_{lat}$ ) using the same data records are shown in Fig. 5.23. For this response pair there is no acceptable identification result for the linked doublet maneuver, as seen in the coherence function of less than 0.6 over the entire frequency range of identification. The identification result from the sweep input is satisfactory over a frequency range of 0.5–4.5 rad/s, and this will provide important dynamic response data for the helicopter coupling response. In general, the sweep maneuver is a superior test input for the identification of a fully coupled vehicle dynamics model.

Keller et al.<sup>94</sup> compared on-axis frequency-response identification results and handling-qualities metrics for a hovering helicopter as obtained from 1) linked records of dedicated frequency sweeps, 2) linked records of common flight-test pulse inputs, and 3) linked records of hovering flight. The results obtained using CIFER<sup>®</sup> showed generally excellent agreement between the results obtained from sweeps and from pulses. A poorer result was obtained for the data from hovering flight because of the reduced excitation for this mostly passive task. The study concludes that pulse inputs can be used for *on-axis* frequency-response analysis of handling qualities, thereby reducing the number of overall frequency sweeps that are required for ADS-33 compliance testing. Similarly, Twisdale and Ashurst<sup>42</sup> developed a fixed-wing aircraft flight-testing approach, System Identification from Tracking (SIFT), that achieved frequency-response identification from handling-qualities evaluations of air-to-air tracking and flight refueling.

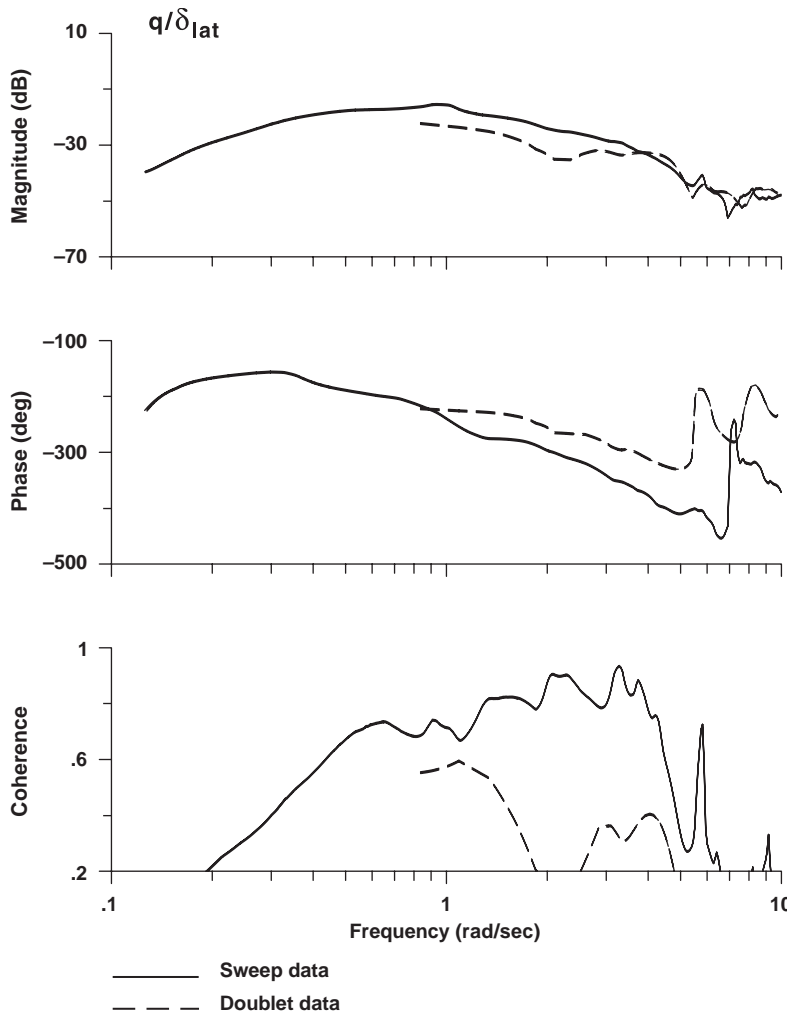


Fig. 5.23 Comparison of off-axis identification results from sweep and doublet maneuvers (UH-60A, hover).

In Hamel,<sup>10</sup> CIFER® identification results for the Bo-105 helicopter were compared for three different inputs (doublet, 3-2-1-1, sweep). Each result was based on concatenated repeat runs. As expected, the frequency sweep displays a more uniform input autospectrum across the frequency range of identification (0.4–30 rad/s). The identified roll frequency response obtained from the sweeps shows higher coherence and lower random error as compared to the other inputs, especially at the lower and higher frequencies (i.e., below 1 rad/s and above

10 rad/s). These results are consistent with the results of the preceding UH-60 example.

Morelli<sup>41</sup> compared lower-order equivalent system identification of the on-axis responses from frequency sweeps vs multisteps (2-1-1 input) for flight-test data from the Tu-144LL aircraft. The on-axis frequency responses and short-period transfer-function models were again adequately determined by CIFER® for a linked set of multistep inputs, showing close agreement to the results obtained using frequency sweeps.

As can be seen, a wide range of inputs can be satisfactory for the identification using the frequency-response method. The key concern is whether the input provides the needed excitation content over the frequency range of interest. Many alternative inputs have been found to provide results of comparable accuracy as the frequency sweeps for the on-axis response, but are often degraded for the off-axis responses.

## Problems

### *Instrumentation requirements*

**5.1** How can filtering of the data affect the system identification? Consider the effect of common filters in input and output signals vs when different filters are used.

**5.2** How would you determine the dynamic characteristics of an aircraft engine from a ground test? What would you measure?

### *Collection of time-history data from a simulation model for system identification*

**5.3** Generate an automated sweep using Eqs. (5.13–5.17), but for a record duration of  $T_{\text{rec}} = 180$  s and a sample rate of  $f_s = 100$  Hz.

**5.4** Exercise your pendulum simulation model (**Problem 3.1**) with your automated sweep generator (**Problem 5.3**), and plot the results  $(\theta, \dot{\theta})$  to ensure that the response stays in the linear range.

**5.5** Store the input  $\bar{M}_{\text{ext}}$  and output  $(\theta, \dot{\theta})$  time-history data from **Problem 5.4** in a format suitable for analysis using CIFER®. (Hint for MATLAB® users: use the ‘save’ command for a ‘.mat file’ or ‘fprintf’ to print to a CIFER® text format.)

### *Piloted frequency-sweep design*

**5.6** Why is it important not to suppress coupling responses (i.e., off-axis responses) in frequency-sweep maneuvers for system identification?

**5.7** You are a flight-test engineer and are given a UAV helicopter to test. Simulation results indicate that the modes are spread between 0.5–30 rad/s. Design the frequency-sweep characteristics, sampling rate, and filter cutoff frequency. Use your frequency-sweep generator to generate this frequency sweep.

## 118 AIRCRAFT AND ROTORCRAFT SYSTEM IDENTIFICATION

*Verification maneuvers*

**5.8** When verifying a system-identification model obtained with a frequency sweep, why is it necessary to use a dissimilar input (i.e., an input different from the frequency sweep in this case)? What are some maneuvers that would make good dissimilar inputs?

**5.9** Generate and plot a doublet input similar to the one shown in Fig. 5.2, using a series of step inputs in external moment of amplitude  $0.75 \text{ rad/s}^2$  (5 s trim, 5 s positive, 5 s negative, 5 s trim). Produce and save the time history of the doublet and the corresponding response of the inverted pendulum in a format suitable for using CIFER®.

## 6

## Data Consistency and Reconstruction

The preceding chapter examined in considerable detail how to properly design and conduct a flight test to generate a high-quality database for use in system identification and model validation. Regardless of how much care is taken in instrumentation and flight testing, there will often exist kinematic inconsistencies between independent measurements of dynamically related variables. This chapter covers typical sources of data inconsistencies and presents both sophisticated and simple methods for isolating and correcting for such errors.

Inconsistencies arising from systematic or *deterministic* sources can range in complexity from simple differences in sign convention or measurement system calibration errors to a difficult combination of unknown biases and drifts in attitude and rate gyro measurements. Random or *nondeterministic* sources of data inconsistency include data dropouts, electrical noise, and air data disturbances, just to name a few of the practical glitches to be expected in the flight database. Data consistency and reconstruction techniques evaluate the flight-test data set as a whole to detect, model, and resolve these potential problems prior to formal system identification (Fig. 2.1). If not resolved at this point, countless hours can be wasted in an attempt to identify a consistent mathematical model from a kinematically inconsistent data set.

Pioneering work in the field of kinematic consistency analysis and flight data reconstruction was done by Gerlach,<sup>95</sup> Wingrove,<sup>96</sup> Klein and Schiess,<sup>97</sup> and Breeman and Simons.<sup>98</sup> Methods of instrumentation error modeling, data consistency, and data reconstruction with excellent flight-test examples are well covered in the AGARD Report on Rotorcraft System Identification.<sup>10</sup> The use of the SMACK Kalman filter/smoothen tool,<sup>99</sup> developed on the basis of Wingrove's work, is discussed in detail by Fletcher<sup>100</sup> in an application to the system-identification analysis of the AGARD Bo-105 helicopter data and is summarized herein. A fixed-wing example showing the importance of data consistency on system-identification results is presented by Friehmelt<sup>101</sup> based on X-31 flight data.

The following topics are covered in this chapter: types of measurement errors in flight-test data, basic concept of kinematic data consistency, case study using SMACK: Bo-105 flight-test data, simple methods for data consistency and reconstruction using CIFER®, and conclusions and recommendations.

### 6.1 Modeling Measurement Errors in Flight-Test Data

Measurement errors are broadly classified as *deterministic* (systematic) or *nondeterministic* (random). Common sources of deterministic errors in one or more of the measurements include bias, scale factor, and drift. These errors can arise from misalignment in the measurement devices relative to the body axes and either steady-state or slowly growing offsets in the output of the measurement

device. Another deterministic error is caused by time shifts that can arise from asynchronous sampling of the data or nonuniform filtering of the various data channels. Each sketch in Fig. 6.1 depicts hypothetical “error-free” (i.e., ideal) signals shown as dotted lines vs “actual” measurement signals as solid lines that have one of these types of deterministic errors.

Examples of random errors are shown in Fig. 6.2. The first sketch shows an instrumentation dropout caused by an unpredictable loss of telemetry or tracking data. The second error is associated with a random disturbance or interference—mechanical, electrical, or atmospheric. A common aerodynamic disturbance in rotorcraft is associated with the impingement of the rotor wake on an air data system measurement sensor, such as a flow angle vane. The third sketch shows that finite sensor resolution leads to a quantization type of random error, whose characteristics resemble white noise.

### 6.1.1 Using Kinematic Consistency Methods to Remove Measurement Errors from Flight-Test Data

There are two main steps to the process of removing measurement errors: 1) formulate a model of measurement errors in the flight-test data and 2) determine error parameters based on kinematic relationships to reconstruct error-free signals. The error model should be physically realistic in the sense that the model is parameterized in terms of the physical properties of the measurement system, such as instrument bias errors or scale factors. A single error model is sought that is valid for the entire data set, based on the assumption, generally acceptable, that the measurement system and environmental characteristics are sufficiently constant over the flight-test period (e.g., several days).

The theoretical basis for data consistency analysis is the set of first-order differential equations (e.g., Ref. 56) that relates the kinematic measurements for the translational and rotational degrees of freedom in an Eulerian (body-fixed) frame (Fig. 6.3).

The equations for the translational degrees of freedom are

$$\dot{U} = RV - QW + A_{x_{cg}} - g \sin \Theta \quad (6.1)$$

$$\dot{V} = PW - RU + A_{y_{cg}} + g \cos \Theta \sin \Phi \quad (6.2)$$

$$\dot{W} = QU - PV + A_{z_{cg}} + g \cos \Theta \cos \Phi \quad (6.3)$$

For the rotational degrees of freedom, the equations are

$$\dot{\Phi} = P + Q \sin \Phi \tan \Theta + R \cos \Phi \tan \Theta \quad (6.4)$$

$$\dot{\Theta} = Q \cos \Phi - R \sin \Phi \quad (6.5)$$

$$\dot{\Psi} = R \cos \Phi \sec \Theta + Q \sin \Phi \sec \Theta \quad (6.6)$$

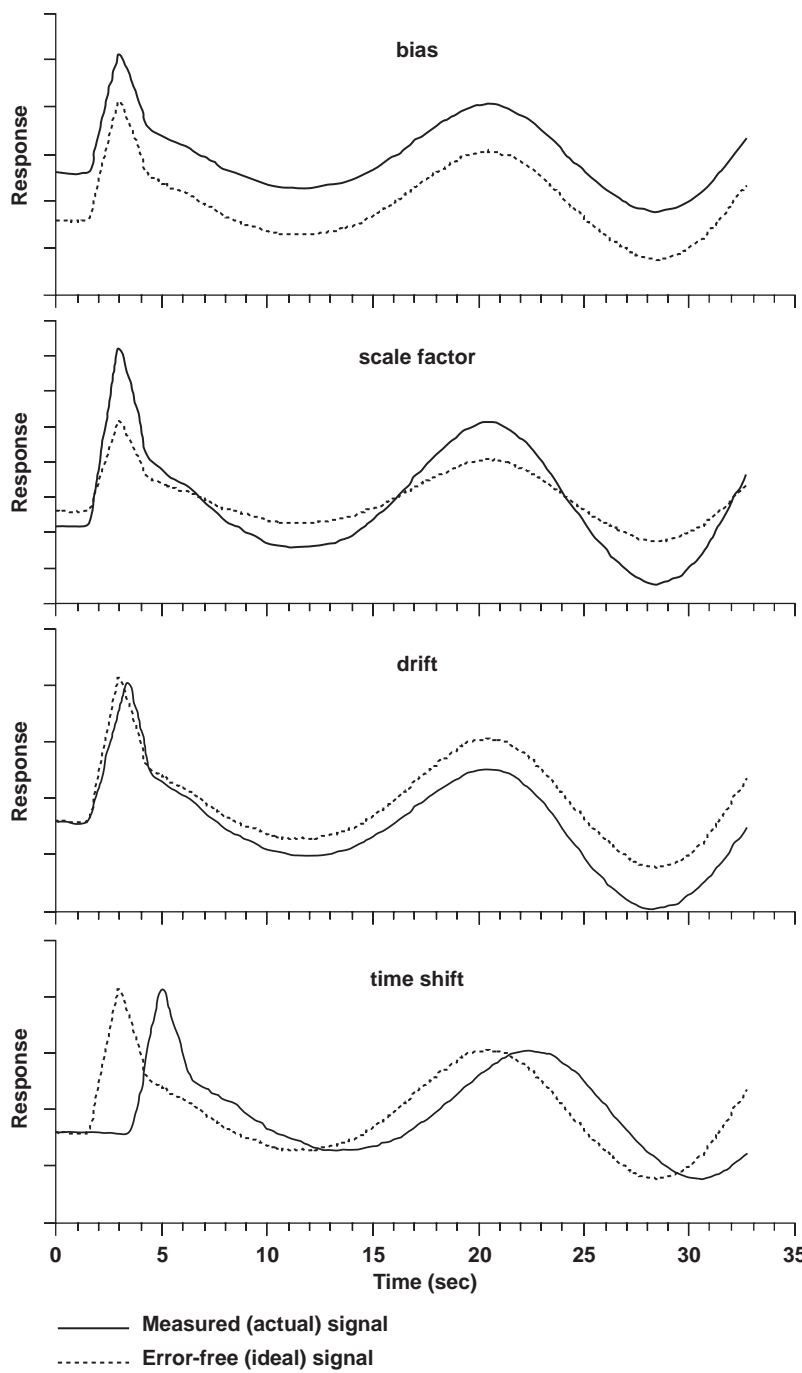


Fig. 6.1 Deterministic measurement errors.

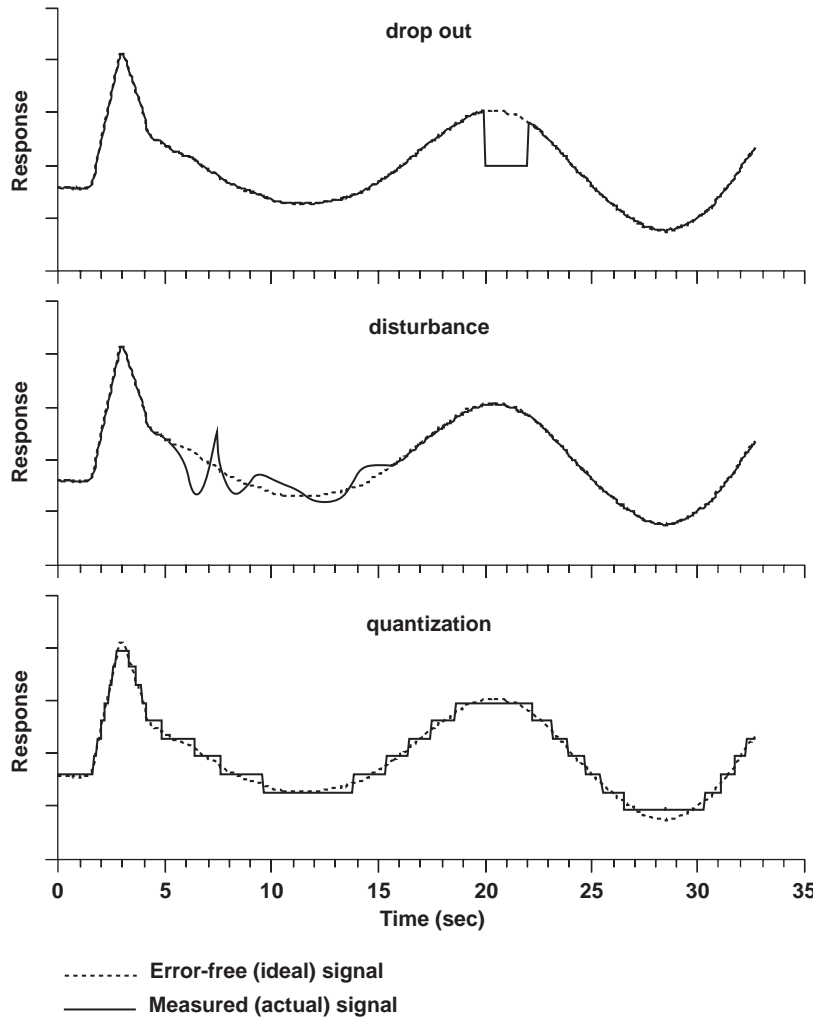


Fig. 6.2 Random measurement errors.

The right side of these six equations involves the measured quantities of translational velocities ( $U$ ,  $V$ , and  $W$ ), Euler rotation angles ( $\Phi$ ,  $\Theta$ , and  $\Psi$ ), body angular rates ( $P$ ,  $Q$ , and  $R$ ), and accelerometer measurements corrected to the center of gravity ( $A_{x_{cg}}$ ,  $A_{y_{cg}}$ ,  $A_{z_{cg}}$ ); the three accelerometer signals are measurements of the specific external forces excluding gravity.<sup>102</sup> By substituting these flight-test measured quantities into Eqs. (6.1–6.6), we can obtain time histories of the translational state rates ( $\dot{U}$ ,  $\dot{V}$ , and  $\dot{W}$ ) and the Euler rates ( $\dot{\Phi}$ ,  $\dot{\Theta}$ , and  $\dot{\Psi}$ ). Then, in principle, the time integration of these rate variables' time histories should produce derived states that match the original measurements. In practice,

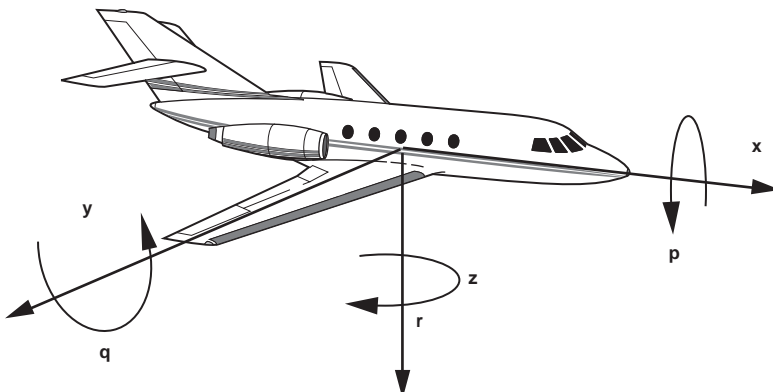


Fig. 6.3 Body-axis coordinate system.

however, errors in the original flight-test data will result in an imperfect match, a *kinematic inconsistency*, between the calculated quantities and those measured in the flight test.

A simple parametric model can be formulated that encompasses both deterministic and random-error contributions to the kinematic inconsistency. As an example, consider the measurement of the Euler roll angle  $\Phi$ . In most cases, we can express the flight measurement  $\Phi_m$  in terms of the estimated (i.e., corrected) value  $\Phi_e$  by the parametric equation

$$\Phi_m(t - \tau_\phi) = \lambda_\phi \Phi_e(t) + b_\phi + n_\phi \quad (6.7)$$

where the error parameters lumped as  $b_\phi$   $\equiv$  bias,  $\lambda_\phi$   $\equiv$  scale factor, and  $\tau_\phi$   $\equiv$  time shift to account for the deterministic errors, such as sensor misalignment, calibration error, and zero offset. The last parameter,  $n_\phi$   $\equiv$  noise, is generally modeled as zero-mean white noise and encompasses all three types of random (nondeterministic) errors.

The general error-model structure would consist of a set of equations similar to Eq. (6.7), one for each of the measured quantities. The error-model parameters are determined by minimizing the least-squares error between the measured and estimated state variables in Eqs. (6.1–6.6). However, it is not possible to determine an error model that contains scale factors and biases on all measured parameters because this results in a high correlation in the error parameters, causing the least-squares solution to become singular (indeterminate). For example, the effects of a pitch attitude bias  $b_\theta$  and a longitudinal accelerometer bias  $b_{a_x}$  on the longitudinal kinematics solution of Eq. (6.1) will be the same (i.e., correlated), so that they can not be independently determined. Therefore, engineering judgement must be used to select the types of errors expected to occur in the measurement signals and avoid correlating effects. For example, in the AGARD study,<sup>10</sup> the researchers included scale factors on the attitude angles and translational speeds and/or biases on the angular rates and translational

accelerations. During the analysis process, some of the error parameters in the initial selection are sequentially eliminated from the model structure if they are found to make insignificant contributions to the overall fit cost function. The resulting “error-free” data [e.g.,  $\Phi_e$  in Eq. (6.7)] are then used for the actual system identification.

The SMACK (smoothing for aircraft kinematics) program developed by Bach<sup>99</sup> is a highly effective tool for kinematic consistency analysis, error parameter determination, and data reconstruction. In addition, SMACK is useful for correcting sensor measurements to the aircraft c.g. and estimating winds and gusts. The SMACK algorithms are based on the Kalman filter/smooth formulation of Wingrove.<sup>96</sup> In his work with the AGARD Bo-105 flight database, Fletcher<sup>100</sup> developed a systematic approach based on SMACK for helicopter kinematic consistency analysis and data reconstruction as a preprocess to system identification with CIFER®. The results of the Bo-105 case study are summarized in the next section.

### 6.1.2 Bo-105 Flight-Test Analysis Using SMACK

Fletcher<sup>100</sup> made extensive use of the SMACK tool to examine and correct data consistency errors in a flight-test database of the Bo-105 helicopter at a flight condition of 80 kn. This flight-test database was collected by the DLR Institute for Flight Mechanics, Braunschweig, Germany, with the specific application of system identification in mind. Flight tests were conducted with several features that made the resulting database excellent for comprehensive and comparative studies by the AGARD Working Group 18 members.<sup>10</sup> There were 52 separate flight-test events, sufficient to provide valuable statistical variation, and the runs were all made within a single week, which meant that the data system characteristics were likely to be fairly stationary.

The initial selection of the error model by Fletcher had 24 parameters, but the data consistency analysis reduced this number to only five important parameters: scale factors in the three velocity component measurements and small biases in  $P$  and  $Q$ . Each of these error parameters varied less than 11% over the entire database, which indicates that they were all physically meaningful and consistent. The results of the analysis were applied to the flight-test data, and the estimated data (i.e., with corrected variables) were then used for the system identification.

Figure 6.4 compares the time-history data before and after the flight-test data were reconstructed by removing the measurement errors. The measured data are shown by the solid line, and the reconstructed data are shown by the dashed line. The first three graphs show that for roll angle, roll rate, and lateral acceleration the measured and reconstructed data are virtually the same. In the case of lateral velocity, there are periods of time where the corrected estimate is quite different from the measurement. This discrepancy is caused by the impingement of the rotor-wake vortices on the air data system vanes that measure angle of attack and sideslip. These sections of “bad data” were visually identified (vertical dotted lines in Fig. 6.4) and given zero weighting in the Kalman filter/smooth solution, allowing the SMACK algorithm to ignore the flight data in these sections and estimate what the lateral velocity should have been during the periods of rotor-wake interference.

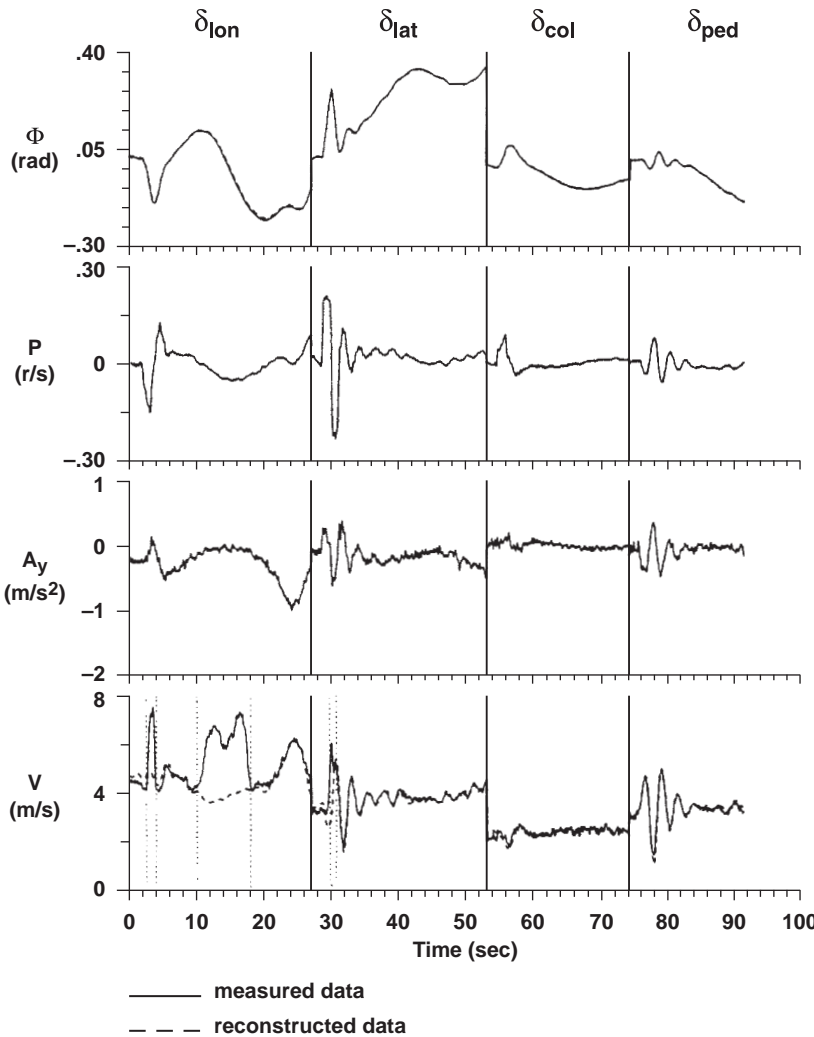


**Fig. 6.4** Comparison of flight data and reconstructed responses for the Bo-105 (80 kn).

Figure 6.5 compares the lateral velocity frequency response to pedal input ( $v/\delta_{\text{ped}}$ ) using the original (measured) flight data vs the reconstructed data. The magnitude plots show a scale factor difference of about 3 dB, which corresponds to the 30% scale factor error ( $\lambda_v = 0.7$ ) in the velocity component  $V$  that was identified (and corrected) in the SMACK data consistency analysis and reconstruction. This scale factor reflects the influence of the fuselage on the local airflow measured by the sideslip vane  $\beta_{\text{nb}}$  as compared to the freestream sideslip.

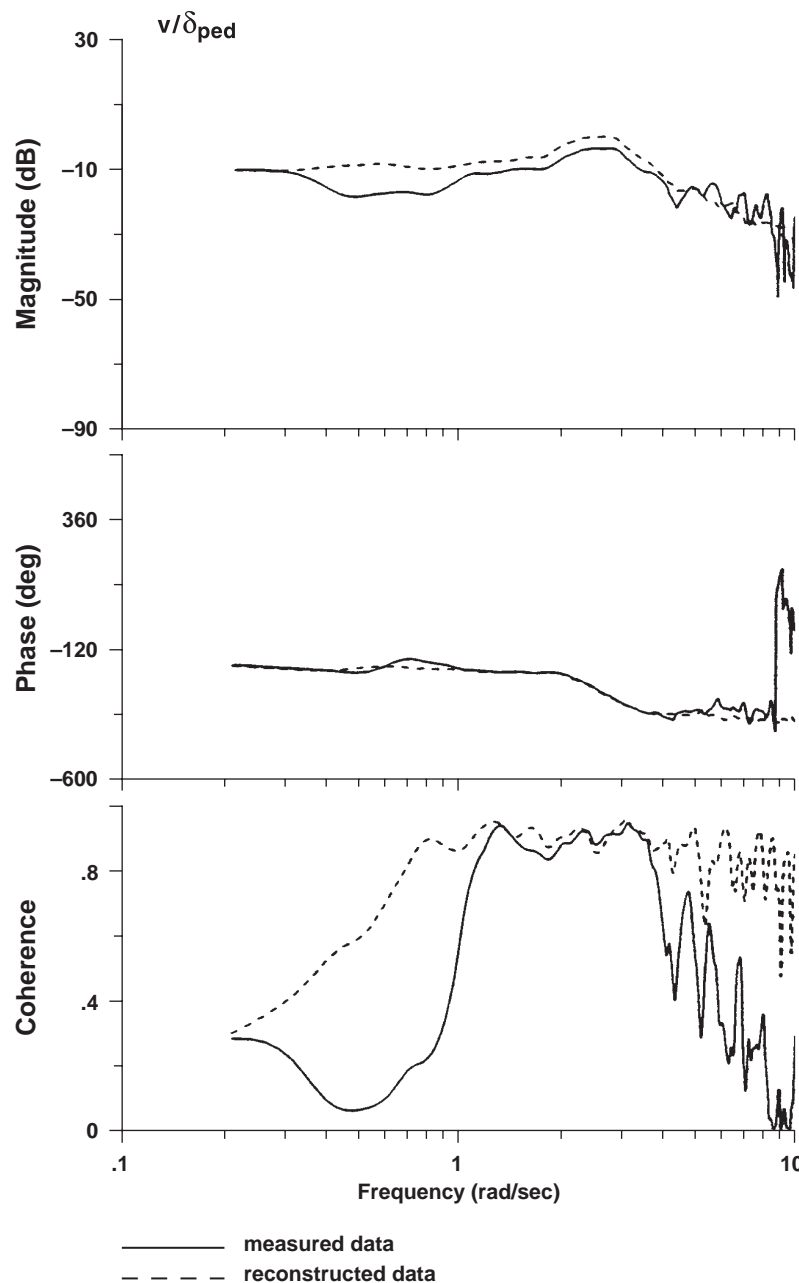


Fig. 6.5 Lateral velocity response identification using flight vs reconstructed data.

The coherence plot of Fig. 6.5 shows that the frequency response from the reconstructed data has improved identification accuracy over a much broader frequency range. The removal of errors in the velocity measurements associated with the rotor-wake disturbances increases the signal-to-noise ratio, as reflected in the improved coherence. Another contributing factor is the complementary filter action of the Kalman filter, which merges the lateral velocity measurements with lateral acceleration measurements. The velocity measurements generally have improved signal to noise at higher frequencies, whereas the roll attitude measurements generally have improved signal to noise at lower frequencies. The resulting reconstructed signal has excellent spectral content over a much greater frequency range than that of the original velocity measurement.

Fletcher found that the accuracy in determining the error-model parameters was significantly enhanced when the SMACK analysis was conducted on concatenated data files, each file containing four maneuvers, one in each of the four control axes—lateral, longitudinal, directional, and collective. From the original 52 separate events, this resulted in 13 distinct runs, each run now with good information content in all axes. To demonstrate the benefit of this concatenation process, consider first Fig. 6.6, which shows the average value and the scatter of the lateral velocity scale factor  $\lambda_v$  as estimated by individually analyzing each of the 52 separated runs. The average and statistical values are computed by grouping the results by axis. As expected, the scatter in lateral velocity scale factor is the least for the directional runs, in which there was the most excitation of the lateral variables. Conversely, the scatter was the greatest for the longitudinal runs, which had the least excitation of the lateral variables. This clearly

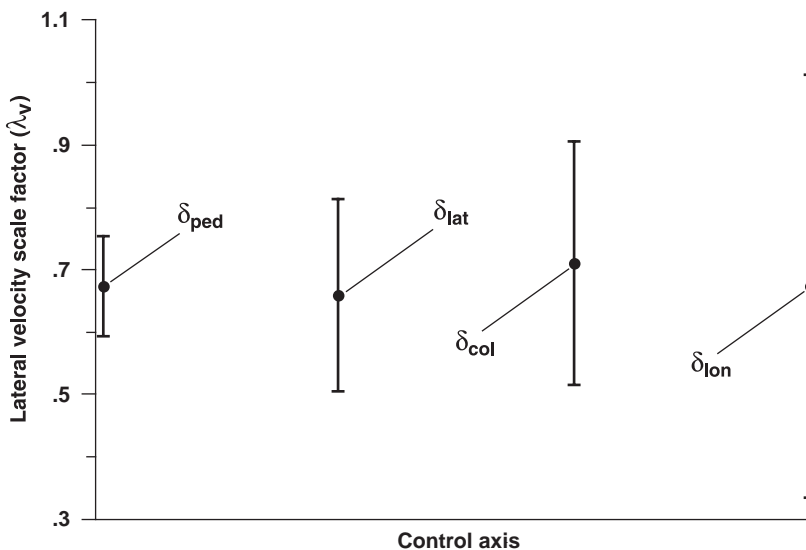


Fig. 6.6 Effect of excitation on lateral velocity scale factor.

shows that there must be sufficient information content in the lateral degrees of freedom to estimate the lateral velocity scale factor. Analogous results were obtained for the error parameters in the other axes. Therefore, to accurately extract a single integrated error model that includes parameters for all axes it is crucial that each data run has sufficient information content in all of the degrees of freedom.

Figure 6.7 compares the identification results obtained from the individual records with those obtained from the 13 linked runs—each linked run containing four maneuvers, one maneuver for each of the control axes. The average values and variances of the scale factors  $\lambda$  and biases  $b$  are shown, organized by dynamic variable:  $u$ ,  $v$ ,  $w$ ,  $p$ , and  $q$ . The parameter scatter is significantly reduced in each case for the linked records.

The results of Fletcher's analysis of the Bo-105 database show the following:

- 1) A fairly simple stationary error model is valid for data collected over a relatively short time span (e.g., several days).
- 2) Linking the maneuvers to ensure good information content in all axes reduces the variability of the identified error parameters.
- 3) Signals should be weighted according to their accuracy, with bad sections of data deweighted.
- 4) The action of Kalman filter/smooth extends the bandwidth of the reconstructed data.

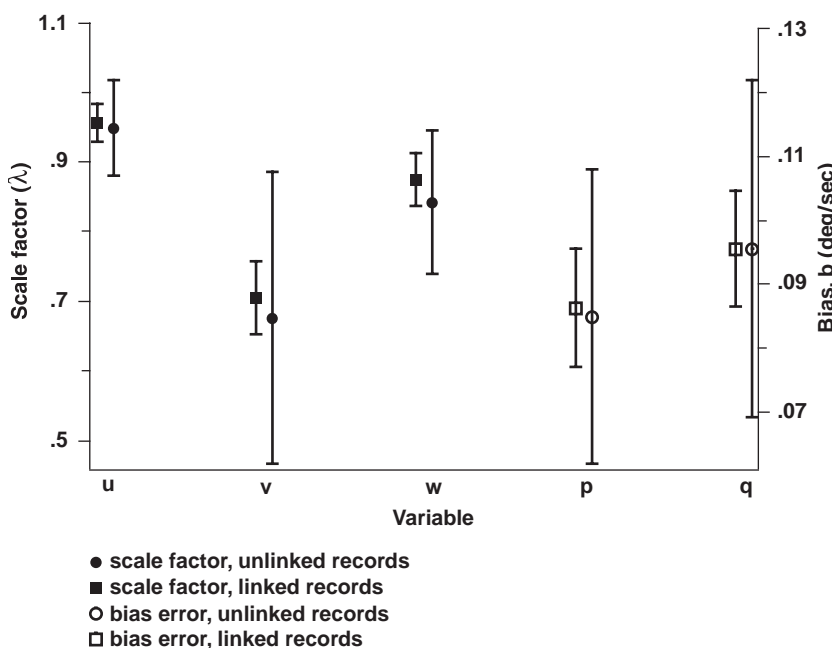


Fig. 6.7 Effect of linking on scale factor and bias determination.

### 6.1.3 Further Experience with Data Consistency Analysis Using SMACK

Additional examples of data consistency analysis using SMACK are documented in system-identification studies of the UH-60 RASCAL<sup>103</sup> and the S-92<sup>117</sup> helicopters. In all cases, the system-identification results were highly improved by using the error-free (corrected) data in place of the raw flight data. In one undocumented study, some difficulties with the analysis were encountered with a linked single-axis approach when the vehicle's states at the end of one maneuver were significantly different from those at the beginning of the next. A single dedicated multi-axis *kinematic consistency maneuver*, consisting of a doublet in each of the four control axes, would avoid this problem.

The following are general recommendations for data consistency analysis as a preprocessing step to system identification:

- 1) Effective data consistency analysis requires that the flight maneuvers excite all of the kinematic variables.
- 2) Dedicated data consistency maneuvers should be flown whenever calibration changes are made, or at least every 10 flight hours.
  - a) A single continuous flight record with doublet excitations in each of the control axes is recommended.
  - b) Single-axis maneuvers can be concatenated to effectively create runs that excite all of the kinematic variables if care is taken to start and stop each flight-test maneuver at the same trim condition.
- 3) Air data signals (angle-of-attack and angle-of-sideslip vanes and airspeed probe) should be augmented with tracking data whenever possible because these measurements can often be noisy as a result of aerodynamic disturbances and subject to considerable hysteresis (as illustrated in Section 6.2.3). Also, air data signals are unreliable for flight helicopter testing in hovering and low-speed conditions.
- 4) The data consistency analysis should use an optimal filter/smooth.

## 6.2 Simple Methods for Data Consistency and State Reconstruction

The Kalman filter/smooth data consistency and reconstruction methods of SMACK demonstrated in Sec. 6.1.2 analyze the *entire data set as a whole* using the nonlinear kinematics equations to determine a multivariable error model and reconstruct data when the measurements are subject to dropouts and disturbances. The SMACK tool was developed by NASA at Ames Research Center to support flight data reconstruction and accident investigations for extreme aircraft maneuvers (e.g., high angle-of-attack stalls and spins) and extreme weather conditions. When dynamic maneuvers are restricted to the range of linear kinematics and the winds are calm, the relationships simplify greatly, and frequency-response identification methods can be used to provide a rapid means for consistency checking and response reconstruction. These procedures will quickly reveal, for example, the presence of sign errors or calibration scale factors that might be present in the data. These simple methods are a good precursor to the more sophisticated Kalman filter/smooth methods and in many cases might

suffice by themselves. An example illustration of velocity-response reconstruction is presented for a hovering flight condition in Section 6.2.3.

The following topics are covered in this section: angular consistency, correction for instrumentation system dynamics, translational consistency, detection of faulty data, and control rigging calibration.

### 6.2.1 Angular Consistency

If we assume small trim angles and small perturbation motion during system-identification maneuvers, the Euler relationships of Eqs. (6.4–6.6) simplify greatly to the linearized equations:

$$p = \dot{\phi} \quad (6.8)$$

$$q = \dot{\theta} \quad (6.9)$$

$$r = \dot{\psi} \quad (6.10)$$

where the lower-case notation (e.g.,  $p$ ,  $\phi$ , etc.) refers to small perturbation variables. The Laplace transform of these linearized equations yields

$$p = s\phi \quad (6.11)$$

$$q = s\theta \quad (6.12)$$

$$r = s\psi \quad (6.13)$$

So the integral relationship of dynamics variables (e.g.,  $\phi$  and  $p$ ) becomes simply an algebraic one involving the Laplace variable  $s$ .

We adopt an error model that includes scale factors on both the rates and attitudes and (uncorrelated) random noise on the rate measurements only. Figure 6.8

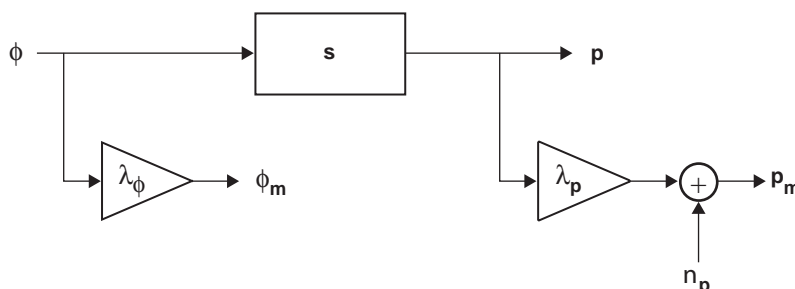


Fig. 6.8 Roll-axis error model.

illustrates this model for the roll axis. So for the roll-angle measurement,

$$\phi_m(t) = \lambda_\phi \phi(t) \quad (6.14)$$

and for the roll-rate measurement,

$$p_m(t) = \lambda_p p(t) + n_p \quad (6.15)$$

where  $\phi_m(t)$  and  $p_m(t)$  are the measurements of the “true” values  $\phi(t)$  and  $p(t)$ .

Taking the measured roll angle  $\phi_m$  as the input and measured roll rate  $p_m$  as the output, we can determine the frequency response:

$$\frac{p_m(s)}{\phi_m} = K s e^{-\tau s} \quad (6.16)$$

where the constant  $K$  is the ratio of scale factors,

$$K = \frac{\lambda_p}{\lambda_\phi} \quad (6.17)$$

and any relative time shift in the data caused by filtering or skewing will be absorbed in  $\tau$ , the effective time delay. The values of  $K$  and  $\tau$  are determined from a transfer-function fit of the frequency response  $p_m/\phi_m$ .

This analysis method yields the scale factor ratio  $K$ , but it cannot separate the roll-angle scale factor  $\lambda_\phi$  vs roll-rate scale factor  $\lambda_p$ . However, the analysis will show if the measurements, as provided, are kinematically consistent. If they are consistent, then the error-model parameters will be very nearly  $K = 1$ ,  $\tau = 0$ . If they are not consistent, then it might be possible to isolate the source of error by conducting the same analysis on redundant sources of the same measurement—for example, by comparing the measurement of roll rate from the flight-test inertial measurement unit (IMU) vs an aircraft-based system, such as the SCAS.

Figure 6.9 shows a consistency check for roll measurements from the AGARD Bo-105 flight-test database described earlier (Sec. 6.1.2). The identified frequency response ( $1/s$ )( $p_m/\phi_m$ ) is shown in the solid line of Fig. 6.9. The very high coherence over a wide range of frequencies (0.30–12 rad/s) verifies the linearity assumption and indicates a lack of significant measurement noise. Remember that the dynamic response being identified in this case is simply the kinematic relationship between the related variables and not the vehicle response to control inputs. The transfer-function model of Eq. (6.16), shown as the dashed line in the figure, fits the flight response perfectly. The identified error-model parameters are

$$K = 1.006 \quad (6.18)$$

$$\tau = -0.003 \text{ s} \quad (6.19)$$

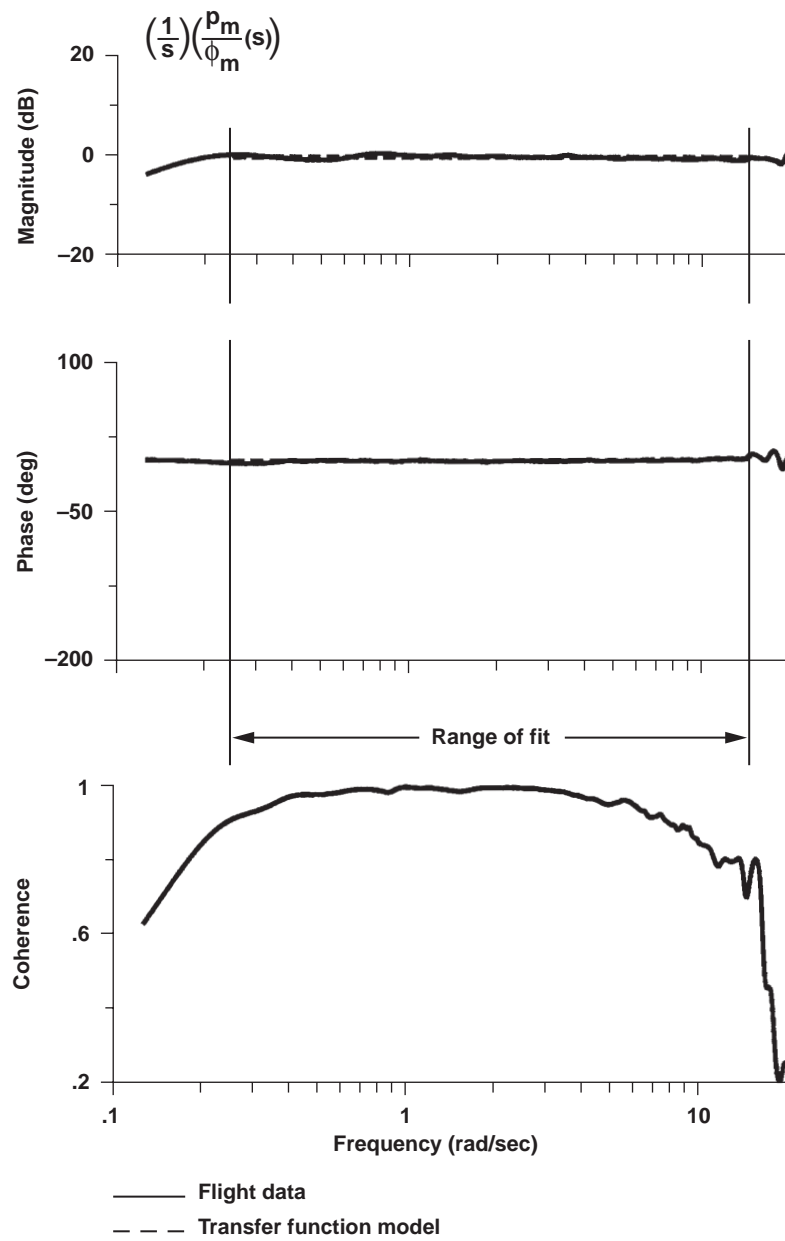


Fig. 6.9 Roll-response consistency check for Bo-105 (80 kn).

indicating essentially perfect angular data consistency. This agrees with the earlier SMACK analysis of the AGARD Bo-105 data set, in which no scale factors were found to be needed in the angular measurements (Sec. 6.1.2).

In summary, frequency-response methods provide a straightforward way of evaluating the kinematic consistency of the angular measurements. It is difficult to quantify the nature of these differences by comparing time histories, as is done when using time-domain methods. The next example demonstrates that instrumentation system dynamics can cause relative phase shifts between the data signals and distort the extracted values of important handling qualities and flight-control performance metrics.

### 6.2.2 Correction for Instrumentation System Characteristics

So far, we have ignored the influence of the dynamics and filtering characteristics of the measurement devices (stick sensors, gyros, noise filters, etc.) on the identification results. For example, when filter characteristics differ between the input and output signals, the identified responses will contain spurious lags or leads. These spurious characteristics introduced by the instrumentation system elements can be isolated and corrected to extract the actual aircraft response to control inputs.

The block diagram in Fig. 6.10 depicts the instrumentation system used in an actual flight-test program to document helicopter handling-qualities characteristics vs ADS-33. Referring to the center path of the block diagram, the lateral stick input  $\delta_{lat}$  drives the aircraft (as represented by the response block  $p/\delta_{lat}$ ) to produce the true roll rate  $p$ . We seek to identify the roll-rate response ( $p/\delta_{lat}$ ), but we only have access to the *digitized measurements* of pilot stick  $\delta_{latm}$  and roll rate  $p_m$  for analysis. The upper path of the diagram shows the *analog* measurement of lateral stick deflection as obtained from a potentiometer (labeled as “stick sensor” in the figures). This signal is low-pass filtered within a data conditioning system to avoid aliasing prior to sampling. The sampled measurement signal  $\delta_{latm}$  is used as the input for frequency-response identification. Clearly, the dynamic characteristics of the final digital signal available for analysis will be altered from actual pilot inputs  $\delta_{lat}$ . This observation applies to roll rates and all other measured quantities as well. In our example, the digital data available for

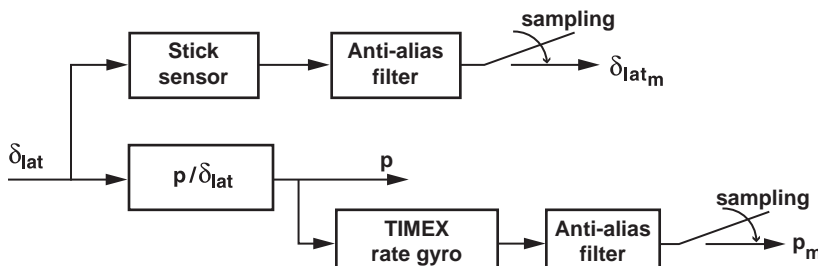


Fig. 6.10 Instrumentation system elements for handling-qualities flight testing.

analysis are not the actual aircraft roll-rate response  $p$  observed by the pilot, but rather a signal  $p_m$ , which is the filtered version of the output of the TIMEX rate gyro instrument. The rate gyro instrument will often contain embedded filtering and signal processing that adds additional lags to the measured signal. So the identified frequency response  $p_m/\delta_{latm}$  can be a significantly distorted characterization of true aircraft response ( $p/\delta_{lat}$ ).

In this actual flight-test example, the sample rate was  $f_s = 113$  Hz, and the stick sensor was a simple string pot with no appreciable added dynamics. The anti-alias filter bandwidth frequency was 20 Hz, but fortunately these filters were the same for input and output (as recommended in Sec. 5.4), and so their influence drops out of the analysis. The dynamic characteristics of the mechanical rate gyro were provided by the manufacturer as

$$H_{RG} = \frac{1.518 \cdot 10^5}{[\zeta = 1, \omega_n = 389.6]} \quad (6.20)$$

An embedded filter was also contained in the rate gyro package, with characteristics provided as

$$H_{EF} = \frac{31.4}{s + 31.4} \quad (6.21)$$

The product of Eqs. (6.20) and (6.21) gives the dynamics of the box marked TIMEX rate gyro in Fig. 6.10:

$$H_{TRG} = H_{RG} H_{EF} \quad (6.22)$$

The CIFER® transfer-function fitting tool (NAVFIT, Sec. 11.4) can be used to extract a simple model that is accurate over the frequency range of interest (1–15 rad/s):

$$H_{TRG} \approx e^{-0.0357s} \quad (6.23)$$

which is a time delay of  $\tau = 0.0357$  s. This is a significant fraction (20%) of the end-to-end aircraft response delay, determined from  $p_m/\delta_{latm}$  to be  $\tau = 0.180$  s.

Using this instrumentation system model, we can correct  $p_m/\delta_{latm}$  to allow a handling-qualities analysis of  $p/\delta_{lat}$ , which is what the pilot experiences:

$$\frac{p}{\delta_{lat}} = \frac{p_m/\delta_{latm}}{H_{TRG}} = \left[ \frac{p_m}{\delta_{latm}} \right] e^{(-0.0357)s} \quad (6.24)$$

In other words, the actual transfer function is the measured transfer function back-corrected for the effective time delay ( $\tau = 0.0357$  s), as introduced by the TIMEX rate gyro unit. This correction is easily accomplished by direct arithmetic

**Table 6.1 Effect of correcting for instrumentation system dynamics**

Parameters	Uncorrected	Corrected
Bandwidth	2.24 rad/s	2.48 rad/s
Phase delay	0.182 s	0.154 s

manipulation of the frequency-response data files. A dedicated function is provided in CIFER® to facilitate frequency-response arithmetic calculations.

Table 6.1 summarizes the results of the sensor dynamics correction for the current example. After accounting for the distortion caused by instrumentation system dynamics, the key HQ parameters (Sec. 7.14.3) of bandwidth  $\omega_{BW}$  are increased, and the phase delay  $\tau_p$  is reduced. Based on the ADS-33 requirements, the helicopter handling qualities are actually level 1 (“satisfactory without improvement”) rather than borderline level 2 (“deficiencies warrant improvement”), as would have been indicated by the uncorrected response.

### 6.2.3 Translational Consistency

In this section, we examine the kinematic consistency of the translational data signals. We adopt the same body-fixed axis system of Fig. 6.3. It is important to recognize that, owing to the test-mass measuring device, the accelerometers can be considered as measuring all specific external forces ( $\equiv$  force/mass) *excluding gravity*.<sup>102</sup> So if the total external X-force component is represented as follows:

Total X-external:

$$X_{\text{tot}} = (X_{\text{aero}} + X_{\text{landing-gear}} + X_{\dots}) + X_{\text{grav}} \quad (6.25)$$

then the  $x$ -axis accelerometer sensor measures the specific external X-force, excluding gravity:

$$A_{x_{\text{cg}}} = \frac{(X_{\text{aero}} + X_{\text{landing-gear}} + X_{\dots})}{m} \text{ ft/s}^2 \quad (6.26)$$

Similarly, the total external  $z$ -force component is represented as follows:

Total Z-external:

$$Z_{\text{tot}} = (Z_{\text{aero}} + Z_{\text{landing-gear}} + Z_{\dots}) + Z_{\text{grav}} \quad (6.27)$$

and the  $z$ -axis accelerometer sensor measures specific external  $Z$  force, excluding gravity:

$$A_{z_{\text{cg}}} = \frac{(Z_{\text{aero}} + Z_{\text{landing-gear}} + Z_{\dots})}{m} \text{ ft/s}^2 \quad (6.28)$$

So, for example, when the aircraft is sitting on the ground, the vertical accelerometer registers a constant value from Eq. (6.3) of  $A_{z_{\text{cg}}} = -g \cos \Theta \cos \Phi \approx -1$  g

(*up*, because of the ground pressing up on the landing gear), *not*  $+1g$  (*down*), as might otherwise be expected. This subtlety is sometimes missed and leads the measurement system engineer to introduce a sign error in the accelerometer calibration.

The translational acceleration in the inertial frame (e.g.,  $d^I W/dt$  in the  $z$  axis) can now be related to the external forces using Newton's Second Law. We express the linear acceleration in rotating body-axis coordinates and linearize the equations for small-perturbation motion about the reference condition. The measurements are also expressed as small-perturbation values about a reference (rectilinear) trim condition:

$$A_{z_{cg}} = (A_{z_{cg}})_0 + a_{z_{cg}} \quad (6.29)$$

where as in the preceding:

$$(A_{z_{cg}})_0 = -g \cos \Theta_0 \approx -g \quad (6.30)$$

Then the linearized equation for small-perturbation motion simplifies to

$$\frac{d^I w}{dt} = \dot{w} + V_0 p - U_0 q = \left( \frac{Z_{tot}}{m} \right) = a_{z_{cg}} - (g \sin \Theta_0) \theta \quad (6.31)$$

which gives finally the following:

$z$  accelerometer:

$$a_{z_{cg}} = \dot{w} + V_0 p - U_0 q + (g \sin \Theta_0) \theta \quad (6.32)$$

The other accelerometer signals are as follows:

$x$  accelerometer:

$$a_{x_{cg}} = \dot{u} + W_0 q - V_0 r + (g \cos \Theta_0) \theta \quad (6.33)$$

$y$  accelerometer:

$$a_{y_{cg}} = \dot{v} + U_0 r - W_0 p - (g \cos \Theta_0) \phi \quad (6.34)$$

The body-axis accelerations can then be reconstructed from the measurements using

$$\dot{u} = a_{x_{cg}} - W_0 q + V_0 r - (g \cos \Theta_0) \theta + b_x \quad (6.35)$$

$$\dot{v} = a_{y_{cg}} - U_0 r + W_0 p + (g \cos \Theta_0) \phi + b_y \quad (6.36)$$

$$\dot{w} = a_{z_{cg}} - V_0 p + U_0 q - (g \sin \Theta_0) \theta + b_z \quad (6.37)$$

which are linearized small-perturbation versions of Eqs. (6.1–6.3), with the components  $b_x$ ,  $b_y$ ,  $b_z$  included to represent the accumulated measurement biases in the component signals. These biases drop out in the frequency-response calculation of  $[\dot{u}/\delta, \dot{v}/\delta, \dot{w}/\delta]$ . Kinematic consistency of the translational signals is then checked by comparing the reconstructed velocity responses [e.g.,  $u/\delta = (1/s)(\dot{u}/\delta)$ ] with the measured velocity responses as obtained using the actual airspeed measurement or GPS data.

A kinematic consistency check of frequency-sweep flight data from the Shadow™ 200 fixed-wing UAV (Sec. 13.11) was completed on the vertical velocity frequency response ( $w/\delta_e$ ). Figure 6.11 compares the response

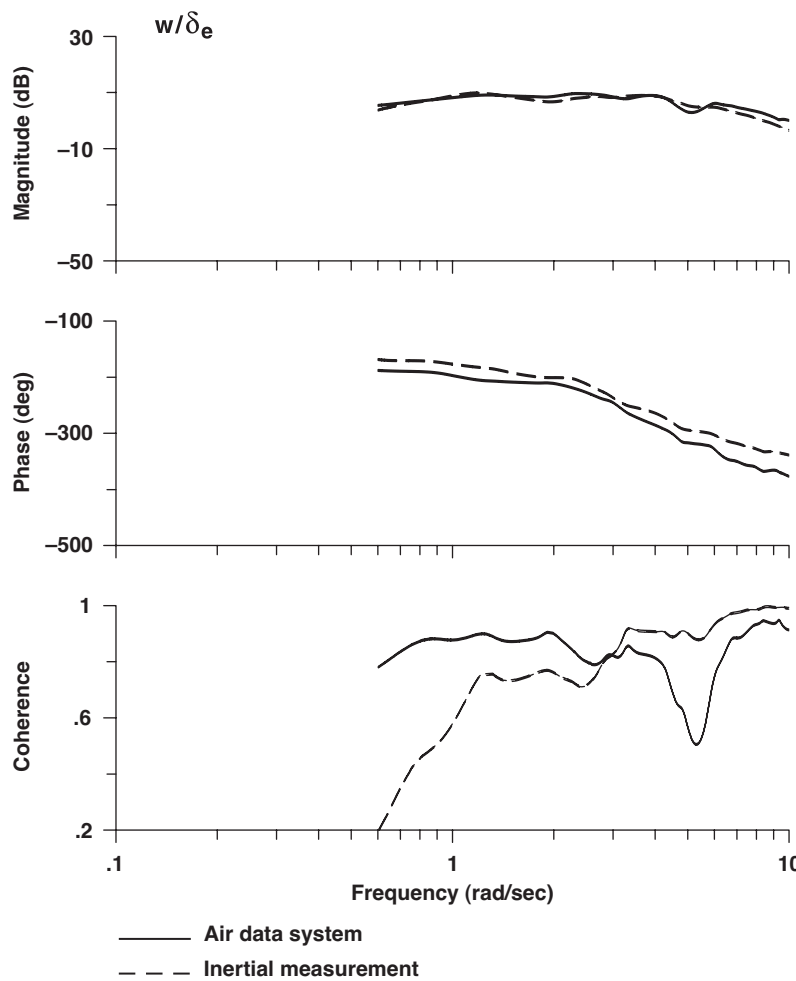


Fig. 6.11 Kinematic consistency check for the Shadow™ 200 fixed-wing UAV.

$[(1/s)(\dot{w}/\delta_e)]$  based on the reconstructed body-axis acceleration of Eq. (6.37) with the response  $[U_0(\alpha_{cg}/\delta_e)]$  obtained from air boom angle-of-attack data corrected to the c.g. The coherence functions are good for both responses in the frequency range of 1–10 rad/s, which corresponds to the short-period response where the vertical velocity response to elevator input is greatest. The results shown in the figure generally reflect good kinematic consistency for these flight-test data in this frequency range. The magnitude curves are in excellent agreement, while the phase curves track well except for a small offset. The increased phase lag seen for the air data measurement amounts to an equivalent time delay of  $\tau = 77$  ms (compared to the inertial measurement) and is associated with the response lag/hysteresis of the angle-of-attack vane device.

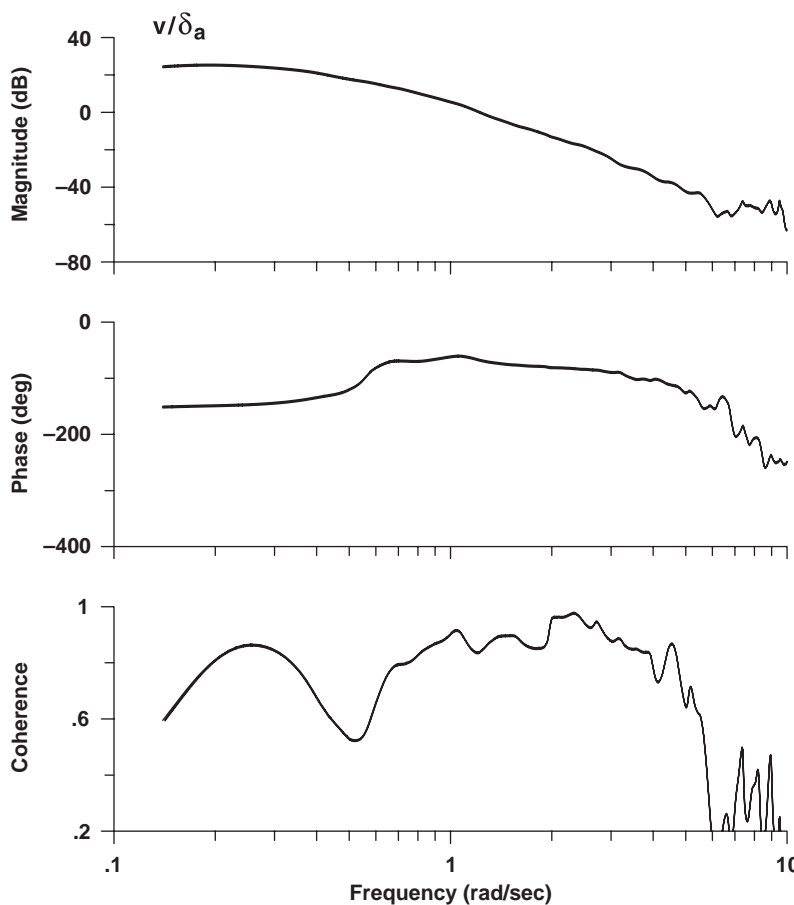


Fig. 6.12 Reconstructed lateral velocity response for XV-15 in hover.

Three-axis air data measurements are often not available or reliable, especially for low-speed flight conditions (e.g., helicopters near hover). When GPS data are also unavailable, we can use the reconstructed body-axis accelerations of Eq. (6.35–6.37) to obtain the velocity frequency responses that are needed for system identification. Figure 6.12 shows the reconstructed velocity response  $[(1/s)(\dot{v}/\delta_a)]$  for the XV-15 roll sweeps at the hover reference condition ( $U_0 = V_0 = W_0 = 0$ ). The response is accurately identified over the wide frequency range of 0.14–5.5 rad/s, as indicated by the good coherence function value ( $\gamma_{xy}^2 \geq 0.6$ ). This rather simple method of velocity-response reconstruction has been found to be quite satisfactory for many identification studies of low-speed and hovering vehicles.

#### 6.2.4 Detection of Faulty Data

The analysis of kinematic consistency ensures that the proper relationships hold between the various response (output) signals. Additional data problems that are associated with the bad input data are commonly encountered, and these will go undetected in such an analysis. For example, string potentiometers (“string pots”) are generally used for measurement of pilot stick, actuators, and control surface deflections. These string pots can start to exhibit slippage or cease to function altogether. Another common problem is inadvertent swapping of input signals in the processing and digital storage of data or the mislabeling of data channels. An excellent and quick method to detect these various sources of *faulty data* is to examine the frequency responses and, especially, the associated coherence functions for the primary input-output pairs on a record-by-record basis.

The detection of faulty data is illustrated in Fig. 6.13, which shows the accelerometer frequency-response identification results ( $a_x/\delta_{\text{lon}}$ ) for three pitch-sweep events. The data are from a flight test of an AH-64 helicopter at a flight condition of 120 kn (documented in the AGARD study<sup>10</sup>). Note that the magnitude and phase plots for two records (events 3 and 5) are virtually identical, but the results for event 6 show that these data clearly were bad. The high coherence for events 3 and 5 indicates a linear system response from longitudinal input to longitudinal accelerometer response, as would be expected. The very low coherence for event 6 confirms that these data were bad. Further checking of the data showed that either the data for the input signal  $\delta_{\text{lon}}$  were incorrectly processed or the signal was bad for this event. When all three records were concatenated (per Sec. 7.11), the overall coherence was reduced, but, more importantly, the character of the frequency-response phase was corrupted significantly (because of the phase difference seen in Fig. 6.13 for event 6). It was only by examining plots of the individual records that the faulty data were isolated and the phase response problem corrected.

In this case, all three records showed good kinematic consistency between the response channels, including the accelerometers, and the problem could only be revealed by checking for a linear relationship (high coherence) between the input and the output for each record. In this example, the check was based on an analysis of the primary translational response ( $a_x/\delta_{\text{lon}}$ ). The primary angular responses (e.g.,  $q/\delta_{\text{lon}}$ ) should also be checked.

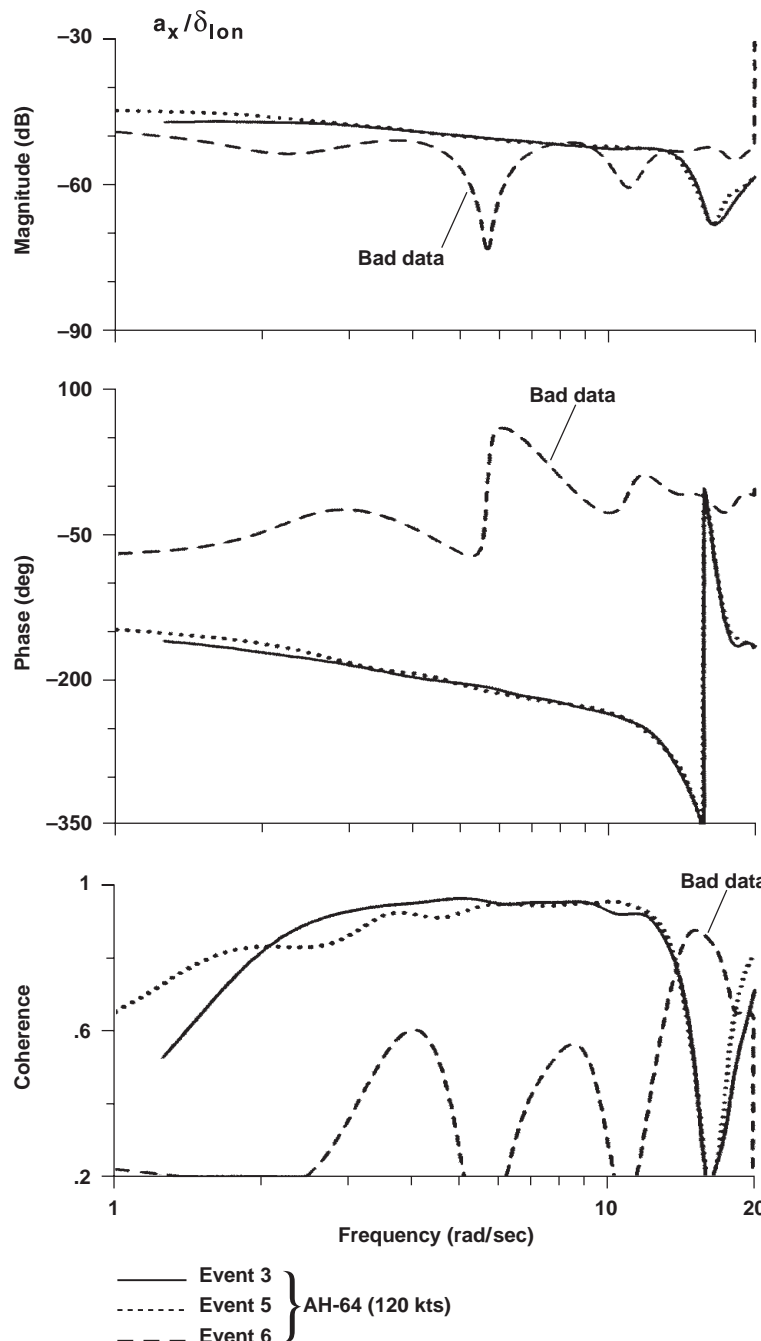


**Fig. 6.13** Detection of faulty data (AH-64).

### 6.2.5 Control Rigging Calibration

In a final application of data consistency analysis, we can use frequency-response identification to quickly and accurately determine control rigging and unit conversions and check these against mechanical drawings and simulation models. For example, in the XV-15 with SCAS off, the measurements of pedal input  $\delta_{\text{ped}}$  and rudder deflection  $\delta_r$  are related through control gearing and mechanical linkage dynamics, as represented in the block diagram of Fig. 6.14.

Engineering documentation for the XV-15 (Ref. 62) indicates theoretical travel limits of  $\pm 20$  deg for rudder associated with 0–100% of pedal input, or

$$\frac{\delta_r}{\delta_{\text{ped}}} = 0.4 \text{ deg}/\% \quad (6.38)$$

Inconsistencies between this expected gearing and actual flight-test data can occur for a variety of reasons. The control calibration (referred to as *control rigging*) could have been conducted using ground tests, with no load, or perhaps there was some “give” or flexure in the control linkages. Rigging checks for complicated control mechanical mixers (*mixer boxes* in rotorcraft) often expose considerable differences relative to simulation schematic drawings. Regardless of the cause, these control calibration scale-factor errors propagate as errors in the identified aerodynamic control sensitivity (e.g.,  $N_{\delta_r}$ ).

An effective test method for determining all of the relevant rigging constants is to perform frequency-sweep tests of the pilot controls. This can be done in flight or on the ground, with proper control surface loading, in a hangar test. The frequency response of  $\delta_r/\delta_{\text{ped}}$  identified from XV-15 flight data is shown in Fig. 6.15. The transfer-function identification method (Chapter 11) is used to determine a simple model of the form

$$\frac{\delta_r}{\delta_{\text{ped}}} = K e^{-\tau s} \quad (6.39)$$

which models the data very accurately, as seen in Fig. 6.15. The identified parameters are

$$K = 0.449 \text{ deg}/\% \quad (6.40)$$

$$\tau = 0.0121 \text{ s} \quad (6.41)$$

The rigging factor  $K$  is 12% above the theoretical value given in Eq. (6.38). The small equivalent time delay  $\tau$  indicates there are no significant linkage dynamics (i.e., no hysteresis).



Fig. 6.14 System representation of gearing and linkage dynamics.

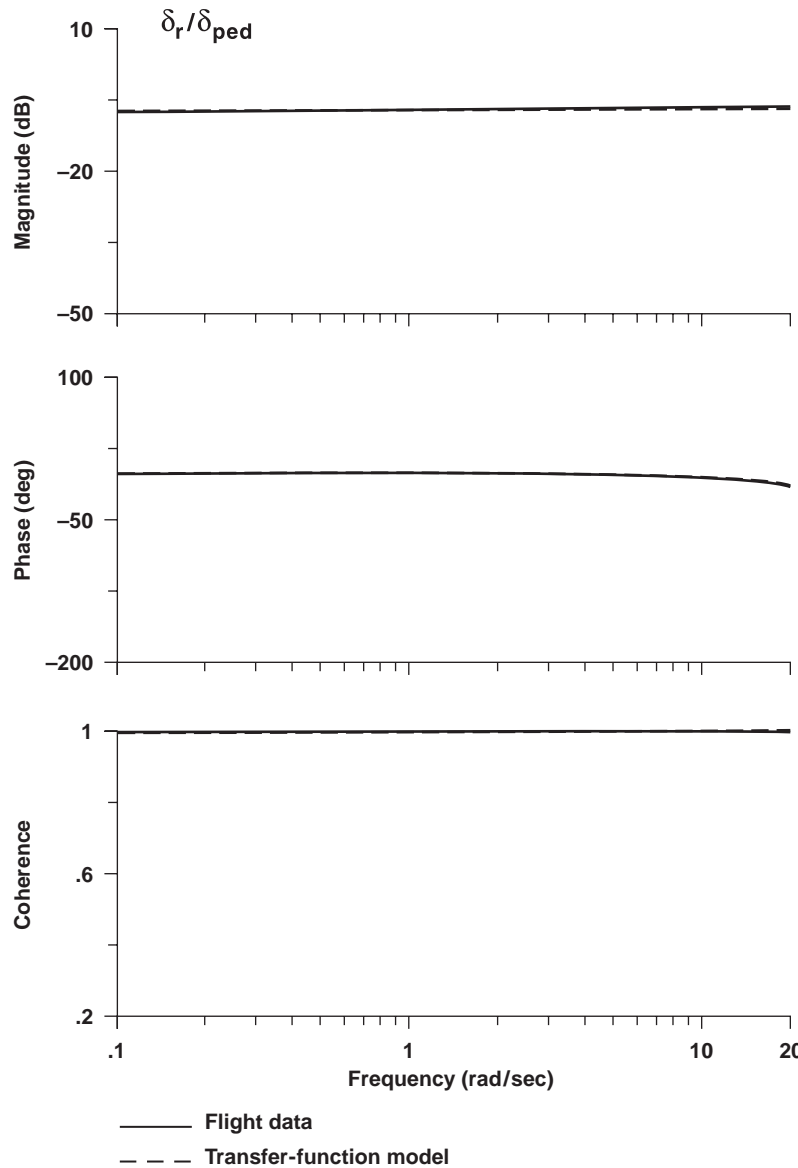


Fig. 6.15 Yaw control rigging identification for the XV-15.

## Problems

### *Equations of motion for data consistency analysis*

**6.1** Derive (a) the translational equations of motion from Newton's laws and (b) the rotational equations of motion from Euler's equation.

**6.2** The accelerometers on your aircraft are located distance vector  $[x, y, z]$  from the center of gravity of the aircraft. Derive the equations that relate the accelerations at the center of gravity ( $a_x, a_y, a_z$ ) to the accelerations measured ( $a_{xm}, a_{ym}, a_{zm}$ ).

**6.3** The nose boom from which angle-of-attack  $\alpha$  and angle-of-sideslip  $\beta$  measurements are taken is located at a distance  $x$  forward of the center of gravity of the aircraft. Derive the relationships between the measured angle of attack  $\alpha_m$  and measured angle of sideslip  $\beta_m$  to the  $\alpha$  and  $\beta$  at the center of gravity.

### *Angular consistency*

**6.4** Create and upload an integral response ( $1/s$ ) into the CIFER<sup>®</sup> database (using utility 15). Plot your integral response using utility 19.

**6.5** Check the angular consistency of the pendulum simulation data ( $\dot{\theta}$  vs  $\theta$ ) vs the ideal response ( $\dot{\theta}/\theta = 1/s$ ), which was created in **Problem 6.4**.

**6.6** Check the angular consistency of the XV-15 roll response data ( $p$  vs  $\phi$ ) for hover (database 1, use Tables 3.1–3.3 for setup) using the lateral sweep data. Plot the flight data vs the ideal case ( $\dot{\phi}/\phi = 1/s$ ). Over what frequency range is the data consistency satisfactory?

### *Instrumentation dynamics*

**6.7** Consider an instrumentation system that samples and filters the input and output data for a system to be identified. Suppose that the filter for the input data has a transfer function  $100/(s + 100)$  and that the output data filter is  $30/(s + 30)$ . Overlay Bode plots of the two filters, calculate the phase offset at 10 rad/s, and then determine the relative time delay.

### *Translational consistency*

**6.8** Check the translational consistency of the lateral velocity data for the XV-15 by comparing the reconstructed lateral velocity [using Eq. (6.36) and then integrating with SIMULINK or another tool] vs the aerodynamic measurement corrected to the center of gravity [ $\beta_{cg}(V_{tot})_0$ ]. Link the roll and yaw step data (database 2, use Tables 3.4 and 3.5 for setup) for this analysis, and export the conditioned time histories. Then compare the two velocity signals in the time domain using overlaid plots.

### *Control gearing identification*

**6.9** Determine the control gearing from pilot lateral stick to aileron surface deflection ( $\delta_a/\delta_{lat}$ ) for the XV-15 in cruise using the lateral sweep data (database 2, use Tables 3.4 and 3.5 for setup).

This page intentionally left blank

## Single-Input / Single-Output Frequency-Response Identification Theory

This chapter introduces the basic concepts of single-input/single-output (SISO) frequency-response identification theory. An understanding of these concepts is an important prerequisite to the success of the system-identification process. The reader is referred to many excellent textbooks on Laplace transform analysis of dynamic systems (for example, see Franklin et al.<sup>104</sup>). A clear and succinct primer that presents a physical interpretation of the frequency-domain, time-series analyses, and the fast Fourier transform (FFT) is that of Ramirez.<sup>105</sup> The details of spectral analysis and frequency-response identification principles are covered in books by Bendat and Piersol<sup>106,107</sup> and Otnes and Enochson.<sup>108</sup> The method of tapered *overlapped windows* or *periodograms* is key to achieving spectral estimates with low random error from real test data. Analytical and computational results can be found in the very useful reports by Nuttal<sup>109,110</sup> and Carter et al.<sup>111</sup>

The analysis of a signal or input-to-output process as a function of frequency (rather than time) is referred to as *spectral analysis*. Spectral analysis is often considered “more art than science” because of the many aspects of sampling, filtering, windowing, and FFT calculations that require user selection of processing parameters. CIFER® incorporates into its graphical user interface many practical guidelines for aircraft, rotorcraft, and subsystem identification, based on extensive practical experience. With much of the nuts and bolts of the analysis machinery taken care of, the analyst can focus more on the correct interpretation of the frequency-domain results.

To put this chapter into the proper context, refer to the system-identification block diagram in Fig. 2.1. This chapter deals with the block labeled multi-variable spectral analysis. Additionally, as shown in Fig. 4.2, this chapter discusses the CIFER® module FRESPID; it also will touch on MISOSA and COMPOSITE, although the latter two modules are discussed more fully in later chapters. FRESPID, MISOSA, and COMPOSITE, three of the main components of CIFER®, are all used in performing a multivariable spectral analysis of flight-test data, which is the key to the rest of the system-identification process.

The following topics are covered in this chapter: 1) definition of frequency response, including information conveyed about system dynamics and relationship to physical system parameters; 2) methods of calculating frequency response, such as Fourier transform, discrete Fourier transform (DFT), fast Fourier transform (FFT), and chirp z-transform (CZT); 3) interpretation of frequency response and related functions, such as spectral density, coherence, and random error; 4) frequency response in CIFER® using FRESPID; and 5) applications.

The mathematics and algorithm details of the Fourier transforms will be summarized at a high level only because these are covered well in the literature (e.g.,

Bendat and Piersol,<sup>107</sup> Otnes and Enochson,<sup>108</sup> and Rabiner and Gold<sup>112</sup>) and the mechanics of the CZT calculation is fully automated in CIFER® and other standard tools (e.g., MATLAB®, IMSL®). We focus herein on the key concepts, selection of important parameters in the algorithms, and flight-vehicle applications.

## 7.1 Definition of Frequency Response

For the purposes of defining the frequency response, it is convenient to perform a “thought experiment” on a very simple dynamic system that is single-input/single-output, linear, stable, and time invariant. Suppose we excite this system with a sine-wave (periodic) input  $x(t)$  of amplitude  $A$  and frequency  $f$ :

$$x(t) = A \sin(2\pi ft) \quad (7.1)$$

where  $f$  is the frequency in hertz.

After the transient response has died out, the system output  $y(t)$  will also be a sine (periodic) wave of the same frequency  $f$ , but with an associated amplitude  $B$  and a phase shift  $\varphi$ :

$$y(t) = B \sin(2\pi ft + \varphi) \quad (7.2)$$

In other words, for this linear and time-invariant system a constant sine-wave input results in a constant sine-wave output at the same frequency  $f$ , also referred to as the *first harmonic frequency*. For linear systems, we do not need to consider the higher harmonics in the response (e.g.,  $2f$ ,  $3f$ ,  $4f$ , ...). Because the time function is the same for the input and output [i.e.,  $\sin(2\pi ft)$ ], the dependency on time  $t$  drops out of this *harmonic analysis*, and we can focus solely on the amplitudes  $A$ ,  $B$  and phase shift  $\varphi$ , which can be obtained from the time-history plots. For the present case of periodic input and output signals, the parameter values  $A$ ,  $B$ , and  $\varphi$  can also be calculated numerically using the Fourier series, including only the first harmonic (sine and cosine) terms.<sup>105</sup>

The frequency-response function  $H(f)$  is a complex-valued function defined by the data curves for the magnification and phase shift at each frequency  $f$ :

$$|H(f)| = \text{Magnification factor} = \frac{B(f)}{A(f)} \quad (7.3)$$

and

$$\angle H(f) = \text{Phase shift} = \varphi(f) \quad (7.4)$$

The frequency response can be obtained experimentally using this method of exciting the system with discrete sine-wave inputs. This quite tedious method was used to obtain frequency responses in the early flight-test experiments, such as on the S-55 helicopter, as reported by Kaufman and Peress.<sup>30</sup>

The frequency response  $H(f)$  fully characterizes the system's dynamic behavior, in terms of the best linear description of the input-to-output behavior, without imposing a requirement for any a priori knowledge about the internal structure of the system's governing equations of motion. However, in this simple example we made certain simplifying assumptions, namely, that the system is single-input/single-output, linear, stable, and time invariant.

## 7.2 Relating the Fourier Transform of the Time Signals to the Frequency Response $H(f)$

Next we will extend the simple concepts presented in the preceding section from a constant sine-wave input to arbitrary, nonperiodic inputs, and we will consider systems with stable or unstable dynamic response characteristics. We will make use of the Fourier transform,<sup>107</sup> which is closely related to the Fourier series<sup>105</sup> but is also applicable to nonperiodic wave forms. The Fourier transform takes nonperiodic time-based input and output signals  $x(t)$  and  $y(t)$ , respectively, and transforms them into two equivalent frequency-based signals  $X(f)$  and  $Y(f)$ , where

$$X(f) = \int_{-\infty}^{\infty} x(t) e^{-j2\pi ft} dt \quad (7.5)$$

and

$$Y(f) = \int_{-\infty}^{\infty} y(t) e^{-j2\pi ft} dt \quad (7.6)$$

are referred to as the *Fourier coefficients*. The frequency response  $H(f)$  is now the complex-valued function that relates Fourier coefficients of the input  $X(f)$  and output  $Y(f)$  by means of the equation

$$Y(f) = H(f)X(f) \quad (7.7)$$

This is the same function that was obtained for constant sine-wave inputs [Eqs. (7.3) and (7.4)].

The frequency-response function  $H(f)$  is just the ratio of the output to the input transforms. Expressed in terms of the real and imaginary parts, we have

$$H(f) = \frac{Y(f)}{X(f)} = H_R(f) + jH_I(f) \quad (7.8)$$

which is consistent with the sign convention for the phase angle  $\varphi$  in Eq. (7.2). The magnification factor of Eq. (7.3) can now be obtained as

$$\text{Magnification factor} = |H(f)| = \sqrt{H_R^2(f) + H_I^2(f)} \quad (7.9)$$

and the phase shift of Eq. (7.4) is obtained by calculating the argument of  $H(f)$ :

$$\text{Phase shift} = \phi(f) = \angle H(f) = \tan^{-1} \left[ \frac{H_I(f)}{H_R(f)} \right] \quad (7.10)$$

The key restriction we encounter<sup>107</sup> in applying Eqs. (7.5) and (7.6) in practical applications is that the area under the input and output curves in the time domain must remain bounded (referred to as the *Dirichlet condition*; Ref. 105):

$$\int_{-\infty}^{\infty} |x(t)| \, dt < \infty \quad \text{and} \quad \int_{-\infty}^{\infty} |y(t)| \, dt < \infty \quad (7.11)$$

Clearly, this condition eliminates *open-loop* frequency-sweep testing of unstable systems. A bounded sweep excitation of a system with unstable dynamic modes will result in an unbounded response and thus violate Eq. (7.11).

Recall that the guidelines for the execution of the frequency-sweep test require 1) starting and ending in trim and 2) regulating the aircraft dynamics to ensure that the transients are bounded and roughly symmetric about the reference flight condition. When conducting a frequency-sweep test as described herein, the pilot (or control system) will provide the needed feedback regulation to ensure that the *closed-loop* response is bounded, regardless of the inherent stability properties of the bare-aircraft dynamics. Thus for systems with *inherently stable or unstable bare-airframe dynamic characteristics*, the Dirichlet condition of Eq. (7.11) will be satisfied, and therefore the frequency-response function can be determined using frequency-sweep testing techniques. Conducting frequency-sweep tests under closed-loop conditions will introduce some bias error in the frequency-response estimate, as described in Chapter 8, but in practice the level of bias errors is not significant when the noise levels are a small fraction of the forced excitation.

The bounding requirement of Eq. (7.11) does eliminate certain types of pilot maneuvers from consideration for frequency-response testing. Suppose, for example, that the pilot executes a pure forward step input of longitudinal stick, and the aircraft response is an associated constant angular rate. The aircraft responses will build up (e.g., speed, rate of descent) until the maneuver is abruptly terminated by the pilot. This would not be a good input to use for frequency-response identification because the integral of  $x(t)$  in Eq. (7.11) is diverging until the point of record termination, which is analogous to the problem with frequency-response identification for unstable system dynamics without feedback.

In summary, subject to the test guidelines (1 and 2), and given only the experimental measurements of the forcing function (input) and associated system response (output), the frequency response can be determined, thus providing a wealth of information about the dynamic system characteristics without making any a priori assumptions about the system structure or stability properties. These frequency-response functions readily support dynamic system analysis, control system design, and simulation model validation, using standard Bode, Nichols, and Nyquist methods, without resorting to parametric (i.e., transfer-function and

state-space) models. Further, when the system dynamics are nonlinear, the frequency response extracted using Fourier transform methods will be a first harmonic *describing function*, which is the best linear model of the nonlinear behavior,<sup>55</sup> as discussed in more detail later (Sec. 7.7.4).

### 7.3 Simple Example of Frequency-Response Interpretation

To illustrate the interpretation of the frequency response in an actual system, consider a simple one-DOF model of the aircraft roll-rate response,

$$\dot{p} = L_p p + L_\delta \delta \quad (7.12)$$

Taking the Laplace transform yields

$$sp(s) - p(0) = L_p p(s) + L_\delta \delta(s) \quad (7.13)$$

We are concerned with the response to control inputs, so that the initial condition is set equal to 0,

$$p(0) = 0 \quad (7.14)$$

and Eq. (7.13) is rewritten as a *transfer function*:

$$H(s) = \frac{p(s)}{\delta(s)} = \frac{L_\delta}{s - L_p} \quad (7.15)$$

The frequency response is obtained by substituting  $j\omega$  for the Laplace variable  $s$  to yield

$$H(j\omega) = \frac{L_\delta}{j\omega - L_p} \quad (7.16)$$

where the frequency  $\omega$  (rad/s) is related to the frequency  $f$  (Hz) used in the definitions of the frequency-response function [Eqs. (7.3), (7.4), and (7.7)] by

$$\omega = 2\pi f \quad (7.17)$$

So the physical model description of Eq. (7.12) allows the use of the Laplace transform to achieve a closed-form expression for the frequency response  $H(f)$ . This is the same frequency response that would be produced from the Fourier transform of the time-history data [ $\delta(t)$  and  $p(t)$ ] as obtained from the time integration of Eq. (7.12).

A convenient graphical visualization of the frequency-response function is a Bode plot,<sup>104</sup> which is a semilog plot of the magnitude of  $H$  in decibels ( $H_{\text{dB}}$ ) and the phase of  $H$  in degrees ( $H_{\text{deg}}$ ), both vs frequency, herein usually in radians/second. The vertical axis (dB, deg) uses a linear scale, and the horizontal

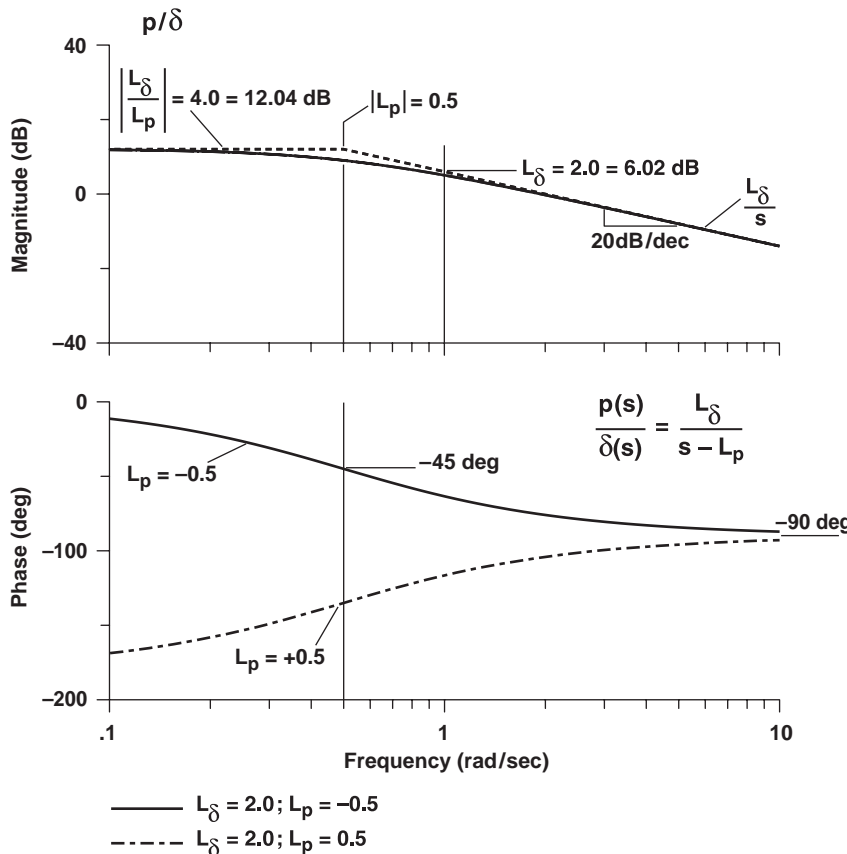


Fig. 7.1 Bode plot for one-DOF system.

axis (frequency) uses a log scale. These quantities are obtained using Eqs. (7.9) and (7.10) and the defining equations:

$$H_{\text{dB}} = 20 \log_{10}|H(j\omega)| \quad (7.18)$$

and

$$H_{\text{deg}} = \angle H(j\omega) \text{ deg} \quad (7.19)$$

When the frequency is taken as  $\omega$  (rad/s), simple rules are available for sketching the asymptotes of the Bode diagram.<sup>104</sup>

Figure 7.1 shows the Bode plot that was obtained for the system transfer function of Eq. (7.16). The asymptotic sketch for the magnitude curve is shown in the short dashes. In this example,  $L_\delta = 2$  and  $L_p$  will be assumed to be either  $-0.5$ , which would be a stable system, or  $+0.5$ , which would be an unstable system.

Consider first the magnitude plot. The magnitude has a flat (constant) characteristic at low frequencies. The asymptotic magnitude value is obtained by setting  $s = 0$  in Eq. (7.15)

$$\left| \frac{p}{\delta}(s) \right|_{s \rightarrow 0} = \left| \frac{L_\delta}{L_p} \right| = 4.0 = 12.04 \text{ dB} \quad (7.20)$$

The magnitude begins to decrease or roll off for frequencies above the break point in the asymptotic curve:

$$\omega = |L_p| = 0.5 \text{ rad/s} \quad (7.21)$$

The asymptotic line that closely approximates the high-frequency magnitude curve is obtained by setting  $s \gg L_p$  in Eq. (7.15),

$$\left. \frac{p}{\delta}(s) \right|_{s \rightarrow \infty} = \frac{L_\delta}{s} \rightarrow -20 \text{ dB/decade slope} \quad (7.22)$$

and is anchored at a frequency of  $\omega = 1 \text{ rad/s}$ , with a magnitude from Eq. (7.22) of

$$\frac{L_\delta}{1} = 2.00 = 6.02 \text{ dB} \quad (7.23)$$

Notice in Fig. 7.1 that the magnitude plot is the same in both cases ( $L_p = -0.5$  or  $L_p = 0.5$ ).

Next, consider the phase plot in Fig. 7.1. In the case of the stable system ( $L_p = -0.5$ ), shown with the solid line, the phase starts near  $H_{\text{deg}} = 0 \text{ deg}$  and rolls off to  $H_{\text{deg}} = -90 \text{ deg}$ . At the break frequency in the magnitude plot ( $\omega = 0.5 \text{ rad/s}$ ), there is a  $-45\text{-deg}$  phase shift. For the unstable system ( $L_p = 0.5$ ), shown with the dashed line, the phase starts near  $H_{\text{deg}} = -180 \text{ deg}$  and then rises to  $H_{\text{deg}} = -90 \text{ deg}$ ; the phase shift at the break frequency is now  $+45 \text{ deg}$  relative to the start.

So the key observation is the difference in phase-curve change for stable vs unstable system dynamics. When the phase rolls off (becomes more negative) in the frequency range where the magnitude breaks downward, a stable dynamic mode is indicated. Alternatively, if the phase increases (becoming more positive) at the magnitude break frequency, an unstable dynamic mode is indicated. The phase characteristic becomes more complicated when there are zeros (numerator terms in the transfer function) in the same proximity.

Given the Bode plot, we could reverse engineer, or “identify,” the parametric transfer-function model of the aircraft dynamics in terms of  $L_\delta$  and  $L_p$ . That is, starting with a Bode plot of the frequency response that was extracted from test data, the aerodynamic parameters  $L_\delta$  and  $L_p$  could be estimated by a quick examination of the graphs of Fig. 7.1. The Bode plot could also be used to update and validate a math model of an aircraft system. For the simple example of Eq. (7.15), suppose that the magnitude plots of the flight-test data and the

simulation (i.e., transfer-function) model are offset from each other across the frequency range, but the phase curves agree well. Then the error must be in the control effectiveness parameter  $L_\delta$  rather than in the damping parameter  $L_p$ . On the other hand, if both the break frequency and associated phase characteristic are in error, then this indicates that  $L_p$ , and not  $L_\delta$ , should be updated.

## 7.4 General Observations

Summarizing what has been covered so far, a number of general observations can be made about the frequency response of a system:

- 1) It fully characterizes the dynamics of the aircraft.
- 2) It contains no inherent assumptions about the structure or order of the system. Some simplifying assumptions were made for the purposes of illustration, but in general no *a priori* assumptions about the aircraft other than linearity and time invariance are necessary. The frequency-response function constitutes a nonparametric model.
- 3) It is defined for stable or unstable systems. Frequency-domain methods are especially well suited to the identification and analysis of unstable systems.
- 4) When aircraft dynamics are nonlinear (e.g., aerodynamic nonlinearities, hysteresis, or even an actuator limit), the frequency-response function, as extracted using the Fourier transform, constitutes a describing function, namely, the linear model that best characterizes the nonlinear behavior of the system.<sup>55</sup> Rotorcraft and other aircraft generally possess nonlinear response characteristics, but they can most often be well characterized by these linearized describing function models.

## 7.5 Calculating the Fourier Transform and Spectral Functions

Although Eqs. (7.5–7.7) serve to define the frequency response of a system in terms of the Fourier transforms of the input and output frequency signals, the equations do not convey a practical method for actually calculating the frequency response. First of all, the time signal does not exist for all time,  $t = -\infty$  to  $+\infty$ . Instead, the record will start at  $t = 0$  and end at  $t = T$ , leading to the *finite* Fourier transform<sup>106</sup>

$$X(f, T) = \int_0^T x(t) e^{-j2\pi ft} dt \quad (7.24)$$

which is based on continuous time, but with a finite flight data record length ( $T = T_{\text{rec}}$ ). Next, we recognize that the data are collected from instruments reporting at a certain sample rate, resulting in a time-history data record  $x_n$  at a sequence of discrete time points, rather than a continuous stream in time  $x(t)$  as in Eq. (7.24). The *discrete* Fourier transform (DFT) determines  $X(f)$  at discrete frequencies  $f_k$  from a finite record of *sampled data*<sup>106</sup>:

$$X(f_k) = X(k\Delta f) = \Delta t \sum_{n=0}^{N-1} x_n \exp\{[-j2\pi(kn)]/N\} \quad (7.25)$$

where

- $X(f_k)$  = Fourier coefficients, for  $k = 0, 1, 2, \dots, N - 1$
- $x_n = x(n\Delta t)$  = time-domain data record, for  $n = 0, 1, 2, \dots, N - 1$
- $\Delta t$  = time increment
- $\Delta f = 1/N\Delta t$  = frequency resolution
- $N$  = number of discrete frequency points

Notice that in the DFT calculation of Eq. (7.25), the number of discrete frequency points in the identified Fourier transform  $X(f_k)$  is the same as the number of discrete time points in the time-history data record  $x_n$ , namely,  $N$ . The frequency points are distributed evenly from  $f_{\min} = \Delta f$  to the sample rate ( $f_s = 1/\Delta t$ ).

### 7.5.1 Spectral Functions

The products of the Fourier transform computation are the Fourier coefficients of the input (excitation)  $X(f)$  and output (response)  $Y(f)$ . From these, three important spectral functions are defined by the equations that follow. Following the terminology of Bendat and Piersol,<sup>107</sup> a *rough estimate* (denoted by  $\tilde{\cdot}$ ) of the *input autospectrum* is determined from the Fourier coefficients by

$$\tilde{G}_{xx}(f) = \frac{2}{T} |X(f)|^2 \quad (7.26)$$

where again for a single flight record  $T = T_{\text{rec}}$ . The input autospectrum, also referred to as the input power spectral density (PSD), displays the distribution of the squared input  $x^2$  or excitation power as a function of frequency  $f$ . Note the use of the symbol  $G_{xx}$  for the one-sided spectral function following the convention of Bendat and Piersol.<sup>106,107</sup> (Note also that the book by Klein and Morelli<sup>6</sup> adopts the symbol  $S_{xx}$  for the one-sided spectral function.)

A rough estimate of the *output autospectrum*, or output PSD, determined by

$$\tilde{G}_{yy}(f) = \frac{2}{T} |Y(f)|^2 \quad (7.27)$$

displays the distribution of the squared output  $y^2$  or response power as a function of frequency. Finally, a rough estimate of the *cross spectrum*, or cross PSD, is determined by

$$\tilde{G}_{xy}(f) = \frac{2}{T} [X^*(f)Y(f)] \quad (7.28)$$

where  $*$  denotes the complex conjugate value. The cross spectrum displays the distribution of the product of input times output  $xy$  or input-to-output power transfer as a function of frequency. The cross spectrum is a complex-valued function and thus also conveys input-to-output phase information.

The PSD magnitude functions are plotted in decibels. For power variables, the decibel is expressed in terms of *power decibels* defined as, for example,<sup>108,113</sup>

$$\tilde{G}_{xx_{\text{dB}}}(f) = 10 \log_{10} \tilde{G}_{xx}(f) \quad (7.29)$$

This is equivalent to displaying the frequency distribution of the input rms in conventional  $\text{dB} = 20 \log_{10}(x)$ . For example, a 6-dB drop in  $\tilde{G}_{xx_{\text{dB}}}$  corresponds to a factor of 2 reduction in the rms of  $x(t)$  at that frequency. Analogous defining equations and interpretations apply to  $\tilde{G}_{yy_{\text{dB}}}$  and  $\tilde{G}_{xy_{\text{dB}}}$ .

### 7.5.2 Bias and Random Errors in Spectral Function Identification

The estimation and minimization of errors in the spectral-function calculations [Eq. (7.26–7.28)] and the associated frequency response (Sec. 7.7) are the key to the practical application of system identification. This is especially true for obtaining useful results for flight vehicles from measured data with high noise contamination. An excellent reference that covers engineering methods for addressing errors in spectral analyses is that of Bendat and Piersol.<sup>107</sup> The current chapter summarizes some of the key concepts, with an emphasis on engineering methods and flight-test results.

Errors that arise in the estimation of the spectral functions can be broadly classified as *deterministic* (systematic) or *nondeterministic* (random)—just as was the case in the time domain (Sec. 6.1). Systematic or *bias* errors are average differences (or offsets) of magnitude and/or phase characteristics between the estimated quantity (e.g., spectral function or frequency response) and the true quantity. Key sources of bias errors in system identification of flight vehicles are the following: extraneous noise in the measurements of the input (excitation) (Sec. 7.7), insufficient frequency resolution for identifying lightly damped modes (Sec. 7.10.4), and correlation between the atmospheric disturbances and control excitation caused by feedback (Chapter 8). Random error is seen as a haphazard scatter in the estimated magnitude and/or phase characteristics around the true response. The error is statistical in nature and is characterized by a standard deviation in the estimated response about its expected value. Key sources of random errors in system identification of flight vehicles are the following: extraneous noise in the measurement of the output (response) (Sec. 7.7.1, Sec. 7.8) and unmeasured inputs (e.g., gusts) that contribute to the output and are uncorrelated with the measured input (Sec. 7.8). Random error can be greatly reduced using windowing methods as discussed next.

### 7.5.3 Windowing

The method of *overlapped windowing*, also called the method of *periodograms*, is a key technique in practical spectral analysis that greatly reduces the level of random error in the spectral estimates (as quantified later in Sec. 7.9). This technique produces *smooth* spectral estimates by averaging the rough estimates (Sec. 7.5.1) for multiple segments of data.

The original time-history record (duration  $T_{\text{rec}}$ ) is segmented into a sequence of  $n_r$  shorter overlapping time segments or *windows* of length  $T_{\text{win}}$ , each window

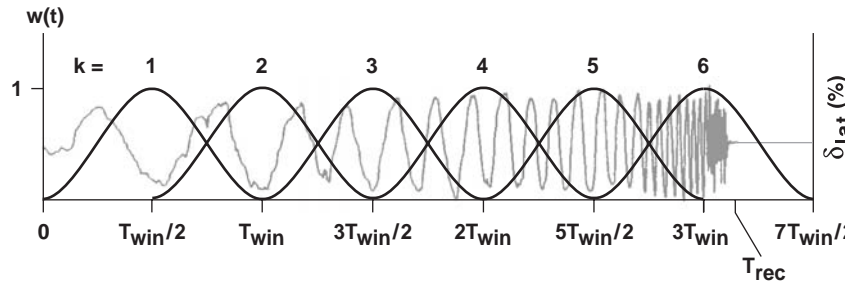


Fig. 7.2 Overlapped windowing of flight data (adapted from Bendat and Piersol<sup>106</sup>).

( $k = 1, 2, \dots, n_r$ ) containing  $L$  points, as depicted for a lateral stick record  $\delta_{\text{lat}}$  in Fig. 7.2 (adapted from Bendat and Piersol<sup>106</sup>). The illustration of Fig. 7.2 is for a 50% overlap of  $n_r = 6$  windows. So, the first window ( $k = 1$ ) spans the time interval from 0 to  $T_{\text{win}}$ , the second ( $k = 2$ ) from  $T_{\text{win}}/2$  to  $3T_{\text{win}}/2$ , and so on. The time history for the last window ( $k = 6$ ) is filled out to its completion by appending the trim value (i.e., zero values after the mean has been subtracted) to the time history beyond the flight record duration ( $T_{\text{rec}} < t \leq 7T_{\text{win}}/2$ ).

The time-history data in each window segment are weighted by the window shaping function  $w(t)$  to form the weighted time-history segment  $w(t)\delta_{\text{lat}}(t)$ . This window tapering reduces the spectral errors associated with side-lobe leakage that is a characteristic of strict rectangular windowing. There are many possible choices of window tapering functions, and CIFER® employs the commonly used (1-cos) window shape, also referred to as a Hanning window<sup>106</sup> and depicted in Fig. 7.2. The Fourier transforms  $X(f)$  [and  $Y(f)$ ] for each weighted time-history window segment  $w(t)\delta_{\text{lat}}(t)$  are then determined from Eq. (7.25) with  $T = T_{\text{win}}$ . Window overlap, shown in Fig. 7.2, counteracts the increased variability introduced by the window edge tapering.<sup>106</sup>

The *smooth estimate*<sup>107</sup> of the input autospectrum, denoted by  $\hat{G}_{xx}(f)$ , is the average of the rough estimates over the  $n_r$  overlapped window segments

$$\hat{G}_{xx}(f) = \left( \frac{1}{U n_r} \right) \sum_{k=1}^{n_r} \tilde{G}_{xx,k}(f) \quad (7.30)$$

with a correction  $U$  to the overall spectral density magnitude for the energy loss associated with the taper function  $w(t)$ . For the Hanning window, the correction is given by Bendat and Piersol<sup>107</sup> as  $U = \sqrt{3}/8 = 0.612$ .

The number of window segments [ $n_r$  in Eq. (7.30)] depends on the overlap fraction

$$n_r = 1 + \left[ \frac{(T_{\text{rec}}'/T_{\text{win}}) - 1}{1 - x_{\text{frac}}} \right] \quad (7.31)$$

where

$T_{\text{win}} = L\Delta t$  = time duration or *width* of the spectral window  
 $T_{\text{rec}}'$  = length of the extended record that we filled out with trim values (e.g.,  
 $T_{\text{rec}}' = 7T_{\text{win}}/2$  in Fig. 7.2)  
 $x_{\text{frac}}$  = overlap fraction, with a range ( $0 \leq x_{\text{frac}} < 1$ ) (the lower value for no overlap and the upper limit representing 100% overlap)

The smooth spectral estimates for the output autospectrum  $\hat{G}_{yy}(f)$  and cross-spectrum  $\hat{G}_{xy}(f)$  are determined from analogous equations with  $G_{xx,k}(f)$  replaced in Eq. (7.30) by  $\tilde{G}_{yy,k}(f)$  and  $\tilde{G}_{xy,k}(f)$ , respectively:

$$\hat{G}_{yy}(f) = \left( \frac{1}{Un_r} \right) \sum_{k=1}^{n_r} \tilde{G}_{yy,k}(f) \quad (7.32)$$

$$\hat{G}_{xy}(f) = \left( \frac{1}{Un_r} \right) \sum_{k=1}^{n_r} \tilde{G}_{xy,k}(f) \quad (7.33)$$

The window width  $T_{\text{win}}$  determines directly the minimum frequency  $f_{\text{min}}$  and frequency resolution  $\Delta f$  of the DFT:

$$f_{\text{min}} = \Delta f = \frac{1}{T_{\text{win}}} = \frac{1}{L\Delta t} = \frac{f_s}{L} \quad (7.34)$$

where the sampling frequency is  $f_s = 1/\Delta t$ .

As an example, suppose that we have a flight-test record with a length  $T_{\text{rec}} = 100$  s. If the record is segmented into 20-s segments or windows, the minimum frequency that can be identified is  $f_{\text{min}} = 1/20 = 0.05$  Hz. There is no information content for periods greater than the length of the window  $T_{\text{win}}$  or for corresponding frequencies of less than  $f_{\text{min}}$  (0.05 Hz in this case). A sometimes held *misconception* is that increased (or even arbitrary) frequency resolution can be achieved by simply “padding” the input sequence with zeros (thereby artificially increasing  $L$ ). Padding with zeros, however, only allows *interpolation* between true frequency resolution points ( $\Delta f = f_s/L$ ) and *does not increase the frequency resolution*.<sup>108</sup> The only way to increase the true frequency resolution of the identification is to increase the width of the window (up to a maximum of the record length), which decreases the number of averages included in the calculation of the smoothed spectra [e.g.,  $\hat{G}_{yy}(f)$ ] and so increases the random error (Sec. 7.9). Further increases in window length require a longer data record.

Viewed in the  $z$  plane,<sup>79</sup> the  $N = L$  discrete frequency points of  $X(f_k)$  are distributed evenly around the entire unit circle up to the sampling frequency  $f_s$ . The  $z$  transform is a mirror image with respect to the Nyquist frequency ( $f_{\text{Nyq}} = f_s/2$ ), so that the useful spectrum is composed of the first  $N/2$  frequency points. The second half of the spectrum ( $f_{\text{Nyq}} < \omega \leq f_s$ ), composed of the remaining  $N/2$  frequency points, is redundant and is not actually calculated in the Fourier transform procedure. In summary, identification results obtained from

the Fourier transform cover the frequency range from the minimum frequency  $f_{\min}$  of Eq. (7.34) up to the maximum frequency

$$f_{\max} = f_{\text{Nyq}} = \frac{f_s}{2} \quad (7.35)$$

Reference to Eq. (7.35) indicates that identification results are achievable at  $f_{\max}$  based on only two data points for an excitation sine wave at this frequency. As a practical matter, experience with flight-test data indicates a somewhat lower effective frequency for which accurate identification is achieved:

$$(f_{\max})_{\text{effective}} = \frac{f_s}{5} = \frac{f_{\text{Nyq}}}{2.5} \quad (7.36)$$

which amounts to five data points for a sine wave with a frequency of  $f_{\max}$ . Even so, this maximum effective identification frequency is always well beyond the frequency range of modeling interest, considering the factor of 25 separation guideline of Sec. 5.4. Therefore, many of the  $L$  frequency points that are calculated up to  $f_{\max}$  are wasted in the DFT (or FFT) in the sense that they provide no additional information in the frequency range of interest.

Some authors (e.g., Otnes and Enochson<sup>108</sup> and Klein and Morelli<sup>6</sup>) discuss an additional processing step referred to as *frequency averaging* or *binning*. In this approach the time-domain data are padded with zeros to provide (interpolated) spectral estimates over a finer mesh around each actual frequency point  $f$ . Then the neighboring frequency points are averaged to yield a single spectral estimate for a band, or *bin*, of frequencies. This procedure reduces random error, but at the expense of reduced effective spectral resolution, and is not recommended herein. The combination of spectral overlapped tapered windowing and multirun concatenation, discussed in this chapter and adopted in CIFER®, provides low random error without compromising spectral resolution. Then *composite windowing* (presented in Chapter 10) achieves a final overall frequency-response identification with excellent dynamic range, low random error, and maximum resolution without the compromise of a single window size selection.

#### 7.5.4 Fast Fourier Transform and Chirp z Transform

Frequency-response determination using the discrete Fourier transform (DFT) of Eq. (7.25) is computationally intensive, requiring  $L^2$  complex multiplication-addition operations for each window of  $L$  data points.<sup>106</sup> The fast Fourier transform (FFT) is a numerically more efficient algorithm for determining the Fourier transform, involving the equivalent of only  $4L(\log_2 L)$  computations.<sup>106</sup> For a typical calculation involving  $L = 1024$  data points (e.g., approximately 20-s windows of data at a 50-Hz sample rate), this is a 25-to-1 efficiency advantage of the FFT over the DFT.

A specialized implementation of the FFT is the chirp z-transform (CZT), also known as the *zoom transform*.<sup>112,114</sup> Developed at Bell Labs for noise spectrum identification, the CZT is capable of a highly accurate frequency-response determination over an arc of the unit circle. The following key properties of the CZT

algorithm make it highly flexible and particularly well suited to frequency-response identification from flight-test data:

1) For the CZT, the number of frequency points  $N$  is specified independently of the number of time-history points  $L$ , subject only to the conditions that  $N \leq L$  and that the sum  $N + L$  must be a power of 2. This relaxes the rather severe FFT restriction that  $N = L$  and that  $N$  and  $L$  must each be a power of 2.

2) The  $N$  frequency points of the CZT are distributed over an arbitrary *arc* of the unit circle (i.e., only in the frequency range of interest), not over the frequency range of the entire unit circle [limited only by the frequencies given in Eqs. (7.34) and (7.35)] as in the case of the FFT. Consider again the example of a 50-Hz sample rate time-history record and a window with  $L = 1024$  points ( $T_{\text{win}} = 20.48$  s). The FFT will return a frequency response with a uniform frequency resolution  $\Delta f = 1/20.48 = 0.0488$  Hz. The response will comprise  $N/2 = 1024/2 = 512$  points from  $f_{\text{min}} = 1/20.48 = 0.0488$  Hz to  $f_{\text{max}} = f_s/2 = 50/2 = 25$  Hz. However, for handling-qualities applications the frequency range of interest (and frequency range of suitable excitation) is typically 0.3–12 rad/s (i.e., 0.0478–1.910 Hz), which includes only 39 frequency points, so that most of the 1024 total frequency points are wasted. For the CZT, the computation produces the same number of frequency points (1024) but distributed only from 0.3–12 rad/s, which improves the resolution by a factor of 27, to  $\Delta f = (12 - 0.3)/(2\pi \cdot 1024) = 0.00182$  Hz.

3) The CZT is subject to reduced leakage, or digital contamination, and it has improved accuracy as compared to the FFT.<sup>112</sup> This has been confirmed by the leading author in many back-to-back tests of the CZT vs the FFT using aircraft flight-test data.

Taken together, these three key characteristics of the chirp z-transform provide excellent flexibility in the selection of sample rates, window length, and frequency resolution, with improved frequency-response accuracy for aircraft flight-test data analysis. The CZT, as implemented in CIFER®, has provided consistent and reliable frequency-response identification from flight-test data, even in cases of low signal-to-noise ratios (typical of helicopters in hover).

## 7.6 Interpreting Spectral Functions

A direct application of the PSD functions is in the evaluation of the excitation and vehicle-response frequency content for a system-identification maneuver. For example, the frequency point beyond which the input autospectrum drops by 6 dB (i.e., a 50% drop in rms) defines the bandwidth of the excitation. A “hole” in the input autospectrum indicates that the pilot input might have passed through that frequency too quickly. Calculated in real time using telemetered data,<sup>115</sup> the input autospectrum can be a highly useful tool in evaluating the quality of the test maneuvers and determining if the recommended limits on turbulence levels have been reached [Eq. (8.20)]. As an example of their utility in postflight analysis, the PSDs provide valuable information for selecting the best individual records for linking in the identification and for uncovering possible resonances in the structure and sensor systems.

Figure 7.3 shows an example of the lateral stick PSD  $\hat{G}_{\delta_{\text{lat}} \delta_{\text{lat}}}$  for concatenated roll-axis frequency-sweep tests of the XV-15 in hover ( $T_{\text{win}} = 25$  s). The excitation

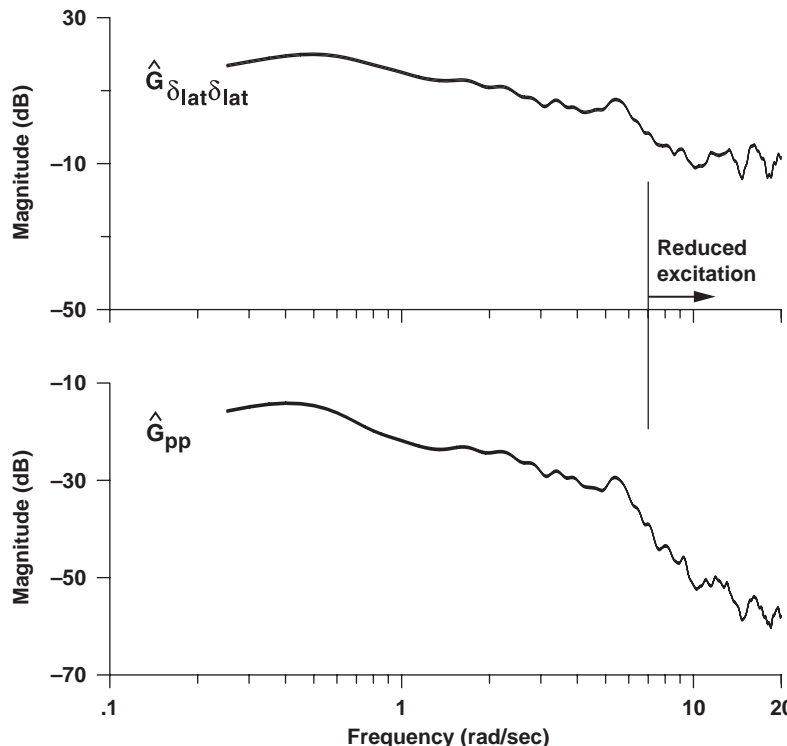


Fig. 7.3 Spectral density functions for SCAS-on roll sweep (XV-15, hover).

is seen to be fairly uniform with frequency, dropping off rapidly beyond  $\omega = 7$  rad/s, and the associated output autospectrum  $\hat{G}_{pp}$  (based on roll rate in rad/s) rolls off even faster at this point. This reflects preflight instructions to the pilot to terminate the sweep when a frequency of about 1.0–1.5 Hz was reached. These data flights were among the first sweeps conducted on the experimental XV-15 aircraft, and so the maximum excitation frequency was intentionally selected to be very conservative. It is clear from the PSD curves that the frequency sweep provides a good excitation in the frequency range of interest, rolling off rapidly once the selected “knock-it-off” frequency is reached. The presence of excitation power at higher frequencies (beyond 1.5 Hz) reflects the irregularities in the wave form of the piloted sweep (Sec. 5.5).

## 7.7 Frequency-Response Calculation

The frequency-response function  $H(f)$  can be estimated directly from the smooth spectral function estimates [Eqs. (7.30), (7.32), and (7.33)] at each frequency point  $f$  using one of two expressions. The standard expression is

$$\hat{H}_1(f) = \frac{\hat{G}_{xy}(f)}{\hat{G}_{xx}(f)} \quad (7.37)$$

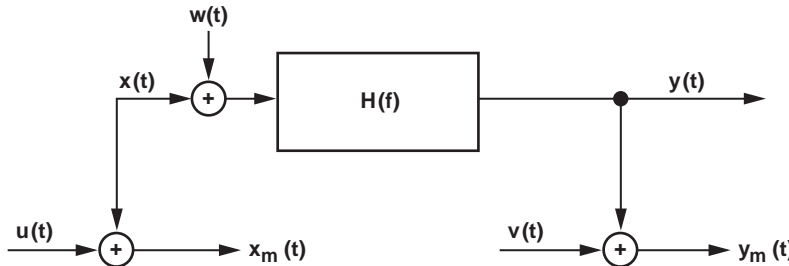


Fig. 7.4 Measurement noise at the input and output.

also referred to herein by simply  $\hat{H}(f)$ . An alternate expression is

$$\hat{H}_2(f) = \frac{\hat{G}_{yy}(f)}{\hat{G}_{yx}(f)} \quad (7.38)$$

Both give the same answer for the frequency-response estimate when the measurements are *noise free*.

In practical applications of system identification, noise will be present in the input and output measurements  $u$  and  $v$ , as depicted in Fig. 7.4. Process noise and other unmeasurable (secondary) inputs will also be present (denoted as  $w$  in Fig. 7.4) and *pass through the system* and thus can be reflected to the output. These can be considered to contribute to the output noise  $v$  and appear in the measured output  $y_m$ , but they do not contribute to the measured input  $x_m$ . So, in the discussion that follows the process noise  $w$  is not considered separately—its effect on the spectral analysis is the same as the output noise  $v$ . Finally, all noise signals  $u$ ,  $v$ , and  $w$  are considered to be uncorrelated with the true signals  $x$  and  $y$ .

The appropriate expression to use for estimating the frequency response [ $\hat{H}_1(f)$ ,  $\hat{H}_2(f)$ , or a combination of these] depends on whether the key source of measurement noise is associated with the inputs or outputs ( $u$  or  $v$ , respectively). In the next sections, we evaluate the influence of measurement noise at the output  $v$  and the input  $u$  on the proper choice (and accuracy) of the frequency-response calculation.

### 7.7.1 Effect of Output Noise on $H_1(f)$ Estimate, with Noise-Free Input Measurements

The frequency-response estimate based on the measurements  $x_m$  and  $y_m$  and using  $H_1(f)$  [Eq. (7.37)] is

$$\hat{H}_1(f) = \frac{\hat{G}_{x_m y_m}(f)}{\hat{G}_{x_m x_m}(f)} \quad (7.39)$$

The assumption commonly made is that extraneous noise is present at the output measurement only (e.g., vehicle response) and that the input (e.g., control surface) measurement is noise free [ $u(t) = 0$ ]. In this situation,

$$\hat{G}_{x_m x_m}(f) = G_{xx}(f) \quad (7.40)$$

and

$$\hat{G}_{x_m y_m}(f) = G_{xy}(f) \quad (7.41)$$

because the noise is uncorrelated [ $G_{xv}(f) = 0$ ]. From Eqs. (7.40) and (7.41), we see that

$$\hat{H}_1(f) = H(f) \quad (7.42)$$

so that  $\hat{H}_1(f)$  provides an *unbiased estimate* of the true frequency response  $H(f)$ . An interesting result by Bendat and Piersol<sup>106</sup> is that  $H_1(f)$  is the *least-squares estimator* for

$$Y(f) = H(f)X(f) + V(f) \quad (7.43)$$

and thus provides an *optimum model* for Eq. (7.7) when output noise is present.

Figure 7.5 shows an example Bode plot for the roll-rate response to lateral stick ( $p/\delta_{\text{lat}}$ ; rad/s/%) of the XV-15 in hover with SCAS-on (a continuation of the analysis results of Fig. 7.3,  $T_{\text{win}} = 25$  s). The frequency response was estimated using the standard expression for  $\hat{H}_1(f)$  given in Eq. (7.37).

The use of Eq. (7.37) ensures that the frequency-response estimate is unbiased for all uncorrelated *output measurement noise* [ $v(t) \neq 0$  in Fig. 7.4], as long as the inputs are noise free. The assumption of noise-free input measurements is appropriate for most system-identification tests and is a standard implementation in most automated analysis tools, including CIFER®. It generally is a good assumption because typical input signals, such as the measurement of the deflection of pilot stick, actuators, and irreversible control-surface deflections, are largely free of disturbances and can be measured with considerable accuracy. On the other hand, there are many sources of noise at the output. Vehicle responses caused by atmospheric disturbances, secondary inputs, and the effect of nonlinearities are important sources of process noise and are reflected as contributions to the output measurement noise  $v(t)$ . Typical vehicle dynamic response measurements, such as angular-rate gyros, accelerometers, and aerodynamic sideslip and angle of attack, are subject to considerable contamination from mechanical, electrical, and aerodynamic disturbances and are key sources of output measurement noise  $v(t)$ . In summary, the assumption of noise at the output and noise-free input measurements is a very good one for most applications.

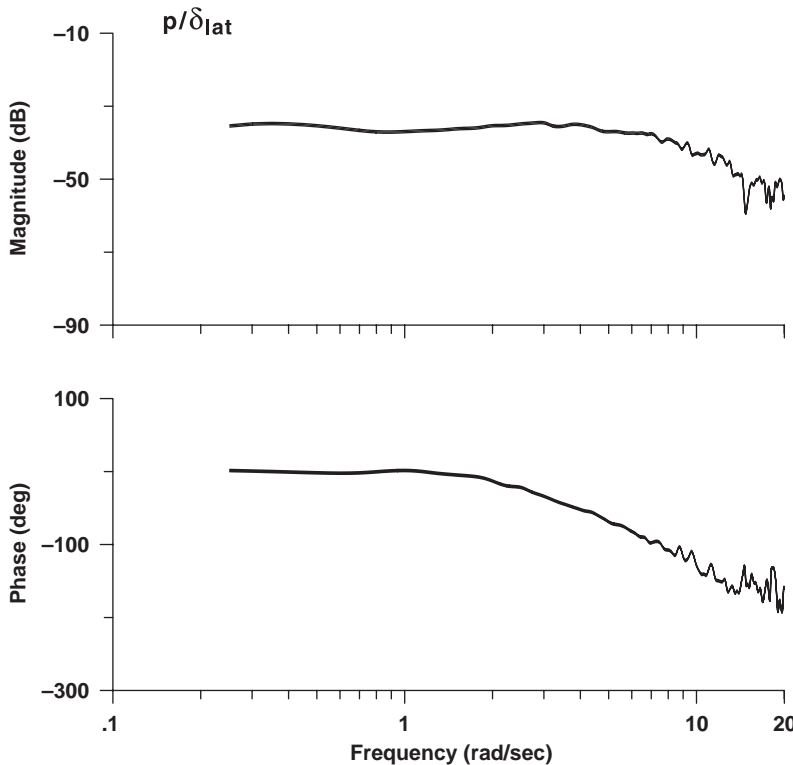


Fig. 7.5 Roll-rate response to lateral stick: SCAS on (XV-15, hover).

### 7.7.2 Effect of Input Noise on the $H_1(f)$ Estimate

The assumption of noise-free input made in the preceding section, though generally valid, is not necessarily true in every situation. In this section we will examine the effect of input noise on the  $H_1(f)$  frequency-response estimate. The output will initially be assumed to be noise free; then, in Sec. 7.7.3 we will extend the discussion to the case of noise being present in both input and output measurements.

Let us assume, then, that there is noise contamination to the input measurements only [ $u(t) \neq 0, v(t) = 0$ ], arising from, for example, electrical or structural disturbances. The input noise  $u(t)$  is assumed to be uncorrelated with the excitation input  $x(t)$ , so that

$$\hat{G}_{x_m y}(f) = G_{xy} \quad (7.44)$$

which shows that an unbiased estimate of the true cross spectrum (and therefore the frequency-response phase) is obtained. The autospectrum of the measured input signal is

$$\hat{G}_{x_m x_m}(f) = G_{xx}(f) + G_{uu}(f) \quad (7.45)$$

Thus the  $H_1(f)$  frequency response as estimated from the measurements will be

$$\hat{H}_1(f) = \frac{G_{xy}(f)}{G_{xx}(f) + G_{uu}(f)} \quad (7.46)$$

or

$$\hat{H}_1(f) = \frac{H(f)}{1 + G_{uu}(f)/G_{xx}(f)} \quad (7.47)$$

This result shows that the estimated magnitude response is biased with respect to the true response  $H(f)$ . We define the normalized bias error  $\epsilon_b$  as

$$\epsilon_b(f) = \frac{\hat{H}(f) - H(f)}{H(f)} \quad (7.48)$$

and substitute Eq. (7.47) to obtain

$$\epsilon_b = \frac{-\alpha_n(f)}{1 + \alpha_n(f)} \quad (7.49)$$

where we have defined the noise-to-signal (PSD) ratio of the input signal, following Bendat and Piersol,<sup>107</sup> as

$$\alpha_n(f) = \frac{G_{uu}(f)}{G_{xx}(f)} \quad (7.50)$$

This analysis shows that input measurement noise will result in an underestimate of the frequency-response magnitude [because  $\alpha_n(f) \geq 0$ ], but an unbiased estimate of the phase angle [Eq. (7.44)]. To ensure that the bias error in the estimate is as low as possible, the noise-to-signal ratio must be minimized. This is accomplished by a good choice of sensor placement and careful ground-based calibrations of the sensors. For the XV-15 flight data, the noise-to-signal ratio is about  $\alpha_n(f) = 1/40$  (Ref. 87), and the resulting bias error is very small ( $\epsilon_b = -0.024 = -2.4\%$ ), especially in comparison to the typical random errors ( $\epsilon_r$ , Sec. 7.9).

So far we have assumed that all measurement noise is uncorrelated with the true signals. Correlated measurement noise at the input or output, or both, is an additional cause of bias in the estimate and therefore must also be minimized. One such source of correlated output noise arises when the pilot or flight control introduces a feedback to counteract the effect of process noise (e.g., gusts). In this case, the excitation signal  $x$  will contain a component that is correlated with the gust. This will introduce a bias in the frequency-response estimate that is a function of the noise-to-excitation signal ratio, as discussed at length in Chapter 8. By conducting the flight tests in conditions of low winds and turbulence (Sec. 5.7), these bias errors can be minimized.

### 7.7.3 Alternate Forms for Frequency-Response Calculation

There are special applications of frequency-response testing where alternate forms for the frequency-response estimate are used. One such application is the identification of structural responses using ground-based rigs and shakers.<sup>116</sup> For frequencies near structural resonances, the measured excitation signal level is small and highly contaminated by noise, and the response signal is large, so that we can assume that noise exists in the *input measurement only*, with no output measurement noise [ $v(t) = 0$  in Fig. 7.4]. When there is no output measurement noise, an unbiased frequency-response estimate can be obtained using  $\hat{H}_2(f)$  of Eq. (7.38). However, Bendat and Piersol<sup>107</sup> caution against using this expression in all but certain special situations because output noise caused by measurements, secondary inputs, and nonlinearities will all result in a biased estimate when  $\hat{H}_2(f)$  is used. Fabunmi<sup>116</sup> also shows that the  $H_1(f)$  estimate is preferred to obtain an accurate response at antiresonances (where the signal-to-noise ratio of the response will be very small).

Rocklin et al.<sup>117</sup> point out as herein that the  $\hat{H}_1(f)$  and  $\hat{H}_2(f)$  forms [Eqs. (7.37) and (7.38), respectively] provide different estimates of frequency-response magnitude but the same estimate of phase. The conventional  $\hat{H}_1(f)$  estimate minimizes the error caused by noise at the output, but is susceptible to noise at the input, resulting in an underestimation of the true response  $H(f)$ , as seen from reference to Eq. (7.47). Conversely, the  $\hat{H}_2(f)$  estimate minimizes the error caused by noise at the input, but is susceptible to noise at the output, thus resulting in an overestimation of the true response. In the case where noise is present in both the input and output signals, Rocklin et al.<sup>117</sup> propose the *robust transfer-function estimate*  $\hat{H}_v(f)$ , which for the SISO case is simply the geometric mean of the  $\hat{H}_1(f)$  and  $\hat{H}_2(f)$  estimates.

Brenner et al.<sup>91</sup> compared the various frequency-response estimates in a flight-test study of the F/A-18 structural responses. In-flight excitation was achieved using a specially designed aerodynamic force generator system mounted at the wing tips. The excitation drive signal (i.e., torque or equivalent aerodynamic surface deflection) could not be measured directly; instead, a strain measurement was used as the input for the spectral analysis. This strain signal was an indirect measurement of the true excitation and was subject to noise arising from aeroelastic responses of the aircraft and excitation systems. The output signals were wing-tip mounted accelerometer measurements, which were subject to noise arising from vibration, electrical, and atmospheric disturbances. In this application, where both input and output measurements were subject to considerable noise, the  $\hat{H}_v(f)$  calculation provided improved estimates of the structural frequency response. Fabunmi<sup>116</sup> developed an algorithm based on a modification to the  $\hat{H}_v(f)$  estimate that demonstrates improved accuracy at both resonances and antiresonances for ground-based structural response testing.

### 7.7.4 Interpretation of Frequency Response When Nonlinear Effects Are Present: Describing Functions

In the context of nonlinear systems analysis, the  $H_1(f)$  frequency-response estimate is a classical *describing function*<sup>55</sup> because it determines that part of the output that can be linearly related to the input. More precisely, the result of

Eq. (7.37) is the equivalent linear system model that is optimum in the sense that it minimizes the mean square difference between the actual output signal and its approximation by the fundamental harmonic (first sinusoidal component of the Fourier series). Nonlinear effects in the input-to-output response that cannot be characterized as an equivalent linear function are associated with higher harmonics terms in the Fourier series expansion. These will appear as an effective noise remnant in the measured outputs and thus reduce the coherence, but they will not bias the frequency-response estimate. This is the same result as in Eq. (7.43) for the case of output measurement noise. Most of these remnants are largely filtered out by the low-pass nature of the aircraft dynamics.

The piloted sweep technique and the concatenation of repeat time-history records result in input amplitudes that are not constant over the frequency range. Therefore the resulting describing function is representative of the average input amplitude over the ensemble time history. Because the pilot inputs are typical of those experienced during normal flight operations, this approximation produces a satisfactory description of the vehicle in its normal operating environment. System-identification experience by the leading author, associated with many and varied flight-vehicle programs, has shown that the frequency responses extracted using these procedures and the resulting parametric models (transfer-functions and state-space representations) are highly accurate over a large range of maneuver amplitudes and deviations from the reference flight condition. This can be seen, for example, in the excellent prediction of XV-15 control response achieved by the identified models in cruise (Figs. 2.9 and 2.10) and hover conditions (Fig. 2.12).

## 7.8 Coherence Function

Another important product of the smooth spectral functions of Eqs. (7.30), (7.32), and (7.33) is the coherence function estimate  $\hat{\gamma}_{xy}^2$ , defined at each frequency  $f$  by

$$\hat{\gamma}_{xy}^2(f) = \frac{|\hat{G}_{xy}(f)|^2}{|\hat{G}_{xx}(f)||\hat{G}_{yy}(f)|} \quad (7.51)$$

The coherence function  $\gamma_{xy}^2$  can be interpreted physically as the fraction of the output spectrum  $G_{yy}$  that is linearly attributable to the input spectrum  $G_{xx}$  at frequency  $f$  (Ref. 106). The values of  $\gamma_{xy}^2$  will range between 0 and 1. If the process under investigation were perfectly linear, and all of the output spectrum were attributable to all of the input spectrum, the coherence would have the constant ideal value of 1. In practical applications, there are several reasons why the coherence function will always be less than 1:

1) Noise contamination in the measured output signal [ $v(t) \neq 0$  in Fig. 7.4] causes a reduction in coherence. Following Bendat and Piersol,<sup>107</sup> the coherence function can be expressed as

$$\gamma_{xy}^2(f) = \frac{1}{1 + \beta_n(f)} \quad (7.52)$$

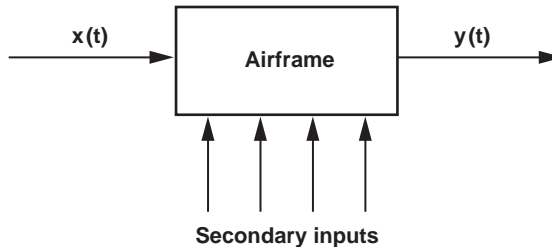


Fig. 7.6 Secondary inputs in single-input/single-output identification.

where we have defined the output noise-to-signal (PSD) ratio in a manner analogous to the input noise ratio of Eq. (7.50):

$$\beta_n(f) = \frac{G_{vv}(f)}{G_{yy}(f)} \quad (7.53)$$

2) There are nonlinearities in the input-to-output system that cannot be described by the frequency response  $H(f)$ , which is a linear (first harmonic) describing function relating the input spectrum to the output spectrum. Nonlinearities enter the analysis as a remnant component in the output noise  $v(t)$ . Once again, this lowers the coherence [Eq. (7.52)].

3) Process noise associated with unknown or unmeasured inputs, such as gusts or off-axis control activity (Fig. 7.6) that are not correlated to the measured input, is present. These *secondary inputs* pass through the system and can be considered as contributing an effective output noise component to  $v(t)$ , which is reflected in reduced coherence [Eq. (7.52)]. Associated with this reduced coherence will be *random error* or scatter in the frequency-response estimate (Sec. 7.9), which is a variability in the estimate about the true response. However, on average the frequency-response estimate of Eq. (7.37) tracks the true response, and so does not produce a *bias error*, which is an offset with respect to the true response.

The spectral quantities in the coherence calculation must be obtained using the method of windowing (Sec. 7.5.3). If only one window section is used ( $n_r = 1$ ), in which case there is no averaging, then the coherence calculation produces a degenerate (meaningless) result of  $\gamma_{xy}^2 \equiv 1$ , regardless of the presence of noise or nonlinearities (see also Ref. 107).

Following some basic rules of thumb, we can use the coherence function to effectively and rapidly assess the accuracy of the frequency-response identification. Generally speaking, as long as the coherence function satisfies the condition

*Guideline:*

$$\gamma_{xy}^2 \geq 0.6 \quad (7.54)$$

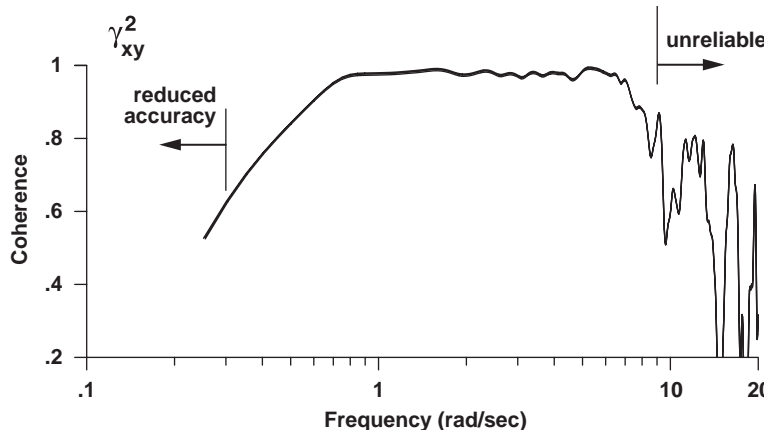


Fig. 7.7 Coherence function for roll-rate response identification: SCAS-on (XV-15, hover).

and is not oscillating, the frequency response will have acceptable accuracy. A rapid drop or oscillation in the coherence function for a particular range of frequencies indicates poor frequency-response identification accuracy in that region.

Figure 7.7 shows the coherence function corresponding to the  $p/\delta_{\text{lat}}$  frequency response of Fig. 7.5. For frequencies in the region of  $\omega > 8$  rad/s, the coherence function begins to oscillate dramatically, and so the frequency-response identification would be considered unreliable starting at that point, despite the fact that the coherence, though dropping, has not yet fallen below the rule of thumb that  $\gamma_{xy}^2 \geq 0.6$ . The poor coherence for frequencies above 8 rad/s reflects the drop in excitation and associated response, as can be seen in the input and output PSDs (Fig. 7.3). Figure 7.5 shows that rather than the expected smooth roll off in phase for a rigid-body-type behavior, the phase curve oscillates (an example of random error) starting at roughly the same frequency point ( $\omega > 8$  rad/s), confirming a loss of frequency-response identification accuracy. This relationship between a drop or oscillation in coherence and an accompanying oscillation in phase is commonly observed in a frequency range where there is a loss of adequate signal-to-noise ratio in the experimental data. There is a reduction in coherence for frequencies below about 0.7 rad/s, but for frequencies above 0.3 rad/s, the coherence value remains above the guideline and does not oscillate. Overall, the coherence function indicates that the frequency-response identification result can be considered reliable in the frequency range of 0.3–8 rad/s, as can also be seen in the smooth frequency-response function (Fig. 7.5).

## 7.9 Random Error in the Frequency-Response Estimate

In the preceding section, the coherence function has been shown to provide excellent qualitative insight into the reliability of the identified frequency response. A quantitative estimate of the expected normalized random error  $\varepsilon_r$  in

the magnitude of the frequency-response identification can be calculated at each frequency point<sup>107</sup> as follows:

$$\varepsilon_r = C_e \frac{[1 - \gamma_{xy}^2]^{1/2}}{|\gamma_{xy}| \sqrt{2n_d}} \quad (7.55)$$

where  $C_e$  is a constant to account for window overlap and  $n_d = T_{\text{rec}}/T_{\text{win}}$  represents the number of independent (i.e., nonoverlapping) time-history averages. The uncertainty in the phase estimate of the frequency response  $\Delta\hat{\phi}_{\text{rad}}$  is the same numerical value (in radians) as the normalized magnitude error:

$$\Delta\hat{\phi}_{\text{rad}} = \varepsilon_r \quad (7.56)$$

Window overlap, illustrated in Fig. 7.2, counteracts the increased variability introduced by the window edge tapering.<sup>106</sup> A detailed analysis showing the error reduction for increasing overlap fraction  $x_{\text{frac}}$  was developed by Nuttall and is explained in his highly insightful reports.<sup>109,110</sup> There is close agreement between the analytical results of Nuttall<sup>109</sup> and the numerical results of his colleague Carter.<sup>111</sup> A significant (26%) reduction in random error is achieved for a 50% window overlap ( $C_e = \sqrt{0.55}$ ), with only small additional improvements realized for increased overlap fractions. For an overlap fraction of 80%, Carter et al.'s results<sup>111</sup> reach an asymptotic improvement in random-error reduction (29% and a corresponding  $C_e = \sqrt{0.50}$ ), or about an additional 3% reduction compared to the 50%-overlap case.

The increased window overlap reduces random error but comes at a cost of a rapidly growing number of calculations [caused by increasing  $n_r$ , the number of overlapping window sections, in Eq. (7.31)]. However, the greatly improved computational capability of modern computers makes the use of larger overlap fractions feasible, especially for off-line data processing.<sup>89</sup> Numerical experiments using CIFER® have shown some benefit in random-error reduction for an overlap ratio of up to 80%, in agreement with the findings of Carter et al.<sup>111</sup> The improvements are most apparent for flight dynamics applications at low frequencies (e.g., 0.1–1 rad/s), which require larger windows and thus a small number of independent, nonoverlapping window sections  $n_d$ . Based on these results, the 80% overlap value is used in CIFER®.

It is easy to see from Eq. (7.55) that for the ideal case of  $\gamma_{xy}^2 = 1.0$  the random error would be eliminated ( $\varepsilon_r = 0$ ), and the frequency-response estimate would match perfectly the true frequency response of the tested system. However, for reasons discussed in the preceding section the coherence will never be unity for real-world applications of system identification.

With a knowledge of the key sources of coherence loss and their relationships to the noise-to-signal ratio [Eq. (7.52)] and random error [Eq. (7.55)], we can infer means of enhancing frequency-response identification accuracy. For example, flight tests should be conducted on days of minimum winds and turbulence (per Sec. 5.7, 5 kn or less, typical of conditions early in the morning at many test sites) to achieve the smallest possible noise-to-signal ratios and maximize coherence [Eq. (7.52)]. Repeat data records of frequency-sweep tests for a given axis

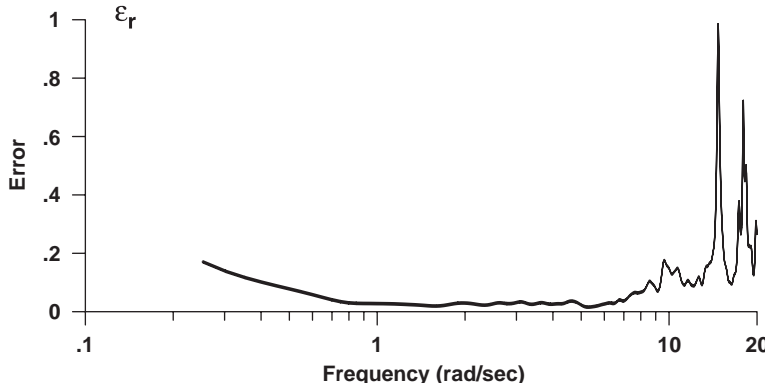


Fig. 7.8 Random-error function for roll-rate response identification: SCAS on (XV-15, hover).

(Sec. 5.7) should be concatenated to form a single linked record ( $T = T_F$ ) for analysis. This increases the number of independent time-history averages (now that  $n_d = T_F/T_{\text{win}}$ ), and therefore the random error is reduced, per Eq. (7.55). Shorter windows  $T_{\text{win}}$  also increase  $n_d$ , but compromise the identification at low frequency. If the minimum coherence is restricted per the guideline of Eq. (7.54) to  $\gamma_{xy}^2 \geq 0.60$ , we can ensure that  $\epsilon_r \leq 0.2$  (i.e., the random error will always be less than 20% error in magnitude and 11.5-deg error in phase, which is generally considered acceptable) by selecting  $n_d$  such that the following is true:

*Guideline:*

$$n_d \geq 5 \quad (7.57)$$

Consider the handling-qualities example discussed in Sec. 5.6, with a maximum period of interest of  $T_{\text{max}} = 12$  s. A typical window width would be twice that, or  $T_{\text{win}} = 24$  s. Suppose that the available flight database consists of two typical repeat frequency-sweep records of  $T_{\text{rec}} = 60 = 5T_{\text{max}}$  s each, for a total of  $T_F = 120$  s. This results in  $n_d = T_F/T_{\text{win}} = 5$  segments of data across two concatenated records, which achieves the preceding guideline. Setting a stricter requirement on the coherence of  $\gamma_{xy}^2 \geq 0.85$  results in  $\epsilon_r \leq 0.1$ , or errors in the frequency-response estimate that are less than 10% and 5.7 deg for the same  $n_d$ . These parameters are close to those of the XV-15 SCAS-on identification of roll-rate response to lateral stick (Fig. 7.5). The random-error function for this case is shown in Fig. 7.8. As expected, the random error remains less than 10% over the frequency range (0.4–9.4 rad/s), which corresponds closely to the frequency range of good coherence (Fig. 7.7), and also corresponds to the frequency range of good piloted excitation ( $G_{xx}$ , Fig. 7.3).

## 7.10 Window Size Selection and Tradeoffs

This section presents additional guidelines on window size selection and discusses the tradeoffs that are encountered as window size is varied.

### 7.10.1 Nominal Window Size Selection ( $T_{\text{win}}$ )

According to Eq. (7.34), the *theoretical minimum* frequency  $f_{\text{min}}$  that can be identified is the reciprocal of the selected window length  $T_{\text{win}}$ . In practical applications, test data are subject to the effects of measurement/process noise, nonlinearities, and secondary control inputs. Therefore, satisfactory coherence will generally be seen starting from frequencies that are about twice the theoretical minimum frequency, so that two periods of oscillation are captured in the window:

$$(f_{\text{min}})_{\text{effective}} \cong 2 \left( \frac{1}{T_{\text{win}}} \right) \quad (7.58)$$

We wish to achieve good coherence (good identification accuracy) starting at the longest period of interest  $T_{\text{max}}$ :

$$(f_{\text{min}})_{\text{effective}} = \frac{1}{T_{\text{max}}} \quad (7.59)$$

so a good choice of nominal window size is the following:

*Guideline:*

$$T_{\text{win}} = 2T_{\text{max}} \quad (7.60)$$

Using this guideline,  $T_{\text{win}} = 24$  s was selected for the handling-qualities application example ( $\omega_{\text{min}} = 0.5$  rad/s) presented in Sec. 7.9. As mentioned in Sec. 5.11, flight-mechanics applications might require accuracy to lower frequencies (e.g.,  $\omega_{\text{min}} = 0.35$  rad/s;  $f_{\text{min}} = 0.055$  Hz) resulting in a larger window size of  $T_{\text{win}} = 36$  s.

The guideline of Eq. (7.60) shows a dependency only on modal period (i.e., inverse dependency on modal frequency). More precisely, however, the required window length for accurate identification is inversely proportional to total modal damping  $\zeta\omega_n$ , as shown for example in the application to structural systems (Sec. 7.10.4). So, the accurate frequency-response identification of a lightly damped low-frequency mode might require a significantly larger window length. But, the guideline is a good starting point. The main effect of further increasing the window length can be seen in better identification of the effective damping ratio, with a more accurate determination of the peak magnitude value and rate of change in phase response near the low-frequency mode of interest. The modal frequency will be well determined using the preceding guidelines.

### 7.10.2 Maximum Window Size

Choosing larger windows will allow the accurate identification of the frequency response to lower frequencies. However, the window size cannot be greater than the individual record length  $T_{\text{rec}}$ , as discussed in Sec. 7.5. When multiple records of varying lengths are concatenated, the maximum window size is limited to the

shortest of the *individual record lengths* and not the overall concatenated record length  $T_F$ . Analogous to the padding-with-zeros caution (Sec. 7.5), linking short records together cannot provide information content for a period longer than the individual record length  $T_{\text{rec}}$ . For example, a single record of length  $T_{\text{rec}} = 10$  s has information content starting at a minimum frequency  $f_{\text{min}} = 1/10$  Hz. Linking together five repeat maneuvers to achieve  $T_F = 50$  s allows more averaging (i.e., larger  $n_d$ ) and thus reduced random error [Eq. (7.55)], but the information content in the linked record still has a minimum frequency (0.1 Hz) associated with the individual record length. Experience with flight data analyses indicates that maximum window size should usually be further limited to about 50% of the individual record length:

*Guideline:*

$$T_{\text{win}} \leq 0.5T_{\text{rec}} \quad (7.61)$$

This provides at least  $n_d = 2$  time-history segments for each individual record. The two relationships [Eqs. (7.58) and (7.61)] can be combined to yield

$$(f_{\text{min}})_{\text{effective}} \geq 4\left(\frac{1}{T_{\text{rec}}}\right) \quad (7.62)$$

Combining this with Eq. (7.59) yields

$$T_{\text{rec}} \geq 4T_{\text{max}} \quad (7.63)$$

which is satisfied by the rule of thumb for individual record lengths [Eq. (5.11)].

Finally, for acceptable levels of random error the recommended number of segments [ $n_d$ , in Eq. (7.57)] limits the maximum window size as a function of the *concatenated record length*  $T_F$ :

*Guideline:*

$$T_{\text{win}} \leq \left(\frac{1}{5}\right)T_F \quad (7.64)$$

In summary, the maximum window size is determined by Eq. (7.61) or Eq. (7.64), whichever is lesser. By linking two or three of the recommended individual records of length  $T_{\text{rec}}$  to make up the total concatenated record length, we can easily ensure that these guidelines are achieved.

The use of these guidelines is now demonstrated based on the XV-15 flight-test databases. The starting period of the all of the sweeps is about  $T_{\text{max}} = 20$  s, and the individual record lengths are about  $T_{\text{rec}} = 95$  s. By linking two repeat sweeps, the concatenated record length is  $T_F = 190$  s. A nominal window length to achieve the broadest bandwidth of flight dynamics identification is  $T_{\text{win}} = 40$  s, which is twice the starting period of excitation [Eq. (7.60)]. This satisfies the maximum window length guideline [Eq. (7.61)] for a single record ( $n_d = 2.4$ ) and nearly meets the window requirement [Eq. (7.64)] for the linked

## 172 AIRCRAFT AND ROTORCRAFT SYSTEM IDENTIFICATION

records ( $n_d = 4.8$ ). For handling-qualities and flight-control analysis, where the emphasis is on higher accuracy for short-term response identification, a smaller window  $T_{\text{win}} = 20$  s yields twice as many averages ( $n_d = 9.5$ ), thereby improving accuracy while sacrificing some of the identification at the lowest frequencies.

The various rules of thumb discussed in this chapter for the relationships between the maximum window sizes, individual record lengths, and concatenated record lengths are all automatically checked within the CIFER® graphical user interface (GUI) for the FRESPID program. The user is alerted if one or more of the guidelines are not met.

### 7.10.3 Minimum Window Size

A typical choice of window size would provide at least a decade of data bandwidth between the minimum effective frequency [Eq. (7.58)] and the maximum frequency of interest  $\omega_{\text{max}}$ . Based on these considerations, the minimum window size should be at least the following:

*Guideline:*

$$T_{\text{win}} \geq 20 \frac{2\pi}{\omega_{\text{max}}} \quad (7.65)$$

### 7.10.4 Window Size Requirements for Structural Response Identification

System identification of structural system responses seeks to extract accurate estimates of the damping ratio  $\zeta$  and the undamped natural frequency  $\omega_n$  for each critical mode from frequency-sweep tests. Excitation inputs can be mass shakers for ground tests, aerodynamic flapperons for fixed-wing aircraft, and high-frequency small-amplitude swashplate inputs for rotorcraft. The response variables are generally structural strains as measured by strain gauges or wing-tip accelerometers (e.g., Acree and Tischler<sup>87</sup>).

Modal damping ratios and frequencies are determined from the fit of a second-order transfer-function model to the extracted frequency response at each mode. Nominal damping ratios for structural modes are small (e.g.,  $0.02 < \zeta < 0.05$ ). For some flight and loading conditions, this might leave only a small margin before flutter occurs ( $\zeta \rightarrow 0$ ). So accurate tracking of these modal estimates with flight conditions can be of the utmost importance for flight vehicles, thus imposing a requirement for small bias errors in the identified frequency response near each modal peak  $\omega_n$ .

Bias errors in the frequency-response estimate are introduced because of the finite resolution of the FFT calculation [ $\Delta f$ , Eq. (7.34)]. The normalized bias error is determined<sup>89</sup> by

$$\epsilon_b = \frac{2}{3} \left( \frac{B_e}{B_r} \right)^2 \quad (7.66)$$

where  $B_e \equiv \Delta f$ . For the small damping ratios typical of a structural response, the half-power bandwidth  $B_r$  can be estimated<sup>106</sup> from the resonance peak

frequency  $f_r$  by

$$B_r \equiv 2\zeta f_r = \frac{\zeta \omega_n}{\pi} \quad (7.67)$$

Referring to Eq. (7.66), if we wish to limit the normalized error to 5% ( $\varepsilon_b = 0.05$ ), the required resolution is

$$\frac{B_e}{B_r} = \frac{1}{3.65} \quad (7.68)$$

For a standard FFT, this indicates fewer than four data points over the bandwidth of concern, which would seem to be too coarse.

Young<sup>76</sup> suggests a finer resolution of

$$\frac{B_e}{B_r} = \frac{1}{7.0} \quad (7.69)$$

Combining Eqs. (7.69) and (7.67),

$$B_e = \frac{\zeta \omega_n}{7\pi} \quad (7.70)$$

from which we finally obtain the required window size,  $T_{\text{win}} = 1/B_e$ , and the restriction on minimum window size of

$$T_{\text{win}} \geq \frac{7\pi}{\zeta \omega_n} \quad (7.71)$$

This should be a conservative result for the chirp z-transform used in CIFER®, which is capable of a much greater frequency resolution for the same window size  $T_{\text{win}}$  than a standard FFT, as discussed in Sec. 7.5.

The influence of window size selection for structural response identification is clearly seen in the results of Fig. 7.9. System-identification tests were conducted to determine the structural modes of a rotor test stand used in wind-tunnel tests. A frequency-sweep excitation was applied using a heavy hydraulic shaker mounted on top of the test stand. The results of the analysis using three window sizes of 10, 5, and 2 s are shown in Fig. 7.9.

The coherence functions show that the large window produces good results at low frequencies but very noisy results at high frequencies. The small window, which provides a much larger number of averages  $n_d$ , greatly attenuates the random error and associated fluctuations and is preferable at higher frequencies. Referring to the results for the second structural peak at  $\omega_n = 55$  rad/s, it can be seen that the 5-s and 10-s windows produce the same magnitude and phase results. For the 2-s window, significant bias errors in the estimated response characteristics are seen. These results indicate that the 5-s window can be considered as the minimum acceptable window size for identification of the mode at 55 rad/s.

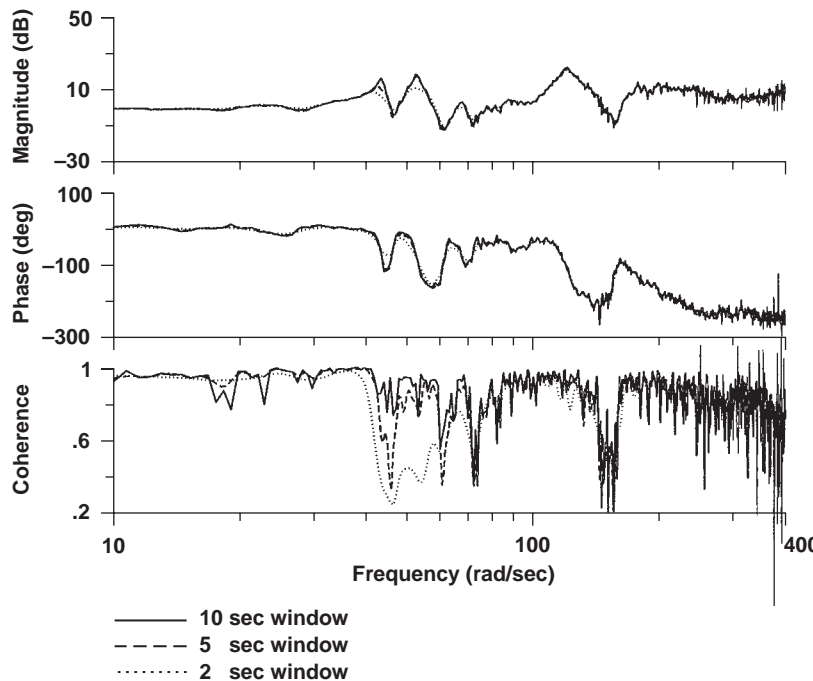


Fig. 7.9 Structural system identification of test stand using three window sizes.

Assuming a typical structural damping ratio of  $\zeta = 0.04$ , we arrive at the following guideline for structural system identification:

*Guideline:*

$$T_{\text{win}} \geq \frac{11}{\zeta \omega_n} \quad (7.72)$$

which is nearly the same as the first (coarser) guideline in Eq. (7.68). This confirms that the resolution bias estimates for the standard FFT are somewhat conservative when applied to the CZT. In the case of identifying multiple structural modes with a single spectral window, the guideline [Eq. (7.72)] should be applied to the lowest-frequency mode of interest. As can be seen in Fig. 7.9 and in accordance with Eq. (7.66), the bias errors are reduced for each increasing modal frequency. So if the resolution is satisfactory for the lowest-frequency mode, the errors will be even smaller for each higher-frequency mode.

By combining the window length requirement of Eq. (7.72) and the associated record length requirement of Eq. (7.61), we obtain the single sweep record length guideline in terms of the minimum structural mode:

*Guideline:*

$$T_{\text{rec}} \geq \frac{22}{\zeta \omega_n} \quad (7.73)$$

and the concatenated record length requirement based on Eq. (7.64) and Eq. (7.72):

*Guideline:*

$$T_F \geq \frac{55}{\zeta \omega_n} \quad (7.74)$$

Structural response tests of the F/A-18<sup>91</sup> sought to determine modal characteristics beginning with the symmetric wing bending mode (5.72 Hz). To obtain accurate identification of the symmetric wing bending mode for conditions close to the flutter boundary (e.g.,  $\zeta = 0.02$ ), the required sweep duration and concatenated record lengths are obtained from Eqs. (7.73) and (7.74) as  $T_{\text{win}} \geq 30.6$  s and  $T_F \geq 76.5$  s, respectively. The flight-test study evaluated sweep durations of 15, 30, and 60 s, as well as the concatenation of repeated 30-s sweeps. The identification results were improved when the sweep duration was increased from 15 s to 30 s, but showed little advantage for longer records. Also, the concatenation of repeated 30-s records provided improved results compared to single, longer sweeps. The flight-test results are seen to be fully consistent with the guidelines recommend herein.

### 7.10.5 Window Selection Tradeoffs

Increasing the window size lowers the effective minimum frequency of identification, thereby yielding data at lower frequencies of interest. However, the use of larger windows reduces the number of time-history averages  $n_d$  and thereby increases the random error  $\epsilon_r$ . This is especially problematic at the higher frequencies where the noise-to-signal ratio is greater, resulting in low coherence and thus higher random error [Eq. (7.55)]. Increased random error is usually manifested by an oscillation in the magnitude and phase curves at higher frequencies, as seen, for example, in Fig. 7.5. Adopting larger windows generally improves the low-frequency identification but degrades the accuracy of the high-frequency identification. Choosing smaller windows will result in the opposite tradeoff. Thus, in conventional single-window methods of spectral analysis a compromise is made to balance the requirements for satisfactory low- and high-frequency identification quality. Manual optimization of window size can involve a tremendous amount of iterative tuning, which contributes to a perception by some that frequency-domain identification methods are more an art than a science.

Multiwindow optimization, discussed in Chapter 9, is a key and unique innovation in CIFER<sup>®</sup> that provides a much more flexible alternative to the single-window compromise already discussed. Up to five window sizes can be selected, ranging from small windows (for accurate identification at higher frequencies) to large windows (for accurate identification at lower frequencies). The individual window results are then automatically merged using a numerical optimization procedure to give a single, highly accurate frequency response (i.e., high coherence, low random error) over a very broad frequency range.

## 7.11 Frequency-Response Identification in CIFER<sup>®</sup> Using FRESPID

Figure 7.10 shows a flowchart summarizing the computational and data-handling procedures carried out by the FRESPID function of CIFER<sup>®</sup> to perform

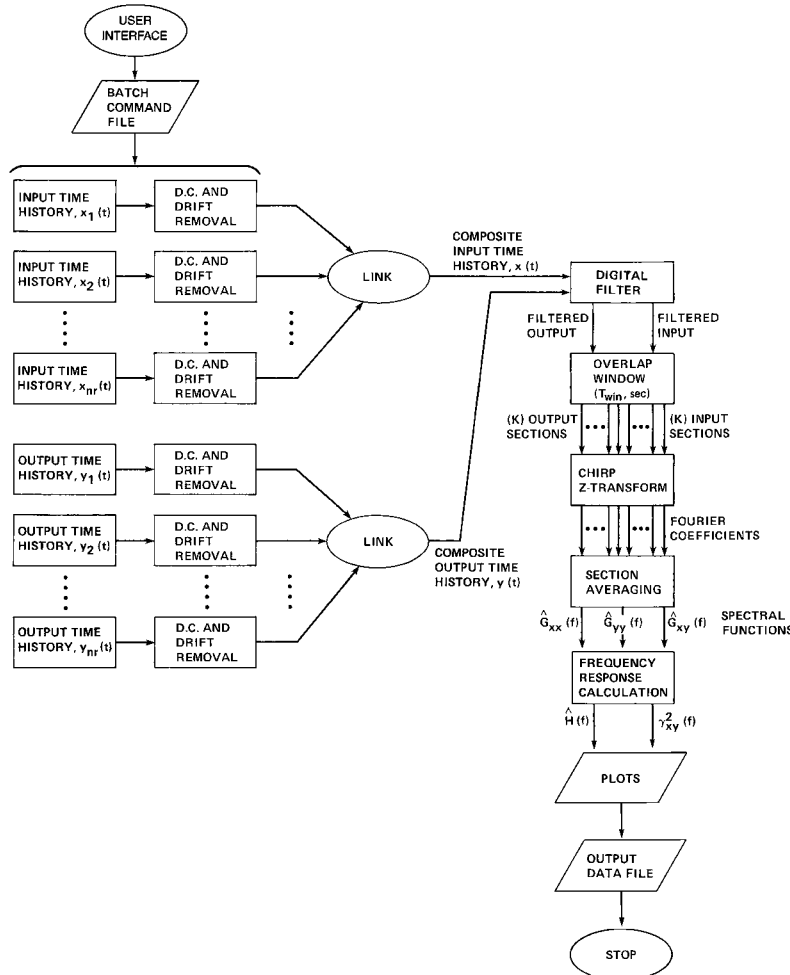


Fig. 7.10 Flowchart of computational procedures performed by the FRESPID program.

frequency-response identification. The user specifies the individual records to be concatenated and processed into frequency-domain data. FRESPID determines and removes the average value and linear drift from each individual record and then concatenates these perturbation time histories into a single linked record with length  $T_F$ . The concatenated input and output time histories are then digitally filtered to eliminate potential aliasing of high-frequency noise by the chirp z-transform. Digital filtering is also used as a precursor to data decimation, which improves the computational speed of the CZT.

Next, the linked records are segmented and weighted using the overlapped windowing method (Sec. 7.5.3) for the (first) window size specified by the user.

These overlapped windows of data are transformed into the frequency domain, using the chirp z-algorithm, and the resulting rough spectral functions are averaged to obtain the smooth spectra. Finally, the frequency-response and associated coherence functions are obtained for the given window size. This process is repeated for each of the user-selected window sizes. Finally, at the end of the processing the software generates plots of the data and stores the frequency-domain data in a relational database.

## 7.12 Summary of Guidelines for Frequency-Response Identification

The recommended approach for vehicle dynamics-response identification includes the following key guidelines:

1) Identify the angular rate responses (e.g.,  $p/\delta$ ), and apply a  $1/s$  correction in the frequency domain to easily calculate the associated attitude responses:  $\phi/\delta = (1/s)(p/\delta)$ ,  $s \rightarrow j\omega$ . (There is a frequency-response arithmetic function in CIFER® that automates this correction.) This amounts to a rotation of the  $\phi/\delta$  frequency-response plot about the  $\omega = 1$  rad/s point. Similarly, for the translational responses it is preferable to identify the response  $u/\delta$  and calculate the speed response:  $u/\delta = (1/s)(\dot{u}/\delta)$ . The reason to do this is that for test data analysis the higher-derivative measurements (angular rates and translational accelerations) generally have better signal-to-noise content over a wider frequency range than do the attitude and speed measurements.

2) Always remove the mean and drift prior to performing the frequency-response calculations (This is the default selection in CIFER®.)

3) Make appropriate selections of conditioning parameters: a) for digital filters, use  $\omega_f = 5\omega_{\max}$ ; and b) to maximize data-rate decimation for increased computational speed, use  $\omega_s = 5\omega_f = 25\omega_{\max}$ .

4) Select a window size  $T_{\text{win}}$  that is about twice the maximum period of interest ( $T_{\text{win}} = 2T_{\max}$ ), and evaluate all of the sweeps individually to select the records with satisfactory coherence.

5) Pick out the best sweeps, based on coherence, and concatenate them together. The total linked record length  $T_F$  should ensure  $n_d \geq 5$  for acceptable random error in the frequency-response estimate. Remember that overall frequency-response accuracy can never be improved by adding in bad data (i.e., data with poor coherence), even if doing so increases the number of averages  $n_d$ .

## 7.13 Pendulum Example

In this section, the frequency-response identification concepts are demonstrated using the pendulum example problem of Sec. 3.1. The time-history data are those obtained for the 180-s record sweep obtained in **Problems 5.3–5.5**. The angular variations of the pendulum for this case are limited to  $\pm 10$  deg, which are well within the linear range ( $\sin \theta_{\text{rad}} \approx \theta_{\text{rad}}$ ), so that good agreement with the ideal linearized model [Eq. (3.7)] can be expected. A nominal window of  $T_{\text{win}} = 15$  s is selected for the identification. Before proceeding, we will check that the various guidelines are satisfied:

1) The frequency range of interest for this example is from  $0.3\omega_n$  to  $3.0\omega_n$ , or  $0.9$ – $9.0$  rad/s [ $\omega_n = 3$  rad/s, Eq. (3.7)]. The dynamics in this range are well excited by the sweep (0.3–12 rad/s).

2) The starting period of the sweep  $T_{\max} = 2\pi/0.3 = 21$  s is compatible with the record length ( $T_{\text{rec}} = 180$  s), per the guideline of Eq. (5.11).

3) We select a nominal window length of  $T_{\text{win}} = 15$  s to provide a minimum frequency of identification of  $\omega_{\min} = 2\pi/15 = 0.42$  rad/s. This is satisfactory for the frequency of interest for our pendulum case, but the minimum effective frequency for this window as obtained from Eq. (7.58) is 0.84 rad/s, which is somewhat above the starting frequency of the sweep. The  $T_{\text{win}} = 15$  s window provides  $n_d = 180/15 = 12$  averages, thereby amply satisfying the guideline of Eq. (7.57).

The identification results for the stable pendulum response  $\theta/\bar{M}_{\text{ext}}$  are presented in Fig. 7.11, as obtained from CIFER®. The frequency range of the identification is 0.42–12 rad/s. The lower limit is determined by  $\omega_{\min}$ , and the upper limit is user selected (for the CZT) to cover the frequency range of interest and corresponds to the maximum frequency of the autosweep. The autosweep (Sec. 5.11) provides a uniform excitation with no holes, as can be seen from the input PSD  $G_{xx}$ . The output PSD  $G_{yy}$  rolls off beyond the natural frequency of the pendulum dynamics ( $\omega_n = 3$  rad/s). The magnitude curves show the expected characteristics, with a peak at the natural frequency and a –20-dB/decade roll off thereafter. The phase curve has a corresponding roll off to –180 deg. The coherence function shows excellent identification accuracy, exceeding  $\gamma_{xy}^2 = 0.90$  for all frequencies. The associated random error is less than 4%, again indicating excellent identification accuracy.

Figure 7.12 shows perfect agreement between the identified frequency response obtained from the nonlinear simulation and the ideal (linearized) transfer-function model (3.7), as expected. These results verify the SIMULINK implementation of the pendulum simulation model, the autosweep testing method, and the identification procedures presented thus far for the application to known (and simple) dynamics.

## 7.14 Applications and Examples

The remainder of this chapter presents typical examples of flight dynamics and controls analyses of air vehicles using power-spectral density and frequency-response methods that build on the concepts presented in the preceding sections.

### 7.14.1 Spectral Analysis of Time-History Signals

Spectral analysis of time-history signals is a key application of frequency-domain identification, providing valuable insight into the dominant frequency components in a signal. For example, as illustrated earlier, the input autospectrum of the aerodynamic control surface (e.g.,  $G_{\delta_a \delta_a}$  for aileron) provides information about the frequency distribution and bandwidth of the dynamic excitation, whereas the output autospectrum reveals the frequency distribution and bandwidth of the measured response and the contribution of noise sources to the measured signal content.

The integral of the input autospectrum  $G_{xx}$  over the entire range of frequencies provides the mean square of the time-domain vibration signal  $x_n$  (Ref. 106):

$$\sigma_x^2 = \int_0^\infty G_{xx}(f) df = \frac{1}{N-1} \sum_{n=1}^N (x_n - x_{\text{ave}})^2 \quad (7.75)$$

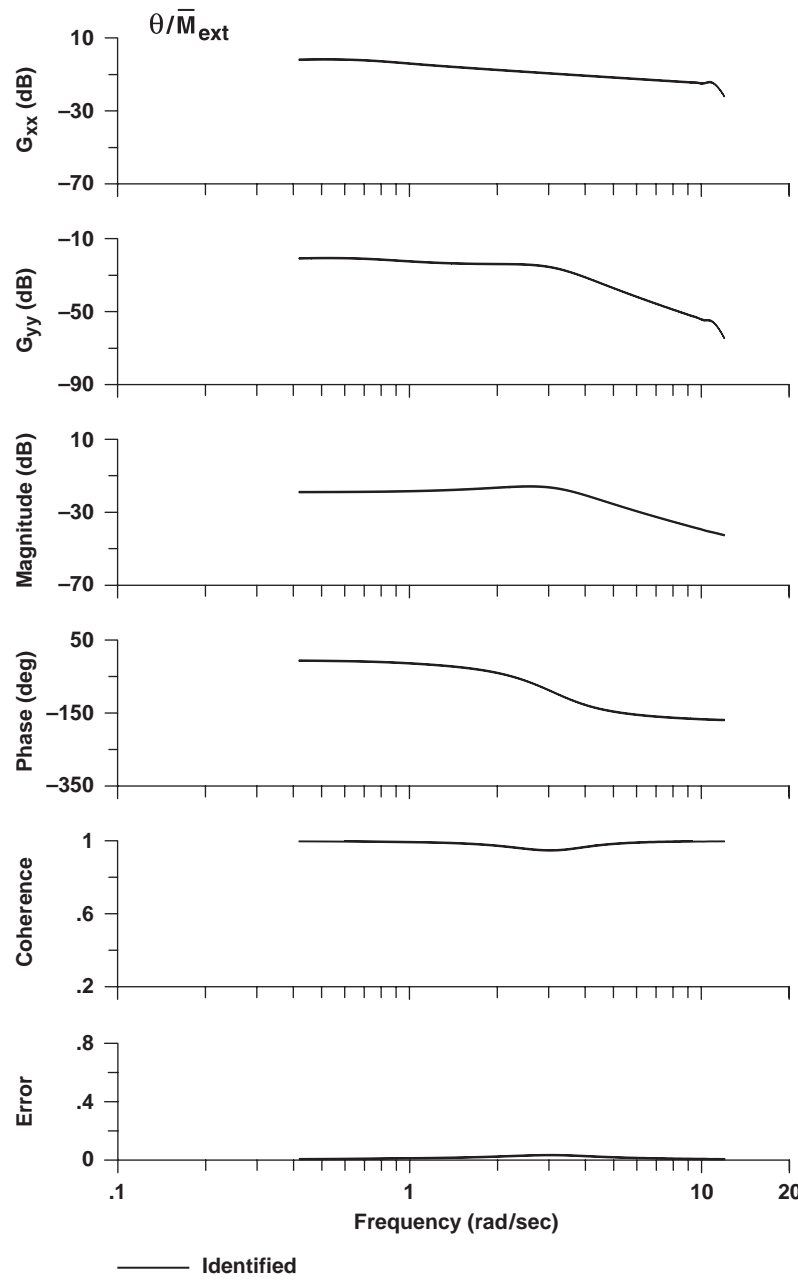


Fig. 7.11 Pendulum example identification.

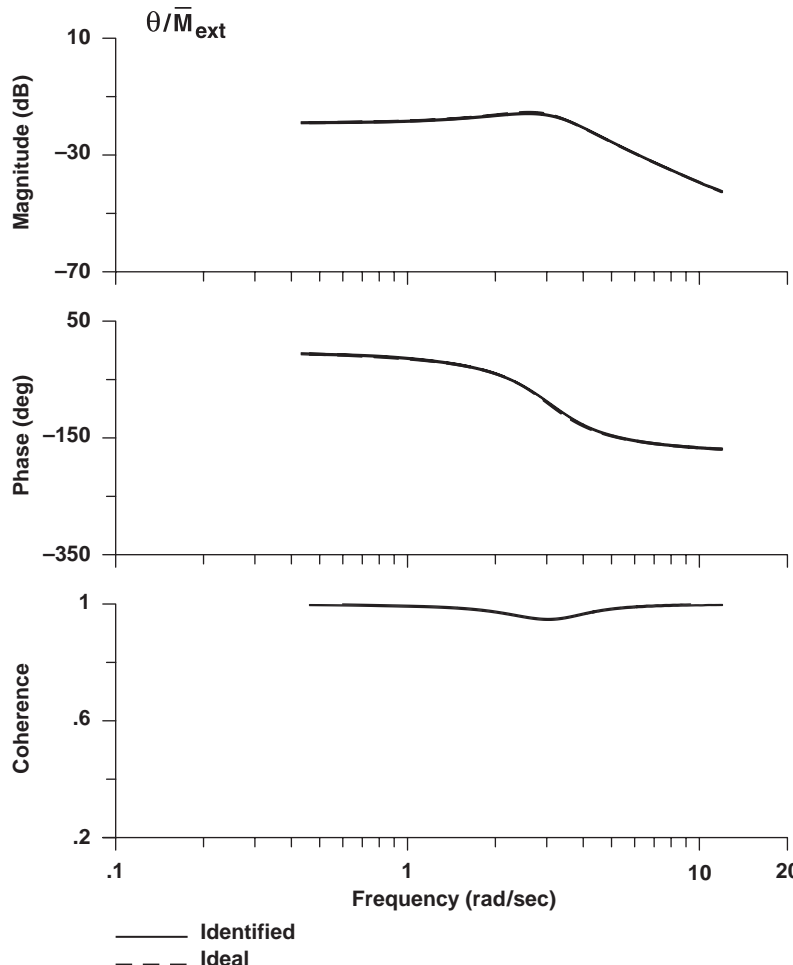


Fig. 7.12 Comparison between identified and ideal frequency responses (pendulum).

By calculating the integral of the input autospectrum  $G_{xx}$  over the frequency range  $f_1$  to  $f_2$ , we obtain the mean square of the time signal  $x_n$  about its mean value within this frequency band:

$$\sigma_x^2(f_1, f_2) = \int_{f_1}^{f_2} G_{xx} \, df \quad (7.76)$$

Such an analysis of the autospectrum can isolate the vibration levels associated with individual structural modes.

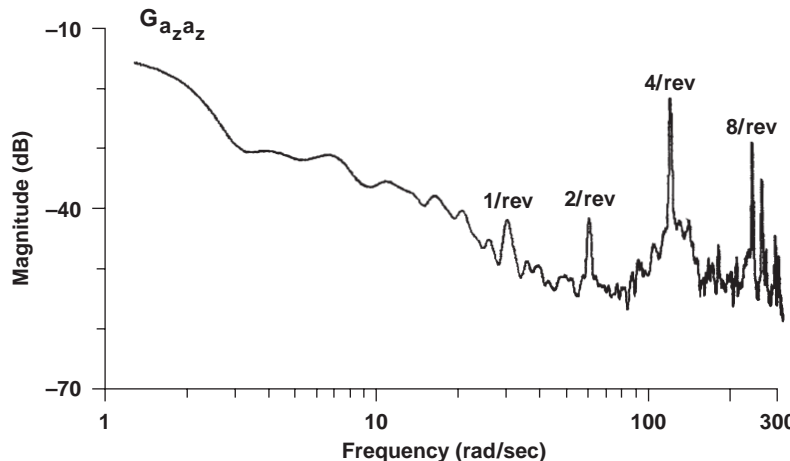


Fig. 7.13 AH-64 vertical vibration autospectrum (130 kn).

In an example of this analysis method, Fig. 7.13 shows the vertical acceleration autospectrum  $G_{a_z a_z}$  of the AH-64 helicopter at a flight condition of 130 kn. The four peaks in the autospectrum plot are dominant vibration components in the signal and occur at integer multiples of the rotor revolution frequency  $\Omega$ , given in radians/second:  $\Omega$ ,  $2\Omega$ ,  $4\Omega$ , and  $8\Omega$ . Denoting the time interval for one rotor revolution as “rev” leads to the common expression for integer multiples of the rotational frequency in hertz as 1/rev, 2/rev, 4/rev, and 8/rev, where  $1/\text{rev} \equiv \Omega/(2\pi)$ . The dominant frequency corresponds to the number of blades  $n_b$ , or 4/rev for a four-bladed helicopter such as the AH-64. For the AH-64, the rotational frequency is  $\Omega = 30.16 \text{ rad/s}$  or  $1/\text{rev} = 4.8 \text{ Hz}$ . The CIFER® rms utility is used to perform the spectral integration of Eq. (7.76) between two frequencies that bracket the 4.8-Hz peak. In this case, we have selected the frequency range of 25–35 rad/s. The resulting rms for 1/rev vibration is 0.00856 g, as shown in Table 7.1. The rms vibration for the 2/rev, 4/rev, and 8/rev peaks are also listed in Table 7.1. As expected, the dominant vibration component is associated with the

Table 7.1 AH-64 vibration analysis (130 kn)

/rev	Hz	$\Omega_1 - \Omega_2$ , rad/s	$\sigma$ , g	Typical limit, g
1	4.8	25–35	0.00856	0.0234
2	9.6	50–80	0.00932	0.0469
4	19.2	100–170	0.0705	0.0937
8	38.4	220–260	0.0316	0.1875
Total	—	25–260	0.0796	—

4/rev peak ( $\sigma_{a_z a_z} = 0.0705 \text{ g}$ ). The total (i.e., overall) rms of the vibration signal is determined by integrating over the entire frequency range ( $\sigma_{\text{tot}} = 0.0796 \text{ g}$ ), which matches the time-domain result using Eq. (7.75).

Maintenance specifications on helicopter rotor tracking and vibration limits are typically defined in terms of aircraft velocities at the rotor harmonic frequencies in units of inches/second or ips. The associated acceleration  $n_z$ , expressed in terms of  $g$ , is calculated as

$$n_z = \text{ips} \cdot (1/12) \cdot 2\pi f \cdot (1/g) \quad (7.77)$$

A typical limit on vertical vibrations is 0.3 ips for forward-flight conditions. The associated acceleration limits  $g$  at each rotor harmonic are listed in Table 7.1. As can be seen, the measured vibrations fall well within these limits for the 130-kn test condition.

### 7.14.2 Pilot Cutoff Frequency Determination

This next application shows a spectral analysis method for determining the pilot operating frequency or *cutoff frequency*  $\omega_{\text{co}}$ , a good estimate of the pilot crossover frequency  $\omega_c$  for pilot-in-the-loop flying tasks.

The block diagram in Fig. 7.14 represents a simplified representation of the closed-loop pilot-vehicle system, in which the pilot attempts to fly a commanded pitch profile  $\theta_c$ . The pilot senses the error  $\theta_e$  between the current pitch of the aircraft  $\theta$  and the commanded pitch  $\theta_c$  and applies a proportional correction to the pitch stick  $\delta$ . The aircraft response is denoted  $Y_c$ . Manual control studies<sup>118</sup> show that the pilot will adopt a compensation strategy  $Y_p$  over a broad frequency range such that

$$Y_p Y_c = \omega_c \frac{e^{-\tau s}}{s} \quad (7.78)$$

where  $\omega_c$  is the pilot's crossover frequency, defined as the frequency at which the gain of the product  $Y_p Y_c = 1$  ( $= 0 \text{ dB}$ ) is the pilot's fundamental frequency of closed-loop regulation.

The rms of the stick input signal  $\delta$  for the frequency range of  $0-\omega_1$  is defined as  $\sigma_1$ . Applying Eq. (7.76), we have

$$(\sigma_1)^2 = \frac{1}{2\pi} \int_0^{\omega_1} G_{\delta\delta} \text{ d}\omega \quad (7.79)$$

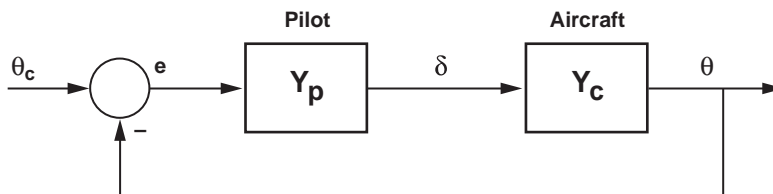


Fig. 7.14 Block diagram for pilot-in-the-loop analysis.

The total stick mean square is determined from Eq. (7.75):

$$(\sigma_{\text{tot}})^2 = \frac{1}{2\pi} \int_0^{\infty} G_{\delta\delta} d\omega \quad (7.80)$$

Next we define the *pilot cutoff frequency*  $\omega_{\text{co}}$  as the half-power frequency<sup>113</sup>; that is,  $\omega_{\text{co}}$  is the frequency  $\omega_1$  such that

$$\left(\frac{\sigma_1}{\sigma_{\text{tot}}}\right)^2 = 0.5 \quad (7.81)$$

or

$$\frac{\sigma_1}{\sigma_{\text{tot}}} = \sqrt{0.5} = 0.7071 \quad (7.82)$$

Subject to the manual control theory result of Eq. (7.78), the pilot cutoff frequency as obtained from the spectral analysis of the cockpit control input  $\delta$  is also a good estimate of the pilot/vehicle broken-loop gain crossover frequency  $\omega_c$  of Eq. (7.78). This analytical result has also been confirmed in analyses of flight data by Anderson and Klyde.<sup>119</sup>

Atencio<sup>120</sup> conducted a detailed fidelity assessment study of the Ames Vertical Motion Simulator vs flight for the UH-60 helicopter based on common flying tasks. The study used the Sikorsky General Helicopter flight-dynamics simulation program (GENHEL), a blade-element math model, which represents accurately the UH-60 aircraft dynamics.<sup>85</sup> Every effort was also made to set up the task and visual representation in the simulator to duplicate actual flight cueing as closely as possible. The test pilots gave a subjective report that the simulator environment was in fact a very good representation of the flight environment of the UH-60. The cutoff frequencies for the simulation and flight test were determined and compared to make a quantitative assessment of pilot cueing fidelity.

Figure 7.15 plots the ratio  $\sigma_1/\sigma_{\text{tot}}$  vs  $\omega$  for simulation and flight for one of the evaluation tasks. The pilot cutoff frequency  $\omega_{\text{co}}$  is determined by reading off the value of frequency corresponding to  $\sigma_1/\sigma_{\text{tot}} = 0.707$ . The pilot cutoff frequency is approximately  $\omega_{\text{co}} = 2$  rad/s, which is a representative value of piloted crossover frequency.<sup>118</sup> The cutoff frequency is essentially the same for both the flight-test and simulation data, thereby indicating that the pilot operating frequency is the same in both flight and simulation environments.

Even when the simulation math model is accurate, as in the present case, the motion or visual cues introduce spurious dynamics that can subtly alter the pilot's perception of the task and thus cause a change in the operating frequency. In this case, the cutoff frequency agreement confirms the excellent simulation fidelity of the UH-60 VMS experiment. Additional examples showing the use of the pilot cutoff frequency in interpreting piloting comparisons between simulator and flight studies are presented by Blanken and Pausder<sup>121</sup> and Lusardi et al.<sup>122</sup>

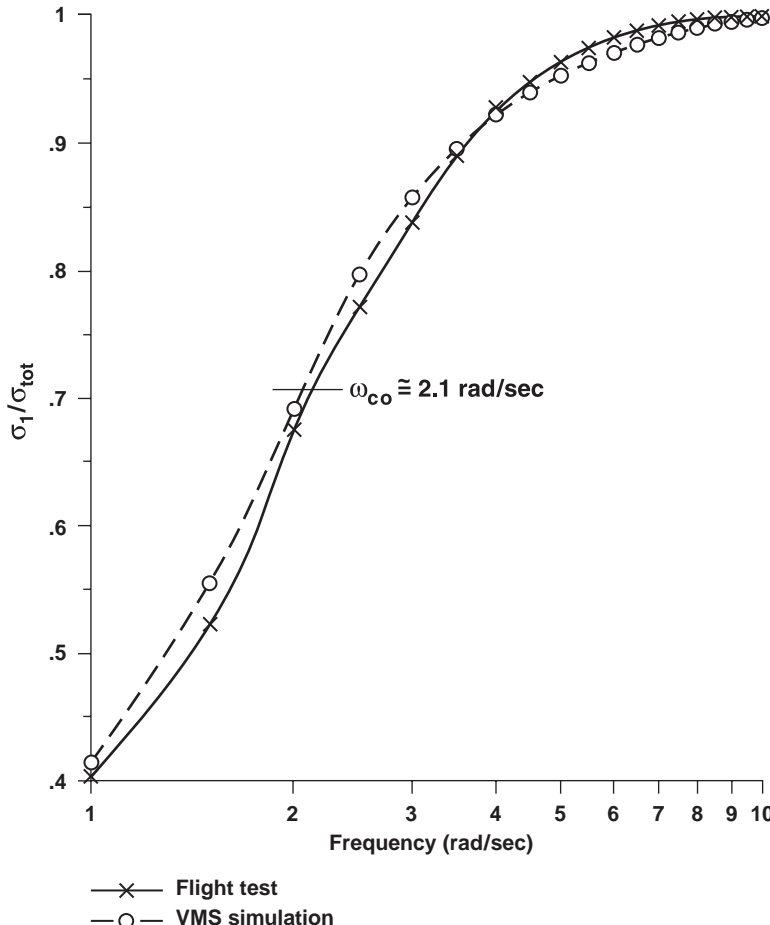


Fig. 7.15 Pilot control activity: simulation vs flight (UH-60, hover).

### 7.14.3 Handling-Qualities Specification Compliance

A key application of frequency-response identification methods to aircraft is for checking compliance of the closed-loop dynamic response with modern frequency-domain handling-qualities criteria. The fixed-wing<sup>5</sup> and rotary-wing<sup>4</sup> design standards give acceptable values for the two important parameters considered herein: bandwidth  $\omega_{\text{BW}}$  and phase delay  $\tau_p$ . These parameters are determined from the on-axis attitude responses to piloted control inputs (e.g.,  $\theta/\delta_{\text{lon}}$ ,  $\phi/\delta_{\text{lat}}$ ,  $\psi/\delta_{\text{ped}}$ ). As discussed in Sec. 7.12, the identification is best conducted using the rate responses (e.g.,  $q/\delta_{\text{lon}}$ ), and then a  $1/s$  correction is applied to the data in the frequency domain to give the needed attitude response. A typical result for the pitch response of the OH-58D helicopter (see photo in Fig. 11.12) is shown in Fig. 7.16. Detailed system-identification results for this helicopter are presented by Ham et al.<sup>123</sup>

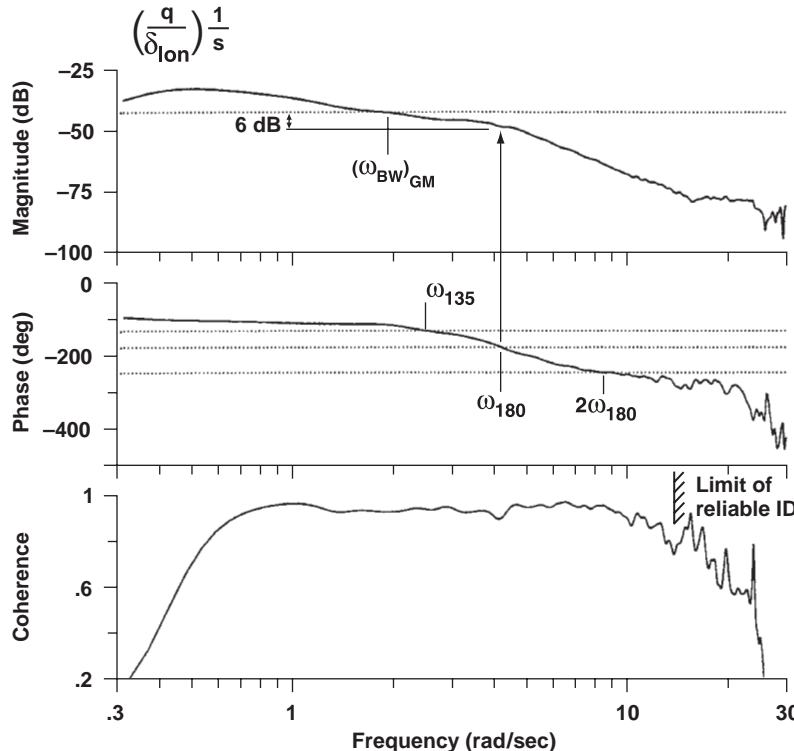


Fig. 7.16 OH-58D pitch response in hover (SCAS-off).

An examination of the coherence curve indicates that the identification accuracy is quite good for frequencies between 0.5 and 12 rad/s (that is, up to 2 Hz), which was the frequency at which the pilot was instructed to terminate the manual sweep. The determination of the bandwidth and phase-delay metrics has specific definitions for handling-qualities analysis as shown in the figure. The bandwidth  $\omega_{BW}$  is based on the  $-135$ -deg phase (corresponding to  $45$ -deg phase margin) frequency  $\omega_{BW_{phase}}$ , or the  $6$ -dB gain margin frequency  $\omega_{BW_{gain}}$ , whichever is less. The phase delay  $\tau_p$  is determined from the frequency  $\omega_{180}$ , where the phase has a value of  $-180$  deg and the phase value  $\varphi_{2\omega_{180}}$  is measured at twice this frequency  $2\omega_{180}$ :

$$\tau_p \equiv -\left[ \frac{\varphi_{2\omega_{180}} + 180\text{deg}}{(57.3)(2\omega_{180})} \right] \quad (7.83)$$

An examination of Fig. 7.16 shows that the range of good coherence encompasses all of the frequencies needed to determine important handling-qualities metrics. A utility in CIFER® (utility 8: handling qual & stab marg) extracts the needed metrics from the frequency-response data, and the results are shown for the OH-58D pitch response in Table 7.2.

**Table 7.2 Handling-qualities characteristics for the OH-58D pitch response in hover (SCAS-off)**

HQ characteristics	Identified value
-180-deg frequency $\omega_{180}$	4.22 rad/s
-135-deg bandwidth frequency $\omega_{BW_{phase}}$	2.52 rad/s
6-dB bandwidth frequency $\omega_{BW_{gain}}$	1.9 rad/s
Bandwidth frequency $\omega_{BW}$	1.9 rad/s
Two-point phase delay $\tau_p$	0.143 s

A least-squares determination of phase delay, as shown by the dashed line in Fig. 7.17, is more reliable than the two-point calculation of Eq. (7.83); it is obtained by the bandwidth utility in CIFER®. The least-squares calculation includes a weighting function based on the coherence to emphasize the most accurate data. For the present case, the least-squares value of phase delay is  $\tau_p = 0.136$  s, which is close to the value from the two-point calculation.

Finally, the extracted handling-qualities metrics are plotted against the ADS-33E rotorcraft specification for level 1 (satisfactory without improvement), level 2 (deficiencies that warrant improvement), and level 3 (deficiencies that require improvement). The pitch-response specification boundaries shown in Fig. 7.18

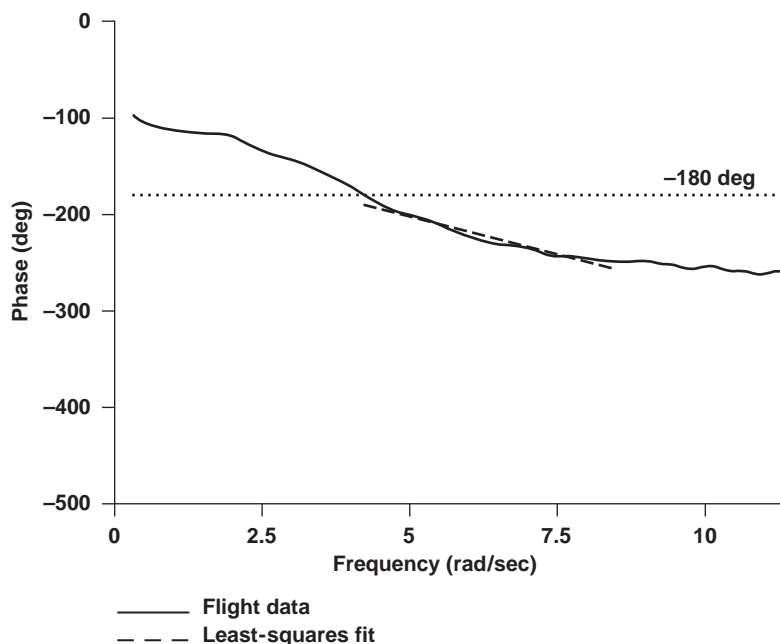


**Fig. 7.17 Least-squares determination of phase delay.**

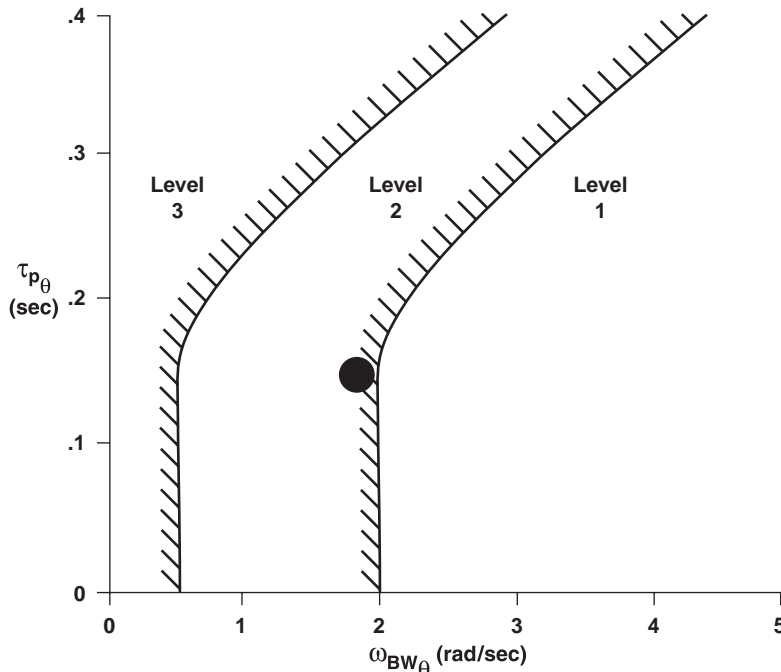


Fig. 7.18 OH-58D SCAS-off hover comparison with ADS-33E.

are for *target acquisition and tracking tasks*, which involve precise pilot-in-the-loop regulation. Some examples of such tasks (also referred to as *high-gain tasks*) are precision hover, the pirouette, and a slope landing. The identification results show that the OH-58D SCAS-off handling qualities are on the borderline between levels 1 and 2 for high-gain piloting tasks, which is consistent with the pilot evaluations.<sup>123</sup>

#### 7.14.4 Numerical Extraction of Linear Models

Numerical perturbation methods are commonly used to extract linear state-space models from complex nonlinear simulation models. Two common applications of the state-space models are for control system design and pilot-in-the-loop handling-qualities analyses. For both applications, the extracted model should exhibit frequency-response characteristics that track those of the nonlinear simulation over the frequency range of interest [e.g., Eq. (5.3)].

The first step in the extraction process is to trim the nonlinear simulation model for a desired flight condition. Then small perturbations are applied sequentially to each element of the state vector (e.g.,  $\Delta x_1$ ), and the resulting state rate  $\dot{x}_1$  is obtained from the nonlinear equations of motion to provide the corresponding value of the  $A$  matrix in Eq. (2.4), which in this case is  $A_{11} = \dot{x}_1 / \Delta x_1$ . Applying a perturbation to the control input  $\Delta u_1$  provides the corresponding value of the  $B$  matrix (in this case,  $B_{11} = \dot{x}_1 / \Delta u_1$ ). The same approach provides the  $C$  and  $D$

matrices of the measurement equation (2.5). Although this approach is straightforward in principle, the extraction of a linear model using numerical perturbation can be very problematic for complex nonlinear simulations (see also Capone, Ref. 124).

In practice, real-time simulation models of aircraft and rotorcraft flight mechanics are typically structured as libraries of individual modules, one for each major component of the aircraft (e.g., wing, fuselage, tail, engine, control system). Computational constraints often preclude the simultaneous update of all of the modules, and a series update or “daisy chain” time-integration approach can be used. Further complications arise when the individual modules are not updated at a common sample rate. These considerations result in embedded integrations within individual modules and iterative solutions for the coupled interactions between the modules. Simulation models that are structured in this manner are generally accurate in the time domain as long as the integration rates are sufficiently fast (small time steps). However, the numerical extraction of higher-order linear models from such models is no longer straightforward.

The issues just discussed are commonly encountered in rotorcraft flight-dynamics simulations. Often, specialized embedded integrations are adopted for the rotor system states to retain the periodic dynamics at real-time sample rates (UH-60 GENHEL).<sup>85</sup> Linear model extraction is accomplished by perturbing the six-DOF fuselage states and allowing the higher-frequency (e.g., rotor and engine) modules to reach steady-state conditions. This results in a six-DOF or *quasi-steady* linear representation of the helicopter (rotor/body) dynamic system. Another technique involves coupling the linear results obtained from extracting isolated models of the individual modules; the overall model that results will be high order, but might not capture accurately the fully coupled dynamics of the nonlinear simulation. The model extraction algorithms, perturbation step sizes, and final linear model accuracy can best be checked by comparing the frequency responses of the linear model [Eq. (2.6)] with system-identification results obtained from frequency sweeps of the nonlinear simulation.

Mansur and Tischler<sup>16</sup> present an example of the limitations of linear model extraction for the simulation model of the AH-64 helicopter dynamics. This application was introduced in Sec. 5.11.1. The nonlinear model implementation used the series update structure and thus precluded the possibility of high-order model extraction beyond a six-DOF quasi-steady model. However, system identification can be used to extract accurate frequency responses from the time responses of the nonlinear simulation. As discussed in Sec. 5.11.1, feedback loops are added to stabilize the bare-airframe dynamics. Then, the simulation model is exercised using frequency sweeps and white noise. The total (pilot + feedback) mechanical (mixer) inputs and helicopter response are used to determine the complete high-order frequency responses for the bare-airframe inputs (e.g.,  $p/\delta_{lat,_{mx}}$ ). This provides the true dynamic response for comparison with the results obtained from perturbation methods.

As can be seen in Fig. 7.19, there are significant errors in the key on-axis ( $q/\delta_{lon}$ ) and off-axis ( $p/\delta_{lon}$ ) responses of the six-DOF model, as compared with those obtained from the nonlinear simulation using system identification. Of particular concern for handling-qualities and control system applications is the additional phase lag associated with the rotor transient response and actuators that appears in

## SINGLE-INPUT / SINGLE-OUTPUT FREQUENCY-RESPONSE 189

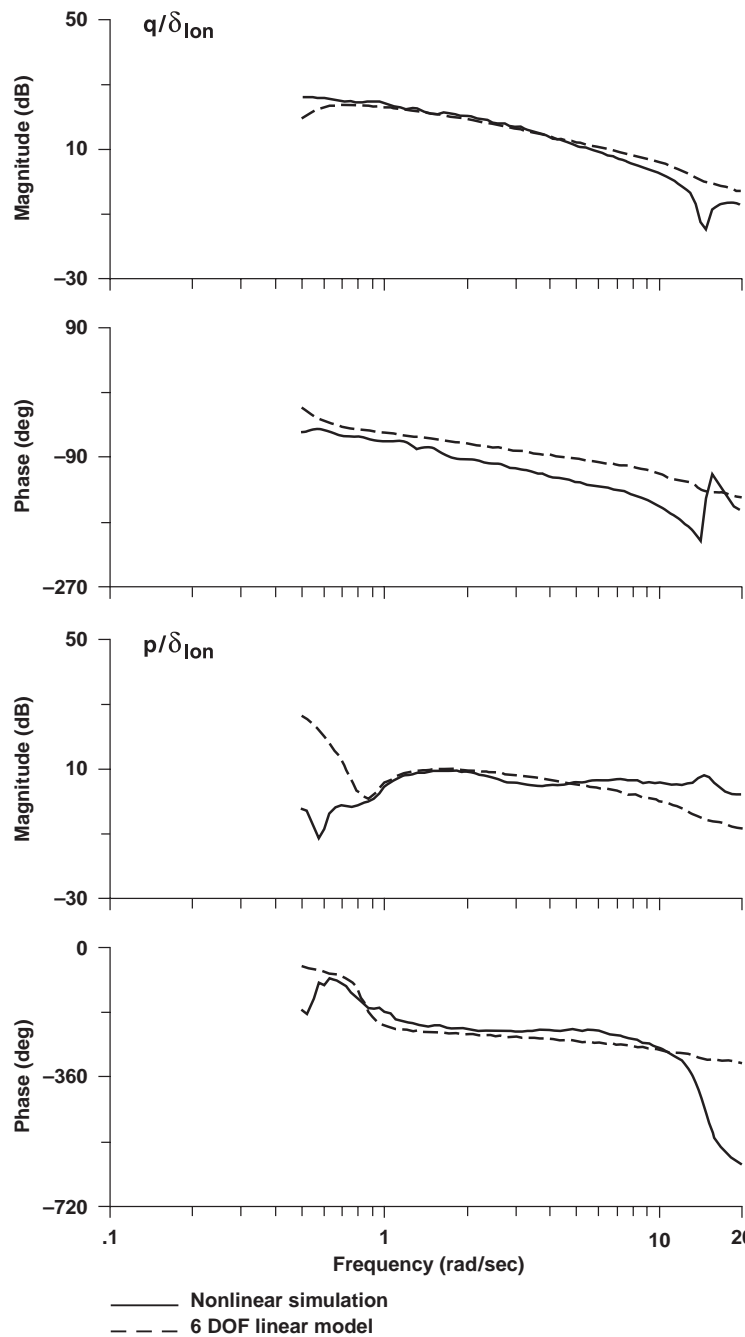


Fig. 7.19 Comparison of six-DOF perturbation and nonlinear simulation models (AH-64, hover).

the nonlinear model but is missing from six-DOF quasi-steady linear model. The roughly 70-deg (= 1.22 rad) additional phase lag at 10 rad/s is equivalent to a considerable amount of added time delay of  $\tau = 1.22/10 = 0.122$  s, associated with the dynamics of the rotor ( $\tau_f$ , Sec. 11.7.1) and actuator systems. Substantially improved accuracy can be achieved by appending transfer-function model representations for these dynamics as demonstrated by Tischler.<sup>125</sup> Alternatively, the real-time rotorcraft simulation can be rearchitected (with considerable effort) so that the state-integration updates are completed simultaneously (as opposed to the series approach of the daisy chain). Kim et al.<sup>126</sup> rearchitected the GENHEL model to allow the extraction of an accurate fully coupled high-order model of the UH-60 from the nonlinear simulation model using the direct numerical perturbation method. The extracted higher-order linear model tracked accurately the frequency responses as obtained from system identification of the nonlinear simulation.

#### 7.14.5 Flight Simulation Validation

The overlay of flight-test and simulation frequency responses is a direct and efficient means to validate model fidelity and assess model improvements. After making modifications to the simulation model, the comparison is repeated to determine whether or not the validity of the model has been improved. The same approach is highly effective in assessing the dynamic performance of simulator motion and visual systems.<sup>45,120</sup>

The simulation vs flight comparison can be evaluated effectively by defining the simulation error response function as

$$\varepsilon_{\text{sim}}(f) \equiv \frac{H_{\text{sim}}(f)}{H_{\text{flight}}(f)} \quad (7.84)$$

which is easily accomplished in CIFER<sup>®</sup> by dividing the two data curves using the frequency-response arithmetic utility.

The magnitude and phase of the error response functions for the XV-15 GTR simulation model in cruise (data from Fig. 2.5) are shown as the dashed curves in Fig. 7.20. Here, 0-dB magnitude and 0-deg phase indicate perfect tracking of the flight and simulation results. Also shown in the figure are the solid curves that are math model mismatch boundaries proposed herein for the highest-fidelity training simulators (FAA Level D). These boundaries correspond to limits on *maximum unnoticeable added dynamics*, or MUAD, beyond which a pilot will detect a deviation in the aircraft response characteristics<sup>127</sup>; they are used in the fixed-wing handling-qualities criteria<sup>5</sup> to evaluate the mismatch criteria between an actual aircraft response and a lower-order equivalent system (LOES) model (Sec. 11.2).

Tischler<sup>11,128</sup> proposed the use of the MUAD boundaries as FAA level D simulation fidelity criteria. The same approach of mismatch boundaries in the frequency domain was also independently proposed and applied by DLR researchers to detect the effects of unnoticeable dynamics in the case of helicopters<sup>24</sup> and for evaluating the fidelity of in-flight simulation.<sup>129</sup>

The XV-15 simulation math model for cruise complies with the proposed Level D (high-fidelity) criteria. This result is consistent with the very favorable pilot

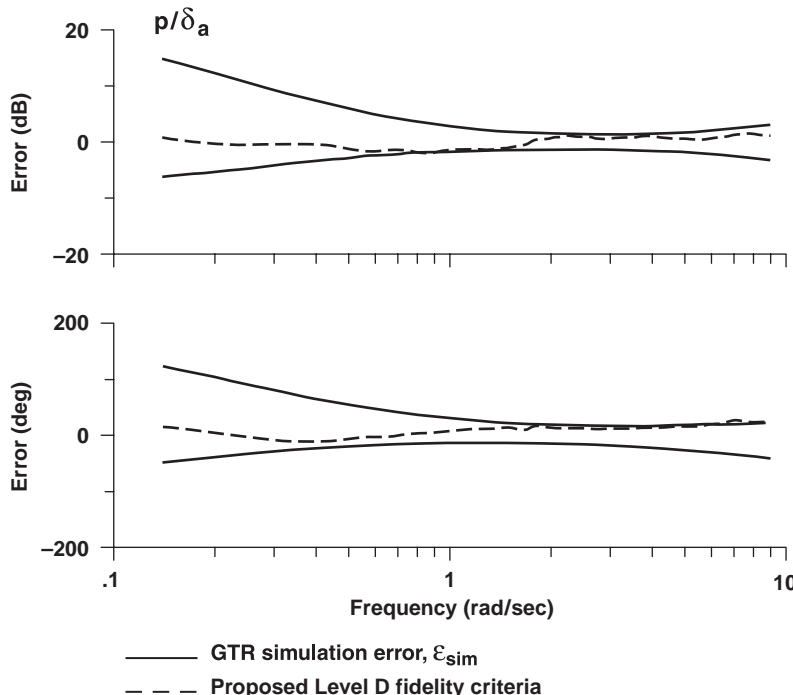


Fig. 7.20 XV-15 error functions (cruise) and proposed level D simulation fidelity criteria.

comparison of simulator and flight behavior.<sup>130</sup> Other examples of helicopter simulation validation using the proposed criteria have been published by Cicolani et al.<sup>131</sup> and Strope et al.<sup>132</sup>

A comprehensive simulation model was developed in conjunction with the solar Pathfinder project (Fig. 5.18) to support flight dynamics and control studies and for preflight planning. The model included a detailed treatment of structural elasticity and unsteady aerodynamics, which are both very important for this vehicle's light wing-loading (0.7 lb/ft<sup>2</sup>). The comparison of flight-test data and simulation for the bare-airframe directional response presented in Fig. 7.21 (reproduced from Lisoski and Tischler<sup>93</sup>) shows that significant discrepancies remained even after model improvements were made. Flight-control analysis and optimization during development tests were based on direct manipulations of the frequency-response data plots using classical control techniques. Then gain adjustments were made in real time from an assessment of the identified broken-loop responses (and stability margins) as obtained from frequency-sweep testing conducted at every 10,000 ft in altitude.

#### 7.14.6 Stability-Margin Testing

The stability characteristics of aircraft rigid-body and structural dynamics can be greatly affected by the feedback loops of the flight control system. Feedback

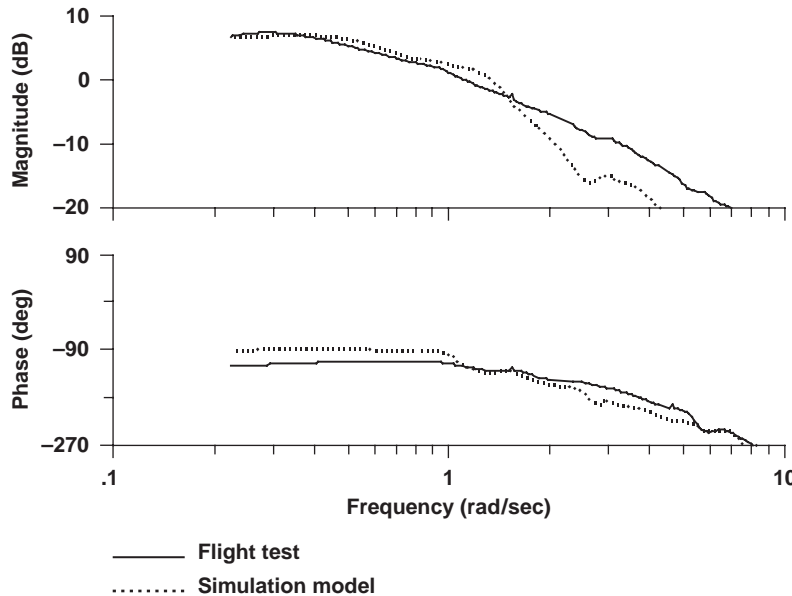


Fig. 7.21 Comparison of flight and simulation directional responses for solar Pathfinder.

can degrade the stability margins for the structural modes at the same time that it improves the rigid-body stability and handling qualities. Military specification 9490D (Ref. 133) defines minimum levels of control system gain-and-phase margin as determined from the broken servoloop frequency response

$$GH(s) = \frac{f(s)}{e} \quad (7.85)$$

shown in Fig. 7.22. The test procedure involves exciting the dynamic response using a piloted or automated sweep input  $r$ . Then the *direct* estimate of the broken-loop response is determined from the measurements  $e$  and  $f$  and Eq. (7.37):

$$GH(f) = \frac{G_{ef}(f)}{G_{ee}(f)} \quad (7.86)$$

When noise ( $n$  of Fig. 7.22) contributes to the measured output, such as caused by measurement system noise or process noise (e.g., turbulence and secondary inputs), it becomes correlated with the error signal  $e$ , because of the presence of feedback (Chapter 8). This correlation yields a biased estimate of the broken-loop response based on Eq. (7.86). Alternatively, the broken-loop response can be determined using an *indirect estimate* from the error response

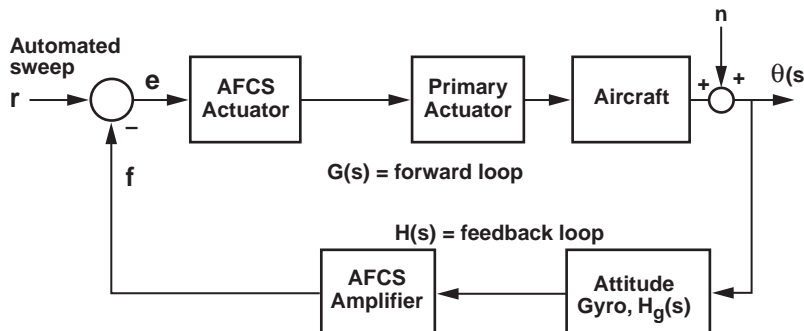


Fig. 7.22 Block diagram for stability-margin test.

( $e/r$  of Fig. 7.22):

$$\frac{e}{r}(s) = \frac{1}{1 + GH(s)} \quad (7.87)$$

This response, determined from the measurements  $r$  and  $e$  by the equation

$$\frac{e}{r}(f) = \frac{G_{re}(f)}{G_{rr}(f)} \quad (7.88)$$

is unbiased for output noise because the sweep input  $r$  and the noise signal  $n$  are uncorrelated.<sup>134</sup> The required broken-loop response is then obtained by manipulating the frequency-response data at each frequency:

$$GH(f) = \left[ \frac{1}{e(f)/r(f)} \right] - 1 \quad (7.89)$$

The gain-margin calculation is based on the frequency-response data beyond the crossover frequency [where  $GH(f) < 1$ ], so that there is a reduced signal/noise level and thus reduced coherence and greater data scatter. In contrast, the error function of Eq. (7.87) approaches a value of unity at higher frequency and thus maintains a higher coherence and reduced scatter. McCoy<sup>135</sup> compared the direct and indirect methods for stability-margin determination of the UH-60A helicopter using piloted sweeps and found that the indirect method produced a more reliable result. Dryfoos et al.<sup>134</sup> also found the indirect method preferable for the stability-margin analysis of the RAH-66 Comanche helicopter using automated sweeps.

The MIL-F-9490D specifications are given as a function of frequency range, with larger gain margins required for the aeroservoelastic (ASE) modes (Table 7.3).

Table 7.3 MIL-F-9490D gain-and-phase margin requirements (dB, deg)  
 (from Ref. 88)

Mode freq., Hz	Air Speed			
	Below $V_o$ min	$V_o$ min to $V_o$ max	At limit speed $V_L$	At $1.15^* V_L$
$f_M < 0.06$	GM <sup>a</sup> = 6 db No phase reqt.	GM = $\pm 4.5$ PM <sup>b</sup> = $\pm 30$	GM = $\pm 3.0$ PM = $\pm 20$	GM = 0.0 PM = 0.0
$0.06 f_M$ 1st ASE	below $V_o$ min	GM = $\pm 6.0$ PM = $\pm 45$	GM = $\pm 4.5$ PM = $\pm 30$	Stable at nominal
1st ASE $< f_M$		GM = $\pm 8.0$ PM = $\pm 60$	GM = $\pm 6.0$ PM = $\pm 45$	phase and gain

<sup>a</sup>GM = gain margin.

<sup>b</sup>PM = phase margin.

Figure 7.23 shows the broken servoloop frequency response  $GH(s)$  of a large single-rotor helicopter as obtained by computer-generated frequency-sweep flight-test procedures. A utility in CIFER® (utility 8: handling qual & stab marg) analyzes the frequency-response data to determine a table of stability margins corresponding to each 0-dB gain and  $-180$ -deg phase crossing. The 0-dB gain

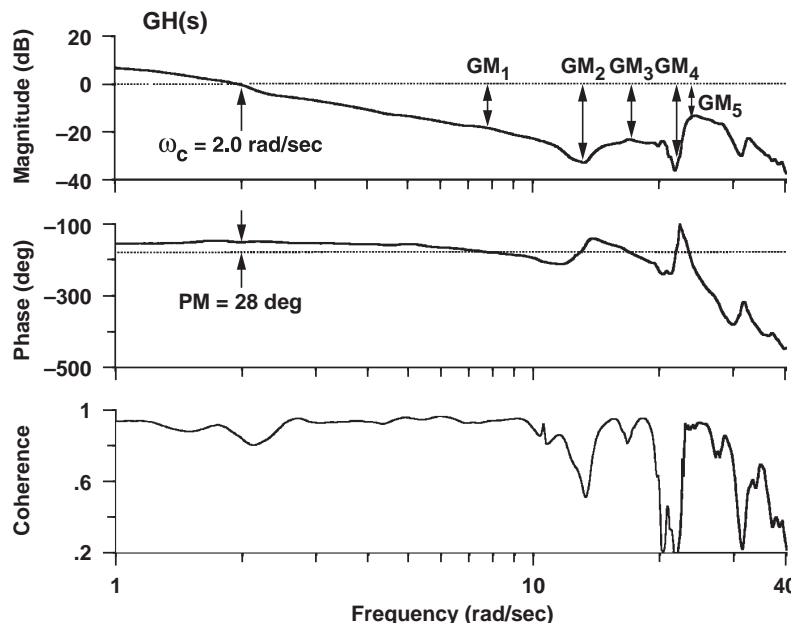


Fig. 7.23 Stability-margin determination for a large helicopter.

Table 7.4 Stability-margin results for a large helicopter

Critical frequencies, rad/s	Gain margin, dB
7.8	17.8
13.0	32.1
17.1	22.8
21.8	36.0
23.4	14.2

crossover frequency at  $\omega_c = 2.0$  rad/s is associated with the closed-loop rigid body and shows an associated phase margin of  $PM = 28$  deg. This margin is substantially below the recommended specification value.

The gain margin is checked at each crossing of the  $-180$  deg ( $\pm k360$ ,  $k = 1, 2, 3, \dots$ ) phase line as shown in the figure, with the values listed in Table 7.4. The critical margin is the minimum value (GM5), which is 14.2 dB at a frequency of  $\omega = 23.4$  rad/s. This frequency corresponds to the first vertical bending mode for the tail boom of this aircraft. Reference to Table 7.3 indicates that this gain margin is well within accepted design specifications.

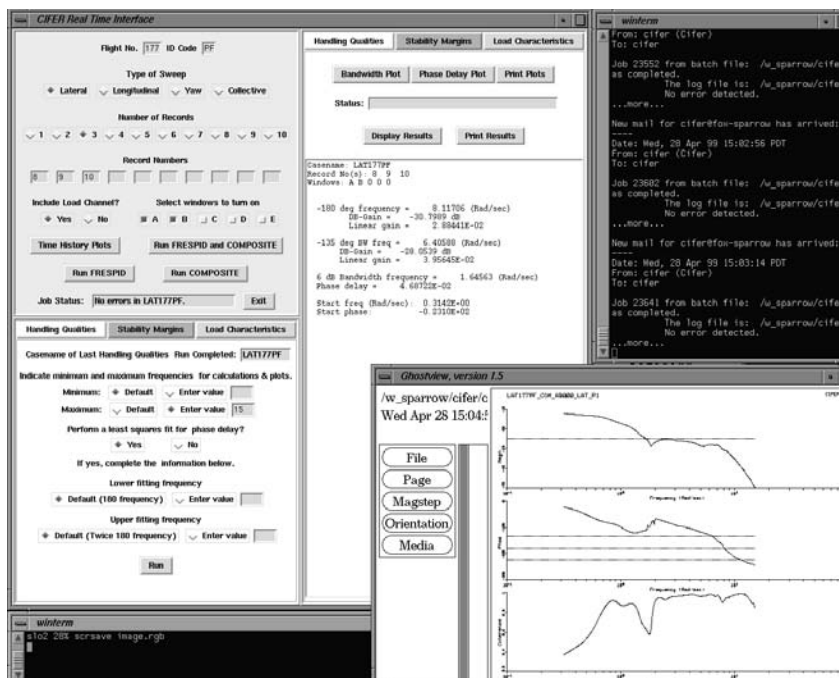


Fig. 7.24 Real-time CIFER® interface.

The coherence function of Fig. 7.23 shows excellent identification accuracy for this flight test across the broad frequency range of interest (1–30 rad/s). Sharp drops (holes) or peaks in the coherence function reflect structural anti-nodes and nodes, respectively. Examples of fixed-wing programs using frequency-domain system identification for elastic mode stability-margin evaluation include the X-29,<sup>136</sup> the European Aircraft Programme (EAP<sup>88</sup>), Euro-fighter high-performance manned aircraft,<sup>89</sup> and the Pathfinder solar-powered unmanned aircraft.<sup>93</sup>

Sahai and her colleagues developed and demonstrated a specialized interface for CIFER® (Fig. 7.24) for automated determination of stability margins (and transfer-function models) from real-time telemetry data.<sup>115,131</sup> This interface implemented the indirect method [Eq. (7.89)] for determining the broken-loop response. Excellent agreement was seen between real-time results based on telemetered data containing noise and dropouts with postflight analysis based on the cleaner onboard recorded data, thus validating the analysis technique.

#### 7.14.7 Control System Model Validation

Stability and control augmentation systems for modern aircraft and helicopters are developed directly in block diagram form using tools such as SIMULINK®. These block diagrams also serve as control system models for piloted-simulation evaluation, stability analysis, troubleshooting, and flight-test optimization of control system performance. The accurate prediction of broken-loop and closed-loop frequency responses for an initial (*baseline*) control system configuration establishes a critical *anchor point* for the control system model.

Tischler et al.<sup>20</sup> documented the development of modernized control laws (MCLAWS) to provide an attitude-command/attitude-hold response type for the UH-60 and thereby afford improved handling qualities for near-Earth operation in night and poor weather. Initial flight tests of the baseline gain set showed significant qualitative discrepancies with the predicted characteristics based on the SIMULINK® analysis model. An immediate project decision was made to conduct ground and flight tests to establish the source of these discrepancies and achieve a reliable anchor point for further analysis design optimization using the CONDUIT® (Control Designer's Unified Interface) tool.<sup>64</sup>

A simplified schematic for the roll axis, shown in Fig. 7.25, illustrates the flight-test measurements that were available. As can be seen by the mnemonic labels indicated next to signal arrows, many of the internal flight-control-computer (FCC) signals were recorded in the flight tests—a result of careful preflight planning. This allowed frequency-response identification of the key elements of the block diagram, which proved invaluable for isolating and correcting several modeling discrepancies. Some examples that demonstrate the excellent agreement for the roll axis once these discrepancies were resolved follow.

The roll-rate command-model response [ $sM_\phi(s)$ ] of Fig. 7.25] is identified from the recorded time histories

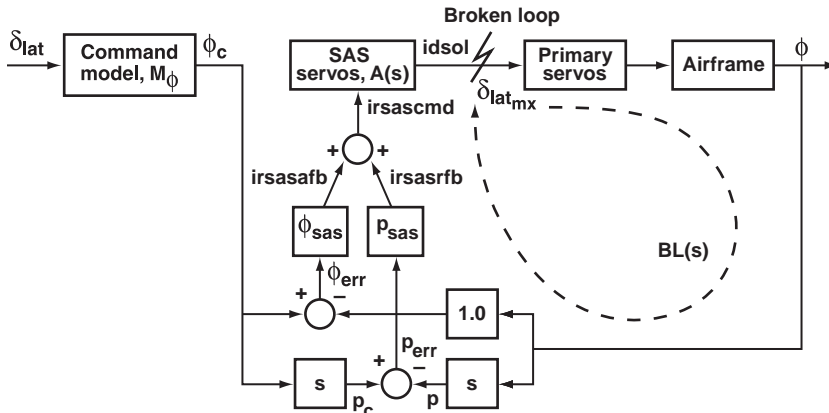


Fig. 7.25 Simplified schematic of roll-axis modernized control system (UH-60 MCLAWS).

$$sM_\phi(s) = \frac{p_c(s)}{\delta_{lat}(s)} \quad (7.90)$$

and is seen in Fig. 7.26 to match the ideal command model as represented in the CONDUIT® analysis

$$[sM_\phi]_{\text{CONDUIT}} = \frac{7.16s}{(0.625s + 1)(0.625s + 1)} \text{ deg/s/in.} \quad (7.91)$$

The coherence is nearly unity, indicating excellent accuracy, as would be expected for identifying software elements as compared to airframe dynamics. The roll-rate SAS dynamics  $P_{sas}(s)$  of Fig. 7.25 are identified [ $P_{sas}(s) = \text{irsasrb}(s)/p_{err}(s)$ ] and again match the CONDUIT® model precisely, as shown in Fig. 7.27, validating this branch of the block diagram model.

The broken-loop response [indicated as  $BL(s)$  in Fig. 7.25] is fundamental to stability and performance of the system. The crossover frequency  $\omega_c$  defines the speed with which the closed loop will reject disturbances, whereas the broken-loop stability margins define robustness to uncertainty and closed-loop damping ratio. Therefore, accurate prediction of the broken-loop response is a critical aspect of control system model validation. Validation based only on the closed-loop response is inadequate because the feedback loops suppress the dynamic responses (especially the frequencies up to crossover).

The broken-loop response is commonly obtained in flight test by injecting an electronic chirp signal at the actuator command, such as indicated by  $r$  in Fig. 7.22 and, for example, in control law development of the Comanche helicopter as discussed by Dryfoos et al.<sup>134</sup> In the current flight-test program such a

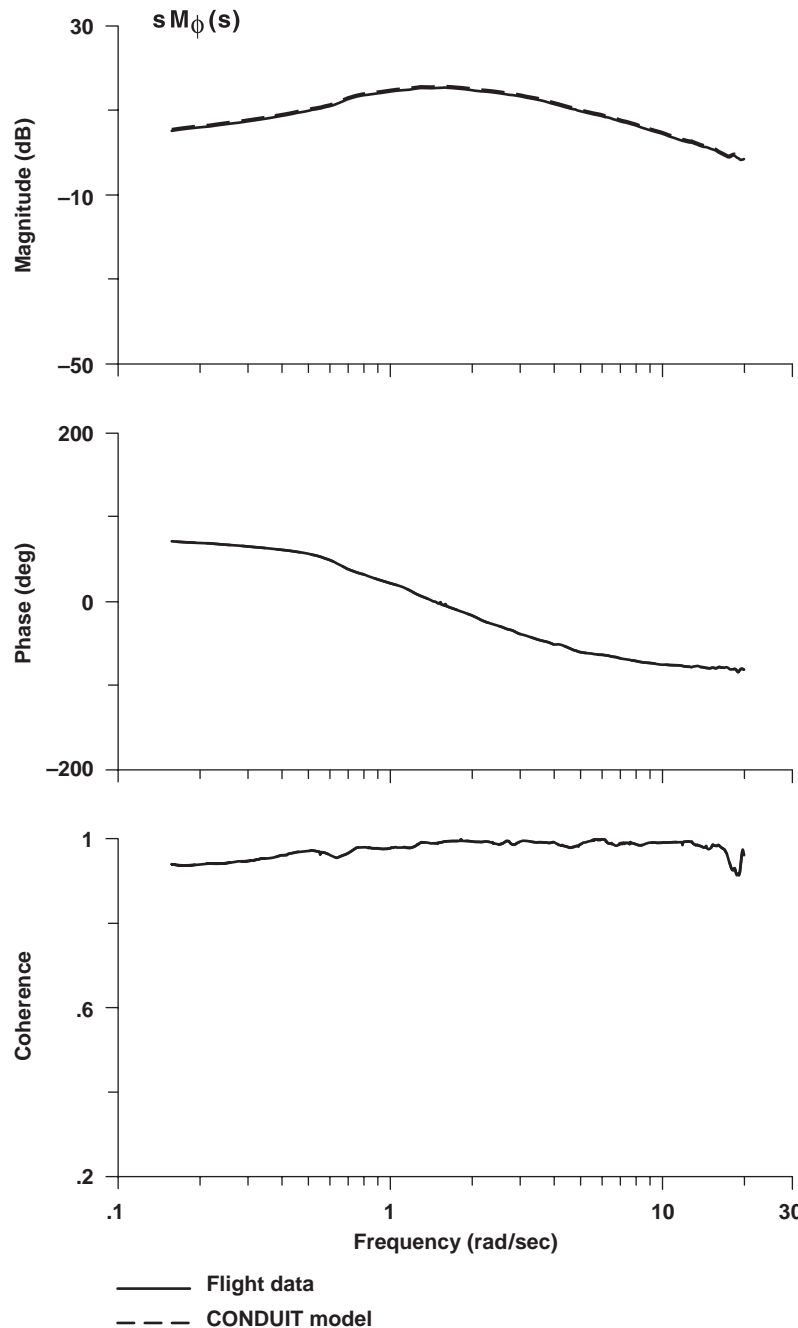


Fig. 7.26 Command model comparison for roll axis (UH-60 MCLAWS).

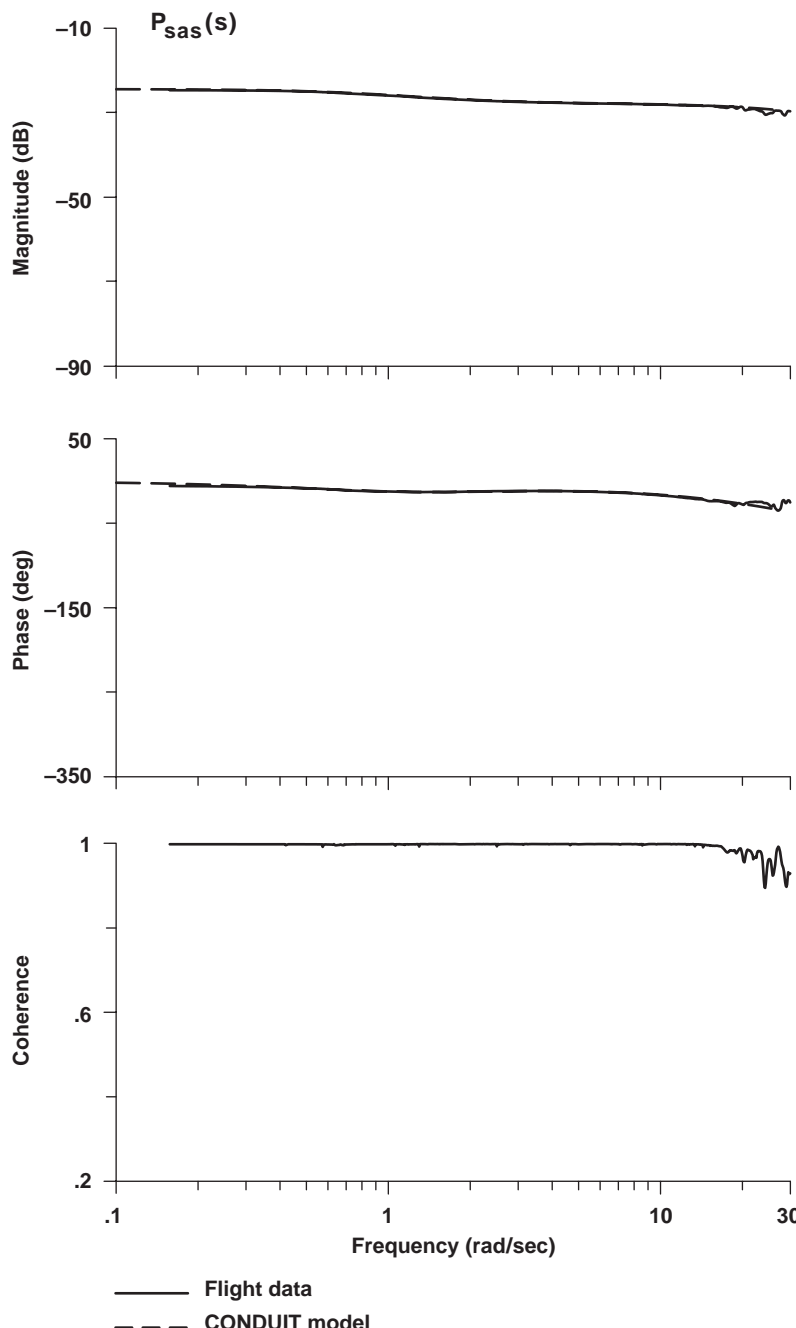


Fig. 7.27 Roll-rate SAS compensation comparison (UH-60 MCLAWS).

specialized input was not available, and model validation was based only on the data obtained from piloted sweeps ( $\delta_{\text{lat}}$  input in Fig. 7.25). In the MCLAWS model-following architecture of Fig. 7.25, the piloted input is introduced in two places in the feedback path ( $\phi_{\text{err}}$  and  $p_{\text{err}}$ ). This precludes the identification of the broken-loop response using the *direct method* [ $f/e$  error response of Eq. (7.86)] or the *indirect estimate* [based on  $e/r$  of Eq. (7.88)]. Instead, from reference to Fig. 7.25, the broken-loop response can be built up from its components as

$$BL(s) = [sP_{\text{sas}}(s) + \phi_{\text{sas}}(s)] \left\{ [p(s)/\delta_{\text{lat}_{\text{mx}}}(s)] \frac{1}{s} \right\} [A(s)] \quad (7.92)$$

making direct use of the frequency-response data for the identification of the various elements in the equation (e.g., Fig. 7.27). The calculation is performed using the frequency-response arithmetic function in CIFER®.

As seen in Fig. 7.28, the analysis model shows very good agreement with the identified response in the frequency range of interest for flight control (1–10 rad/s). This ensures that the key control system metrics of crossover frequency, gain margin, and phase margin will be well predicted. Errors at low frequency (below 1 rad/s) are associated with modeling inaccuracies in the bare-airframe response simulation  $p/\delta_{\text{lat}_{\text{mx}}}$ .

Control law optimization can also be conducted using this frequency-response arithmetic approach, without having access to an identified state-space model of the bare airframe (i.e.,  $p/\delta_{\text{lat}_{\text{mx}}}$  herein). As demonstrated by in-flight tests of the solar Pathfinder<sup>93</sup> and in a simulation-based study of a ducted fan UAV by Spaulding et al.,<sup>137</sup> the bare-airframe frequency response is determined, and then the gains and filters of the control system components [ $P_{\text{sas}}(s)$  and  $\phi_{\text{sas}}(s)$ , in this case] can be tuned to achieve the desired broken-loop response characteristics [ $BL(s)$ ].

Finally, the overall closed-loop response  $p/\delta_{\text{lat}}$  shows good agreement, as can be seen in Fig. 7.29, thereby ensuring that the handling-qualities parameters (bandwidth and phase delay) will be well predicted.

This analysis established that the MCLAWS model provided a satisfactory prediction of broken-loop and closed-loop response characteristics, thus establishing a solid *anchor point* from which design optimization using CONDUIT® was conducted. This ensured that the improvements seen in analysis and simulation would be realized in flight. A full discussion of control law validation and final handling-qualities performance is presented in Tischler et al.<sup>20</sup>

Numerical linearization of complex block diagram models (e.g., using the MATLAB® function linmod) for the purpose of obtaining a state-space representation can be problematic and should be checked before using the result in linear analyses. Time integration of the block diagram model can be considered to be accurate. Thus, an effective means to validate the linearization results is to compare the Bode plots obtained using the numerical perturbation model with those obtained using system identification for an automated sweep input.

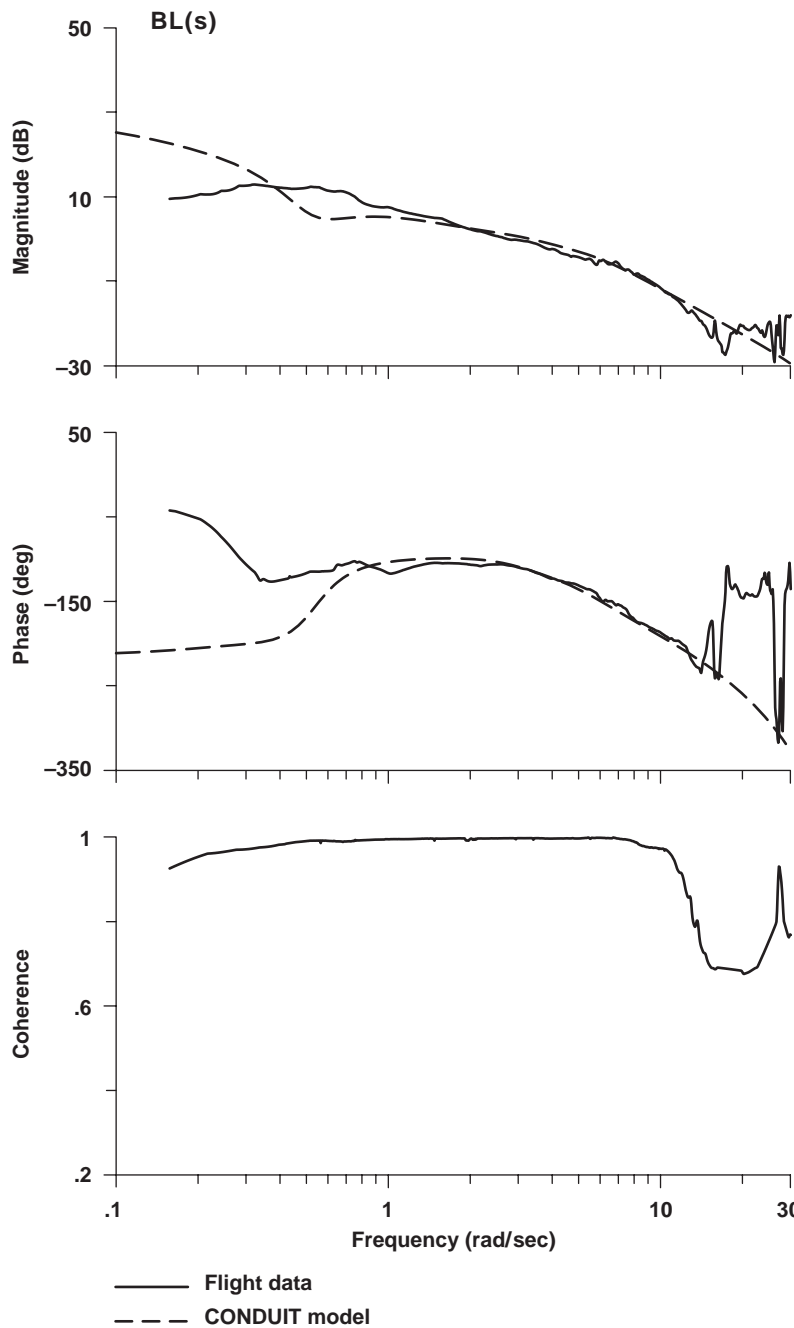


Fig. 7.28 Roll broken-loop response comparison (UH-60 MCLAWS).

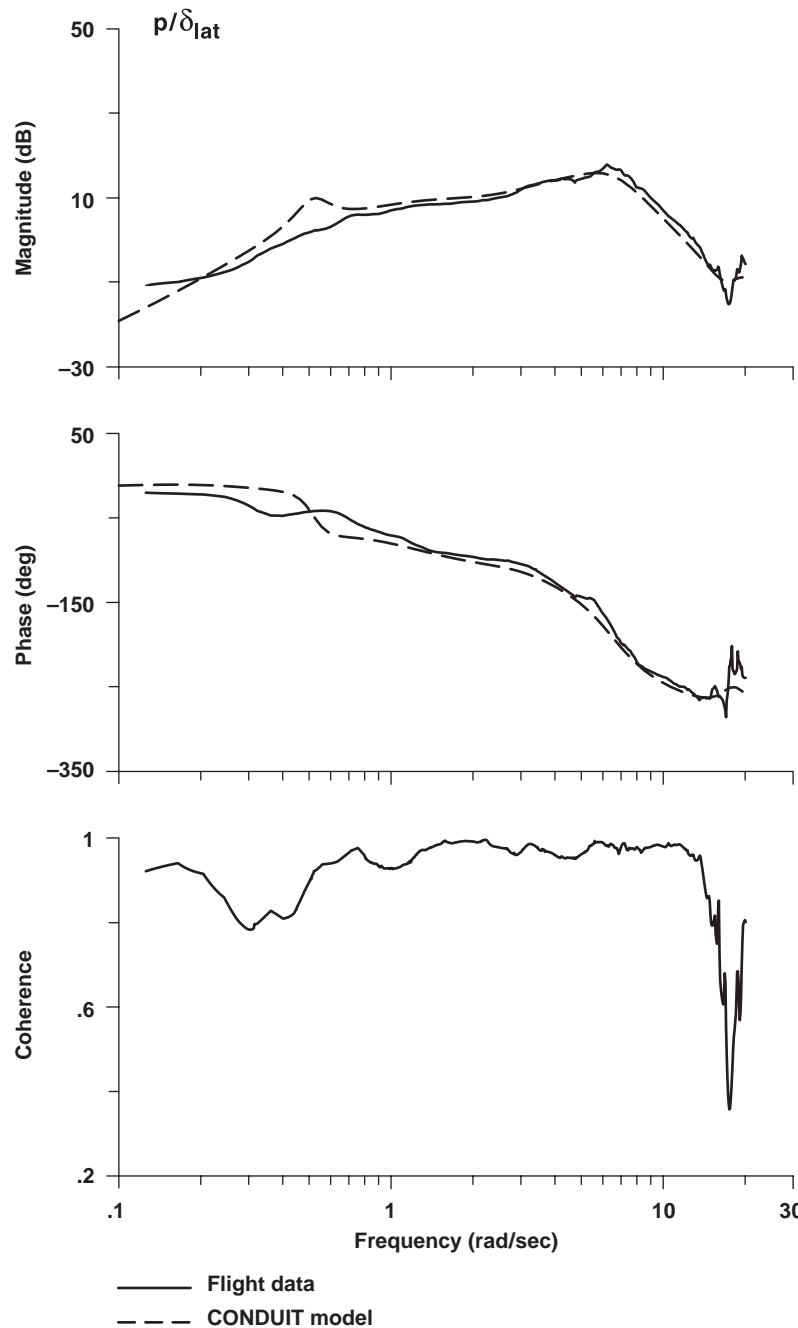


Fig. 7.29 Roll closed-loop response comparison (UH-60 MCLAWS).

## Problems

### *Assumptions of SISO frequency-response identification with FRESPID*

**7.1** Is the assumption of *noise-free input* measurements reasonable for the XV-15 flight data in both the piloted input signals and the control effector input signals? Use the input and output time histories plotted in **Problem 3.9** for these analyses.

### *Identification of XV-15 closed-loop SISO frequency responses using FRESPID*

**7.2** Obtain the closed-loop frequency-response  $p/\delta_{\text{lat}}$  for the XV-15 in hover using the two concatenated records (883 and 884 in database 1). Process with a single 20-s window, and generate the following plots: filtered input and output time histories, input autospectrum, frequency response, and coherence.

**7.3** Examine the log file generated in **Problem 7.2**, and verify that all of the anticipated actions occurred during the FRESPID run. Notice the calculation of the average and rms values of the input and output signals. If any errors occurred, make the appropriate corrections and repeat the run.

**7.4** Based on the autospectrum plots generated in **Problem 7.2**, what is the frequency range over which the excitation can be considered satisfactory? What is the range for which the coherence indicates satisfactory frequency-response identification?

### *Closed-loop handling qualities of the XV-15 in hover*

**7.5** Starting with the closed-loop frequency-response data generated in **Problem 7.2**, use the CIFER® Bandwidth Utility (#8), or direct reference to the frequency-response plots, to determine the following handling-qualities parameters following the example of Sec. 7.14.3. Remember that the analysis is based on  $\phi/\delta_{\text{lat}} = ([p/\delta_{\text{lat}}]/s)$ : (a) -135-deg frequency (phase bandwidth frequency), (b) 6-dB gain bandwidth frequency, (c) handling-qualities bandwidth  $\omega_{\text{BW}}$ , which is minimum of (a) and (b), and (d) phase delay  $\tau_p$  using the two-point calculation.

**7.6** Continuing the handling-qualities analysis, generate linear frequency plots of the phase and coherence and perform a least-squares fit for phase delay using utility 8. Compare the two-point phase delay with the least-squares phase delay.

### *Calculating the rms of the XV-15 piloted input signal*

**7.7** Starting with the closed-loop frequency-response data generated in **Problem 7.2**, use the CIFER® RMS Utility (#7) to determine the rms of  $\delta_{\text{lat}}$  from the autospectrum  $G_{\delta_{\text{lat}} \delta_{\text{lat}}}$  for the entire frequency range of data available.

**7.8** Compare the rms value obtained in the frequency domain (**Problem 7.7**) with the standard deviation result obtained from the time history of  $\delta_{\text{lat}}$ . (The

time-domain rms is given in the log file examined in **Problem 7.3.**) Explain any differences between the frequency-domain and time-domain determination of the rms.

**7.9** Return to utility 8, and calculate the rms of  $\delta_{\text{lat}}$  over a smaller range of frequencies (than in **Problem 7.7**). Explain why the resulting rms is smaller than that obtained in **Problem 7.7**.

**7.10** Determine the pilot cutoff frequency ( $\omega_{\text{co}}$  of Sec. 7.14.2) for the lateral sweep. Is this consistent with the autospectrum curve? What does this value tell you about the piloted sweep?

*SISO frequency-response identification of an inverted pendulum using FRESPID*

**7.11** Identify the frequency-response  $\theta/\bar{M}_{\text{ext}}$  using your pendulum simulation time histories from **Problem 5.5**. Use three windows: 35 s, 25 s, and 20 s. Compare your results with those presented in Sec. 7.13.

**7.12** Identify the frequency response of  $\dot{\theta}/\bar{M}_{\text{ext}}$ . Apply a  $1/s$  correction in the frequency domain and compare with the identified  $\dot{\theta}/\bar{M}_{\text{ext}}$  from **Problem 7.11**.

**7.13** Overlay the ideal frequency response [Eq. (3.7)] with the system-identification result from the nonlinear simulation for  $\theta/\bar{M}_{\text{ext}}$ .

**7.14** Look at the effect of measurement noise (try once in the input and again in the output) and process noise on the frequency response  $\theta/\bar{M}_{\text{ext}}$ . Add noise to the pendulum system as shown in Fig. P7.14. Then overlay the identified response (use the 35-s window) with the noise-free case from **Problem 7.11**. What is the effect on coherence? What are reasonable guidelines for allowable noise-to-signal levels?

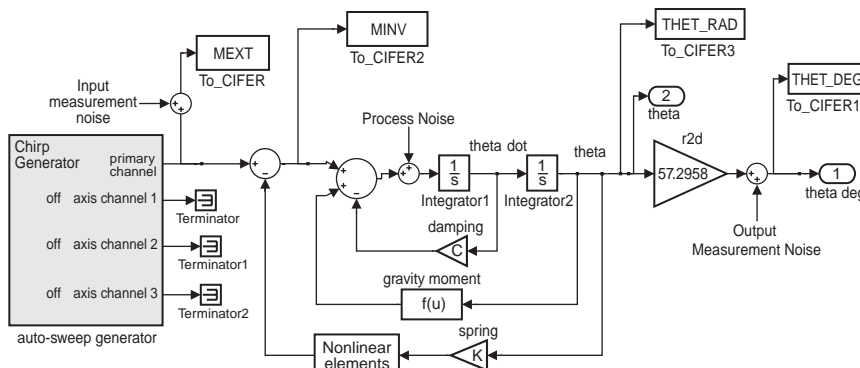


**Fig. P7.14** Diagram showing insertion of input measurement noise, output measurement noise, and process noise.

**7.15** Look at the effect of nonlinearity on system identification of  $\theta/\bar{M}_{\text{ext}}$  by including (a) spring limiting of  $\pm 1.9 \text{ rad/s}^2$ , (b) spring backlash with deadband width of  $0.3 \text{ rad/s}^2$ , and (c) large-amplitude frequency sweeps of  $\bar{M}_{\text{ext}} = 10 \text{ rad/s}^2$  in your pendulum simulation. Figure P7.14 depicts where nonlinear elements should be introduced into the simulation. Use the frequency-sweep generator specifications from **Problem 5.3** to exercise your pendulum. Coplot the identified frequency responses (35-s window) with the ideal pendulum frequency response (**Problem 7.11**). What are the effects of the nonlinear elements on the magnitude, phase, and coherence of the identified frequency responses?

*SISO bare-airframe frequency-response identification of the XV-15*

**Students should choose to work on either the hover configuration (Problem 7.16) or the cruise configuration (Problem 7.17) and then continue with the chosen configuration when working on the problems in the rest of this book.**

**7.16 Hover configuration:** Using the XV-15 hover data in database 1, create separate FRESPID cases, each with two inputs  $\delta_a$  and  $\delta_r$ , and four outputs  $\dot{v}$ ,  $p$ ,  $r$ , and  $a_y$ . The first case will use the lateral sweep data (except for record 882, which was of poor quality), and the second case will use the yaw sweep data. Set up FRESPID to run with plots turned off and control cross correlation on (the latter so as to generate data that will be used in the next chapter for multi-input conditioning). Use three windows with 45, 30, and 20 s. Determine the SISO frequency responses from all of the inputs to all of the outputs, making sure that the outputs are in the following units:  $\dot{v}$  and  $a_y$  in  $\text{ft/s}^2$  and  $p$  and  $r$  in  $\text{rad/s}$ .

**7.17 Cruise configuration:** Using the XV-15 cruise data in database 2, create separate FRESPID cases, each with two inputs  $\delta_a$  and  $\delta_r$ , and four outputs  $p$ ,  $r$ ,  $a_y$ , and  $\beta$ . The first case will use the lateral sweep data, and the second case will use the yaw sweep data. Set up FRESPID to run with plots turned off and control cross correlation on (the latter so as to generate data that will be used in the next chapter for multi-input conditioning). Use three windows with 45, 30, and 20 s. Determine the SISO frequency responses from all of the inputs to all of the outputs, making sure that the outputs are in the following units:  $p$  and  $r$  in  $\text{rad/s}$ ,  $a_y$  in  $\text{ft/s}^2$ , and  $\beta$  in  $\text{rad}$ . Do not forget to correct the sideslip data to take into account the difference between measurements taken at the nose boom instead of the center of gravity.

*Window-size selection*

**7.18** Compare the  $p/\delta_a$  frequency responses of windows A, B, and C from **Problem 7.16** or **Problem 7.17** by overlaying plots of magnitude, phase, and coherence. How is the identified frequency response affected by window length?

**7.19** A UAV helicopter project has two frequency-sweep records that can be concatenated; one 85 s long, and one 92 s long. The dynamic modes of interest are between 0.5 and 30 rad/s. What are the five window lengths you would choose for this project?

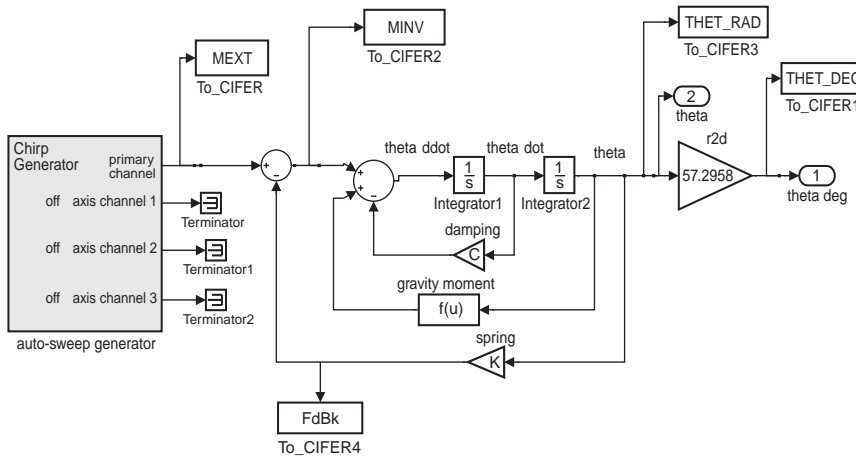


Fig. P7.20 Signals for control system validation and design.

#### Control system model validation

**7.20** Identify the frequency responses  $\theta/\bar{M}_{\text{inv}}$  and  $(\text{FdBk})/\theta$  from your pendulum simulation as shown in Fig. P7.20. Validate the identified response for the feedback block (which is just a simple gain in this case). Then, using frequency-response arithmetic reconstruct  $\theta/\bar{M}_{\text{ext}}$  using the known transfer function for a closed-loop system with feedback;

$$\frac{\theta}{\bar{M}_{\text{ext}}} = \frac{\theta/\bar{M}_{\text{inv}}}{1 + (\theta/\bar{M}_{\text{inv}})(\text{FdBk}/\theta)} \quad (\text{P7.20})$$

compare the reconstructed  $\theta/\bar{M}_{\text{ext}}$  with the identified  $\theta/\bar{M}_{\text{ext}}$  frequency response from **Problem 7.11**.

**7.21** Use frequency-response arithmetic and the frequency responses identified in **Problem 7.20** to reconstruct the broken-loop response  $(\text{FdBk})/\bar{M}_{\text{inv}}$  using the known equation for a broken-loop system:

$$\frac{\text{FdBk}}{\bar{M}_{\text{inv}}} = \left( \frac{\theta}{\bar{M}_{\text{inv}}} \right) \left( \frac{\text{FdBk}}{\theta} \right) \quad (\text{P7.21})$$

Calculate the crossover frequency and phase margin using utility 8. Then using frequency-response arithmetic, add a 0.1-s time delay to the pendulum feedback. The time delay can be modeled using a Padé filter [Eq. (15.23)]. Examine the effect of the time delay on phase margin. What is the gain margin?

## SINGLE-INPUT / SINGLE-OUTPUT FREQUENCY-RESPONSE 207

**7.22** Design a new feedback gain  $\bar{K}$  for the pendulum feedback with 0.1s time delay from **Problem 7.21** to achieve a larger phase margin. Use only frequency-response arithmetic to construct a new feedback transfer function ( $F_{dBk}/\theta$ ) that incorporates the new feedback gain. Use utility 8 to show that the phase margin has improved.

**7.23** Using frequency-response arithmetic, determine the closed-loop transfer-function  $\theta/M_{ext}$  for the system with the new feedback gain  $\bar{K}$  design (and added time delay) from **Problem 7.22**. Then use utility 8 to determine the bandwidth for the new closed-loop pendulum and compare to the value for the nominal pendulum.

This page intentionally left blank

## 8

## Bare-Airframe Identification from Data with Feedback Regulation Active

The identification of bare-airframe dynamics from flight-test data with feedback regulation active raises some important issues and limitations. The SCAS feedbacks generally suppress the bare-airframe excitation signal, especially at lower frequencies (Fig. 5.6), and introduce cross-control correlation that also reduces the effective input autospectrum for multi-input analyses (Chapter 9).

Perhaps the greatest concern in the identification of the bare-airframe response under closed-loop test conditions is that the SCAS feedback introduces correlation between the output noise and the bare-airframe excitation signal ( $v$  and  $x$ , respectively, in Fig. 7.4). This correlation leads to bias errors in the frequency-response estimate. The analytical and numerical simulation results presented herein show that bare-airframe dynamics can be determined without incurring significant bias errors, subject to modest restrictions on the noise-to-signal ratio. These restrictions are consistent with the flight-testing guidelines discussed previously (Sec. 5.7). Although this chapter refers to SCAS feedback, the same considerations also apply to piloted feedback regulation as well.

The following topics are covered in this chapter: situations requiring closed-loop testing, theoretical analysis of bias errors caused by feedback, and numerical study of bias errors in closed-loop testing.

### 8.1 Limiting Conditions in Closed-Loop Identification

Some situations require that the identification of bare-airframe dynamics be based on test data collected with one or more of the SCAS channels engaged. Possible reasons for these circumstances to arise include the following:

1) The bare-airframe dynamics might have lightly damped, unstable, or highly coupled modes that make it too difficult for the pilot to execute a satisfactory frequency sweep with the SCAS disengaged. For example, the unaugmented characteristics of high-performance fixed-wing aircraft exhibit a rapid pitch divergence (with a typical time-to-double amplitude of less than 1 s) because of a large unstable static margin. This precludes the possibility of piloted frequency-sweep testing without engaging the SCAS pitch channels. Helicopters typically exhibit an unstable low-frequency oscillation in hover (20-s period), and so the sweeps are often conducted with the SCAS engaged in one or more channels.

2) Computer-generated sweeps will cause the aircraft to drift away from the trim condition. This is true both for flight testing and ground-based simulation studies. When automated sweep inputs are used, low-gain SCAS (or pilot) feedbacks will generally be required to keep the aircraft variations centered about the reference condition (as illustrated in Sec. 5.11.1).

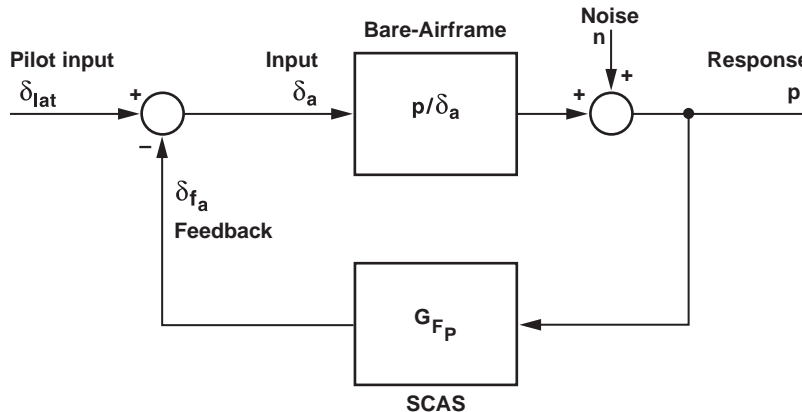


Fig. 8.1 Single degree-of-freedom closed-loop roll-response model.

3) Sometimes the only data available for use in system identification are from prior flight tests conducted for an entirely different reason and flown with the SCAS engaged.

Figure 8.1 illustrates the identification of the single-input/single-output roll-rate response to aileron  $p/\delta_a$  under closed-loop conditions. The block diagram includes a noise input  $n$ , which, as discussed in Chapter 7, accounts for the presence of response measurement noise and process noise as reflected to the output. Typical sources of process noise are turbulence, response to neglected secondary inputs, remnants associated with nonlinearities in the response, and even integration errors in the case of off-line simulation studies.

The closed-loop system responds to the piloted-sweep input  $\delta_{lat}$  and noise  $n$ . Measurement of the control surface input  $\delta_a$  and response  $p$  allows the direct identification of the bare-airframe response

$$\hat{H} = \left( \frac{\hat{p}}{\delta_a} \right) = \frac{G_{\delta_a p}}{G_{\delta_a \delta_a}} \quad (8.1)$$

even when the SCAS is engaged, as discussed previously in Sec. 3.4. [Note that Eq. (8.1) is an application of Eq. (7.37).] However, the problem that arises when noise is present is that feedback of noise via the SCAS (and/or the pilot) causes the frequency-response estimate  $\hat{H}$  to be biased relative to the true frequency response  $p/\delta_a$ . This can be easily seen by observing that the (total) surface deflection  $\delta_a$  is made up of components from the pilot  $\delta_{lat}$  and the SCAS feedback  $\delta_{f_a}$ . Thus the frequency response being identified  $\hat{p}/\delta_a$  is also expressed as

$$\hat{H}(s) = \frac{\hat{p}}{\delta_a}(s) = \frac{p(s)}{\delta_{lat}(s) - p(s)G_{F_p}(s)} \quad (8.2)$$

For the limiting situation when there is no noise ( $n = 0$ ), the spectral calculation of Eq. (8.1) gives us the true (i.e., unbiased) estimate, independent of the level of feedback  $G_{F_p}$ . However, when the feedback is dominated by the response to noise  $n$ , then

$$pG_{F_p} \gg \delta_{\text{lat}} \quad (8.3)$$

$$\frac{\hat{p}}{\delta_a}(s) \rightarrow \frac{-1}{G_{F_p}} \quad (8.4)$$

which is the troublesome result of identifying the inverse feedback frequency-response ( $-1/G_{F_p}$ ) in closed-loop pilot tracking tasks when there is no significant exogenous input.<sup>138</sup> The *limiting condition* of Eq. (8.4) is reached only in the case when there is no pilot input ( $\delta_{\text{lat}} = 0$ ) and the system excitation is completely caused by output noise  $n$  (e.g., effects of turbulence). However, biases in the open-loop response estimate obtained from Eq. (8.1) will occur even with nonzero pilot input ( $\delta_{\text{lat}} \neq 0$ ) whenever output noise is present; this occurs because the feedback loop causes the surface deflection to be partially correlated with the noise. The amount of bias error depends on the noise-to-signal ratio at each frequency, as shown in the following sections.

## 8.2 Quantification of Bias Errors

In practice, the actual closed-loop situation will fall somewhere between the two limiting cases of zero noise ( $n = 0$ ) or zero piloted inputs ( $\delta_{\text{lat}} = 0$ ) just discussed. By quantifying the level of bias error, we can establish testing guidelines that will ensure adequate identification accuracy.

This section presents analysis and numerical simulation results for the extraction of the bare-airframe response from closed-loop data as given by Tischler.<sup>61</sup> Consider the identification of the single-input/single-output bare-airframe roll-rate response to aileron presented in Fig. 8.1, but now formulated for convenience with a unity feedback architecture as shown in Fig. 8.2.

The elements of the block diagram are as follows:

$\delta_{\text{lat}}$  = pilot lateral stick input

$G_c$  = SCAS compensation dynamics

$p$  = measured roll rate resulting from control surface and noise inputs

$p_{\delta}$  = aircraft response to the controls

$\delta_a$  = total aileron surface deflection, resulting from piloted input and SCAS feedback

$H(s) \equiv p_{\delta}(s)/\delta_a(s)$  = bare-airframe roll-rate response

$n$  = roll-rate measurement noise and process noise reflected to the output, where the noise and external inputs from the pilot are assumed to be uncorrelated, that is to say,

$$G_{\delta_{\text{lat}}n} = 0$$

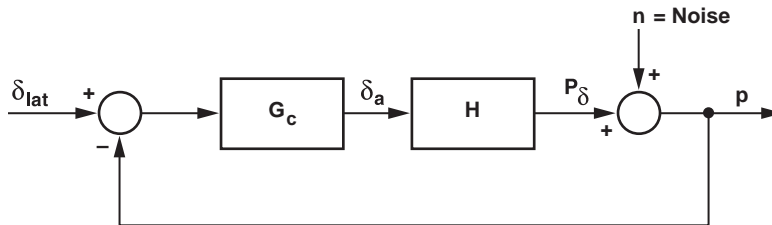


Fig. 8.2 Analysis model of closed-loop identification.

The bare-airframe frequency-response estimate  $\hat{H}$  is determined from Eq. (8.1) using the available (measured) quantities  $\delta_a$  and  $p$ . The resulting cross spectrum  $G_{\delta_a p}$  from Fig. 8.2 (Ref. 106) is

$$G_{\delta_a p} = G_{\delta_a p_\delta} + G_{\delta_a n} \quad (8.5)$$

Substituting Eq. (8.5) into Eq. (8.1),

$$\hat{H} = \frac{G_{\delta_a p_\delta} + G_{\delta_a n}}{G_{\delta_a \delta_a}} \quad (8.6)$$

which can also be expressed as

$$\hat{H} = H + \frac{G_{\delta_a n}}{G_{\delta_a \delta_a}} \quad (8.7)$$

The first term on the right side of Eq. (8.7) is the true frequency response, and the second term is a bias error. In other words,

$$\text{Estimated response} = \text{true response} + \text{bias error} \quad (8.8)$$

This result shows that the estimate is *biased* by correlation between the aileron surface and output noise signals. (This bias term is zero for *open-loop* systems because in this case the control surface and noise signals are uncorrelated, and thus  $G_{\delta_a n} = 0$ .) The undesirable correlation results from the feedback of the noise around the loop. This correlation causes  $G_{\delta_a n} \neq 0$  and results in the bias in the estimate of Eq. (8.7). The true (unbiased) bare-airframe frequency response [ $H(s) \equiv p_\delta / \delta_a(s)$ ] is identified for *stable* or *unstable bare-airframe dynamics* as long as 1) the airframe excitation  $\delta_a$  is recorded and 2) no output noise is present ( $n = 0$ ), so that  $G_{\delta_a n} = 0$ . If these conditions hold, the frequency-response estimate obtained is unbiased *regardless of the level of feedback compensation*.

For the general case that includes both noise and feedback, Tischler<sup>61</sup> expanded the relationship of Eq. (8.7) to derive the result

$$\hat{H} = H - \frac{G_{nn}}{[G_c/(1 + G_c H)][G_{\delta_{\text{lat}}\delta_{\text{lat}}} + G_{nn}]} \quad (8.9)$$

When the closed-loop system is excited *only by process noise* (i.e., no pilot inputs),  $G_{\delta_{\text{lat}}\delta_{\text{lat}}} = 0$ , and hence

$$\hat{H} = H - \frac{G_{nn}}{[G_c/(1 + G_c H)]G_{nn}} \quad (8.10)$$

This expression reduces to

$$\hat{H} = -\frac{1}{G_c} \quad (8.11)$$

which is the limiting condition of identifying the inverse compensation, as was shown in the simple analysis leading to Eq. (8.4). Clearly, the estimated frequency response  $\hat{H}$  of Eq. (8.11) bears no relation to  $H$ , the true bare-airframe response  $p/\delta_a$ . This is a general problem for bare-airframe identification from closed-loop test data, and it applies equally to time-domain and the frequency-domain methods.

### 8.3 Bias Errors Defined

The normalized bias error in the identified frequency response  $\hat{H}$  is defined as in Eq. (7.48) based on the true (unbiased) frequency response  $H$ :

$$\text{Frequency-response bias error} = \varepsilon_b(f) = \frac{\hat{H}(f) - H(f)}{H(f)} \quad (8.12)$$

Tischler<sup>61</sup> derived a simple approximation for the bias error that is accurate below crossover frequency ( $\omega < \omega_c$  and  $\omega_c$  is frequency where at which  $G_c H = 1$ ):

$$\varepsilon_b \approx \frac{-1}{S^2(\omega) + 1} \quad (8.13)$$

where

$$S^2(\omega) \equiv \frac{G_{\delta_{\text{lat}}\delta_{\text{lat}}}}{G_{nn}} \quad (8.14)$$

## 214 AIRCRAFT AND ROTORCRAFT SYSTEM IDENTIFICATION

is the excitation signal-to-noise (PSD) ratio. If we define the output noise-to-excitation signal ratio

$$\lambda_n(\omega) = \frac{G_{nn}(\omega)}{G_{\delta_{\text{lat}}\delta_{\text{lat}}}} \quad (8.15)$$

then

$$S^2(\omega) = \frac{1}{\lambda_n(\omega)} \quad (8.16)$$

and

$$\varepsilon_b \equiv \frac{-\lambda_n(\omega)}{1 + \lambda_n(\omega)} \quad (8.17)$$

which is the same form as Eq. (7.49). This result shows that the increase of bias error with feedback of output noise has the same characteristic as that caused by input measurement noise. Also, in both cases the bias error produces an underestimate of the true frequency response. As before, the noise-to-signal ratio ( $\lambda_n$  in this case) must be minimized to obtain an accurate estimate.

When the signal-to-noise level is very high ( $S \gg 1$ ), the bias error will be very small. In the limiting case of no noise ( $S \rightarrow \infty$ ), the bias error will be zero regardless of the level of feedback, as stated earlier. On the other hand, as the external excitation vanishes ( $S \rightarrow 0$ ), then  $\varepsilon_b \rightarrow -1$ , that is, the bias error is 100% and the identification of the bare-airframe frequency response  $H$  is not possible, again as stated earlier.

As a general guideline, Eq. (8.13) shows that if the signal-to-noise ratio is greater than 3, then the frequency-response bias error will be less than 0.1 that is,

*Guideline:*

$$S(\omega) > 3 \quad (8.18)$$

results in  $\varepsilon_b < 0.1$ . This reflects a bias in the magnitude of 10% (about 0.9 dB). Alternatively, by defining the frequency distribution of the noise-to-excitation signal rms ratio to be

$$\bar{\sigma}_n(\omega) \equiv \frac{1}{S(\omega)} \quad (8.19)$$

The guideline of Eq. (8.18) can be expressed as

*Guideline:*

$$\bar{\sigma}_n(\omega) < 0.33 \quad (8.20)$$

and results in  $\varepsilon_b < 0.1$ . Because a bias error of less than 10% is generally acceptable, this leads to the conclusion that the external input amplitude, whether generated by a pilot or by computer, must exceed the noise amplitude by at least a factor of three. The approximate analytical solution is seen to be independent of the level of feedback gain  $G_c$ .

## 8.4 Numerical Study of Identification Results Obtained Under Closed-Loop Conditions

In this section, the closed-loop identification concepts will be demonstrated using a numerical simulation based on the XV-15 dynamics in hover. Referring to the block diagram in Fig. 8.2, the vehicle dynamics are approximated by

$$H(s) = \frac{e^{-0.005s}}{s - 0.5} \quad (8.21)$$

This system has unstable dynamics, with a right half-plane pole at  $s = 0.5$  rad/s and a small time delay ( $\tau = 5$  ms). For this example, two very simple control system configurations will be considered. The first case is for a control system with a moderate gain, representative of the XV-15 tilt-rotor SCAS:

$$G_c = K = 3.0 \text{ deg/deg/s} \quad (8.22)$$

The second case is representative of a high-gain SCAS:

$$G_c = K = 6.5 \text{ deg/deg/s} \quad (8.23)$$

Both feedback gains produce a stable closed-loop roll-rate response:

$$\frac{p}{\delta_{\text{lat}}}(s) = \frac{KH(s)}{1 + KH(s)} \quad (8.24)$$

and  $\omega_c = K$ . For the purposes of calculating the analytical result  $p/\delta_{\text{lat}}$  from Eq. (8.24), the time delay in Eq. (8.21) is represented by a Padé approximation.<sup>104</sup>

In the following analysis based on a numerical simulation, the identification results for the closed-loop and bare-airframe responses are compared for the two gain levels and checked against the analytical results of Eqs. (8.21) and (8.24), respectively. Initially, the analysis will be performed assuming that no noise is present. Then the effect of low and high noise ratios on the bare-airframe identification will be examined.

#### 8.4.1 Identification of Closed-Loop Response $p/\delta_{\text{lat}}$ and Bare-Airframe Response $p/\delta_a$ for Noise-Free Case ( $n = 0$ )

Figure 8.3 shows the identification results for the (stable) closed-loop response ( $p/\delta_{\text{lat}}$  of Fig. 8.2) with moderate feedback gain ( $K = 3.0$ ) and no noise ( $n = 0$ ). The identified closed-loop frequency response matches the analytical (true response) as obtained from Eqs. (8.22) and (8.24). The coherence function is very nearly unity, indicating excellent identification accuracy, as expected for this simple linear case with no noise.

Next, the (unstable) bare-airframe response  $p/\delta_a$  of Fig. 8.2 is identified [using Eq. (8.1)] under the closed-loop test conditions with the low-gain control system and no noise. In this case, the system is still excited via the exogenous sweep input  $\delta_{\text{lat}}$ , but the identification is completed using the surface actuator  $\delta_a$ .

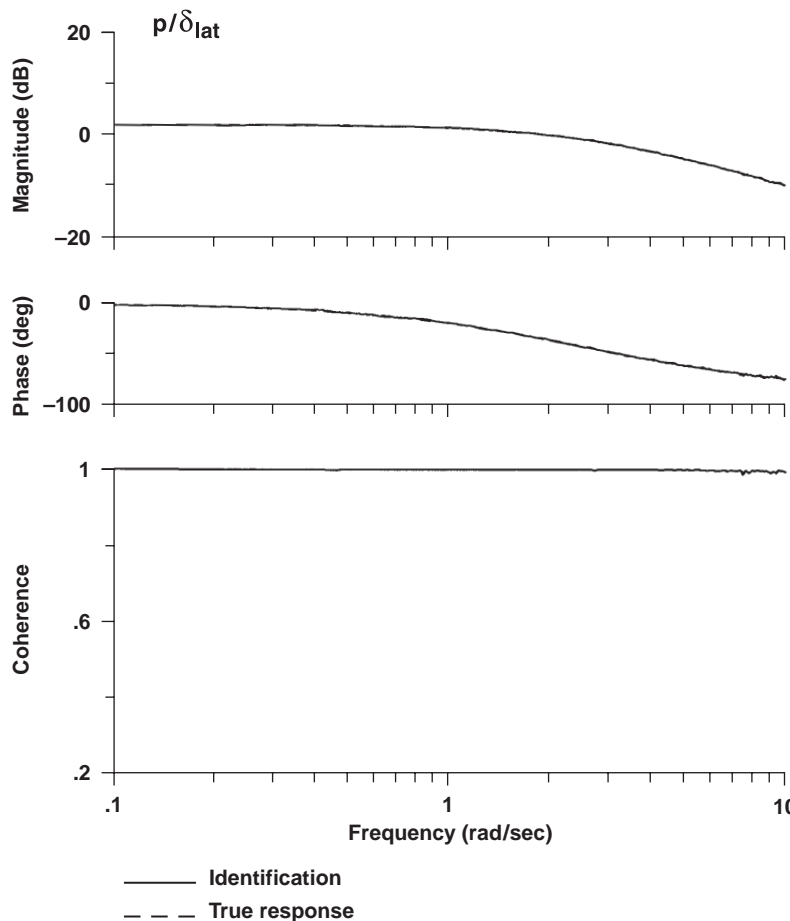


Fig. 8.3 Verification of closed-loop response ( $K = 3.0$ , no noise).

as the input. The analytical (true) response of Eq. (8.21) plotted in Fig. 8.4 shows a phase shift of (positive) 45 deg at the break frequency ( $\omega = 0.5$  rad/s), as expected for the unstable response. The identification result essentially matches that of the true response. The coherence remains very high, as expected, indicating excellent identification accuracy for the linear (and unstable) response. This demonstrates again that the frequency response for the unstable bare-airframe system can indeed be accurately identified from a closed-loop experiment. The SCAS (or piloted) feedback ensures that the input  $\delta_a$  and output  $p$  remain

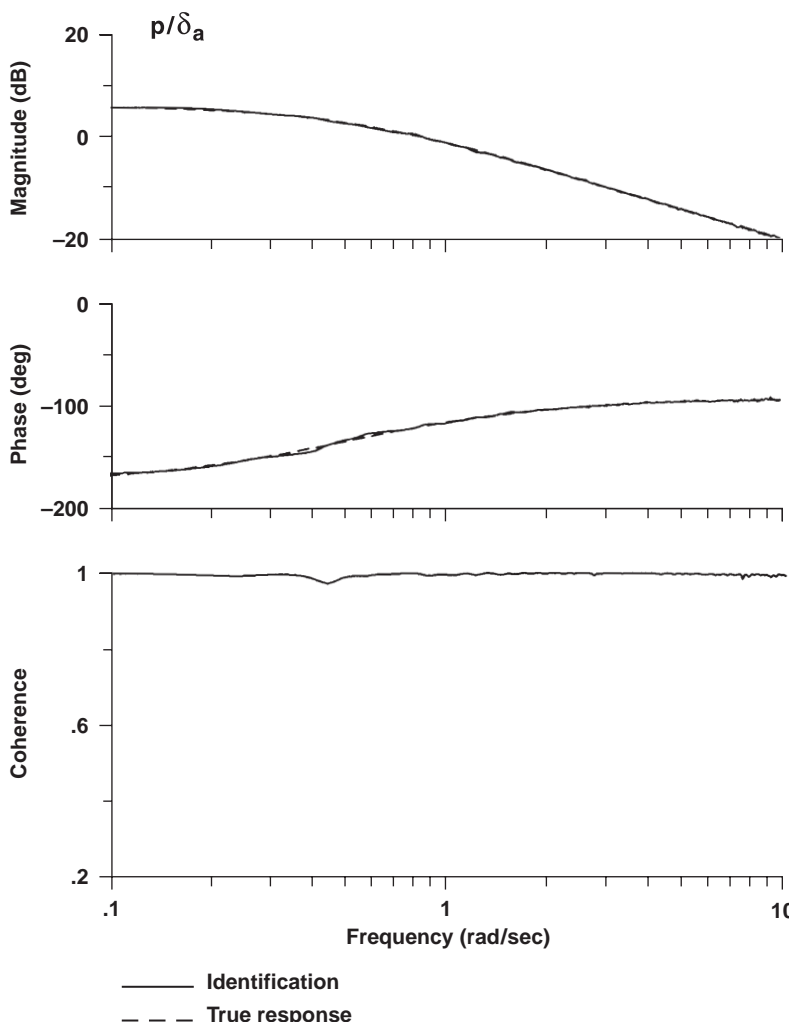


Fig. 8.4 Identification of unstable bare airframe ( $K = 3.0$ , no noise).

bounded. Therefore, the Dirichlet condition (7.11) is met for the desired frequency-response calculation.

Figure 8.5 shows the identification of the (stable) closed-loop response  $p/\delta_{\text{lat}}$  for the high-gain case ( $K = 6.5$ ), but still with no noise ( $n = 0$ ). As was the case for the moderate-gain configuration, the identified closed-loop response matches the true response [Eqs. (8.23) and (8.24)] exactly.

Finally, the identification of the (unstable) bare-airframe response is repeated, this time using the high-gain feedback ( $K = 6.5$ ) control system, but still with no noise ( $n = 0$ ). As shown in Fig. 8.6, there continues to be nearly perfect agreement between the identified and the true response of Eq. (8.21). The coherence also remains very high. There is no significant difference in the bare-airframe identification results obtained for the moderate-gain compared to the high-gain

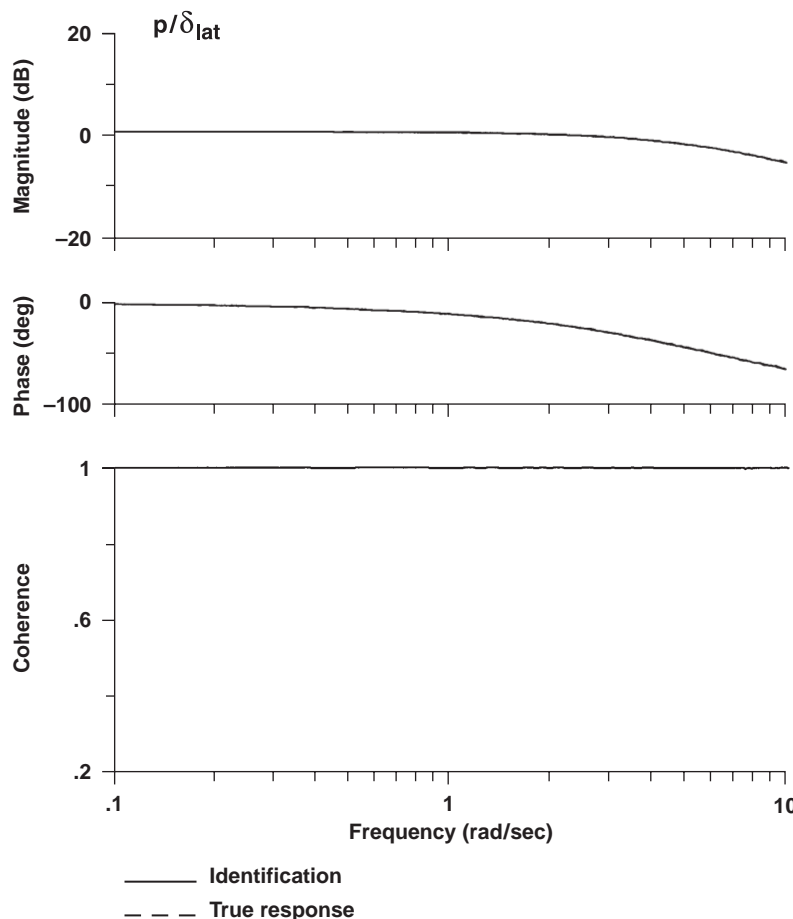


Fig. 8.5 Verification of closed-loop response ( $K = 6.5$ , no noise).

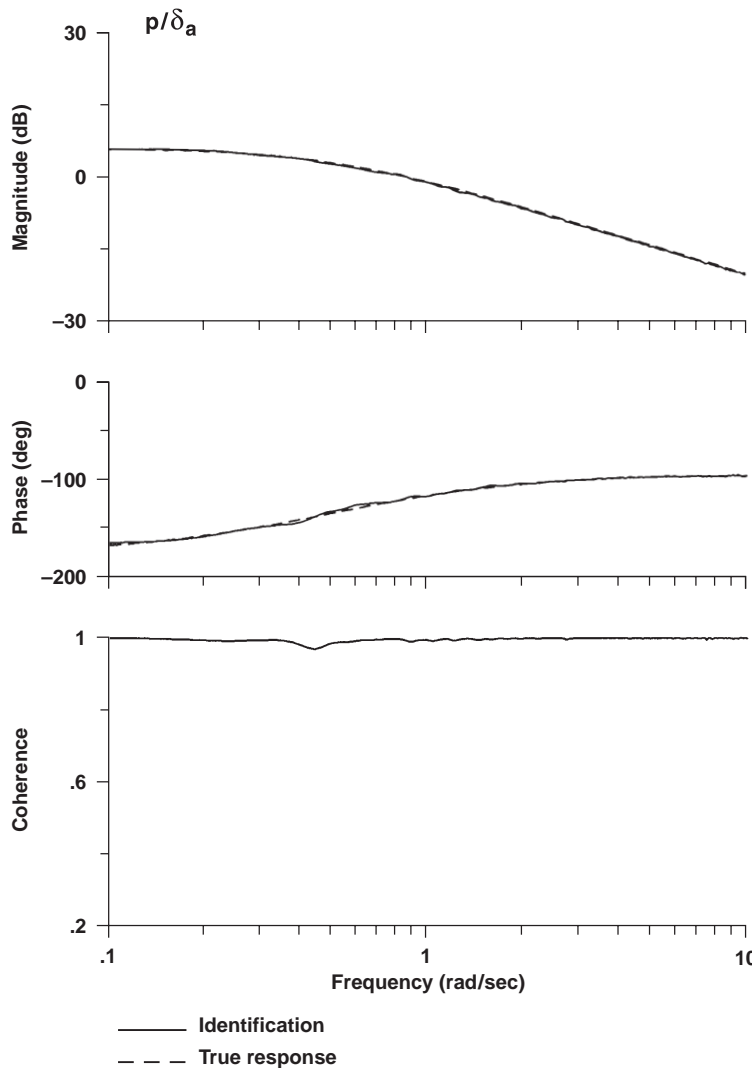


Fig. 8.6 Identification of bare airframe ( $K = 6.5$ , no noise).

feedback systems (Fig. 8.4 vs Fig. 8.6), in agreement with the discussion of Sec. 8.2.

Summarizing the results of this section, it is clear that for the case without noise the unstable bare-airframe response  $p/\delta_a$  can be accurately extracted from data obtained under closed-loop test conditions. The only requirements are that the feedback stabilizes the test configuration (to satisfy the Dirichlet condition) and that the control surface deflections (bare-airframe inputs) are recorded. Further, the level of feedback gain has no significant influence on the result.

### 8.4.2 Effect of Noise on Identification of Bare-Airframe Response Under Closed-Loop Conditions

So far, we have demonstrated the identification of the bare-airframe response under closed-loop test conditions, but with no external noise. Next, we will examine the effect of noise ( $n$ , in Fig. 8.2) on the bare-airframe identification results. Figure 8.7 shows the effect of relatively low noise levels for the moderate-feedback-gain case ( $K = 3$ ). The rms noise levels  $\sigma_n$  are normalized by the pilot

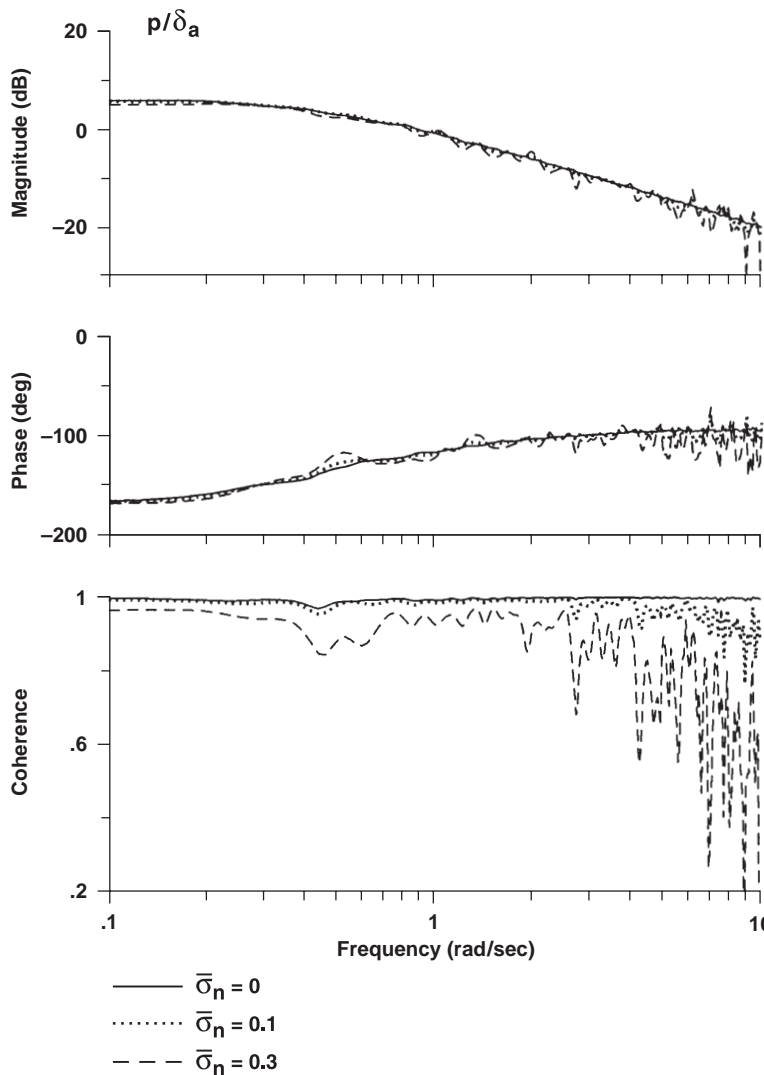


Fig. 8.7 Effect of low noise ratios on bare-airframe identification ( $K = 3.0$ ).

excitation rms levels  $\sigma_{\text{lat}}$  to obtain the noise-to-excitation signal rms ratio introduced in Eq. (8.19):

$$\bar{\sigma}_n = \frac{\sigma_n}{\sigma_{\text{lat}}} \quad (8.25)$$

Three noise levels are shown in Fig. 8.7:  $\bar{\sigma}_n = 0$  (i.e., no noise, repeated from Fig. 8.4 for comparison purposes),  $\bar{\sigma}_n = 0.1$ , and  $\bar{\sigma}_n = 0.3$ .

As shown earlier in Fig. 8.4, the solid line corresponds to no noise and reflects an accurate identification of the bare-airframe response. When the noise level rises to 10%, some scatter or *random error* is apparent. However, on average the identification tracks the true response, so that there is no significant *bias error*. There is a loss in coherence, reflecting the increased noise-to-signal ratio [from Eq. (7.52)] and associated random error [from Eq. (7.55)].

For the 30% noise level ( $\bar{\sigma}_n = 0.3$ ), the random error is now considerable, as reflected in the oscillations in magnitude and phase. There is an associated significant drop in coherence. Note, however, that the bias error remains small [which can be seen only a slight underestimate in the response in accordance with Eq. (8.13)]. So on average an accurate estimate of the response is still obtained. This case can be considered as the maximum acceptable noise level, and it is in good agreement with the upper-limit guideline Eq. (8.20) obtained from the earlier theoretical analysis.

Figure 8.8 shows the effect of higher noise ratios on the identification of the bare airframe under closed-loop conditions. The solid line still represents no noise, but the other two lines correspond to  $\bar{\sigma}_n = 1$  and 10. In the latter case there is nearly total noise and no piloted excitation.

For the case of  $\bar{\sigma}_n = 1$ , there is increased random error, as reflected in the large oscillation in the frequency-response plots and the considerable oscillation in the coherence function. More importantly, major differences are now seen between the average identified response and the true response. Thus the *bias error* has grown considerably. For frequencies below crossover (i.e.,  $\omega < 3$ ), there is a significant underestimation that becomes more pronounced with decreasing excitation signal-to-noise ratio as predicted [Eq. (8.13)]. These results clearly demonstrate a breakdown in the bare-airframe identification under closed-loop conditions.

The plots corresponding to the high noise case of  $\bar{\sigma}_n = 10$  demonstrate what happens close to the limiting condition of no piloted excitation signal, when the noise-to-signal ratio becomes infinite. Note that the magnitude and the phase plots have both become quite flat. The magnitude for this case is approximately  $20 \log(\frac{1}{3})$  with a corresponding constant phase of  $-180$  deg, in agreement with the limiting condition  $\hat{H} = -1/G_c$  of Eq. (8.11). What is quite unsettling is that the coherence is now close to unity, which could create the false impression that the bare-airframe identification was in fact quite accurate, and that the identified "aircraft dynamics" correspond to those of a simple constant gain system. Clearly, this identification result does not reflect the bare-airframe response at all.

For a physical system response, the frequency-response plots associated with the linear and angular velocities of the aircraft fuselage should show some roll-off

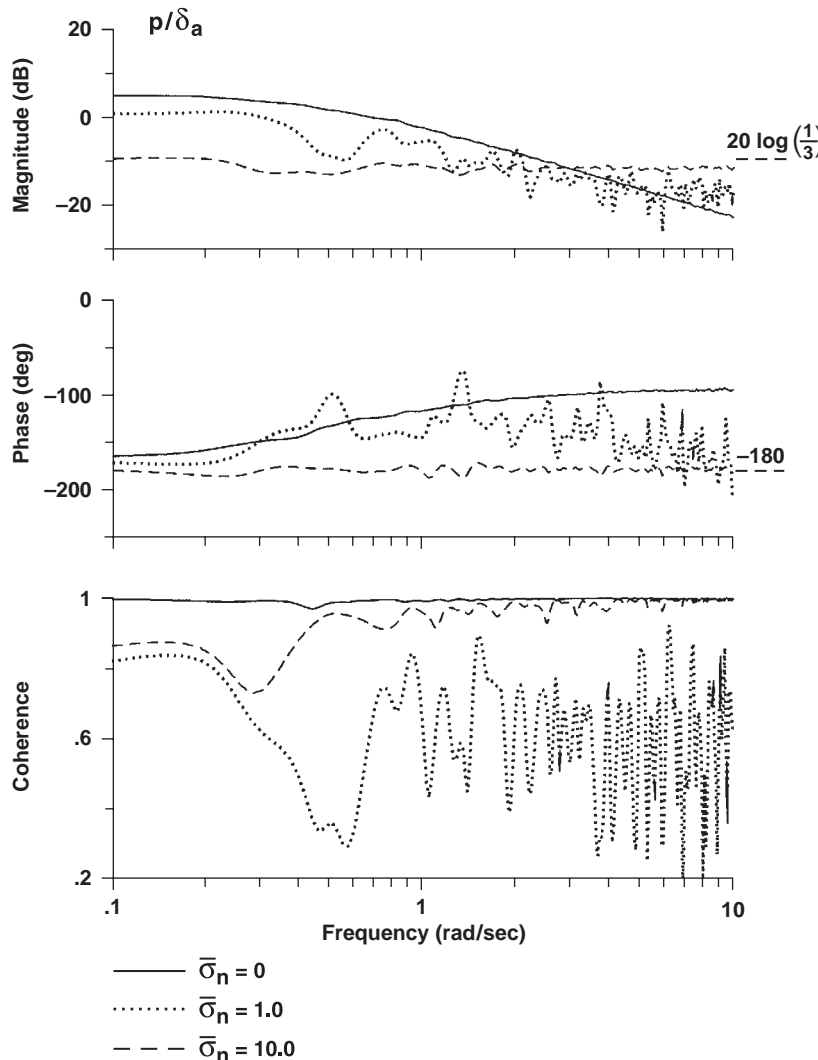


Fig. 8.8 Effect of high noise ratios on bare-airframe identification ( $K = 3.0$ ).

or low-pass characteristic, such as that seen, for example, in the asymptotic response of Eq. (7.22) and illustrated in Fig. 7.1. When the magnitude and phase curves are flat over a wide frequency range and the phase remains at 0 deg or -180 deg, coupled with an unexpectedly high coherence value of the function, a significant noise feedback correlation problem in the closed-loop test setup should be suspected. When these telltale signs appear, it is likely that the bare-airframe identification will contain serious bias errors.

#### 8.4.3 Quantifying the Bias Errors in Parametric Identification

Parametric models (transfer-function or state-space representations), often the ultimate goal of the system-identification process, are determined from the frequency responses. Therefore bias errors that occur in the identified frequency response will also be manifested as bias errors in the identified parametric models. For transfer-function modeling (Chapter 11), the identification structure appropriate to the present example is

$$H(s) = \frac{ke^{-\tau s}}{s + a} \quad (8.26)$$

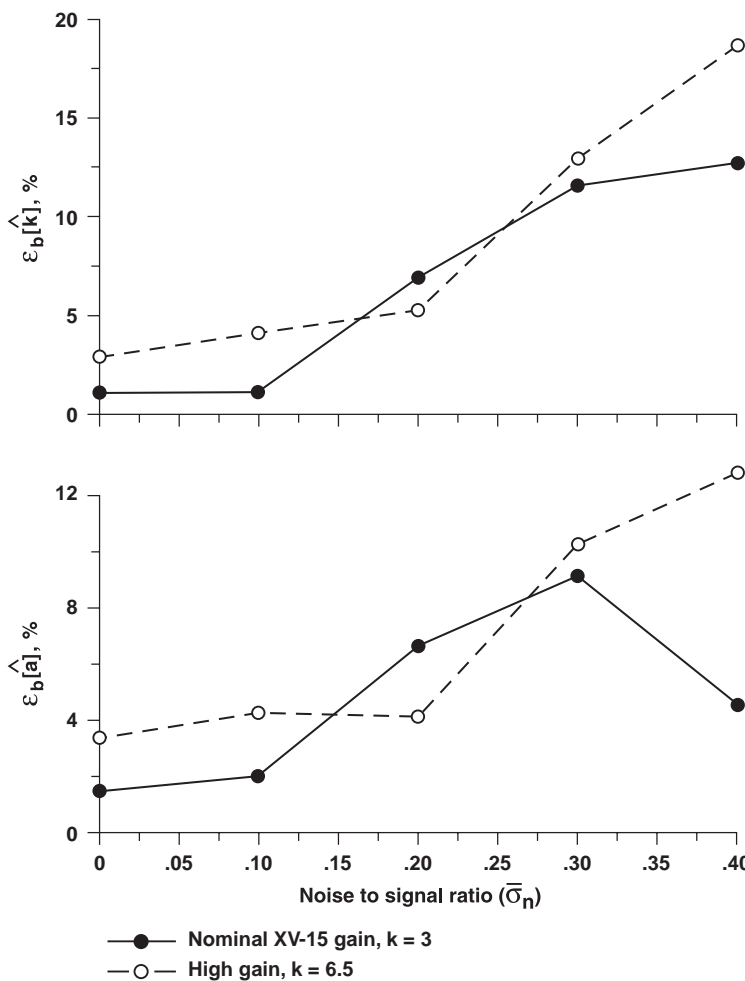


Fig. 8.9 Bias errors in identification of model parameters ( $K, a$ ).

where a bias-free model extraction would return the true response of Eq. (8.21):

$$k_{\text{true}} = 1, \quad a_{\text{true}} = -0.5, \quad \tau_{\text{true}} = 0.005 \quad (8.27)$$

Transfer-function models can be determined for each of the bare-airframe frequency responses of Figs. 8.7 and 8.8 using NAVFIT (Chapter 11). The normalized bias error in the identified value of the gain  $\hat{k}$  is then defined as

$$\varepsilon_b[\hat{k}] = \left| \frac{\hat{k} - k_{\text{true}}}{k_{\text{true}}} \right| \quad (8.28)$$

and similarly for the other parameters. The normalized errors for the transfer-function gain  $\varepsilon_b[\hat{k}]$  and modal frequency  $\varepsilon_b[\hat{a}]$  are plotted in Fig. 8.9 as a function of the noise-to-signal rms ratio  $\bar{\sigma}_n$ . The small bias errors for no noise are associated with the accumulated errors of the numerical simulation and overall identification procedure. The increase in bias error for the high-gain case at low noise levels ( $\bar{\sigma}_n < 0.1$ ) probably results from integration errors in generating the simulation data, which become more significant at the higher closed-loop natural frequencies (for a fixed time step). Restricting the maximum bias error (gain and modal frequency) to within 10% indicates a requirement for noise-to-excitation signal ratios limits of  $\bar{\sigma}_n < 0.3$ , which is in good agreement with the theoretical results of Eq. (8.20). The trends are generally independent of gain level (at least for noise up to 30%), which is also in agreement with the earlier analytical results.

## 8.5 Flight-Test Implications

We now consider how the preceding results can be applied in practice. Suppose a flight test is carried out on a day with moderate wind gusts that cause the aircraft in a trim state to oscillate in roll with an amplitude of about  $\pm 1$  deg/s. This oscillation can be thought of as the roll-rate noise component. To ensure that the bias error will be acceptably small, the response to the piloted sweep inputs should exceed those of the noise inputs by at least a factor of three, resulting in a forced response of  $\pm 3$  deg/s. In practical terms, this will not represent a difficult requirement because for a typical sweep the response amplitudes are about  $\pm 10$  deg/s (Sec. 5.5). When winds are light, as required for frequency-sweep testing (Sec. 5.7), the trim variations must remain within the 1/3 guidelines of  $\pm 3$  deg/s.

On the other hand, if the winds are considered sizeable and gusty, the aircraft might already be oscillating considerably (e.g.,  $\pm 5$  deg/s) just because of the turbulence. The SCAS (or pilot) will provide feedback proportional to the gust disturbances, which produces correlated noise that can result in significant bias errors. In the limiting case of large disturbance inputs and small piloted excitation inputs, the frequency response that is identified will approach the inverse feedback response of Eq. (8.11). In general, it is advantageous to disengage as many SCAS channels as possible for bare-airframe identification testing, as was also recommended in Sec. 5.8. While conducting the sweep, the piloted regulation of response caused by turbulence is a secondary, lower-frequency task (Sec. 5.9) and so does not generally introduce a high degree of correlation to turbulence inputs.

Therefore piloted feedback is generally much less problematic than the true SCAS feedbacks as considered herein.

## 8.6 Identification of Unstable Inverted Pendulum Dynamics

The unstable dynamics of the inverted pendulum with rate damping only  $\theta/\bar{M}_{\text{inv}}$  were identified using the simulation data from the stable closed-loop system of Fig. 3.2. Here the sweep input  $\bar{M}_{\text{ext}}$  excites the system, but the input for identification is the time history of  $\bar{M}_{\text{inv}}$ . As seen in Fig. 8.10, there is perfect agreement between the identified response (15-s window) and theory [Eq. (3.8)]. This result again validates the concept of identifying unstable system dynamics under closed-loop test conditions. The effect of output noise on these results is evaluated in **Problem 8.5**.

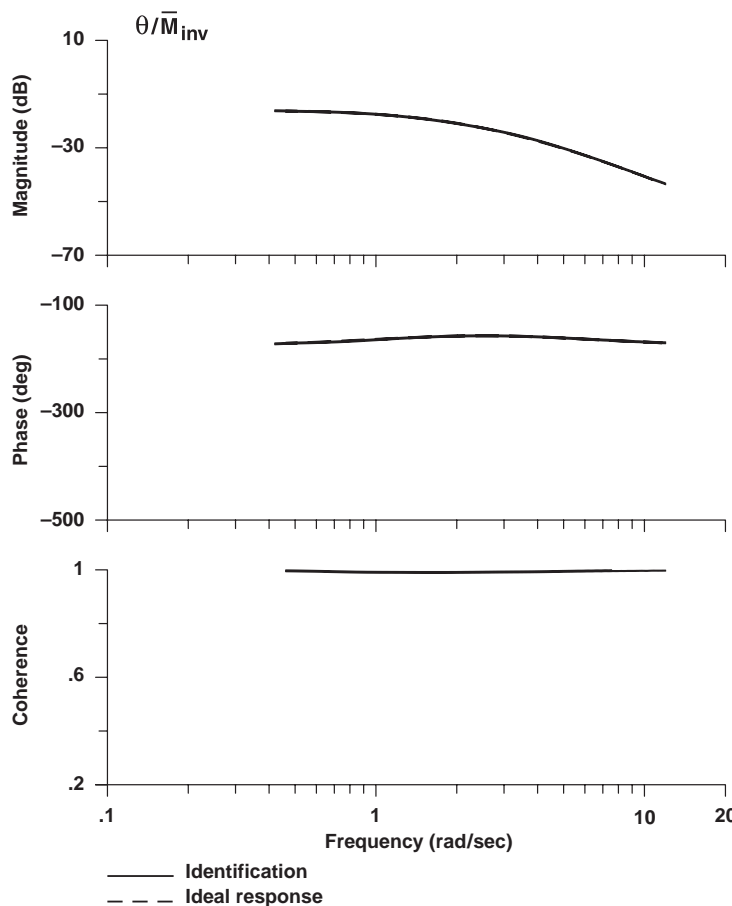


Fig. 8.10 Comparison between identified and ideal responses for (unstable) inverted pendulum.

## 8.7 Conclusions

This chapter can be summarized with the following conclusions:

- 1) The bare-airframe frequency response for stable or unstable system dynamics can be accurately extracted from data obtained under closed-loop test conditions when no noise is present. The only requirements are that the feedback (piloted or SCAS) stabilizes the test configuration (to satisfy the Dirichlet condition) and that the control surface deflections (bare-airframe inputs) are recorded. Further, under these conditions the level of feedback gain has no significant influence on the accuracy of the result.
- 2) Bias errors will arise in the identification of the bare-airframe response under closed-loop test conditions when noise is present, but they do not become important until noise ratios reach  $\bar{\sigma}_n(\omega) \geq 0.33$ . The coherence is a reliable indicator of bare-airframe identification accuracy for noise levels in this range.
- 3) Be aware of the potential for large bias errors caused by the correlated feedback of noise. This situation is often detected visually when the identified response approaches  $\hat{H} = -1/G_c$  rather than the expected low-pass-type characteristic of the aircraft rigid-body response.

## Problems

### *Identification of an unstable system from closed-loop frequency sweep tests*

**8.1** Simulate the response of the inverted pendulum system with feedback stabilization using the configuration parameters:  $\bar{K} = 13$ ,  $\bar{C} = 1.2$ , and  $l = 4$ . Generate simulation time histories using a sweep excitation with appropriate minimum and maximum frequencies, making sure to store the channel data for  $\bar{M}_{\text{inv}}$ ,  $\bar{M}_{\text{ext}}$ , and  $\theta$ .

**8.2** Identify the closed-loop (stable) response  $\theta/\bar{M}_{\text{ext}}$  from the time-history data saved in **Problem 8.1**, and check the result against the analytical transfer function [Eq. (3.5)]. Process the data with 35-, 25-, and 20-s windows.

**8.3** Identify the frequency response for the unstable subsystem associated with the inverted pendulum and rate damping  $\theta/\bar{M}_{\text{inv}}$  from the time-history data stored in **Problem 8.1**. Process the data with 35-, 25-, and 20-s windows. If you did not already know that the subsystem was unstable, how could you determine that from a visual inspection of the identification result?

**8.4** Compare the identified response  $\theta/\bar{M}_{\text{inv}}$  from **Problem 8.3** with the analytical result.

**8.5** Now, we will introduce varying levels of process noise into the pendulum simulation and look at the effect on the identified frequency response  $\theta/\bar{M}_{\text{inv}}$ . Continue using the pendulum configuration parameters given in **Problem 8.1** and insert process noise into the system as shown in Fig. P8.5. Overlay these identified responses (35-s window) with the ideal response obtained in **Problem 8.3**. How does the presence of process noise affect the identification?

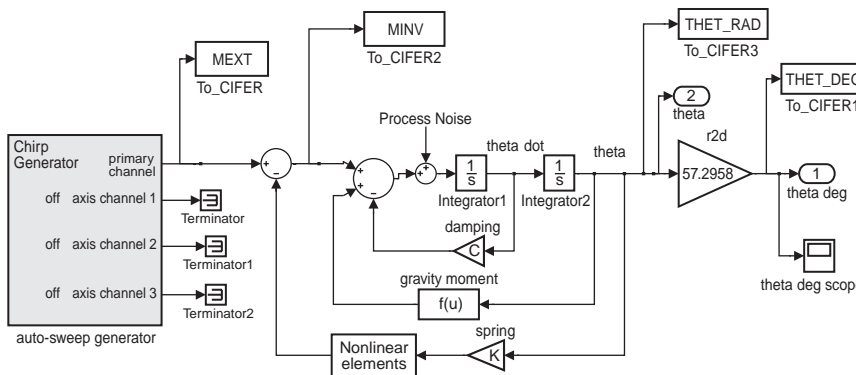


Fig. P8.5 Process noise for unstable pendulum problem.

**8.6** Derive Eq. (8.13). Hint: Start with Eq. (8.6), and use the identities  $G_{\delta_a n} = G_{n \delta_a}^*$ , where  $*$  represents the complex conjugate and  $G_{n \delta_a} = G_{nn}(\delta_a/n)$ . Also note that for frequencies  $\omega < \omega_c$ , we can approximate  $G_c H / (1 + G_c H) \approx 1$ .

**8.7** Introduce process noise with a very high noise-to-signal ratio in the pendulum simulation (continuing with configuration parameters given in **Problem 8.1**). Add the noise to the attitude feedback as shown in Fig. P8.7. Does  $\theta/\bar{M}_{\text{inv}} = -1/G_{F_p}$  as Eq. (8.4) predicts?

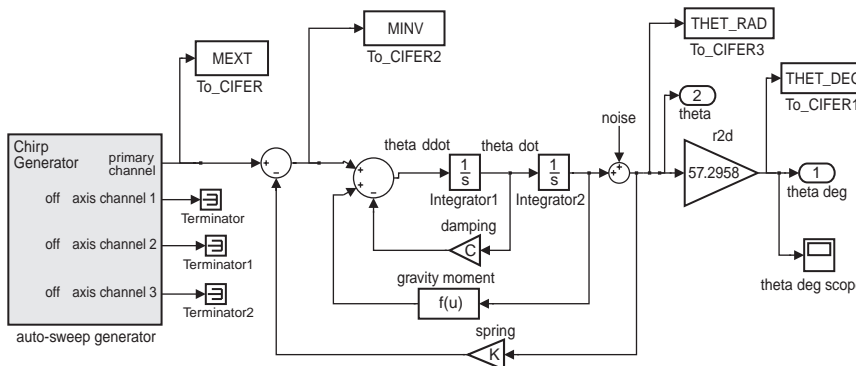


Fig. P8.7 Process noise reflected to output.

**8.8** Look at the effect of nonlinearity on system identification for  $\theta/\bar{M}_{\text{inv}}$  by including (a) spring limiting of  $\pm 3.8 \text{ rad/s}^2$ , (b) spring backlash with deadband width of  $0.5 \text{ rad/s}^2$ , and (c) large-amplitude frequency sweeps of  $\bar{M}_{\text{ext}} = 6 \text{ rad/s}^2$  in your pendulum simulation. Use the pendulum configuration parameters given in **Problem 8.1** and the frequency-sweep generator specifications from **Problem 5.3**. Figure P8.5 depicts how nonlinear elements should be introduced

into the simulation. Coplot these frequency responses (35-s window) with the ideal unstable pendulum frequency response. What is the effect of the nonlinear elements on the magnitude, phase, and coherence of the identified frequency responses? How does this compare to the closed-loop (stable) pendulum case of **Problem 7.15**

*Identification of broken-loop frequency-responses*

**8.9** Determine the broken-loop response ( $f/e$ ) of the pendulum simulation (using the configuration parameters given in **Problem 8.1**). Use the signal labeled “E” in Fig. P8.9. as the input to the broken-loop response, and use the signal labeled “F” as the output of the broken-loop response. Use utility 19 to create a hard copy of the broken-loop response.

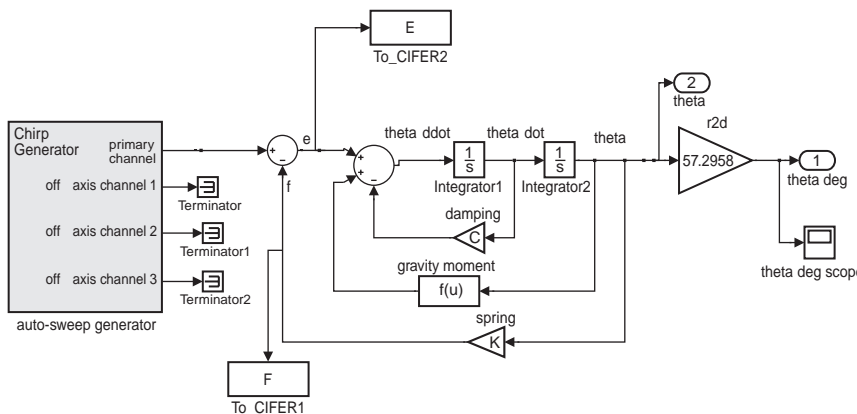


**Fig. P8.9** Pendulum broken-loop exercise.

**8.10** Use CIFER utility 8 to determine the phase margin of the pendulum broken-loop frequency response identified in **Problem 8.9**.

## 9

## Multi-Input Identification Techniques

The frequency-response identification techniques of Chapters 7 and 8 were limited to the consideration of single-input/single-output (SISO) systems (e.g.,  $p/\delta_{\text{lat}}$ ). Of course, aircraft systems and subsystems generally consist of several inputs and outputs, and generally more than one input is present during the test maneuvers. For example, whereas a typical flight-test record can be characterized as a lateral stick frequency sweep, there will be secondary inputs in the remaining axes as supplied by the pilot and/or SCAS to maintain a roughly constant reference condition (Sec. 5.9). The response will be influenced by both the primary and secondary inputs. So we need techniques that are applicable to the identification of multi-input/multi-output (MIMO) systems from flight-test records with multiple channels of excitation.

In this chapter, we will see that the starting point for MIMO system identification is the single-input/single-output (SISO) frequency-response identification method of Chapter 7. The SISO analysis is first conducted on the pair-wise combinations of inputs and outputs. Additional procedures are then necessary to *condition*, or correct, these frequency responses to take into account the effects of multiple partially correlated inputs. These procedures are referred to as *multi-input identification techniques*. The results of the multi-input identification are the *conditioned frequency responses and partial coherence* shown in the system-identification flowchart (Fig. 2.1). Bendat and Piersol<sup>106</sup> provide an excellent derivation and physical insight into this conditioning process and the relationship of the conditional spectral quantities to the SISO or *ordinary* equivalents. Twisdale and Ashurst<sup>42</sup> implemented the multi-input frequency-response identification for aircraft in the FRA tool of the Air Force Flight Test Center. The reference provides a succinct explanation of the key multi-input identification concepts and insightful flight-test examples. The CIFER<sup>®</sup> module for multi-input frequency-response determination is MISOSA (Multiple-Input/Single-Output System Analysis), as shown in Fig. 4.1. The CIFER<sup>®</sup> algorithm is based on the compact matrix formulation of Otnes and Enochson.<sup>108</sup>

This chapter covers the following topics: reasons to be concerned about the presence of multiple inputs, analytical solution for identification with two inputs, example with two inputs using the XV-15 flight data, general matrix solution for arbitrary number of inputs, multiple-input identification in CIFER<sup>®</sup> using MISOSA, and additional flight-test examples.

### 9.1 Multi-Input Terminology

This section defines some basic terminology in order to facilitate the discussion of multi-input identification. Consider the example of an aileron frequency-sweep test of a fixed-wing aircraft in cruise. For simplicity, we consider only the

lateral-directional controls and responses. The aileron  $\delta_a$  is referred to as the *primary control* for these sweep tests. Rudder control inputs are associated with maintaining a relatively constant reference condition during the sweep (Sec. 5.9), and so the rudder  $\delta_r$  is therefore referred to as the *secondary control*.

We conduct the aileron sweep  $\delta_a$  to obtain the lateral-directional responses to aileron inputs ( $p/\delta_a$ ,  $r/\delta_a$ ,  $a_y/\delta_a$ ,  $\beta/\delta_a$ ). Aileron inputs mostly produce a rolling moment (about the fuselage  $x$  axis, Fig. 6.3), so that the *primary* response of the aircraft is in roll rate  $p$ , which is a motion also about the fuselage  $x$  axis (Fig. 6.3). Therefore we refer to  $p/\delta_a$  as the *on-axis* response. If the aerodynamic center of the vertical tail is located above the c.g., an aircraft roll rate will induce a yawing moment (about the fuselage  $z$  axis, Fig. 6.3). In addition, the aileron deflection causes a differential drag on the wing, which also contributes a yawing moment. These yawing moments will cause associated responses in yaw rate  $r$ , lateral accelerometer  $a_y$ , and sideslip  $\beta$ . Because these responses are all about axes other than that of the primary roll control moment ( $x$  axis), we refer to  $r/\delta_a$ ,  $a_y/\delta_a$ , and  $\beta/\delta_a$  as *off-axis* responses. In this case, we describe the aircraft as exhibiting *dynamic coupling* because a moment input about one axis produces responses about other axes.

## 9.2 Need for Multiple-Input Identification Technique

System-identification analysis from aircraft data nearly always involves consideration of multiple inputs. Flight-test data, whether obtained using a piloted input or an automated excitation signal, usually involve both primary and secondary controls. Similarly, data from off-line simulation models usually involve inputs in all control axes because of the need to artificially stabilize the system about the reference trim condition (Sec. 5.11.1).

The presence of multiple inputs, however, does not necessarily mean that the usual single-input/single-output identification procedures will be inadequate. The SISO solution explained in Sec. 7.7 [Eq. (7.37)] is satisfactory for multi-input/multi-output system identification if *at least one* of the following conditions is satisfied:

- 1) Interaxis dynamic coupling is negligible.
- 2) Secondary inputs are uncorrelated with the primary input

### 9.2.1 *Interaxis Dynamic Coupling (Condition 1)*

The influence of the secondary inputs on the identification of the *off-axis response* is generally very significant. For example, as will be demonstrated in Sec. 9.5, identification of the *off-axis bare-airframe response*  $p/\delta_r$  from rudder frequency-sweep  $\delta_r$  data is distorted by the presence of secondary aileron inputs  $\delta_a$  if they are at least partially correlated with the primary (rudder) input. Yet the identification of the *on-axis bare-airframe response*  $r/\delta_r$  from the same sweep data will be much less influenced by the secondary inputs. The influence of coupling is further reduced for the identification of the *on-axis closed-loop (SCAS-on) response* (e.g.,  $p/\delta_{lat}$  of Fig. 7.5). These last two cases illustrate situations where the interaxis coupling is low (condition 1) and the SISO solution (for the on-axis response) is generally satisfactory.

### 9.2.2 Control Input Correlation (Condition 2)

When the secondary inputs are essentially uncorrelated with the primary (sweep) input, the SISO solution is also applicable to MIMO system identification. Consider again the case of SCAS-off frequency-sweep testing of the fixed-wing directional response. Using the flight-test technique described in Sec. 5.9, the pilot might be responsible solely for the primary input (rudder  $\delta_r$ ), while the copilot (or pilot) pulses the secondary controls (i.e., aileron  $\delta_a$  and elevator  $\delta_e$ ) as necessary to maintain a constant reference condition. This renders the secondary inputs uncorrelated with the primary sweep input, thereby satisfying condition 2. In this case, the SISO solution is thus applicable to the determination from the rudder-sweep record of each of the responses to rudder inputs, namely (for cruise),  $p/\delta_r$ ,  $\beta/\delta_r$ ,  $r/\delta_r$ , and  $a_y/\delta_r$ .

### 9.2.3 General Considerations

When the closed-loop response is to be identified (e.g.,  $p/\delta_{lat}$ ), conditions 1 and 2 can both be largely satisfied. By design, the SCAS systems for modern flight vehicles are intended to suppress off-axis response coupling and achieve diagonalized closed-loop response to control inputs. The requirement for piloted regulation in the off axes is also minimized by the high-bandwidth feedback loops that suppress the response to disturbances. Therefore the SISO solution is often satisfactory for the identification of the *closed-loop* on-axis response needed for bandwidth and phase-delay analysis of handling qualities (Sec. 7.14.3). Handling-qualities requirements for the on-axis responses based on frequency-response characterizations are given in ADS-33<sup>4</sup> for rotorcraft and MIL-STD-1797<sup>5</sup> for fixed-wing aircraft. Although these documents do not refer to multi-input flight-data analysis methods, the solution method presented herein should be used to ensure an accurate identification even though the effects of secondary inputs are less for the on-axis responses.

In the case of MIMO identification of the coupled *bare-airframe* dynamics, the dynamics generally exhibit interaxis coupling for some input/output combinations *and* the inputs are partially correlated. In other words, neither condition 1 nor condition 2 is satisfied. As demonstrated in the next section, the SISO solution for such cases can give a very inaccurate identification result, so that the multi-input identification methods of this chapter are required to achieve a correct solution. Fortunately, the multi-input analysis is completed very rapidly, and there is usually no harm in performing the identification using MIMO solution conditioning. As already mentioned, when at least one of the two conditions apply, the multi-input solution simply reduces to the SISO solution without modification. Thus it is generally recommended to always run the MIMO solution rather than trying to decide in advance whether the conditions actually require its use.

## 9.3 Simple Two-Input Example

In this section, a simple two-input/one-output identification problem is presented. This simple case can be solved analytically, thereby illustrating the relationship to the SISO solution and the limiting conditions (i.e., conditions 1 and 2) already discussed.

Consider the simple dynamic model for the bare-airframe roll-rate response  $p$  to rudder  $\delta_r$  and aileron  $\delta_a$  inputs, as shown in the schematic of Fig. 9.1. The aircraft dynamics are represented by two (unknown) transfer functions  $p/\delta_r$  and  $p/\delta_a$ , whose combined response produces the aircraft roll rate  $p$ . The two control inputs present during the tests  $\delta_r$  and  $\delta_a$  produce the measured roll-rate response  $p$ . The schematic also includes a crossfeed path between the two inputs  $K_{CF}$ . This crossfeed can be a model of the pilot strategy for using some secondary aileron input to maintain an average zero-roll-rate reference condition during the rudder sweeps, or it can be an actual block in a SCAS, or both. So this transfer function  $K_{CF}$ , which is assumed to be composed of unknown dynamics, can range in complexity from a simple constant to a higher-order dynamic function of frequency owing to a combination of SCAS/pilot feedbacks and crossfeeds.

Following the flight-testing procedures of Chapter 5, a set of rudder frequency sweeps  $\delta_r$  will be conducted for the purpose of identifying the off-axis frequency response  $p/\delta_r$ , and then a set of aileron sweeps  $\delta_a$  will be conducted for the purpose of identifying the on-axis frequency response  $p/\delta_a$ . The analysis that follows addresses the identification of the off-axis response  $p/\delta_r$  from the rudder-sweep flight data.

As shown in the block diagram for this system (Fig. 9.1), the (secondary) aileron input can be considered as being made up of two components:

$$\delta_a = \delta_{a_C} + \delta_{a_{UC}} \quad (9.1)$$

where  $\delta_{a_C}$  is the component of the aileron input that is *correlated* with the rudder input and  $\delta_{a_{UC}}$  is the component of the aileron input that is *uncorrelated* with the rudder. First, the results of using the SISO solution to identify  $p/\delta_r$  are illustrated. In this case, the influence of  $K_{CF}$  is ignored.

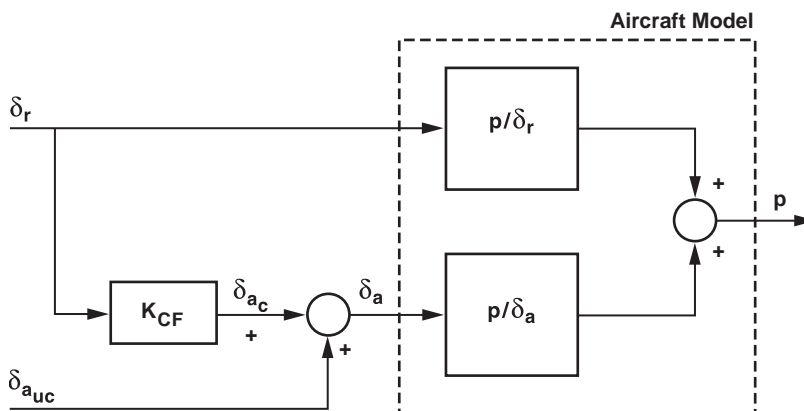


Fig. 9.1 Schematic model of roll-rate response to rudder and aileron inputs.

### 9.3.1 Using the Single-Input/Single-Output Solution

A SISO estimate of the desired response  $p/\delta_r$  is easily obtained from the measured rudder and roll-rate signals:

$$\frac{\hat{p}}{\delta_r} = \frac{G_{\delta_r p}}{G_{\delta_r \delta_r}} \quad (9.2)$$

The cross spectrum  $G_{\delta_r p}$  can be expressed in terms of the input autospectrum  $G_{\delta_r \delta_r}$  and the transfer function from the input to the output (as obtained from an inspection of Fig. 9.1):

$$G_{\delta_r p} = G_{\delta_r \delta_r} \left( \frac{p}{\delta_r} + K_{CF} \frac{p}{\delta_a} \right) \quad (9.3)$$

which shows that the SISO solution can also be expressed as

$$\frac{\hat{p}}{\delta_r} = \frac{G_{\delta_r \delta_r} \left( \frac{p}{\delta_r} + K_{CF} \frac{p}{\delta_a} \right)}{G_{\delta_r \delta_r}} \quad (9.4)$$

which simplifies to

$$\frac{\hat{p}}{\delta_r} = \frac{p}{\delta_r} + K_{CF} \frac{p}{\delta_a} \quad (9.5)$$

In other words,

$$\text{Estimated response} = \text{true response} + \text{bias error} \quad (9.6)$$

where

$$\text{bias error} = K_{CF} \frac{p}{\delta_a} \quad (9.7)$$

Reference to Eq. (9.5) demonstrates precisely the conditions of Sec. 9.2 under which the SISO solution will produce the correct results even though two inputs  $\delta_r$  and  $\delta_a$  are present. The estimated frequency response will be *correct* (i.e., unbiased) if and only if *either* of the following two conditions is true:

1) The first condition is  $p/\delta_a = 0$ , which means the roll response is fully decoupled from the secondary aileron input (not possible herein because this is the on-axis response for aileron input). This corresponds to condition 1 of Sec. 9.2.

or

2)  $K_{CF} = 0$ , which implies  $\delta_{a_C} = 0$ , and hence the two inputs are completely uncorrelated. This corresponds to condition 2 of Sec. 9.2.

In either situation, the bias error of Eq. (9.5) will be zero, and a simple SISO analysis [based on Eq. (9.2)] would yield the true response  $p/\delta_r$ . Expressing this in the reverse manner, frequency-response calculations using single-input/single-output methods will be *incorrect whenever both* of the following conditions are true:

- 1) The MIMO system exhibits interaxis coupling.  
*and*
- 2) The inputs are partially correlated.

### 9.3.2 Two-Input/Single-Output Solution

When the system to be identified exhibits interaxis coupling and the inputs are partially correlated, a multiple-input/single-output (MISO) procedure is used to determine the true (unbiased) response from the measured control inputs. In the present case, we want to determine accurately the off-axis response  $p/\delta_r$  from rudder-sweep data in which both control inputs  $\delta_r$  and  $\delta_a$  are present. The solution method starts with the equations for the cross spectra:

$$G_{\delta_r p} = \left( \frac{p}{\delta_r} \right) G_{\delta_r \delta_r} + \left( \frac{p}{\delta_a} \right) G_{\delta_r \delta_a} \quad (9.8)$$

$$G_{\delta_a p} = \left( \frac{p}{\delta_r} \right) G_{\delta_a \delta_r} + \left( \frac{p}{\delta_a} \right) G_{\delta_a \delta_a} \quad (9.9)$$

Simultaneous solution of Eqs. (9.8) and (9.9) provides the relationships for estimating the two unknown frequency responses in terms of the spectral SISO spectral quantities:

$$\frac{p}{\delta_r} = \frac{G_{\delta_r p} [1 - (G_{\delta_r \delta_a} G_{\delta_a p}) / (G_{\delta_a \delta_a} G_{\delta_r p})]}{G_{\delta_r \delta_r} (1 - \gamma_{\delta_r \delta_a}^2)} \quad (9.10)$$

$$\frac{p}{\delta_a} = \frac{G_{\delta_a p} [1 - (G_{\delta_a \delta_r} G_{\delta_r p}) / (G_{\delta_r \delta_r} G_{\delta_a p})]}{G_{\delta_a \delta_a} (1 - \gamma_{\delta_r \delta_a}^2)} \quad (9.11)$$

The solution of these equations involves several spectral quantities that are calculated using SISO identification: cross spectra between each input and the output  $G_{\delta_r p}$  and  $G_{\delta_a p}$ ; cross spectra between the two inputs  $G_{\delta_r \delta_a}$  and the complex conjugate  $G_{\delta_a \delta_r}$ ; input autospectra  $G_{\delta_r \delta_r}$  and  $G_{\delta_a \delta_a}$ ; and cross coherence between the inputs  $\gamma_{\delta_r \delta_a}^2$ , also called the *cross-control coherence*.

Next, each spectral quantity is expressed analytically—for the present case using the aileron input, as defined in Eq. (9.1). By definition, the uncorrelated part of the aileron input has no correlation with the rudder input, so that

$$G_{\delta_r \delta_{a_{UC}}} = 0 \quad (9.12)$$

## MULTI-INPUT IDENTIFICATION TECHNIQUES

235

and therefore

$$G_{\delta_r \delta_a} = G_{\delta_r \delta_r} K_{CF} \quad (9.13)$$

Furthermore,

$$G_{\delta_a \delta_a} = G_{\delta_r \delta_r} |K_{CF}|^2 + G_{\delta_{a_{UC}} \delta_{a_{UC}}} \quad (9.14)$$

The cross-control coherence is defined as

$$\gamma_{\delta_r \delta_a}^2 = \frac{|G_{\delta_r \delta_a}|^2}{G_{\delta_r \delta_r} G_{\delta_a \delta_a}} \quad (9.15)$$

Substituting Eqs. (9.13) and (9.14) into Eq. (9.15) results in

$$\gamma_{\delta_r \delta_a}^2 = \frac{G_{\delta_r \delta_r}^2 |K_{CF}|^2}{G_{\delta_r \delta_r} (G_{\delta_r \delta_r} |K_{CF}|^2 + G_{\delta_{a_{UC}} \delta_{a_{UC}}})} \quad (9.16)$$

which simplifies to

$$\gamma_{\delta_r \delta_a}^2 = \frac{G_{\delta_r \delta_r} |K_{CF}|^2}{G_{\delta_r \delta_r} |K_{CF}|^2 + G_{\delta_{a_{UC}} \delta_{a_{UC}}}} \quad (9.17)$$

There are two limiting cases for the cross-control coherence, each with an important consequence for the identification:

1) *Complete correlation of the controls:* In this case, there is no uncorrelated component, so that  $G_{\delta_{a_{UC}} \delta_{a_{UC}}} = 0$ , and hence  $\gamma_{\delta_r \delta_a}^2 = 1$ . Reference to Eqs. (9.10) and (9.11) immediately shows that the solution breaks down and the two aircraft dynamics responses  $p/\delta_r$  and  $p/\delta_a$  can not be separately identified. This is the same multipath propagation problem illustrated in Fig. 5.7, and it cannot be solved without independent excitation inputs. Clearly, complete correlation between the control inputs is undesirable. In practice, it is generally possible to avoid high levels of cross coherence between the inputs by directing the pilot to treat the secondary control regulation as a lower priority (Sec. 5.9). The use of uncorrelated pulse-type inputs for the secondary control generally achieves this goal as well. If the aircraft has a wing-leveling system, then a rudder frequency-sweep input generates a fully correlated aileron input (i.e.,  $K_{CF}$  of Fig. 9.1). In this case the pilot or copilot can introduce some uncorrelated aileron inputs via the lateral stick  $\delta_{a_{UC}}$  to reduce the otherwise high levels of cross-control coherence.

As a rule of thumb, the average value of the cross-control coherence between two control inputs  $\delta_1, \delta_2$  should be limited by the following:

*Guideline:*

$$(\gamma_{\delta_1 \delta_2}^2)_{\text{ave}} < 0.5 \quad (9.18)$$

to ensure a satisfactory MIMO solution.

2) *No control cross correlation:* In this case,  $K_{CF} = 0$  (i.e., condition 2), and hence  $\gamma_{\delta_r \delta_a}^2 = 0$ . The simultaneous solution of Eqs. (9.10) and (9.11) will now reduce to the single-input/single-output solution. To see why this is so, it is convenient to rewrite Eq. (9.10) as

$$\frac{p}{\delta_r} = \frac{G_{\delta_r p}}{G_{\delta_r \delta_r}} \cdot \frac{[1 - (G_{\delta_r \delta_a} G_{\delta_a p}) / (G_{\delta_r \delta_a} G_{\delta_r p})]}{(1 - \gamma_{\delta_r \delta_a}^2)} \quad (9.19)$$

When there is no control cross correlation,  $\gamma_{\delta_r \delta_a}^2 = 0$ , and  $G_{\delta_r \delta_a} = 0$ , and so Eq. (9.19) reduces to

$$\frac{p}{\delta_r} = \frac{G_{\delta_r p}}{G_{\delta_r \delta_r}} \quad (9.20)$$

demonstrating, as expected, that the MISO result reduces to the SISO solution of Eq. (9.2) when there is no correlation between the inputs.

### 9.3.3 Two-Input/Multi-Output Solution

The MISO solution for two inputs described in Sec. 9.3.2 can be extended to multiple outputs by using two sets of flight data: one set for the rudder sweeps and the other for the aileron sweeps. First, the MISO solution of Eqs. (9.10) and (9.11) is carried out using the data from rudder sweeps for each of the aircraft outputs (e.g., in a fixed-wing aircraft,  $p$ ,  $\beta$ ,  $r$ , and  $a_y$ ). This yields a set of four frequency responses for the primary rudder input ( $p/\delta_r$ ,  $\beta/\delta_r$ ,  $r/\delta_r$ ,  $a_y/\delta_r$ ) and four frequency responses for the secondary aileron input ( $p/\delta_a$ ,  $\beta/\delta_a$ ,  $r/\delta_a$ ,  $a_y/\delta_a$ ). However, for rudder sweeps the spectral energy of the secondary aileron input is much less than that of the primary rudder input. Therefore, in this case of the rudder sweeps, the aileron data are only used for the multi-input solution of the rudder frequency responses [e.g., Eq. (9.10)], and the frequency responses corresponding to the aileron inputs [e.g., Eq. (9.11)] are discarded. This completes the identification of frequency responses for the rudder inputs ( $p/\delta_r$ ,  $\beta/\delta_r$ ,  $r/\delta_r$ ,  $a_y/\delta_r$ ).

This procedure is repeated, this time using the aileron-sweep data. Once again, the MISO calculations applied to each output generate a set of four frequency responses for the rudder input ( $p/\delta_r$ ,  $\beta/\delta_r$ ,  $r/\delta_r$ ,  $a_y/\delta_r$ ) and four frequency responses for the aileron input ( $p/\delta_a$ ,  $\beta/\delta_a$ ,  $r/\delta_a$ ,  $a_y/\delta_a$ ), but this time the rudder input is secondary, and the aileron input is primary. Because the rudder input

has much lower spectral content in this case, the frequency responses obtained for the rudder inputs are discarded, but we retain the frequency responses for the aileron inputs ( $p/\delta_a$ ,  $\beta/\delta_a$ ,  $r/\delta_a$ ,  $a_y/\delta_a$ ).

Thus, we have carried out the MISO calculations for each output, using one set of flight data records for sweeps of each input. In each analysis, we save the frequency responses only for the dominant input because these will have the most accuracy (i.e., highest coherence). This completes the MIMO identification of the lateral-directional frequency-response matrix. The MIMO procedure presented in this section, based on two inputs, will be generalized for an arbitrary number of inputs in Sec. 9.6.

#### 9.4 Conditioned Spectral Quantities

The form of Eq. (9.19) allows the definition of spectral quantities for the MISO solution in terms of the familiar SISO quantities. The numerator of Eq. (9.19) is defined as the *conditioned* cross spectrum:

$$G_{\delta_r p \cdot \delta_a} \equiv G_{\delta_r p} \left[ 1 - \frac{(G_{\delta_r \delta_a} G_{\delta_a p})}{(G_{\delta_a \delta_a} G_{\delta_r p})} \right] \quad (9.21)$$

which can be seen as the SISO or *ordinary*<sup>106</sup> cross spectrum  $G_{\delta_r p}$ , conditioned with the correction term

$$\left[ 1 - \frac{(G_{\delta_r \delta_a} G_{\delta_a p})}{(G_{\delta_a \delta_a} G_{\delta_r p})} \right] \quad (9.22)$$

This *conditioning*, indicated (from Ref. 106 by the notation  $(\cdot \delta_a)$ ), eliminates the linear effects of the partially correlated aileron inputs. Similarly, the conditioned rudder input autospectrum is defined from the denominator of Eq. (9.19)

$$G_{\delta_r \delta_r \cdot \delta_a} \equiv G_{\delta_r \delta_r} (1 - \gamma_{\delta_r \delta_a}^2) \quad (9.23)$$

which is seen as the ordinary autospectrum  $G_{\delta_r \delta_r}$ , conditioned with the correction term

$$(1 - \gamma_{\delta_r \delta_a}^2) \quad (9.24)$$

to eliminate the linear effects of the partially correlated aileron inputs  $(\cdot \delta_a)$ . Finally, the conditioned frequency response is obtained by rewriting Eq. (9.19) using the conditioned spectral quantities

$$p/\delta_r \cdot \delta_a \equiv \frac{G_{\delta_r p \cdot \delta_a}}{G_{\delta_r \delta_r \cdot \delta_a}} \quad (9.25)$$

which has exactly the same form as the SISO solution of Eq. (9.2), but now using the conditioned spectral quantities rather than the SISO spectral quantities. So the conditioned frequency response is the SISO solution conditioned to eliminate the linear effects of partially correlated aileron inputs ( $\cdot \delta_a$ ).

The multi-input identification begins with the calculation of the SISO spectral quantities, including the cross-control spectra and cross-control coherence. The SISO spectral quantities are then conditioned to remove the effect of any correlation between the inputs, leading to the final corrected spectral quantities and frequency responses.

The conditioned frequency response  $p/\delta_r \cdot \delta_a$  can also be thought of as the frequency response that would have been identified from the flight-test data if there had been no partially correlated component of aileron during the maneuver (i.e.,  $\delta_{a_C} = 0$ ). In particular, the conditioned frequency response is the SISO frequency-response solution that would have been obtained if the pilot had been instructed to use only the rudder for input, with no use of the aileron at all.

The magnitude of the conditioned autospectrum  $G_{\delta_r \delta_r \cdot \delta_a}$  is reduced from the unconditioned value in direct proportion to the cross-control coherence [Eq. (9.23)]. This is the result of removing the component of  $\delta_a$  that is partially correlated with  $\delta_r$ . In other words, the effective rudder excitation level is only the part that is uncorrelated with the aileron input. When the average cross-control coherence is limited to 50% [i.e.,  $(\gamma_{\delta_r \delta_r}^2)_{ave} < 0.5$ , per the guideline of Eq. (9.18)], the reduction in average effective rudder autospectrum will be limited to 50%. This is equivalent to a 30% reduction in the primary control rms ( $\sigma_{\delta_r}$  in this case) because  $\sigma_{\delta_r} \propto \sqrt{G_{\delta_r \delta_r \cdot \delta_a}}$  [Eq. (7.75)].

A generalization of the ordinary coherence function concept of Sec. 7.8 allows the accuracy and quality of the conditioned frequency-response estimate to be assessed. The *partial coherence* function ( $\gamma_{\delta_r p \cdot \delta_a}^2$  in this case) is obtained<sup>106</sup> from the definition for the ordinary coherence [Eq. (7.51)], with the ordinary spectral quantities now replaced by the conditioned spectral quantities:

$$\gamma_{\delta_r p \cdot \delta_a}^2 = \frac{|G_{\delta_r p \cdot \delta_a}|^2}{|G_{\delta_r \delta_r \cdot \delta_a}| |G_{p p \cdot \delta_a}|} \quad (9.26)$$

where the conditioned roll autospectrum is defined as

$$G_{p p \cdot \delta_a} \equiv G_{p p} (1 - \gamma_{\delta_a p}^2) \quad (9.27)$$

which is seen as the SISO output autospectrum  $G_{p p}$ , conditioned with the correction term

$$(1 - \gamma_{\delta_a p}^2) \quad (9.28)$$

to eliminate the linear effects of the partially correlated aileron inputs.

The partial coherence is that fraction of the output  $p$  that can be linearly related to the primary (rudder) input in the test data, with the linear effects of partially correlated aileron inputs removed. The partial coherence is interpreted in exactly the same way as the ordinary coherence for SISO systems.

Similarly, the partial coherence for the aileron inputs ( $\gamma_{\delta_a p, \delta_a}^2$ ) indicates that fraction of the output  $p$  which can be related to the secondary (aileron) input for the test data, with the linear effects of partially correlated rudder inputs removed. This secondary input partial coherence is obtained by reversing the controls in Eq. (9.26) and is useful in showing the importance of the secondary control  $\delta_a$  on the identification of  $p/\delta_r$ .

The normalized random error  $\epsilon_r$  associated with the conditioned frequency-response estimate  $p/\delta_r \cdot \delta_a$  can be determined directly from Eq. (7.55), using the partial coherence  $\gamma_{\delta_r p, \delta_a}^2$  instead of the ordinary coherence:

$$\epsilon_r = C_\epsilon \frac{[1 - \gamma_{\delta_r p, \delta_a}^2]^{1/2}}{|\gamma_{\delta_r p, \delta_a}| \sqrt{2n_d}} \quad (9.29)$$

A final useful quantity for MIMO system identification is the multiple coherence:

$$\gamma_{\delta_r \delta_a: p}^2 = \frac{(p/\delta_r) G_{\delta_r p}^* + (p/\delta_a) G_{\delta_a p}^*}{G_{pp}} \quad (9.30)$$

where the  $*$  denotes the complex conjugate. The multiple coherence is the fraction of the output that is linearly related to *all of the inputs* included in the analysis ( $\delta_r$  and  $\delta_a$  in our current two-input example). The multiple coherence will be less than unity when noise at the output or nonlinearities are present, or when additional secondary control inputs contribute to the aircraft response but are not included in the multi-input analysis.

## 9.5 Example of a Two-Input Identification Solution Using the XV-15 Flight Data

In this section, the two-input solution is demonstrated for the identification of the bare-airframe off-axis (coupling) response  $p/\delta_r$  of the XV-15 in cruising flight (database 2, Table 3.4). The flight-test data are from directional sweeps, which were completed with the *SCAS off* in both the yaw and roll channels. The primary input is rudder  $\delta_r$ , but secondary aileron inputs  $\delta_a$  are also present in these piloted sweeps to keep the aircraft motions centered about the reference condition (i.e., roughly wings level). As will be seen, the identification of the off-axis response  $p/\delta_r$  will be significantly influenced by secondary control inputs  $\delta_a$ , so that the SISO solution must be conditioned to obtain an unbiased identification.

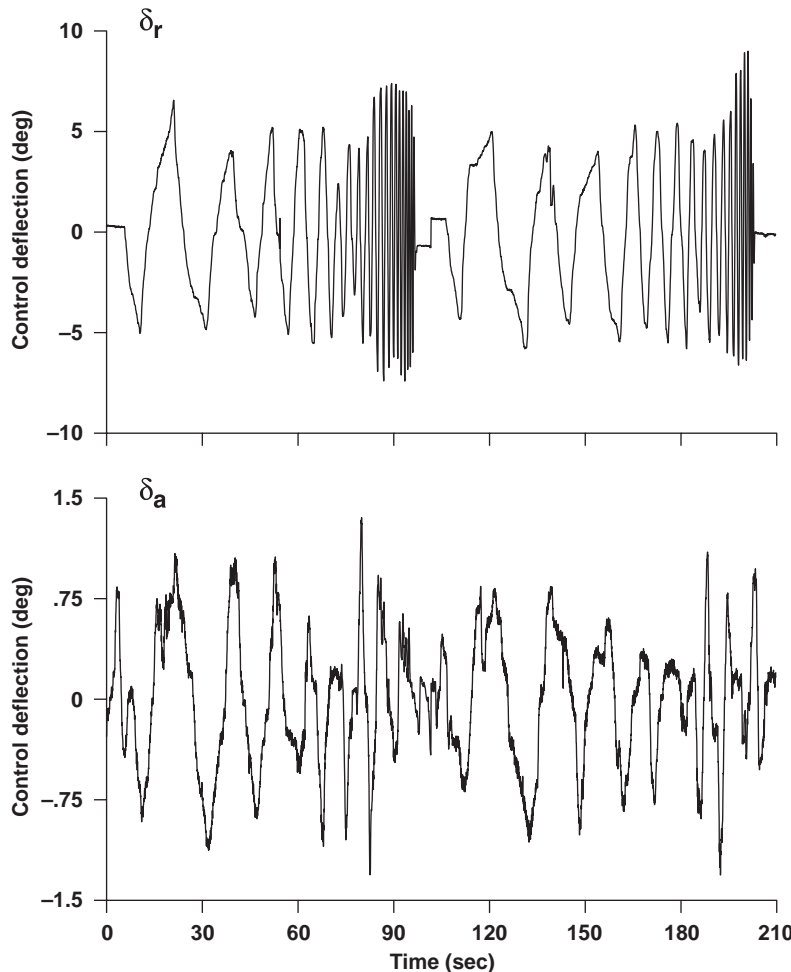


Fig. 9.2 Rudder and aileron control inputs during directional sweep (XV-15, cruise).

Figure 9.2 shows the rudder  $\delta_r$  and aileron  $\delta_a$  inputs. The aileron inputs are less than 20% of the rudder inputs. (Note the expanded scale for the aileron plot to provide a clearer view of the waveform.) Although the time-history plot appears to show some correlation between the two inputs, it is difficult to tell how significant this is just from a visual inspection.

As seen in Fig. 9.3, the cross-control coherence has a maximum value of  $\gamma_{\delta_r \delta_a}^2 = 0.75$  at low frequency, where it is associated with piloted trim (i.e., secondary) inputs. There is also an increase in the cross-control coherence near the Dutch-roll mode (about 2 rad/s), where roll-yaw dynamic coupling is the

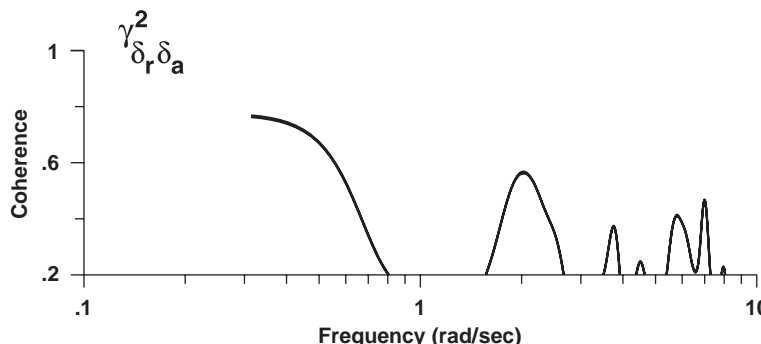


Fig. 9.3 Cross-control coherence (XV-15, cruise).

most significant, resulting in piloted roll regulation. The average value is calculated as  $(\gamma_{\delta_r \delta_a}^2)_{\text{ave}} \approx 0.20$ , which is well within the guideline of Eq. (9.18). The cross-control coherence situation for these data is definitely not at either extreme ( $\gamma_{\delta_r \delta_a}^2 = 0$  or  $\gamma_{\delta_r \delta_a}^2 = 1.0$ ). The cross correlation is high enough that it should not be ignored, but not so high that it will make the identification impossible.

Figure 9.4 shows the input autospectrum for  $\delta_r$ . The SISO solution  $G_{\delta_r \delta_r}$  is shown as the dashed line. The conditioned MISO solution  $G_{\delta_r \delta_r \cdot \delta_a}$ , which takes out the correlated part of  $\delta_a$ , is shown as the solid line. The input autospectrum is lower for the MISO solution than for SISO solution, illustrating that the conditioning process reduces the effective energy of the identification excitation [Eq. (9.23)].

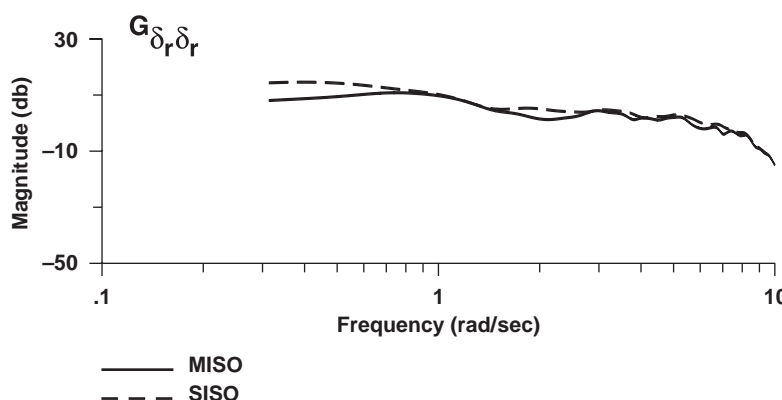


Fig. 9.4 Rudder input autospectrum: SISO vs MISO (XV-15, cruise).

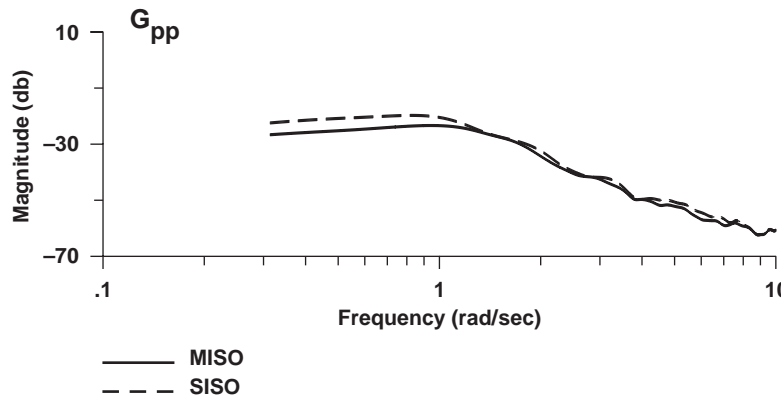


Fig. 9.5 Roll-rate output autospectrum: SISO vs MISO (XV-15, cruise).

The same characteristic of energy reduction is seen in the output autospectrum of Fig. 9.5. The conditioned cross spectrum is compared to the SISO solution in Fig. 9.6.

The frequency-response identification results for the SISO ( $p/\delta_r$ , long dashes) vs MISO ( $p/\delta_r \cdot \delta_a$ , solid line) solutions are shown in Fig. 9.7. In this case, the conditioning process results in an increase in the coherence compared to the SISO result. The partial coherence is well above 0.6, indicating an accurate identification.

Also shown in Fig. 9.7 is the GTR simulation response (short dashes) obtained directly from the stability and control derivative model. The simulation model is seen to track the MISO (i.e., correct) flight response nearly perfectly, as would be expected, because the aerodynamic look-up tables that are the basis for the simulation model were obtained from full-scale wind-tunnel tests. The

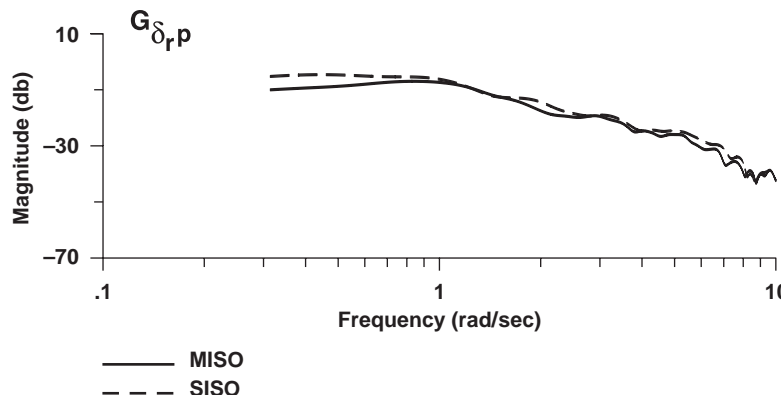


Fig. 9.6 Rudder-to-roll-rate cross spectrum: SISO vs MISO (XV-15, cruise).

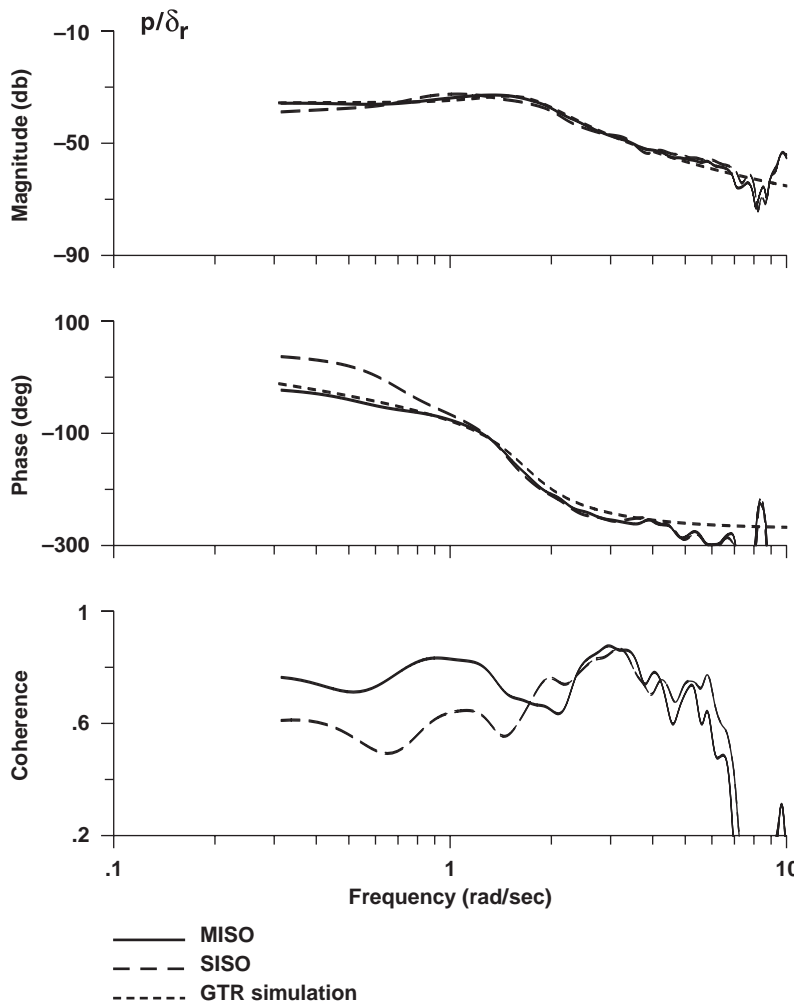


Fig. 9.7 Off-axis frequency-response identification: SISO vs MISO (XV-15, cruise).

results show a significant phase error in the SISO results at frequencies below 1 rad/s and some magnitude error near the Dutch-roll mode (1–2 rad/s). These errors reflect the considerable influence of the piloted secondary inputs  $\delta_a$  during the sweep and are largest in the region of high cross-control coherence (Fig. 9.3). If the SISO data were used to evaluate the off-axis response of the XV-15 simulation, one might conclude that there was a problem with the math model, but in reality the problem would be with the use of the SISO identification analysis.

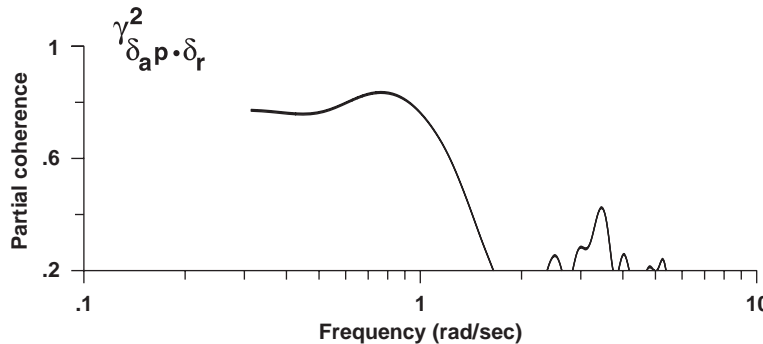


Fig. 9.8 Partial coherence for aileron inputs (XV-15, cruise).

The partial coherence for aileron inputs (Fig. 9.8) is strongest in the same low frequency range, reflecting the significant on-axis response  $p/\delta_a$ .

Finally, as shown in Fig. 9.9, the multiple coherence  $\gamma_{\delta_r, \delta_a, p}^2$  is high over the frequency range of piloted sweep excitation (up to 8 rad/s). This indicates that most of the output is attributable to the two measured inputs included in the analysis  $\delta_r$  and  $\delta_a$ , with little influence from other inputs (e.g., pitch controls and turbulence) or from nonlinearities.

The key on-axis response for handling-qualities analyses  $\beta/\delta_r$  was identified using the same directional sweep data. Figure 9.10 compares the results for the SISO and MISO analyses. As expected from the discussion of Sec. 9.2, there is much less influence of the secondary control inputs on the on-axis response identification. The influence of secondary inputs is further reduced for the identification of the on-axis *closed-loop* responses (as is demonstrated in **Problem 9.6**) because the feedback loops suppress the sideslip/roll response coupling and render the system essentially as SISO (per condition 1).

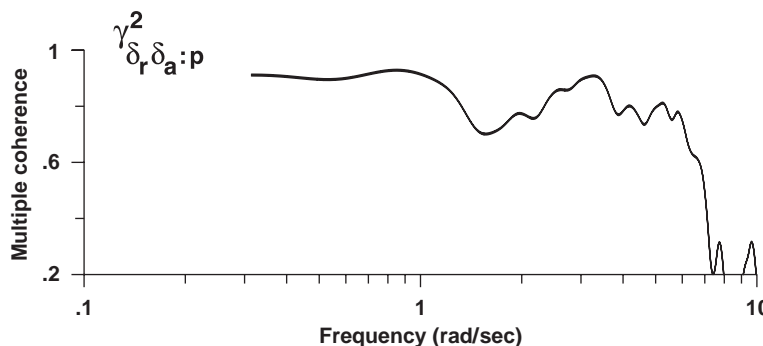


Fig. 9.9 Multiple coherence (XV-15, cruise).

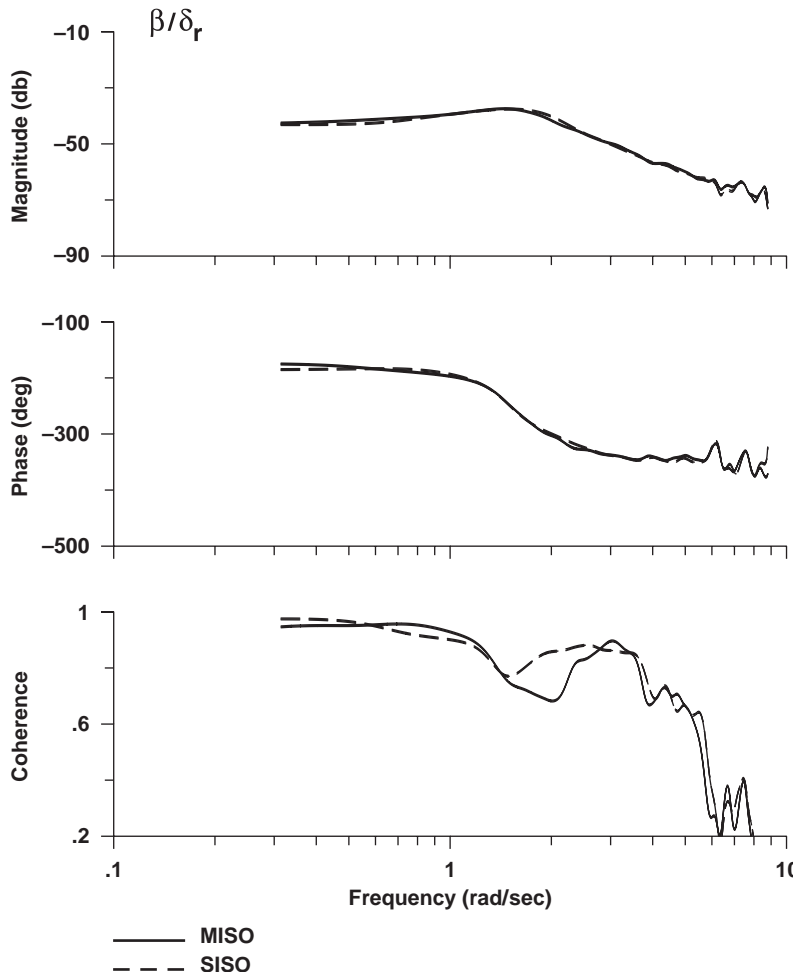


Fig. 9.10 On-axis frequency response and coherence: SISO vs MISO (XV-15, cruise).

## 9.6 General MIMO Solution

The method for solving the general MIMO problem, presented in this section, is a generalization of the techniques for two inputs discussed in Sec. 9.3.2. First we will present the equations used to solve the general MISO problem (Sec. 9.6.1). The general MIMO problem can then be solved by repeated application of the MISO analysis, once for each of the  $n_o$  outputs (Sec. 9.6.2).

There are two flight-test procedures that can be used to generate the data appropriate for the MIMO identification. The most common approach is to use a series

of data sets, each one consisting of sweep maneuvers for one of the  $n_c$  inputs. In this approach, the  $n_o$  MISO solutions are successively calculated for each of these data sets, and the frequency responses with the highest coherence are obtained (MIMO extension of Sec. 9.3.3). Alternatively, the calculations can be made using a single data set if it contains sufficient information content for all inputs. This can be achieved by employing appropriate multi-input maneuvers during the flight test (Sec. 9.10).

### 9.6.1 General MISO Solution

The generalized MISO identification problem can be solved numerically at each frequency point  $f$  in a direct matrix formulation<sup>108</sup>:

$$\hat{\mathbf{H}}(f) = \hat{\mathbf{G}}_{xx}^{-1}(f) \hat{\mathbf{G}}_{xy}(f) \quad (9.31)$$

which can be seen to be directly analogous to the  $\hat{H}_1$  scalar solution in the SISO case [Eq. (7.37)]. [From here on we again drop the estimate designation  $(\hat{\cdot})$  for notational convenience, though it is implied.] The solution of Eq. (9.31) is an  $n_c \times 1$  column vector of conditioned frequency responses  $\mathbf{H}(f)$  for a selected output  $y$ :

$$\mathbf{H}(f) = \frac{y}{x_i}(f), \quad \text{for } i = 1, 2, \dots, n_c \quad (9.32)$$

where  $x_i$  are the control inputs. The quantity denoted  $\mathbf{G}_{xy}(f)$  in Eq. (9.31) is an  $n_c \times 1$  column vector of SISO cross spectra between each control input and the single output  $y$ .

The quantity denoted  $\mathbf{G}_{xx}(f)$  in Eq. (9.31) is an  $n_c \times n_c$  matrix of auto- and cross spectra between the  $n_c$  control inputs. The diagonal terms of  $\mathbf{G}_{xx}$  are the control autospectra, such as

$$G_{11} = G_{\delta_a \delta_a}, \quad G_{22} = G_{\delta_e \delta_e}, \quad G_{33} = G_{\delta_r \delta_r}, \dots \quad (9.33)$$

and the off-diagonal terms are pair-wise control cross spectra and their complex conjugates, such as

$$G_{12} = G_{\delta_a \delta_e}, \quad G_{13} = G_{\delta_a \delta_r} = G_{\delta_r \delta_a}^*, \quad G_{21} = G_{\delta_e \delta_a} = G_{\delta_a \delta_e}^*, \dots \quad (9.34)$$

If any two of the inputs exhibit a cross-control coherence of near unity, then the autospectrum matrix  $\mathbf{G}_{xx}(f)$  becomes nearly singular ("ill conditioned"), and the MISO solution of Eq. (9.31) breaks down at this frequency  $f$ . This is a direct extension of the guideline [Eq. (9.18)] for the two-input solution. Further, if all of the controls are *fully uncorrelated*, then the  $\mathbf{G}_{xx}$  matrix is diagonal, and the inverse is just the reciprocal of the diagonal elements. This renders the MIMO matrix solution the same as the SISO solution of Eq. (7.37) (Sec. 9.2, condition 2). When the output is only affected by the primary input, only one element of the cross-spectrum vector  $\mathbf{G}_{xy}$  and the associated element of the frequency response vector  $\mathbf{H}(f)$  have non-zero values. Once again, this reduces the MIMO matrix solution to the SISO solution, even for a fully populated input autospectrum matrix (Sec. 9.2, condition 1).

Each of the  $n_c$  frequency responses in  $\mathbf{H}$  [Eq. (9.31)] has an associated partial coherence:

$$\gamma_{x_i y \cdot (n_c - 1)!}^2 = \frac{|G_{x_i y \cdot (n_c - 1)!}|^2}{|G_{x_i x_i \cdot (n_c - 1)!}| |G_{y y \cdot (n_c - 1)!}|} \quad (9.35)$$

where each quantity in this equation involves fairly complex manipulations of the spectral matrices.<sup>108</sup> Note that Eq. (9.35) is a generalization of Eq. (9.26) from two inputs to  $n_c$  inputs. Further, the factorial notation used in expressions such as  $\gamma_{x_i y \cdot (n_c - 1)!}^2$  is not to be taken as a literal factorial, but to indicate that the spectral quantity for one input  $x_i$  is conditioned by each of the other  $(n_c - 1)$  inputs.

The associated conditioned random error is obtained using the partial coherence functions:

$$\epsilon_{r \cdot (n_c - 1)!} = C_\epsilon \frac{[1 - \gamma_{x_i y \cdot (n_c - 1)!}^2]^{1/2}}{|\gamma_{x_i y \cdot (n_c - 1)!}| \sqrt{2n_d}} \quad (9.36)$$

A matrix formulation for the multiple coherence function (to show the combined influence all  $n_c$  inputs) is also given by Otnes and Enochson<sup>108</sup>.

### 9.6.2 Combining MISO Analyses to Obtain the MIMO Solution

The MIMO solution, consisting of the frequency-response vectors  $\mathbf{H}$  for each output, is obtained by repeating the MISO calculation of Eq. (9.31) for each of the  $n_o$  outputs. However, in order to achieve an accurate identification (high coherence) of the frequency responses in the MIMO solution, there are some important issues to consider with respect to the flight data used in these calculations. This is directly analogous to the two-input discussion of Sec. 9.3.3.

In most testing procedures for system identification, a maneuver is executed with a dominant input. Consider the MIMO bare-airframe identification of a hovering helicopter with fully coupled dynamics. There are four primary controls ( $\delta_{\text{lat}}$ ,  $\delta_{\text{lon}}$ ,  $\delta_{\text{ped}}$ , and  $\delta_{\text{col}}$ ) and generally (Sec. 13.4.3) nine outputs ( $p$ ,  $q$ ,  $r$ ,  $a_x$ ,  $a_y$ ,  $a_z$ ,  $u$ ,  $v$ ,  $w$ ). When a roll-sweep maneuver (or 3-2-1-1, Schroeder phase, etc.) is conducted, the flight-test data involve mostly lateral stick inputs  $\delta_{\text{lat}}$ . There will also be considerable control activity for the remaining inputs  $\delta_{\text{lon}}$ ,  $\delta_{\text{ped}}$ , and  $\delta_{\text{col}}$ . These are associated with piloted (or augmentation system) stabilization of the off-axis excursions as a result of the highly coupled nature of the helicopter system dynamics. The information content for the dominant input ( $\delta_{\text{lat}}$  in this case) will also be the greatest for the roll sweep data. Therefore, although the calculation of Eq. (9.31) will return the frequency responses of the outputs for *all four control inputs*, only the nine responses to lateral stick input (i.e.,  $p/\delta_{\text{lat}}$ ,  $q/\delta_{\text{lat}}$ ,  $r/\delta_{\text{lat}}$ , etc.) will have high coherence. The partially correlated effect of the secondary controls will be removed from these lateral stick frequency responses, and these will be accurately identified from the roll-sweep data. But the frequency responses for the other inputs (e.g.,  $p/\delta_{\text{lon}}$ ,  $q/\delta_{\text{ped}}$ ,  $r/\delta_{\text{col}}$ , etc.) available from Eq. (9.31) will generally not exhibit acceptable coherence from the roll-sweep data and are discarded. The lateral-stick

responses will constitute the first column (corresponding to the first control  $\delta_{\text{lat}}$ ) of the  $(n_o \times n_c)$  of the MIMO frequency-response estimate matrix  $\hat{\mathbf{T}}$ .

The identification is next repeated for yaw sweep data, where the pedal input  $\delta_{\text{ped}}$  is dominant. In this yaw-sweep case, the responses to pedal (i.e.,  $p/\delta_{\text{ped}}$ ,  $q/\delta_{\text{ped}}$ ,  $r/\delta_{\text{ped}}$ , etc.) will now have high coherence and will be corrected for the presence of secondary inputs. These pedal responses will constitute the second column (corresponding to the second control  $\delta_{\text{ped}}$ ) of the MIMO frequency-response estimate matrix  $\hat{\mathbf{T}}$ . The responses to lateral stick, although available from Eq. (9.31), will exhibit poor coherence for the yaw-sweep data and are generally discarded. This procedure is continued for each of the four sweep axes, and a complete MIMO frequency-response estimate matrix  $\hat{\mathbf{T}}$  of dimension  $n_o \times n_c$  is compiled (9  $\times$  4 in this case).

The preceding approach is based on a set of flight-data records, each consisting of frequency sweeps with a primary input limited to one of the control axes. In the special case of a multi-input maneuver, sufficient information content is achieved for all controls in a single maneuver (Sec. 9.10), and the frequency responses for all inputs can be determined from Eq. (9.31) from the single data set.

## 9.7 High Control Correlation

In some situations, the secondary inputs can be highly correlated with the primary inputs, but the amplitude of the secondary inputs can still be quite small. This will render the MISO solution indeterminate [ $\mathbf{G}_{xx}$  of Eq. (9.31) is nearly singular], although the secondary controls have little real importance in the test data and can be safely ignored. Such situations are detected by high values of the average cross-control coherence functions, together with very low levels of the input autospectrum for the secondary inputs as compared to the primary inputs. So, for example, if the primary input is denoted  $\delta_1$  and the secondary input is denoted  $\delta_2$ , high cross-control coherence can be reflected [e.g.,  $(\gamma_{\delta_1 \delta_2}^2)_{\text{ave}} > 0.80$ ], while the secondary input autospectrum  $G_{\delta_2 \delta_2}$  has a low value (e.g., 20 db lower) compared to the primary input autospectrum  $G_{\delta_1 \delta_1}$ . In such situations, it might be necessary (and sufficiently accurate) to drop one (or more) of the secondary controls from the MISO analysis.

One common cause of this problem occurs when a pilot sweep in one control bleeds into a secondary control input as a result of mechanical rigging—sometimes referred to as *mechanical cross talk*. This can cause a small, inadvertent, but highly correlated, off-axis input. A similar situation occurs as a result of pilot biodynamic effects, where the pilot's body can transmit a very small but highly correlated secondary input—sometimes referred to as a *bob-weight* effect. For example, the pilot might execute a pedal sweep, but inadvertently transmit via his body motions a small, but highly correlated input to the lateral cyclic axis. In the case of the biodynamic coupling, the problem can be eliminated by the pilot bracing his/her arm against the cockpit to avoid the inadvertent cyclic inputs. The small off-axis inputs will be seen as a very low power-spectrum as compared to the primary inputs, and can be ignored in the analysis.

The problem of high control correlation has also been encountered by the leading author in the identification of the bare-airframe response of small highly coupled ducted-fan rotorcraft UAVs under closed-loop test conditions.<sup>12</sup> In this case the high cross-control coherence was the result of gyroscopic coupling induced by the large rotational momentum of the fan. Again, the MISO identification could not be

conducted because a cross-control coherence of nearly unity was detected—even though the amplitudes of the off-axis inputs were small. An accurate analysis was completed by dropping the secondary inputs and reverting to the SISO solution.

## 9.8 Multiple-Input Identification in CIFER® Using MISOSA

The MIMO frequency-response matrix identification of Sec. 9.6 is implemented in the CIFER® module MISOSA (Multi-Input/Single-Output Spectral Analysis) shown in Fig. 4.1. The solution for a typical flight vehicle (e.g., four control inputs, nine outputs) involves a large number of spectral matrix calculations and poses a significant bookkeeping challenge for which the CIFER® database is an important resource. At the user interface level, MISOSA is quite simple and only requires the selection of primary and secondary inputs, outputs, and SISO spectral windows. This section reviews some key aspects of the overall MIMO frequency-response identification using CIFER®.

Consider again the MIMO bare-airframe identification of a hovering helicopter. The identification starts with one FRESPID (SISO) case named LATSWP for a linked set of time histories associated with the first primary control  $\delta_{\text{lat}}$ . The FRESPID case should be run with “control cross-correlation on,” so that the needed cross-control spectral quantities are determined. An associated MISOSA (MISO) case (also named LATSWP for ease of bookkeeping) is processed, with one control designated as “primary” ( $\delta_{\text{lat}}$  in this case) and the remaining controls designated as “secondary” ( $\delta_{\text{ped}}$ ,  $\delta_{\text{ion}}$ , and  $\delta_{\text{col}}$ ). The users also select the desired outputs. As explained in Sec. 9.6.2, the output of this MISOSA case will be only those responses associated with the primary input. This FRESPID / MISOSA process is then repeated for the linked record associated with the next primary control (LONSWP case for the linked set of  $\delta_{\text{lon}}$  sweep records), with the remaining controls designated as secondary. This process continues for each of the  $n_c$  controls in the MIMO analysis to arrive at the  $n_o \times n_c$  ( $9 \times 4$  in this case) frequency-response estimate matrix  $\hat{T}$ . Identification of the closed-loop responses will be based on the piloted controls as inputs, whereas the identification of the bare-airframe response will be based on the aerodynamic surface deflections as inputs.

Tables 9.1 and 9.2 illustrate the solution of the two-input bare-airframe identification problem  $\delta_a$  and  $\delta_r$  for the XV-15 cruise condition (discussed in Sec. 9.5). Table 9.1 tracks the analysis for the lateral-stick sweep data, which produces all

**Table 9.1 Lateral-sweep-data analysis (cruise)**

Time-history set	FRESPID	MISOSA
Lateral-sweep data	FRESPID case: LATSWP	MISOSA case: LATSWP
Two inputs	Two inputs (cross correlation on)	Primary input: $\delta_a$ Secondary input: $\delta_r$
Four outputs	Four outputs	Four outputs
Number of frequency responses generated	$(n_c \cdot n_o) + (n_c/2)(n_c - 1) = 9$	$n_o = 4$

Table 9.2 Pedal-sweep-data analysis (cruise)

Time-history set	FRESPID	MISOSA
Pedal-sweep data	FRESPID case: PEDSWP	MISOSA case: PEDSWP
Two inputs	Two inputs (cross correlation on)	Primary input: $\delta_r$ Secondary input: $\delta_a$
Four outputs	Four outputs	Four outputs
Number of frequency responses generated	$(n_c \cdot n_o) + (n_c/2)(n_c - 1) = 9$	$n_o = 4$

of the conditioned frequency responses for the primary aileron  $\delta_a$  input ( $p/\delta_a$ ,  $\beta/\delta_a$ ,  $r/\delta_a$ ,  $a_y/\delta_a$ ). Similarly, Table 9.2 tracks the analysis for the pedal-sweep data, which produces all of the conditioned frequency responses for the primary rudder  $\delta_r$  input ( $p/\delta_r$ ,  $\beta/\delta_r$ ,  $r/\delta_r$ ,  $a_y/\delta_r$ ). Note that the assignment of primary and secondary inputs is reversed for the two cases.

The MISOSA software calculates the conditioned frequency responses for the primary input only, following the approach of Sec. 9.6.2. The remaining inputs are designated as the secondary inputs for this analysis and are used for conditioning purposes only. The order of the secondary inputs is immaterial in the solution, so that there is no need to be concerned with ordering the controls in terms of most important. Furthermore, there is no disadvantage to including controls that turn out to be totally uncorrelated, and so it is generally best to include all of the controls that are active in the flight record rather than trying to make an a priori judgement about which secondary controls are important in the solution and which secondary controls could be ignored. The cross-control coherences for each pair-wise combination of controls are checked to ensure that they are within the guideline of Eq. (9.18), and the user is alerted if this guideline is exceeded.

The MISO frequency-response solution of Eq. (9.31) is completed at each discrete frequency  $f$ . If a numerical singularity is encountered for a particular frequency (e.g., because of high cross-control coherence), then the program will drop that frequency point, issue a warning message, and then continue on with the remaining frequency points in the analysis. This procedure is repeated for all of the selected SISO spectral windows.

## 9.9 Example of MISO Solution for a Hovering Helicopter

Tischler and Tomashofski<sup>139</sup> identified accurate high-order models of the SH-2G helicopter over a range of flight conditions from hover to 100 kn to support flight-control system development. The results are presented in detail in Sec. 15.3. This helicopter exhibits a high level of cross coupling between pitch and roll, resulting in considerable cross-control correlation for the piloted sweeps. Figure 9.11 shows the MISO identification of SH-2G helicopter bare-airframe dynamics in a hover flight condition. The analysis shown is for the roll-sweep flight data, so that the primary input in this case is  $\delta_{lat}$ . The key frequency responses of interest are associated with the on-axis response (roll rate  $p/\delta_{lat}$ ) and the main off-axis response (pitch rate  $q/\delta_{lat}$ ).

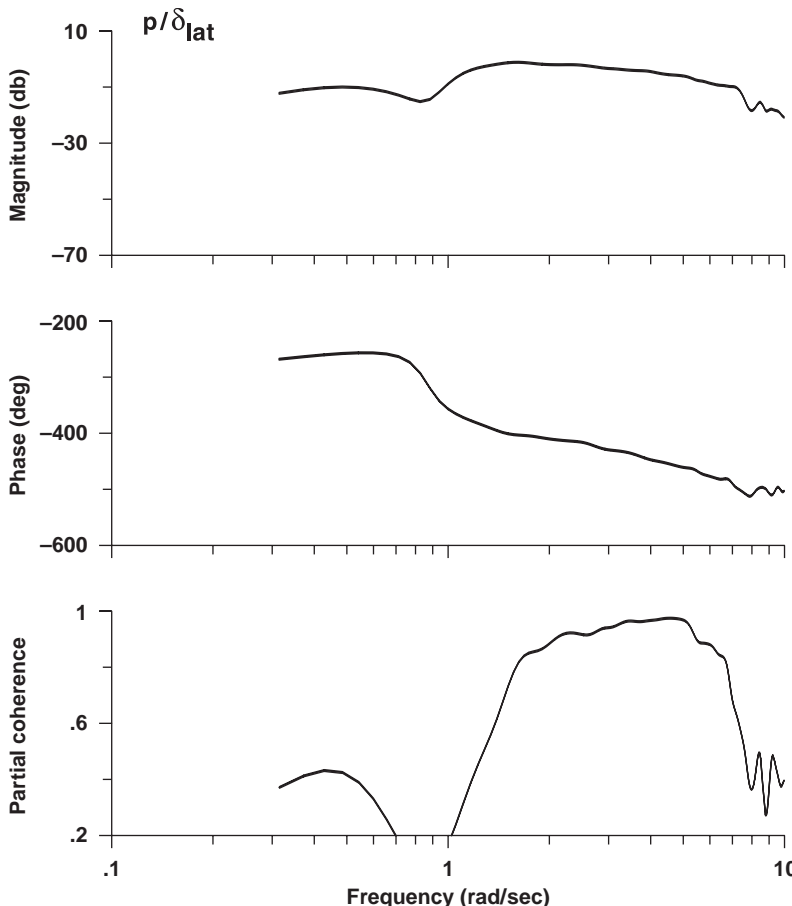


Fig. 9.11 MISO identification of roll-rate response for SH-2G (four inputs).

Figure 9.11 shows the frequency-response identification of the conditioned on-axis roll-rate response  $p/\delta_{\text{lat}}$ . There is good (partial) coherence for on-axis response to the primary input  $\delta_{\text{lat}}$  in the frequency range of interest for flight control (1.5–7 rad/s). The noticeable “hole” in the coherence function at about 0.8 rad/s is associated with a peak in the lateral-to-longitudinal cross-control coherence.

Figures 9.12a–9.12e show the partial coherence for each secondary control, with the effects of the other three inputs taken out. There are important contributions arising from the roll response to pitch inputs ( $\delta_{\text{lon}}$ , Fig. 9.12a) at lower frequency and to pedal inputs ( $\delta_{\text{ped}}$ , Fig. 9.12b) in the frequency range of the Dutch-roll mode. Not surprisingly, there is little partial coherence associated with the roll response because of the secondary collective (i.e., vertical) control ( $\delta_{\text{col}}$ , Fig. 9.12c). The  $p/\delta_{\text{col}}$  response is not significant unless the helicopter has a canted tail rotor (e.g., UH-60). Figure 9.12d shows that the multiple coherence is very high, indicating

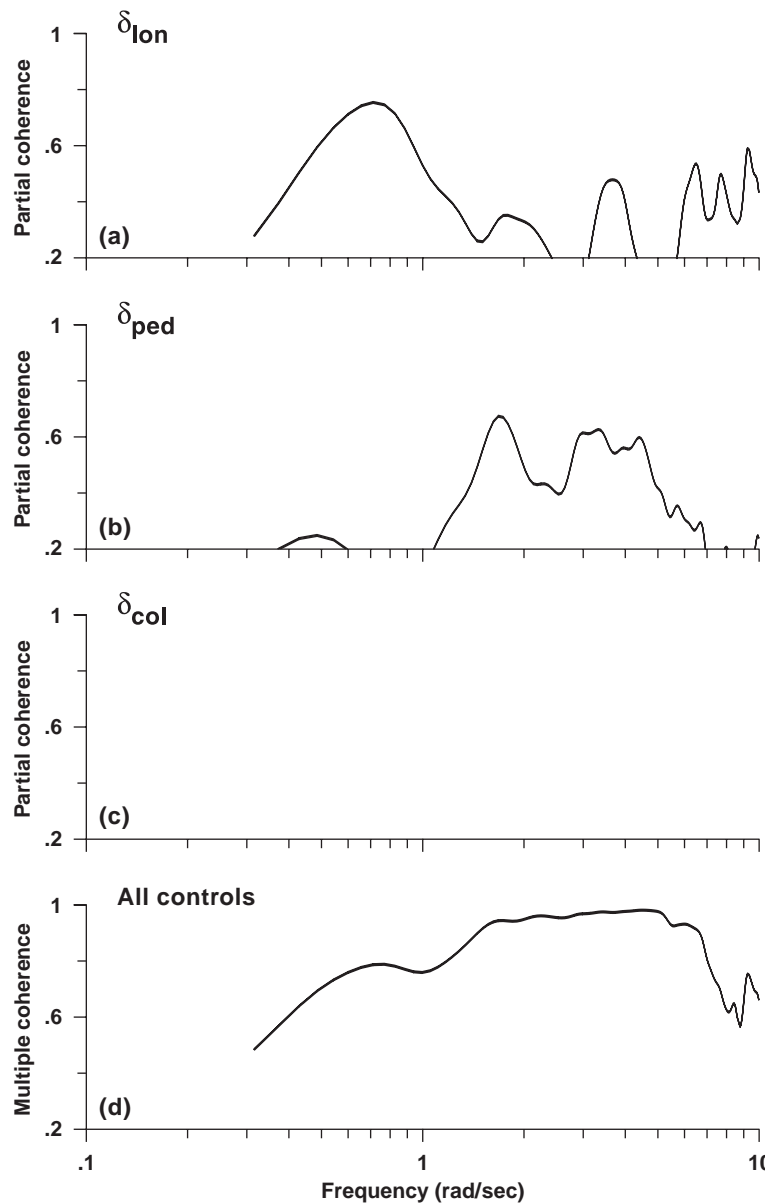


Fig. 9.12 Partial coherences for secondary inputs and multiple coherence.

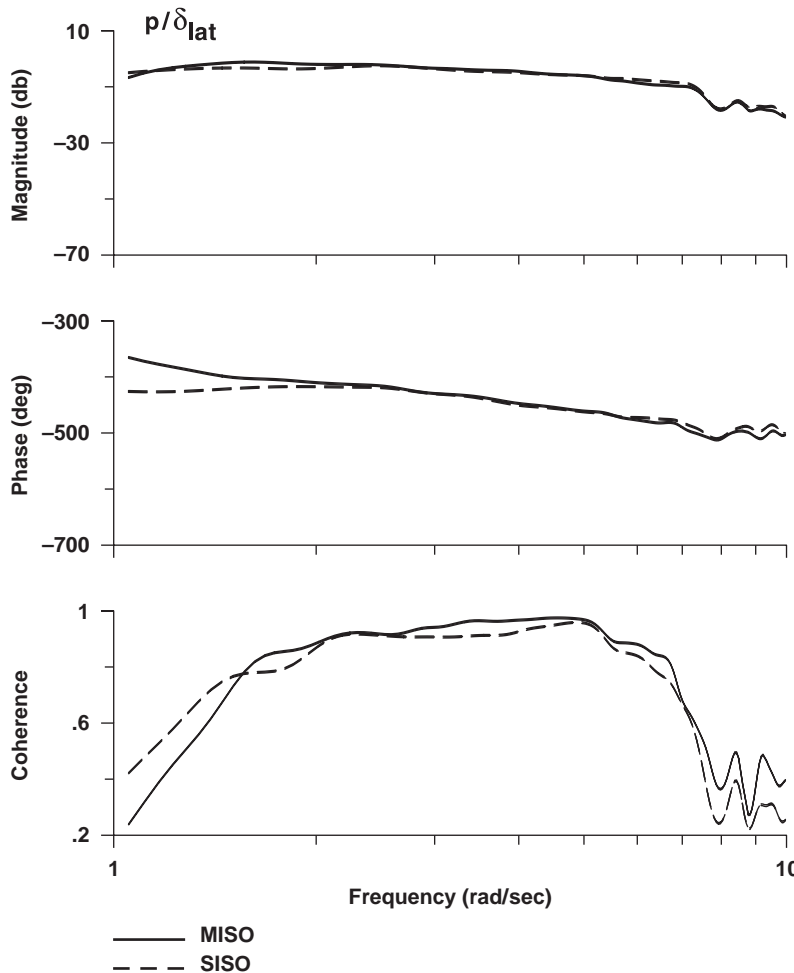


Fig. 9.13 Comparison of MISO and SISO solutions for on-axis roll-rate response.

that nearly all of the roll-rate response is caused by the four pilot control inputs, and the effects of other excitations (such as wind gusts) and nonlinearities are minimal.

The significance of secondary inputs to the identification of the on-axis response  $p/\delta_{lat}$  is demonstrated in Fig. 9.13. The solid line shows the MISO, result and the dashed line shows the SISO result. The differences between these two results are fairly minor in the frequency range over which the coherence is good (1.5–7 rad/s) and could be ignored in this case. The differences are much more important for the off-axis response identification  $q/\delta_{lat}$ , as can be seen in Fig. 9.14. Although the coherence is still poor for the MISO analysis at the low and high frequency ends of the plotted results, it is acceptable in the important frequency range of the short-term response (2–5 rad/s). The magnitude and

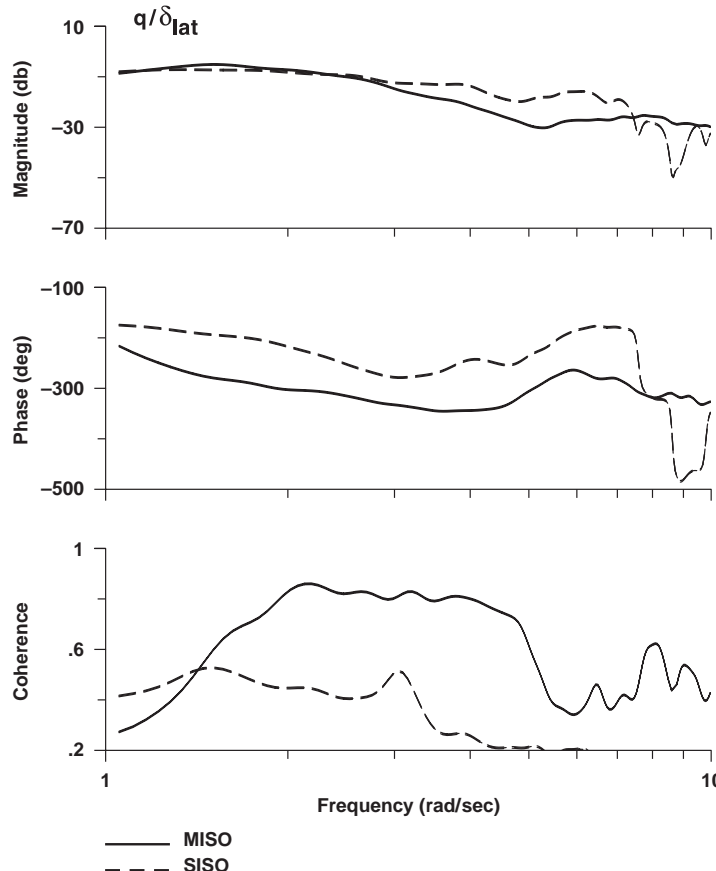


Fig. 9.14 Comparison of MISO and SISO solutions for off-axis pitch-rate response.

phase response for the MISO solution is the correct result and much different from the SISO solution. These results emphasize the need for the multi-input solution for identification of dynamics where response coupling is significant (consistent with Sec. 9.2 and the XV-15 results of Sec. 9.5).

### 9.10 MIMO Identification Using a Multi-Input Maneuver

In some cases, the flight-test technique might involve a sequenced series of identification inputs in a single flight record. Figure 9.15 shows a multi-axis maneuver for an experimental aircraft involving a sequenced individual excitation of six independent controls in a single flight record.<sup>140</sup> The aircraft tests were conducted under closed-loop conditions, and the leading author used CIFER<sup>®</sup> to identify a MIMO bare-airframe flight-dynamics model, as indicated in the aircraft dynamics block of Fig. 5.7.

The multi-axis maneuver contains all of the  $n_c$  primary control excitations in the same maneuver; consequently, a *single* FRESPID case is used to analyze the linked

## MULTI-INPUT IDENTIFICATION TECHNIQUES

255

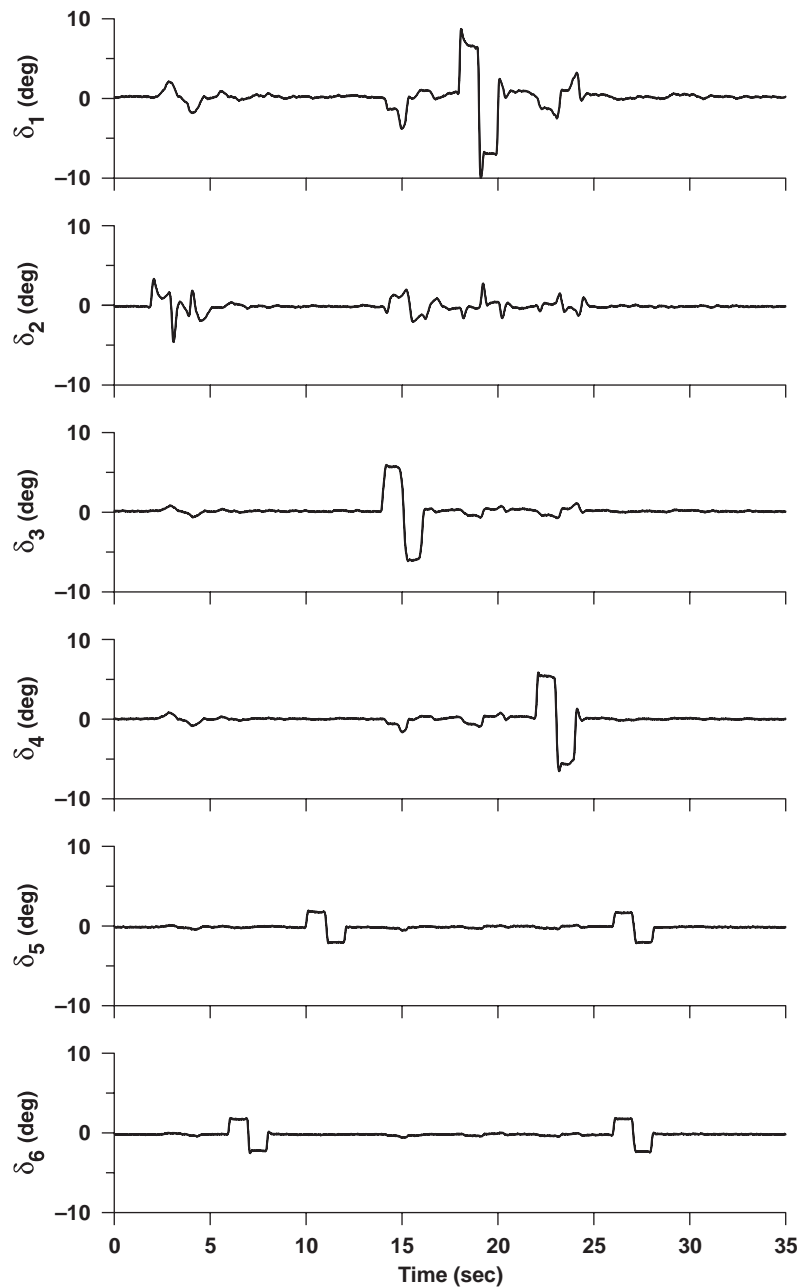


Fig. 9.15 Multi-input maneuver.

set of repeat records. Next, there are  $n_c$  MISOSA cases: each case designates one of the controls as primary and the remaining controls as secondary. The identification of the complete frequency-response matrix is completed by repeating the solution method of Sec. 9.6.1  $n_c$  times, using a different control as the primary input for each pass. This process was used to provide the complete MIMO frequency-response estimate matrix  $\hat{T}$  from flight data from a single multi-axis maneuver and yielded an accurate MIMO state-space model of this aircraft using CIFER®.

### 9.11 Determination of Broken-Loop Response for MIMO Control System

A special situation arises in the determination of the broken-loop response for a MIMO closed-loop system. Consider again the MIMO helicopter control system of Fig. 5.12 repeated in Fig. 9.16. In stability-margin determination for MIMO system, we wish to determine the stability margins for one loop at a time, *with the*

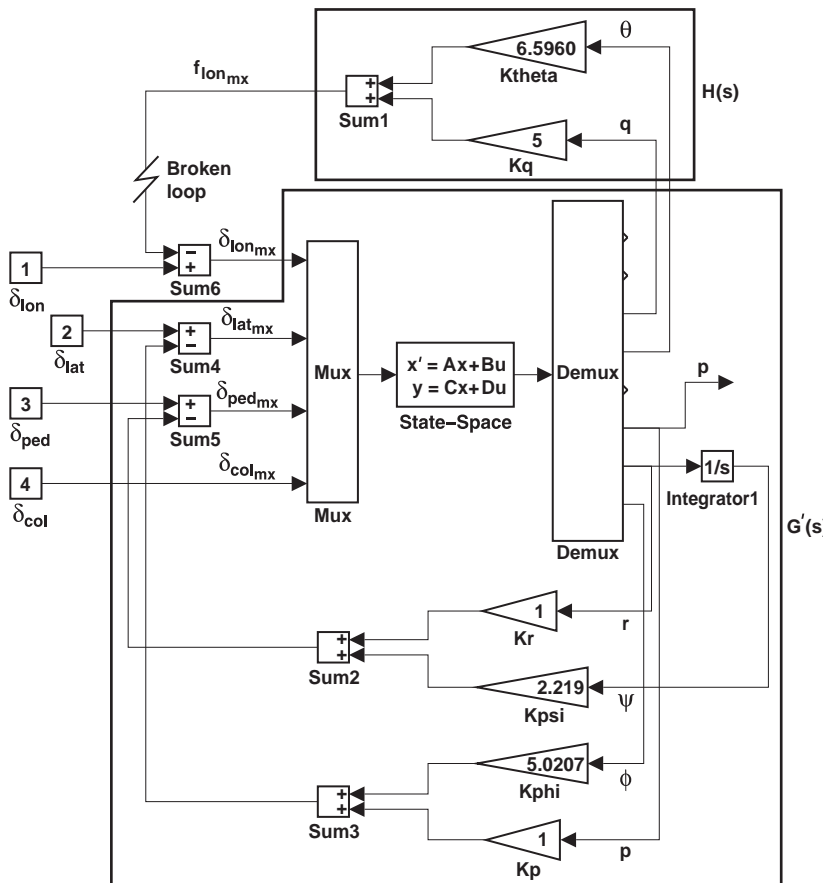


Fig. 9.16 Determination of broken-loop pitch response for MIMO control system.

*remaining loops closed.* For example, in Fig. 9.16 we would like to determine the stability margin for the pitch loop [indicated as  $BL(s)$ ], with the roll and yaw loops closed. So, in this analysis, we specifically want to include the effect of the suppression of the off-axis responses by the remaining loops.

The desired response is now the *equivalent* bare-airframe response [ $G'(s)$ ]. This is the bare-airframe SISO pitch response with the remaining closed, as indicated by the box in Fig. 9.16. The relevant feedback controller is  $H(s)$ , also indicated in Fig. 9.16. Then, using the direct method of Eq. (7.86), we determine the broken-loop pitch response using the *SISO analysis* method with  $e = \delta_{\text{lon}_{\text{mx}}}$  and  $f = f_{\text{lon}_{\text{mx}}}$ , where both signals are shown in the figure. We specifically *do not use* the *MIMO* identification solution. The equivalent bare-airframe frequency response  $G'(s)$  as obtained in this SISO analysis is well approximated by the pitch response with roll and yaw degrees of freedom constrained obtained using the method of coupling numerators (for example, see Tischler<sup>125</sup>).

## Problems

### *Methods and guidelines for multi-input identification techniques*

**9.1** Given flight data, explain how you could use the SISO frequency responses and autospectrum data to determine that a SISO solution for a MISO system is sufficient.

**9.2** Using Eq. (9.10), show what happens to an off-axis response when cross-control correlation is zero. What happens when cross-control correlation is one?

**9.3** Plot the cross-control correlation of the control deflections (the coherence of the aileron to the rudder, for example) for the lateral and directional sweeps for either the cruise or hover data from the XV-15. Would you say that the cross-control correlation meets the guideline given in Eq. (9.18)?

### *Conditioning of bare-airframe XV-15 frequency responses for multiple inputs with MISOSA*

**Students who worked with the hover configuration in Problem 7.16 should continue with that configuration in Problem 9.4a. Those who worked with the cruise configuration in Problem 7.17 should continue with that configuration in Problem 9.4b.**

**9.4a Hover configuration:** Use MISOSA (no plots) to condition the frequency responses generated in **Problem 7.16**. Choose MISOSA case names that correspond to those of the FRESPID cases. For the lateral-sweep case  $\delta_a$  is the primary input and  $\delta_r$  is the secondary input, whereas for the directional-sweep case the reverse is true. The outputs ( $v$ ,  $p$ ,  $r$ , and  $a_y$ ) will be the same for both cases.

**9.4b Cruise configuration:** Follow instructions for **Problem 9.4a**, except the outputs will now be  $p$ ,  $r$ ,  $a_y$ , and  $\beta$  from **Problem 7.17**.

**9.5** Compare the SISO and MISO solutions of either **Problem 9.4a** or **Problem 9.4b** using utility 19. Plot the magnitude, phase, and coherence for the off-axis bare-airframe responses  $r/\delta_a$  and  $p/\delta_r$ . Repeat the comparison for the on-axis bare-airframe responses  $p/\delta_a$  and  $r/\delta_r$ . What can you conclude from these results?

*Conditioning of closed-loop XV-15 frequency responses for multiple inputs with MISOSA*

**9.6** Compare the SISO and MISO solutions for the closed-loop roll response in hover  $p/\delta_{\text{lat}}$ . First, return to your FRESPID case (**Problem 7.2**), and add the input  $\delta_{\text{ped}}$ , making sure to indicate that you want the analyze the cross correlation of the controls. Then run MISOSA to condition out  $\delta_{\text{ped}}$  from the response. Compare the SISO and MISO results for the closed-loop response. How much do the bandwidth and phase delay change from the SISO calculations of **Problem 7.5**?

**9.7** Plot cross-control coherence of the piloted inputs for the hover lateral-sweep case from **Problem 9.6**. Is there considerable control correlation at any frequency? How can you explain that the closed-loop MISO solution is nearly identical to the SISO solution at all frequencies that are within the region of good coherence?

## 10 Composite Windowing

Data windowing was introduced in Chapter 7 as a standard method of spectral analysis to reduce the random error in the spectral estimates. Repeat maneuvers are first linked into concatenated records, which are then segmented into a sequence of shorter overlapping time records called *windows* or *periodograms*. The guidelines for window-size selection (Sec. 7.10) provide a range of possible window lengths  $T_{\text{win}}$ . The ultimate choice of window length is a balance between increased information content at low frequency (larger windows) vs better random error suppression which is important at higher frequencies (smaller windows). Hence no single window size selection will produce optimal results over the entire frequency range of interest. Furthermore, a window that is best suited to a particular input/output frequency-response pair might be much less desirable for other input/output pairs in the MIMO frequency-response estimate matrix  $\hat{T}$ .

To obtain the most accurate identification estimates for a particular situation, the spectral calculations (SISO and multi-input conditioning) would have to be performed repeatedly using several different window sizes. The best window size could then be selected based on the compromise just discussed and an individual assessment based on each frequency-response pair. Clearly, this would be a manually intensive exercise, and in the end it would still be a compromise. The optimization-based *composite-windowing* technique both eliminates the need for manual assessment and overcomes the compromises entailed with a single window-size selection. This technique merges the results obtained from the range of window sizes into a single, MIMO composite frequency-response estimate matrix  $\hat{T}_c$  of exceptional quality and dynamic range. The COMPOSITE program in CIFER® integrates the composite-windowing technique with the automated management of the large amount of spectral data for the various window sizes. This completes the database of *conditioned frequency responses and partial coherences*, shown in Fig. 2.1, and it is the last step in the nonparametric identification process (Sec. 1.4). From this point, more detailed analyses can be conducted on the frequency responses, or more detailed parametric models can be determined (Fig. 2.1).

Key topics to be covered in this chapter include the following: background for the composite-windowing method, composite-windowing approach, choice of windows, composite windowing in CIFER® using COMPOSITE, and examples.

### 10.1 Background

Section 7.5.3 introduced the standard technique of windowing in spectral analysis to reduce the random error in the frequency-response estimates. The problem of choosing a suitable window size was investigated at some length in Sec. 7.10. It involves a fundamental balance between dynamic range vs random error, as illustrated in Fig. 10.1 and summarized in the following.

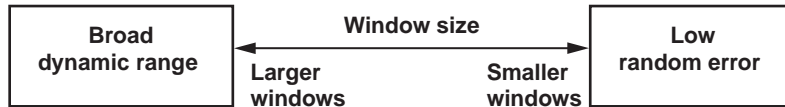


Fig. 10.1 Fundamental tradeoff in window-size selection.

For larger window sizes, the effective minimum frequency of identification is reduced, thereby yielding better information content at lower frequencies of interest. However, the number of window sections is also reduced, which means fewer windows to be averaged in the spectral calculations (lower  $n_d$ ), resulting in higher random error  $\epsilon_r$ . There is an increased oscillation of the magnitude and phase curves, especially at higher frequencies, where noise-to-signal ratios are generally higher and there is a need for more averaging.

Smaller windows means more averaging, which reduces the random error. This greatly improves the identification accuracy at higher frequencies, but at the expense of diminished information content at the lower frequencies of interest (higher effective minimum frequency). Smaller windows can also cause resolution bias error in the identification of lightly damped modes (e.g., in Fig. 7.9).

Selecting a single window size thus requires that a compromise be made in order to improve the accuracy of the frequency response at some frequencies at the expense of other frequencies. The window selection depends on the specific identification application at hand and is likely to be different for each pair in the MIMO frequency-response estimate matrix  $\hat{T}$ . For a typical helicopter, the MIMO system model consists of four inputs and nine outputs, yielding a total of  $4 \times 9 = 36$  frequency responses. A range of windows would need to be manually evaluated to arrive at an optimum window size for each frequency response. Yet even after all of this work, the selected window would be best suited to only a limited portion of the overall frequency range of interest. All of these considerations have led to a widespread perception that frequency-response analysis is somewhat of a “black art.”

Clearly, what is needed is a method that does the following: eliminates the need for repeated, manual optimization of window sizes and produces a single, optimized frequency response that is accurate over the entire frequency range of interest. The composite-windowing method discussed herein achieves these two objectives. This technique merges the results obtained with a range of window sizes into a single MIMO *composite frequency-response estimate matrix*  $\hat{T}_c$  of exceptional quality and dynamic range.

## 10.2 Composite-Window Approach

Windowing with a single window produces a smoothed spectrum (e.g.,  $\hat{G}_{xx}$ ; Sec. 7.5.3) from a rough spectrum ( $G_{xx}$ ; Sec. 7.5.1). Composite windowing refines the spectral calculations by combining the smooth results for multiple windows to produce the *composite spectral estimate*  $\hat{G}_{xx_c}$ .

Composite windowing starts with the selection of a range of windows sizes to be combined. Upper and lower limits of window size are selected based on the guidelines of Sec. 7.10. Additional windows are then selected to span these two

limits. We denote the total number of window sizes selected as  $n_w$ . The SISO frequency-response identification is then performed for each of the selected window sizes. For MIMO system analysis, this is followed by multi-input conditioning to produce the conditioned frequency responses for each selected window size.

Next, a weighting function  $W_i$  is determined for each window  $i$  and frequency  $f$  to be used for combining the windows into a single composite result. To emphasize the windows with the most accurate data, we select a function that varies inversely with  $(\epsilon_r)_i$ , the random error for that window and frequency-response pair [Eq. (7.55) for SISO or Eq. (9.36) for MISO applications]. The function used in CIFER® is

$$W_i = \left[ \frac{(\epsilon_r)_i}{(\epsilon_r)_{\min}} \right]^{-4} \quad (10.1)$$

so that the data with the minimum error  $(\epsilon_r)_{\min}$  are given a weight of  $W_i = 1$  and the windows with higher errors are deweighted accordingly. The weighting function is also tapered at the start and end of the frequency range over which the data for the particular window are used to avoid discontinuities in the composite result.

An initial solution for the composite values of each of the spectral functions is based on a simple weighted average.<sup>141</sup> For example, the weighted-average solution for the composite input autospectrum  $\widehat{G}_{xx}$  at each discrete frequency  $f$  is obtained from the  $n_w$  individual (smooth) window results at the same frequency  $\widehat{G}_{xx_i}$ :

$$\widehat{G}_{xx} = \frac{\sum_{i=1}^{n_w} W_i^2 \widehat{G}_{xx_i}}{\sum_{i=1}^{n_w} W_i^2} \quad (10.2)$$

The data used in this calculation start at the minimum identification frequency [ $f_{\min}$ , Eq. (7.34)] for the largest window and the minimum effective frequency [ $(f_{\min})_{\text{effective}}$ , Eq. (7.59)] for the remaining (smaller) windows. This ensures the use of the most accurate data in the averaging process.

The weighted-average calculation of Eq. (10.2) is repeated to provide the analogous results for the remaining three spectral quantities: the output autospectrum  $\widehat{G}_{yy}$ , the real part of the cross spectrum  $\text{Re}(\widehat{G}_{xy})$ , and the imaginary part of the cross spectrum  $\text{Im}(\widehat{G}_{xy})$ .

Next, the coherence based on the weighted-average spectral quantities is determined from Eq. (7.51):

$$\widehat{\gamma}_{xy}^2(f) = \frac{|\widehat{G}_{xy}(f)|^2}{|\widehat{G}_{xx}(f)| |\widehat{G}_{yy}(f)|} \quad (10.3)$$

The final *composite values* for spectral functions are those that minimize the weighted least-squares cost function  $J$  at each discrete frequency  $f$ :

$$J(f) = \sum_{i=1}^{n_w} W_i \left\{ \left( \frac{\hat{G}_{xx_c} - \hat{G}_{xx_i}}{\hat{G}_{xx}} \right)^2 + \left( \frac{\hat{G}_{yy_c} - \hat{G}_{yy_i}}{\hat{G}_{yy}} \right)^2 + \left[ \frac{\operatorname{Re}(\hat{G}_{xy_c}) - \operatorname{Re}(\hat{G}_{xy_i})}{\operatorname{Re}(\hat{G}_{xy})} \right]^2 \right. \\ \left. + \left[ \frac{\operatorname{Im}(\hat{G}_{xy_c}) - \operatorname{Im}(\hat{G}_{xy_i})}{\operatorname{Im}(\hat{G}_{xy})} \right]^2 + 5.0 \left( \frac{\hat{\gamma}_{xy_c}^2 - \hat{\gamma}_{xy_i}^2}{\hat{\gamma}_{xy}^2} \right)^2 \right\} \quad (10.4)$$

where  $\hat{G}_{xx_c}$  is the *composite* input autospectrum estimate at frequency  $f$ , and the analogous notation is used for the other composite spectral quantities. Including the last term (coherence) in the cost function of Eq. (10.4) ensures that the coherence function of the composite frequency response will track the coherence of the most reliable windows over the entire frequency range.

The cost function  $J$  of Eq. (10.4) has a nonlinear dependency on the (unknown) composite spectral quantities (because of the coherence term), and so the minimization must be determined iteratively. A quick and robust solution is obtained using standard gradient-based methods. The startup values are the weighted-average results [e.g., Eq. (10.2)], which correspond to the exact solution for the minimization of  $J$  when the last term in Eq. (10.4) is dropped. The optimization returns composite spectral functions and a composite frequency-response result that tracks the windows with the highest coherence and lowest random error (most reliable data) over the entire frequency range.

The composite frequency-response estimate is then determined using Eq. (7.37) and the composite auto- and cross spectra

$$\hat{H}_c(f) = \frac{\hat{G}_{xy_c}(f)}{\hat{G}_{xx_c}(f)} \quad (10.5)$$

and the associated coherence function, determined from Eq. (7.51), is

$$\hat{\gamma}_{xy_c}^2(f) = \frac{|\hat{G}_{xy_c}(f)|^2}{|\hat{G}_{xx_c}(f)| |\hat{G}_{yy_c}(f)|} \quad (10.6)$$

An estimate of the random-error function for the composite window result is obtained from Eq. (7.55), using the composite-window coherence result of Eq. (10.6). In this case, the calculation of window section parameter  $n_d$  is calculated at each frequency  $f$  based on the weighted-average window length  $\hat{T}_{\text{win}}$  at each frequency:

$$\hat{T}_{\text{win}}(f) = \frac{\sum_{i=1}^{n_w} W_i^2 T_{\text{win}_i}}{\sum_{i=1}^{n_w} W_i^2} \quad (10.7)$$

### 10.3 Choice of Window Sizes

The selection of window sizes for the composite window procedure is easily accomplished based on the guidelines in Sec. 7.10. The maximum window length is defined as the lesser value from the guidelines of Eqs. (7.61) and (7.64). The minimum window length is given in Eq. (7.65). Once the maximum and minimum window sizes are chosen, the remaining windows are selected to provide a fairly uniform distribution for the total number of window sizes selected (maximum:  $n_w = 5$ ). With the computer processing capability currently available, the processing time for additional windows is negligible, and the maximum number of window sizes is usually selected. Experience with this technique has consistently shown that the composite result is robust to changes in the specific distribution of windows. Thus the choice of window distribution is not crucial. Finally, it is best to set the maximum frequency for all windows at the same value  $\omega_{\max}$ , rather than trying to second guess the best frequency ranges for each window.

### 10.4 Composite-Window Calculations in CIFER® using COMPOSITE

The CIFER® module that implements the composite-window calculations of Sec. 10.2 is named COMPOSITE. The user has only to specify the source of the frequency-response data (SISO or MIMO calculations) and which windows (up to five max) are to be used. The solution algorithm in COMPOSITE is based on an unconstrained optimization using quasi-Newton–Raphson methods.<sup>142</sup>

For particular frequencies, numerical problems can occur during the solution for the optimum cost function of Eq. (10.4). For example, the optimization might not converge for certain frequencies, or the process might converge to a local minimum where the resulting composite curves exceed the allowable deviation from the individual curves. Extensive experience has shown that such numerical problems generally occur in frequency ranges where the data quality is very poor (as indicated by low coherence and large oscillations in frequency-response curves). When this happens, the optimizer simply drops the particular frequency point from the frequency-response calculation and continues on to the next point. For typical flight-data-analysis applications, the number of dropped points is small (generally 1–5%) relative to the number of points that are generated for the final composite frequency response.

Extensive experience to date has shown the composite-windowing method to be highly robust and effective for a wide range of applications, including flight data, ground testing, and simulation. This technique for frequency-response estimation dependably outperforms standard (single window) frequency-response identification tools and eliminates the tedious manual optimization of window sizes. The composite-windowing technique is illustrated in the next section using the simple pendulum example.

### 10.5 Composite-Window Results for Pendulum Example

The SISO frequency response for the closed-loop (stable) pendulum example  $\theta/\bar{M}_{\text{ext}}$  was identified from simulation time-history data in Sec. 7.13 using a nominal window,  $T_{\text{win}} = 15$  s. The identification was repeated for four additional windows ( $T_{\text{win}} = 30$  s, 25 s, 20 s, 10 s). For clarity in the plot, Fig. 10.2 compares the results for only three windows ( $T_{\text{win}} = 30$  s, 20 s, 10 s).

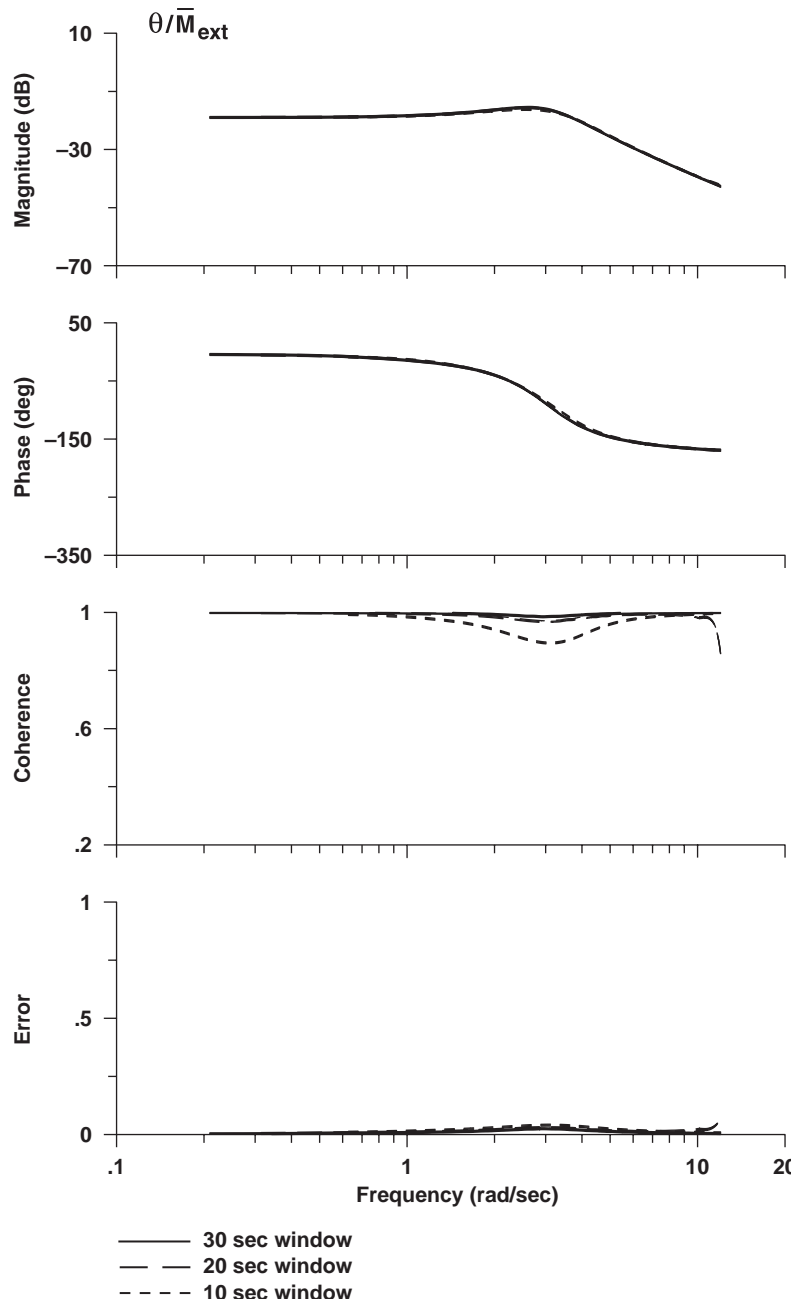


Fig. 10.2 Identification results for pendulum example using three window sizes.

The larger window is seen to be effective down to lower frequencies, and it provides for the highest coherence (nearly unity) and lowest random error over most of the frequency range. At the highest end of the identification frequency range, the smallest window provides slightly lower random error. The composite window result (five windows) is compared with the nominal (15-s) window in Fig. 10.3. The composite result tracks the individual windows in the frequency range over which they are most accurate. The result is an identification of great dynamic range, improved coherence (seen especially at the closed-loop pendulum

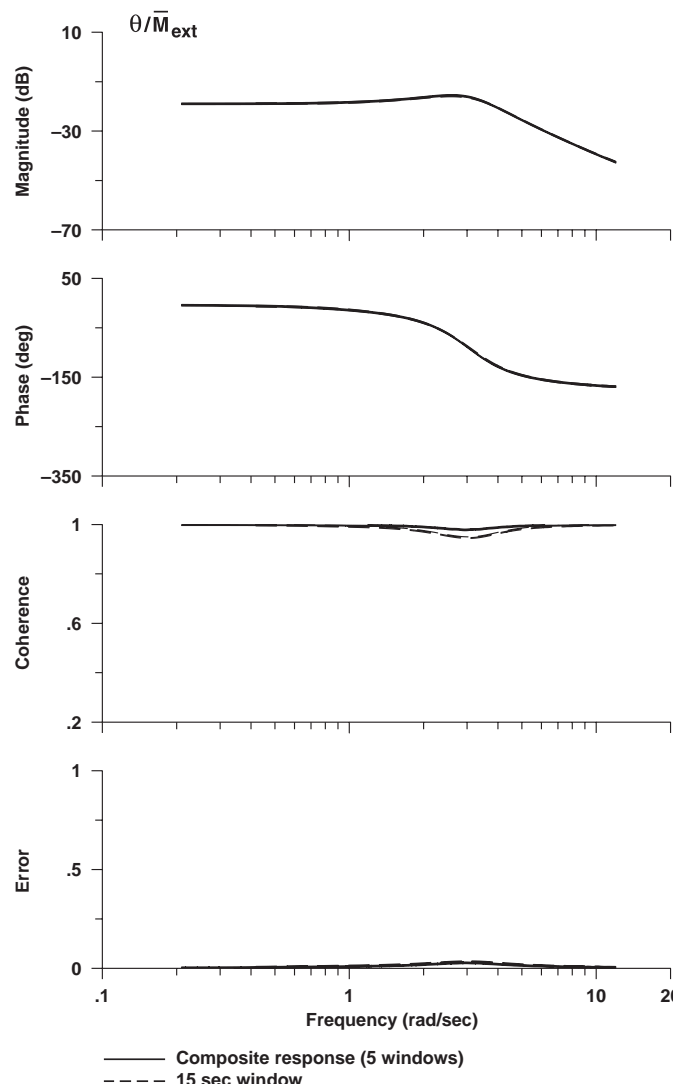


Fig. 10.3 Comparison of composite and nominal (15-s) window for pendulum.

frequency of 3 rad/s), and reduced random error at higher frequencies. The differences between the individual and composite-window frequency-response results are insignificant for this case of noise-free simulation data. However, there is considerable improvement in the results using the composite-windowing method for flight-test data as will be demonstrated in examples later in this section.

The next section will discuss composite windowing as an integrated step in the overall CIFER® approach.

## 10.6 COMPOSITE Windowing in Single-Input and Multi-Input Analyses

The work-flow path to identify frequency responses from a linked test record based on the single-input solution (FRESPID) is shown in Fig. 10.4. A good example of this work flow is the identification of the closed-loop (SCAS-on) response to a pitch control input (e.g.,  $q/\delta_{\text{lon}}$ ,  $\alpha/\delta_{\text{lon}}$ ,  $a_z/\delta_{\text{lon}}$ ) as needed for handling-qualities analyses. In this case, the time histories are a linked set of repeated longitudinal stick sweeps, and the small secondary control inputs are ignored. If  $n_w$  window sizes are selected, the SISO analysis will produce a total of  $n_o \cdot n_w$  frequency responses. The COMPOSITE program combines the results for the  $n_w$  windows, to achieve a final set of  $n_o$  optimized frequency responses that forms the  $n_o \times 1$  composite frequency-response estimate matrix  $\hat{T}_c$ . Another application of the use of the single-input analysis work path is the determination of the broken-loop response for a MIMO control system (Sec. 9.11). Here, the single-input solution provides the response of one loop broken, with the remaining control loops closed.

The analogous workflow for a multi-input analysis of the same identification problem (e.g.,  $q/\delta_{\text{lon}}$ ,  $\alpha/\delta_{\text{lon}}$ ,  $a_z/\delta_{\text{lon}}$ ) is shown in Fig. 10.5. In this case, both the (one) primary and  $(n_c - 1)$  secondary controls (for  $n_c$  controls in total) are included in the analysis. This SISO (FRESPID) step now produces many additional frequency responses associated with the secondary inputs as well as the cross-control spectra needed to condition the responses (MISOSA). After multi-input conditioning, there are the same number of frequency-response files as in the SISO case ( $n_o \cdot n_w$ ) and seen from reference to Fig. 10.4. As before, the last step is composite windowing, which combines the results for the  $n_w$  windows to achieve the final  $n_o$  optimized (and conditioned) frequency responses that form the  $n_o \times 1$  composite frequency-response estimate matrix  $\hat{T}_c$ . In both cases (single-input and multi-input analysis), composite windowing is the final step in the generation of the frequency-response database.

In the process of generating the frequency-response database, a large number of intermediate frequency responses are generated. The CIFER® modules (FRESPID,

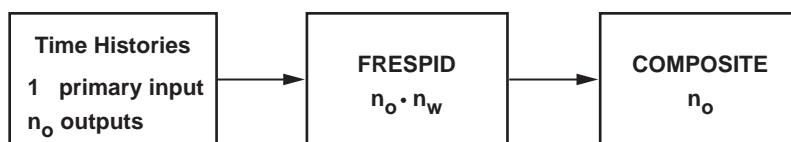


Fig. 10.4 COMPOSITE windowing in single-input analyses.

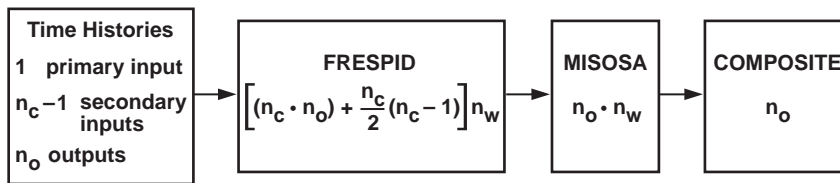


Fig. 10.5 COMPOSITE windowing in multi-input analysis.

MISOSA, and COMPOSITE) are highly integrated and provide a transparent progression from one step to the next. For example, the unique naming and database storage of all of the generated frequency-response files are automatically handled by the software.

The work-flow path for the more complex problem of bare-airframe 2 input MIMO identification is illustrated in Tables 10.1 and 10.2 for the XV-15 in cruise. The work-flow path of Table 10.1 is for the analysis of the lateral sweeps; it is a continuation of Table 9.1, which completed the multi-input conditioning step. This work-flow path, which carries the case name LATSWP, starts with concatenated time-history records for lateral frequency sweeps: the primary input is aileron  $\delta_a$ , and the secondary input is rudder  $\delta_r$ . Processing with MISOSA conditions the response to the primary input by removing the linear effect of the partially correlated secondary input  $\delta_r$ . So, the influence of the secondary control input is removed from the system-identification results. In other words, by the time the COMPOSITE windowing step is reached, there is only one input to consider for the LATSWP cases, namely,  $\delta_a$ , as seen in Table 10.1. The number of frequency responses generated for the LATSWP case by MISOSA and COMPOSITE is  $n_o \cdot n_w$  and  $n_o$ , respectively, shown in the last row of the table.

The work-flow path for the analysis of the pedal sweeps is shown in Table 10.2, which is a continuation of Table 9.2. In this case the primary input is  $\delta_r$ , and the secondary input is  $\delta_a$ . As in the first work-flow path, COMPOSITE works with only a single input ( $\delta_r$  in this case), because the effects of the

Table 10.1 Lateral-sweep-data analysis (cruise)

Time-history set	FRESPID	MISOSA	COMPOSITE
Lateral-sweep	case: LATSWP	case: LATSWP	case: LATSWP
Two inputs	Two inputs (cross correlation on)	Primary input: $\delta_a$ Secondary input: $\delta_r$	Input: $\delta_a$
Four outputs	Four outputs	Four outputs	Four outputs
Number of frequency responses generated	$[(n_c \cdot n_o) + (n_c/2)(n_c - 1)] n_w$ $= 9n_w$	$n_o \cdot n_w = 4n_w$	$n_o = 4$

Table 10.2 Pedal-sweep data analysis (cruise)

Time-history set	FRESPID	MISOSA	COMPOSITE
Pedal-sweep	case: PEDSWP	case: PEDSWP	case: PEDSWP
Two inputs	Two inputs (cross correlation on)	Primary input: $\delta_r$ Secondary input: $\delta_a$	Input: $\delta_r$
Four outputs	Four outputs	Four outputs	Four outputs
Number of frequency responses generated	$[(n_c \cdot n_o) + (n_c/2)(n_c - 1)]n_w$ $= 9n_w$	$n_o \cdot n_w = 4n_w$	$n_o = 4$

partially correlated secondary input  $\delta_a$  have been conditioned out by MISOSA. Once again, the number of frequency responses generated by MISOSA and COMPOSITE are  $n_o \cdot n_w$  and  $n_o$ , respectively.

Summarizing this section, one work-flow path (single-input or multi-input analysis) yields  $n_o$  final frequency responses for the primary input of that path. The completion of all work-flow  $n_c$  paths generates the set of  $n_c \cdot n_o$  frequency responses. This can be expressed as the  $n_o \times n_c$  MIMO composite frequency-response estimate matrix  $\bar{T}_c$  used for state-space model identification (Chapters 12 and 13).

## 10.7 Composite-Windowing Results for XV-15 Closed-Loop SISO Identification in Hover $p/\delta_{\text{lat}}$

In this example, the XV-15 closed-loop roll response  $p/\delta_{\text{lat}}$  for hover is determined using composite windowing for comparison with the single (nominal) window results of Chapter 7. As seen in **Problem 9.6**, the influence of secondary inputs on the closed-loop on-axis response identification is small and can be ignored, so that COMPOSITE windowing is completed using the SISO workflow of Fig. 10.4.

The individual lateral sweep records are  $T_{\text{rec}} = 99$  s (record 883) and  $T_{\text{rec}} = 95$  s (record 884) in length (Table 3.1). A maximum window size of  $T_{\text{win}} = 40$  s was selected based on the guidelines of Eqs. (7.61) and (7.64). The maximum frequency of interest in this case was selected as  $\omega_{\text{max}} = 12$  rad/s, resulting in a minimum window of  $T_{\text{win}} = 10$  s [consistent with Eq. (7.65)]. The SISO frequency-response results for the 40-s and 10-s windows are shown in Fig. 10.6. The larger window ( $T_{\text{win}} = 40$  s) is seen to provide data with good coherence starting at a frequency of about  $\omega = 0.4$  rad/s. However, the limited amount of spectral averaging at higher frequencies causes an increase in random error, as is seen in Fig. 10.6 and reflected in the oscillations in the magnitude and phase characteristics. Good coherence for the smaller window ( $T_{\text{win}} = 10$  s) is achieved starting at about  $\omega = 1$  rad/s, with a reduced random error seen at higher frequencies. The results for the nominal ( $T_{\text{win}} = 25$  s) window used in Figs. 7.5, 7.7, and 7.8 lie as expected in between the smaller and larger windows.

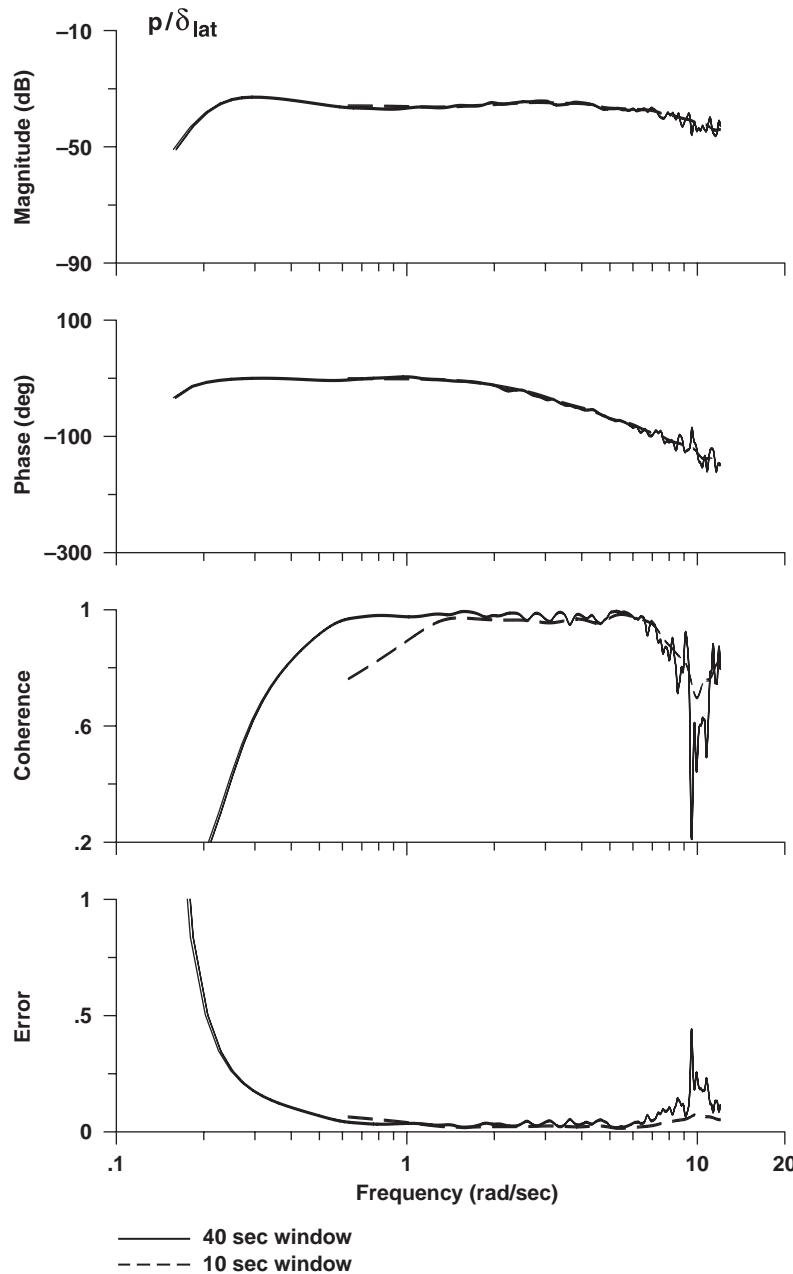


Fig. 10.6 Closed-loop roll-rate response for 40-s and 10-s windows (XV-15, hover).

A composite-window result for this response was generated using five windows uniformly spanning the range from the largest to the smallest ( $T_{\text{win}} = 40$  s, 35 s, 30 s, 20 s, 10 s). The resulting composite frequency response  $p/\delta_{\text{lat}}$  is shown in Fig. 10.7. An excellent identification is obtained over a wide frequency range (0.3–12 rad/s). In an improvement to the single (nominal) window results of Fig. 7.7, acceptable coherence is maintained even out to higher frequencies (8–12 rad/s), where excitation results only from the nonsinusoidal details of the piloted inputs (Sec. 5.9). The composite response is seen to generally track

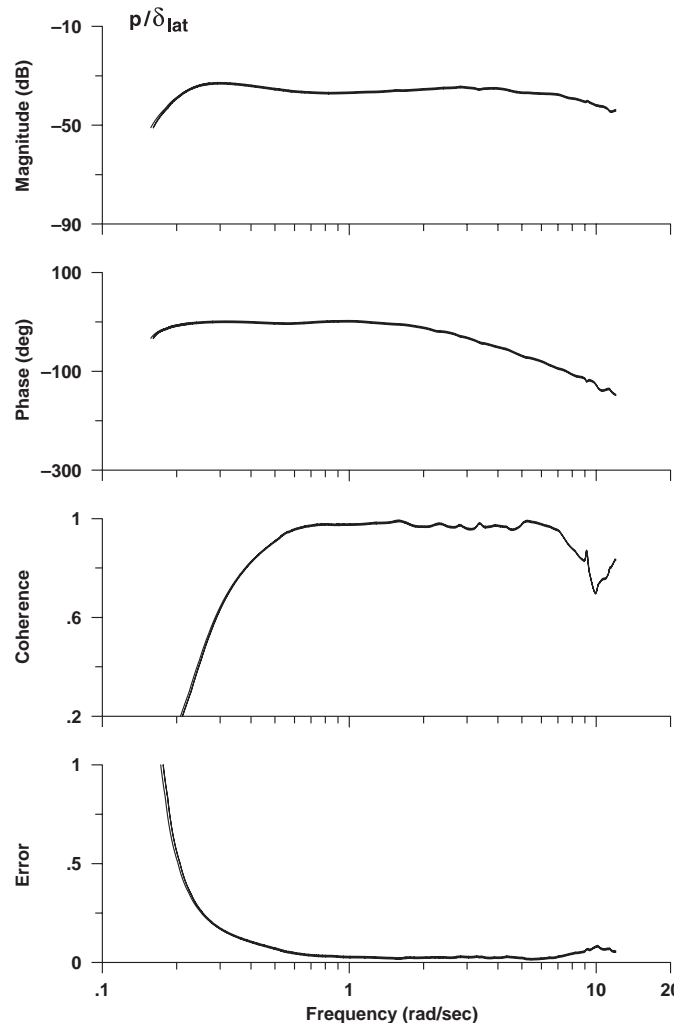


Fig. 10.7 Composite closed-loop roll-rate response using five spectral windows (XV-15, hover).

both the good coherence (and low random-error) results of the large window at low frequencies and the low random-error (smaller oscillations) results of the small window at higher frequencies. The composite frequency response is rapidly determined and is clearly an improved result compared to the single (nominal) window results of Chapter 7. Further analysis is not required to manually evaluate the potential tradeoffs in window size selection.

The next example demonstrates composite windowing for a MIMO bare-airframe identification application.

### 10.8 Composite-Windowing Results for Bo-105 Helicopter MIMO Identification

The MIMO work-flow of Fig. 10.5 is illustrated using lateral frequency-sweep data for the Bo-105 helicopter. This data set, obtained by the DLR in support of AGARD Flight Mechanics Panel Working Group 18 on Rotorcraft System Identification,<sup>10</sup> provides a dynamically rich and challenging example. The helicopter exhibits a high level of interaxis coupling, unstable flight-dynamics modes, highly coupled rotor and fuselage dynamics, and lightly damped rotor modes.<sup>15</sup>

Figure 10.8 shows the coherence functions that were obtained for three typical windows ( $T_{\text{win}} = 50$  s, 25 s, 5 s) from the MISO analysis of the on-axis roll-rate response  $p/\delta_{\text{lat}}$ . The minimum frequency for each window corresponds to  $\omega_{\text{min}} = 2\pi/T_{\text{win}}$  [from Eq. (7.34)]. As seen from the 50-s window, the sweep excitation produces a satisfactory identification starting at about  $\omega = 0.4$  rad/s, which is above the minimum effective frequency [ $(\omega_{\text{min}})_{\text{effective}} = 0.25$  rad/s]. As expected, the coherence for the 25-s and 5-s windows rises to roughly meet the coherence for the 50-s window at their respective effective minimum frequencies.

The results of Fig. 10.8 show that no single window size produces a fully satisfactory coherence across the entire frequency range. The 5-s window produces

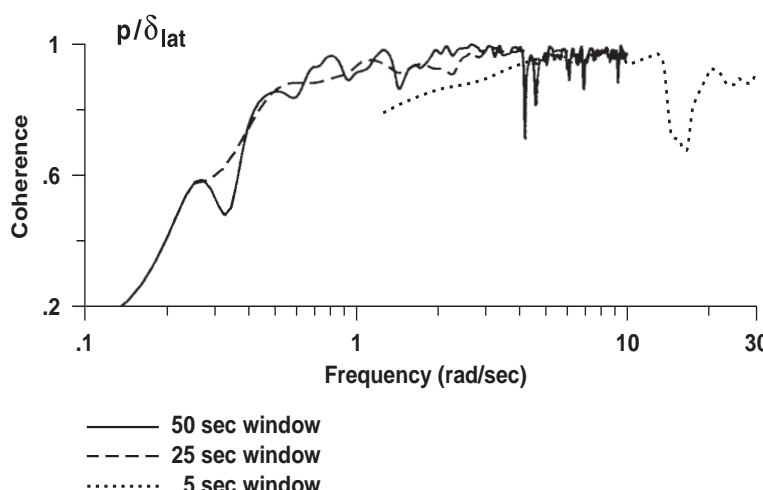


Fig. 10.8 Coherence functions for three different window sizes (Bo-105 helicopter).

good results for the higher frequencies, but the coherence drops off at lower frequencies. Conversely, the 50-s window works well for low frequencies, but the frequency response shows considerable random error at higher frequencies. The intermediate window size of 25 s might be considered as a good compromise in this case, but it does not produce the best coherence at most frequencies.

Figure 10.9 shows the COMPOSITE result obtained by combining five spectral windows ( $T_{\text{win}} = 50$  s, 35 s, 25 s, 10 s, 5 s) into a single, optimized frequency-response identification. The coherence function indicates that the identification is of very high quality across the entire range of excitation frequencies. The lightly damped mode at about 16 rad/s, well captured in the composite-window frequency response, is associated with the lead-lag rotor dynamics of the hingeless rotor design (no lag dampers), as discussed in Sec. 15.2.2.

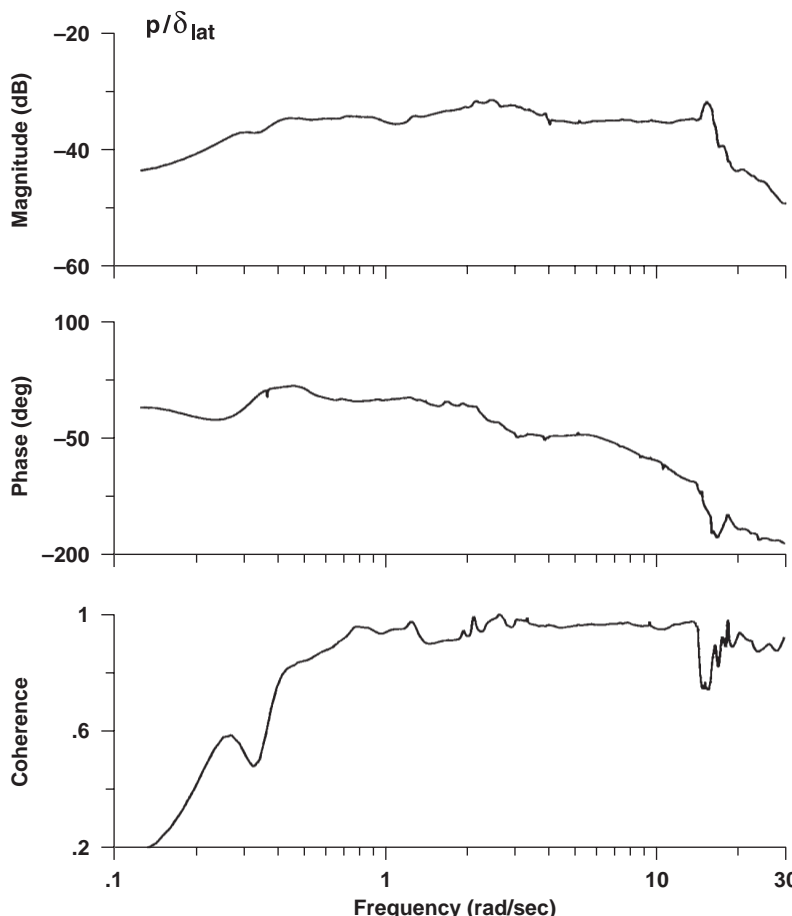


Fig. 10.9 Frequency response and coherence for composite window result (Bo-105 helicopter).

### 10.9 Composite Results for Structural System Identification

The structural system response of a rotor test stand was presented in Sec. 7.10.4. The result for three different window sizes, as illustrated in Fig. 7.9, showed that no single window produced a fully satisfactory result over the entire frequency range of interest. Although the 10-s window is free of bias errors, it produced considerable random error at higher frequencies because of the lack of sufficient averaging. The 5-s and 2-s windows resulted in frequency-response estimates with significant bias errors for the lower-frequency modes.

The COMPOSITE result for the three windows is shown in Fig. 10.10. A substantial improvement is achieved, with good frequency-response resolution at the modal peaks (no bias error) and good suppression of the high-frequency random error. The coherence plot for the composite-window result shows generally

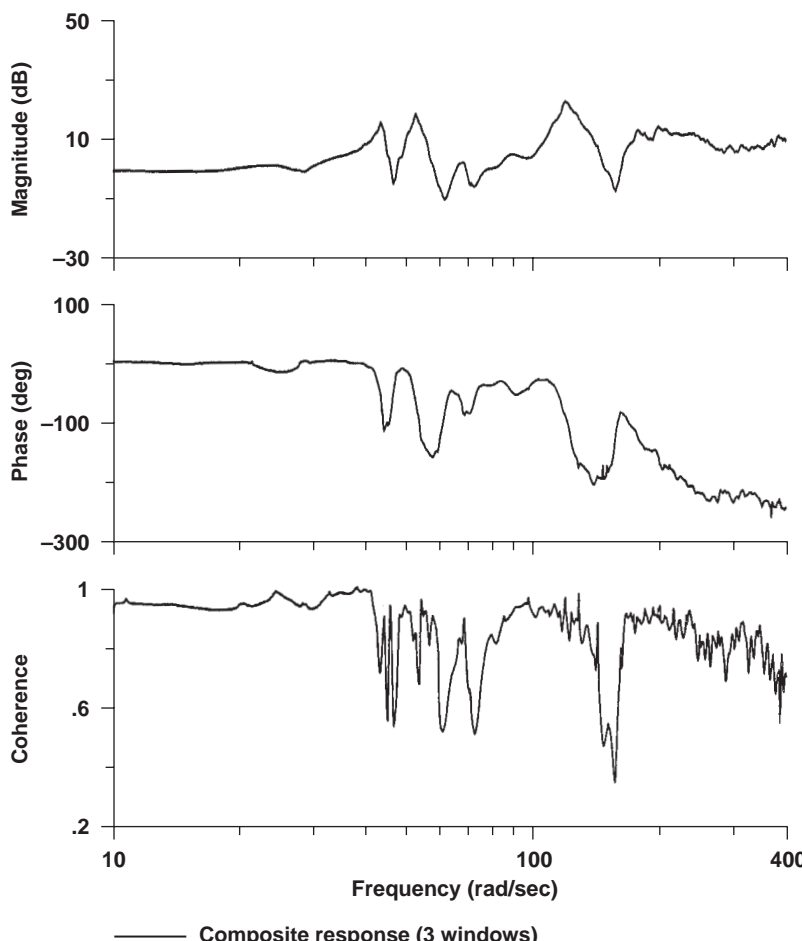


Fig. 10.10 Structural system identification using composite windowing.

excellent identification accuracy over the broad frequency range of the identification. The dips in coherence correspond to the antinodes in the structural response, where the signal-to-noise ratio is greatly reduced.

### 10.10 Composite Windowing in Spectral Analysis of Time-History Signals

Many applications of system identification seek to extract a mathematical description of the vehicle input-to-output response dynamics from flight-test data. For such applications, the composite windowing algorithm of Sec. 10.2 combines the individual window results to achieve a set of consistent spectral functions ( $\hat{G}_{xx_c}$ ,  $\hat{G}_{yy_c}$ , and  $\hat{G}_{xy_c}$ ) that together yield a frequency response of minimum random error that tracks the coherence of the most reliable frequency-response data. By contrast, spectral analysis applications such as those illustrated in Secs. 7.14.1 and 7.14.2 require an accurate estimate of the autospectrum of an isolated signal; the coherence of the input-to-output pair process is not relevant. Then the optimization of Eq. (10.4) is reduced to the weighted-average solution of Eq. (10.2). In this case, the weighting function of Eq. (10.1) retains only the window length dependency ( $\epsilon_r \propto 1/\sqrt{2n_d}$ ) of Eq. (7.55). This is triggered in COMPOSITE by designating the same time-history signal for both the input and the output.

Lusardi et al.<sup>122</sup> extracted accurate models of UH-60 helicopter response to turbulence from specially conducted flight tests. Figure 10.11 shows an example

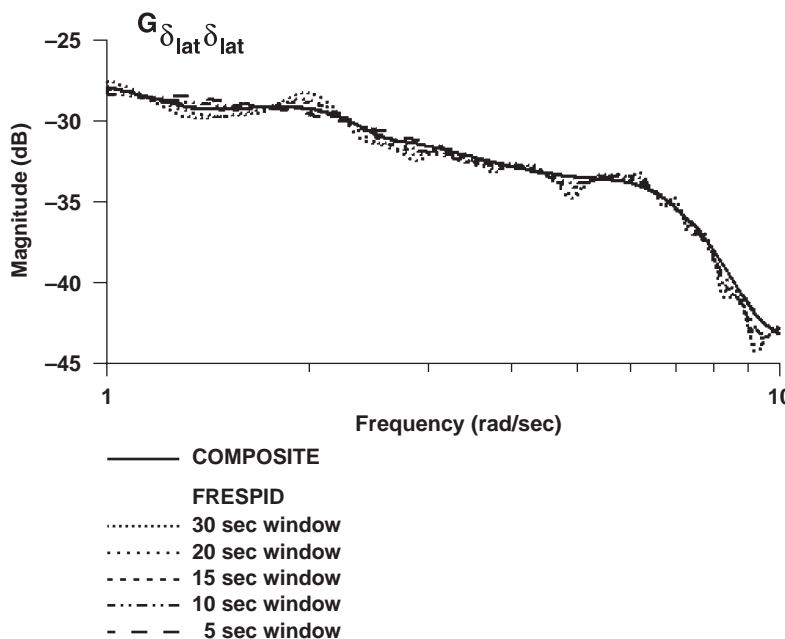


Fig. 10.11 Composite-window result for spectral analysis.

from this flight-test work of the autospectrum for lateral stick  $\delta_{\text{lat}}$ . The figure plots the autospectrum  $G_{\delta_{\text{lat}} \delta_{\text{lat}}}$  for five individual window sizes along with the result of composite-window processing using COMPOSITE. The figure clearly illustrates that a smooth autospectrum has been achieved that tracks the larger windows at low frequencies and the smaller windows at high frequencies.

## 10.11 Summary

It is important to reiterate that the improved accuracy of the composite frequency responses as demonstrated for the examples herein was obtained without having to select/optimize a single optimum window size. In fact, no single window could have produced these excellent results. It was only necessary to specify the minimum and maximum window sizes, together with a few other intermediate sizes spread roughly uniformly across this range. The composite-windowing optimization algorithm is fast and robust to specific choice of intermediate window sizes.

## Problems

*Use of COMPOSITE to combine multiple windows for the inverted pendulum system identification*

**10.1** Revert to the original pendulum parameters given in Eq. (3.6), and repeat the SISO identification (**Problem 8.3**) of the unstable response  $\theta/M_{\text{inv}}$  using a range of windows, and combine the windows using COMPOSITE windowing. Use the guidelines given in Chapter 7 to choose the window sizes.

**10.2** Repeat the SISO identification (**Problem 7.11**) of the stable pendulum response  $\theta/\bar{M}_{\text{ext}}$  using a range of windows, and then combine the windows using COMPOSITE windowing. Be sure to revert to the original pendulum parameters given in Eq. (3.6). Use the guidelines given in Chapter 7 to choose the window sizes.

*Use of COMPOSITE to combine multiple windows for closed-loop XV-15 system identification*

**10.3** Repeat the SISO identification of the closed-loop XV-15 response  $p/\delta_{\text{lat}}$  for hover performed in **Problem 7.2** for a range of windows, and then combine the windows using COMPOSITE. (Hint: Use guidelines in Chapter 7 for choosing window sizes.)

**10.4** Use the general plotting utility (19) to compare the result of the composite window with that obtained from a single window.

**10.5** Rerun your FRESPID and COMPOSITE closed-loop  $p/\delta_{\text{lat}}$  cases from **Problem 10.3** using the same minimum and maximum window lengths, but change the intermediate window sizes. Examine the sensitivity of the COMPOSITE result to the intermediate window lengths.

*Use of COMPOSITE to combine multiple windows for the open-loop XV-15 system identification*

*Students should continue with their choice of configuration (hover or cruise) made in the Chapter 7 Problems.*

**10.6** Rerun the FRESPID and MISOSA analyses obtained for the hover or cruise configuration using a range of windows and adding  $\phi$  as an additional output to the lateral-sweep hover case. Choose window sizes based on the Chapter 7 guidelines. Use COMPOSITE to combine the windows for a final set of eight (cruise) or nine (hover) frequency responses. Generate hard-copy plots of these optimized frequency responses.

**10.7** Use utility 19 to coplot the composite window and individual MISO windows for the  $p/\delta_a$  frequency responses obtained in **Problem 10.6**. Based on analysis of this plot, describe how the individual windows are combined in COMPOSITE to make one window.

*Use of COMPOSITE for spectral analysis of a signal*

**10.8** Rerun the SISO calculation of the lateral-stick autospectrum  $G_{\delta_{\text{lat}}\delta_{\text{lat}}}$  from the closed-loop XV-15 data in hover. This time use output = input =  $\delta_{\text{lat}}$  and run the results for five spectral windows. Use a different case name to avoid overwriting your old results.

**10.9** Use COMPOSITE (and the results of **Problem 10.8**) to determine a new lateral-stick autospectrum  $G_{\delta_{\text{lat}}\delta_{\text{lat}}}$ . Then compare the COMPOSITE result with the SISO result from **Problem 10.8**. Why are these autospectra different?

**10.10** Determine the rms of the input  $\delta_{\text{lat}}$ , using the input autospectrum  $G_{\delta_{\text{lat}}\delta_{\text{lat}}}$  calculated with COMPOSITE (in **Problem 10.9**). Use utility 7 for this analysis, and calculate the rms over the entire frequency range available. Is the rms value the same as the SISO solution obtained in **Problem 7.7**? Is the COMPOSITE rms a closer match to the time-domain calculation from the log file of **Problem 7.3**?

# 11

## Transfer-Function Modeling

The theory and procedures discussed through Chapter 10 address the identification of a high-quality MIMO frequency-response database from the initial frequency-sweep time-history records. This MIMO database of *conditioned frequency responses and partial coherences*, shown in Fig. 2.1, constitutes the *non-parametric model* of Sec. 1.4. As the flowchart in Fig. 2.1 shows, there are two classes of *parametric models* that can be obtained at this point: transfer-function and state-space representations. The detailed topics of parametric model identification will be the focus of the next three chapters.

This chapter discusses the determination of transfer-function representations, which are the parametric model forms that are the simplest to extract from the numerical frequency-response databases. Transfer-function models are (linear) input-to-output descriptions of the dynamic system; they can be represented by pole-zero descriptions. A transfer-function fit that best matches the frequency-response data (magnitude and phase) on a Bode plot over the frequency range of interest is obtained.

For many applications these models are found to be quite sufficient, including handling-qualities analysis, actuator and other subsystem models, aeroelastic mode determination, and models for root-locus-based control system design. Even if the ultimate goal is the determination of a fully coupled state-space representation, as discussed in Chapters 12 and 13, obtaining transfer-function models is a useful intermediate step that provides information on the fundamental dynamic characteristics and a good estimate of key parameter values.

The transfer-function identification approach presented in this chapter is based on the lower-order equivalent system (LOES) concepts initially put forth by Hodgkinson et al.,<sup>49</sup> and later covered, for example, in Hodgkinson,<sup>59</sup> Bischoff and Palmer,<sup>50</sup> and Bischoff.<sup>143</sup>

The main topics to be covered in this chapter include the following: motivation for transfer-function modeling, transfer-function model identification method, selection of model structure, SISO transfer-function identification in CIFER<sup>®</sup> using NAVFIT, and applications and examples.

### 11.1 Motivations for Transfer-Function Modeling

Transfer-function models, that accurately match the flight-data frequency responses and thus characterize the overall input-to-output response dynamics can be identified. Although such models can be used to represent the complete MIMO behavior, they are most commonly used to represent the single-input/single-output on-axis response of the flight vehicle or subsystem (e.g.,  $p/\delta_{\text{lat}}$ ). The system to be modeled is, in essence, treated like a “black box” because there generally is no attempt to represent the actual physics of the aircraft using force and moments

equations and the associated physical constraints (e.g., gravity and kinematics). Instead, transfer-function models are composed of a numerator and denominator polynomial in the Laplace variable  $s$ , and they can include an equivalent time delay to account for additional, unmodeled, high-frequency dynamics, and actual transport delays in the system. The transfer-function model results are best presented in factored form to expose the gain, poles and zeros (or time constants), and time delay. Although the complete aircraft or helicopter dynamics for a bare-airframe or closed-loop system can be composed of many states (even hundreds, in the case of a modern fly-by-wire airframe), the overall end-to-end frequency response can be well characterized over the frequency range of interest by a very simple LOES transfer function composed of only a few dominant modes. In spite of this apparent simplicity, these transfer-function models can provide a very accurate representation of the system-response behavior, including the prediction of time response to control inputs. Furthermore, these models constitute a fully satisfactory “end result” of identification for many key applications, such as handling-qualities analyses, flight-mechanics characterization, flight-dynamics modeling for control system design, subsystem component modeling, and aeroelasticity modeling. Examples of each of these applications are presented in this chapter.

## 11.2 Transfer-Function Modeling Identification Method

A transfer-function model is sought that best fits the frequency-response data for a given input-output pair over a selected frequency range. This chapter presents identification methods and results that are based, for the most part, on single transfer-function fits. In MIMO system applications, this is directly applicable to the on-axis (diagonal) response for largely uncoupled systems. Transfer-function models based on coupled single-input/two-output and two-input/two-output identification techniques are also commonly used in aircraft handling-qualities and flight-mechanics analyses. These applications involve simultaneous fits of two transfer functions, with constraints imposed to ensure that the responses have the same denominators (as they must physically). These topics are covered in excellent references by Bischoff and Palmer,<sup>50</sup> MIL-STD-1797,<sup>5</sup> and Field et al.<sup>144</sup> Extending the transfer-function fitting approach for model structures beyond the two-input/two-output case becomes cumbersome. The generalized modeling of coupled MIMO systems is best accomplished by representing the dynamics in state-space form as covered in Chapters 12 and 13.

A transfer-function model of the generalized form

$$T(s) = \frac{(b_0 s^m + b_1 s^{m-1} + \dots + b_m) e^{-\tau_{eq}s}}{(s^n + a_1 s^{n-1} + \dots + a_n)} \quad (11.1)$$

is sought that best matches the identification frequency-response data. For physical systems, the causality condition<sup>145</sup> states that the response (output) cannot depend on the input at a future time, which implies

$$m \leq n \quad (11.2)$$

The transfer-function model can also be displayed in the factored form

$$T(s) = \frac{k(1/T_{z_1})(1/T_{z_2})\cdots(1/T_{z_m})e^{-\tau_{eq}s}}{(1/T_{p_1})(1/T_{p_2})\cdots(1/T_{p_n})} \quad (11.3)$$

where the parameters of the model are as follows:

- $k$  = high-frequency gain ( $s \rightarrow \infty$ )
- $(1/T_{z_i})$  = shorthand notation for the  $i$ th zero,  $s + 1/T_{z_i}$
- $(1/T_{p_i})$  = shorthand notation for the  $i$ th pole,  $s + 1/T_{p_i}$
- $\tau_{eq}$  = equivalent time delay

When the zeros (or poles) are complex conjugate pairs, they are displayed in terms of the damping ratio and natural frequency as

$$[\zeta, \omega] \Rightarrow [s^2 + 2\zeta\omega s + \omega^2]$$

The orders of the numerator  $m$  and denominator  $n$  are chosen so as to achieve a good fit of the frequency-response data in the frequency range of interest and to be consistent with the physics of the system and causality [Eq. (11.2)]. So transfer-function models of fixed-wing flight dynamics typically have an order  $n$  of four or less (LOES modeling), which corresponds to the classical flight-mechanics modes. For rotorcraft applications, the order can reach as high as 10 or more, to include the coupled fuselage/rotor responses.<sup>18</sup> A satisfactory model of mechanical linkage responses and other elements with dynamics at frequencies much higher than the frequency-response data range can be as simple as  $ke^{-\tau_{eq}s}$ . The equivalent time delay  $\tau_{eq}$  is a lumped parameter to account for the phase lag caused by all unmodeled higher-frequency dynamics modes, but it can also include actual transport delay (e.g., computational delays in the flight control and navigation systems).

In the transfer-function identification process, each of the coefficients  $a_i$  and  $b_i$  of the polynomials and the equivalent time delay  $\tau_{eq}$  can be individually fixed or freed (in the latter case, to be optimized). For example, an examination of the slope of the frequency-response magnitude data at high frequency can provide a direct value of the high-frequency gain  $b_0$ . Fixing this value can be effective to ensure that it does not vary as a result of correlation with the other free parameters. The low-frequency gain of the transfer-function  $b_m/a_n$  is the steady-state response to control inputs and provides useful information on aircraft agility. For example, the low-frequency gain of  $p/\delta_a$  indicates the steady-state roll rate per degree of aileron input (deg/sec/deg-aileron).

A numerical optimization algorithm determines the set of unknown (i.e., freed) quantities in Eq. (11.1) that minimizes the magnitude and phase errors between the desired SISO transfer-function model  $T$  and the associated composite frequency-response estimate (i.e., *data*)  $\hat{T}_c$ . Typically, the models of interest are for the key on-axis response pairs (e.g.,  $p/\delta_a$ ,  $q/\delta_e$ , etc.) of the identified  $n_o \times n_c$  composite

frequency-response estimate matrix  $\hat{\mathbf{T}}_c$  introduced in Sec. 10.6. The quadratic cost function  $J$  to be minimized is

$$J = \frac{20}{n_\omega} \sum_{\omega_1}^{\omega_{n_\omega}} W_\gamma [W_g (|\hat{\mathbf{T}}_c| - |T|)^2 + W_p (\angle \hat{\mathbf{T}}_c - \angle T)^2] \quad (11.4)$$

where

- $||$  = magnitude (dB) at each frequency  $\omega$
- $\angle$  = phase (deg) at each frequency  $\omega$
- $n_\omega$  = number of frequency points (typically selected as  $n_\omega = 20$ )
- $\omega_1$  and  $\omega_{n_\omega}$  = starting and ending frequencies of fit (typically covering 1–2 decades)

By selecting the  $n_\omega$  frequency points  $\omega_1, \omega_2, \dots, \omega_{n_\omega}$  in a uniform spacing over a log-frequency scale (rad/s), the minimization achieves a best fit as displayed on the Bode plot. The other parameters in Eq. (11.4) are as follows:

1)  $W_\gamma$  is a weighting function dependent on the value of the coherence function at each frequency  $\omega$ . The function used in CIFER® is

$$W_\gamma(\omega) = \left[ 1.58 \left( 1 - e^{-\gamma_{xy}^2} \right) \right]^2 \quad (11.5)$$

thereby emphasizing the most reliable data. For a coherence of  $\gamma_{xy}^2 = 0.6$ , this function reduces the weight on the squared errors by 50%.

2)  $W_g$  and  $W_p$  are the relative weights for magnitude and phase squared-errors. The normal convention<sup>5</sup> is to use the values

$$W_g = 1.0 \quad (11.6)$$

$$W_p = 0.01745 \quad (11.7)$$

which sets 1-dB magnitude error comparable with 7.57-deg phase error. As was pointed out by S. Boyd of Stanford University,<sup>125</sup> this choice of weighting is also equivalent to equal weighting of the real and imaginary parts of the transfer-function error. However, the transfer-function fitting results are largely insensitive to the exact choice of these weighting values.<sup>5</sup>

As a guideline, a cost function of

*Guideline:*

$$J \leq 100 \quad (11.8)$$

generally reflects an acceptable level of accuracy for flight-dynamics modeling, whereas a cost function  $J \leq 50$  can be expected to produce a match that is nearly indistinguishable from the flight data.

The transfer-function model accuracy can also be evaluated in terms of the error-response function [Eq. (7.84)] defined as

$$\varepsilon_{\text{model}}(f) \equiv \frac{T(f)}{\hat{T}_c(f)} \quad (11.9)$$

or in terms of the magnitude (dB) and phase (deg) responses,

$$\text{Mag}_{\text{err}}(f) = (|T| - |\hat{T}_c|) \quad (11.10)$$

$$\text{Phase}_{\text{err}}(f) = (\angle T - \angle \hat{T}_c) \quad (11.11)$$

These functions are checked against the frequency-dependent envelopes of maximum unnoticed added dynamics (MUAD) provided in MIL-STD-1797<sup>5</sup> and shown earlier in Fig. 7.20. If the error functions fall within these boundaries, then the model response would be judged by a pilot as being indistinguishable from the actual flight response, thereby providing a good basis for handling-qualities analyses.

### 11.3 Model Structure Selection

The method for transfer-function identification as explained in Sec. 11.2 is quite simple. The difficult aspect is the selection of the appropriate transfer-function model structure for Eq. (11.1). The proper selection of the different aspects of model structure depends on the ultimate application for the model, the frequency range of interest, the quality of the available frequency-response data, and an understanding of basic flight dynamics and linear systems. The considerations for model structure selection are discussed in detail in the following paragraphs because these same considerations are applicable to multi-input/multi-output state-space identification, which is a direct extension of the transfer-function identification process.

The critical factors to be considered in selecting the model structure include ultimate application of the model, selection of the input-output variable pair, frequency range of the fit ( $\omega_1$  to  $\omega_{n_0}$ ), order of numerator and denominator  $m$  and  $n$ , inclusion of equivalent time delay  $\tau_{\text{eq}}$ , and fixing or freeing specific coefficients in the fitting process.

#### 11.3.1 Ultimate Application of the Model

The first step in model structure selection is to consider the ultimate application of the model because this will have a major impact on the complexity of the transfer-function form selected (i.e., the values of  $m$  and  $n$ ) and the frequency range of interest. The same physical system might require different model structures depending on the application. For example, when the ultimate application of the model is for handling-qualities analysis, the model structure can be a classical lower-order equivalent system form, whereas flight-control applications

such as SCAS design might require additional complexity for a more accurate representation at higher frequencies.

### 11.3.2 Selection of the Input-Output Variable Pair

The next step is to select the input/output pair of concern. The dominant input/output pair that best reflects the overall dynamics of the system is selected. For example, in fixed-wing air vehicles (and rotorcraft at higher forward speeds) the pairs  $p/\delta_a$  and  $\beta/\delta_r$  characterize well the aircraft lateral/directional flight dynamics. The longitudinal response is characterized well by the pairs  $q/\delta_e$ ,  $n_z/\delta_e$ , and  $a_x/\delta_t$ . For rotorcraft in hover and low-speed flight, the transfer-function model identification will be based on the dominant angular-rate responses to the pilot control input:  $q/\delta_{\text{lon}}$ ,  $p/\delta_{\text{lat}}$ , or  $r/\delta_{\text{ped}}$ . In the vertical axis, the pair of interest is  $a_z/\delta_{\text{col}}$ . In each case, these response pairs reflect the dominant flight-dynamic response to control input and as such are primary inputs for piloted or automatic control.

### 11.3.3 Frequency Range of the Fit ( $\omega_1$ to $\omega_{n_\omega}$ )

The frequency range of the fit ( $\omega_1$  to  $\omega_{n_\omega}$ ) must be restricted to the frequency range over which the coherence function is satisfactory [e.g.,  $\gamma_{xy}^2 \geq 0.6$ , per the guideline in Eq. (7.54)], but it must also be consistent with the ultimate application of the model. For example, a simple first- or second-order response model can be selected to characterize the flight-dynamics response of a highly augmented closed-loop helicopter for comparison with the LOES handling-qualities database. This model can adequately capture the dynamics in the frequency range of interest (0.1–10 rad/s). But such a model will not adequately capture the higher-frequency dynamics of a rotor system (or structural) response, even though the coherence might be adequate at such frequencies. Therefore the frequency range of the fit must be restricted to exclude the rotor response. Transfer-function models needed to support flight-control analysis and design must be accurate for frequencies near the crossover frequency  $\omega_c$ , generally encompassing  $0.3\omega_c$  to  $3.0\omega_c$ . This will ensure that the key characteristics are accurately modeled, such as stability margins, disturbance rejection, and aircraft and actuator responses to commands. A typical range of fit for this application is 1–20 rad/s.

### 11.3.4 Order of Numerator and Denominator ( $m$ and $n$ )

The selection of the appropriate order of the transfer-function model numerator  $m$  and denominator  $n$  is based on a physical understanding of the response characteristics in the frequency range of interest and an awareness of the ultimate application of the model. For example, an appropriate transfer-function model for the handling-qualities analysis of bare-airframe fixed-wing dynamics should be based on the classical flight-mechanics response and will be composed of short-period, roll aperiodic, Dutch-roll modes, etc. For rotary-wing aircraft in hovering and low-speed flight, the analogous modes are the longitudinal and lateral hovering cubics and decoupled heave and yaw modes. Excellent background on the classical transfer-function forms for fixed-wing and rotary-wing vehicles is given by McRuer et al.,<sup>56</sup> Blakelock,<sup>146</sup> Hodgkinson et al.,<sup>49</sup> Hodgkinson,<sup>59</sup> and Bischoff.<sup>143</sup>

Stability augmentation systems (SAS) are often implemented to improve the handling qualities of the bare-airframe response while retaining the classical response modes. In this case, these same classical forms would also be appropriate to characterize the closed-loop response and are referred to as LOES. In contrast, modern stability and control augmentation systems (SCAS) can provide closed-loop responses that are greatly altered from the classical forms. For example, the model-following architecture, commonly adopted for control system designs in modern fixed- and rotary-wing aircraft, causes the closed-loop response to follow a first- or second-order command model (e.g., ADOCS; Ref. 84). Here, transfer-function model forms are better selected based on the command model response rather than the classical forms.

The transfer-function model form used for the fit should be the lowest orders  $m$  and  $n$  that adequately characterize the frequency-response behavior over the frequency range of interest. In this case, a satisfactory model fit is indicated by the value of the cost function ( $J \leq 100$ ). Increasing the order of the transfer-function model can provide incremental reductions in the cost function. However, these extra parameters might not have any physical meaning, and they can result in a model with poorer predictive capability.<sup>7</sup> Models with extraneous parameters are referred to as *overparameterized* or *overmodeled*, and they exhibit increased uncertainty in the identified parameters.<sup>2</sup> Thus a tradeoff exists between reduced fitting error and increased parameter uncertainty. This can also be viewed as a tradeoff of model complexity vs model variability.<sup>2</sup> The goal of a model with the minimum number of parameters is also consistent with the principal of parsimony (Sec. 1.4).

Further, a model that accurately characterizes the response in the frequency range of interest might not provide a good prediction when extrapolating to frequencies well outside the frequency range of the fit. So while a LOES handling-qualities model can track the frequency response well in the frequency range important for the transient dynamics (e.g., 0.1–10 rad/s), it might not predict accurately the steady-state (trim) response (at  $\omega = 0$  rad/s) or the very high-frequency response (i.e., well above 10 rad/s).

The ultimate selection of appropriate transfer-function models generally requires a careful case-by-case consideration of the important dynamics modes and data quality in the frequency range of interest.<sup>68</sup> These various considerations are best illustrated with the practical examples in the following sections.

### 11.3.5 Inclusion of Equivalent Time Delay $\tau_{eq}$

The inclusion of an equivalent time delay  $\tau_{eq}$  can be used to account for the phase-lag effects caused by unmodeled high-frequency dynamics (e.g., high-frequency filters and sensor dynamics) associated with a particular selection of transfer-function model orders  $m$  and  $n$ , as just discussed. For example, if the aircraft dynamics contain a pole at frequency  $p_1$  that is well above the upper fitting frequency  $\omega_{n_\omega}$ , then

$$\frac{1}{T_{p_1} s + 1} \approx e^{-T_{p_1} s} \quad (11.12)$$

where the time constant is simply  $T_{p_1} \equiv 1/p_1$ . In the general case of multiple zeros and poles at frequencies above the upper fitting frequency, the total equivalent time delay [included in the expression  $e^{-\tau_{eq}s}$  in Eq. (11.3)] is

$$\tau_{eq} \approx \sum_{i=1}^n T_{p_i} - \sum_{i=1}^m T_{z_i} \quad (11.13)$$

The equivalent time delay accounts for the effect of these unmodeled high-frequency dynamics via their contribution to the frequency-response phase lag:

$$\phi = -\tau_{eq}\omega \text{ rad} \quad (11.14)$$

Additional contributions to the identified value of equivalent time delay are the true time lags (e.g., control and measurement processing delays). But the identified equivalent delay will also “absorb” modeling error and an incorrect model structure, which can result in an identified transfer-function model with a lower cost function but physically meaningless parameters. Therefore an initial transfer-function model should be identified without the additional time delay, and the resulting model structure should be evaluated for correctness. If additional phase lag is apparent at high frequency that cannot be captured by the appropriate transfer-function model, then the equivalent delay should be included as a free parameter, but only if it results in a significant reduction in the identification cost function.

### 11.3.6 Fixing or Freeing Specific Coefficients in the Fitting Process

The parameters of the transfer-function model structure (numerator coefficients, denominator coefficients, and time delay) can be individually fixed or freed during the identification process. Sometimes a priori knowledge that permits a particular parameter value to be assigned to ensure that the physical significance of the results is maintained is available. For example, independent knowledge of computational or throughput delays can allow the equivalent delay to be assigned and fixed. Gravity and kinematic constants often appear as isolated coefficients in transfer-function models and can be fixed.

## 11.4 SISO Transfer-Function Identification in CIFER® Using NAVFIT

Transfer-function identification is accomplished in CIFER® using the NAVFIT program developed by Hodgkinson and his colleagues at McDonnell Aircraft Company.<sup>147</sup> NAVFIT is a generalized tool for single-input/single-output transfer-function model determination from frequency-response data. Cost-function minimization is accomplished using Rosenbrock’s multivariable search method.<sup>148</sup> The program was originally developed to enable LOES fitting of fixed-wing aircraft simulation models for handling-qualities analysis. NAVFIT was enhanced for flight-test applications by Tischler with the incorporation of coherence weighting  $W_\gamma$ . The first extensive identification of rotorcraft transfer-function models from frequency-sweep flight-test data, reported by Tischler et al.<sup>53</sup> and Tischler,<sup>54,61</sup> used

NAVFIT. This program was subsequently incorporated into CIFER® and has been applied to many fixed-wing and rotorcraft flight-test data projects.

Considerable experience with NAVFIT by Tischler has shown the program to be highly robust, even for difficult flight-test applications. For the typical problems involving the identification of relatively low-order transfer-function models (e.g., up to fourth order), the algorithms in NAVFIT have been found to avoid convergence to local minima, and they are quite insensitive to initial parameter guesses. In fact, selecting default initial guesses of 1.0 for all of the coefficients is usually quite satisfactory. Tilly<sup>149</sup> published a comparative study of three algorithms for SISO transfer-function model identification in the frequency domain, of which NAVFIT was one. In applications where the structure (model order) was known and reasonable initial parameter guesses were available, NAVFIT was found to be the preferred tool. NAVFIT was also found to be especially well suited to control system applications because it allows the explicit determination of the zeros of the system (as well as the poles).

## 11.5 Pendulum Example

In this section, the transfer-function identification methods are illustrated for the stable and unstable pendulum dynamics. The identified transfer functions are compared with the analytical expressions to illustrate the accuracy of the overall process.

The frequency-response data for the stable pendulum case were those obtained using the composite-windowing results of Fig. 10.3. The transfer-function model structure for this case is the second-order analytical expression [Eq. (3.5)], with  $m = 0$ ,  $n = 2$ . The identification results obtained using NAVFIT for a fitting range of 0.3–12 rad/s are

$$\frac{\theta}{M_{\text{ext}}}(s) = \frac{1.01}{[0.353, 3.013]} \text{ rad/(rad/s}^2\text{)} \quad (11.15)$$

yielding parametric values that are accurate to within 1% of the analytical result [Eq. (3.7)]. The frequency response of the identified transfer-function model is seen in Fig. 11.1 to be essentially identical to the simulated test data, which is consistent with the very low value of the identification cost function ( $J = 0.054$ ). This verifies the end-to-end identification process for the simple stable case. The influence of the model structure in obtaining the correct model parameters is examined in **Problem 11.3**.

The frequency response of the unstable inverted pendulum  $\theta/\bar{M}_{\text{inv}}$  was determined in **Problem 10.1**. A transfer-function model was identified using NAVFIT by fitting over the frequency range of excitation (0.3–12 rad/s):

$$\frac{\theta}{\bar{M}_{\text{inv}}}(s) = \frac{1.01}{(-1.67)(3.77)} \text{ rad/(rad/s}^2\text{)} \quad (11.16)$$

which matches the analytical parameters of Eq. (3.8) to within 1%. As was the case for the stable pendulum, the associated cost function is quite low ( $J = 0.060$ ),

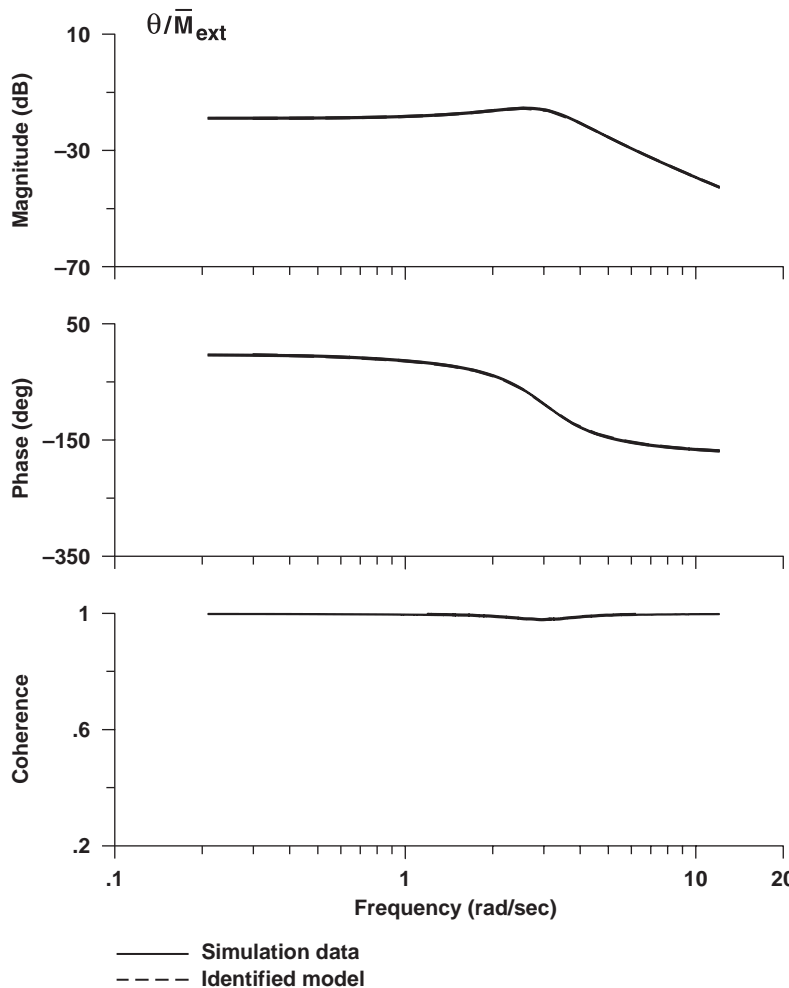


Fig. 11.1 Comparison of identified transfer-function model and frequency-response data for stable pendulum.

indicating a near perfect fit. This result verifies again that the characteristics of an unstable dynamic system can be determined accurately from closed-loop test data (Chapter 8). The remainder of this chapter will present detailed flight-test examples of transfer-function identification for a range of applications.

## 11.6 Handling-Qualities Applications

Transfer-function modeling is well suited to handling-qualities applications because the pilot opinion of dynamic response and pilot-in-the-loop performance both involve vehicle response to cockpit control inputs, not the detailed stability

and control derivatives of a state-space representation. The transfer-function models, also referred to as *lower-order equivalent system* or LOES models, are typically fairly simple low-order approximations of the actual end-to-end dynamic response. Such models allow handling qualities of highly varied and dynamically complex vehicles to be characterized by a common set of fundamental flight-mechanics models.

A significant body of literature that provides guidance on desirable values of LOES parameters for achieving good handling-qualities ratings is available. One such excellent document is the background guide for the fixed-wing military handling-qualities requirement.<sup>5</sup> This comprehensive document is actually a compilation of much of the extant data from flight-test and simulation studies in terms of LOES parameters. Another excellent reference on this topic is Hodgkinson's book.<sup>59</sup> Practical issues that are encountered in LOES modeling and handling-qualities analysis are discussed by Mitchell and Hoh.<sup>51</sup> Morelli<sup>41</sup> presented LOES model identification and handling-qualities analysis from flight-test data of the TU-144LL supersonic transport aircraft. Additional recent experience with LOES identification for flying-qualities analysis of transport aircraft is presented by Field et al.<sup>144</sup> The characterization of helicopter handling qualities using LOES models extracted from flight-test data is illustrated by Tischler<sup>61</sup> and Tischler et al.<sup>84</sup> Handling-qualities analyses of vertical/short takeoff and landing (V/STOL) aircraft based on LOES concepts is given by Franklin.<sup>150</sup>

### 11.6.1 LOES Handling-Qualities Evaluation of the ADOCS Demonstrator

The Advanced Digital Optical Control System (ADOCS) Demonstrator (Fig. 5.8) was based on a UH-60A helicopter. The demonstrator featured a side-stick controller, full-authority fly-by-wire/fly-by-light control system hardware and an explicit model-following control system architecture to provide task-tailored response characteristics and improved handling qualities compared to the standard UH-60A Blackhawk.<sup>151</sup> The many control system innovations that were developed and flight validated under this program formed the basis of fly-by-wire systems for a generation of modern rotorcraft, such as the RAH-66 (Comanche) helicopter and the V-22 (Osprey) tilt rotor, as discussed by Landis et al.,<sup>152</sup> and the fly-by-wire variants of the AH-64D, UH-60M, and CH-53E helicopters that are in current development.

The ADOCS explicit model-following flight control system provided an attitude-command, attitude-hold (ACAH) response type for reduced workload at low-speed and hovering conditions. An important feature was the automatic trim follow-up function to null out any long-term force inputs needed to maintain trim. System-identification studies on the ADOCS flight-test data were conducted by Tischler et al.<sup>84</sup> to document the performance of the system and to compare the dynamic characteristics with the proposed military handling-qualities requirements<sup>83</sup> that evolved into ADS-33E (Ref. 4).

An example longitudinal frequency sweep from the ADOCS flight tests was shown in Fig. 5.9. The identified pitch-rate response  $q/\delta_{\text{lon}}$ , as obtained from CIFER® using concatenated sweeps, is shown in the solid curve of Fig. 11.2. The associated coherence function, also shown in the figure, indicates an accurate

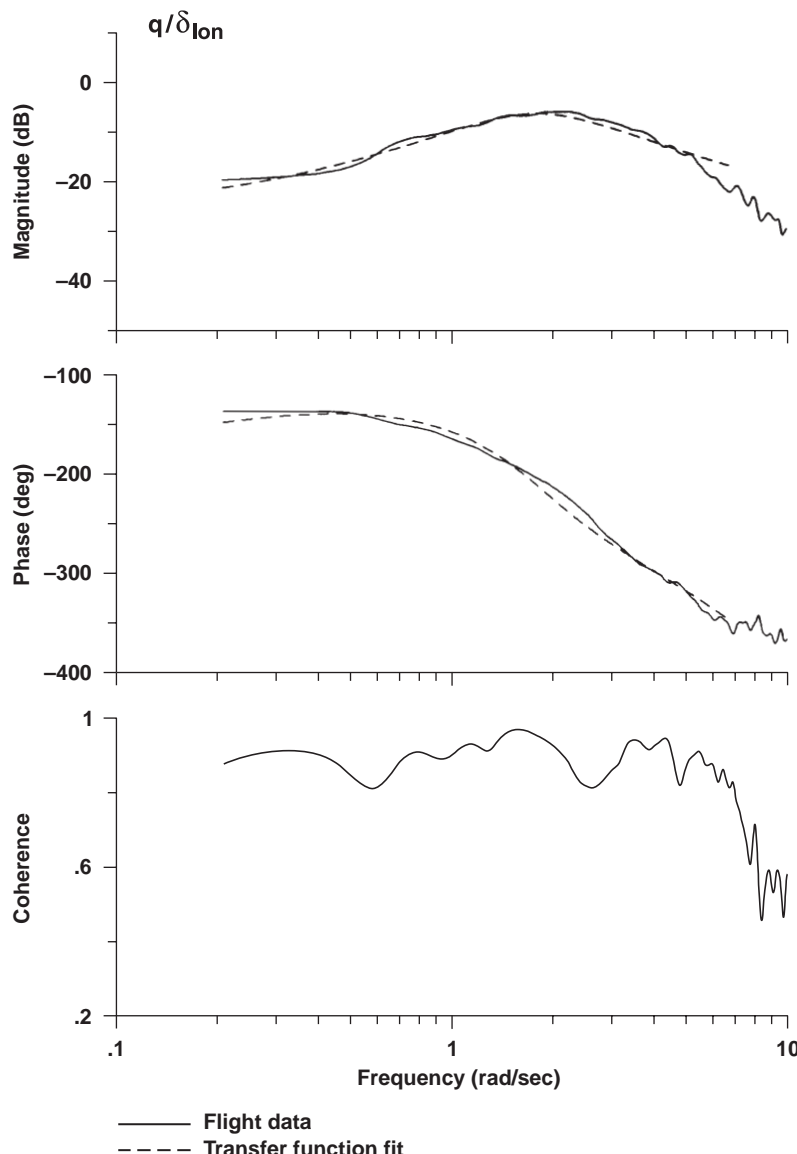


Fig. 11.2 ADOCS pitch-rate response and transfer-function model (hover).

identification in the frequency range of 0.2–7 rad/s. At higher frequencies, the coherence drops, which reflects the intentionally reduced piloted inputs.

For an ACAH system, the mid-frequency (short-term) response (around 1 rad/s) would be expected to produce a constant gain characteristic. The associated pitch-rate response would then follow a derivative  $s$  characteristic (i.e., +20dB/decade slope) because

$$\frac{q}{\delta_{\text{lon}}}(s) = \frac{s\theta}{\delta_{\text{lon}}}(s) \quad (11.17)$$

This can be seen in the identified response of Fig. 11.2 for the frequency range (0.3–2 rad/s). The rate-command characteristic at low frequency (below 0.3 rad/s) is associated with the autotrim function<sup>84</sup> for this side-stick controller. The rate response follows a  $k/s$  roll off at frequencies above 2 rad/s, which reflects the second-order ACAH control system.

An appropriate model structure for the ADOCS pitch-rate response is selected based on the flight data response

$$\frac{q}{\delta_{\text{lon}}}(s) = s \left( \frac{k(s+a)e^{-\tau_{\text{eq}}s}}{s[\zeta, \omega_n]} \right) \quad (11.18)$$

where the response in the large parentheses is the attitude response  $\theta/\delta_{\text{lon}}$  of Eq. (11.17). The parameters in this model are as follows:

$k$  = stick gain

$(s+a)/s$  = trim follow-up

$[\zeta, \omega_n]$  = short-term second-order attitude response

$\tau_{\text{eq}}$  = equivalent time delay that accounts for the lumped effect of rotor transient response and control-system dynamics

The transfer-function model was identified using NAVFIT with a fitting range of 0.2–7 rad/s, corresponding to the range of good coherence. Further, this fitting range is consistent with the frequency range of applicability of the short-term attitude response representation. The dominant rotor-flap mode frequency at approximately 10 rad/s (Ref. 153) causes an increasingly sharp roll off in the magnitude curve for frequencies beyond about 8 rad/s (Fig. 11.2) that cannot be adequately captured by the short-term attitude response representation. Explicit identification of rotor dynamics using extended transfer-function model structures is demonstrated in Secs. 11.7 and 11.8.

The identified transfer-function model is based on Eq. (11.18):

$$\frac{q}{\delta_{\text{lon}}}(s) = s \left[ \frac{-0.876(s+0.229)e^{-0.238s}}{s[0.539, 1.82]} \right] \text{deg/s/%-lon} \quad (11.19)$$

The dashed line in Fig. 11.2 shows that this transfer-function model matches the frequency response very well over the frequency range of the fit. The parameters

in Eq. (11.19) reveal important aspects about the ADOCS response characteristics. The closed-loop response is dominated by a well-damped second-order short-term characteristic ( $\zeta = 0.539$ ,  $\omega_n = 1.82$  rad/s). The integral term  $(s + 0.229)/s$  provides trim follow-up (self-trimming), with a time constant of  $(T = 1/0.229 = 4.4$  s). The equivalent time delay of  $\tau_{eq} = 0.238$  s reflects the combined influences of the important higher-frequency dynamics, namely, computer processing delays, filtering, and rotor dynamics.<sup>84</sup>

Transfer-function modeling based on the classical short-period form of Eq. (11.18) allows an evaluation of ADOCS handling qualities using the LOES approach.<sup>59</sup> For example, Fig. 11.3 presents a compilation of handling-qualities results<sup>154</sup> from flight and simulation experiments for low-speed and hovering vehicles. These data are presented in terms of the effective (i.e., equivalent system) total damping ( $2\zeta_n\omega_n$ ) and natural frequency  $\omega_n$  for the short-term response. The handling qualities are characterized using the Cooper-Harper rating scale and the associated *levels* of handling qualities (see also Sec. 7.14.3). An average handling-qualities rating (HQR) of HQR = 3.5 indicates that the system falls into the *level 1* category or “satisfactory without improvement.” An average rating from HQR = 3.5 to 6.5 indicates that the system falls into the *level 2*

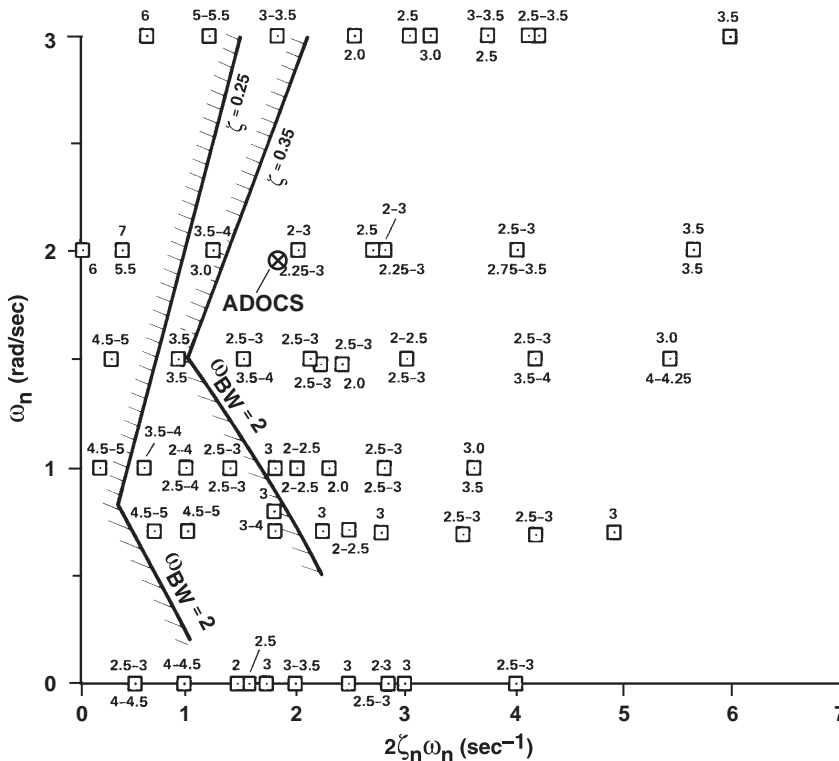


Fig. 11.3 Analysis of ADOCS handling qualities based on equivalent system data (from Ref. 154).

category or “deficiencies that warrant improvement,” and an average rating of  $HQR = 6.5$  or greater indicates *level 3* handling qualities where “deficiencies require improvement.”

The LOES parameters for ADOCS are obtained directly from Eq. (11.19):

$$2\zeta_n\omega_n = 2(0.539)(1.82) = 1.96 \text{ s}^{-1} \quad (11.20)$$

$$\omega_n = 1.82 \text{ rad/s} \quad (11.21)$$

As indicated in Fig. 11.3, this places the ADOCS short-term pitch response in hover well within the level 1 region.

A second important characteristic of the ADOCS transfer-function model is the relatively large equivalent time delay,  $\tau_{eq} = 0.238$  s. Handling-qualities experience, summarized in Fig. 11.4,<sup>155</sup> indicates that the equivalent time delay should not greatly exceed  $\tau_{eq} = 0.120$  s, thereby suggesting degradation of ADOCS handling qualities for high-gain tasks. Comparable levels of equivalent time delay in the roll axis were considered to be a key contributor to pilot-induced oscillations (PIO) and attendant level 2 HQRs for high-gain piloting tasks such as slope landing.<sup>84</sup>

The excellent predictive capability of this rather simple transfer-function model is demonstrated in the time domain for a step input in Fig. 11.5. The first plot shows the pilot input  $\delta_{lon}$ , which is used as a forcing function for the transfer-function model. The model responses for pitch rate  $q$  and pitch attitude  $\theta$ , shown as a dashed line, track the flight data (solid line) very closely. It is remarkable that the closed-loop response of this very complex system can be modeled accurately

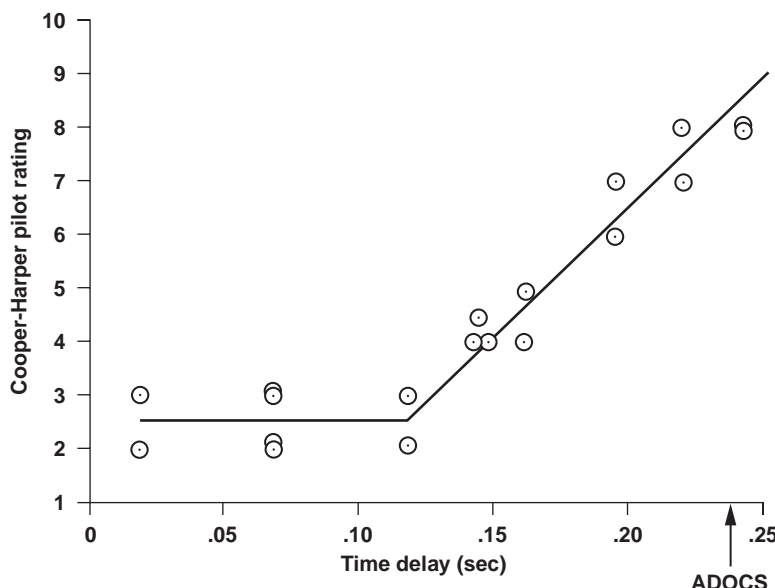


Fig. 11.4 Effect of equivalent time delay on handling qualities (from Ref. 155).

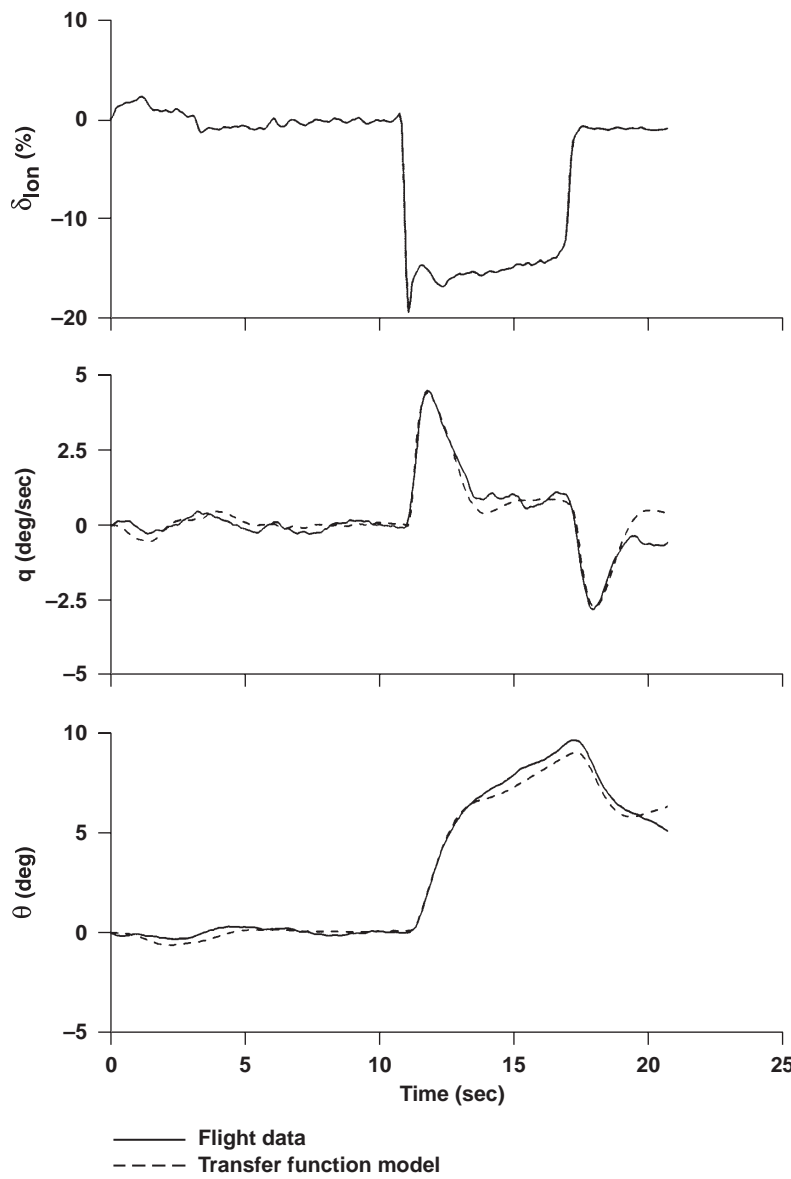


Fig. 11.5 ADOCS transfer-function model verification (hover).

with such a simple LOES transfer-function model. Further, the rather large amplitudes seen in the time-response comparison demonstrate that the model is accurate for sizeable maneuvers and *is not restricted to small perturbations*. Thus system identification of LOES models provides a simple and very accurate approach for obtaining closed-loop simulation models for flight dynamics and handling-qualities studies.

### 11.6.2 Lateral / Directional Dynamics Identification for Fixed-Wing Aircraft

In this example, transfer-function models that accurately describe the bare-airframe lateral-directional response of the XV-15 in the cruise flight condition are extracted. The simplest model structure is obtained under the assumption that the roll and sideslip dynamics are completely decoupled,<sup>50,59</sup> that is, aileron deflections produce pure aperiodic rolling motion (with no sideslip) and rudder inputs produce pure sideslip/yaw Dutch-roll motions (with no roll rate). This assumption results in the one-DOF model for roll response to aileron:

$$\frac{p}{\delta_a}(s) = \frac{L_{\delta_a} e^{-\tau_a s}}{(s + 1/T_r)} \quad (11.22)$$

where

$L_{\delta_a}$  = aileron roll-control sensitivity

$T_r$  = roll mode time constant and inverse of the roll damping stability derivative ( $1/T_r = -L_p$ )

$\tau_a$  = equivalent time delay for aileron inputs

The transfer-function model for the sideslip for rudder inputs (with no roll motion) is

$$\frac{\beta_{cg}}{\delta_r}(s) = \frac{Y_{\delta_r} e^{-\tau_\beta s}}{[\zeta_{dr}, \omega_{dr}]} \quad (11.23)$$

where

$Y_{\delta_r}$  = rudder sideslip sensitivity

$[\zeta_{dr}, \omega_{dr}]$  = Dutch-roll complex mode

$\tau_\beta$  = equivalent time delay for rudder inputs

Clearly, this decoupling simplification ignores both the control coupling  $N_{\delta_a}$ ,  $L_{\delta_r}$  and response coupling (primarily caused by  $L_\beta$ ) in the roll and sideslip equations of motion, but it allows the identification to proceed using SISO transfer-function identification tools. Bischoff and Palmer<sup>50</sup> showed that transfer-function identifications based on these simpler forms were easily obtained and resulted in acceptable model matches both in the time and frequency domain as compared to the completely coupled forms. They concluded that this approach was satisfactory for determining the natural modes of lateral/directional motion ( $1/T_r$ ,  $[\zeta_{dr}, \omega_{dr}]$ ) and time delays that are important in handling-qualities evaluations.

A simplified roll-rate model for the bare-airframe XV-15 response in cruise is obtained using NAVFIT with a fitting range of 0.14–9 rad/s (good coherence):

$$\frac{p}{\delta_a}(s) = \frac{-5.21 e^{-0.0628s}}{(s + 0.894)} \text{ deg/s/deg-ail} \quad (11.24)$$

The associated cost function is somewhat higher than desirable ( $J = 132$ ), reflecting a considerable mismatch when compared with the flight data in Fig. 11.6a (denoted as SISO model). This mismatch is more clearly seen in terms of the magnitude and phase error functions [Eqs. (11.10) and (11.11)] as presented in Fig. 11.7. Also shown in this figure are allowable mismatch boundaries from MIL-STD 1797,<sup>5</sup> introduced earlier in Fig. 7.20. When the error functions lie within these boundaries of *unnoticeable dynamics*, the pilots consider the original response and the LOES transfer function as indistinguishable (see also Sec. 7.14.5). In this case, both the magnitude and phase boundaries are slightly exceeded (1–3 rad/s). The mismatch results from the omission of Dutch-roll coupling in the simple roll-response model, as will be shown later [Eq. (11.29)].

The simplified model for the XV-15 sideslip response in cruise is obtained using NAVFIT with a fitting range of 0.14–5.5 rad/s (good coherence):

$$\frac{\beta_{cg}}{\delta_r}(s) = \frac{-1.16 e^{-0.0s}}{[0.237, 1.67]} \text{ deg/deg-rud} \quad (11.25)$$

indicating a lightly damped Dutch-roll mode ( $\zeta_{dr} = 0.237$ ), which is characteristic of the bare-airframe dynamics. The associated cost function is very low ( $J = 35$ ), reflecting the excellent model fit seen in Fig. 11.6b. The magnitude and phase error functions are within the mismatch corridor limits of Fig. 11.7b, showing the good suitability of the simplified sideslip model structure in this case.

An improved roll-response fit can be obtained using the complete transfer-function model structure that includes both the Dutch-roll and spiral modes,<sup>59</sup> with the Dutch-roll mode fixed from the sideslip response model obtained in Eq. (11.25):

$$\frac{p}{\delta_a}(s) = \frac{L_{\delta_a} s [\zeta_\phi, \omega_\phi] e^{-\tau_a s}}{(1/T_s)(1/T_r)[\zeta_{dr}, \omega_{dr}]} \quad (11.26)$$

where  $[\zeta_\phi, \omega_\phi]$  are complex zeros that determine the appearance of the Dutch-roll mode in the roll response and  $T_s$  is the spiral mode time constant.

The model structure of Eqs. (11.23) and (11.26) comprise a *one-way coupling* approximation, where we have accounted for the coupling of sideslip motion into the roll response but have neglected the coupling of the roll motion into the sideslip response. To fix the Dutch-roll mode and identify the remaining parameters in Eq. (11.26) using NAVFIT, the roll-rate flight data  $[p(\omega)/\delta_a(\omega)]$  are multiplied by the frequency response associated with the Dutch-roll mode  $[(j\omega)^2 + 2\zeta_{dr}\omega_{dr}(j\omega) + \omega_{dr}^2]$ , as identified in Eq. (11.25). This is accomplished

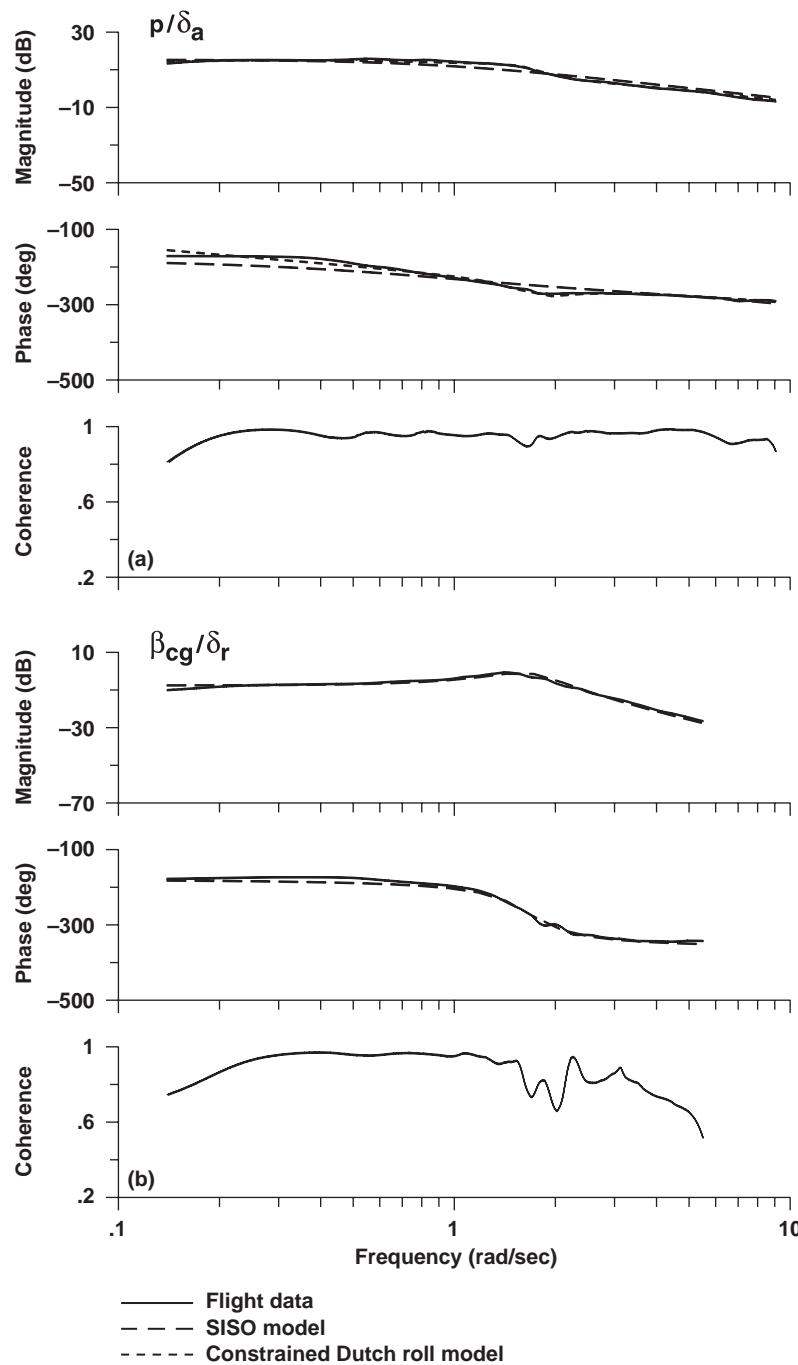


Fig. 11.6 Roll-rate and sideslip transfer-function models (XV-15, cruise).

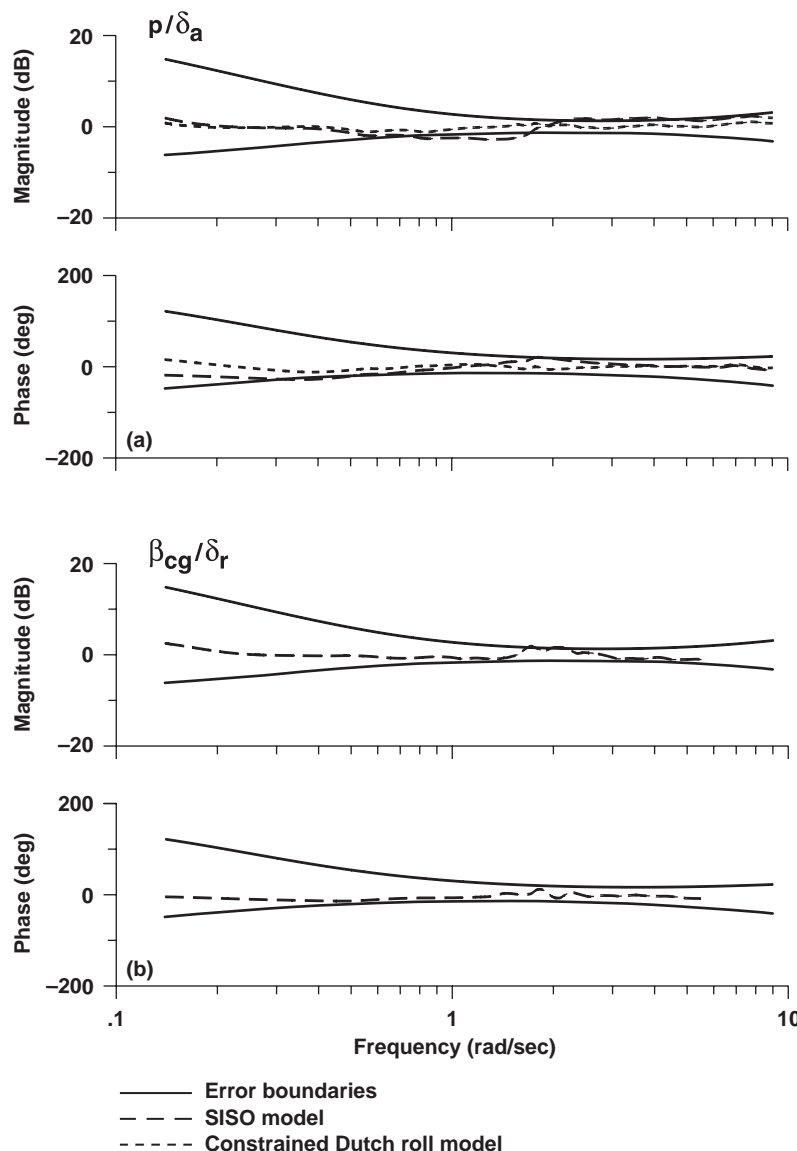


Fig. 11.7 Error functions for transfer-function models (XV-15, cruise).

using arithmetic manipulation of the frequency-response functions at each identification frequency  $\omega$ . The resulting roll-rate transfer-function model structure is

$$[\zeta_{dr}, \omega_{dr}] \frac{p}{\delta_a}(s) = \frac{L_{\delta_a} s[\zeta_{\phi}, \omega_{\phi}] e^{-\tau_a s}}{(1/T_s)(1/T_r)} \quad (11.27)$$

which can be obtained using SISO transfer-function identification. A very accurate model ( $J = 16.7$ ) is then achieved using NAVFIT:

$$[\zeta_{dr}, \omega_{dr}] \frac{p}{\delta_a}(s) = \frac{-4.60s[0.278, 1.93] e^{-0.0533s}}{(0.0912)(1.00)} \quad (11.28)$$

Finally, the complete roll-rate transfer function is obtained as

$$\frac{p}{\delta_a}(s) = \frac{-4.60s[0.278, 1.93] e^{-0.0533s}}{(0.0912)(1.00)[0.237, 1.67]} \text{ deg/s/deg-ail} \quad (11.29)$$

which fits the data very closely ( $J = 16.9$ ), as seen in Fig. 11.6a (denoted as constrained Dutch-roll model). The roll-response mismatch errors are considerably reduced compared to the simplified model results and now stay within the envelopes for both magnitude and phase (Fig. 11.7). This modeling method achieves good fits for both the roll and sideslip responses, while preserving the physical constraint of common poles. A comparison of Eqs. (11.29) with (11.24) shows that the simplified roll-response model structure indeed provides a reasonable estimate of the roll mode, roll sensitivity, and roll time delay, in agreement with Bischoff and Palmer.<sup>50</sup>

Table 11.1 compares the dynamic characteristics of the XV-15 bare-airframe response in cruise with the handling-qualities recommendations of MIL-STD-1797<sup>5</sup> for flight category B (gradual maneuvers; see reference for definitions). The XV-15 parameters for the bare-airframe (SCAS-off) vehicle comply easily with all of the recommendations for this category. Compliance is also achieved for the most aggressive recommendations under category A (rapid maneuvering), except for the Dutch-roll damping ratio specification. Improved Dutch-roll damping is easily achieved with a simple Dutch-roll augmentation system, common on many aircraft, including the XV-15.

**Table 11.1 Evaluation of XV-15 lateral-directional handling qualities in cruise**

Parameter	MIL-STD-1797A level I, cat. B requirement	XV-15
Roll-mode time constant $T_r$	$\leq 1.4$ s	1.0 s
Time-to-double for spiral mode ( $T_2$ ) <sub>s</sub>	$\geq 20$ s	Stable
Dutch-roll damping ratio $\zeta_{dr}$	$\geq 0.08$	0.24
Dutch-roll frequency $\omega_{dr}$	$\geq 0.4$ rad/s	1.67 rad/s
Dutch-roll total damping $\zeta_{dr}\omega_{dr}$	$\geq 0.15$ rad/s	0.40 rad/s
Roll time delay $\tau_a$	$\leq 0.10$ s	0.053 s

Transfer-function identification of the  $p/\delta_a$  and  $\beta_{cg}/\delta_r$  responses based on the complete forms for both roll and sideslip responses must be completed simultaneously to ensure that the denominators (poles) are the same, as they are physically. The identification package LATFIT, which was developed by the same researchers<sup>156</sup> that developed NAVFIT, provides such a capability. A third package LONFIT, developed by the same team, provides a simultaneous fit of  $q/\delta_e$  and  $n_z/\delta_e$  for determination of longitudinal short-period dynamics, thereby avoiding the “galloping  $1/T_{\theta_2}$  problem”<sup>157</sup> that occurs in the SISO fit of  $q/\delta_e$ . The LATFIT and LONFIT tools were used in the original identification of XV-15 transfer-function dynamics in cruise.<sup>125</sup> These tools evolved into the LOES analysis package SLAP.<sup>144</sup> Another modern tool for simultaneous LOES matching of two transfer functions is included in CONDUIT® (Ref. 64).

Simultaneous transfer-function matching can also be accomplished using the transfer-function model structure that is included in the state-space modeling method (Sec. 12.2.2). The result for this case produces models with very low-cost functions:

$$\frac{p}{\delta_a}(s) = \frac{-4.52s[0.361, 1.85]}{(0.085)(1.09)[0.296, 1.54]} e^{-0.052s} \text{ deg/deg-ail with } J = 13 \quad (11.30)$$

$$\frac{\beta_{cg}}{\delta_r}(s) = \frac{-1.34(0.061)(0.728)}{(0.085)(1.09)[0.296, 1.54]} e^{-0.00s} \text{ deg/deg-rud with } J = 8 \quad (11.31)$$

There is an additional (third) zero at high frequency that appears in the complete high-order form for  $\beta_{cg}/\delta_r$  (Ref. 50). However, in the present case the identified value of this zero is well beyond the frequency range for which the data are reliable, and so it is dropped. A comparison of the simultaneous identification of Eqs. (11.30) and (11.31) with the earlier results of Eqs. (11.29) and (11.25) demonstrates the good accuracy of the approximate (one-way coupling) method. Generalized matching of multiple degrees of freedom is more easily accomplished with a state-space formulation directly in terms of the stability and control derivatives. This is the primary role of DERIVID (Chapter 13).

Field et al.<sup>158</sup> have made extensive use of LOES modeling and MUAD boundary assessment to validate the implementation of large transport aircraft models in an advanced motion-based simulator. Manual and automated frequency-sweep testing was conducted to document the simulation math models, control loaders, and simulator motion system drives and responses.

## 11.7 Flight-Mechanics Characterization Studies

Transfer-function models are a very useful intermediate result in the overall flight-mechanics modeling process because they are minimum-parameter realizations of the input-to-output dynamic behavior of a system. In other words, a transfer-function model contains the *least possible number of parameters* that will characterize the system response. In contrast, state-space realizations are nonunique and can take many possible forms. All realizations (e.g., controller canonical form, observer canonical form, block diagonal form, as discussed in

Sec. 12.5.1 and Chen<sup>159</sup>), will fit the frequency-response data equally well and have the same eigenvalues as the transfer-function model. Physics-based state-space models, characterized in terms of stability and control derivatives, might again fit the measured response well, but they might have extraneous parameters that offset one another and therefore can lose physical meaning.

Thus initial models based on SISO transfer-function models can provide critical information on fundamental flight-mechanics response characteristics, appropriate state-space model structure (order and form), and initial values of the key derivatives. They provide an important stepping stone in the overall system-identification process, even when the ultimate goal is a MIMO state-space model in stability and control derivative form. Examples of transfer-function modeling for the study of basic rotorcraft flight mechanics are given by Chen and Tischler<sup>68</sup> and Houston.<sup>160</sup> This section uses the transfer-function identification method to characterize the coupled rotor/fuselage dynamics of the OH-58D helicopter. The example is drawn from the results presented by Ham et al.<sup>123</sup>

### 11.7.1 Helicopter Rotor-Body Coupling Fundamentals

The flight dynamics of the roll (and pitch) motion of helicopters are dominated by the coupling of the fuselage inertia response and the rotor flapping. This leads to a second-order response of roll (and pitch) rate to swashplate inputs. Very insightful explanations of the coupled roll/fuselage dynamics are given by Heffley et al.<sup>21</sup> and Curtiss.<sup>161</sup> Rotor flapping can be visualized as a deflection in the rotor disc (referred to as the *tip-path plane deflection*). Following the nomenclature of Johnson<sup>162</sup> and Tischler and Tomashofski,<sup>139</sup> lateral flapping relative to the shaft is denoted as  $\beta_{1s}$  and is positive for flapping down to the left. Lateral tip-path plane deflection imparts a proportional rolling moment, acting like a spring between the fuselage and the rotor plane. This causes a negative (i.e., left wing down) fuselage roll acceleration:

$$\dot{p} = L_{\beta_{1s}} \beta_{1s} \quad (11.32)$$

so that the effective flap-stiffness constant ( $L_{\beta_{1s}}$ ,  $s^{-2}$ ) will have a negative value in our notation, opposite from Heffley et al.<sup>21</sup> The primary contributions to this constant are the height of the rotor hub above the fuselage center of gravity  $h_r$ , the offset (or effective offset) of the rotor-blade flapping hinge from the center of rotation of the rotor shaft  $e$ , and the rotor-blade flap spring stiffness  $K_\beta$ . These contributions are normalized by the fuselage roll moment of inertia  $I_{xx}$ , to give an estimate for  $L_{\beta_{1s}}$  as<sup>21</sup>

$$-L_{\beta_{1s}} = \frac{Wh_r}{I_{xx}} + \frac{n_b M_\beta \Omega^2 e}{2I_{xx}} + \frac{n_b K_\beta}{2I_{xx}} \quad (11.33)$$

where

$W$  = helicopter weight, lbs

$n_b$  = number of rotor blades

$M_\beta$  = first mass moment of rotor blade, slug-ft

$\Omega$  = rotor rotation speed, rad/s

Typical values are in the range of  $20 < -L_{\beta_{1s}} < 90$ , as tabulated by Heffley et al.<sup>21</sup> The lower end of the range is representative of a helicopter with small or no hinge offset, such as a teetering rotor design of the UH-1H or AH-1G. The higher end of the range is representative of helicopters with a large effective hinge offset, such as the Bo-105 (12%) and RAH-66 (10%) hingeless rotor systems or helicopters with a high rotor mast and low fuselage roll inertia. The analogous values for the pitch axis  $M_{\beta_{1c}}$  will be considerably smaller because of the increased moment of inertia in this axis (for example, see the SH-2G identification results of Table 15.1).

If we ignore the coupling between lateral and longitudinal flap motion for now (and the effect of the flapping spring), the primary lateral flap response (referred to as the *regressive flapping mode*) is well approximated<sup>21</sup> by the first-order response:

$$\tau_f \dot{\beta}_{1s} = -\beta_{1s} + \tau_f p + \theta_{1c} \quad (11.34)$$

where  $\tau_f$  is the rotor flap time constant and the control input  $\theta_{1c}$  denotes the (cosine) deflection of the swashplate that results in a positive lateral flapping response and a (negative) fuselage roll response. Considering the rotor in isolation ( $p = 0$ ), the flapping equation (11.34) shows that one rad of control input ( $\theta_{1c} = 1$ ) with the shaft fixed results in one rad of cyclic lateral flapping ( $\beta_{1s} = 1$ ) at steady state.

Heffley et al.<sup>21</sup> gives a useful expression for the inverse rotor-flap time constant as a function of rotor geometry:

$$\frac{1}{\tau_f} = \frac{\gamma \Omega}{16} \left( 1 - \frac{8e}{3R} \right) \quad (11.35)$$

where  $\gamma$ , the Lock number representing the (nondimensional) ratio of aerodynamic to centrifugal forces,<sup>163</sup> is given by

$$\gamma = \frac{\rho a c R^4}{I_b} \quad (11.36)$$

with

$\rho$  = atmospheric density, slug/ft<sup>3</sup>

$a$  = lift-curve slope

$c$  = rotor chord, ft

$R$  = rotor radius, ft

$I_b$  = moment of inertia of the blade about the flapping axis, slug·ft<sup>2</sup>

Heffley provides a table of inverse rotor time constant values for many common helicopters. However, the expression of Eq. (11.35) (and tabulated values) for the inverse rotor-flap time constant must be corrected for the influence of dynamic inflow (transient dynamics of airmass flow through the rotor). This correction, based on the pioneering work in dynamic inflow theory by Curtiss,<sup>161</sup> replaces the

geometric Lock number  $\gamma$  with an effective (reduced) Lock number  $\gamma^*$ :

$$\gamma^* = \frac{\gamma}{1 + a\sigma/(16\bar{v}_0)} \quad (11.37)$$

where  $\sigma = n_b c / \pi R$  is defined as the rotor solidity and  $\bar{v}_0$  is the nondimensional inflow ratio [Eq. (15.13)].

The effect of the correction is most significant in hover, increasing the value of the rotor time constant by about 50%, and washes out in forward-flight conditions (as seen in the SH-2G results of Sec. 15.3.4). For most hovering helicopters, the rotor-flap time constant is in the fairly narrow range of  $\tau_f = 0.10$  to  $0.15$  s (corrected table from Heffley et al.<sup>21</sup>). Teetering rotors and fully articulated rotors with small hinge offset will have values at the lower end of this range, and large hinge-offset (and hingeless) rotors will have values at the upper end of this range.

Finally, the linkage and actuator between the pilot cockpit stick  $\delta_{\text{lat}}$  and the swashplate is characterized by a gain and an equivalent time delay:

$$\theta_{1c} = (K_{\delta_{\text{lat}}} e^{-\tau_{\text{lat}} s}) \delta_{\text{lat}} \quad (11.38)$$

so that a negative value of linkage gain is needed to provide a positive roll-rate response to a positive lateral-stick input (typical sign convention).

The coupling of Eqs. (11.32–11.38) can be visualized in a block diagram, as seen in Fig. 11.8, remembering that  $L_{\beta_{1s}} < 0$ , which results in a stable feedback loop.

A typical root locus of the feedback loop as a function of the rotor-flap stiffness  $L_{\beta_{1s}}$  is illustrated in Fig. 11.9 using a nominal value of the rotor time constant,  $\tau_f = 0.125$  s.

Many modern helicopters feature articulated or hingeless rotor designs with associated higher values of flap stiffness. Then the fuselage and rotor responses are a coupled second-order response as seen in Fig. 11.9 and discussed in depth by Curtiss.<sup>161</sup> The roll-rate response to swashplate inputs  $p/\theta_{1c}$  is obtained from Fig. 11.8 as

$$\frac{p}{\theta_{1c}}(s) = \frac{L_{\beta_{1s}}}{\tau_f s^2 + s - \tau_f L_{\beta_{1s}}} \quad (11.39)$$

and

$$\frac{p}{\delta_{\text{lat}}}(s) = \frac{K_{\delta_{\text{lat}}} L_{\beta_{1s}} e^{-\tau_{\text{lat}} s}}{\tau_f s^2 + s - \tau_f L_{\beta_{1s}}} \quad (11.40)$$

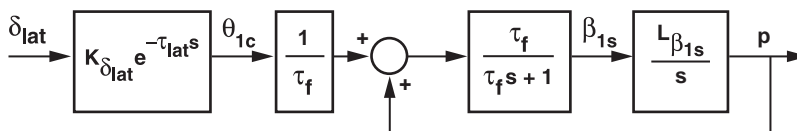


Fig. 11.8 Block diagram representation of rotor-body coupling.

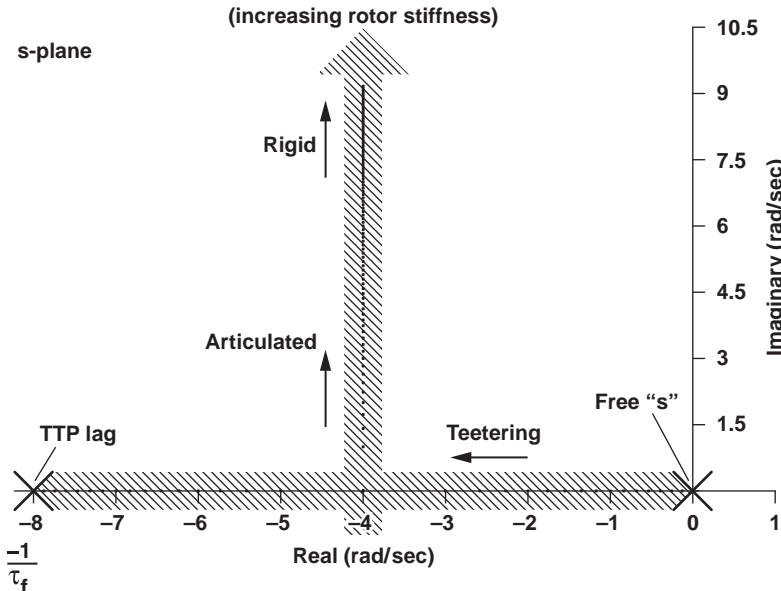


Fig. 11.9 Root locus of rotor-body coupling with increasing rotor-flap stiffness (following Heffley et al.<sup>21</sup>).

which is the appropriate transfer-function model structure for system identification of the coupled roll-flap dynamics. From this expression, we see that the natural frequency for the roll-rate response is given as

$$\omega_n = \sqrt{(-L_{\beta_{1s}})} \quad (11.41)$$

The high values of flap stiffness (i.e., low roll inertia and large hinge offset) common to most modern attack helicopters provide a faster (more agile) response to controls, as characterized by an increased response frequency  $\omega_n$  and an associated increase in response bandwidth  $\omega_{BW}$ .

Many helicopters do not require high levels of agility, so that rotor hub designs with reduced flap stiffness (lower  $L_{\beta_{1s}}$ ) are incorporated. This reduces the structural moments and vibration on the airframe. When the condition

$$(\tau_f)^2 \ll \left| \frac{1}{L_{\beta_{1s}}} \right| \quad (11.42)$$

applies, the fuselage and rotor responses are only lightly coupled<sup>161</sup> and the second-order (oscillatory) response of Eq. (11.39) factors into two real roots. In such cases, the roll-rate flight-mechanics response of Fig. 11.8 is well approximated by a cascade model combining the first-order rotor response and a first-order quasi-steady roll-rate response, as depicted in Fig. 11.10. This can be seen

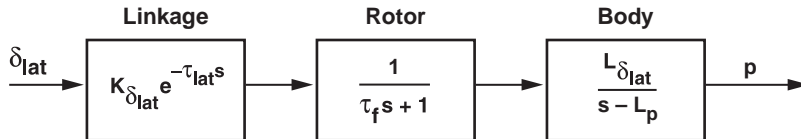


Fig. 11.10 Cascade model of rotor-body response applicable to small flap stiffness.

as a *one-way coupled* (i.e., actuator-type) approximation of the two-way coupled rotor-body dynamics.<sup>125</sup>

The first-order rotor response is

$$\frac{\beta_{1s}}{\theta_{1c}}(s) = \frac{1}{\tau_f s + 1} \quad (11.43)$$

A *more accurate model* of this rotor-response block is the first-order over fourth-order transfer-function model, given by Landis and Glusman,<sup>164</sup> that was used in the flight-control design study based on the UH-60 helicopter.<sup>125</sup>

The first-order quasi-steady roll-rate response is

$$\frac{p}{\delta_{\text{lat}}}(s) = \frac{L_{\delta_{\text{lat}}} e^{-\tau_{\text{lat}} s}}{s - L_p} \quad (11.44)$$

where the quasi-steady parameters of equation Eq. (11.44) are determined by dropping the  $s^2$  term in the denominator of the coupled response of Eq. (11.40). The effective (or quasi-steady) roll-control sensitivity is

$$(L_{\delta_{\text{lat}}})_{\text{effective}} = K_{\delta_{\text{lat}}} L_{\beta_{1s}} \quad (11.45)$$

and the effective (or quasi-steady) roll-damping derivative is

$$(L_p)_{\text{effective}} = \tau_f L_{\beta_{1s}} \quad (11.46)$$

So the condition of Eq. (11.42) simply ensures that the flap time constant is much smaller than the quasi-steady roll time constant:

$$\tau_f \ll \left| \frac{1}{(L_p)_{\text{effective}}} \right| \quad (11.47)$$

resulting in two distinct modes in Fig. 11.9.

The *simplest model* of rotorcraft flight dynamics combines the time constant of the rotor-flap response and the actuator/linkage delays into an equivalent time delay

$$\tau_{\text{eq}} = \tau_f + \tau_{\text{lat}} \quad (11.48)$$

and then

$$\frac{p}{\delta_{\text{lat}}}(s) = \frac{L_{\delta_{\text{lat}}} e^{-\tau_{\text{eq}} s}}{(s - L_p)} \quad (11.49)$$

provides the required transfer-function model structure for identification.

The first-order model of Eq. (11.49) is referred to as the *quasi-steady approximation* because it accounts only for the influence of the steady-state rotor response on the helicopter flight mechanics. The decoupled roll-rate model of Eq. (11.49) has the same structure as the decoupled fixed-wing roll rate of Eq. (11.22). Figure 11.11 compares the coupled model structure [Eq. (11.40)] and the quasi-steady model [Eq. (11.49)] for the UH-1H helicopter, which has a teetering rotor. As can be seen, the roll-rate response of the quasi-steady model is fairly accurate over the range of frequencies of interest for flight mechanics (0.1–10 rad/s) for this type of rotor system.

Consider now generalizing these modeling techniques to the fully coupled motion of the fuselage degrees of freedom. The adoption of the quasi-steady approximation results in a six-DOF representation for the complete helicopter as indicated in Table 1.2. The quasi-steady model formulation is a very useful starting point for helicopter system-identification and works well for a large

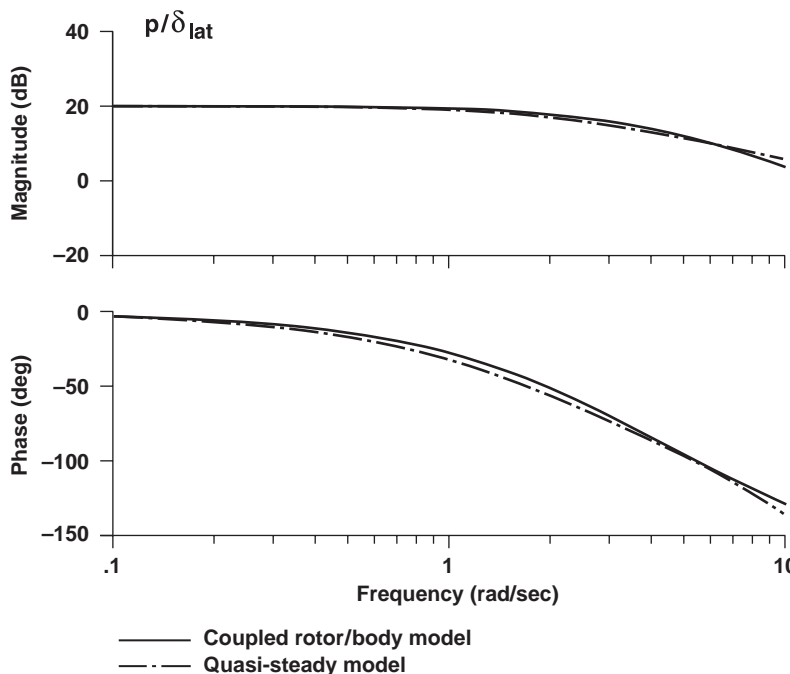


**Fig. 11.11** Comparison of coupled rotor-body and quasi-steady model structures for the UH-1 helicopter.

number of helicopters. Colbourne et al.<sup>19</sup> used the quasi-steady model structure to identify very accurate models of the Fire Scout P2 demonstrator, a variant of the Schweizer 333 helicopter (Sec. 13.12), which has a small hinge offset. These models were shown to capture well the frequency-response and time-domain response behavior, and they were subsequently used in control law development for the unmanned version of this helicopter, as discussed in the same reference.

When the coupling between the lateral/directional and longitudinal/vertical rotorcraft dynamics is negligible, the six-DOF system reduces further to two three-DOF systems of quasi-steady equations (Table 1.2) that are directly analogous to the rigid-body dynamics of fixed-wing aircraft.<sup>165</sup> This three-DOF quasi-steady assumption is appropriate to the XV-15 tilt-rotor identification because of the symmetrical configuration, high aircraft inertias, and gimballed (zero hinge-offset) rotor system, and it provides a very accurate representation of the flight-dynamics response in hovering flight (Chapters 13 and 14). It is also appropriate for other symmetrical rotorcraft configurations (e.g., the tandem-rotor CH-47).

As vehicle size is reduced, dynamic (Froude) scaling relationships<sup>166</sup> show that the flap stiffness increases:

$$\omega_n \propto \sqrt{N} \quad (11.50)$$

where  $N$  denotes the vehicle scale ratio. (For example,  $N = 2$  refers to a one-half-scale aircraft.) The flap stiffness then scales according to

$$|L_{\beta_{1s}}| \propto N \quad (11.51)$$

These relationships show that a reduction in vehicle size by a factor of 5 ( $N = 5$ ) results in a factor of 5 increase in the flap stiffness and a factor of 2.2 increase in response bandwidth (agility). This can be seen in the very agile response of hobby-size radio-controlled helicopters. Consider the comparison of the Yamaha R-50 small-scale unmanned helicopter to the UH-1H manned helicopter as discussed by Mettler et al.<sup>166</sup> The R-50 has a large effective flap stiffness ( $L_{\beta_{1s}} = -142.5$ ) as compared to the UH-1H ( $L_{\beta_{1s}} = -19.2$ ), which is consistent with the scale ratio between these aircraft ( $N = 5$ ). The quasi-steady model was fully adequate for characterizing the roll/flapping dynamics of the UH-1H, as was shown in Fig. 11.11. However, for the case of the much smaller R-50, the condition of Eq. (11.42) no longer applies. The coupled rotor body model of Eq. (11.40) must therefore be used for system identification of the R-50 and other small-scale UAV helicopters.<sup>167</sup>

### 11.7.2 Application to OH-58D Identification (High-Flap-Stiffness Example)

A good illustration of the helicopter flight-mechanics modeling concepts is the identification study of the OH-58D helicopter, presented by Ham et al.<sup>123</sup> and summarized herein. The key characteristics of this helicopter (Fig. 11.12) are



Fig. 11.12 OH-58D helicopter.

given by Heffley et al.<sup>21</sup>; this helicopter exhibits a rather high value of rotor-flap stiffness ( $L_{\beta_{1s}} = -47.4 \text{ s}^{-2}$ ) based on analytical predictions. The analytical value of the flap time constant, corrected for dynamic inflow effects, is  $\tau_f = 0.130 \text{ s}$ . These values indicate that the condition of Eq. (11.42) for the use of the quasi-steady model will no longer apply.

The solid line in Fig. 11.13 shows the frequency-response flight data for the SAS-off roll response  $p/\delta_{\text{lat}}$  in hover. The coherence is generally acceptable for the entire range of the plot (1–16 rad/s). The two model structures of Eqs. (11.40) and (11.49) were used to identify a transfer function for the fitting range of 1–16 rad/s. This range excludes the rotor lead-lag (in-plane) response (Sec. 15.2.2), visible for frequencies beyond 16 rad/s, because this is not included in the model structure for this example.

The identified quasi-steady model using the structure of Eq. (11.49) was

$$\frac{p}{\delta_{\text{lat}}}(s) = \frac{0.184e^{-0.161s}}{(s + 9.27)} \text{ rad/s/%} \quad (11.52)$$

This result is a poor fit of the flight response, as is shown by Fig. 11.13 and also reflected in the high associated transfer-function cost ( $J = 125.6$ ).

The identified coupled roll/flapping model using the structure of Eq. (11.40) was

$$\frac{p}{\delta_{\text{lat}}}(s) = \frac{0.988e^{-0.051s}}{s^2 + (1/0.155)s + 55.35} \text{ rad/s/%} \quad (11.53)$$

resulting in a much better fit, as seen in Fig. 11.13 and reflected by the low cost function ( $J = 21.4$ ). The time delay included in the identification of the coupled model  $\tau_{\text{eq}} = 0.051 \text{ s}$  accommodates the effects of actuator and linkage dynamics. The identified rotor-flap stiffness ( $L_{\beta_{1s}} = -55.35 \text{ s}^{-2}$ ) and rotor time constant ( $\tau_f = 0.155 \text{ s}$ ) compare well with the analytical values just given. Also, the relationship between the identified parameters of the coupled and quasi-steady models are in good agreement with Eqs. (11.46–11.48).

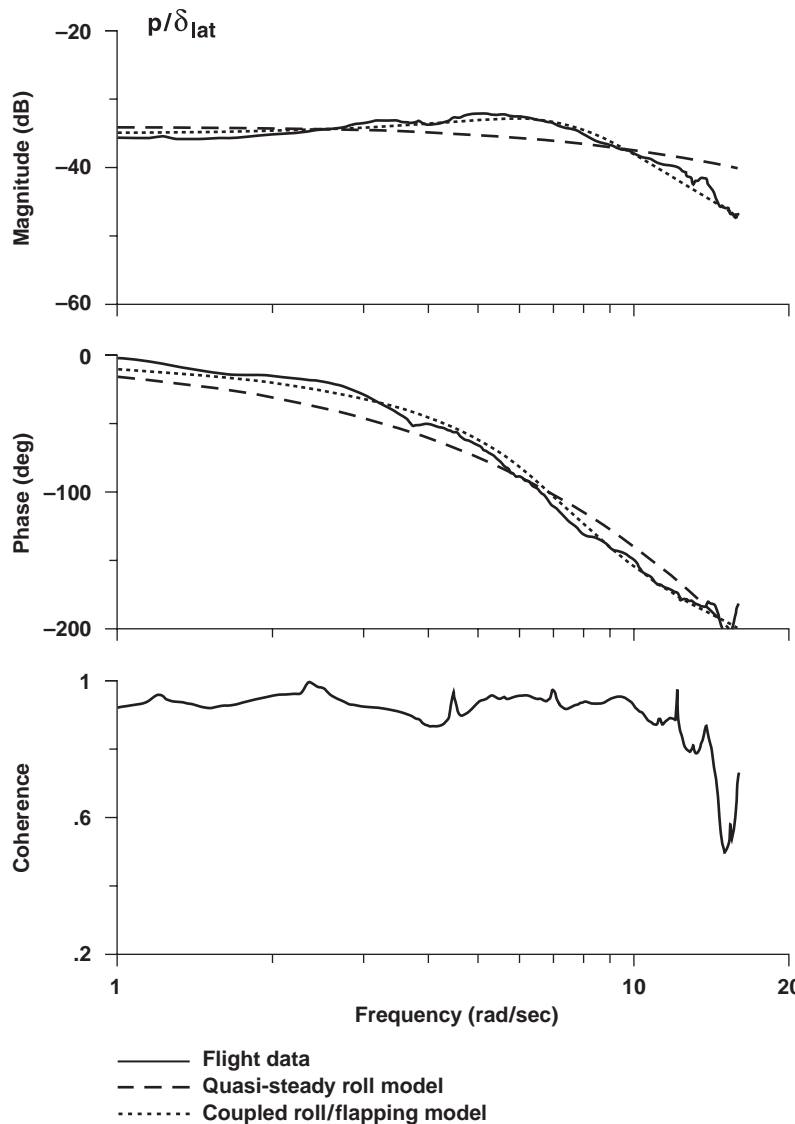


Fig. 11.13 Roll-response transfer-function models (OH-58D, hover).

## 11.8 Flight-Dynamics Models for Control System Design

Classical design and analysis techniques using Bode plots, Nichols plots, and root-locus plots continue to be in wide use in the aircraft and helicopter communities. These techniques are based on SISO transfer-function descriptions of end-to-end dynamics, as obtained in this chapter. Examples of such applications are found widely in the literature (e.g., Refs. 56 and 146). In the development of the

Fire Scout P2 demonstrator (unmanned helicopter), SISO transfer-function models were extracted from piloted flight tests of the test vehicle and then used in the development of a flight-control system for autonomous operations, as described by Colbourne et al.<sup>19</sup>

Tischler<sup>18</sup> investigated the system-identification requirements for high-bandwidth control system design, based on the roll-attitude response  $\phi/\delta_{\text{lat}}$  of the Bo-105 helicopter. The flight data were obtained by the DLR in support of AGARD Flight Mechanics Panel Working Group 18. (Ref. 10). A range of identification model structures was examined, with the simplest being the quasi-steady form of Eq. (11.44). Accurate prediction of closed-loop flight-control performance (i.e., crossover frequency, stability margins, bandwidth, and phase delay) required that the model needed to include the following: roll-angle integrator state (first order), coupled body roll/regressive flap (second order), lead-lag air resonance (second order), Dutch-roll dynamics (second order), and actuator dynamics (equivalent time delay). The result is a seventh-order *baseline model*:

$$\frac{\phi}{\delta_{\text{lat}}} = \frac{2.62[0.413, 3.07][0.0696, 16.2]e^{-0.0225s}}{(0)[0.277, 2.75][0.509, 13.7][0.0421, 15.8]} \text{ rad/%-lat} \quad (11.54)$$

The identified transfer-function model provides an excellent characterization of the frequency-response data, as is seen in Fig. 11.14, and as also reflected in a very low cost function,  $J = 12.1$ . The transfer-function model indicates a highly coupled roll/flapping model ( $\zeta_{\text{rf}} = 0.51$ ,  $\omega_{\text{rf}} = 13.7 \text{ rad/s}$ ), as is expected for the high flap stiffness ( $L_{\beta_{1s}} = -89.1 \text{ s}^{-2}$ ; Ref. 21) for the hingeless rotor system (large effective hinge offset) of the Bo-105. The low damping value of regressive lead-lag mode ( $\zeta_{\text{ll}_r} = 0.0421$ ,  $\omega_{\text{ll}_r} = 15.8 \text{ rad/s}$ ) reflects only the structural damping of the hingeless rotor because there are no mechanical dampers for this rotor system. The total modal damping ( $\sigma = -\zeta\omega = -0.665 \text{ rad/s}$ ) agrees very well with previously published experimental data.<sup>168</sup> There is also a nearby complex zero ( $\omega_n = 16.2 \text{ rad/s}$ ) associated with the lead-lag response to control inputs. This complex zero-pole pair (dipole) is a key characteristic of the dynamics of the coupled flap/lag/fuselage system, as explained in detail by Curtiss.<sup>161</sup> The Dutch-roll mode ( $\zeta_{\text{dr}} = 0.277$ ,  $\omega_{\text{dr}} = 2.75 \text{ rad/s}$ ) is lightly damped, as is also generally the case for the bare-airframe response of fixed-wing aircraft [e.g., Eq. (11.25)]. Significant roll-yaw coupling is apparent from the separation of the complex zero ( $\zeta_{\phi} = 0.413$ ,  $\omega_{\phi} = 3.07 \text{ rad/s}$ ) from the Dutch-roll mode. Finally, the equivalent time delay corresponds well to the known control system hydraulics and linkage lags.

Figure 11.15 shows a root-locus plot for variation of roll-rate feedback  $K_p$  (%/rad/s). In the nominal case based on the identified roll-rate response, rotor/flapping model stability is seen to set the limitation on rate feedback gain, although lead-lag modal damping is clearly reduced for moderate gain levels. When 50 ms of additional time delay is included to account for the filters and computational delay in a practical digital control system implementation,<sup>125</sup> the lead-lag mode becomes rapidly destabilized and sets the limit on rate feedback—as also concluded by Curtiss.<sup>161</sup> This result illustrates the need for

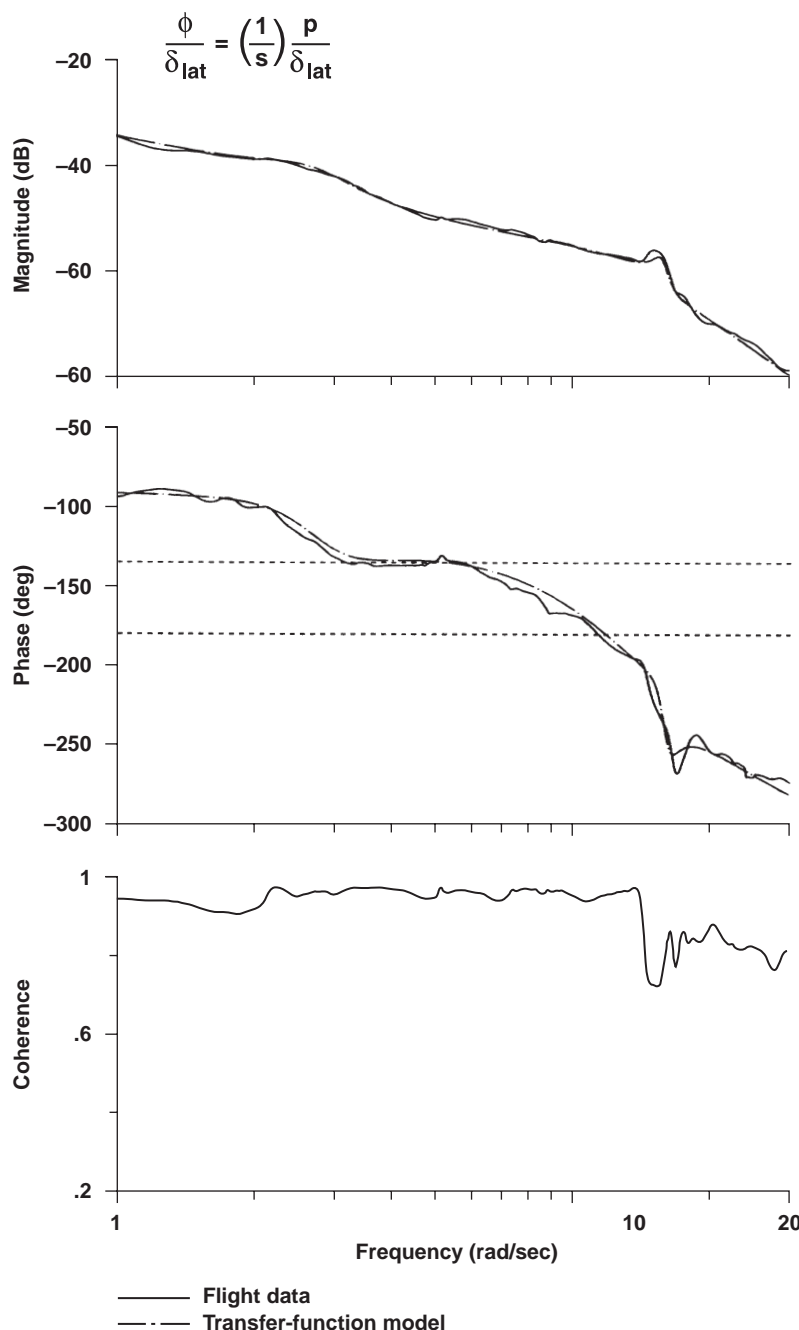


Fig. 11.14 Helicopter roll-attitude response model (Bo-105, hover).

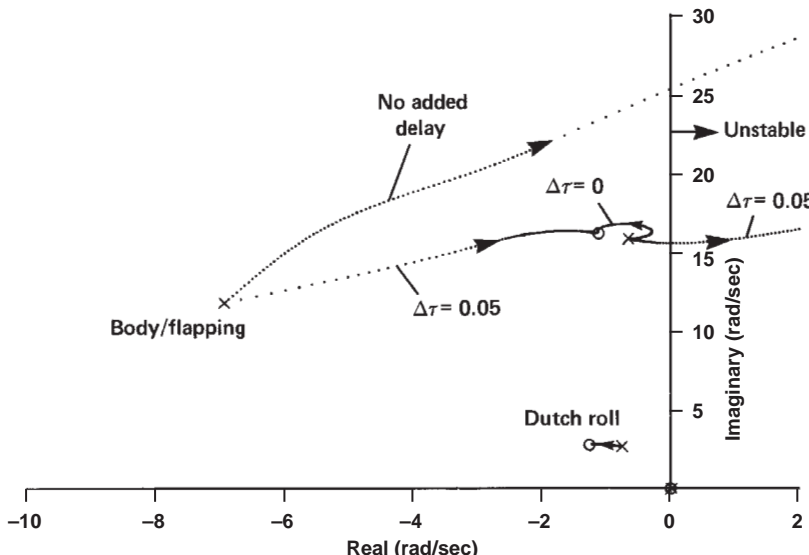


Fig. 11.15 Root-locus varying roll-rate gain (Bo-105, 80 kn).

accurate knowledge of lead-lag dynamics in high-bandwidth control system design. The coupling of lead-lag and roll/flapping dynamics was a key characteristic of the integrated rotor/control system development for the RAH-66 (Comanche) bearingless rotor helicopter.<sup>169</sup> Transfer-function model identification methods have also been widely used to characterize the coupled heave/rotor/inflow dynamics of helicopters, as demonstrated by Ham et al.<sup>123</sup> for the OH-58D and by Chen and Tischler<sup>68</sup> for the CH-47B.

### 11.9 Aeroelastic Model Identification

The aeroelastic response of a flight-vehicle structure is generally characterized by a series of modes, each represented by a second-order (spring-mass damper) system with an associated modal frequency and damping ratio. These modal characteristics are rapidly and accurately determined from frequency-sweep test data by fitting the measured aircraft response in the frequency range over which the mode is well excited. As demonstrated for the XV-15 by Acree and Tischler,<sup>87</sup> plots of modal damping vs airspeed provide a basis for comparison with analytical models, and they provide important trends for predicting the potential onset of wing flutter (zero damping).

The key advantages of this approach compared to the classical exponential dwell-decay (time-domain) method are as follows<sup>87</sup> 1) elimination of the effects of uncorrelated noise by using the frequency-response function, which is important for the typically low signal-to-noise ratio of structural response testing; 2) isolation and identification of individual modes by fitting transfer functions to

the frequency-response data with a narrow frequency band, which is important for handling closely spaced modes; 3) availability of the coherence function as a direct measure of the adequacy of modal excitation, level of random error, and signal-to-noise ratio, which allows the identification to emphasize the most reliable data; and 4) concatenation of repeat records, which reduces random error in frequency-response identification.

In the XV-15 tilt-rotor project, frequency-sweep flight-testing and transfer-function modeling methods were extensively used to establish aeroelastic mode stability for a range of airspeeds.<sup>87</sup> Automated frequency sweeps of the wing flaperons  $\delta_f$ , as shown in Fig. 11.16, were used to excite six primary aeroelastic modes of interest. Symmetric excitations of the right and left flaperons were used to identify the symmetric modes, and asymmetric excitations were used to identify the asymmetric modes. The direct measurement of the flaperon deflections provides

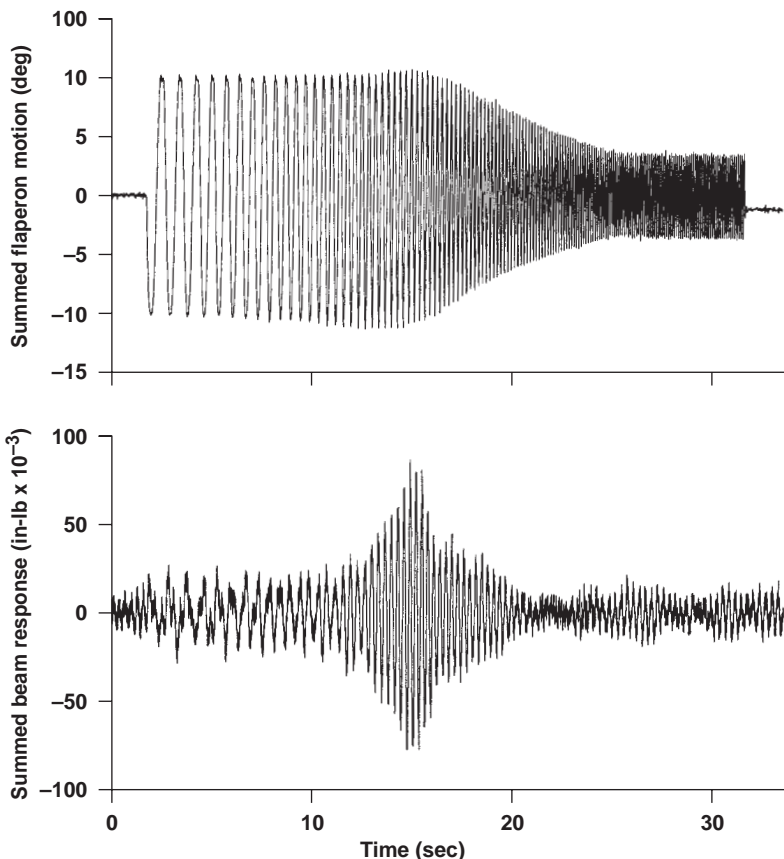


Fig. 11.16 Frequency-sweep input and wing-bending strain-gauge response (XV-15, 180 kn).

## 312 AIRCRAFT AND ROTORCRAFT SYSTEM IDENTIFICATION

an essentially noise-free input signal, and so the standard frequency-response estimate [Eq. (7.37)] is appropriate.

Data were collected from strain gauges that measured the wing-bending strain  $\varepsilon_{wb}$  at the wing root. As described in detail in the cited reference, the symmetric response was identified by using the summed (right and left) flapperon measurements as the input and the summed (right and left) wing strain-gauge measurements as the output. This technique greatly improved the coherence for the symmetric mode identification. Similarly, the coherence for the asymmetric mode identification was enhanced by using the differenced right- and left-wing flapperons as the input and the differenced wing strain measurements as the output. The time-history data for the symmetric response at 180 kn (true airspeed, Fig. 11.16) clearly show a “ringing” of the structure as the sweep passed through the symmetric beam-bending mode occurring at about 17 s. Notice also the shorter records that are used in structural response identification compared to typical flight-dynamics applications (Sec. 5.3) because of the higher modal frequencies involved.

The frequency response for the symmetric strain response to summed flapperon inputs  $\varepsilon_{wb}/\delta_f$  is shown with the solid line of Fig. 11.17. This result was achieved by concatenating several repeat flight records, of which Fig. 11.16 is typical. The Bode plot clearly shows the first symmetric bending mode of the wing. The coherence is good for the frequency range of interest, which includes the frequencies from below to just above this peak. A second-order transfer-function model provides the aeroelastic damping and natural frequency of the first wing-bending (symmetric) mode:

$$\frac{\varepsilon_{wb}}{\delta_f}(s) = \frac{k}{[0.026, 20.74]} \quad (11.55)$$

where the rigid-body response of Eq. (11.22) can be ignored in this model because it is well separated in frequency from the aeroelastic response (more than a factor of 20). As seen in Fig. 11.17, there is very good agreement between the transfer-function model (dashed line) and the flight response in the area of good coherence. The low damping ratio ( $\zeta = 0.026$ ) is typical of aircraft structural modes, and the natural frequency location ( $\omega_n = 20.74 \text{ rad/s} = 3.3 \text{ Hz}$ ) reflects the high cantilever inertia associated with the engine/prop-rotor systems that are placed in the wing tips of the tilt-rotor configuration (Fig. 3.4).

This procedure was repeated several times at the baseline condition of 180 kn to evaluate the scatter in the modal identification. As seen in Fig. 11.18, there is very little scatter in the results obtained from CIFER® (less than 1% in natural frequency and less than 9% in modal damping). Tests were then also conducted over a range of airspeeds to assess aeroelastic stability over the flight envelope. As also seen in Fig. 11.18, there is a linear (but small) effect of airspeed on the symmetric mode damping ratio and frequency. An extensive statistical analysis<sup>87</sup> showed that the CIFER® results exhibited significant reductions in scatter, both at the baseline and as a function of airspeed, compared to the exponential decay (Prony) analysis.

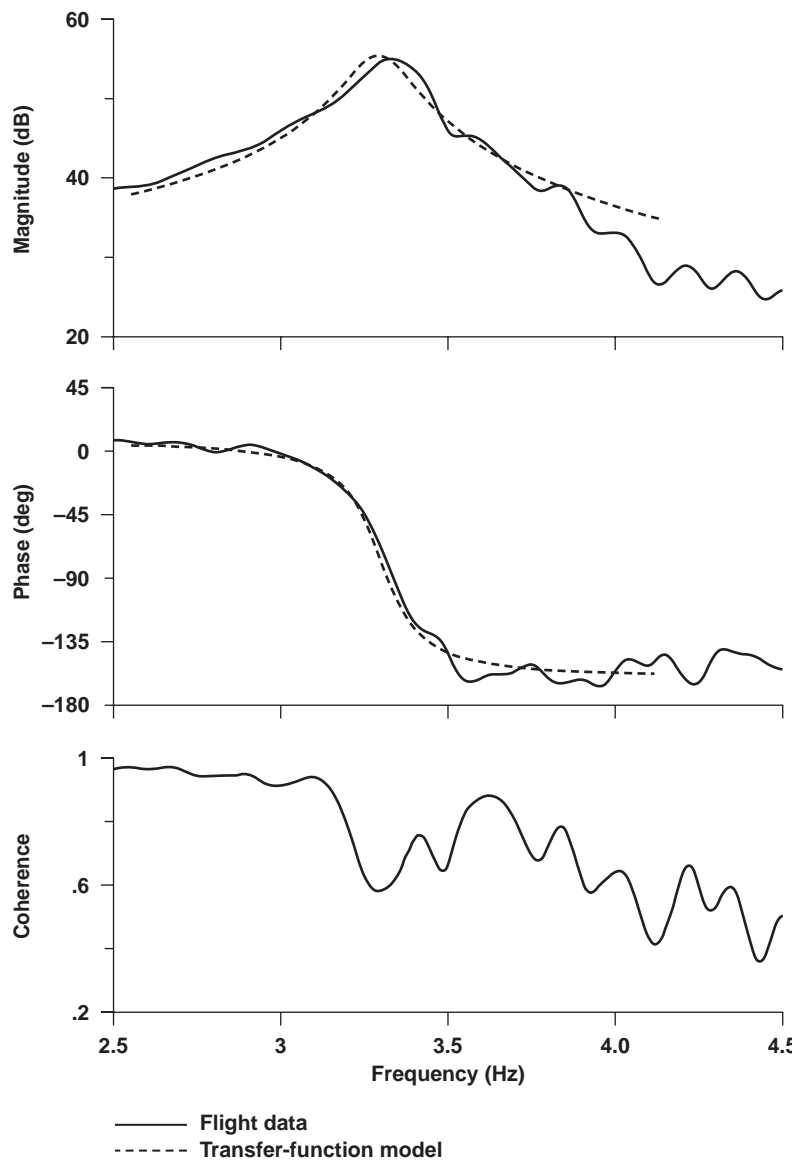


Fig. 11.17 Aeroelastic transfer-function model (XV-15, 180 kn).

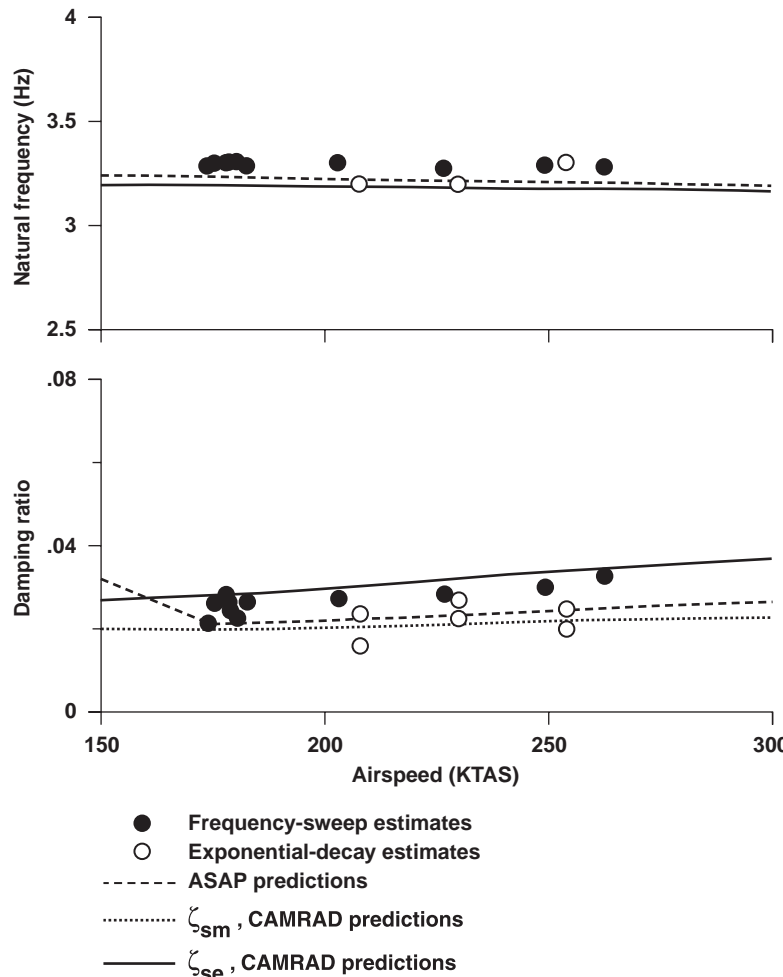


Fig. 11.18 Symmetric wing beam mode (XV-15, 180 kn).

### 11.10 Subsystem Component Modeling

A complete flight-vehicle analysis or simulation model can include a considerable library of subsystem components, including actuators, sensors, filters, linkages, and various sources of equivalent time delays (e.g., digital system zero-order hold and throughput delays associated with onboard processing). Transfer-function models are typically used to represent the input-to-output dynamic response of subsystem components because for flight-dynamics applications there is no need to model the detailed fluidic motion of a hydraulic actuator, the internal dynamics of an angular rate gyroscope, or the exact kinematics of the linkage system. Here

the only concern is an accurate model of the subsystem's overall dynamics response.

As an example of subsystem modeling, actuators are generally characterized as a second-order transfer function with given natural frequency, steady-state gain, and performance limits (rate and position authority). An added time delay can be included to account for additional unmodeled dynamics or an internal servoloop control system. Rate gyros and other sensors can be modeled by a second-order system, such as that of Eq. (6.20), and perhaps an added time delay to account for embedded filtering. Linkage kinematics are well modeled by a simple gain and perhaps an added time delay to account for deadband/hysteresis effects. Another example of subsystem modeling is the measurement data consistency model [Eq. (6.16)] of Sec. 6.2.1. Additional examples of typical subsystem models are contained in the case studies compiled by Tischler.<sup>11</sup> The following example demonstrates the identification of an actuator model from helicopter flight data.

Actuator system response is a key aspect in the flight-control design process and in determining overall flight-control performance.<sup>64</sup> System stability margins and overall closed-loop performance and handling qualities can be significantly degraded if the actuator dynamics do not agree with the design models. Accurate models of actuator dynamics have been found to be especially important for small-scale UAV development,<sup>12</sup> where flight-mechanics modes become faster with decreasing vehicle size. An accurate model of actuator dynamics can be quickly determined using a frequency sweep in a bench test under representative loading conditions, or in flight if measurements of the actuator command input  $r$  and position response  $\delta$  are available. An example of frequency-response identification and transfer-function modeling of a helicopter actuator from flight-test data is shown in Fig. 11.19. Excellent coherence is achieved over a broad frequency range (0.2–40 rad/s) using a computer-generated frequency-sweep excitation. The actuator dynamics are seen to be characterized very accurately by the well-damped second-order transfer-function model

$$\frac{\delta}{r}(s) = \frac{42.2^2}{[\zeta = 0.74; \omega_n = 42.2]} \quad (11.56)$$

as confirmed by the very low cost function ( $J = 6$ ).

A simulation model of the actuator for control system analysis combines these linear dynamic response characteristics with the performance limits as shown in Fig. 11.20. The gains in the simulation model are obtained directly from the identification results:

$$k_1 = \frac{\omega_n}{2\zeta} \quad (11.57)$$

$$k_2 = 2\zeta\omega_n \quad (11.58)$$

The rate limits  $\pm\dot{\delta}_{\max}$  and position limits  $\pm\delta_{\max}$  are implemented in the limited integrator blocks.

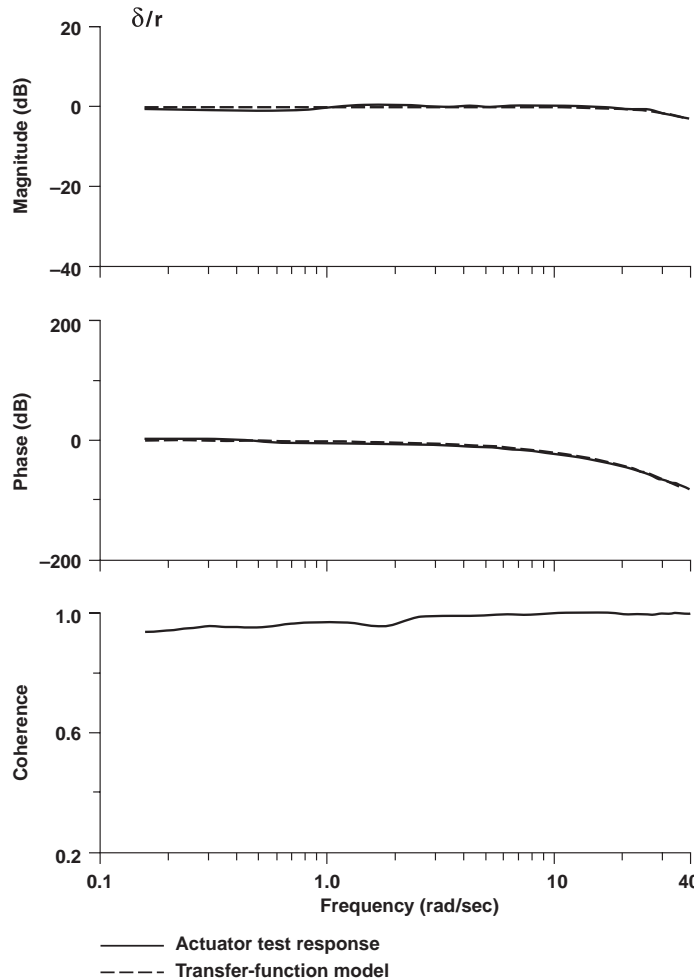


Fig. 11.19 AFCS actuator model identification.

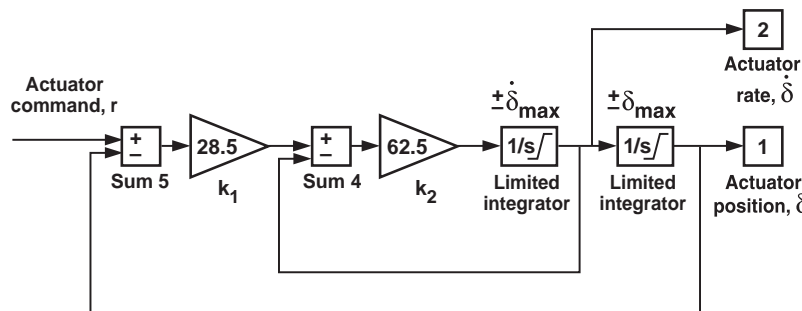


Fig. 11.20 Simulation model of actuator.

## 11.11 Summary and a Look Ahead

There is a broad range of system-identification applications to fixed-wing and rotorcraft projects that only require a model of the input-to-output process that can be achieved using the frequency-response identification and transfer-function models that have been discussed so far. These models, which are generally obtained with a very modest level of effort, provide a wealth of information about the characteristics of the system. They are often the “end goal” for many users of system identification (actually, perhaps a majority of users). Chapters 12 and 13 present the techniques for the identification of generalized multi-input/multi-output models in a state-space formulation. These methods build on the frequency-response fitting concepts of SISO transfer-function modeling. The results that have been presented in this chapter are often a useful intermediate step towards the more sophisticated MIMO response modeling using the more advanced state-space identification techniques. Chapter 14 presents the time-domain verification of both transfer-function models and state-space models.

## Problems

*SISO transfer-function fitting for the inverted pendulum system using NAVFIT*

**11.1** Identify a transfer-function model of the stable closed-loop pendulum frequency-response (**Problem 10.2**)  $\theta/\bar{M}_{\text{ext}}$ , using the known model structure of Eq. (3.5). Only use the frequency range of acceptable coherence in your identification ( $\gamma_{xy}^2 \geq 0.6$ ). Compare your identified model to the known analytical transfer function. Then, examine the sensitivity of the identification results to the initial guesses for the parameters and the effect of process and measurement noise (input and output) introduced into the simulation (continue with frequency responses from **Problem 7.14**, remembering to use COMPOSITE windowing).

**11.2** Obtain a transfer-function model for the unstable pendulum frequency response (**Problem 10.1**)  $\theta/\bar{M}_{\text{inv}}$ , using the known model structure. Only use the frequency range of acceptable coherence in your identification ( $\gamma_{xy}^2 \geq 0.6$ ). Compare your identified model to the known analytical transfer function. Then examine the sensitivity of the identification to process noise for the unstable case (remember to use COMPOSITE windowing).

**11.3** What would be the effect of using an incorrect model structure in **Problems 11.1** and **11.2** that included (a) an extra pole? (b) an extra zero? (c) an extra pole and an extra zero? What is the sensitivity to noise now? What does this tell you about the importance of proper model structure selection?

**11.4** Simulate the stable pendulum’s response to a doublet (amplitude of  $0.75 \text{ rad/s}^2$  as described in **Problem 5.9**) with the transfer-function model  $\theta/\bar{M}_{\text{ext}}$  identified in **Problem 11.1**, using MATLAB® or another suitable tool. Compare the time responses of your transfer-function model and the nonlinear model.

*SISO transfer-function fitting of XV-15 open- and closed-loop frequency-responses using NAVFIT*

**11.5** Identify a transfer-function model from the XV-15 closed-loop response  $p/\delta_{\text{lat}}$  in hover (**Problem 10.3**). Start with the model structure:  $m = 1$ ,  $n = 2$ , and  $\tau_{\text{eq}}$ . Next, try the simpler model structure:  $m = 0$ ,  $n = 2$ . Only use the frequency range of acceptable coherence in your identification ( $\gamma_{xy}^2 \geq 0.6$ ). Are these models satisfactory in terms of the cost function and reasonableness of the parameter values? Try alternative model structures, and look at the effect on the cost function and model parameters.

**11.6** Refer to the bare-airframe roll-attitude frequency response  $\phi/\delta_a$  as obtained using the roll-attitude data  $\phi$  in **Problem 10.6**. Identify a bare-airframe roll-attitude transfer-function model for hover using the model structure of the *hovering cubic*<sup>56</sup>:

$$\frac{\phi}{\delta_a} = \frac{L_{\delta_a}(1/T_{\phi_2})e^{-\tau_a s}}{(1/T_r)[\zeta_r, \omega_r]} \quad (\text{P11.6})$$

Only use frequencies of acceptable coherence in your identification ( $\gamma_{xy}^2 \geq 0.6$ ). Reference to Table 3.1 shows that a positive input  $\delta_a$  produces a negative roll rate  $p$ . Therefore, we should choose an initial guess for numerator coefficients (or steady-state gain) with negative values to achieve best results. Are the hovering dynamics stable or unstable? If unstable, what is the time-to-double amplitude for the unstable roots?

**11.7** Identify a transfer-function model for the cruise bare-airframe roll-rate response  $p/\delta_a$  using the simple first-order model structure given in Eq. (11.22). Then identify a transfer-function model for  $\beta/\delta_r$  using the model structure given in Eq. (11.23). Only use the frequency range of acceptable coherence in your identifications ( $\gamma_{xy}^2 \geq 0.6$ ). Reference to Table 3.4 shows that a positive input  $\delta_a$  produces a negative roll rate  $p$ . Therefore, we should choose an initial guess for numerator coefficients (or steady-state gain) with negative values to achieve best results. Check your answers with Eq. (11.24) and Eq. (11.25). Are the cruise dynamics stable or unstable?

*One-way coupling solution for the XV-15 bare airframe using NAVFIT*

**11.8** Identify a model for the decoupled yaw-rate response to rudder input for hover using the structure [based on data with acceptable coherence ( $\gamma_{xy}^2 \geq 0.6$ )]:

$$\frac{r}{\delta_r} = \frac{N_{\delta_r} e^{-\tau_r s}}{(1/T_y)} \quad (\text{P11.8})$$

**11.9** Identify a complete fourth-order bare-airframe model for roll at hover:

$$\frac{\phi}{\delta_a} = \frac{L_{\delta_a}(1/T_{\phi_1})(1/T_{\phi_2})e^{-\tau_a s}}{(1/T_y)(1/T_r)[\zeta_r, \omega_r]} \quad (\text{P11.9})$$

with the yaw response mode  $1/T_y$  fixed at the value obtained in **Problem 11.8**. Only use frequencies of acceptable coherence in your identification ( $\gamma_{xy}^2 \geq 0.6$ ). Remember again, because of the sign convention of the data, to start with negative numerator coefficients or negative steady-state gain for your initial guess. Compare the cost function and parameter values with those obtained using the hovering cubic of **Problem 11.6**. What can you say about the level of roll-yaw coupling in the XV-15 at hover?

**11.10** Identify a complete fourth-order bare-airframe model for roll at the cruise condition:

$$\frac{p}{\delta_a} = \frac{L_{\delta_a} s [\zeta_\phi, \omega_\phi] e^{-\tau_a s}}{(1/T_s)(1/T_r)[\zeta_{dr}, \omega_{dr}]} \quad (P11.10)$$

with the Dutch-roll mode fixed at the values obtained in **Problem 11.7**. Make sure to choose a frequency range with acceptable coherence ( $\gamma_{xy}^2 \geq 0.6$ ). Compare your results with those given in Eq. (11.29). What can you say about the level of roll-yaw coupling in the XV-15 at cruise?

This page intentionally left blank

## 12

## State-Space Model Identification— Basic Concepts

The previous chapter presented a parametric modeling approach using transfer-function identification, with primary application to the characterization of single-input/single-output decoupled responses. Transfer-function modeling is generally accomplished in quick fashion and provides important insight into the appropriate model structure and dynamic characteristics (i.e., dominant modes, time delay, and key derivatives) required to track the primary responses. In the many applications illustrated in Chapter 11, these transfer-function models provide the needed endproduct of system identification. However, the transfer-function model structure is not easily extended to generalized MIMO systems, where the state-space representation is better suited. Also, state-space models are often the needed final product of system identification for applications such as simulation model development and control system design.

The frequency-response method for state-space model identification is a direct extension of the transfer-function identification, using the same cost function based on frequency-response error. Here we seek a state-space model that produces a frequency-response matrix  $T$  that best fits the (measured) MIMO composite frequency-response estimate matrix  $\hat{T}_c$  obtained from Chapter 10. State-space model identification is covered in two chapters (Chapters 12 and 13). This chapter presents the basic concepts of the frequency-response method for state-space model identification and applications to canonical representation of SISO systems. Chapter 13 extends the discussion to the identification of physical structure representations of MIMO systems.

There is a wealth of reference material on state-space model identification of aircraft and helicopter dynamics in the time and frequency domains. An excellent overview and reference list of the maximum likelihood (ML) time-domain formulation is given by Iliff.<sup>170</sup> Aircraft state-space model identification based on maximum likelihood in the frequency domain was developed by Klein<sup>33</sup> and then applied extensively for helicopters and aircraft by the DLR of Germany (e.g., Refs. 34 and 37) and others, as summarized in Chapter 1. The frequency-response method for state-space model identification was developed by DiMarco and Magdaleno<sup>48</sup> and Tischler,<sup>171</sup> and has some key advantages compared to the other methods, especially for flight-vehicle identification from test data. A detailed development of the parameter accuracy analysis and associated metrics (such as the Cramér–Rao bounds and insensitivities used both in ML estimation and herein) is presented by Maine and Iliff.<sup>172</sup>

This chapter covers the following topics: background and motivation for using state-space models, state-space identification method, accuracy analysis and model structure determination, canonical vs physical model structures, state-space

model identification in CIFER® using DERIVID, and example results for canonical model structures.

## 12.1 Background

The transfer-function identification method presented in Chapter 11 rapidly provides an accurate lower-order equivalent system (LOES) parametric model that is needed (and, in fact, sufficient) for many applications, as illustrated in Sec. 11.6 to Sec. 11.10. LOES modeling also provides important insight into model structure, dynamic modes, and key dynamic parameters. Though still highly useful as a first modeling step, the transfer-function modeling method is not well suited to the more complex flight-vehicle applications involving higher-order or coupled MIMO behavior. Correlations can often occur among the identified transfer-function parameters that are not easily detected. The converged solution might have a low cost function, but with poles and zeros that offset each other and thus lack physical meaning. Also, it might be difficult to detect an overparameterized model in which there is insufficient information content to identify accurately some of the parameters, leading again to some values for the identified poles and zeros that might not have any real physical meaning. Finally, the identification of a consistent MIMO model based on a transfer-function structure becomes quite cumbersome beyond the two-input/two-output applications of Chapter 11. These limitations are largely overcome by considering the complete MIMO system response and recasting the identification model structure in state-space form.

In many applications the required endproduct of system identification is a state-space model expressed in terms of the stability and control derivatives or even the physical system parameters. For example, modern MIMO flight-control-system design methods, such as LQR,  $H_{\infty}$ , dynamic inversion, or eigenstructure assignment,<sup>11</sup> are based on state-space theory and require an accurate state-space model. State-space identification results are also very useful for simulation model validation and troubleshooting. Correction factors are often incorporated to improve the fidelity of physics-based simulation models. System-identification methods provide a systematic means for determining and implementing these correction factors, as illustrated in Sec. 13.9.3. Many recent flight-vehicle programs rely entirely on identified state-space models, rather than physics-based models, for flight-control design and training simulators. This was the case for the Burro (autonomous KMAX),<sup>173</sup> Fire Scout P2 demonstrator (autonomous variant of Schweizer 333),<sup>19</sup> SH-2G,<sup>139</sup> and the Autonomous Rotorcraft Project RMAX.<sup>174</sup> The identified state-space models are also useful for comparison with stability derivatives derived from wind-tunnel test data, as demonstrated for a fixed-wing aircraft application by Lewis and Catterall<sup>175</sup> and a helicopter application by Kaletka and Langer.<sup>176</sup> Taking a completely general view, the state-space methods described herein can be used to identify linear-time-invariant (LTI) models for any dynamic system, once the equations of motion are formulated and unknown constant coefficients are specified.

The state-space model structure is formulated from the first-order differential equations of motion. The unknown parameters can be the stability and control derivatives of the classical flight-mechanics equations, or physical constants

(such as equivalent spring, mass, and damper constants) in a generalized system representation. Initial guesses for the model parameters can be obtained from previous transfer-function identification results, from a priori estimates based on first principles, or from rapid equation-error regression methods.<sup>6,10</sup> Constraints on known relationships (e.g., kinematics) and a priori parameter values (e.g., lift-curve slope or gravity constant) are included directly in the state-space formulation. The SISO transfer-function models of Chapter 11 are also easily identified using the state-space methods by simply adopting an equivalent canonical model structure (Sec. 12.5.1). A sensitivity analysis provides reliable information on parameter value accuracy and correlation that is critical for model structure refinement.

In addition to providing a more general formulation for model *identification* in the frequency domain, the state-space description also allows the direct *verification* of the model in the time domain. The dynamic response of a state-space model is obtained by direct time integration of the differential equations of motion using the measured control inputs. Flight data for inputs dissimilar to the identification maneuvers are used to verify the utility and robustness of the model. An accurate prediction of the flight responses is an important gauge of the model's usefulness for many applications.

## 12.2 MIMO State-Space Model Identification Using the Frequency-Response Method

In this section, we adopt a general analytical model of a dynamic system in terms of the differential equations of motion. These equations are then converted into a state-space model structure with some known and some unknown coefficients. An identification algorithm for determining the unknown parameters in the model structure is then presented.

The perturbation equations of motion of a MIMO linear-time-invariant (LTI) system can be written in the form

$$\begin{aligned} m_{11}\dot{x}_1 + m_{12}\dot{x}_2 + \cdots + m_{1n}\dot{x}_n &= (f_{11}x_1 + f_{12}x_2 + \cdots + f_{1n}x_n) + (g_{11}u_1 + g_{12}u_2 + \cdots + g_{1n_c}u_{n_c}) \\ m_{21}\dot{x}_1 + m_{22}\dot{x}_2 + \cdots + m_{2n}\dot{x}_n &= (f_{21}x_1 + f_{22}x_2 + \cdots + f_{2n}x_n) + (g_{21}u_1 + g_{22}u_2 + \cdots + g_{2n_c}u_{n_c}) \\ &\dots \\ m_{n1}\dot{x}_1 + m_{n2}\dot{x}_2 + \cdots + m_{nn}\dot{x}_n &= (f_{n1}x_1 + f_{n2}x_2 + \cdots + f_{nn}x_n) + (g_{n1}u_1 + g_{n2}u_2 + \cdots + g_{nn_c}u_{n_c}) \end{aligned} \quad (12.1)$$

This system of equations is composed of  $n$  states  $x_1, x_2, \dots, x_n$ , and  $n_c$  control inputs  $u_1, u_2, \dots, u_{n_c}$ . This general formulation can accommodate model structures ranging from SISO canonical forms—equivalent to the transfer-function models of Chapter 11—to complex representations of complete mechanical systems. The mass terms  $m_{ij}$  are included because some physical parameters show

up on the left side of the equations of motion. An example is the rotor-flap time constant  $\tau_f$  on the left-hand side of Eq. (11.34). Other situations where these mass terms arise are for inclusion of forces and moments that depend on state rates and the inclusion of algebraic states that often arise for physical model structures (Sec. 15.2). In the case of the classical flight-mechanics equations, the mass matrix is usually unity (but can also include rate terms like  $\dot{N}_v$ ). The  $f_{ij}$  coefficients are the *stability derivatives*, and the  $g_{ij}$  coefficients are the *control derivatives*. The  $m_{ij}$ ,  $f_{ij}$ , and  $g_{ij}$  coefficients are the parameters to be determined by the identification process.

### 12.2.1 State-Space Model Structure

The equations of motion (12.1) are written concisely in matrix form

$$\dot{\mathbf{Mx}} = \mathbf{Fx} + \mathbf{Gu}(t - \tau) \quad (12.2)$$

The matrices  $\mathbf{M}$ ,  $\mathbf{F}$ ,  $\mathbf{G}$ , and the vector  $\tau$  contain model parameters to be identified, but can also contain a priori model parameters and constants (e.g., gravity  $g$ ). The time delays can be included to account for unmodeled dynamics. A *measurement* (also called *output*) vector  $\mathbf{y}$  is introduced because the states  $\mathbf{x}$  might not be directly measurable or only a subset might be measurable. The  $n_o$  available measurement signals  $y_1, y_2, \dots, y_{n_o}$  depend on the states and controls, but are conveniently expressed in matrix form as functions only of the state and state rate

$$\dot{\mathbf{y}} = \mathbf{H}_0\mathbf{x} + \mathbf{H}_1\dot{\mathbf{x}} \quad (12.3)$$

The matrices  $\mathbf{H}_0$  and  $\mathbf{H}_1$  are composed of known constants (e.g., units conversions, gravity, kinematics). The state-rate term  $\mathbf{H}_1\dot{\mathbf{x}}$  allows a simple kinematic relationship for the accelerometer measurements [Eqs. (6.32–6.34)]; *it does not contain the unknown stability and control derivatives*. Once the identification parameters are determined, the model equations (12.2) and (12.3) are easily expressed in conventional state-space form:

$$\dot{\mathbf{x}} = \mathbf{Ax} + \mathbf{Bu}(t - \tau) \quad (12.4)$$

$$\dot{\mathbf{y}} = \mathbf{Cx} + \mathbf{Du}(t - \tau) \quad (12.5)$$

where

$$\mathbf{A} = \mathbf{M}^{-1}\mathbf{F} \quad (12.6)$$

$$\mathbf{B} = \mathbf{M}^{-1}\mathbf{G} \quad (12.7)$$

$$\mathbf{C} = \mathbf{H}_0 + \mathbf{H}_1\mathbf{M}^{-1}\mathbf{F} \quad (12.8)$$

$$\mathbf{D} = \mathbf{H}_1\mathbf{M}^{-1}\mathbf{G} \quad (12.9)$$

We choose not to start with this standard state-space form because if mass matrix terms exist [e.g., Eq. (11.34)], this would result in elements of the ( $\mathbf{A}$  and  $\mathbf{B}$ ) matrices that are a complex combination of the desired physical parameters.

The identification model structure and unknown parameters are defined entirely in terms of the ordinary differential equations, which are expressed in state-space form by Eqs. (12.2) and (12.3). The identification is conducted by comparing the resulting MIMO frequency responses of the state-space model with those of the flight data. In Chapter 11, transfer-function identification was achieved by minimizing a cost function [Eq. (11.4)] of the weighted sum of the squared errors between the single-input/single-output (SISO) transfer-function model and the frequency-response data. The identification of multiple-input/multiple-output (MIMO) state-space models is achieved by a direct extension of the SISO cost function to matrix form. The identification cost function for the complete MIMO system is simply the sum of the individual cost functions [Eq. (11.4)].

The frequency-response matrix of the identification model  $\mathbf{T}(s)$  relates the Laplace transform of the output vector  $\mathbf{y}$  to the Laplace transform of the input vector  $\mathbf{u}$ :

$$\mathbf{Y}(s) = \mathbf{T}(s)\mathbf{U}(s) \quad (12.10)$$

or, in expanded form

$$\begin{bmatrix} Y_1(s) \\ Y_2(s) \\ \dots \\ Y_{n_o}(s) \end{bmatrix} = \begin{bmatrix} T_{11}(s) & T_{12}(s) & \dots & T_{1n_c}(s) \\ T_{21}(s) & T_{22}(s) & \dots & T_{2n_c}(s) \\ \dots & & & \dots \\ T_{n_o 1}(s) & T_{n_o 2}(s) & \dots & T_{n_o n_c}(s) \end{bmatrix} \begin{bmatrix} U_1(s) \\ U_2(s) \\ \dots \\ U_{n_c}(s) \end{bmatrix} \quad (12.11)$$

The frequency-response matrix of the model to be identified  $\mathbf{T}(s)$  is expressed as a function of the state-space identification model matrices  $\mathbf{M}$ ,  $\mathbf{F}$ ,  $\mathbf{G}$ ,  $\mathbf{H}_0$ , and  $\mathbf{H}_1$  by taking the Laplace transform of Eqs. (12.2) and (12.3) and performing some matrix algebra. Ignoring the time delay,

$$\mathbf{T}(s) = [\mathbf{H}_0 + s\mathbf{H}_1][(s\mathbf{I} - \mathbf{M}^{-1}\mathbf{F})^{-1}\mathbf{M}^{-1}\mathbf{G}] \quad (12.12)$$

In a generalization of the SISO equivalent time delay  $\tau_{eq}$  concept of Sec. 11.3, time delays  $\tau$  are included to account for unmodeled higher-order states. An individual equivalent time delay can be included in the model structure for each individual frequency-response pair resulting in a matrix

$$\boldsymbol{\tau}(s) = \begin{bmatrix} e^{-\tau_{11}s} & e^{-\tau_{12}s} & \dots & e^{-\tau_{1n_c}s} \\ e^{-\tau_{21}s} & e^{-\tau_{22}s} & \dots & e^{-\tau_{2n_c}s} \\ \dots & & & \dots \\ e^{-\tau_{n_o 1}s} & e^{-\tau_{n_o 2}s} & \dots & e^{-\tau_{n_o n_c}s} \end{bmatrix} \quad (12.13)$$

However, in most cases a common time delay is included for all output responses to a particular control. This corresponds to one time delay for each column (or  $n_c$  time delays in total) reducing to a time-delay vector [Eq. (12.2)]. Equations (12.12) and (12.13) can be combined to give

$$\mathbf{T}(s) = [\mathbf{H}_0 + s\mathbf{H}_1][(s\mathbf{I} - \mathbf{M}^{-1}\mathbf{F})^{-1}\mathbf{M}^{-1}\mathbf{G}] \circ \boldsymbol{\tau}(s) \quad (12.14)$$

where the operator ‘ $\circ$ ’ denotes the element-by-element multiplication of the *Schur product*  $\mathbf{A} \circ \mathbf{B} \equiv [a_{ij}b_{ij}]$  (Ref. 145).

### 12.2.2 Including the Transfer-Function Model Form in the Complete Structure

As discussed so far in this chapter, MIMO bare-airframe dynamics are best represented in a state-space model structure. Yet many subsystem components, such as sensors, actuators, and filters, are more conveniently represented by retaining the SISO transfer-function model structures of Eq. (11.1). An overall identification model structure that combines these two model forms (state space and transfer function) can represent a wide range of dynamic systems. In CIFER®, an individual transfer-function modeling element can be appended to each input-output pair of the state-space structure.

The overall model response is obtained by combining the state-space and transfer-function (TF) responses:

$$\mathbf{T}(s) = [\mathbf{T}(s)]_{\text{state-space}} \circ [\mathbf{T}(s)]_{\text{TF}} \quad (12.15)$$

Constraints can be introduced to ensure individual coefficients that comprise the transfer-function model element  $[\mathbf{T}(s)]_{\text{TF}}$  to have common values. This allows the identification of LOES transfer-function models with common denominators, as in the example of the lateral-directional model determination (Sec. 11.6.2). Individual transfer-function model coefficients can be free for identification or fixed at a priori values. Accuracy analyses are conducted on the combined models, thereby providing important data on parameter reliability and model structure selection (Sec. 12.3). Time-domain verification of this model structure is also useful to check the predictive accuracy (Chapter 14). The transfer-function model structure is referred to in CIFER® software as *sensor dynamics* because this is the most common use of this capability.

If we choose the state-space model structure to be an input-to-output process of unity, the overall model structure of Eq. (12.15) reduces to just that of a MIMO transfer-function model structure  $[\mathbf{T}(s)]_{\text{TF}}$ . This is an extension of the SISO transfer-function identification of Chapter 11. To accomplish this, a state-space equation is introduced for each transfer-function pair,

$$\dot{x} = 0x + 1u \quad (12.16)$$

The output equation is then defined as

$$y = (1.0s)x = u \quad (12.17)$$

which results in

$$\frac{y}{u} = 1.0 \quad (12.18)$$

for each response pair. Hence the overall model reduces to

$$\mathbf{T}(s) = [\mathbf{T}(s)]_{\text{TF}} \quad (12.19)$$

which is the transfer-function model structure. This capability was used to identify the two-input LOES transfer model with a common denominator [Eqs. (11.30) and (11.31)].

### 12.2.3 Identification Cost Function and Solution Algorithm

The solution of the MIMO identification problem involves determining the model matrices  $\mathbf{M}$ ,  $\mathbf{F}$ ,  $\mathbf{G}$ , and  $\boldsymbol{\tau}$  that produce a frequency-response matrix  $\mathbf{T}(s)$  that most closely matches the frequency responses obtained from the flight data ( $\hat{\mathbf{T}}_c$  from Chapter 10). The associated cost function to be minimized is a direct extension of the SISO formulation of Eq. (11.4) and is now simply the summed cost for the  $n_{\text{TF}}$  transfer functions:

$$J = \sum_{l=1}^{n_{\text{TF}}} \left\{ \frac{20}{n_{\omega}} \sum_{\omega_1}^{\omega_{n_{\omega}}} W_g [W_g (|\hat{T}_c| - |T|)^2 + W_p (\angle \hat{T}_c - \angle T)^2] \right\}_l \quad (12.20)$$

which is analogous to the cost function for the maximum likelihood method.

In most cases, the matrix of flight-test responses will not have good data for several of the theoretically possible ( $n_o \cdot n_c$ ) input-to-output combinations, as indicated by poor coherence for the entire frequency range of interest. Such responses are dropped entirely from the cost function. So only a subset  $n_{\text{TF}}$  of the frequency-response pairs of Eq. (12.11) will be included in the cost function of Eq. (12.20). The frequency-response pairs retained in the identification are denoted by  $T_l$ ,  $l = 1, 2, 3, \dots, n_{\text{TF}}$ .

The accuracy of the identified model is best characterized by the average overall cost function:

$$J_{\text{ave}} = \frac{J}{n_{\text{TF}}} \quad (12.21)$$

We note that all transfer functions included in the cost function of Eq. (12.20) use a common number of frequency points  $n_{\omega}$ . However, the choice of frequency-range points ( $\omega_1, \omega_2, \dots, \omega_{n_{\omega}}$ ) is made separately for each response pair  $T_l$ , corresponding to the region of acceptable overall coherence of that response, and in accordance with the frequency range of applicability of the overall model structure—just as in the transfer-function identification method. Also, as before,

the frequency points  $\omega_1, \omega_2, \dots, \omega_{n_{\omega}}$  are nominally selected to span the frequency range in a linear distribution across a logarithmic frequency scale. Although the overall frequency range is selected to ensure good coherence, it is also useful to define a coherence cutoff parameter  $(\gamma_{xy}^2)_{\text{cut}}$ . The distribution of points is then automatically adjusted to avoid data that exhibit local drops in coherence below this threshold. Experience indicates that a good choice is the following:

*Guideline:*

$$(\gamma_{xy}^2)_{\text{cut}} = 0.4 \quad (12.22)$$

The weighting functions  $W_{\gamma}$ ,  $W_g$ , and  $W_p$  all retain the same definitions as in the transfer-function identification method [Eqs. (11.5), (11.6), and (11.7), respectively] and are evaluated at each frequency point  $(\omega_1, \omega_2, \dots, \omega_{n_{\omega}})$  for each frequency-response pair  $T_l$ .

The  $n_p$  parameters to be identified in the model matrices  $\mathbf{M}$ ,  $\mathbf{F}$ ,  $\mathbf{G}$ , and  $\mathbf{\tau}$  are collected into an identification vector  $\boldsymbol{\Theta} = [\theta_1 \ \theta_2 \ \dots \ \theta_{n_p}]$ . Because frequency-response errors are a nonlinear function of the identification parameters, the solution for the minimum cost function  $J$  *must* be completed using an iterative process. As mentioned earlier, initial guesses for the model parameters can be obtained from the results of transfer-function identification (i.e., as obtained in Chapter 11), from a priori estimates based on first principles, or from rapid equation-error regression methods.<sup>6,10</sup>

An optimization algorithm varies the identification parameters  $\boldsymbol{\Theta}$  until a minimum value of the average cost  $J_{\text{ave}}$  is obtained. Depending on the model structure, the cost function can be highly nonlinear in the state-space identification parameters and can also involve correlated effects of multiple parameter variations. Therefore a gradient-based minimization method, as was used for transfer-function identification, is not recommended. A pattern search method, such as the secant method (Ref. 177; used in Tischler et al.<sup>178</sup>), is much better suited for this application and is the method used in CIFER®. The secant method starts from a set of trial guesses, which is obtained by perturbing the starting values of the identification parameters  $\boldsymbol{\Theta}$ . For each trial guess in this set, there is an associated vector of magnitude and phase errors relative to the flight data and an overall average cost function  $J_{\text{ave}}$ . The algorithm then selects the next estimate of the parameter set that reduces the cost function, based on a weighted average of the trial guesses. This process continues until a minimum cost function value is achieved. The solution is then restarted at this point to ensure that the converged solution is not just a local minimum, and eventually a final converged identification solution is reached.

The method can be thought of as a “crawling net,” and it is very robust to sharp changes and discontinuities in the optimization space  $J_{\text{ave}}(\boldsymbol{\Theta})$ . The secant method has been found to be especially adept at coping both with poor initial guesses and local minima. The new estimate cannot “jump” far away from the best choice of among the previous guesses, and so the minimum is generally reached in a smooth

and reliable (if sometimes slow) manner to arrive at the converged identification parameter set denoted by  $\Theta_0$ . Although the pattern method solution might involve many more iterations than a corresponding gradient method, each evaluation is computationally inexpensive because no matrix inversions are required. Extensive experience covering a wide range of aircraft, rotorcraft, and subsystem applications shows the solution process is highly reliable and does not suffer from the numerical problems that arise from the need to determine the inverse of the Jacobian matrix in gradient methods. The solution method has been found to work very well even for high-order model structures involving large numbers of identification parameters and frequency-response pairs. The restart method effectively avoids getting “stuck” in local minima. Also, the converged identification results are robust to large variations in the initial parameter guesses (**Problems 13.3** and **13.7**).

The interpretation of the converged MIMO cost function extends directly from the transfer-function identification method [Eq. (11.4)]. An overall average cost function that achieves

*Guideline:*

$$J_{\text{ave}} \leq 100 \quad (12.23)$$

is generally considered as reflecting an acceptable level of accuracy for flight-dynamics modeling and is typical of hovering helicopters. Some of the individual cost functions, especially for the off-axis responses, can reach the guideline of

*Guideline:*

$$J_l \leq 150 \text{ to } 200 \quad (12.24)$$

without resulting in a noticeable loss of overall predictive accuracy. The measurement data associated with fixed-wing and forward-flight helicopter applications are typically of higher quality than for hovering helicopters. Also, the required model structure is less complex because of the reduced coupling that is generally present for air vehicles in forward flight. These factors result in average cost functions that are usually much lower than the goals suggested herein. This is seen in the XV-15 forward-flight examples of Sec. 13.8. An average cost function  $J_{\text{ave}} \leq 50$  can be expected to produce time-response predictions that are nearly indistinguishable from the flight data.

Finally, a note of caution is in order about model applicability, as was sounded in the case of transfer-function model identification (Sec. 11.3.3). The identified state-space model might exhibit a low cost function, reflecting excellent frequency-response agreement *within the frequency range for which accurate (i.e., acceptable coherence) test data are available*. But the model might not predict accurately the response for frequencies below the available test data [e.g., steady-state (trim) response at  $\omega = 0 \text{ rad/s}$ ] or at frequencies well above the available test data (e.g., structural resonances outside the test data range). These limitations can be assessed using the time-domain verification methods of Chapter 14.

### 12.3 Accuracy Analysis

The identification process returns the state-space model of Eqs. (12.2) and (12.3) that best matches the frequency-response flight data. A measure of the accuracy or relative degree of confidence of the identification parameters  $\Theta_0$  is needed for a number of reasons, including the following:

1) The model structure might need to be refined. If the confidence of a parameter value is found to be very poor because of a lack of information content or correlation with other parameters, then it is better to eliminate that parameter from the model structure or replace it with a value that is reasonable from physical concepts. This process of *model structure determination* increases the accuracy and reliability of the final identified model.

2) A measure of parameter accuracy is needed to design/analyze a control system to ensure robustness. Many control design procedures use estimates of expected uncertainties in the design process. Once a control system design is completed, the estimated uncertainties are used to evaluate expected degradation with respect to the nominal performance.<sup>20</sup>

3) The evaluation of apparent differences between flight-test parameters and simulation parameters requires knowledge of the level of confidence with which both sets of parameters are known.

The two techniques for assessing identification parameter accuracy are scatter analysis and theoretical accuracy analysis. When many repeated test maneuvers are available, the statistical scatter in the converged estimates provides an important measure of parameter accuracy. However, the reasons for large parameter scatter are important for model structure determination, and these are not easily exposed. Also, this approach is not suitable for most flight-test applications, where the number of repeat maneuvers is generally too small to achieve a statistically significant result.

In the frequency-response method, two or three repeated runs are concatenated (Sec. 7.9) to achieve the most reliable frequency-response database and a single converged parameter set  $\Theta_0$ . The theoretical accuracy analysis method then provides an estimate of the expected parameter variability, based on a sensitivity analysis of the converged identification result. In theory, this is the same result as the standard deviation of parameter estimates that would be obtained from repeating the identification for multiple data sets. The theoretical accuracy analysis also provides a wealth of additional information on the cause of parameter variability that is valuable in refining the model structure.

The pioneering report by Maine and Iliff<sup>172</sup> provides a complete discussion of the mathematical basis for the theoretical accuracy analysis. This widely referenced work also demonstrates that time-correlated (or *colored*) noise is the primary cause of the well-known underprediction of the estimated parameter standard deviation based on the Cramér–Rao bounds. Morelli and Klein<sup>179</sup> validated these concepts using flight-test data of the F-18 aircraft. Milne<sup>180</sup> provides an excellent discussion of the key equations for theoretical accuracy analysis, physical interpretations of the metrics, and a systematic approach to model structure determination based on these results. The following sections summarize the development of the theoretical accuracy concepts and metrics and the use of these metrics in an integrated and reliable method for state-space model structure

refinement. The reader is directed to the references for a more complete mathematical development of the theory.

### 12.3.1 Cramér–Rao Inequality and Determining the Cramér–Rao Bounds

The Cramér–Rao inequality provides the fundamental basis for the theoretical accuracy analysis. This inequality establishes the *Cramér–Rao bounds*  $\text{CR}_i$  as the minimum expected standard deviation  $\sigma_i$  in the parameter estimate  $\theta_i$  that would be obtained from many repeated maneuvers. Thus

$$\sigma_i \geq \text{CR}_i \quad (12.25)$$

The relative values of the Cramér–Rao bounds among the identification parameters are of key significance for refining the model structure. Large relative Cramér–Rao bounds for individual parameters indicate poor identifiability and suggest that these parameters should be eliminated (or fixed) in the model structure.

The Cramér–Rao bound of the  $i$ th identified parameter of the converged solution  $\Theta_0$  is determined from the associated diagonal element of the inverse of the Hessian matrix  $\mathcal{H}$ :

$$\text{CR}_i = \sqrt{(\mathcal{H}^{-1})_{ii}} \quad (12.26)$$

where the  $n_p \times n_p$  matrix  $\mathcal{H}$  is defined as

$$\mathcal{H} = \nabla_{\Theta}^2 J = \frac{\partial^2 J}{\partial \Theta \partial \Theta^T} = \begin{bmatrix} \frac{\partial^2 J}{\partial \theta_1^2} & \frac{\partial^2 J}{\partial \theta_1 \partial \theta_2} & \cdots & \frac{\partial^2 J}{\partial \theta_1 \partial \theta_{n_p}} \\ \frac{\partial^2 J}{\partial \theta_2 \partial \theta_1} & \frac{\partial^2 J}{\partial \theta_2^2} & \cdots & \frac{\partial^2 J}{\partial \theta_2 \partial \theta_{n_p}} \\ \vdots & & & \\ \frac{\partial^2 J}{\partial \theta_{n_p} \partial \theta_1} & \frac{\partial^2 J}{\partial \theta_{n_p} \partial \theta_2} & \cdots & \frac{\partial^2 J}{\partial \theta_{n_p}^2} \end{bmatrix} \quad (12.27)$$

for the cost function  $J$ , as defined in Eq. (12.20).

The Hessian matrix is thus seen to indicate the curvature of the cost function to variations (and combination of variations) in each of the identification parameters. At one extreme, if the cost function is nearly insensitive to a certain parameter then there is little information content in the data set about that parameter, and its Cramér–Rao bound [from Eq. (12.26)] would be large. The statistical scatter for multiple runs would thus also be expected to be large for that parameter. Conversely, as the sensitivity of the cost function to a specific parameter increases

(and hence its insensitivity decreases), the Cramér–Rao bound decreases, along with the expected scatter for that parameter.

A numerical approximation for the Hessian matrix is determined by evaluating the gradients of the cost function with respect to perturbations in the converged parameter values. Consider the matrix formulation for the cost function in Eq. (12.20):

$$J(\Theta) = \frac{20}{n_\omega} \boldsymbol{\epsilon}^T(\Theta) \mathbf{W} \boldsymbol{\epsilon}(\Theta) \quad (12.28)$$

where  $\boldsymbol{\epsilon}$  is a vector of the magnitude and phase errors between the identified model (dependent on the identification parameters  $\Theta$ ) and the flight data, namely,

$$\boldsymbol{\epsilon}(\Theta) = \begin{bmatrix} (|\hat{T}| - |T|)_1 \\ (|\hat{T}| - |T|)_2 \\ \dots \\ (|\hat{T}| - |T|)_{n_{TF}} \\ (\angle \hat{T} - \angle T)_1 \\ (\angle \hat{T} - \angle T)_2 \\ \dots \\ (\angle \hat{T} - \angle T)_{n_{TF}} \end{bmatrix} \quad (12.29)$$

Each frequency-response row in Eq. (12.29) is associated with one frequency-response pair  $T_l$  and is actually composed of  $n_\omega$  rows corresponding to the number of frequency points. The weighting parameters  $W_y(\omega)$ ,  $W_g$ , and  $W_p$  in the cost function of Eq. (12.20) are collected into the single diagonal weighting matrix  $\mathbf{W}(\omega)$  that is dependent on frequency  $\omega$  but *not* on the parameter set  $\Theta$ .

The cost function associated with the converged identification parameter set  $\Theta_0$  is expressed as

$$J(\Theta_0) = \frac{20}{n_\omega} \boldsymbol{\epsilon}^T(\Theta_0) \mathbf{W} \boldsymbol{\epsilon}(\Theta_0) \quad (12.30)$$

This cost function can be expanded with respect to perturbations  $\partial\Theta$  in the converged identification parameters:

$$J(\partial\Theta) = \left( \frac{20}{n_\omega} \right) [(\boldsymbol{\epsilon}_0 + \mathbf{D}\partial\Theta)^T \mathbf{W} (\boldsymbol{\epsilon}_0 + \mathbf{D}\partial\Theta) + \text{higher-order terms}] \quad (12.31)$$

where  $\mathbf{D}_{ij} \equiv \partial\epsilon_i / \partial\theta_j|_0$  is a matrix of partial derivatives of the frequency-response matching errors (magnitude and phase) at each frequency point with respect to perturbations in each of the converged identification parameter values. The notation

(|<sub>0</sub>) indicates that the partial derivatives are evaluated about the converged parameter set  $\Theta_0$ . Expanding the formulation of Eq. (12.31) and neglecting the higher-order terms yields

$$J(\partial\Theta) = \left(\frac{20}{n_\omega}\right)[(\boldsymbol{\epsilon}_0^T + \partial\Theta^T \mathbf{D}^T) \mathbf{W}(\boldsymbol{\epsilon}_0 + \mathbf{D}\partial\Theta)] \quad (12.32)$$

which is further expanded to yield

$$J(\partial\Theta) = \left(\frac{20}{n_\omega}\right)[\boldsymbol{\epsilon}_0^T \mathbf{W} \boldsymbol{\epsilon}_0 + \boldsymbol{\epsilon}_0^T \mathbf{W} \mathbf{D} \partial\Theta + \partial\Theta^T \mathbf{D}^T \mathbf{W} \boldsymbol{\epsilon}_0 + \partial\Theta^T \mathbf{D}^T \mathbf{W} \mathbf{D} \partial\Theta] \quad (12.33)$$

The partial derivative of each term is evaluated with respect to the perturbations in the identified parameters  $\partial\Theta$  using the rules for gradients of matrix products.<sup>181</sup> When we note that  $\mathbf{W}^T = \mathbf{W}$ , the first derivative result is

$$\frac{\partial J}{\partial\Theta} = \left(\frac{20}{n_\omega}\right)[0 + 2\mathbf{D}^T \mathbf{W} \boldsymbol{\epsilon}_0 + 2\mathbf{D}^T \mathbf{W} \mathbf{D} \partial\Theta] \quad (12.34)$$

Taking the partial derivative again gives the following approximation for the Hessian matrix  $\mathcal{H}$ :

$$\mathcal{H} = \frac{\partial^2 J}{\partial\Theta^2} \equiv \left(\frac{20}{n_\omega}\right)[2\mathbf{D}^T \mathbf{W} \mathbf{D}] \quad (12.35)$$

which is also consistent with the result by Raisinghani and Goel.<sup>57</sup>

As already mentioned, the Cramér–Rao inequality of Eq. (12.25) dictates that the Cramér–Rao bound is always less than or equal to the standard deviation that would be obtained from a scatter analysis. In ML identification methods, scale factors of 5 to 10 are commonly needed in Eq. (12.26) to arrive at a reasonable estimate of expected scatter (e.g., Section 5.5.3.1 of Ref. 10; Ref. 172; Ref. 6):

$$\sigma_i \approx (5 \text{ to } 10) \text{ CR}_i \quad (12.36)$$

Maine and Iliff<sup>172</sup> show that these factors account for the effects of non-Gaussian (i.e., *colored*) noise and modeling errors in the identification process. Even when the noise is properly modeled, or eliminated as in frequency-response identification, a scale factor of about 2 typically remains necessary:<sup>172</sup>

$$\sigma_i \approx 2\text{CR}_i = 2\sqrt{(\mathcal{H}^{-1})_{ii}} \quad (12.37)$$

The factor of 2 in Eq. (12.37) is included in the Cramér–Rao results provided by CIFER®:

$$(\text{CR}_i)_{\text{CIFER}} \equiv 2\sqrt{(\mathcal{H}^{-1})_{ii}} \approx \sigma_i \quad (12.38)$$

In the remainder of this book, the symbol  $\text{CR}_i$  refers to  $(\text{CR}_i)_{\text{CIFER}}$ , with the factor of 2 in Eq. (12.38) included.

The required matrix of partial gradients  $\mathbf{D}$  in Eq. (12.35) is obtained numerically by applying small perturbations  $\Delta\theta_i$  to each of the  $n_p$  converged parameters in  $\boldsymbol{\Theta}_0$  and determining the change in the fitting error  $\Delta\epsilon$  [in Eq. (12.29)] as a function of frequency. Progressively smaller perturbations in the parameters are used until successive calculations return the same partial gradient result to within an acceptable tolerance, thus indicating that the accuracy results are valid.

The Cramér–Rao bounds are best expressed as a percentage of the converged identification values:

$$\overline{\text{CR}_i} = \left| \frac{\text{CR}_i}{\theta_i} \right| \times 100\% \quad (12.39)$$

Extensive experience with identification of state-space models from simulation and flight-test data using the frequency-response method suggests a reasonable guideline is to achieve Cramér–Rao bounds satisfying the following:

*Guideline:*

$$\overline{\text{CR}_i} \leq 20\% \quad (12.40)$$

which, together with a converged average cost function of  $J_{\text{ave}} \leq 100$ , reflects a highly reliable state-space model identification with good predictive accuracy. Several of the largest Cramér–Rao bounds may be in the range of 20%–40% without loss of reliability or cause for concern.

### 12.3.2 Validation of Cramér–Rao Bound Calculation

Table 12.1 shows the identification parameters and associated Cramér–Rao bounds for the XV-15 identification in hover obtained from CIFER® (Sec. 13.9.3). Also shown are the average parameters and sample standard deviation obtained by the DLR using the time-domain (ML) identification method for repeated maneuvers.<sup>13</sup> The differences seen in some of the identified parameters (note especially the angular damping derivatives  $L_p$  and  $N_r$ ) arise from the inherent weighting (magnitude vs phase weighting and frequency weighting) for the frequency-domain and time-domain methods, as is explained in more detail in the cited reference and by Kaletka et al.<sup>14</sup> for the comparison of results for the Bo-105 helicopter. Despite the differences in several of the individual derivatives, there is excellent overall agreement of the model for the time-domain validation maneuvers.<sup>13</sup> There is also reasonable qualitative agreement between the Cramér–Rao bounds obtained from CIFER® [Eqs. (12.38) and (12.39)] and the ML sample standard deviation results.

Another case study is for the Bo-105 helicopter (80 kn), as shown in Table 12.2. The identification results for the key on-axis angular parameters of the Bo-105 helicopter obtained from CIFER® are compared with the time-domain ML method (results obtained by the DLR; see Section 6.2.4 of Ref. 10). Again, the identification parameters show reasonable overall agreement given the considerable differences between the methods. The Cramér–Rao bounds (%) are

**Table 12.1 Comparison of identification and parameter scatter results (XV-15, hover)**

Parameter	Value: CIFER®	CR%: CIFER®	Value: ML	Sample scatter, %
$Y_v$	-0.0976	6.65	-0.0749	19.1
$Y_p$	-1.49	12.78	0	—
$L_v$	-0.00437	5.38	-0.0179	13.3
$L_p$	-0.237	15.41	-0.559	18.1
$L_r$	0	—	-0.349	33.0
$N_v$	0.00072	7.67	0.00141	132
$N_p$	0.0386	29.88	0	—
$N_r$	-0.142	13.17	-0.0715	3.42
$Y_{\delta_a}$	-0.0452	5.83	-0.0116	3.37
$L_{\delta_a}$	-0.0578	2.41	-0.0617	2.81
$N_{\delta_a}$	0.00591	5.13	0.00615	7.53
$N_{\delta_r}$	0.0119	4.58	0.0127	3.30

comparable between the two methods once the typical scale factor of 5–10 is included in the ML results.

The two examples presented herein provide empirical validation of the theoretical accuracy metrics values and predicted standard deviations obtained from Eq. (12.38). Similarly, Klein and Morelli<sup>6</sup> demonstrate good agreement between accuracy metrics obtained in the frequency domain and those obtained in the time domain, once the latter were corrected for colored noise effects.

### 12.3.3 Interpretation of the Cramér–Rao Bounds and Related Metrics

The level of confidence in the accuracy of an identified parameter is ascertained directly from the Cramér–Rao percentage. A Cramér–Rao bound that significantly exceeds the guideline of Eq. (12.40) reflects one or both of the following problems: insensitivity and correlation.

**Table 12.2 Comparison of key identification and parameter scatter results (Bo-105, 80 kn)**

Parameter	Value: CIFER®	CR%: CIFER®	Value: ML	Sample scatter, %
$L_p$	-8.78	7.3	-8.50	1.3
$M_q$	-4.49	5.2	-3.50	1.3
$N_r$	-1.07	5.7	-0.858	0.79
$L_{\delta_{\text{lat}}}$	0.179	7.8	0.185	1.2
$M_{\delta_{\text{lon}}}$	0.098	4.4	0.093	1.1
$N_{\delta_{\text{ped}}}$	0.057	4.0	0.049	0.61

High *insensitivity* occurs when changes in a single parameter  $\theta_i$  have *little or no* effect on the converged cost function  $J(\Theta_0)$ , indicating that the parameter is not important in the selected model structure. Parameter insensitivity is determined from the diagonal elements of the Hessian matrix<sup>172</sup>:

$$I_i = \frac{1}{\sqrt{\mathcal{H}_{ii}}} \quad (12.41)$$

The parameter insensitivities are also best presented as normalized percentages of the converged parameter values:

$$\bar{I}_i = \left| \frac{I_i}{\theta_i} \right| \times 100\% \quad (12.42)$$

Maine and Iliff<sup>172</sup> show that the insensitivity value is the lower limit of the Cramér–Rao bound; thus,

$$\bar{I}_i \leq \overline{CR}_i \quad (12.43)$$

Taking into account the Cramér–Rao scaling introduced in Eq. (12.38), the relationship becomes

$$\bar{I}_i \leq 0.5 \overline{CR}_i \quad (12.44)$$

Much experience shows that a reasonable goal for insensitivities as obtained from the frequency-response method is as follows:

*Guideline:*

$$\bar{I}_i < 10\% \quad (12.45)$$

which from reference to Eq. (12.44) is also consistent with the goal for the Cramér–Rao bound [Eq. (12.40)]. Several of the largest insensitivities are typically in the range of 10–20% without loss of reliability or cause for concern.

A common situation that produces a value of insensitivity considerably in excess of the guideline [Eq. (12.45)] is when a parameter is included in a selected model structure but it turns out to be unimportant to the vehicle dynamics. For example, coupling response derivatives are often initially included in a generalized model structure of a flight-vehicle response. These couplings will be of negligible importance in a flight vehicle with a largely decoupled response, and the extraneous coupling derivatives will display large insensitivities and result in large associated Cramér–Rao bounds.

Another situation that produces high insensitivities is when there is insufficient information content in the frequency-response database to determine an identification parameter. For example, suppose that we have selected an identification model structure that includes a high-frequency structural mode with associated identification parameters  $[\zeta, \omega_n]$  to account for expected flexible system dynamics. If the test excitation and resulting frequency-response database is only

## STATE-SPACE MODEL IDENTIFICATION—BASIC CONCEPTS 337

adequate at lower (rigid-body response) frequencies, the insensitivities of these structural mode parameters will be very large. This indicates that the parameters are not important in defining the responses in the frequency range over which the data are available. The accurate determination of these parameters would require the test excitation to be repeated out to higher frequencies.

High *correlation* occurs when two or more parameters can be simultaneously varied in a linear relationship and have an offsetting effect on the cost function  $J(\Theta)$ . In such a situation, the parameters cannot be independently determined. To illustrate this point with a very simple example, consider an algebraic SISO system

$$y = kx \quad (12.46)$$

to be identified from input measurements  $x$  and output measurements  $y$ . There is just one physical parameter  $k$  that characterizes the input-to-output process. Suppose that the identification model structure is (incorrectly) selected to include two identification parameters  $k_1$  and  $k_2$  such that

$$y = (k_1 + k_2)x \quad (12.47)$$

Clearly the effects of modeling parameters  $k_1$  and  $k_2$  are fully correlated because

$$k_2 = k - k_1 \quad (12.48)$$

and the model structure parameters ( $k_1$  and  $k_2$ ) cannot be independently determined. Any value of  $k_1$  with a corresponding value of  $k_2$  given in Eq. (12.48) will produce a model that fits the data equally as well. The only way out of this problem is to assign a fixed value to one of the parameters (e.g., set  $k_1 = 0$ ) and then identify the remaining parameter ( $k_2 = k$ ).

The preceding example presents a very simple correlation problem. If the actual physical system description of Eq. (12.46) were known a priori, then only a single identification parameter  $k$  would be introduced in the model structure to begin with, thus avoiding the correlation problem. However, identification is based solely on the input and output data, and we seek to determine the underlying model. The presence of pair-wise correlation can be detected numerically by examining the correlation coefficients.<sup>172</sup> For two identification parameters  $\theta_i$  and  $\theta_j$  the correlation coefficient is

$$\rho_{ij} = \frac{(\mathcal{H}^{-1})_{ij}}{\sqrt{(\mathcal{H}^{-1})_{ii}(\mathcal{H}^{-1})_{jj}}} \quad (12.49)$$

where

$$-1 \leq \rho_{ij} \leq 1 \quad (12.50)$$

In the preceding simple case, the parameters  $k_1$  and  $k_2$  would display a correlation coefficient of  $\rho_{12} = -1$ , indicating that the model structure needs to be

reduced. However, this method of analysis is not reliable when there are correlations among multiple parameters.<sup>172</sup>

In more complex identification problems involving MIMO state-space model structures, the physical system is represented by a set of differential equations with many unknown coefficients as the identification parameters. The identification parameters can have duplicating (i.e., correlated) effects on the frequency-response fits, which can compromise greatly the accuracy of the results, as reflected by high Cramér–Rao bounds. Reliable numerical tools are needed to expose potential parameter correlations and provide guidance for model structure determinations that are suitable for the often complex identification of flight vehicles. High-order model structures and a large number of identification parameters are characteristics of flight-vehicle identification, especially in the case of rotorcraft. The confidence ellipsoid<sup>172</sup> provides a reliable concept for analyzing correlation among multiple parameters. The point on the *scaled confidence ellipsoid*<sup>180</sup> associated with a specific Cramér–Rao bound  $CR_i$  is determined by

$$\bar{\Theta}_{CR_i} = \frac{\mathbf{T}^{-1} \mathbf{H}^{-1}(:,i)}{CR_i} \quad (12.51)$$

In this equation,  $\mathbf{H}^{-1}(:,i)$  denotes the  $i$ th column of  $\mathbf{H}^{-1}$  and  $\mathbf{T} \equiv \text{diag}[I_1, I_2, \dots, I_{n_p}]$  are the insensitivities of Eq. (12.41).

The elements of the confidence ellipsoid vector  $\bar{\Theta}_{CR_i}$  are normalized to unity. When the Cramér–Rao bound of an identification parameter exceeds considerably the guideline of Eq. (12.40) and the associated insensitivity is within the guideline of Eq. (12.45), parameter correlation is indicated. The large relative components of  $\bar{\Theta}_{CR_i}$  reflect the contributions of the correlated parameters that are responsible for a large Cramér–Rao bound  $CR_i$ . The confidence ellipsoid can be thought of as a multidimensional generalization of the pair-wise correlation coefficient result  $\rho_{ij}$ .

### 12.3.4 Systematic Model Structure Determination Using the Theoretical Accuracy Metrics

Milne<sup>180</sup> presents a systematic approach for model structure determination based on achieving a parameter set with all Cramér–Rao bounds within a common limit and therefore a roughly constant degree of confidence. An initial model is identified, with all of the possible derivatives included in the model structure. The converged solution is analyzed to determine the Cramér–Rao bounds and insensitivities, which are then compared against the maximum values for the Cramér–Rao bounds and insensitivities given in the guidelines of Eqs. (12.40) and (12.43), respectively.

The identification parameter with largest insensitivity [greater than the guideline of Eq. (12.43)] is eliminated first from the model structure (i.e., it is set to zero and fixed). For  $I > 40\%$  there will be little discernible initial effect on the cost function, and the reconverged solution will also not change significantly. The reduced model structure and the insensitivities are then calculated again. This procedure is repeated until all of the insensitivities are generally in accordance

## STATE-SPACE MODEL IDENTIFICATION—BASIC CONCEPTS 339

with the guideline. The converged cost function should be monitored with each step in the model reduction. The process is terminated if dropping a parameter and reconverging the model results in a jump increase in the average cost function of

*Guideline:*

$$\Delta J_{\text{ave}} \approx 1 \text{ to } 2 \quad (12.52)$$

or a jump increase in the cost function of an individual frequency-response pair  $T_l$  of

*Guideline:*

$$\Delta J_l \approx 10 \text{ to } 20 \quad (12.53)$$

This will usually occur when the largest insensitivity is close to the guideline of Eq. (12.43). This last parameter is then reinserted, and the parameters with high Cramér–Rao bounds are investigated next.

All of the remaining parameters have acceptable sensitivities, and so individually they have an important effect on the cost function. However, parameters with high Cramér–Rao bounds [in excess of the guideline Eq. (12.40)] have correlated effects with other parameter(s), which compromises the reliability of the identified values. When two or more parameters are found to be correlated, as indicated by large elements in the confidence ellipsoids [Eq. (12.51)], a decision must be made as to which parameters should be dropped from the identification model structure. The parameter that clearly has the largest Cramér–Rao is dropped.

In many situations, however, several parameters are grouped with roughly the same high Cramér–Rao bound values. The correlation analysis might show that a single parameter shows up prominently in the confidence ellipsoids of several parameters with high Cramér–Rao bounds. By dropping this single parameter, the Cramér–Rao bounds of the remaining correlated parameters will be reduced. When several parameters have close Cramér–Rao values, it is sometimes useful to try several options in the sequence of model reduction steps, to see which “path” has the smallest effect on the converged cost function.

Experience shows the Cramér–Rao bounds and confidence ellipsoids to be highly reliable metrics, and usually the alternate paths end at the same final reduced model structure. Finally, the judgment of which parameter to drop next can also be influenced by physical insights associated with the vehicle configuration. For example, an on-axis derivative might be correlated with one or more off-axis (coupling) derivatives. Generally the off-axis coupling derivatives are dropped first if their Cramér–Rao bounds exceed the guidelines, even if the on-axis derivative has the largest Cramér–Rao bound value.

When a parameter with a high Cramér–Rao bound but acceptable insensitivity is dropped, the cost function will initially jump. But after only a few iterations the reduced model solution will rapidly reconverge to nearly the same original cost function, as the correlated parameters readjust. Care must be taken to ensure that the reduced model is fully reconverged, and then the Cramér–Rao bounds are calculated again. The procedure is repeated until all of the Cramér–Rao bounds are generally in accordance with the guideline. As before, the converged cost function

should be monitored with each step in the model reduction. The model reduction proceeds toward a maximum Cramér–Rao bounds within the target value of Eq. (12.40). The model reduction process is finally terminated if dropping a parameter and reconverging the model results in a jump according to the guidelines of Eqs. (12.52) and (12.53). At this point, this last parameter is retained in the model structure, and the previous converged model constitutes the final identification result. This will usually occur when the largest Cramér–Rao bound is close to the guideline of Eq. (12.40).

As discussed in Sec. 11.3, a tradeoff exists for model complexity versus model variability.<sup>2</sup> Retaining extraneous parameters can incrementally reduce the fitting error, but result in a higher variability, as will be seen in the increased Cramér–Rao bounds. Further, models that are *overparameterized* or *overmodeled* can result in a model with poorer predictive capability.<sup>7</sup> Therefore it is desirable to reduce the model structure using the method presented here. This is also in accordance with the principal of parsimony (Sec. 1.4).

## 12.4 Key Features of the Frequency-Response Method for State-Space Model Identification

There are several key features of the frequency-response method for state-space model identification, as compared to other methods, that are advantageous for flight-vehicle applications. Foremost among the advantages of this method is that the identification cost function  $J$  of Eq. (12.20) is based on pair-wise frequency-response fits. This makes it possible to select individually the fitting range for each pair  $T_l$  to coincide with the range for which those data are reliable (i.e., high coherence). In contrast, output and equation-error identification approaches (both time and frequency domain) fit *all responses over the same frequency range*, regardless of data quality. The measured translational velocity responses are typically most accurate (highest coherence) at lower frequencies (e.g., up to 1 rad/s), where the aircraft phugoid dynamics are dominant and the resulting signal-to-noise ratio is typically highest. The measured angular responses are typically most accurate at mid-frequencies (e.g., 1–10 rad/s), where the short-period responses are most significant. Finally, for rotorcraft the flap and lag measured responses (if available) are typically most accurate from about 6 rad/s to near the rotational frequency of the rotor (1/rev, typically about 27 rad/s), which is the key resonant frequency. When all of the measured responses are included over a common frequency range, reduced accuracy data are included in the cost function, which can compromise the accuracy of the identified state-space model parameters.

Using the pair-wise frequency-response fits in the cost function also provides key information on the proper identification model structure. When a particular pair-wise frequency response is dropped entirely for lack of coherence over the entire frequency range of interest, this indicates a lack of information transfer in this input-to-output pair. As explained in Sec. 12.5.3, associated control and response derivatives are then dropped from the model structure. This permits a considerable simplification in the model structure using a very transparent process. Needed final simplifications in the model structure are easily assessed based on the theoretical accuracy metrics (Sec. 12.3.4).

Another key strength of the frequency-response method is that the frequency responses used in the identification process are unbiased in the presence of uncorrelated process and measurement noise (Sec. 7.7). Therefore the identified state-space parameters will also be unbiased for the presence of uncorrelated process and measurement noise. This is a distinct advantage over output and equation-error methods (time domain or frequency domain). In the case of the former method, the process noise is ignored, whereas in the latter case the measurement noise is ignored. Either case can result in biases in the identified parameters.<sup>10</sup> Alternatively, the noise characteristics can be included in the time-domain solution, leading to the more complex maximum likelihood estimation method.<sup>180</sup> Because the output and/or process noise is uncorrelated with the excitation input, it drops out of the frequency-response calculations in the frequency-response method. This also eliminates the primary cause for the larger scale factors in the ML accuracy metric calculations (Sec. 12.3.1).

The MIMO frequency-response matching procedure for state-space model identification is a direct extension of the lower-order equivalent-system concepts for transfer-function model identification presented in Chapter 11. This makes it straightforward to interpret the MIMO identification results, cost function levels, and mismatch behavior. For example, if the Bode plot comparison corresponding to a primary on-axis response pair shows that the magnitude break of the identified model is misplaced, this is an indication that the value for a key time constant is incorrect. When the magnitude curve is offset by a constant value when compared with the flight data, the source is an incorrect control derivative or inconsistent units. Finally, an error in the high-frequency phase roll off is often caused by the effects of time delays or unmodeled high-frequency dynamics. In the case of output-error identification methods, it can be much more difficult to isolate the modeling errors based on an examination of the output time histories (time domain) or Fourier coefficients (frequency domain). The intuition, insight, and extensive literature associated with SISO transfer-function model identification scales up quite naturally to the more complex MIMO system identification.

As in SISO transfer-function identification, the cost function for the MIMO state-space model identification is formulated in terms of fitting errors in decibels (and phase in degrees). Thus the error reflects a percentage magnitude error and phase shift. By minimizing the average of the individual cost functions, a roughly uniform level of fitting accuracy is generally achieved, as seen in the various frequency-response plots. The resulting model prediction, when viewed in the time domain, demonstrates a balance of percentage errors among the various responses.

The availability of the coherence function  $\gamma_{xy}^2$  provides another key advantage to the frequency-response method for state-space model identification. The frequency-response errors are weighted according to the associated coherence value of the flight-data response  $W_\gamma$  [Eq. (12.20)]. This identification scheme returns stability and control derivative values that cause the model to best track the accurate data at the expense of the less reliable data. The coherence weighting is also an important aspect of the Hessian matrix that is the basis for the accuracy metric calculations of Eq. (12.35). When the coherence drops for a particular frequency response, or over a limited frequency range, the weighting  $W$  for the associated data is reduced, and the model parameters that are key to this response also

show an increased insensitivity and Cramér–Rao bound. In other words, as the data quality drops, the calculated reliability of the relevant parameters for this frequency range is also reduced, as would be expected. The result is that the accuracy metrics, as calculated using the frequency-response method, closely reflect the compatibility of the frequency-response database and the selected model structure. Thus the accuracy metrics, as obtained from the frequency-response method, provide reliable tools for an integrated method of model structure determination even when the data are noisy, as is often the case in flight-test applications, especially for rotorcraft.

In the case of output-error identification methods, the relative fitting errors are weighted by the inverse of the prediction-error covariance, also known as the innovations covariance matrix.<sup>180</sup> Because the innovations covariance matrix is itself determined from the errors between the flight-data time histories and the response of the identified model, the model parameters can be skewed to minimize errors even for unreliable data. Errors in the model structure result in colored noise in the innovations, so that the accuracy metrics might not be reliable tools for model structure determination.

Clearly, however, the realization of the advantages of the frequency-response method as discussed herein depends heavily on the availability of a MIMO frequency-response database with the highest possible quality. The methods and guidelines of Chapters 5–10 are essential to this aim.

## 12.5 State-Space Model Structure

The proper definition and refinement of the model structure is a critical aspect in obtaining a satisfactory result from state-space model identification. This applies whether the identification is carried out in the time domain or the frequency domain. As has been emphasized throughout this book, the model structure must be both appropriate to the *frequency range of interest* and appropriate to the information content of the test data. A model structure that excludes dynamic modes within the frequency range of the test data will produce significant variability and bias errors in the remaining identified parameters, as seen clearly in the application to rotorcraft (Sec. 11.7.2 and Tischler<sup>18</sup>). Conversely, extraneous degrees of freedom and/or identification parameters can result in an improved fit (i.e., lower cost function), but can actually degrade the predictive capability of the model and degrade the predictive quality of the basic (fundamental) parameters.<sup>170</sup>

Model structure selection for transfer-function models of single-input/single-output systems, as discussed at length in Sec. 11.4, is fairly simple owing to the transparent relationship between the pole-zero description and the associated frequency response. The state-space equivalents of the SISO transfer functions are the various SISO *canonical model structures* (e.g., Sec. 12.5.1), which retain the same transparency seen in the various applications in Chapter 11. Transfer-function model structure selection becomes more complex in the case of two-input/two-output LOES models, where physical consistency requires that the denominators of the transfer-functions (i.e., natural modes of response) be the same (Sec. 11.6.2). The parameters to be identified are the transfer-function gains, zeros, and (common) poles. The analogous LOES state-space model structure is

more easily formulated from the classical longitudinal or lateral/directional equations-of-motion (as in Hodgkinson<sup>59</sup>). Then, the unknown parameters are the equivalent values of the stability and control derivatives (e.g.,  $M_w$ ,  $M_q$ ,  $M_{\delta_e}$ , etc.). The resulting transfer functions will all “automatically” have a common denominator, from the common characteristic equation and thus be physically consistent.

In the most complex applications of system identification, model structure selection for the complete MIMO flight vehicle response is based directly on the higher-order dynamics equations of motion. Although many of the same considerations discussed in Chapter 11 for transfer-function identification still apply, the model selection and reduction process can be significantly more complex (and crucial). As discussed by Hamel,<sup>10</sup> these *physical model structures* involve consideration of many important aspects, such as the degree of interaxis coupling, the number of states and measurements to be included, the identifiability of the parameters as a function of the available measurements, what parameters are known and should be fixed (e.g., gearing, gravity, filter dynamics), and the physical constraints between the parameters (e.g., common actuator, aerodynamic symmetry, geometry). Many on- and off-axis frequency responses are matched simultaneously (typically up to 36 for a flight mechanics model of a helicopter), and there are potentially a large number of unknown and multiply correlated identification parameters.

As can be seen, there is a wide range of possible model structures. Choosing the appropriate model starts, as always, with the intended application, the associated frequency range of interest, and an assessment of the key physics to be represented. The converged identification cost function, accuracy analysis metrics, and time-domain verification cost function (Chapter 14) are all important for evaluating the many possible tradeoffs in model structure selection. The following sections present an introduction to canonical and physical state-space model structures.

### 12.5.1 Canonical Model Structure

Canonical models, as the state-space equivalents of transfer-function models, are minimal realizations that contain exactly enough parameters to fully represent the input-to-output process. The various canonical forms all contain the same number of model parameters as the transfer-function model [i.e., Eq. (11.1) for the SISO system]. If the model structure contained any fewer parameters, the identified model response could not be made to track the test data. Including additional parameters in the model would result in an overparameterized structure, and the identified parameter values would not be reliable.

As in the case of the transfer-function model structure, the parameters of a canonical model are complex combinations of the physical parameters, such as the stability and control derivatives. Therefore it can be difficult to assign a physical meaning to the individual canonical parameters. Many possible canonical structures will produce the same input-output response, that is, they produce the same transfer-function matrix  $T(s)$ . Common examples of canonical forms include the observable-canonical form, the controllable-canonical form, and the block-diagonal form, among others.<sup>159</sup>

The transfer-function description for a SISO system,

$$T(s) = \frac{y(s)}{u} = \frac{(b_1 s^{n-1} + b_2 s^{n-2} + \dots + b_n) e^{-\tau_{eq}s}}{s^n + a_1 s^{n-1} + \dots + a_n} \quad (12.54)$$

is easily represented in the state-space form of Eqs. (12.2) and (12.3) using the observable-canonical realization:

$$\begin{bmatrix} \dot{x}_1 \\ \dot{x}_2 \\ \dot{x}_3 \\ \dot{x}_4 \\ \vdots \\ \vdots \\ \dot{x}_n \end{bmatrix} = \begin{bmatrix} 0 & 0 & 0 & 0 & -a_n \\ 1 & 0 & 0 & 0 & -a_{n-1} \\ 0 & 1 & 0 & 0 & -a_{n-2} \\ 0 & 0 & 1 & 0 & -a_{n-3} \\ \vdots & \vdots & \vdots & \ddots & \vdots \\ \vdots & \vdots & \vdots & \vdots & \vdots \\ 0 & 0 & 0 & 1 & -a_1 \end{bmatrix} \begin{bmatrix} x_1 \\ x_2 \\ x_3 \\ x_4 \\ \vdots \\ \vdots \\ x_n \end{bmatrix} + \begin{bmatrix} b_n \\ b_{n-1} \\ b_{n-2} \\ b_{n-3} \\ \vdots \\ \vdots \\ b_1 \end{bmatrix} \mathbf{u} \quad (12.55)$$

where  $\mathbf{u} = [u]$  and

$$y = \begin{bmatrix} 0 & 0 & 0 & \dots & 0 & 1 \end{bmatrix} \begin{bmatrix} x_1 \\ x_2 \\ x_3 \\ x_4 \\ \vdots \\ \vdots \\ x_n \end{bmatrix} = x_n \quad (12.56)$$

In this case,  $\mathbf{M} = \mathbf{I}_{n \times n}$ ,  $\mathbf{H}_1 = \mathbf{0}$ , and the matrix of time delays Eq. (12.13) reduces to a scalar:

$$\tau(s) = \left[ e^{-\tau_{eq}s} \right] \quad (12.57)$$

The number of states  $n$  in the SISO canonical form is seen to be the same as the order of the transfer function, and the coefficients in the numerator and denominator of the transfer function are columns in the state-space matrices. The physical system output  $y$  is associated with the state  $x_n$ . The other states are internal canonical state variables and have no transparent physical relationship to the aircraft motion degrees of freedom.

Because the parameters in the canonical model structure are the same as those of the transfer-function model structure, it might seem pointless to go to the extra work of setting up the problem in state-space form, when the much simpler transfer-function identification method of Chapter 11 would have produced essentially the same result. But there are several important advantages to using the methods herein, even for SISO transfer-function model identification. The theoretical accuracy metrics will expose the presence of nearly cancelling pole-zero pairs in the transfer-function model structure and provide the accuracy bounds on the final model parameters. The state-space representation also allows naturally for simultaneous matching of two-input/two-output lower-order equivalent system (LOES) handling-qualities models with common denominators (Sec. 11.6.2). This technique was demonstrated in Eqs. (11.30) and (11.31). Finally, casting the transfer function in state-space form allows the direct time-domain simulation of the model for verification against the flight-data response (Chapter 14).

### 12.5.2 Physical Model Structures

A physical model structure for flight-vehicle dynamics relates the vehicle response variables to control inputs as derived from the dynamics equations of motion and linearized for small motions about the reference trim condition. The state variables are now the physical motion perturbations of the aircraft, and they typically include the angular rates, linear velocities, and attitudes, rather than the canonical states of the earlier canonical model structure [Eq. (12.55)]. As summarized in Tables 1.1 and 1.2, model structures used in state-space system identification vary considerably in complexity, depending on the assumed level of interaxis coupling and the required modeling detail.

System identification of conventional fixed-wing aircraft generally assumes that the longitudinal and lateral/directional rigid-body dynamics are decoupled. This assumption leads to a three-DOF decoupled stability and control model structure (Table 1.1) that is equivalent to the fourth-order LOES transfer-function models, such as in Eq. (11.26). The stability and control derivative models, discussed in most classical flight-mechanics textbooks (e.g., Ref. 56) and commonly used in aircraft vehicle identification, are obtained when the forces and moments are expanded in a Taylor series of the state variables and controls. The equations of motion are generally written in axes aligned either with the fuselage centerline (*body axes*) or aligned with the trim airspeed vector (*stability axes*). For example, the longitudinal acceleration equation is written in body axes as

$$\dot{u} = -W_0 q - (g \cos \Theta_0) \theta + X_u u + X_w w + X_q q + X_{\delta_e} \delta_e \quad (12.58)$$

to form the basis for the states equation (12.2). The terms in these equations include reference velocities and pitch attitude [subscript  $(\cdot)_0$ ], the stability derivatives (e.g.,  $X_u$ ), the control derivatives (e.g.,  $X_{\delta_e}$ ), and the gravity term  $[-(g \cos \Theta_0) \theta]$ . The unknown parameters to be identified are the stability and control derivatives.

The output equation (12.3) defines the measurements in terms of the state and state rates. For example, the longitudinal acceleration equation is obtained from Eq. (6.33) for symmetric flight conditions ( $V_0 = 0$ ) as

$$a_{x_{cg}} = \dot{u} + W_0 q + (g \cos \Theta_0) \theta \quad (12.59)$$

A single time delay is included for each of the control inputs to account for mechanical linkage and other higher-order dynamics. In the current example, the matrix of time delays [Eq. (12.13)] reduces to two column vectors associated with the elevator and throttle control, respectively.

For helicopters with low flap stiffness, the rotor dynamics can be satisfactorily modeled as quasi-steady (Sec. 11.7), resulting in a six-DOF identification model structure<sup>10</sup> as indicated in Table 1.2. The accurate modeling of the vertical response to collective inputs might require the inclusion of an additional state to account for dynamic inflow, as demonstrated in the seven-DOF model identification of the AH-64 helicopter by Schroeder et al.<sup>182</sup> For helicopters with high flap stiffness, the rotor-body coupling becomes increasingly significant, as seen in Fig. 11.9, and the model structure must be extended. An appropriate model in this case includes the dynamics states for rotor flapping and lead-lag dynamics, vertical inflow, and engine torque. The resulting (13-DOF) *hybrid model structure*<sup>139</sup> is valid for a wide range of helicopter configurations and flight conditions (see Table 1.2). Finally, in the most complex case the model structure can be formulated in terms of the constituent element springs, masses, and dampers, with constraint equations to enforce commonality and kinematic interrelationships, such as the work completed by Tischler<sup>92</sup> for the identification of rotor dynamics from a wind-tunnel test.

### 12.5.3 Additional Aspects of Model Structure Definition

As in the case of transfer-function modeling (Chapter 11), there are a number of additional aspects that define the state-space model structure.

An important aspect is to decide which response pairs should be included in the cost function [Eq. (12.20)]. Generally speaking, the accuracy of the identified parameters will be improved as more frequency responses (with acceptable coherence) are included in the identification (larger  $n_{TF}$ ). This results from the increased information content, thereby allowing a separation of otherwise correlated parameters and an improvement in the identification parameter accuracy metrics (i.e., reduced Cramér–Rao bounds). However, including additional frequency responses with poor coherence functions generally degrades the identification results.

The selected frequency range of the identification must be consistent with the frequency range of acceptable coherence and the frequency of applicability of the model structure. So, for example, a three-DOF model for fixed-wing aircraft identification cannot capture the structural mode that might be apparent at higher frequencies. In rotorcraft applications, a quasi-steady model is invalid for frequencies near and beyond the regressive flapping mode (typically about 14 rad/s). If the frequency range of identification is not consistent with the model structure, the identification algorithm can result in a good match of the responses, but the identified parameters might lack physical meaning.

Another aspect of the model structure is the designation of which parameters should be fixed at known values, with the remaining parameters free to be determined in the course of the identification. Some physical parameters, such as gravity, are known a priori and should be fixed. Other parameters might have been identified from input-output ground tests, such as gearing and filter parameters. It is

always desirable to pare down the number of unknown parameters as much as possible to simplify the MIMO identification problem statement.

A final aspect concerns the definition of known physical constraints among the parameters. For example, if the same basic actuator is used for all of the control axes, then the actuator time constants should be constrained to have the same value (a single identification parameter). There might also be aerodynamic symmetry, such as pitch and roll dynamics that use some of the same aerodynamic parameters (e.g., the same lift-curve slope or rotor time constant). If a force producer is at the end of a moment arm, the moment and force equations can contain the single force control derivative with the appropriate geometric constraint. The introduction of constraints in the model structure that correspond to known physical constraints will reduce the level of correlation among the identification parameters and improve the parameter reliability.

## 12.6 State-Space Model Identification in CIFER® Using DERIVID

Multi-input/multi-output state-space model identification, using the frequency-response method, is accomplished in CIFER® with the DERIVID (from derivative identification) module. Model structure setup is facilitated with the generic problem definition of Eqs. (12.2) and (12.3) and a highly flexible user interface. A wide range of physical systems or subsystems that can be described by linear-time-invariant (LTI) differential equations with an arbitrary set of constraints among the parameters can be modeled with DERIVID. The parameters can be given fixed values, allowed to vary freely in the course of the identification, or be linearly constrained to free parameters. The model structure can accommodate up to 40 states and 100 unknown parameters. Some components of the air-vehicle system, such as actuators, sensors, and filters, can be more easily modeled using a MIMO transfer-function structure in DERIVID. The simultaneous identification of transfer-function model structures with a common denominator, as in Eqs. (11.30) and (11.31) of the previous chapter, was easily formulated using DERIVID. The SISO transfer-function definition in DERIVID replicates the capability of NAVFIT (Sec. 11.4) but also includes the accuracy analysis to determine the reliability of the identification result.

The integration of model identification, theoretical accuracy analysis, and model structure reduction (Sec. 12.3.4) in a systematic and reliable procedure is a key aspect of DERIVID. The program uses an iterative, robust secant search algorithm to determine the identification parameter vector  $\Theta$  that minimizes the errors between the state-space model and the frequency-response database. A large number ( $n_{TF} = 80$ ) of frequency-response pairs can be included in the cost function. The Cramér–Rao bounds and insensitivity levels are determined from the method of numerical gradients (Sec. 12.3.1), and the values are checked against the suggested guideline of Eqs. (12.40) and (12.45). When the Cramér–Rao bound guidelines are exceeded, the corresponding confidence ellipsoids are presented to help expose sources of correlation. The model structure is easily adjusted, based on the theoretical accuracy results, and the model is reconverged. This process is repeated until a highly reliable model structure is found. Detailed listings and plots of the completed results are provided. Additional insight into

the dynamic characteristics is achieved via reference to the eigenvalues, eigenvectors, and time vectors<sup>56</sup> that are also presented for output.

Finally, DERIVID is supported by an extensive set of CIFER® utilities. These utilities are useful for examining the results, creating plots or tables of the results in rough or report-quality form, comparing the results of different runs, and organizing the results in the CIFER® database.

## 12.7 Pendulum Example

The identification of the stable pendulum dynamics is accomplished using the state-space model structure in this example. The identification results are then compared with those obtained using the transfer-function model structure (Sec. 11.5).

The analytical transfer-function model of Eq. (3.5) is rewritten in the form of Eq. (12.54):

$$\frac{\theta}{M_{\text{ext}}} = \frac{1}{s^2 + \bar{C}s + (\bar{K} - g/l)} = \frac{b_1s + b_2}{s^2 + a_1s + a_2} \quad (12.60)$$

so that  $n = 2$ ,  $a_1 = \bar{C}$ ,  $a_2 = \bar{K} - g/l$ ,  $b_1 = 0$ ,  $b_2 = 1$ , and  $\tau = 0$ . This transfer-function model is realized in observable-canonical form using Eqs. (12.55–12.57):

$$\mathbf{x} = \begin{bmatrix} x_1 \\ x_2 \end{bmatrix} \quad (12.61)$$

$$\mathbf{y} = x_2 = \theta \quad (12.62)$$

$$\mathbf{u} = \begin{bmatrix} M_{\text{ext}} \end{bmatrix} \quad (12.63)$$

$$\mathbf{M} = \mathbf{I}_{2 \times 2} \equiv \text{two by two identity matrix} \quad (12.64)$$

$$\mathbf{F} = \begin{bmatrix} 0 & -a_2 \\ 1 & -a_1 \end{bmatrix} \quad (12.65)$$

$$\mathbf{G} = \begin{bmatrix} b_2 \\ 0 \end{bmatrix} \quad (12.66)$$

$$\mathbf{H}_0 = \begin{bmatrix} 0 & 1 \end{bmatrix} \quad (12.67)$$

$$\mathbf{H}_1 = \begin{bmatrix} 0 & 0 \end{bmatrix} \quad (12.68)$$

$$\boldsymbol{\tau}(s) = \begin{bmatrix} 1 \end{bmatrix} \quad (12.69)$$

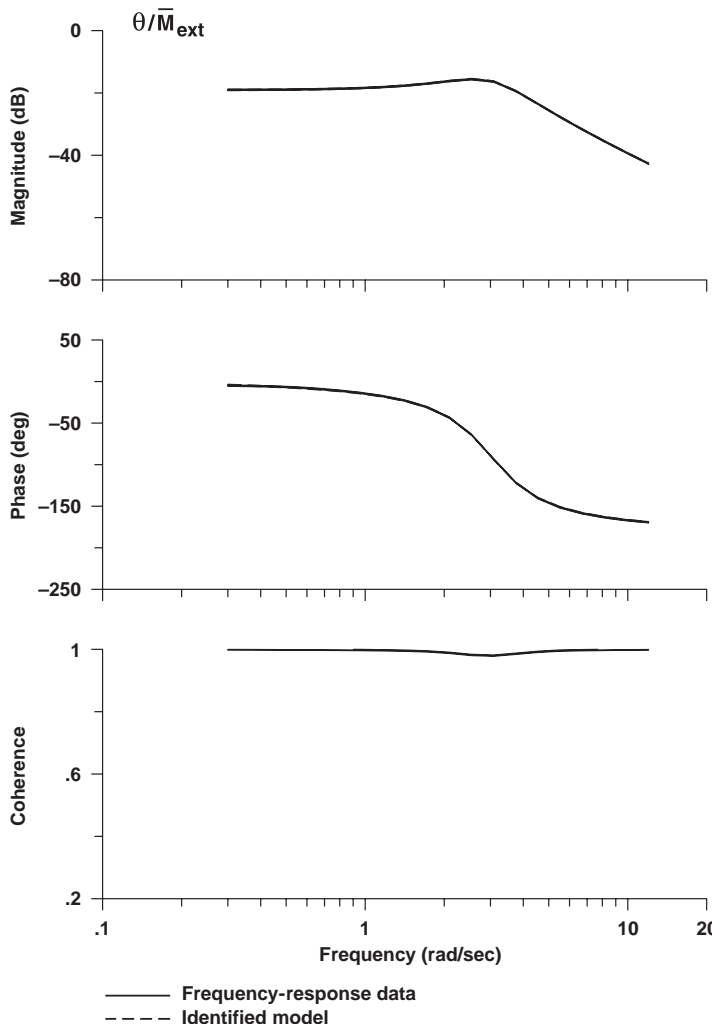


Fig. 12.1 Frequency-response results for stable pendulum identification.

The state-space identification results are shown in Fig. 12.1, as obtained using DERIVID for a fitting range of 0.3–12 rad/s, the same range that was used in the transfer-function identification (Sec. 11.5). The frequency response of the identified model is indistinguishable from the frequency-response data. This is also reflected in a very low value of the identification cost function ( $J_{ave} = 0.053$ ), matching the transfer-function identification result as expected (Sec. 11.5).

The parameter values and associated eigenvalues are listed in Tables 12.3 and 12.4. These results match the transfer-function identification result [Eq. (11.15) and again agree to within 1% of the analytical result Eq. (3.7)].

**Table 12.3 Identification results for stable pendulum example<sup>a</sup>**

Parameter	Parameter value	Cramér–Rao, %	Insensitivity, %
$-a_2$	-9.081	4.88	1.94
$-a_1$	-2.129	9.89	4.02
$b_1$	1.006	5.34	1.83

<sup>a</sup>  $\theta/\bar{M}_{\text{ext}}$  transfer-function cost is  $J_{\text{ave}} = 0.053$ .

**Table 12.4 Eigenvalues for identified stable pendulum model**

	$\zeta$	$\omega_n$
$\lambda_1$	0.353	3.013
$\lambda_2$	0.353	3.013

The theoretical accuracy metrics for the identified parameters are also listed in Table 12.3. The insensitivities and Cramér–Rao bounds are within the guideline values, thus indicating that the model structure is appropriate. Note also that the condition of Eq. (12.44) is met. Based on the Cramér–Rao bounds provided by CIFER® [Eq. (12.38)], the identified parameters are reliable to an expected standard deviation of 10%. The good reliability (low expected standard deviation) reflects the perfect model structure (matches the analytical form) and high coherence of the simulation data.

## 12.8 Identification of a XV-15 Closed-Loop State-Space Model

This example demonstrates the identification of a canonical state-space model to characterize the short-term closed-loop response  $p/\delta_{\text{lat}}$  of the XV-15 in hover. An initial choice of model structure can be selected by considering the transfer-function form that is appropriate for the flight data of Fig. 10.7. In this case, we start out by assuming a first-order over second-order characteristic, which provides a single excess pole, consistent with the -90-deg phase shift near 10 rad/s. The transfer-function form

$$\frac{p}{\delta_{\text{lat}}} = \frac{(b_1 s + b_2) e^{-\tau s}}{s^2 + a_1 s + a_2} \quad (12.70)$$

is realized in an observable canonical model structure using Eqs. (12.55–12.57).

Figure 12.2 shows a good fit between the identified model (CLROLL1) and the flight-data frequency response over the selected fitting range (0.6–10 rad/s), as reflected by the very low cost function ( $J_{\text{ave}} = 5.3$ ).

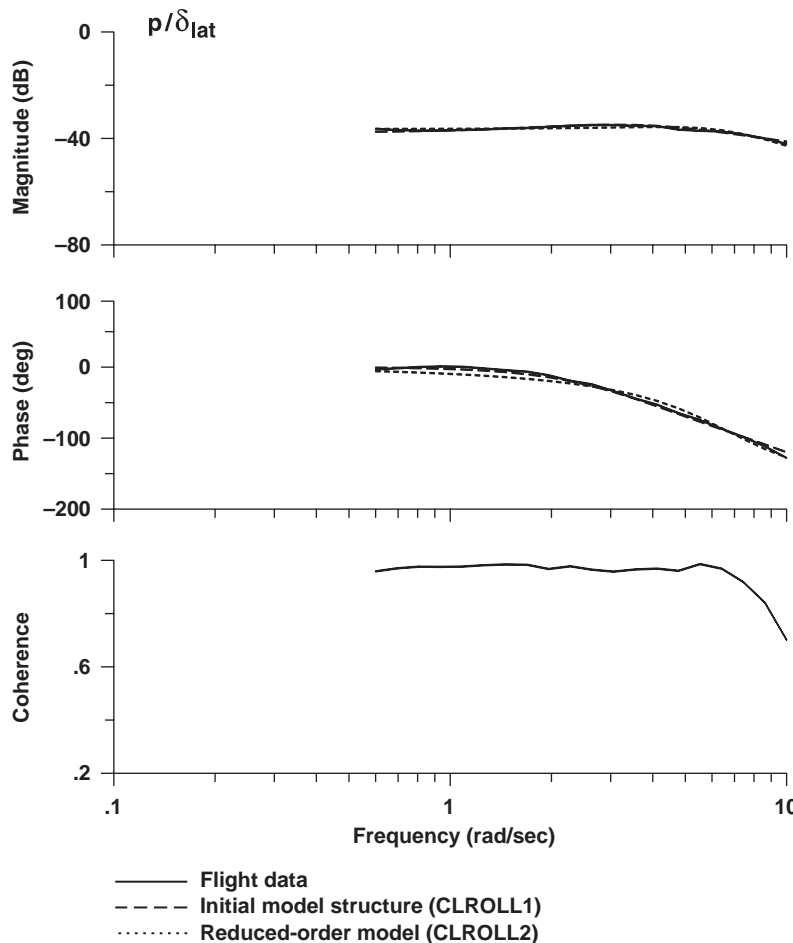


Fig. 12.2 Closed-loop roll-response identification (XV-15, hover).

The identified parameter values and accuracy metrics are shown in Table 12.5. The insensitivities are all well below the 10% threshold. However, the Cramér-Rao bounds for the  $-a_2$  and  $b_2$  parameters are well above the 20% threshold, indicating some parameter correlation. This is confirmed by reference to the confidence ellipsoids shown in Table 12.6, which shows that these parameters are highly correlated, with less contribution from the remaining parameters. The problem can be seen as correlation (i.e., tradeoff) between the real zero and complex pole locations in the transfer function of Eq. (12.70), which suggests that a reduced-order model structure is warranted.

The identification model structure is reduced to the form

$$\frac{p}{\delta_{\text{lat}}} = \frac{b_2}{s^2 + a_1 s + a_2} \quad (12.71)$$

**Table 12.5** Closed-loop roll identification results for initial model structure (XV-15, hover)<sup>a,b,c</sup>

Parameter	Parameter value	Cramér–Rao, %	Insensitivity, %
$-a_2$	-13.72	30.51	2.52
$-a_1$	-5.645	14.83	2.73
$b_2$	0.1765	36.45	2.92
$b_1$	0.08792	16.87	2.63
$\tau$	0.0903	20.78	5.72

<sup>a</sup>Case name: CLROLL1; Case ID: initial model structure [Eq. (12.70)].

<sup>b</sup>All results in English units and control deflections in %.

<sup>c</sup> $p/\delta_{\text{lat}}$  transfer-function cost is  $J_{\text{ave}} = 5.3$ .

**Table 12.6** Confidence ellipsoids for closed-loop response identification (XV-15, hover)

Parameter	$-a_2$	$-b_2$	$\tau$
$-a_2$	-0.987	-0.9560	0.7648
$-a_1$	0.0169	0.0169	-0.7476
$b_2$	1.000	1.000	-0.8871
$b_1$	-0.2434	-0.2432	1.000
$\tau$	-0.0964	-0.1068	0.7036

**Table 12.7** Closed-loop roll identification results for reduced model structure (XV-15, hover)<sup>a,b,c</sup>

Parameter	Parameter value	Cramér–Rao, %	Insensitivity, %
$-a_2$	-44.46	8.66	1.97
$-a_1$	-7.297	12.51	3.35
$b_2$	0.6687	10.38	1.88

<sup>a</sup>Case name: CLROLL2; Case ID: reduced model structure [Eq. (12.71)].

<sup>b</sup>All results in English units and control deflections in %.

<sup>c</sup> $p/\delta_{\text{lat}}$  transfer-function cost is  $J_{\text{ave}} = 21.2$ .

and the canonical model identification is repeated (CLROLL2). The frequency response of the reduced model still tracks the test data, as seen in Fig. 12.2, though not quite as well as the original model structure. The identification cost function for this reduced model structure has increased as expected, but is still acceptable ( $J_{\text{ave}} = 21.2$ ). The identified parameter values, accuracy metrics, and eigenvalues are shown in Tables 12.7 and 12.8. Now the accuracy metrics are

**Table 12.8 Eigenvalues of final closed-loop model identification (XV-15, hover)**

	$\zeta$	$\omega_n$
$\lambda_1$	0.547	6.668
$\lambda_2$	0.547	6.668

well within the guidelines, indicating that a proper model structure has been achieved.

## 12.9 Structural System Identification

The next example presents identification results for the NASA vertical/short takeoff and landing (V/STOL) system research aircraft (VSRA), shown in Fig. 12.3. This was essentially a YAV-8B Harrier aircraft equipped with a fly-by-wire research flight-control system and integrated displays.<sup>183</sup> System identification flight testing using automated frequency sweeps of the ailerons was conducted at a flight condition of 120 kn. The objective of the identification effort was to determine state-space models of the structural responses in support of control system design and stability-margin verification. The measurement of interest in this case was the roll acceleration  $p$ , as measured by an angular accelerometer. The resulting flight-data response  $p/\delta_a$ , shown in the solid line of Fig. 12.4, exhibits high coherence for the frequency range of excitation, 16.5–32 Hz. (The frequency response is plotted in  $\text{dB} = 20 \log(\text{deg/s}^2/\text{aileron})$ , and the units of aileron deflection are instrumentation counts in this case.) The frequency response clearly exposes the first and second bending modes.

A suitable model for the roll-rate response is based on the partial fraction summation of the one-DOF rigid-body roll model and the first two antisymmetric



Fig. 12.3 NASA V/STOL system research aircraft (VSRA) (NASA photo).

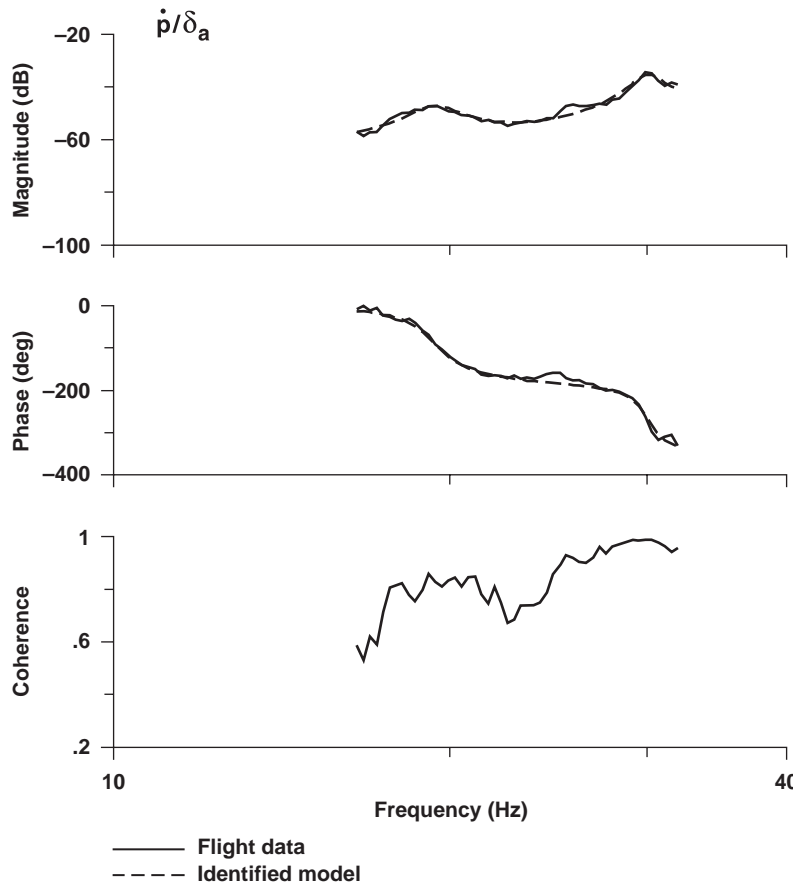


Fig. 12.4 Aeroelastic response identification (VSRA, 120 kn).

structural bending modes<sup>184</sup>:

$$\frac{p}{\delta_a} = \frac{L_{\delta_a}}{(s - L_p)} + \frac{K_1 s}{[s^2 + 2\zeta_1 \omega_{n_1} s + \omega_{n_1}^2]} + \frac{K_2 s}{[s^2 + 2\zeta_2 \omega_{n_2} s + \omega_{n_2}^2]} + \dots \quad (12.72)$$

The first term on the right-hand side is the rigid-body roll response [same form as Eq. (11.22)], followed by the first antisymmetric structural bending mode and the second antisymmetric structural bending mode.

The identification model structure of Eq. (12.72) is conveniently realized in block-diagonal form, with observer-canonical subblocks [Eq. (12.55)]:

$$\mathbf{F} = \begin{bmatrix} L_p & 0 & 0 \\ 0 & \begin{bmatrix} 0 & -\omega_{n_1}^2 \\ 1 & -2\zeta_1\omega_{n_1} \end{bmatrix} & 0 \\ 0 & 0 & \begin{bmatrix} 0 & -\omega_{n_2}^2 \\ 1 & -2\zeta_2\omega_{n_2} \end{bmatrix} \end{bmatrix} \quad (12.73)$$

$$\mathbf{G} = \begin{bmatrix} L_{\delta_a} \\ \begin{bmatrix} 0 \\ K_1 \end{bmatrix} \\ \begin{bmatrix} 0 \\ K_2 \end{bmatrix} \end{bmatrix} \quad (12.74)$$

$$\mathbf{M} = \mathbf{I}_{5 \times 5} \quad (12.75)$$

The equation for the roll acceleration measurement is then

$$y = \dot{p} \quad (12.76)$$

so that

$$\mathbf{H}_0 = \begin{bmatrix} 0 & \begin{bmatrix} 0 & 0 \end{bmatrix} & \begin{bmatrix} 0 & 0 \end{bmatrix} \end{bmatrix} \quad (12.77)$$

$$\mathbf{H}_1 = \begin{bmatrix} 1 & \begin{bmatrix} 0 & 1 \end{bmatrix} & \begin{bmatrix} 0 & 1 \end{bmatrix} \end{bmatrix} \quad (12.78)$$

The identified model shown in the dashed line of Fig. 12.4 matches the frequency-response flight data quite well ( $J_{ave} = 53.3$ ). The model parameters and accuracy metrics are listed in Table 12.9 (aileron deflection now in deg). The rigid-body roll-rate damping parameter  $L_p$  was fixed at the known a priori values, and it does not have any significant effect on the measured response in the frequency range of test excitation (16–32 Hz). All parameter accuracy metrics are within the guidelines, thereby confirming that the model structure is appropriate and that the results are reliable.

**Table 12.9 Aeroelastic response identification (VSRA, 120 kn)<sup>a</sup>**

Parameter	Parameter value	Cramér-Rao, %	Insensitivity, %
$L_{\delta_a}$	6.570	21.0	7.65
$L_p$	-1.000 <sup>b</sup>	—	—
$K_1$	-3.546	8.80	3.14
$-\omega_{n_1}^2$	-1.485E+04	1.08	0.53
$-2\zeta_1\omega_{n_1}$	-11.94	14.07	5.16
$K_2$	8.995	9.03	2.71
$-\omega_{n_2}^2$	-3.579E+04	0.76	0.36
$-2\zeta_2\omega_{n_2}$	-11.82	14.58	5.63

<sup>a</sup>  $\dot{p}/\delta_a$  transfer-function cost is  $J_{ave} = 53.3$ ,  $\dot{p}/\delta_a$  units are deg/sec<sup>2</sup>/deg-ail.

<sup>b</sup> fixed parameter in the identification.

From the parameter values of Table 12.9, the eigenvalues corresponding to the first antisymmetric structural mode are calculated as

$$[\zeta_1 = 0.049; \omega_{n_1} = 19.4 \text{ Hz}] \quad (12.79)$$

The eigenvalues corresponding to the second antisymmetric structural mode are calculated as

$$[\zeta_2 = 0.031; \omega_{n_2} = 30.1 \text{ Hz}] \quad (12.80)$$

Referring to Eq. (12.72) and the results of Table 12.9, the residues show the following characteristics:

$$K_1 < 0 \quad (12.81)$$

$$K_2 > 0 \quad (12.82)$$

which indicates that roll-rate feedback to the aileron surfaces (roll control) will *destabilize* the first structural mode and *stabilize* the second structural mode.<sup>184</sup>

The combined roll-rate transfer function from Eq. (12.72) is

$$\frac{p}{\delta_a} = \frac{12.019[-0.257, 130.76][0.330, 130.35]}{(1)[0.0490, 121.86][0.0312, 189.18]} \text{ deg/s}^2/\text{deg-ail} \quad (12.83)$$

The root-locus plot of Fig. 12.5 confirms that roll-rate feedback destabilizes the first structural mode and stabilizes the second structural mode.

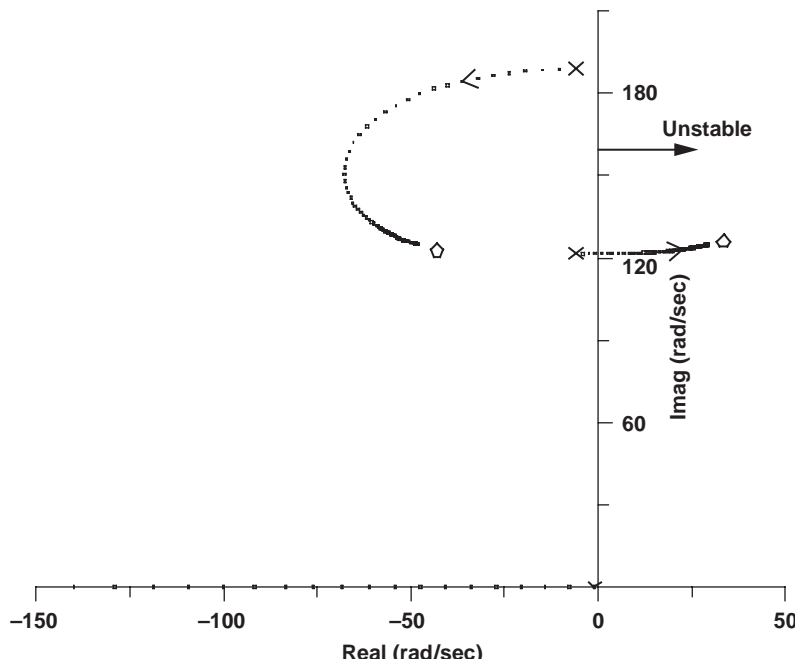


Fig. 12.5 Root locus for roll-rate feedback to aileron (VSRA, 120 kn).

Notch filters were included in the VSRA flight-control system to suppress the coupling of the flight control and aeroelastic dynamics. These notch filters and the control law gains were subsequently updated based on the identification results.

## Problems

### Theoretical accuracy metrics

**12.1** Compare the state-space identification results of Sec. 12.8 with those obtained using transfer-function identification (**Problem 11.5**). You should be able to appreciate the added value of the theoretical accuracy metrics in ascertaining the appropriate model structure.

### Canonical model identification with DERIVID

**12.2** Identify a canonical model of the stable pendulum based on the analytical transfer-function model of Eq. (3.5) using the COMPOSITE frequency-response identified in **Problem 10.2**. Compare the results with the transfer-function identification results of Eq. (11.15).

**12.3** Plot the results of **Problem 12.2** with utility 31. Then create tables of the results with utility 33.

**12.4** Identify a canonical model of the unstable pendulum based on the form of the analytical result of Eq. (3.8) using the COMPOSITE frequency response identified in **Problem 10.1**. Compare your results with the transfer-function identification results of Eq. (11.16).

**12.5** Plot the results of **Problem 12.4** with utility 31, and then create tables of the results with utility 33.

**12.6** Consider the effect of including an extraneous identification parameter in the (1,1) element of the  $F$  matrix of Eq. (12.65) for the second-order unstable pendulum response. Show analytically how this parameter shows up in the transfer-function form of Eq. (12.60). Repeat the identification of the unstable system including this extraneous parameter and examine the effect on the identification cost, parameter values and accuracy metrics. If you started out using this model structure with the extraneous parameter, what procedure would point you to the appropriate reduced model structure?

## 13

## State-Space Model Identification: Physical Model Structures

The previous chapter presented the basic concepts of state-space model identification using the frequency-response method. The example applications were based on canonical model structures, which are state-space equivalents of SISO transfer functions. In this chapter, the concepts and examples focus on the identification of physical model structures for flight-vehicle dynamics. This is the most challenging aspect of system identification, and good results depend heavily on a high-quality MIMO frequency-response database. All of the previous steps of the overall methodology (see Fig. 2.1) must be carefully completed to ensure that the extracted model has reasonable values for the identified parameters and provides good predictive accuracy. Proper collection of flight-test data, kinematic consistency and state reconstruction, advanced FFTs, multi-input conditioning, and multiwindow optimization are all important to achieving the necessary frequency-response database quality. The initial investigation of model structures and key parameter values using SISO transfer-function and canonical identification methods is also very important to establishing the correct physical model structure and initial parameter guesses. Errors in any of these steps will degrade the accuracy and utility of the MIMO physical model—an ultimate product of many system identification studies.

The identification of physical models of flight-vehicle dynamics is discussed extensively in the literature. Iliff<sup>170</sup> is an excellent and succinct reference on the stability and control derivative model structure and identification for fixed-wing applications using time-domain methods. Examples of some recent fixed-wing identification studies include the X-31<sup>35, 82</sup>, and the F-18.<sup>179</sup> An excellent overview of fixed-wing and rotorcraft applications at the DLR is given by Jategaonkar et al.<sup>185</sup> The international effort by AGARD Flight Mechanics Panel Working Group 18 on Rotorcraft System Identification<sup>10</sup> involved comprehensive case studies of three helicopters (Bo-105, SA-330 Puma, and AH-64 Apache) based on quasi-steady (six-DOF) stability and control derivative model structures. This is an excellent reference on model structure considerations and the system identification of helicopter flight dynamics using time- and frequency-domain methods. Higher-order models for helicopters that explicitly include the states of the rotor system and dynamic inflow are discussed by Kaletka and Gimonet<sup>37</sup> and Tischler and Tomashofski.<sup>139</sup> Identification of physical rotor parameters using a model structure based on the complete rotor equations of motion is presented by Fletcher and Tischler<sup>103</sup> and Tischler.<sup>92</sup> A recent compilation of practical identification experience is available in two issues of the *AIAA Journal of Aircraft*.<sup>186, 187</sup>

This chapter relies heavily on the basic state-space model identification concepts introduced in Chapter 12, but now with more emphasis on how the methodology

is applied to MIMO model structures based on the flight-vehicle equations of motion. The topics covered in this chapter include the following: background and general guidelines for physical model structures, equations of motion for flight vehicles, state-space model structure definition, data preparation for system identification, and example applications. The identification of higher-order models of helicopter dynamics is covered in Chapter 15.

### 13.1 Background

Physical model structures are direct implementations of the equations of motion for the flight-vehicle system or subsystem components. These are wide ranging in complexity, depending mostly on the assumed level of coupling and system order. As always in system identification, the choice of model structure depends on the end application of the model, the frequency range of applicability, and the associated key vehicle dynamic characteristics. In the discussion of model structures that follows, the reader should refer back to Tables 1.1 and 1.2.

At the simpler end of the spectrum, the rigid-body flight dynamics of most conventional fixed-wing aircraft, tilt-rotor (e.g., XV-15 and V-22), and tandem rotor (e.g., CH-47) configurations are well represented by the decoupled classical three-DOF longitudinal and three-DOF lateral-directional dynamics equations. The unknown coefficients to be identified in the model structure are the conventional stability and control derivatives, which result from a Taylor-series representation of the aircraft aerodynamics. Model structures for fixed-wing aircraft configurations are widely available in the flight-dynamics literature. They can be expressed in either dimensional form (e.g.,  $X_u, X_w, M_u, M_w, M_q, M_\delta$ ), as by McRuer, et al.<sup>56</sup> and McLean,<sup>81</sup> or in nondimensional form ( $C_{X_u}, C_{X_w}, C_{M_u}, C_{M_w}, C_{M_q}, C_{M_\delta}$ ) as by Blakelock.<sup>146</sup> (The dimensional form is in more common use now because it provides greater insight into the key dynamic characteristics.) These three-DOF model structures involve relatively few identification parameters (fewer than 20) and are generally identified to good accuracy if the recommended guidelines for flight testing and frequency-response database identification are followed. Problems with parameter insensitivity and correlation are generally not very significant. The identified stability and control derivatives are the desired product for many key applications, such as wind-tunnel vs flight comparison, math model validation, and, especially, MIMO flight-control design.

Conventional stability and control model structures can be extended to include the dynamics of airframe flexibility. An example of this is the VSRA model of Eq. (12.72), which appends two antisymmetric bending modes to the one-DOF roll response. Generalized structural dynamics models can become considerably more complex, as presented by McLean<sup>81</sup> and Blakelock.<sup>146</sup> The accurate identification of models that include higher numbers of structural modes will require more extensive structural instrumentation, such as a distributed array of strain gauges and automated frequency-sweep inputs for excitation over a wide range of frequencies.

In single-rotor helicopter configurations, the decoupled three-DOF assumption is not suitable, and the rigid-body dynamics of the fuselage must be considered fully coupled. For helicopters with a low value of flap stiffness, the assumption of

a quasi-steady rotor response is adequate (Sec. 11.7). The resulting six-DOF model structure is composed of the body-axis stability and control derivatives, with equivalent time delays included to represent the rotor system transient response. Now the unknown parameters to be determined simultaneously will number up to 64 in total, thus constituting a significantly more difficult identification problem than in the fixed-wing case. Information content for rotorcraft flight-test data is generally best for the on-axis midfrequency responses (i.e., the dominant short-term response modes), and it degrades for the coupling responses and at lower frequencies. This often results in increased parameter insensitivity and correlation, making model structure selection and reduction much more central to the identification process. Here the theoretical parameter accuracy analysis of Sec. 12.3 is the key tool.

The quasi-steady rotor-response assumption is invalid for rotorcraft with high values of flap stiffness, as demonstrated in Fig. 11.13 for the OH-58D helicopter. In this case, the rotor and fuselage dynamics are tightly coupled, and the hybrid model structure of Chapter 15 is well suited. This higher-order model structure combines a quasi-steady (stability and control derivative) model structure, accurate for lower-frequency motion, with an explicit representation of the coupled fuselage/rotor coupling to accurately model the responses at mid- and higher frequencies (beyond 1 rad/s). The rotor equations include the key degrees of freedom of flap, lead-lag, and dynamic inflow. Formulation of these hybrid models requires a good grasp of the fundamentals of rotorcraft flight mechanics. The identification model setup is also more complex, owing to the additional degrees of freedom and constraints among the identification parameters. However, the completed model structure includes about the same number of identification parameters as the six-DOF model, with no additional difficulty in model convergence or model structure reduction.

The stability and control derivatives are actually complex combinations of the aircraft geometric parameters (e.g., wing span, wing chord, tail volume), aerodynamic parameters (e.g., lift-curve slope and control surface effectiveness), and inertial parameters (mass and moments of inertia). So the model structure could also be implemented in a physics-based formulation in terms of the many fewer and more basic physical quantities, but it would require the implementation of many constraints. For example, a common value of lift-curve slope or tail length could be used in the various places and combinations that these parameters appear throughout the dynamic equations of motion. The formulation and setup of physics-based model structures can be a much more formidable task than what is involved for the stability and control models just mentioned, but the identification results can provide the fundamental parameters needed to update detailed simulation models. An example of this approach was the identification study of the Sikorsky Bearingless Main Rotor (SBMR), using frequency-sweep data obtained from full-scale rotor tests in the NASA 40  $\times$  80 ft wind tunnel.<sup>92</sup> This comprehensive effort provided specific values of 15 rotor physical parameters (e.g., hinge offset, lift-curve slope, blade inertia) needed to update directly the rotor dynamics model for a new developmental helicopter rotor system. The identification results also helped resolve a long-standing problem in characterizing the off-axis rotor response of helicopters.<sup>188,189</sup>

### 13.2 Buildup Approach to Developing the Appropriate Physical Model Structure

The effort required for model setup, model structure determination, and parameter identification increases, as expected, with the increasing degree of complexity in the model structures of Sec. 13.1. The simpler three-DOF fixed-wing models can involve several man-hours to a couple of days of effort, at least for the first complete experience. Coupled six-DOF models of helicopters can involve a week or more the first time. Formulating the hybrid models might require background reading on rotorcraft flight dynamics and are more complex to set up. Finally, the physics-based models of the SBMR<sup>92</sup> and the UH-60<sup>103</sup> each involved several months for model structure derivation from first-principles and parameter identification.

Given the potential complexity of the task, the best approach is to build up knowledge about the appropriate model structure in stages. The frequency-response method is ideally suited for this process. The first step is to study the frequency responses generated from flight data in detail, looking for clues about the model structure. Important aspects include locations of key break frequencies and modes; presence of unstable dynamics, as seen by a phase rise where the magnitude rolls off; and the importance of coupling, as detected by the coherence in the off-axis responses.

In the next step, lower-order SISO transfer-function models should be identified for the key on-axis responses to further establish the appropriate model structure (e.g., quasi-steady vs coupled rotor-body model) and to determine the location of the basic modes and dominant stability and control derivatives. These results provide initial values for the more complete state-space model structures. In some studies, the identification of MIMO physical models can start with lower-order representations (e.g., short-period models of fixed-wing longitudinal dynamics) to “shake out” problems with model structure implementation, sign and units errors, and data consistency before proceeding. In general, simpler models offer more physical insight into the sources of major identification model discrepancies.

At this point, a complete state-space model structure can be implemented that includes enough complexity (coupling and degrees of freedom) to track the MIMO frequency-response data matrix  $\hat{T}_c$ . The model structure should provide an initial converged solution with a cost function  $J_{ave} \leq 100$ , which generally reflects an acceptable level of accuracy for flight-dynamics modeling. Then the selected model structure is refined by dropping unimportant or correlated parameters, following the procedure explained in Sec. 13.4.7, until a final identification model is obtained.

### 13.3 Equations of Motion for Flight Vehicles

The six-DOF flight-dynamics equations of motion provide a general physical model structure that is a useful basis for MIMO system identification of most flight vehicles. As discussed in Sec. 13.1, this structure adequately characterizes the flight dynamics of helicopters with small values of the rotor flap stiffness. Also from this starting point, the equations can be easily simplified to the decoupled three-DOF model structures (longitudinal and lateral/directional) needed for fixed-wing applications. The following derivation is presented in a brief form,

and the reader is referred to classical flight-mechanics references (e.g., Ref. 56) for a more complete development.

### 13.3.1 Force Equations

The derivation of the force equations starts with the Newton's Second Law, expressed in the inertial frame of reference:

$$\frac{d^I m V}{dt} = F \quad (13.1)$$

where  $F$  is the total external force vector. The flight dynamics are obtained in the Eulerian (body-fixed) frame as

$$\frac{d^B V}{dt} + (\boldsymbol{\omega} \times \mathbf{V}) = \frac{\mathbf{F}_{\text{gravity}}}{m} + \frac{\mathbf{F}_{\text{aero}}}{m} \quad (13.2)$$

where  $\boldsymbol{\omega}$  is the angular velocity vector of the body-fixed axis system. On the right-hand side, we have separated the force vector into gravitational and aerodynamic contributions. The body-axis accelerations are given as

$$\frac{d^B V}{dt} = -(\boldsymbol{\omega} \times \mathbf{V}) + \bar{\mathbf{F}}_{\text{gravity}} + \bar{\mathbf{F}}_{\text{aero}} \quad (13.3)$$

with the specific gravity and aerodynamic force vectors defined as

$$\bar{\mathbf{F}}_{\text{gravity}} = \frac{\mathbf{F}_{\text{gravity}}}{m} \quad (13.4)$$

$$\bar{\mathbf{F}}_{\text{aero}} = \frac{\mathbf{F}_{\text{aero}}}{m} \quad (13.5)$$

The equations of motion for fixed-wing aircraft are commonly derived using a *stability-axis coordinate system*, which is a body-fixed frame initially aligned with the trim velocity vector. For hovering and low-speed flight vehicles, it is convenient instead to select the *body-axis coordinate system* of Fig. 6.3, which is also a body-fixed frame but now aligned with the fuselage axes. When comparing identification and analytical results, it is important to be sure that the same axis system (body or stability axes) is used.

Next, the vector equations are expanded in scalar form, and a trim condition is defined by reference Euler angles

$$\Theta = \Theta_0, \quad \Phi = 0, \quad \Psi = 0 \quad (13.6)$$

and reference velocities

$$U = U_0, \quad V = V_0, \quad W = W_0 \quad (13.7)$$

The asymmetric reference state  $V_0$  accommodates helicopter trim in forward flight. The small trim roll angles  $\Phi_0$  that might be also present in hover and forward flight can generally be neglected.

Next, the equations are linearized for small-perturbation motion about the trim flight condition:

$$\text{perturbation speeds: } u, v, w \quad (13.8)$$

$$\text{perturbation angular rates: } p, q, r \quad (13.9)$$

$$\text{perturbation Euler angles: } \phi, \theta \quad (13.10)$$

$$\text{perturbation control deflections: } \delta_a, \delta_e, \delta_r, \delta_t \quad (13.11)$$

The specific aerodynamic forces [Eq. (13.5)] are expanded in a Taylor series for perturbations in the states and controls. The resulting equations of motion from Eq. (13.3) are

$$\begin{aligned} \dot{u} = & -W_0q + V_0r - (g \cos \Theta_0)\theta + X_uu + X_vv + \dots + X_qq + \dots \\ & + X_{\delta_e}\delta_e + X_{\delta_a}\delta_a + \dots \end{aligned} \quad (13.12)$$

$$\begin{aligned} \dot{v} = & -U_0r + W_0p + (g \cos \Theta_0)\phi + Y_uu + Y_vv + Y_qq + \dots \\ & + Y_{\delta_e}\delta_e + Y_{\delta_a}\delta_a + \dots \end{aligned} \quad (13.13)$$

$$\begin{aligned} \dot{w} = & -V_0p + U_0q - (g \sin \Theta_0)\theta + Z_uu + Z_vv + \dots + Z_qq + \dots \\ & + Z_{\delta_e}\delta_e + Z_{\delta_a}\delta_a + \dots \end{aligned} \quad (13.14)$$

The parameters to be identified are the dimensional stability and control force derivatives (e.g.,  $X_u, X_w, Z_w, Z_q, X_{\delta}$ ). These are the partial derivatives of the specific aerodynamic forces with respect to variations in the states and controls:  $X_u \equiv (1/m)(\partial X / \partial u)$ . The trim condition values ( $\cdot_0$ ) are assumed known and are entered as fixed values in the model structure. For example, in Eq. (13.14) the terms involving  $q$  are  $Z_qq$  and  $U_0q$ , and so the associated response derivative for  $q$  is  $\partial \dot{w} / \partial q = [Z_q + U_0]$ . The DERIVID module for state-space system identification in CIFER® allows the user to specify a constant value for  $U_0$  and to indicate that the parameter  $Z_q$  is free and is to be identified.

### 13.3.2 Moment Equations

The moment equations are also derived starting from Newton's Second Law in the inertial frame of reference:

$$\frac{d^I \mathbf{I} \boldsymbol{\omega}}{dt} = \mathbf{M} \quad (13.15)$$

where  $\mathbf{M}$  is the total external moment vector. Expressed in a body-fixed frame of

reference, this becomes

$$\frac{d^B \mathbf{I} \boldsymbol{\omega}}{dt} = -(\boldsymbol{\omega} \times \mathbf{I} \boldsymbol{\omega}) + \mathbf{M}_{\text{aero}} \quad (13.16)$$

where  $\mathbf{I}$  is the inertia tensor and  $\mathbf{M}_{\text{aero}}$  is the vector of external aerodynamic moments.

The vector equation is expanded into its components and linearized as before for small-perturbation motion. The external aerodynamics moments are then expressed in a Taylor series of the dimensional moment stability and control derivatives (e.g.,  $L_u$ ,  $L_w$ ,  $M_w$ ,  $M_q$ ,  $L_\delta$ ). These are the partial derivatives of the specific aerodynamic moments with respect to variations in the states and controls:  $L_p \equiv (1/I_{xx})(\partial L/\partial p)$ . The roll and yaw equations are coupled as a result of the cross-product ( $I_{xz}$ ) terms in the inertia tensor  $\mathbf{I}$ . The equations-of-motion can be re-arranged in standard first-order form as:

$$\dot{p} = L_u' u + L_v' v + \dots + L_p' p + \dots + L_{\delta_e}' \delta_e + L_{\delta_a}' \delta_a + \dots \quad (13.17)$$

$$\dot{q} = M_u u + M_v v + \dots + M_w \dot{w} + M_q q + \dots + M_{\delta_e} \delta_e + M_{\delta_a} \delta_a + \dots \quad (13.18)$$

$$\dot{r} = N_u' u + N_v' v + \dots + N_r' r + \dots + N_{\delta_e}' \delta_e + N_{\delta_a}' \delta_a + \dots \quad (13.19)$$

where *primed derivatives* ( )' are defined following McRuer et al.<sup>56</sup>

$$L_i' = \frac{L_i + (I_{xz}/I_{xx})N_i}{1 - [I_{xz}^2/(I_{xx}I_{zz})]} \quad (13.20)$$

and

$$N_i' = \frac{N_i + (I_{xz}/I_{zz})L_i}{1 - [I_{xz}^2/(I_{xx}I_{zz})]} \quad (13.21)$$

for  $i = u, v, w, p, q, r, \delta_a, \delta_e, \delta_r, \delta_t$ . These primed derivatives account for the influence of the product of inertia  $I_{xz}$ . In the remainder of this book, the primed notation (') is implied but is generally dropped for convenience.

### 13.3.3 Euler Angle Relationships

The small-perturbation equations for the Euler angle rates are

$$\dot{\phi} = p + r \tan \Theta_0 \quad (13.22)$$

$$\dot{\theta} = q \quad (13.23)$$

$$\dot{\psi} = \frac{r}{(\cos \Theta_0)} \quad (13.24)$$

### 13.4 Model Formulation in a State-Space Structure

The equations of motion from Sec. 13.3 are now cast in the state-space form

$$\dot{\mathbf{Mx}} = \mathbf{Fx} + \mathbf{Gu}(t - \tau) \quad (13.25)$$

$$\dot{\mathbf{y}} = \mathbf{H}_0\mathbf{x} + \mathbf{H}_1\dot{\mathbf{x}} \quad (13.26)$$

#### 13.4.1 State and Control Variables

The six-DOF equations of motion are composed of eight states, describing the motion of the fuselage center of gravity and the rotation of the body,

$$\mathbf{x} = \begin{bmatrix} u \\ v \\ w \\ p \\ q \\ r \\ \phi \\ \theta \end{bmatrix} \quad (13.27)$$

and four bare-airframe controls. (Here we have dropped heading angle  $\psi$  because it does not influence the dynamic response of the aircraft.) For fixed-wing aircraft, the control vector consists of the inputs for roll, pitch, yaw, and throttle:

$$\mathbf{u} = \begin{bmatrix} \delta_a \\ \delta_e \\ \delta_r \\ \delta_t \end{bmatrix} \quad (13.28)$$

In the case of rotorcraft applications, the control vector consists of the inputs for roll, pitch, yaw, and heave:

$$\mathbf{u} = \begin{bmatrix} \delta_{lat} \\ \delta_{lon} \\ \delta_{ped} \\ \delta_{col} \end{bmatrix} \quad (13.29)$$

### 13.4.2 State and Control Matrices ( $M$ , $F$ , $G$ )

With the state and input vectors defined, it is a relatively simple matter to cast the equations of motion (13.12–13.14), (13.17–13.19), (13.22), and (13.23) in the form of Eqs. (13.25) and (13.26) and define the structure of the  $M$ ,  $F$ , and  $G$  matrices. The components of the  $F$  matrix reflect the force and moment gradients to state perturbations from trim and thus are *stability derivatives* (e.g.,  $X_u$ ,  $X_w$ ,  $M_w$ ,  $M_q$ ). The components of the  $G$  matrix reflect the gradients to control perturbations from trim and thus are the *control derivatives* (e.g.,  $X_{\delta_e}$ ,  $M_{\delta_e}$ ).

The components of  $M$  include parameters that depend on the rates of change of the state variables. In the case of the canonical models of Chapter 12, the  $M$  matrix in Eq. (13.25) was the identity matrix ( $M = I$ ). For fixed-wing flight-mechanics models, the  $M$  matrix allows the explicit identification of parameters such as  $Y_v$  in Eq. (13.13) and  $M_w$  in Eq. (13.18), which are associated with the effects of sidewash lag and downwash lag.<sup>56</sup> In the identification of more complex integrated systems, the  $M$  matrix is also very useful for including algebraic relationships in the model structure. Examples of this are control system summing junctions and the coupling of the rotor and body dynamics in the hybrid model for rotorcraft (Sec. 15.2.3).

### 13.4.3 Measurement Vector

The measurement (or output) vector for most six-DOF flight-vehicle applications is nominally composed of

$$\mathbf{y} = \begin{bmatrix} u \\ v \\ w \\ p \\ q \\ r \\ a_x \\ a_y \\ a_z \end{bmatrix} \quad (13.30)$$

**Euler angle measurements.** The Euler angles are generally not included in the measurement vector for the frequency-response method. The reason is that the angular-rate frequency responses usually have higher coherence for the entire frequency range of interest, and they have the identical dynamic information because, for example, from Eq. (13.23) we have

$$\frac{\theta}{\delta_e}(s) = \left(\frac{1}{s}\right) \frac{q}{\delta_e}(s) \quad (13.31)$$

when the data are kinematically consistent. Sometimes measurement system characteristics or signal-to-noise issues warrant including both angular rate and attitude measurements. For example, in the case of the XV-15 in hover the data show a degradation in the kinematic consistency between roll rate and roll angle at lower frequencies (below 1.0 rad/s; **Problem 6.6**). Because the roll angle measurement was found to provide a higher coherence frequency response in this frequency range, it is also included in the measurement vector in this case (Sec. 13.9). In other cases, the Euler angle responses ( $\theta/\delta_e$ ) can be found to have acceptable coherence at low frequencies (e.g., 0.1–1 rad/s), where the coherence of the angular rate response ( $q/\delta_e$ ) is not acceptable. This can occur owing to the improved signal-to-noise ratio of the pitch-angle signal for the phugoid response. Good angular response data (either attitude or rate) are especially important at low frequencies for an accurate identification of the rotorcraft speed-stability derivatives  $M_u$  and  $L_v$  in hovering flight.

**Velocity measurements.** Translational velocities ( $u$ ,  $v$ ,  $w$ ) might be available as a measured or reconstructed signal from an onboard inertial measurement unit (IMU) or an embedded GPS/INS (EGI), modern measurement systems that fuse the aircraft measurements into one set of kinematically consistent signals. Alternatively, the reconstructed body-axis accelerations [ $\dot{u}$ ,  $\dot{v}$ ,  $\dot{w}$ , using Eqs. (6.35), (6.36), (6.37), respectively] are used to calculate the acceleration frequency responses [e.g.,  $\dot{v}/\delta_a(s)$ ]. Then the required velocity frequency responses are easily obtained. For example,

$$\frac{\dot{v}}{\delta_a}(s) = \left( \frac{1}{s} \right) \left[ \frac{\dot{v}}{\delta_a}(s) \right] \quad (13.32)$$

An alternate implementation would be to include the body-axis accelerations rather than the velocities in the measurement vector  $\mathbf{y}$ :

$$\dot{u} = su \quad (13.33)$$

$$\dot{v} = sv \quad (13.34)$$

$$\dot{w} = sw \quad (13.35)$$

which is realized using the  $H_1$  matrix of Eq. (13.26). Then the acceleration responses [ $\dot{v}/\delta_a(s)$ , etc.] are used directly in the identification cost function. The result is the same in either case.

**Aerodynamic angle measurements.** At forward-speed flight conditions, aerodynamic angle of attack  $\alpha_{nb}$  and sideslip  $\beta_{nb}$  measurements are often available for aircraft and rotorcraft applications from a flight-test air data system (nose boom). If available, these provide reliable and independent measurements of the perturbation translational velocities, and they would also be included in

the measurement vector [Eq. (13.30)]. The linearized variations of the aerodynamic angles as measured at the nose boom are related to the vehicle states by

$$\alpha_{nb} = \frac{w + py_{nb} - qx_{nb}}{U_0} \quad (13.36)$$

$$\beta_{nb} = \frac{v - pz_{nb} + rx_{nb}}{(V_{tot})_0} \quad (13.37)$$

where the coordinates  $x_{nb}$ ,  $y_{nb}$ ,  $z_{nb}$  give the nose-boom location relative to the c.g. The total reference velocity is defined as

$$(V_{tot})_0 = \sqrt{(U_0)^2 + (V_0)^2 + (W_0)^2} \quad (13.38)$$

For the stability axes system used most commonly in fixed-wing applications,  $U_0$  and  $(V_{tot})_0$  can be used interchangeably.

**Accelerometer measurements.** The accelerometer measurements are very important for model identification because they provide a direct measurement of the specific external forces excluding gravity. Thus they are key responses for identifying the aerodynamic force derivatives (e.g.,  $X_u$ ,  $Y_v$ ,  $Z_w$ ,  $X_{\delta_{lon}}$ ,  $Y_{\delta_{lat}}$ ). These measurements are easily expressed in terms of the state and state rates, repeated from Eqs. (6.33), (6.34), and (6.32), with correction terms included to account for the offsets  $x_a$ ,  $y_a$ ,  $z_a$  of the accelerometer package relative to the center of gravity:

$$a_x = \dot{u} + W_0q - V_0r + (g \cos \Theta_0)\theta + z_a \dot{q} - y_a \dot{r} \quad (13.39)$$

$$a_y = \dot{v} + U_0r - W_0p - (g \cos \Theta_0)\phi - z_a \dot{p} + x_a \dot{r} \quad (13.40)$$

$$a_z = \dot{w} + V_0p - U_0q + (g \sin \Theta_0)\theta + y_a \dot{p} - x_a \dot{q} \quad (13.41)$$

As before, the terms involving linear and angular accelerations are realized by making use of the  $H_1$  matrix.

**Additional measurements.** Depending on the application, there are many other measurements that can be included. Some examples are structural system measurements (strain gauges), engine rpm, engine fuel flow, and rotor system states (flapping, coning, and lead-lag).

### 13.4.4 Measurement Matrices ( $H_0$ , $H_1$ )

The formulation of the measurement vector in terms of the  $H_0$  and  $H_1$  matrices allows the body-axis accelerations [Eqs. (13.33–13.35)] and accelerometer

measurements [Eqs. (13.39–13.41)] to be expressed in terms of the states. This is possible because in the frequency domain the differentiation is realized by the simple arithmetic multiplication by the Laplace variable ( $s = j\omega$ ). (When the frequency response is presented on a Bode plot, the differentiation amounts to a simple rotation of the data curve about the  $\omega = 1 \text{ rad/s}$  point.) By adopting this form, we avoid the repetition of the identification parameters in both the  $\mathbf{F}$  matrix and the conventional output expression ( $y = \hat{\mathbf{C}}\mathbf{x} + \mathbf{D}\mathbf{u}$ ) and thereby avoid the requirement to implement a constraint equation for each parameter.

### 13.4.5 Time-Delay Matrix $\tau$

As in the SISO transfer-function modeling method, time delays are often included to account for unmodeled dynamics, such as actuator dynamics, control linkages, or transient rotor dynamics. The time delay is most commonly associated with the control input, and so the effect will be the same on all outputs. Then the same time-delay value is used for an entire column of the time-delay matrix  $\tau$ , [Eq. (12.13)]. For example, in the case of the four inputs for fixed-wing aircraft [Eq. (13.28)], there are four time delays to be identified ( $\tau_a, \tau_e, \tau_r, \tau_t$ ).

### 13.4.6 Free, Fixed, and Constrained Parameters

The complete six-DOF model structure has 64 aircraft parameters: 36 stability derivatives, 24 control derivatives, and four equivalent time delays. Symmetry assumptions for fixed-wing aircraft reduce the identification problem to nine stability derivatives, six control derivatives, and two equivalent delays each for longitudinal and lateral/directional equations of motion. [Note that there is no dependency of the aerodynamic coefficients on the Euler angles ( $\phi, \theta, \psi$ ).]

In the general identification case, the parameters in the model structure matrices  $\mathbf{M}$ ,  $\mathbf{F}$ ,  $\mathbf{G}$ ,  $\tau$  can be categorized as free, fixed, or constrained. Parameters should be designated as fixed when they are known a priori, thus reducing the complexity of the identification problem and ensuring that the identified model has realistic physical constants. Examples of fixed parameters include gravity  $g$ , trim values  $U_0, V_0, W_0, \Theta_0$ , and known filters, time delays, etc. Most parameters in the model structure are designated as free to be optimized by the identification algorithm.

The initial values for the free parameters in the model structure are obtained from a variety of sources. For example, they might be available from simulation models, such as was the case for the XV-15.<sup>130</sup> Satisfactory initial estimates of the key on-axis rate damping and control moment derivatives (e.g., for rotorcraft,  $L_p, L_{\delta_{\text{lat}}}, M_q, M_{\delta_{\text{lon}}}, N_r, N_{\delta_{\text{ped}}}, Z_w, Z_{\delta_{\text{col}}}$ ) can be made from the identification of simple transfer-function models, as obtained, for example, in Eq. (11.22). Guesses for the remaining parameters can usually be made based on first principles estimates, values for a similar type of aircraft, or simply initialized as zero. Excellent compilations of stability and control derivatives are provided for fixed-wing aircraft<sup>165</sup> and helicopters.<sup>190</sup> Experience indicates that the frequency-response method and the secant algorithm (Sec. 12.2) are very robust to the choice of initial guesses, even for highly complex identification model structures. This is demonstrated for the XV-15 identification in **Problems 13.3 and 13.7**.

In many situations there is a common identification parameter that appears in several places in the four identification matrices  $M$ ,  $F$ ,  $G$ ,  $\tau$ . For example, a second-order representation of an actuator dynamics model can be included in each of the control axes, but with a single (common) natural frequency (bandwidth). When rotor system dynamics are included in an identification structure, the rotor-response time constant is constrained to a single value in pitch and roll, as it should be physically.

Model structures derived from underlying physical equations of motion can be formulated in terms of the constituent element springs, masses, and dampers, with constraint equations to enforce commonality and kinematic interrelationships. For example, Tischler<sup>92</sup> identified a model of dynamic response of a full-scale rotor in a wind tunnel. The highly complex model structure was formulated in terms of the physical (aerodynamic, inertial, and control system) constants of the rotor and required a system of 40 differential equations. The structure included a large number of constraints because the physical constants (e.g., rotor time constant, flap frequency) had to have the same identified values throughout. Other examples of identification studies involving detailed constraint equations are presented by Fletcher and Tischler<sup>103</sup> for the UH-60 and by Colbourne et al.<sup>173</sup> for the multibody dynamics of a helicopter and slung-load.

### 13.4.7 State-Space Model Structures for Generalized Identification

The model structure of Secs. 13.3–13.4.6 was developed to represent the six-DOF aerodynamic model of a general flight vehicle. The same basic approach can be followed to derive the appropriate state-space model structure for more complex multibody systems by including the relevant dynamic degrees of freedom. One example of this was the coupled helicopter/slung-load multibody model identification of the BURRO (Ref. 173) using CIFER®. Hui<sup>191</sup> also used CIFER® system identification methods to obtain an accurate state-space model of the yaw response of the Bell 412HP helicopter in support of high-bandwidth flight-control development. The model structure included a complex representation of the coupled dynamics of the engine, governor, and fuel control systems. At the other end of the spectrum, lower-order physical model structures can be derived for an actuator, control system gyro or filter, or any other dynamic subsystem that can be described in the form of a linear-time-invariant (LTI) set of first-order differential equations.

## 13.5 Frequency-Response Database and Frequency Ranges

In this section the frequency-response database and associated frequency ranges are selected for incorporation in the identification cost function of Eq. (12.20). This leads to a frequency-response table that is then used to eliminate some of the control and response derivatives, thereby achieving an initial reduction in the complexity of the model structure.

### 13.5.1 Frequency-Response Database

In the case of the six-DOF model structure, there are  $n_c = 4$  inputs [Eqs. (13.28) or (13.29)] and  $n_o = 9$  outputs [Eq. (13.30)], yielding a total of 36 possible frequency response pairs  $T_l$  to be included in the identification cost function.

(There are more if aerodynamic angles measurements  $\alpha$  and  $\beta$  are also included.) We recall from Table 10.1 that one work flowpath is used to determine one column of the frequency-response (data) matrix  $\hat{T}_c$ . This is repeated for each primary control (four work flowpaths in total), corresponding to the  $n_c = 4$  columns of  $\hat{T}_c$ . Assuming that  $n_w = 5$  spectral windows are used, the total number of frequency responses that are calculated in creating the frequency-response database are 840 SISO frequency responses, 180 MISO (conditioned) frequency responses, and 36 composite window (final) frequency-response pairs comprising the  $n_o \times n_c$  data matrix  $\hat{T}_c$ . Thus a total of 1056 frequency responses are estimated to determine the flight data matrix  $\hat{T}_c$ . Keeping track of this large number frequency responses can be a bookkeeping challenge without an automated databasing capability such as that provided by CIFER®. Corrections can be easily introduced in the frequency domain to integrate/differentiate the response variable (multiply by a power of  $s$ ) or to perform units corrections (multiply by gain), sign change (shift of 180 deg in phase), or phase wrap (shift of 360 deg of phase).

### 13.5.2 Table of Frequency Ranges

The frequency range to be included in the model identification is determined for each of the 36 flight data frequency responses by examining the Bode plot and coherence function. The selected frequency ranges are best compiled in a table displaying the input-to-output frequency-response combinations, such as Table 13.1. The on-axis responses are highlighted in bold and are key to the model identification. This table is for the flight-test identification of a six-DOF model of a helicopter in hover—the Fire Scout P2 demonstrator. For now we will limit our discussion of this helicopter to the frequency-response table and its use in the initial reduction of the model structure. We will complete the system identification of this helicopter later, in Sec. 13.12, after we have illustrated some key points with somewhat simpler examples.

For each input/output pair in Table 13.1, the range of frequencies to be included in the cost function calculation is established by examining the corresponding

**Table 13.1 Example of frequency-response table  
(Fire Scout P2 demonstrator, hover)**

Measurement (output)	Control (input)			
	$\delta_{\text{lat}}$	$\delta_{\text{lon}}$	$\delta_{\text{ped}}$	$\delta_{\text{col}}$
$\dot{u}$	None	<b>0.7–12.0</b>	None	None
$\dot{v}$	<b>0.8–4.0</b>	None	None	None
$\dot{w}$	None	None	None	<b>0.15–2.0</b>
$p$	<b>0.7–12</b>	2.0–10.0	3.0–12.0	2.0–12.0
$q$	None	<b>0.6–12.0</b>	1.2–7.0	None
$r$	2.0–10.0	None	<b>0.25–10.0</b>	1.0–5.0
$a_x$	None	<b>0.5–12.0</b>	None	0.4–8.0
$a_y$	<b>1.0–10.0</b>	0.15–7.0	2.0–10.0	None
$a_z$	None	None	None	<b>0.15–2.0</b>

magnitude, phase, and coherence plots of the flight data. If the coherence function never reaches the threshold

*Guideline:*

$$(\gamma_{xy}^2)_{\text{threshold}} = 0.6 \quad (13.42)$$

within the frequency range of interest, or if the magnitude or phase plots indicate other serious problems with the data, that pair should be excluded entirely (indicated in the table by “none”). It is useful to also refer to the doublet time history data to verify that this input-to-output response pair is not significant.

For each pair that has acceptable coherence [i.e., Eq. (13.42) is met for some frequencies], an associated fitting range from  $\omega_{\min}$  to  $\omega_{\max}$  [ $\omega_{\min} \equiv \omega_1$ ;  $\omega_{\max} \equiv \omega_{n_{\omega}}$  of Eq. (12.20)] is selected based on the following:

*Guideline:*

$$(\gamma_{xy}^2)_{\text{fitting range}} \geq 0.5 \quad (13.43)$$

Local coherence dips within this frequency range are not of concern because they can be avoided by adjusting the distribution of frequency points [using the coherence cutoff  $(\gamma_{xy}^2)_{\text{cut}}$  described in Sec. 12.2.3]. The primary (on-axis) responses, which are highlighted in bold in the table, all show good coherence in the frequency range of interest for flight-dynamics modeling, so that the database is well suited to this purpose. As can be seen in the table, most of the frequency-response pairs that are dropped are associated with the off-axis (coupled) responses. Note also that for a hover flight condition the frequency content of the vertical acceleration and vertical accelerometer responses are the same [ $\dot{w}/\delta_{\text{col}} \equiv a_z/\delta_{\text{col}}$ , from Eq. (13.41)], and only one is used in the identification cost function.

The maximum frequencies selected in the Table 13.1 must be consistent with the frequency range of model applicability. For example, the quasi-steady model for rotorcraft is not appropriate for frequency ranges that include the rotor modes (flapping, lead-lag, and dynamic inflow)—even if the coherence functions for the responses are acceptable in that higher range. (In CIFER®, the user can select a global frequency range of model applicability that will override, if necessary, the maximum frequencies selected based on coherence only.) The maximum frequencies in Table 13.1 are limited to 12 rad/s, which corresponds to the frequency range of applicability for the six-DOF helicopter model in this case, even though the actual flight data showed good coherence out to somewhat higher frequencies for some of the response pairs. The flight data for  $a_x/\delta_{\text{col}}(s)$  and  $a_z/\delta_{\text{col}}(s)$  have high coherence to about 15 rad/s (as can be seen later in Fig. 13.11). However, as seen in Table 13.1, the responses are restricted to 8 and 2 rad/s, respectively, to avoid fitting the quasi-steady model structure to frequency-response data that include the higher-order effect of dynamic inflow (Sec. 13.12.2).

For each input/output pair, a *decade span* can be defined as

$$\text{dec\_span} = \log\left(\frac{\omega_{\max}}{\omega_{\min}}\right) \quad (13.44)$$

to characterize the fraction of a decade for which acceptable data are available. Practical experience indicates that a frequency response should only be included if

*Guideline:*

$$\text{dec\_span} \geq 0.3 \quad (13.45)$$

If this guideline is not met, “none” is entered for the usable frequency range. Including small *segments* (less than this guideline) generally degrades the identification because frequency points are concentrated in a narrow frequency range, thereby overemphasizing the importance of the limited data in the identification cost function. The frequency responses are better dropped entirely in this case. The final frequency ranges selected for the six-DOF helicopter model are shown in Table 13.1.

### 13.5.3 Model Structure Reduction Based on Frequency-Response Table

When the coherence of a particular frequency-response pair is found to be very low over the frequency range of interest, the corresponding entry in the frequency-response table is designated as “none” and is therefore dropped from the identification cost function of Eq. (12.20). One such case in Table 13.1, which is typical for a hovering helicopter is the off-axis (i.e., coupling) response  $r/\delta_{\text{lon}}$ , indicating a lack of significant energy transfer from pitch control inputs  $\delta_{\text{lon}}$  to the yaw degree of freedom  $r$ . From this we can deduce that

$$\frac{r}{\delta_{\text{lon}}}(s) \approx 0 \quad (13.46)$$

over the entire frequency range of pitch control excitation. Pitch inputs produce primarily a response in the longitudinal degrees of freedom, with significant coupling into roll. The level of coupling into yaw is generally very small, as in the example of Table 13.1.

Considering pitch inputs only, the yaw equation-of-motion (13.19) can be expressed in the frequency domain in terms of the other state responses as

$$\begin{aligned} \frac{r}{\delta_{\text{lon}}}(s) = & \left( \frac{1}{s - N_r} \right) \left\{ N_{\delta_{\text{lon}}} + \left[ N_p \frac{p}{\delta_{\text{lon}}}(s) \right] + \left[ N_q \frac{q}{\delta_{\text{lon}}}(s) \right] \right. \\ & \left. + \left[ N_u \frac{u}{\delta_{\text{lon}}}(s) \right] + \left[ N_v \frac{v}{\delta_{\text{lon}}}(s) \right] + \left[ N_w \frac{w}{\delta_{\text{lon}}}(s) \right] \right\} \end{aligned} \quad (13.47)$$

where we recall that the primes (') are implied on the derivatives but are dropped for notational convenience. The first term  $[1/(s - N_r)]$  is the on-axis yaw-rate damping response and will not vanish, and so the remaining terms in the braces {} must sum to zero to satisfy Eq. (13.46). In general, each term in the braces

[e.g.,  $N_{\delta_{\text{lon}}}$ ,  $N_p p(s)/\delta_{\text{lon}}(s)$ ] will contribute a different magnitude and phase characteristic as a function of frequency to the overall response. The vector sum of these multiple terms will not produce cancelling effects over the entire frequency range that could result in  $r(s)/\delta_{\text{lon}}(s) \approx 0$ . So for the overall response to be negligible, the individual terms must each contribute a negligibly small magnitude.

The first right-hand side term in the braces is the control coupling derivative  $N_{\delta_{\text{lon}}}$ , which will dominate at higher frequencies—that is, beyond the break frequencies of the short-term angular responses (typically 1–5 rad/s). Clearly, for Eq. (13.46) to be satisfied,

$$N_{\delta_{\text{lon}}} \approx 0 \quad (13.48)$$

and  $N_{\delta_{\text{lon}}}$  should be eliminated from the model structure (i.e., given a fixed value of zero). This conclusion can also be deduced by taking the reverse point of view: if the control coupling *had been significant*, this would have resulted in a significant yaw-rate response to pitch inputs, especially at higher frequencies and an associated high value of coherence. Because this response pair has no coherence, the control coupling derivative  $N_{\delta_{\text{lon}}}$  must be negligible.

All of the remaining terms in the braces of Eq. (13.47) involve products of a gain (response coupling derivative) and a frequency response to pitch input  $\delta_{\text{lon}}$ . But two terms contain the dominant (on-axis) responses to longitudinal cyclic (pitch control) input. In hovering flight these are pitch rate and longitudinal velocity [ $q(s)/\delta_{\text{lon}}(s)$  and  $u(s)/\delta_{\text{lon}}(s)$ ], which clearly cannot be small. This can be checked by comparing the on-axis vs the off-axis frequency-response plots, such as  $u(s)/\delta_{\text{lon}}(s)$  vs  $v(s)/\delta_{\text{lon}}(s)$  and  $w(s)/\delta_{\text{lon}}(s)$ . In the present hover case, the latter two responses are negligible, and  $u(s)/\delta_{\text{lon}}(s)$  is clearly the dominant speed response for pitch inputs. Because the responses  $q(s)/\delta_{\text{lon}}(s)$  and  $u(s)/\delta_{\text{lon}}(s)$  are the dominant responses, we can be sure that the coupling derivatives matched with these responses in Eq. (13.47) must be negligible, that is,

$$N_q \approx 0, \quad N_u \approx 0 \quad (13.49)$$

which again is to be expected for a conventional helicopter in hover.

In the case of translational responses, only the dropped accelerometer frequency responses should be considered because these reflect the isolated contribution of the aerodynamic derivatives. The speed (or body-axis acceleration) responses are dominated by gravity contributions through the pitch and roll attitudes and so are not included in this initial model structure reduction analysis. Referring again to Table 13.1, we see that  $a_x/\delta_{\text{lat}}$  is negligible, as would be expected for a hovering helicopter. From this result, we can conclude that

$$X_{\delta_a} \approx 0 \quad (13.50)$$

$$X_p \approx 0, \quad X_v \approx 0 \quad (13.51)$$

and so these must also be eliminated from the model structure.

For fixed-wing aircraft (and rotorcraft in forward flight), the dominant angular state responses are the same as for rotorcraft in hover [i.e.,  $p(s)/\delta_a(s)$ ,  $q(s)/\delta_e(s)$ ,  $r(s)/\delta_r(s)$ ], whereas the dominant translational state responses are now  $w(s)/\delta_e(s)$  and  $v(s)/\delta_r(s)$ . For fixed-wing aircraft, the key state response to throttle is speed [ $u(s)/\delta_t(s)$ ], whereas for rotorcraft in forward flight the dominant state response to collective remains  $w(s)/\delta_{col}(s)$ , the same as in hover. Again, this can be checked by comparing the frequency-response plots.

Thus for each frequency-response pair that is dropped from the table as a result of an overall lack of coherence, there will be one associated control derivative and one or two associated response derivatives to be eliminated from the initial identification model structure. The dropped derivatives are those that are matched with the dominant responses for the particular control input. Table 13.2 shows the derivatives that are dropped based on the frequency-response table (Table 13.1) for the six-DOF lightweight helicopter example.

This process of initial model structure reduction is a key and unique feature of the frequency-response method, made possible by access to the pair-wise coherence functions. A considerable simplification of the initial model structure is clearly achieved in this six-DOF example, reducing the number of control derivatives by nine and the number of stability derivatives by 14. The overall initial model structure is thus reduced from 60 identification parameters in the  $\mathbf{F}$  and  $\mathbf{G}$  matrices to 37. This process is especially useful in the identification of complex flight vehicles, such as helicopters and novel UAV configurations<sup>12</sup> for which the appropriate model structure is not known a priori.

In the next two sections (Secs. 13.6 and 13.7) we will discuss the rest of the system-identification procedure: 1) checking the initial model setup, 2) running the identification algorithm iteratively until a fully converged solution is achieved, 3) checking the time-domain predictive accuracy of the initial identification result, and 4) applying the parameter accuracy metrics to reduce the model structure further and obtain the final system identification. Then, in Secs. 13.8–13.11, we will illustrate the complete system-identification procedure with

**Table 13.2 Dropped derivatives for hover example  
(Fire Scout P2 demonstrator)**

Dropped frequency response	Dropped control derivative	Dropped response derivatives
$q/\delta_{lat}$	$M_{\delta_{lat}}$	$M_p, M_v$
$a_x/\delta_{lat}$	$X_{\delta_{lat}}$	$X_p, X_v$
$a_z/\delta_{lat}$	$Z_{\delta_{lat}}$	$Z_p, Z_v$
$r/\delta_{lon}$	$N_{\delta_{lon}}$	$N_q, N_u$
$a_z/\delta_{lon}$	$Z_{\delta_{lon}}$	$Z_q, Z_u$
$q/\delta_{col}$	$M_{\delta_{col}}$	$M_w$
$a_y/\delta_{col}$	$Y_{\delta_{col}}$	$Y_w$
$a_x/\delta_{ped}$	$X_{\delta_{ped}}$	$X_r$
$a_z/\delta_{ped}$	$Z_{\delta_{ped}}$	$Z_r$

several three-DOF examples: lateral/directional dynamics models of the XV-15 for cruise and hover, longitudinal dynamics model of STOVL from a nonlinear simulation, and a longitudinal dynamics model of a fixed-wing UAV. Finally, we will extend the concepts and techniques introduced to that point by completing the six-DOF system identification of the Fire Scout P2 demonstrator; this example was started in Sec. 13.5.2 with the discussion of the frequency-response table and the corresponding initial model structure reduction.

### 13.6 Checking the Initial Model Setup

Difficulties in obtaining satisfactory results from system identification are often caused by errors in setting up the problem statement. Typical errors are associated with incorrect assumptions about the units and signs of the flight data and incorrect derivation or implementation of the equations of motion in the identification software. These problems are manifested by errors between the flight-data frequency responses and those of the initial identification model. If left uncorrected, the identification algorithm will either not converge, or it will absorb these setup errors (e.g., units and signs) into incorrect values of the converged identified parameters.

The frequency-response format allows the initial model structure and parameter values to be readily evaluated and debugged. Large, consistent mismatches in magnitude and phase comparisons between the initial model and the flight data are easily seen in the individual response pairs and traced back to errors in sign convention, units, and model structure implementation. This constitutes a “sanity check” that should be completed before the optimization process is begun. Listed next are some typical problems and suggested debugging methods:

- 1) The rate responses for a flight-mechanics model should typically exhibit a  $-20$  dB/dec roll off at higher frequencies and an additional constant phase lag of  $-90$  deg. If they do not, check to see that the equations of motion are correct and properly implemented.
- 2) A consistent mismatch of  $\pm 20$  dB/dec magnitude and  $\pm 90$  deg phase between the flight-test response data and the initial model for the entire frequency range often reflects an error in the measurement equations (Sec. 13.4.3) or the need for a correction in the frequency-response data [e.g., Eq. (13.32)]. Check that the measurement equation is correct. For example, the frequency-response data might correspond to an angular rate  $q/\delta_e$ , while the model output as implemented in the  $\mathbf{H}_0$  and  $\mathbf{H}_1$  matrices produces an attitude response  $(\theta/\delta_e)$ .
- 3) A constant magnitude shift by  $36.16$  dB for the entire frequency-response magnitude plot is equivalent to a scale factor of  $57.3$  and generally reflects deg vs rad inconsistencies.
- 4) Phase shifts of  $180$  deg reflect sign inconsistencies.
- 5) Large cost functions or unexpected model stability properties (unstable vs stable eigenvalues) might reflect very poor initial parameter guesses. It is often useful to tune the initial parameter values to improve the frequency-response agreement prior to optimization.
- 6) There might be errors in kinematic consistency. For example, the magnitude and phase curves of the model (and flight data) should be the same for the  $u/\delta_e$  and  $a_x/\delta_e$  responses at higher frequency (typically beyond  $1$  Hz for manned aircraft),

where the gravity contribution to the  $\dot{u}$  signal is negligible. If one response shows good agreement between the model and data and the other does not, there might be a problem with a scale factor, units, or kinematic consistency and state reconstruction.

### 13.7 Model Identification and Structure Reduction

Once the model setup and implementation are checked out, we are ready to apply the model identification and structure reduction procedures first introduced in Chapter 12. The identification algorithm is run until a fully converged solution is achieved. The Secant algorithm (Sec. 12.2.3) can require 500–1000 iterations for more complex model structures to reach convergence, especially if there are several insensitive or highly correlated parameters. The convergence process is nonlinear and might appear to advance slowly for many iterations, but it is very important to continue running the optimization until it reaches a fully converged minimum average cost function  $J_{\text{ave}}$ . The identification algorithm is then restarted from this point, and it often achieves improved convergence away from this local minimum. A global minimum is reached if the solution then returns to the same solution after a restart, thus indicating that a satisfactory identification result is achieved for this model structure.

The guidelines for desirable cost functions are given in Eqs. (12.23) and (12.24). The model and data frequency-response plots should also be checked to verify that the key dynamic characteristics are well represented. If large mismatches occur in regions corresponding to poor coherence, the data might be unreliable, and the associated frequency-response range should be trimmed back (Sec. 13.5.2). Individual frequency-response pairs  $T_l$  with marginal coherence and large costs [in excess of Eq. (12.24)] should sometimes be dropped altogether and the corresponding derivatives removed from the model structure (Sec. 13.5.3). The model setup is refined, and the solution is reoptimized until the converged initial model structure meets the cost-function guidelines of Eqs. (12.23) and (12.24).

The time-domain predictive accuracy of the initial identification result should be checked at this point using the methods of Chapter 14. Problems with time-domain agreement can often be easily traced back to poor frequency-response agreement in a particular response pair. Adjustments can be made in the frequency-response calculations (e.g., choice of flight records and spectral windows) or selection of frequency-response ranges in order to correct this problem.

Next the parameter accuracy metrics should be determined for the initial model result. The model structure is reduced following the method of Sec. 12.3.4, working first on the parameters with the largest insensitivities, followed by the parameters with the largest Cramér–Rao bounds. The sources of parameter correlation are also reviewed at each step. *Only one parameter should be eliminated at each step* of this process, and the solution should be fully converged each time until the target Cramér–Rao bound is reached [Eq. (12.40)] or there is a jump in the cost functions [Eq. (12.52) and Eq. (12.53)]. After reconverging the model for the last two to three model structure reduction steps, it is also important to check that satisfactory time-domain predictive accuracy is still achieved (Chapter 14).

The identification procedure is now complete. If the cost function and parameter accuracy metrics are within the guidelines, the parameters that remain will have reliable values, and the model should exhibit good predictive accuracy. Experience has shown that a complicated model at the current limits of the CIFER® software (40 states, 80 simultaneous frequency-response matches, and 100 identification parameters) can be efficiently and reliably identified using this procedure.

### 13.8 Identification of Three-DOF Lateral/Directional Model for XV-15 in Cruise

This section demonstrates the identification of a three-DOF lateral/directional state-space model of XV-15 flight dynamics in cruise.

#### 13.8.1 Model Structure

The lateral/directional states are  $v$ ,  $p$ ,  $r$ , and  $\phi$ , and the measurements are  $p$ ,  $r$ ,  $a_y$ , and  $\beta$ . In this case no center-of-gravity corrections are needed, because the accelerometer measurements are provided at the center of gravity, and the angle of sideslip has already been corrected to the center of gravity in the frequency-response calculation Eq. (3.11).

The three-DOF equations of motion in body axes are obtained directly from Secs. 13.3 and 13.4 and the assumption of an  $x$ - $z$  plane of geometric, inertial, and aerodynamic symmetry (as is common for fixed-wing aircraft):

$$\dot{v} = -U_0 r + W_0 p + (g \cos \Theta_0) \phi + Y_v v + Y_p p + Y_r r + Y_{\delta_a} \delta_a + Y_{\delta_r} \delta_r \quad (13.52)$$

$$\dot{p} = L_v' v + L_p' p + L_r' r + L_{\delta_a}' \delta_a + L_{\delta_r}' \delta_r \quad (13.53)$$

$$\dot{r} = N_v' v + N_p' p + N_r' r + N_{\delta_a}' \delta_a + N_{\delta_r}' \delta_r \quad (13.54)$$

$$\dot{\phi} = p + r \tan \Theta_0 \quad (13.55)$$

There are nine stability derivatives and six control derivatives to be identified in these equations of motion. Equivalent time delays are included for the aileron input  $\tau_a$  and rudder input  $\tau_r$  to account for unmodeled high-order dynamics.

The measurement (also referred to as the *output* or *observer*) equations relate the measured quantities (shown on the left-hand side of the equations) to the states (appearing on the right):

$$p = p \quad (13.56)$$

$$r = r \quad (13.57)$$

$$a_y = \dot{v} + U_0 r - W_0 p - (g \cos \Theta_0) \phi \quad (13.58)$$

$$\beta = \frac{v}{(V_{\text{tot}})_0} \quad (13.59)$$

We note again the presence of the trim velocities  $U_0$  and  $W_0$  in the equations of motion and the measurement equations. This reflects the fact that we have adopted a body-axis coordinate system (Fig. 6.3) in this case, rather than a stability-axis system. There is no requirement to use the body axes, and the identification can be just as easily completed using a stability-axis system. Alternatively, the stability-axis parameters can be determined from the body-axis identification results via transformation equations.<sup>56</sup>

The trim condition for the flight data is repeated from Eqs. (3.12–3.15):

$$(V_{\text{tot}})_0 = 307.7 \text{ ft/s} \quad (13.60)$$

$$\Theta_0 = 4.57 \text{ deg} \quad (13.61)$$

$$U_0 = 306.7 \text{ ft/s} \quad (13.62)$$

$$W_0 = 24.5 \text{ ft/s} \quad (13.63)$$

The frequency-response ranges for acceptable coherence are listed in Table 13.3, with the maximum values truncated at the upper limit of applicability for the three-DOF model structure (10 rad/s). As can be seen, all of the frequency responses are included in this case, and all meet the dec\_span guideline of Eq. (13.45). Therefore none of the identification parameters are dropped at this initial model structure stage. The frequency-response database for the cruise condition is of very high quality, as is typical of cruise conditions, and the frequency ranges span the overall frequency range of interest for flight dynamics purposes. Of special importance are the good frequency ranges for on-axis responses, shown in bold, which ensure the accurate identification of the key flight-dynamics modes.

Figure 13.1 and 13.2 show the identification model structure for the XV-15 in cruise as summarized by CIFER® (and expressed in terms of the CIFER® mnemonics rather than engineering symbols). As can be seen,  $\mathbf{M}$  is the identity matrix,  $\mathbf{F}$  contains nine free stability derivatives,  $\mathbf{G}$  contains six free control derivatives, and  $\mathbf{\tau}$  contains the two free time delays. Notice where the trim

**Table 13.3 Frequency-response ranges for cruise (XV-15)**

Response	Control (input)	
	$\delta_a$	$\delta_r$
$p$	<b>0.14–9.0</b>	0.16–6.0
$r$	0.14–9.0	<b>0.6–9.0</b>
$a_y$	0.14–3.0	<b>0.14–10.0</b>
$\beta$	0.14–3.0	<b>0.14–5.5</b>

## STATE-SPACE MODEL IDENTIFICATION

381

M Matrix Structure				G Matrix Structure		
V	1.00	P	0	R	0	PHI
P	0	1.00	0	0	* YDA	* YDR
R	0	0	1.00	0	* LDA	* LDR
PHI	0	0	0	1.00	* NDA	* NDR
F Matrix Structure				Tau Matrix Structure		
V	* YV	P	* YP	R	* YR	PHI
			+ 24.5		- 307.	32.07
P	* LV		* LP		* LR	0
R	* NV		* NP		* NR	0
PHI	0		1.0		0.0799	0
					BETA	AIL
						RUD

\* Indicates a free derivative

@ indicates a term tied to a free derivative

Fig. 13.1 Identification model structure for cruise (XV-15).

Summary of free derivative terms					
Total	No. Free M Terms	No. Free F Terms	No. Free G Terms	No. Free Tau Terms	No. Free Sensor Terms
17	0	9	6	2	0
Observer Structure ( $\mathbf{H}_0 + \mathbf{H}_1 s$ )					
P	V 0.0	P 1.0	R 0.0	PHI 0.0	
R					
AY	0.0 + 1.0S	-24.5	0.31E+03	-32.07	
BETA	0.33E-02	0.0	0.0	0	
Active Transfer Functions					
	P / AIL		P / RUD		
	R / AIL		R / RUD		
	AY / AIL		AY / RUD		
	BETA / AIL		BETA / RUD		
All Sensor Coefficients are at default values					
No parameter constraints have been defined					

Fig. 13.2 Identification model structure for cruise (XV-15).

velocities, gravity, and kinematics show up as fixed aspects of the model. For example, the partial derivative  $\partial \dot{v} / \partial r = [Y_r - U_0]$  is implemented with the aerodynamic contribution  $Y_r$  as a free identification parameter (denoted with a \* in Fig. 13.1) and a fixed value for the trim velocity ( $U_0 = 306.7$  ft/s). It should be remembered that any small offsets in the assumed trim condition (i.e., an error in the value of  $U_0$  in this case) will be absorbed in the free term of the partial derivative  $Y_r$ . All of the transfer functions have been included in the cost function (per Table 13.3), and there are no explicit sensor dynamics (no use of the transfer-function model structure, Sec. 12.2.2) and no parameter constraints.

### 13.8.2 Initial Identification Results and Model Structure Reduction

The initial guess values for the identification parameters are obtained from the linearized output of the XV-15 GTR simulation program as determined using numerical perturbations.<sup>192</sup> An overview of the model is also provided by Churchill and Dugan.<sup>130</sup> Full-scale wind-tunnel data of the XV-15 aircraft were obtained in the NASA Ames 40 × 80 ft wind tunnel and form the basis for the simulation model. The GTR simulation model (GTRV170) tracks the flight data well (Figs. 13.3) and provides a close initial guess in this case ( $J_{ave} = 130.1$ , as seen later in Table 13.9). In most cases, such accurate initial guesses are neither available nor necessary. The somewhat discretized nature of the response plots in some cases reflects the fact that only 20 frequency points were used in the identification [ $n_\omega = 20$  in Eq. (12.20)]. Note also that the only frequency points used in the identification are those for which the coherence is greater than the cutoff value  $(\gamma_{xy}^2)_{cut} = 0.4$ .

The converged initial identification result (V170M1) is presented in Table 13.4, and the corresponding cost functions are shown in the V170M1 column of Table 13.5. The parameter values and cost functions are quite robust for wide variations in the choice of the initial parameter values (**Problems 13.3 and 13.7**). The initial model structure converges to an excellent average cost function ( $J_{ave} = 32.8$ , Table 13.5), with a maximum individual cost function of ( $J_{max} = 77.6$ ). These are well within the suggested guidelines of Eqs. (12.23) and Eq. (12.24), respectively.

The accuracy analysis results for the initial model structure are also shown in Table 13.4. We note again that the values of the insensitivities and Cramér–Rao bounds meet the relationship of Eq. (12.44). The derivative  $Y_{\delta_a}$  has a large insensitivity (58.3%) and therefore is not important in matching the flight data. This conclusion can be confirmed by looking at the effect of variations in this parameter on the frequency-response plots (**Problem 13.11**). Because the insensitivity for  $Y_{\delta_a}$  is well in excess of the guideline (10%), it is dropped from the model structure. The model is then reconverged (V170M2) with the parameter results shown in Table 13.6 and cost functions in the V170M2 column of Table 13.5.

The V170M2 model shows little change in the average cost function ( $J_{ave} = 32.9$ ). Now the response coupling derivative  $L_r$  is seen in Table 13.6 to have the largest insensitivity (26.0%), still well in excess of the guideline, and so this parameter is now also dropped from the model structure. The model structure with  $L_r$  dropped is reconverged, and the result is V170M3. As shown in Table 13.5, the average cost function for V170M3 ( $J_{ave} = 33.3$ ) is only slightly higher than

Table 13.4 Initial identification results for cruise (XV-15)<sup>a,b,c</sup>

Engineering symbols	CIFER® mnemonic	Value (V170M1)	CR, %	Insens, %
<b><i>F-matrix</i></b>				
$Y_v$	YV	-0.2805	3.64	1.20
$Y_p$	YP	-2.203	33.00	10.34
$Y_r$	YR	15.23	11.91	4.02
$g \cos \Theta_0$	G	32.07 <sup>d</sup>	—	—
$L_v$	LV	-8.003E-03	4.44	1.34
$L_p$	LP	-0.6896	6.12	1.25
$L_r$	LR	-0.09566	79.36	24.63
$N_v$	NV	7.333E-03	2.97	0.92
$N_p$	NP	-0.2280	7.69	2.24
$N_r$	NR	-0.9796	5.11	1.54
<b><i>G-matrix</i></b>				
$Y_{\delta_a}$	YDA	-0.02825	159.1	58.31
$Y_{\delta_r}$	YDR	-0.2165	8.42	3.57
$L_{\delta_a}$	LDA	-0.07927	4.53	0.99
$L_{\delta_r}$	LDR	-6.554E-03	11.88	4.25
$N_{\delta_a}$	NDA	-0.02193	4.74	1.59
$N_{\delta_r}$	NDR	0.02235	3.23	1.03
<b><i>Time delays</i></b>				
$\tau_a$	AIL	0.09049	11.73	5.36
$\tau_r$	RUD	0.03078	27.24	12.44

<sup>a</sup>Case name: V170M1; Case ID: converged initial model.

<sup>b</sup>All results are in English units.

<sup>c</sup>Control deflections in degrees.

<sup>d</sup>Fixed parameters in model structure.

previously obtained for V170M2, and there are no significant jumps in the individual cost functions. The converged model is shown in Table 13.7. The insensitivities are nearly within the guidelines, and so we turn our attention to the Cramér–Rao values.

As seen in Table 13.7, the parameter  $Y_p$  has the largest Cramér–Rao bound (31.3%), which is somewhat above the guideline (20%). The associated normalized confidence ellipsoid ( $\bar{\Theta}_{\text{CR}_{Y_p}}$ ), shown in Table 13.8, indicates that the elevated Cramér–Rao value results from some correlation (0.6) between the roll-rate derivatives  $Y_p$  and  $L_p$ . The results also show some correlation with several other derivatives. Next we try eliminating the  $Y_p$  parameter from the model structure and reconverge the model (V170M4); the associated cost function results are shown in Table 13.5. There is a jump both in the reconverged average cost function ( $\Delta J_{\text{ave}} = 2.5$ ) and in several of the individual cost functions in the range of

**Table 13.5 Cost functions for cruise model identification (XV-15)**

Engineering symbols	CIFER® mnemonics	V170M1	V170M2	V170M3	V170M4
$p/\delta_a$	P/AIL	37.5	37.4	36.3	40.5
$r/\delta_a$	R/AIL	77.6	78.1	79.3	81.6
$a_y/\delta_a$	AY/AIL	20.7	20.9	21.7	32.9
$\beta/\delta_a$	BETA/AIL	40.2	39.8	41.0	36.8
$p/\delta_r$	P/RUD	39.2	39.5	39.2	39.6
$r/\delta_r$	R/RUD	18.9	18.9	18.3	20.4
$a_y/\delta_r$	AY/RUD	12.4	12.4	12.0	16.1
$\beta/\delta_r$	BETA/RUD	16.2	16.5	18.4	18.1
$J_{ave}$	Average	32.8	32.9	33.3	35.8

Case name: V170M1; Case ID: Converged initial model.

Case name: V170M2; Case ID: DROP YDA.

Case name: V170M3; Case ID: DROP LR.

Case name: V170M4; Case ID: DROP YP.

**Table 13.6 Intermediate model (V170M2) for cruise (XV-15)<sup>a</sup>**

Engineering symbols	CIFER® mnemonic	Value (V170M2)	CR, %	Insens, %
<b><i>F-matrix</i></b>				
$Y_v$	YV	-0.2802	3.64	1.20
$Y_p$	YP	-1.962	31.34	11.62
$Y_r$	YR	15.54	11.35	3.97
$g \cos \Theta_0$	G	32.07 <sup>b</sup>	—	—
$L_v$	LV	-8.004E-03	4.43	1.35
$L_p$	LP	-0.6883	6.12	1.25
$L_r$	LR	-0.09110	83.04	26.00
$N_v$	NV	7.324E-03	2.97	0.91
$N_p$	NP	-0.2281	7.73	2.24
$N_r$	NR	-0.9832	5.09	1.53
<b><i>G-matrix</i></b>				
$Y_{\delta_a}$	YDA	0.000 <sup>c</sup>	—	—
$Y_{\delta_r}$	YDR	-0.2178	8.34	3.56
$L_{\delta_a}$	LDA	-0.07907	4.52	0.99
$L_{\delta_r}$	LDR	-6.562E-03	11.87	4.25
$N_{\delta_a}$	NDA	-0.02188	4.74	1.60
$N_{\delta_r}$	NDR	0.02234	3.23	1.03
<b><i>Time delays</i></b>				
$\tau_a$	AIL	0.09024	11.74	5.37
$\tau_r$	RUD	0.03101	27.04	12.35

<sup>a</sup> Case name: V170M2; Case ID: DROP YDA.

<sup>b</sup> Fixed parameters in model structure.

<sup>c</sup> Eliminated from model structure.

**Table 13.7 Final identified model and GTR simulation for cruise (XV-15)<sup>a,b</sup>**

Engineering symbols	CIFER® mnemonic	Value (V170M3)	CR, %	Insens,%	GTRV170
<i>F-matrix</i>					
$Y_v$	YV	-0.2797	3.64	1.19	-0.2424
$Y_p$	YP	-1.984	31.32	11.54	0.7883
$Y_r$	YR	16.44	9.65	3.76	7.794
$g \cos \Theta_0$	G	32.07 <sup>c</sup>	—	—	32.07 <sup>c</sup>
$L_v$	LV	-8.119E-03	4.23	1.32	-6.605E-03
$L_p$	LP	-0.6780	6.03	1.27	-0.7628
$L_r$	LR	0.000 <sup>d</sup>	—	—	-0.1138
$N_v$	NV	7.240E-03	2.85	0.92	8.484E-03
$N_p$	NP	-0.2308	7.57	2.22	-0.2206
$N_r$	NR	-0.9759	5.05	1.54	-0.9246
<i>G-matrix</i>					
$Y_{\delta_a}$	YDA	0.000 <sup>d</sup>	—	—	-1.400E-03
$Y_{\delta_r}$	YDR	-0.2173	8.35	3.57	-0.1793
$L_{\delta_a}$	LDA	-0.07775	4.27	1.00	-0.08314
$L_{\delta_r}$	LDR	-7.024E-03	10.09	4.03	-4.810E-03
$N_{\delta_a}$	NDA	-0.02166	4.66	1.61	-0.01940
$N_{\delta_r}$	NDR	0.02213	3.14	1.03	0.02920
<i>Time delays</i>					
$\tau_a$	AIL	0.08920	11.84	5.43	0.000
$\tau_r$	RUD	0.03276	25.10	11.69	0.000

<sup>a</sup>Case name: V170M3; Case ID: DROP LR.

<sup>b</sup>All results in English units.

<sup>c</sup>Fixed parameters in model structure.

<sup>d</sup>Eliminated from model structure.

**Table 13.8 Confidence ellipsoid for parameter  $Y_p$  with largest Cramér–Rao bound (V170M3)**

Engineering symbols	CIFER® mnemonics	$\bar{\Theta}_{\text{CR}_{Y_p}}$
$Y_v$	YV	0.0674
$Y_p$	YP	1.0000
$Y_r$	YR	-0.0585
$L_v$	LV	0.2135
$L_p$	LP	0.6093
$N_v$	NV	-0.0673
$N_p$	NP	-0.2834
$N_r$	NR	0.0492
$Y_{\delta_r}$	YDR	-0.0765
$L_{\delta_a}$	LDA	0.2437
$L_{\delta_r}$	LDR	0.0212
$N_{\delta_a}$	NDA	0.2971
$N_{\delta_r}$	NDR	-0.0901
$\tau_a$	AIL	0.0438
$\tau_r$	RUD	-0.0695

Eqs. (12.52) and (12.53). Specifically, the cost function for  $a_y/\delta_a$  jumps by  $\Delta J = 11$ . So the previous model (V170M3), which retains  $Y_p$ , is taken as the final identification result. The final identification parameters can be varied about the converged values based on the Cramér–Rao bounds to see how these metrics relate to the frequency-response error behavior (**Problem 13.12**).

### 13.8.3 Final Identification Results

The parameter results and accuracy metrics for the final identification model (V170M3) are shown in Table 13.7. Also shown in the table are the GTR simulation model values (GTRV170). The cost functions for the final identified model and the GTR simulation are listed in Table 13.9.

There is a good match for most of the derivatives, validating the primary aerodynamics and inertia simulation modeling for this flight condition. The seemingly large discrepancies in the derivatives  $Y_p$  and  $Y_r$  most likely reflect small errors in the assumed flight-test trim velocities ( $W_0$  and  $U_0$ , respectively) because from Eq. (13.13) it can be seen that  $\partial v/\partial p = Y_p + W_0$  and  $\partial v/\partial r = Y_r - U_0$ . The identified model shows substantial improvements compared to the simulation in all individual cost functions as well as the overall average cost  $J_{ave}$ .

The frequency responses of the final identified model and XV-15 simulation are compared with the flight data in Fig. 13.3. The identification results track the flight data very accurately, as expected from the low cost function. The simulation model is only modestly degraded, as reflected by the higher cost function. Overall, however, the simulation model is seen to be quite accurate, as would be expected, because it is largely based on full-scale wind-tunnel data.

The  $n$  eigenvalues  $\lambda_i$  of the identified model in standard state-space form [ $\mathbf{A}$ , Eq. (12.6)] are the *natural modes of motion* of the dynamic response. The associated eigenvectors  $\mathbf{v}_i$  show which state variables are dominant in each mode.

**Table 13.9 Cost functions for identification and GTR simulation models (XV-15, cruise)**

Engineering symbols	CIFER® mnemonics	V170M3 <sup>a</sup>	GTRV170 <sup>b</sup>
$p/\delta_a$	P/AIL	36.3	75.8
$r/\delta_a$	R/AIL	79.3	261.5
$a_y/\delta_a$	AY/AIL	21.7	222.9
$\beta/\delta_a$	BETA/AIL	41.0	158.7
$p/\delta_r$	P/RUD	39.2	51.9
$r/\delta_r$	R/RUD	18.3	123.9
$a_y/\delta_r$	AY/RUD	12.0	58.5
$\beta/\delta_r$	BETA/RUD	18.4	87.4
$J_{ave}$	Average	33.3	130.01

<sup>a</sup> Case name: V170M3; Case ID: DROP LR.

<sup>b</sup> Case name: GTRV170; Case ID: gtrsim v = 170.

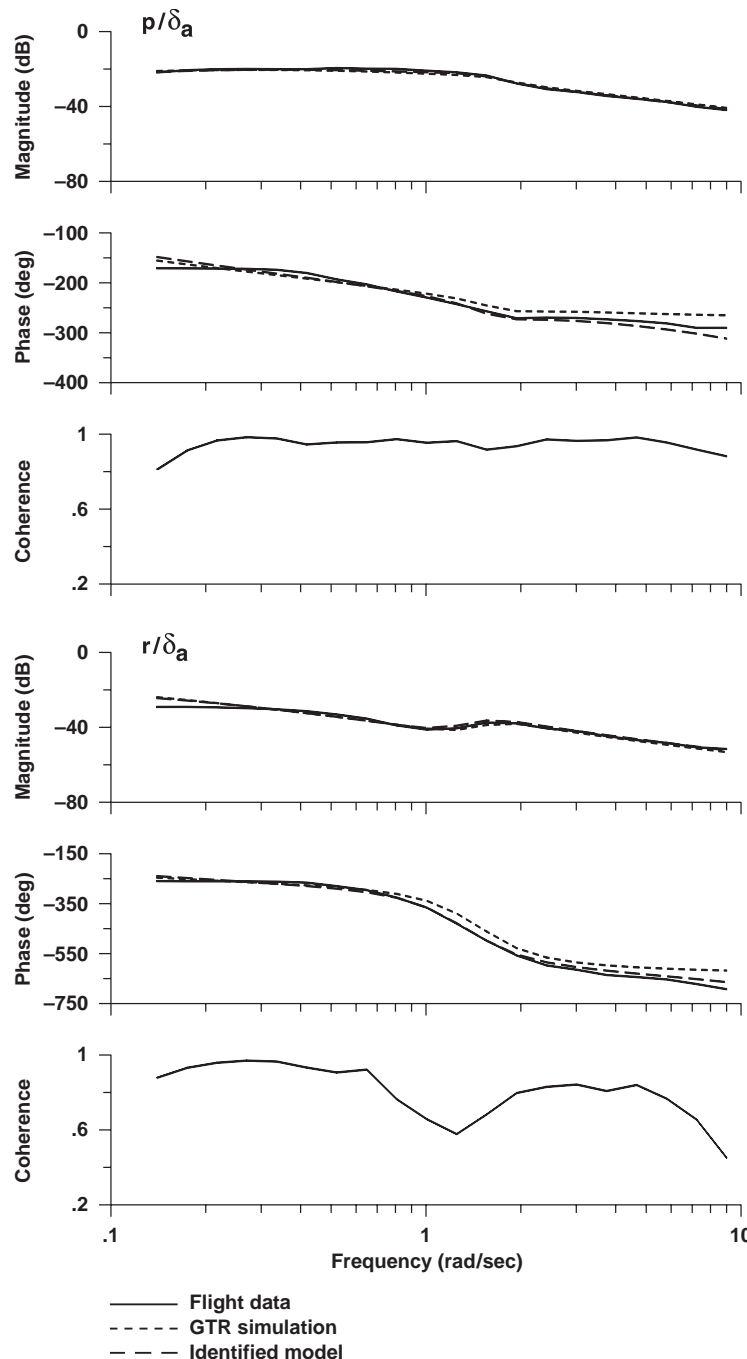


Fig. 13.3 GTR simulation and final identification models for cruise (XV-15).

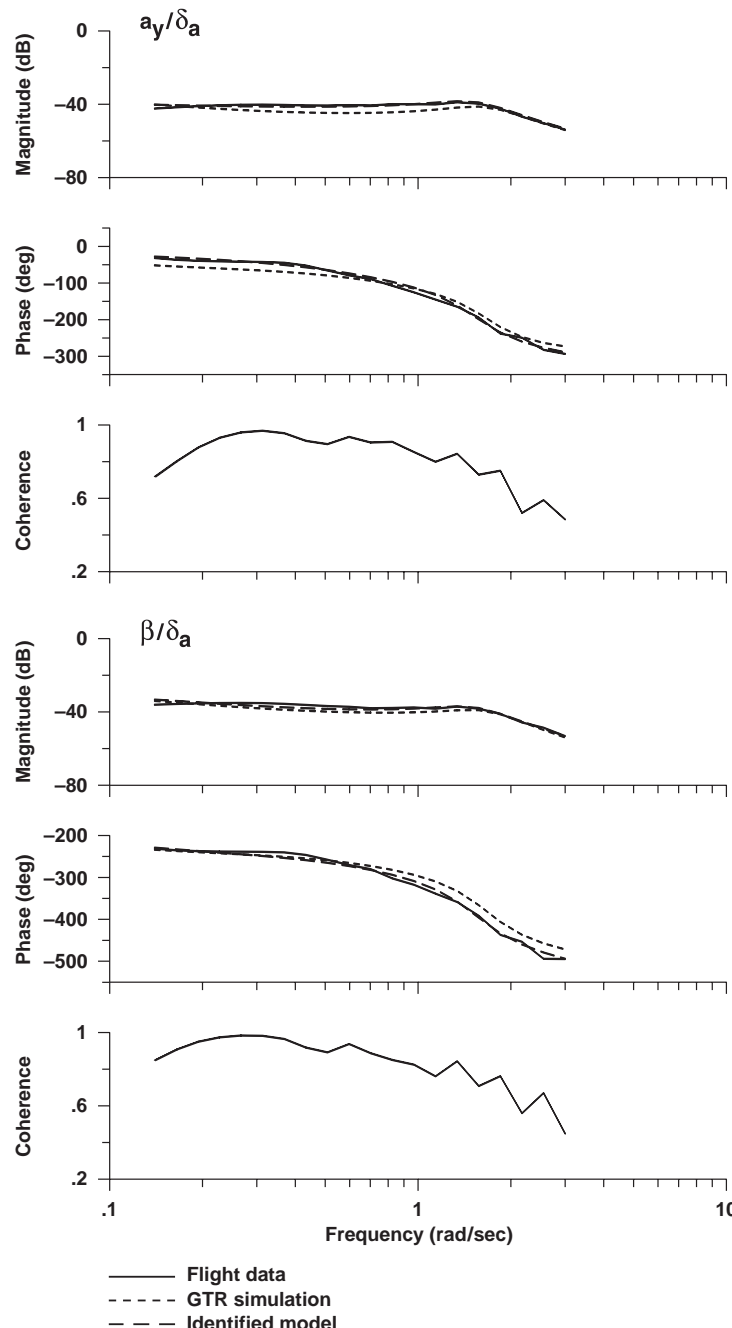


Fig. 13.3 GTR simulation and final identification model for cruise (XV-15) (continued).

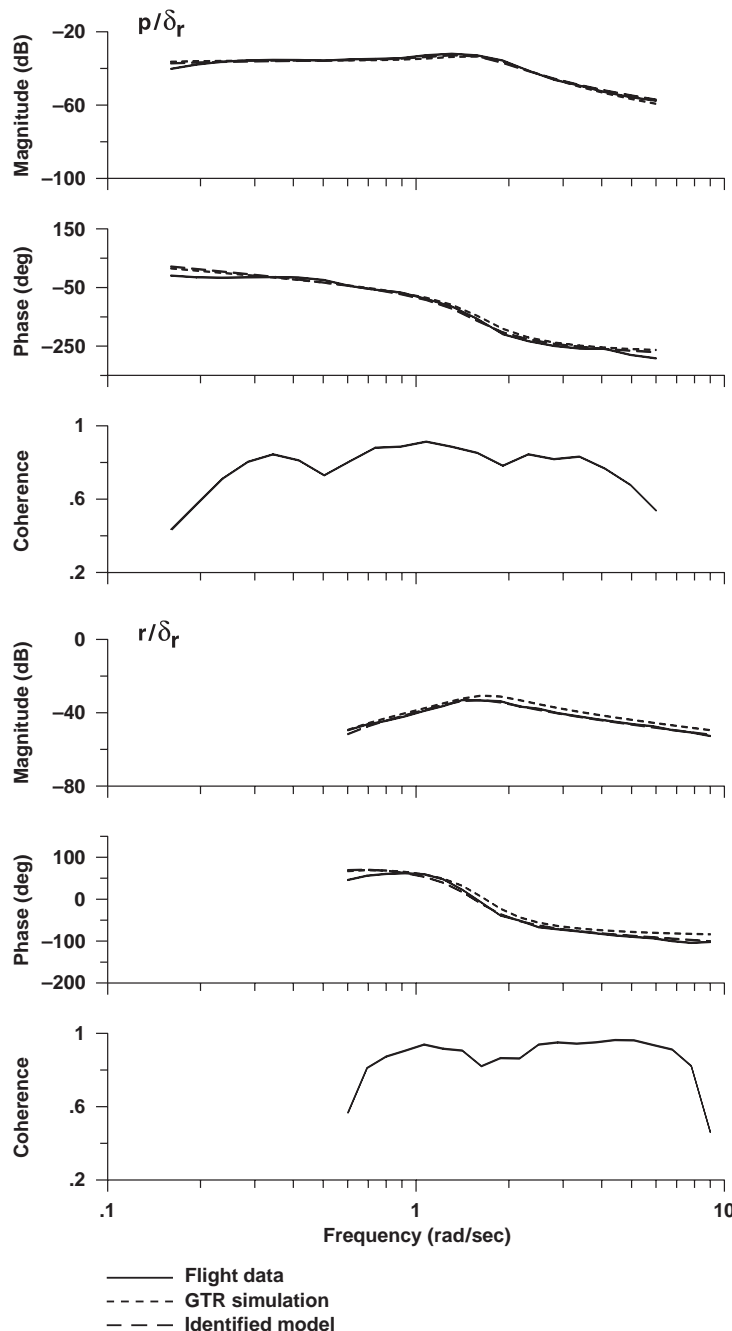


Fig. 13.3 GTR simulation and final identification model for cruise (XV-15) (continued).

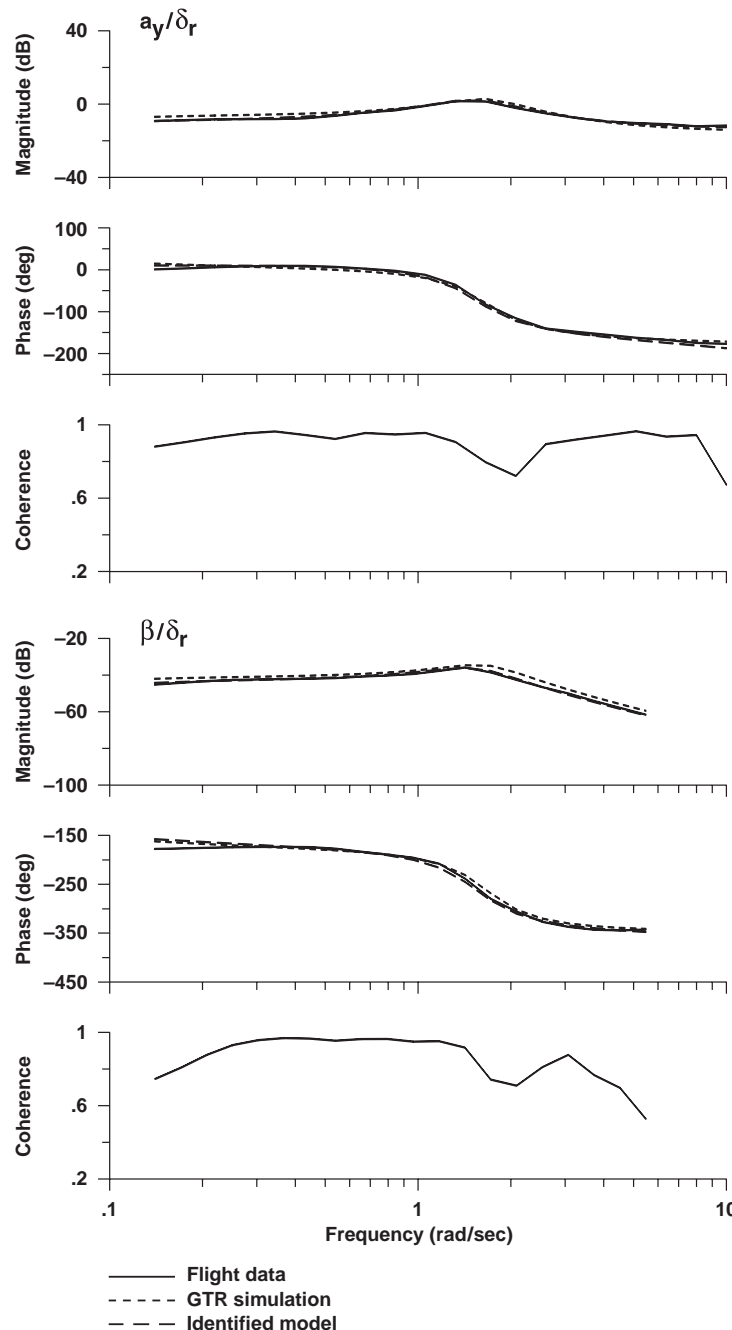


Fig. 13.3 GTR simulation and final identification model for cruise (XV-15) (continued).

These are determined from the solution of the eigenvalue-eigenvector problem<sup>104</sup>:

$$(\lambda_i \mathbf{I} - \mathbf{A}) \mathbf{v}_i = 0 \quad (13.64)$$

To aid in the interpretation of the eigenvector results, the state variables are scaled to more balanced units (e.g.,  $u, v, w \sim \text{ft/s}$ ;  $p, q, r \sim \text{deg/s}$ ;  $\phi, \theta \sim \text{deg}$ ). Finally, each eigenvector is normalized, so that the largest component is unity.

The eigenvalue and eigenvector results for the cruise model (V170M3) are shown in Tables 13.10 and 13.11, respectively. All of the eigenvalues have negative real parts, and so the dynamics are stable. Notice that the eigenvector components ( $v_{pi}, v_{\phi i}, v_{ri}$ ) corresponding to the angular states ( $p, \phi, r$ , respectively) for the  $i$ th eigenvalue ( $\lambda_i$ ) are related according to the Euler rate equation (13.55), so that

$$v_{pi} = \lambda_i v_{\phi i} - v_{ri} \tan \Theta_0; \quad i = 1, 2, 3, 4 \quad (13.65)$$

The lowest-frequency eigenvalue  $\lambda_1$  is associated with the spiral mode. This corresponds to the  $1/T_s$  pole in the transfer-function model of Eq. (11.26). The associated eigenvector shows that this mode is characterized by the aperiodic variation dominated by roll attitude and lateral velocity (sideslip). The roll convergence mode  $\lambda_2$  is an aperiodic response in roll rate [corresponding to  $1/T_r$  in Eq. (11.26)], with some sideslip contribution caused by Dutch-roll coupling. The Dutch-roll mode is periodic (so  $\lambda_3$  and  $\lambda_4$  are complex conjugates, as are the associated eigenvectors), and it involves lightly damped oscillations in sideslip, roll rate, and yaw rate. This corresponds to the complex  $[\zeta_{dr}, \omega_{dr}]$  mode in the transfer-function model in Eq. (11.26). The eigenvector for this mode shows that the roll and yaw-rate oscillations are equal in magnitude and opposite in phase. This characteristic can be seen in the time response to a rudder step input (Fig. 14.5).

The state-space identification results are based on a complete stability and control derivative model formulation that correctly accounts for the interrelationship between the transfer-function parameters. This is in contrast to the earlier LOES transfer-function model identification method that treats the poles and zeros as independent parameters. The close agreement of these models, as seen in the comparison of the eigenvalues of Table 13.10 with the denominator of Eq. (11.29), validates the LOES transfer-function fitting method widely used in handling-qualities analyses.

**Table 13.10 Eigenvalues of identified cruise model (XV-15):  
Eigenvalues ( $\lambda_i$ ) of  $[M_{\text{inverse}}][F]$**

	$(\lambda_i)_R$	$(\lambda_i)_I$	$\zeta_i$	$\omega_i$
$\lambda_1$	-0.1060	0.0000	—	—
$\lambda_2$	-0.9382	0.0000	—	—
$\lambda_3$	-0.4447	1.477	0.2883	1.543
$\lambda_4$	-0.4447	-1.477	0.2883	1.543

Table 13.11 Scaled eigenvectors for cruise model (XV-15)

(Real, Imag) [ $\zeta$ , $\omega_n$ ]	Eigenvalues			
	$\lambda_1$	$\lambda_2$	$\lambda_3$	$\lambda_4$
States				
$v$	0.140	0.000	-0.523	0.000
$p$	-0.114	0.000	-0.936	0.000
$r$	0.0969	0.000	-0.0301	0.000
$\phi$	1.000	0.000	1.000	0.000

The *time vector diagram*<sup>56</sup> provides a useful illustration of the relative phasing and contribution of each term in the equations of motion for a selected modal response. For example, the unforced (i.e., controls fixed) yaw-rate response is obtained from Eq. (13.54) as

$$\dot{r} = N_v'v + N_p'p + N_r'r \quad (13.66)$$

Then we take the Laplace transform to obtain

$$sr - N_v'v - N_p'p - N_r'r = 0 \quad (13.67)$$

The time vector for the yaw rate  $r$  equation that is associated with the Dutch-roll mode is calculated from Eq. (13.67) by substituting the eigenvalue ( $s = \lambda_{dr} = \lambda_3$ ), the associated *unnormalized* eigenvector  $v_{dr}$ , and the identified values of the stability derivatives. Finally, the resulting time vector is normalized by the largest component.

As shown in Fig. 13.4, the plot of the time vector is a closed polygon and illustrates the balance of the inertial moment  $sr$  with the relative importance and phasing of each aerodynamic term in the unforced equation of motion (13.67).

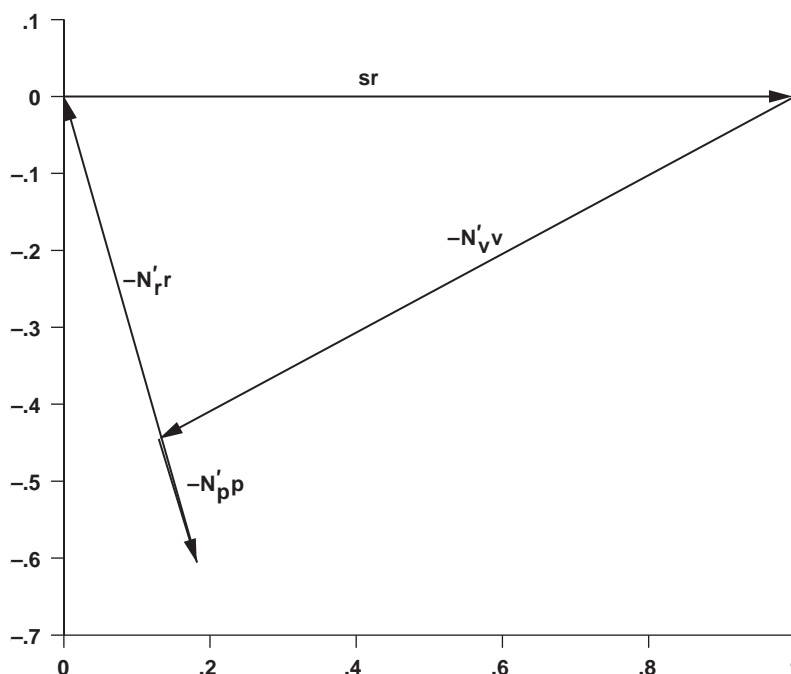


Fig. 13.4 Yaw-equation time vector for Dutch-roll mode.

The primary contributions are from  $-N_v'v$ ,  $-N_r'r$ , and a smaller contribution from  $-N_p'p$  that is out of phase with  $-N_r'r$ . Elimination of the roll-rate contribution leads to the decoupled two-DOF Dutch-roll approximation of Eq. (11.23).

### 13.9 Identification of Three-DOF Lateral/Directional Model for XV-15 in Hover

The identification of a stability and control derivative model for the three-DOF lateral/directional dynamics of the XV-15 in hover is demonstrated in this example.

#### 13.9.1 Model Structure

The equations of motion are the same ones used in the cruise example [Eqs. (13.52–13.55)]. The trim condition in hover is

$$U_0 = V_0 = W_0 = \Theta_0 = 0 \quad (13.68)$$

Analysis of the roll response measurements (**Problem 6.6**) shows a degradation in data consistency ( $p/\delta_a$  vs  $\phi/\delta_a$ ) at low frequency (0.14–0.5 rad/s). Full data reconstruction using SMACK (Sec. 6.1.1) was not possible because a third independent source of response information (e.g., GPS or Doppler radar velocity) was not available. However, in this frequency range the attitude response has improved coherence (as compared to the roll-rate response) and is therefore considered more reliable. So in this case the roll angle  $\phi$  was included in the measurement vector ( $\mathbf{y} = [v, p, r, a_y, \phi]^T$ ). As in cruise, the equivalent time delays (for aileron input  $\tau_a$  and rudder input  $\tau_r$ ) are included to account for unmodeled high-order dynamics.

The frequency-response table for the XV-15 for the hover flight condition is shown in Table 13.12. The information content of the data (up to about 9 rad/s) spans the frequency range of applicability for the three-DOF model (about 10 rad/s). Of special importance are the good frequency ranges for on-axis responses, shown again in bold, which ensure the accurate identification of the key flight-dynamics modes. Notice that the roll-rate response ( $p/\delta_a$ ) is only included for frequencies beyond 0.5 rad/s, because the lack of data consistency in the frequency range of 0.14–0.5 rad/s makes it impossible for an identified model to simultaneously track both the roll-rate and roll-attitude responses. In the mid-frequency range the roll-attitude and roll-rate responses ( $\phi/\delta_a$  and  $p/\delta_a$ ) are

**Table 13.12 Frequency-response ranges for hover (XV-15)**

Response	Control (input)	
	$\delta_a$	$\delta_r$
$v$	<b>0.14–5.5</b>	None
$p$	<b>0.5–9.0</b>	None
$r$	0.15–8.0	<b>0.14–8.0</b>
$a_y$	<b>0.14–9.0</b>	None
$\phi$	<b>0.14–8.0</b>	None

M Matrix Structure				G Matrix Structure		
	V	P	R	PHI	AIL	RUD
V	1.00	0	0	0	V	* YDA
P	0	1.00	0	0	P	* LDA
R	0	0	1.00	0	R	* NDA
PHI	0	0	0	1.00	PHI	0

F Matrix Structure				Tau Matrix Structure		
	V	P	R	PHI	*AIL	* RUD
V	* YV	* YP	YR	32.174	V	AIL
P	* LV	* LP	LR	0	P	AIL
R	* NV	* NP	* NR	0	R	AIL
PHI	0	KIN	0	0	PHI	AIL

\* Indicates a free derivative

@ Indicates a term tied to a free derivative

**Fig. 13.5 Identification model structure for hover (XV-15).**

identical, and both show the same high coherence. Then at high frequencies the improved signal-to-noise ratio of the roll-rate response provides better coherence.

The off-axis responses to rudder input ( $p/\delta_r$  and  $a_y/\delta_r$ ) display no acceptable coherence and therefore are dropped from the table. This is as expected for the tilt-rotor configuration, where yaw control (Fig. 3.5) generates a pure yawing moment in hover. Following the procedure in Sec. 13.5.3, the associated control and angular response derivatives ( $L_{\delta_r}$ ,  $L_r$ ,  $Y_{\delta_r}$ ,  $Y_r$ ) are dropped from the initial model structure and fixed at zero. The reduced initial model structure shown in Figs. 13.5 and 13.6 contains seven free stability derivatives in  $F$ , four free control derivatives in  $G$ , and two time delays in  $\tau$ .

### 13.9.2 Initial Identification Results and Model Structure Reduction

The initial values for the identification parameters are obtained again from the linearized output of the XV-15 simulation model as determined using numerical perturbations (listed in Table 13.13). The GTR simulation model (GTRV0) tracks the flight data fairly well (Fig. 13.7) for the responses  $v/\delta_a$ ,  $p/\delta_a$ ,  $\phi/\delta_a$ , and  $r/\delta_r$ , but is degraded for the responses  $a_y/\delta_a$  and  $r/\delta_a$ . The initial guesses for the parameter values, as obtained from the simulation model, results in a very high cost function of  $J_{ave} = 2717.0$  (Table 13.13), which is reflected in the discrepancies in the frequency-response plots. These clearly show that the simulation model is not as accurate in hover as was the case for the cruise condition.

Despite the poor initial guess, a fully converged identification solution (HVMODM1) is achieved in 239 iterations. The average cost function is  $J_{ave} = 97.1$ , as shown in Table 13.13. The associated accuracy analysis shows that the aileron time delay  $\tau_a$  has the largest insensitivity (233%) and is therefore dropped from the model structure. As expected for the large insensitivity, dropping

Summary of free derivative terms					
Total	No. Free M Terms	No. Free F Terms	No. Free G Terms	No. Free Tau Terms	No. Free Sensor Terms
13	0	7	4	2	0
Observer Structure ( $H_0 + H_1 s$ )					
	V	P	R	PHI	
V	1.0	0.0	0.0	0.0	
P	0.0	1.0	0.0	0.0	
R	0.0	0.0	1.0	0.0	
AY	0.0 + 1.0S	0.0	0.0	-32.174	
PHI	0.0	0.0	0.0	1.0	
Active Transfer Functions					
	V / AIL				
	P / AIL				
	R / AIL		R / RUD		
	AY / AIL				
	PHI / AIL				
All Sensor Coefficients are at default values					
No parameter constraints have been defined					

Fig. 13.6 Identification model structure for hover (XV-15).

 Table 13.13 Cost functions for identification and GTR simulation models (XV-15, hover)<sup>a</sup>

Engineering symbols	CIFER® mnemonics	HV MOD M1	HV MOD M2	HV MOD M3	HV MOD M4	GTR V0
$v/\delta_a$	V/AIL	139.1	139.1	139.0	138.2	235.8
$p/\delta_a$	P/AIL	70.6	71.1	71.1	72.2	54.7
$r/\delta_a$	R/AIL	78.9	79.3	81.2	97.5	5541
$a_y/\delta_a$	AY/AIL	109.4	108.8	108.9	111.1	10201
$\phi/\delta_a$	PHI / AIL	122.5	122.4	122.4	120.7	129.6
$r/\delta_r$	R/RUD	62.1	62.1	67.4	73.0	139.3
$J_{ave}$	Average	97.1	97.1	98.3	102.1	2717

<sup>a</sup>Case name: HVMODM1; Case ID: GTRSIM CONVERGED.

Case name: HVMODM2; Case ID: DROP TAU-AIL.

Case name: HVMODM3; Case ID: DROP TAU-RUD.

Case name: HVMODM4; Case ID: DROP NP.

Case name: GTRV0; Case ID: GTRSIM model.

**Table 13.14** Final identified model and GTR simulation for hover (XV-15)<sup>a,b</sup>

Engineering symbols	CIFER® mnemonics	HVMODM3 value	CR, %	Insens, %	GTRV0 value
<i>F-matrix</i>					
$Y_v$	YV	-0.09755	6.65	2.52	-0.02060
$Y_p$	YP	-1.489	12.78	5.71	-1.736
$Y_r$	YR	0.000 <sup>c</sup>	—	—	-0.6140
$g \cos \Theta_0$	G	32.17 <sup>d</sup>	—	—	32.17 <sup>d</sup>
$L_v$	LV	-4.374E-03	5.38	1.24	-3.700E-03
$L_p$	LP	-0.2365	15.41	5.44	-0.4270
$L_r$	LR	0.000 <sup>c</sup>	—	—	0.1031
$N_v$	NV	7.152E-04	7.67	1.80	1.300E-03
$N_p$	NP	0.03862	29.86	10.64	0.1672
$N_r$	NR	-0.1416	13.17	5.54	-0.02550
	KIN	1.000 <sup>d</sup>	—	—	1.000 <sup>d</sup>
<i>G-matrix</i>					
$Y_{\delta_a}$	YDA	-0.04523	5.83	2.79	8.470E-03
$Y_{\delta_r}$	YDR	0.000 <sup>c</sup>	—	—	0.02940
$L_{\delta_a}$	LDA	-0.05777	2.41	0.91	-0.05960
$L_{\delta_r}$	LDR	0.000 <sup>c</sup>	—	—	1.890E-03
$N_{\delta_a}$	NDA	5.910E-03	5.13	2.06	5.190E-03
$N_{\delta_r}$	NDR	0.01187	4.58	2.14	0.01240
<i>Time delays</i>					
$\tau_a$	AIL	0.000	—	—	0.000
$\tau_r$	RUD	0.000	—	—	0.000

<sup>a</sup> Case name: HVMODM3; Case ID: Drop TAU = RID.

Case name: GTRV0; Case ID: GTRSIM model.

<sup>b</sup> All results in English units.

<sup>c</sup> Eliminated from model structure.

<sup>d</sup> Fixed parameters in model structure.

this derivative results in no change in the reconverged cost function (HVMODM2, Table 13.13). Now the rudder time delay  $\tau_r$  has the largest insensitivity (26%) and is dropped from the model structure. The reconverged model (HVMODM3) shows only a small increase in the cost function ( $J_{ave} = 98.3$ ). The identification results and accuracy metrics for this model are given in Table 13.14.

All insensitivities are now satisfactory, and so we turn our attention now to the Cramér–Rao bounds. As seen in Table 13.14 for the HVMODM3 model, the coupling response derivative  $N_p$  has a satisfactory insensitivity and a somewhat elevated Cramér–Rao bound (29.9%). The associated confidence ellipsoid indicates this is caused by a high correlation (0.79) with the derivative  $N_v$ . Based on these results, we next drop the  $N_p$  parameter from the model structure. Now, however, the reconverged model (HVMODM4, Table 13.13) shows a jump in both the average cost function ( $\Delta J_{ave} = 3.8$ ) and the cost function for the  $r/\delta_a$  response

( $\Delta J = 16.3$ ). Therefore the derivative  $N_p$  must be retained in the model structure (HVMODM3), and the identification is now complete.

### 13.9.3 Final Lateral / Directional Model in Hover

The parameter results and accuracy metrics for the final identification model (HVMODM3) are listed in Table 13.14. There is a fairly significant level of yaw coupling with roll input  $N_{\delta_a}$ . This arises because the differential prop-rotor thrust command used to command a roll moment also produces a torque split—and thus a yawing moment. The pilot crossfeed  $G_{CF}$  that is needed to maintain a fixed heading during lateral maneuvering in hover is approximately

$$G_{CF} = -\left(\frac{N_{\delta_a}}{N_{\delta_r}}\right) = -0.50 \text{ deg-rud/deg-ail} \quad (13.69)$$

This high level of required piloted crossfeed probably contributed to the poor SCAS-off handling qualities for lateral translation in hover.<sup>193</sup>

The identification results are also compared with the simulation parameters in Table 13.14. There are considerable discrepancies in several of the stability and control derivatives for the simulation model, as reflected in the large differences in the cost functions (Table 13.13). Direct comparisons of stability and control derivatives identified from flight tests with values identified from simulation math models can be used to derive correction factors for significantly improving the model fidelity. For example, the correction to the rolling moment equation is of the form

$$L_{\text{corrected}} = L_{\text{original}} + [(L_p)_{\text{flight}} - (L_p)_{\text{sim}}]p + [(L_{\delta_a})_{\text{flight}} - (L_{\delta_a})_{\text{sim}}]\delta_a + \dots \quad (13.70)$$

where  $L_{\text{original}}$  denotes the rolling moment as produced by the original nonlinear simulation equations. The identification method provides a systematic and accurate approach to determining these correction factors that are routinely used by the simulator industry to improve dynamic fidelity.

The frequency responses for the final identification model are compared with the flight data and the six-DOF simulation model in Fig. 13.7. The large mismatches in the simulation responses ( $a_y/\delta_a$  and  $r/\delta_a$ ) are substantially improved in the identification result, as reflected in the much reduced associated cost functions. The sign error in the GTR simulation model control derivative  $Y_{\delta_a}$  is responsible for the large phase error in the lateral acceleration response  $a_y/\delta_a$ , whereas the error in the simulation response coupling derivatives  $N_y$  and  $N_p$  is responsible for the large error in the coupling response  $r/\delta_a$ .

The eigenvalues of the identified hover model are shown in Table 13.15. The low-frequency stable aperiodic mode  $\lambda_1$  is associated with the decoupled damped yaw response and has a frequency that corresponds to the damping derivative  $N_r$ . The remaining three eigenvalues ( $\lambda_2, \lambda_3, \lambda_4$ ) constitute the *hovering cubic* for the lateral/directional dynamics and involve lateral translation and roll motion (a lateral phugoid). The unstable quadratic pair ( $\lambda_2, \lambda_3$ ) has a period of oscillation  $T = 2\pi/\omega_n = 13.5$  s, which is common to hovering V/STOL aircraft (e.g.,

## STATE-SPACE MODEL IDENTIFICATION

399

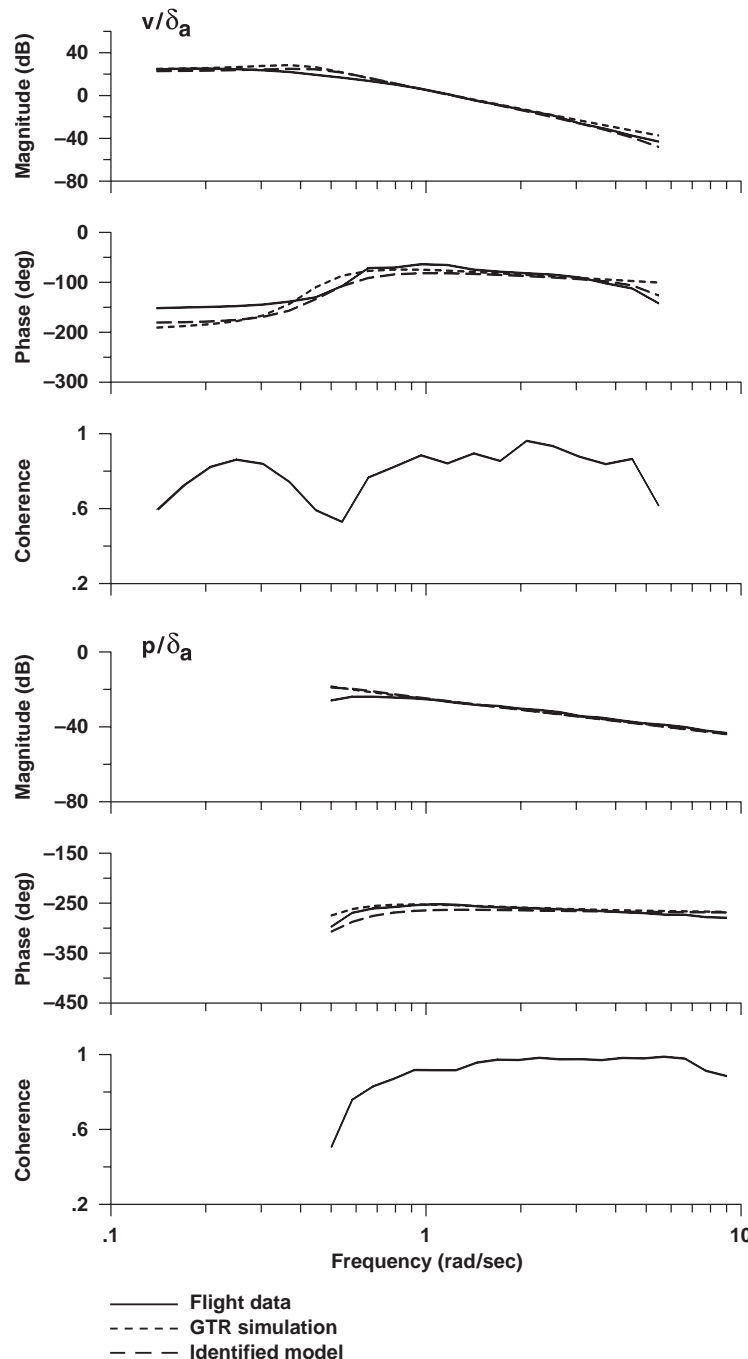


Fig. 13.7 GTR simulation and final identification model for hover (XV-15).

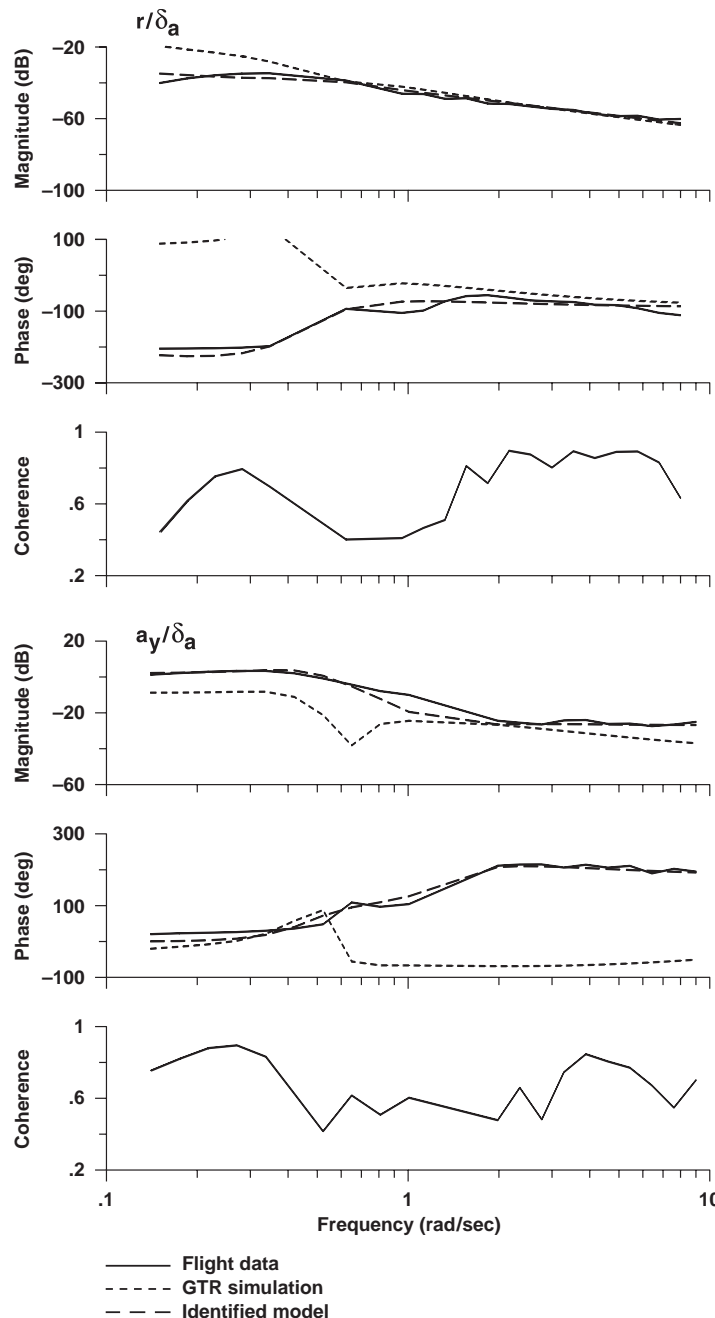


Fig. 13.7 GTR simulation and final identification model for hover (XV-15) (continued).

## STATE-SPACE MODEL IDENTIFICATION

401

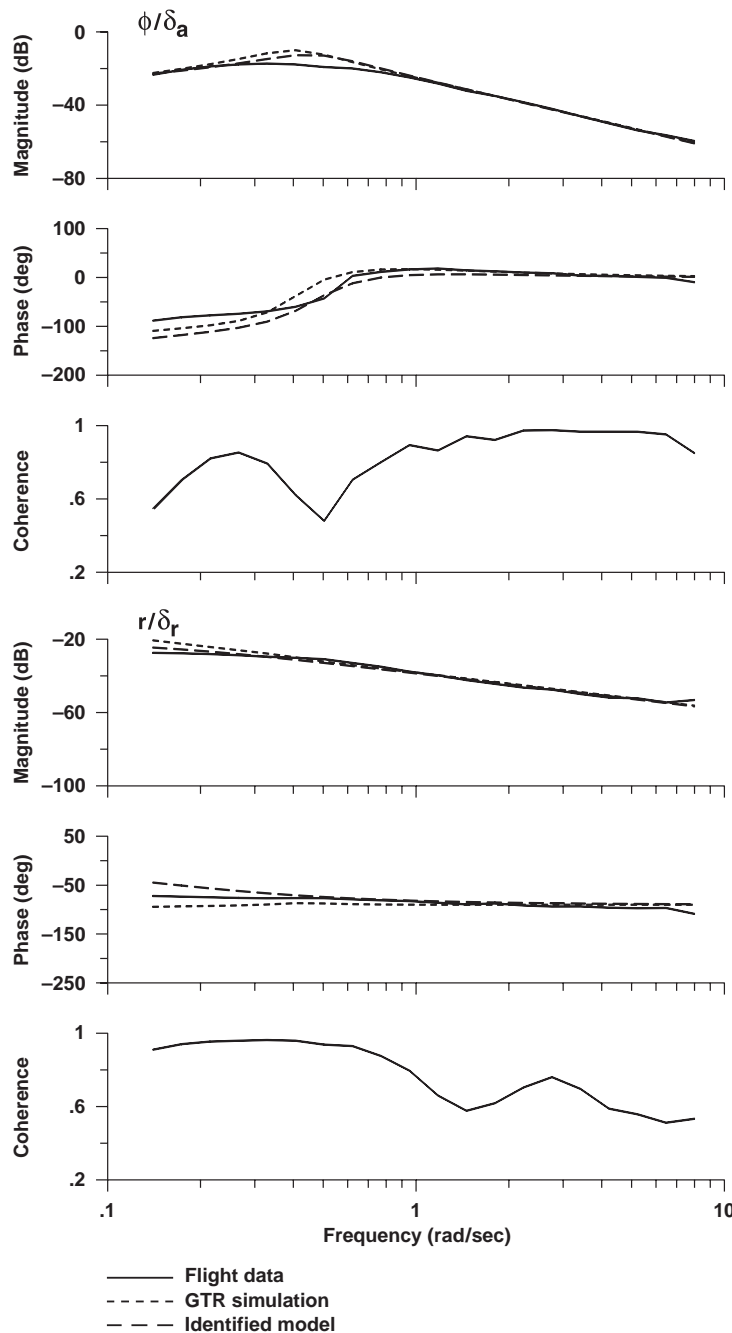


Fig. 13.7 GTR simulation and final identification model for hover (XV-15) (continued).

**Table 13.15 Eigenvalues of identified hover model (XV-15):  
Eigenvalues ( $\lambda_i$ ) of  $[M_{\text{inverse}}][F]$**

	$(\lambda_i)_R$	$(\lambda_i)_I$	$\zeta_i$	$\omega_i$
$\lambda_1$	-0.1416	0.0000	—	—
$\lambda_2$	0.1559	-0.4400	-0.3339	0.4668
$\lambda_3$	0.1559	0.4400	-0.3339	0.4668
$\lambda_4$	-0.6458	0.0000	—	—

Ref. 56) and helicopters.<sup>163</sup> The positive real part of these eigenvalues  $\lambda_R = 0.156$  indicates that disturbances in the states will double in amplitude in a duration of

$$t_{\text{double}} = \left( \frac{0.693}{\lambda_R} \right) = 4.44 \text{ s} \quad (13.71)$$

This falls in the level 3 region (“deficiencies require improvement”) of the ADS33E<sup>4</sup> handling-qualities requirements and is probably the primary cause of the poor reported handling qualities for the SCAS-off lateral flight maneuvers.<sup>193</sup> The stable aperiodic roll mode  $\lambda_4$  is at a lower frequency than for typical helicopters, owing to the high roll inertia of the tilt-rotor configuration.

### 13.10 Accurate Determination of Stability and Control Derivatives from Nonlinear Simulation Using System Identification

Detailed flight-control design efforts are based on very complex high-order and nonlinear simulation models. Force and moment descriptions are developed for each of the aircraft elements, such as the wings or rotors, propulsion system, and flight-control systems, based on wind-tunnel look-up tables, component bench-test data, and analytical theory. The simulation of multiple rigid-body systems or flexible bodies involves sets of dynamic equations of motion linked by constraint conditions. In many simulations these sets of equations are numerically integrated in serial form to reduce the complexity of deriving a fully coupled multibody simulation. The distributed or serial nature of these complex simulations thus might preclude the extraction of an integrated high-order linear model of the fully coupled system that is needed for accurate control design studies. Also, when the simulation models include control system nonlinear elements such as deadzone, hysteresis, saturation, and even Boolean logic, the numerical perturbation methods will often give the wrong result.

Even when the simulation architecture allows for the direct extraction of higher-order linear models using classical numerical perturbation methods, the assumption of independent perturbation results in incorrect phasing of the state variables within the multidimensional look-up tables. For example, the look-up table for aerodynamic pitching moment might depend both on angle of attack and pitch rate, so that  $C_{m_q} = f(\alpha)$ . Thus the correct determination of phugoid dynamics depends on maintaining representative phasing of  $q$  and  $\alpha$  within the linearization process. Selection of perturbation size can also strongly influence the linearization results. These effects can significantly degrade the predictive accuracy of the extracted

linear model. Much more accurate linear models are obtained by simulating piloted frequency-sweep inputs and extracting state-space models using system identification, just as if flight-test data had been used. The improvement obtained by "flying" the simulation model is especially apparent at low frequencies, where the dynamic responses are larger, and correct phasing of the representative motion variables for entry into the multidimensional look-up tables is important.

Engelland et al.<sup>194</sup> extracted accurate stability and control derivative models of a conceptual STOVL aircraft from a complex nonlinear off-line simulation to support control system design studies. The excitation input consisted of computer-generated frequency sweeps and white noise. Using the procedure described in Sec. 5.11.1, artificial feedback control loops were included to keep the aircraft flight condition near the reference trim point during the inputs. Starting from the perturbation model structure and derivative values, CIFER® was used to identify a more accurate six-DOF bare-airframe model.

The perturbation and identified derivatives are compared in Table 13.16. Longitudinal frequency responses of the two linear models are compared with the complete simulation responses in Fig. 13.8 for a flight condition of 120 kn. The control inputs are unique to V/STOL configurations and include the following:

**Table 13.16 Comparison of STOVL perturbation derivatives and identification results (from Engelland et al<sup>194</sup>)**

Engineering symbols	Perturb. value	CIFER® value	CR, %	Insens, %
$X_u$	-0.03471	-0.03602	5.66	2.29
$X_w$	0.03958	0.02852	6.91	2.84
$X_{\dot{w}}$	6.764E-04	6.764E-04 <sup>a</sup>	—	—
$X_q$	0.2451	0.2451 <sup>a</sup>	—	—
$X_{\delta_{PCD}}$	-7.690E-03	-8.303E-03	7.50	3.58
$X_{\delta_{PLA}}$	0.02270	0.02229	3.73	1.84
$X_{\delta_{\theta_N}}$	-0.5150	-0.5586	2.35	1.01
$Z_u$	-0.04596	-0.03312	13.62	4.58
$Z_w$	-0.3704	-0.2817	4.39	1.38
$Z_{\dot{w}}$	-0.01023	-0.01023 <sup>a</sup>	—	—
$Z_q$	-3.754	-3.754 <sup>a</sup>	—	—
$Z_{\delta_{PCD}}$	0.1389	0.1551	5.57	2.70
$Z_{\delta_{PLA}}$	-0.3800	-0.3305	2.25	1.02
$Z_{\delta_{\theta_N}}$	-0.01724	-0.03055	4.65	2.24
$M_u$	1.661E-04	-1.059E-03	6.02	1.75
$M_w$	1.222E-03	3.715E-03	5.26	1.28
$M_{\dot{w}}$	-1.286E-03	-1.286E-03 <sup>a</sup>	—	—
$M_q$	-0.4971	-0.6852	5.56	1.87
$M_{\delta_{PCD}}$	0.02494	0.02818	2.52	0.98
$M_{\delta_{PLA}}$	4.993E-04	4.993E-04 <sup>a</sup>	—	—
$M_{\delta_{\theta_N}}$	2.502E-04	4.953E-04	10.16	4.26

<sup>a</sup>Perturbation value used.

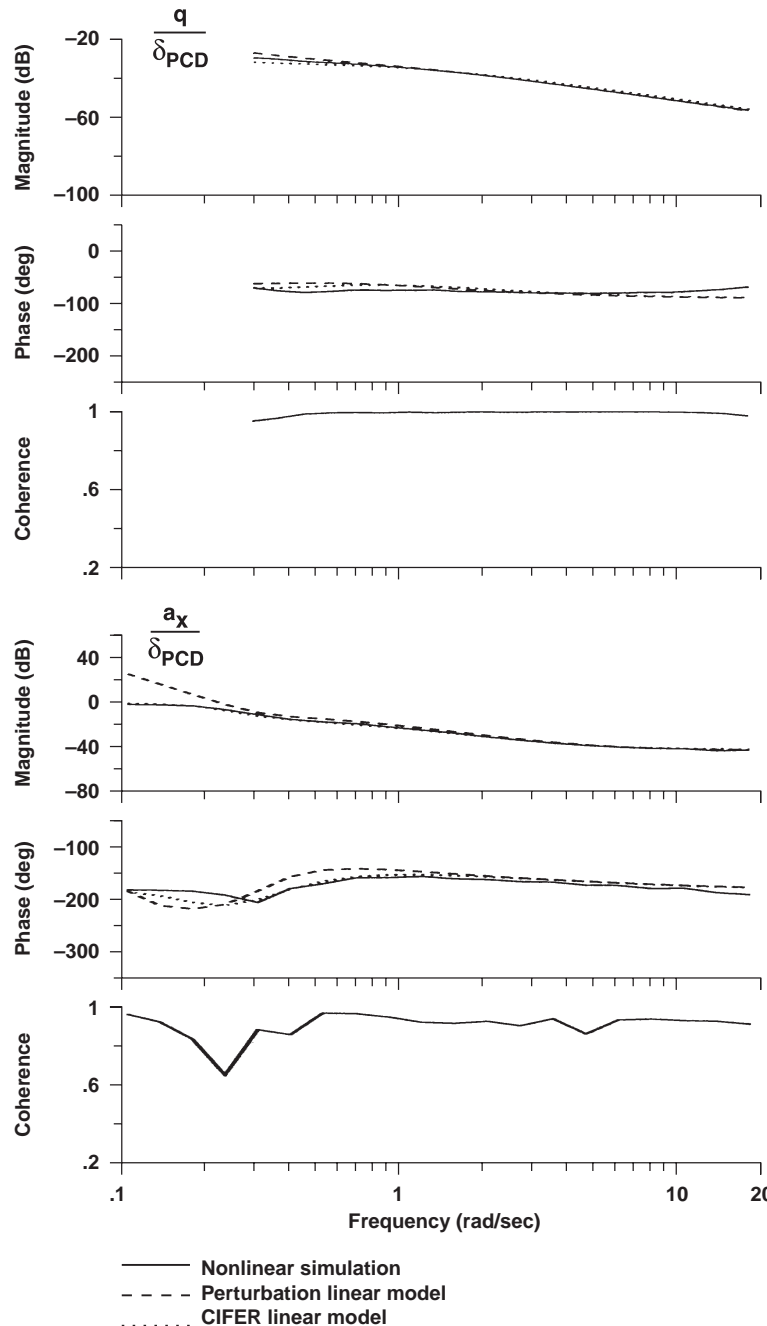


Fig. 13.8 Frequency-response comparison of STOVL perturbation and identification models (from Engelland et al<sup>194</sup>).

$\delta_{\text{PCD}}$  = total pitching-moment command to be distributed among the pitch control effectors (i.e., equivalent to  $\delta_{\text{lon}_{\text{mx}}}$  of Fig. 5.12)

$\delta_{\text{PLA}}$  = power lever angle that commands total thrust from the propulsion system (i.e., equivalent to  $\delta_{\text{col}_{\text{mx}}}$  of Fig. 5.12)

$\delta_{\theta_N}$  = total thrust deflection that is distributed appropriately among the thrust-deflecting nozzles

The linear model obtained using system identification is seen to be much more accurate than the numerical perturbation model for the on-axis pitch-rate response  $q/\delta_{\text{PCD}}$  at higher frequencies (note phase for 3.0–20 rad/s) and for the longitudinal-acceleration response  $a_x/\delta_{\text{PCD}}$  at lower frequencies (note magnitude and phase for 0.1–1.0 rad/s). The models are essentially identical in the midfrequency range. A time-domain comparison of the two linear models with the nonlinear simulation response is shown in Fig. 13.9 for a small (1-deg)

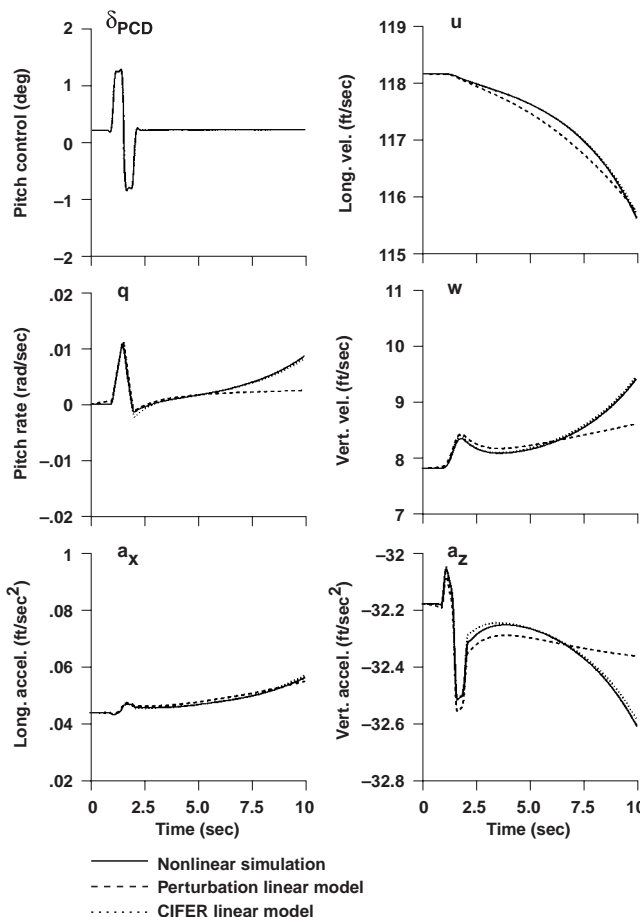


Fig. 13.9 Time-response comparison of STOVL perturbation and identification models (from Engelland et al<sup>194</sup>).

pitch-doublet input. The system identification model is seen to track the nonlinear behavior much more closely than the numerical perturbation model. The improvements are most noticeable for the long-term response (low-frequency) behavior, which is consistent with the frequency-response comparison of Fig. 13.8. The very close agreement of the system-identification model with the nonlinear simulation shows that the method of linear model extraction is much more important in this case than the nonlinear characteristics of the simulation.

Success in achieving maximum control system performance and robustness in flight depends heavily on the predictive accuracy of the linear-design models. The system-identification approach provides highly accurate design models for design at specific flight conditions, but it is clearly more time intensive than the simple numerical perturbation method, so the identification-based approach is not practical for checking control system behavior at the tens or hundreds of off-nominal conditions.

Spaulding et al.<sup>137</sup> evaluated the accuracy of state-space models of a ducted-fan UAV extracted using perturbation methods from a nonlinear simulation model that was also based on extensive multidimensional look-up tables. This work showed that significant errors in the predicted frequency responses resulted from this method. Further, the control system robustness and closed-loop performance, which was indicated as having been acceptable based on the linearized state-space model, was found to degrade considerably when evaluated in the nonlinear simulation. Instead, the frequency responses were identified based on automated sweeps of the nonlinear model, and the control system was optimized by direct manipulation of the broken-loop characteristics [e.g., as in Eq. (7.92)].

### 13.11 Identification of a Three-DOF Longitudinal Model of a Fixed-Wing UAV

Flight tests were conducted on the Shadow<sup>TM</sup> 200 Block IB fixed-wing UAV (Fig. 13.10) for the purposes of extracting a state-space model of the bare-airframe dynamics in support of simulation development and fidelity assessment.<sup>195</sup> This vehicle has a wing span of approximately 11 ft and gross weight for these flight tests of about 350 lb. Test data from piloted frequency sweeps were used for model identification, and doublet test data were used for model verification. A three-DOF state-space model for the longitudinal dynamics was identified. The state vector is

$$\mathbf{x} = \begin{bmatrix} u \\ w \\ q \\ \theta \end{bmatrix} \quad (13.72)$$

and the bare-airframe controls are elevator and engine rpm, so that

$$\mathbf{u} = \begin{bmatrix} \delta_e \\ \delta_{\text{rpm}} \end{bmatrix} \quad (13.73)$$

and the measurement vector is



Fig. 13.10 Shadow™ 200 fixed-wing UAV (U.S. Army photo).

$$\mathbf{y} = \begin{bmatrix} \alpha \\ q \\ a_x \\ a_z \end{bmatrix} \quad (13.74)$$

The frequency-response comparisons of Fig. 13.11 show that the identified model accurately characterizes the short-period responses. The excellent frequency-response agreement is reflected in a very low value for the identification cost function,  $J_{\text{ave}} = 26.3$ .

The identified parameters and accuracy results are listed in Tables 13.17 and 13.18. The low values of the insensitivities (all less than 10%) and Cramér–Rao bounds (all less than 20%) for the stability and control derivatives, together with the low cost function, indicate that an accurate and reliable model has been achieved. The key characteristic of the model is the identified short-period mode:  $[\zeta_{\text{sp}} = 0.58, \omega_{\text{sp}} = 5.3 \text{ rad/s}]$ .

The time-response verification for an elevator  $\delta_e$  and engine rpm doublet  $\delta_{\text{rpm}}$  is shown in Figs. 13.12 and 13.13, respectively. Overall, the model predicts the longitudinal dynamic response of the vehicle with excellent accuracy. For the elevator doublet, there is a discrepancy in the longitudinal acceleration  $a_x$  prediction at about 7 s, which is probably caused by an atmospheric disturbance as reflected in the flight data. But the magnitude of this discrepancy is very small in comparison with the primary response, which is in the normal acceleration  $a_z$ .

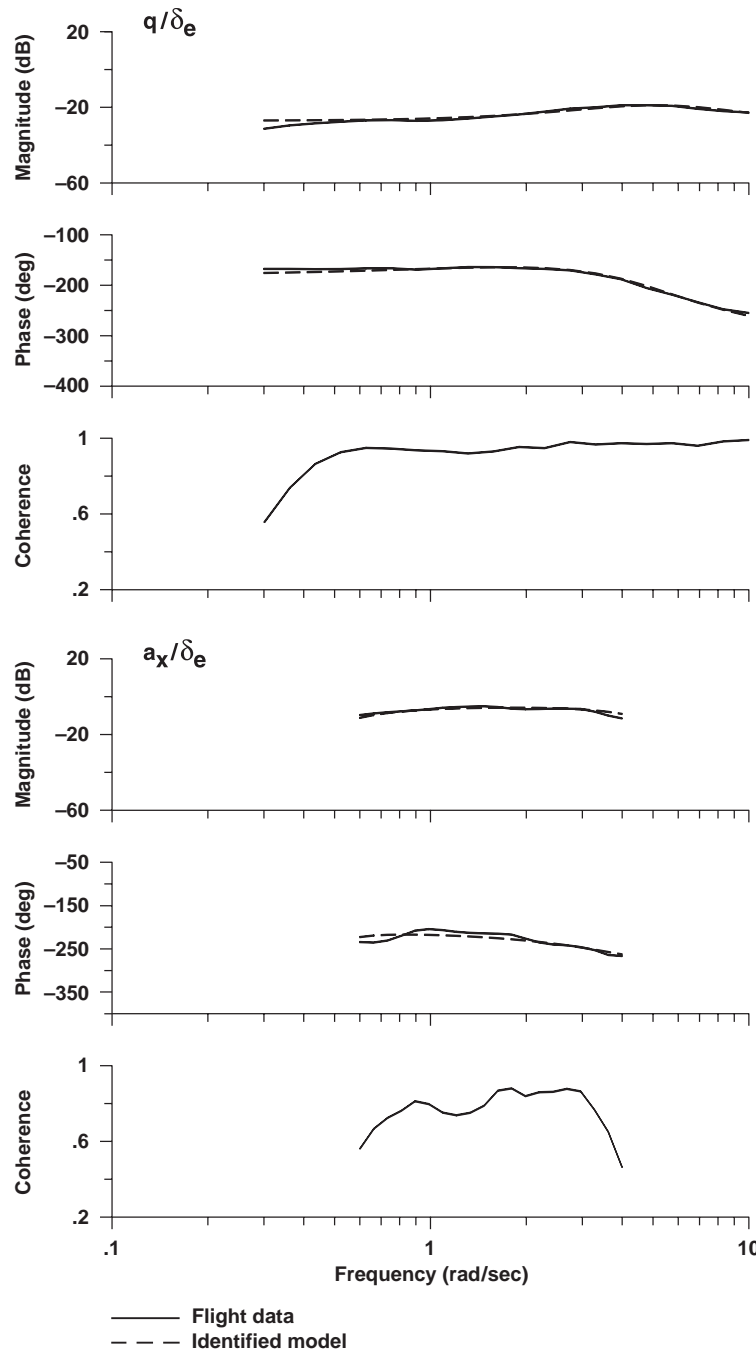


Fig. 13.11 Identification of Shadow™ 200 UAV longitudinal dynamics.

## STATE-SPACE MODEL IDENTIFICATION

409

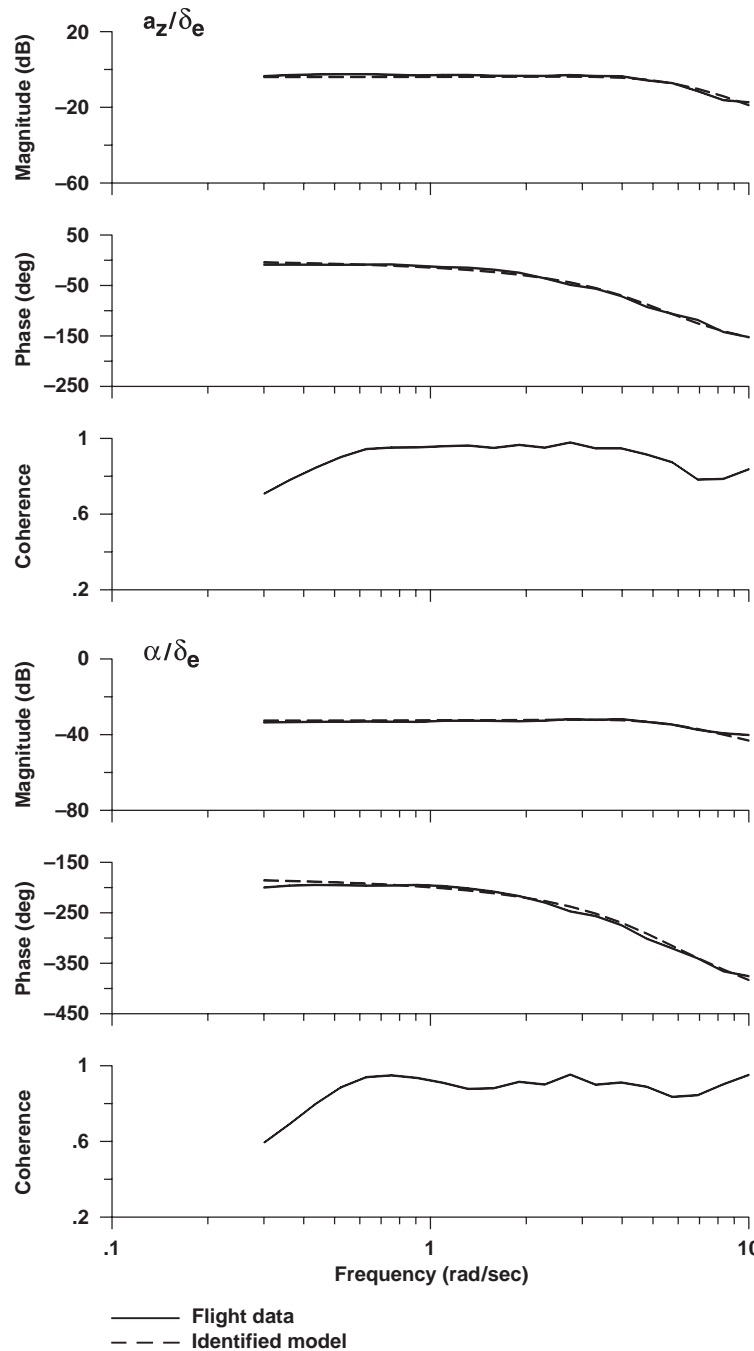


Fig. 13.11 Identification of Shadow™ 200 UAV longitudinal dynamics (continued).

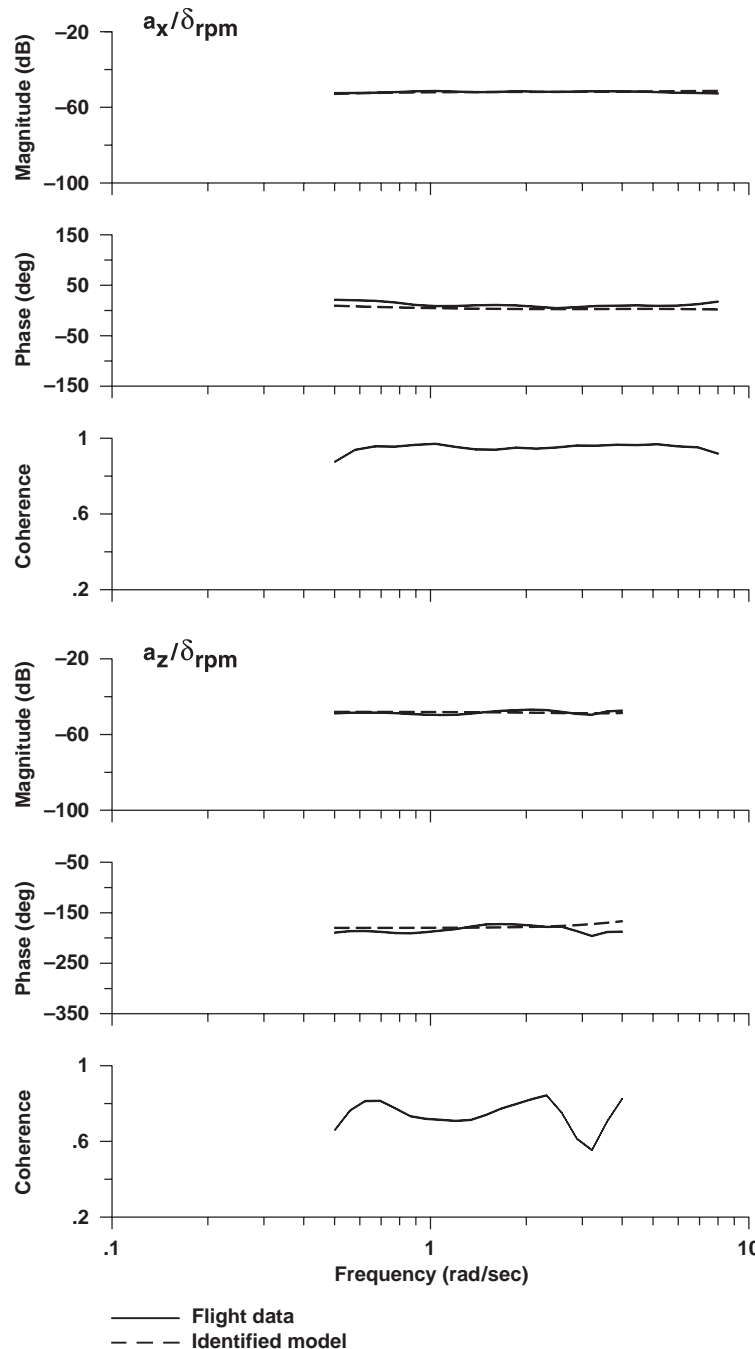


Fig. 13.11 Identification of Shadow™ 200 UAV longitudinal model (continued).

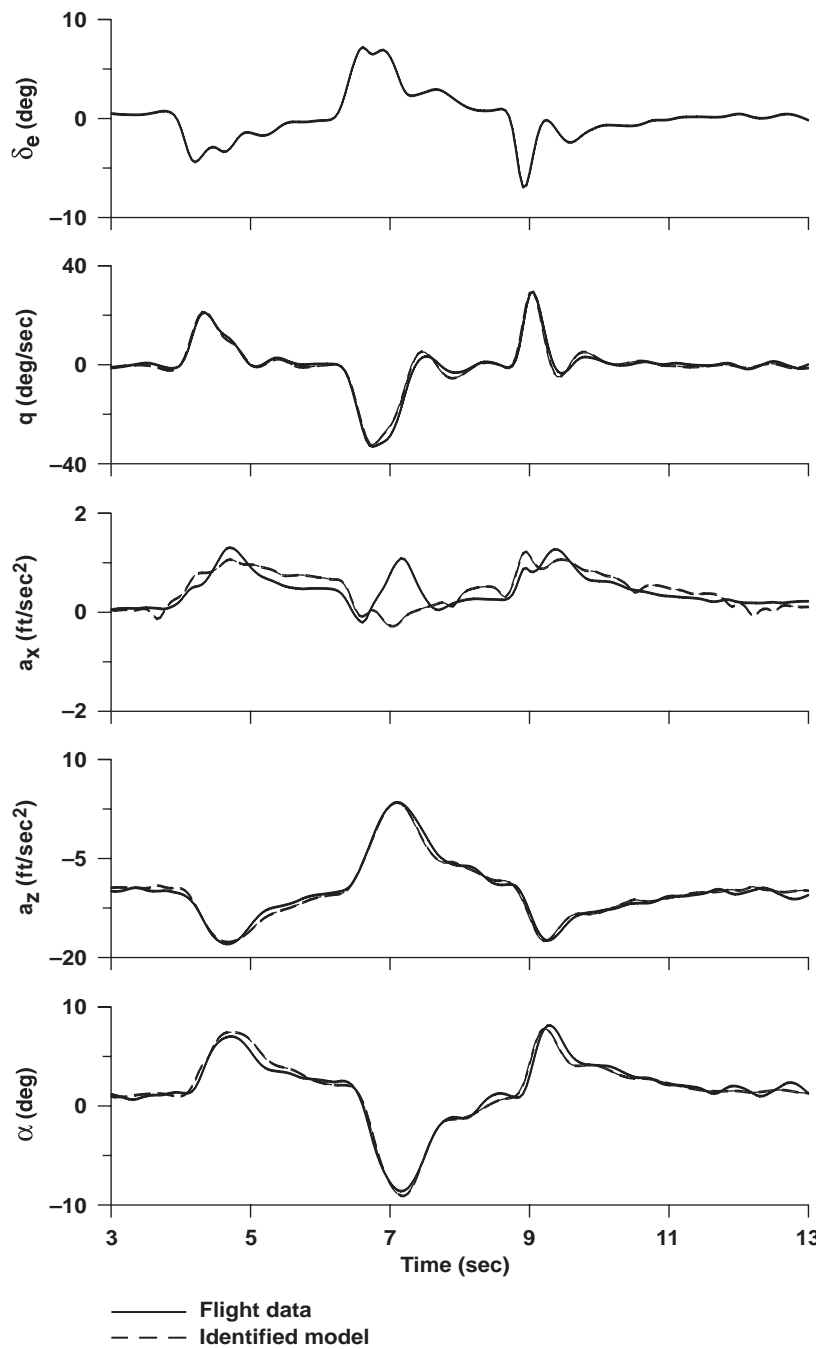


Fig. 13.12 Time-response verification of Shadow™ 200 UAV model for elevator input.

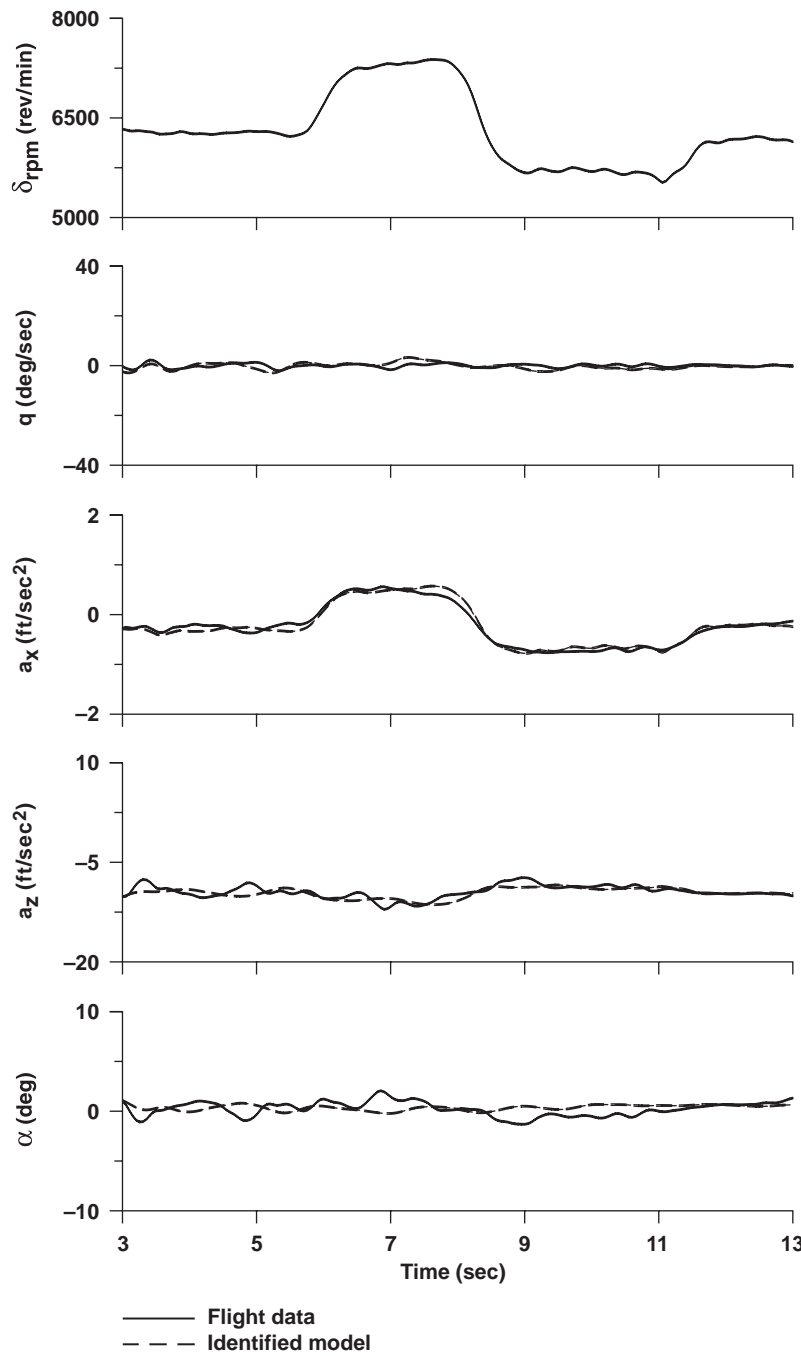


Fig. 13.13 Time-response verification of Shadow™ 200 UAV model for engine RPM input.

**Table 13.17 Identification results for three-DOF longitudinal model of Shadow™ 200 UAV<sup>a,b</sup>**

Engineering symbols	Value	CR, %	Insens, %
$X_u$	-0.07903	18.12	6.55
$X_w$	0.1731	5.25	1.60
$Z_w$	-1.882	4.28	1.66
$M_w$	-0.1404	6.43	1.47
$M_q$	-4.293	11.02	2.06
$X_{\delta_{\text{rpm}}}$	2.721E-03	3.59	1.75
$Z_{\delta_{\text{rpm}}}$	-5.626E-03	4.83	2.19
$M_{\delta_e}$	-0.6607	7.25	1.00
<i>Time delays</i>			
$\delta_{\text{rpm}}$	0.000 <sup>c</sup>	—	—
$\delta_e$	0.03557	25.65	8.65

<sup>a</sup> All results in English units.

<sup>c</sup> Eliminated from model structure.

**Table 13.18 Transfer-function costs**

Engineering symbols	Costs
$q/\delta_e$	26.4
$a_x/\delta_e$	22.4
$a_z/\delta_e$	21.8
$a/\delta_e$	22.7
$a_x/\delta_{\text{rpm}}$	26.6
$a_z/\delta_{\text{rpm}}$	38.1
$J_{\text{ave}}$	26.3

### 13.12 System Identification of a six-DOF MIMO Model of a Lightweight Manned Helicopter

Fully coupled MIMO models of the Fire Scout P2 demonstrator—a variant of the Schweitzer 333 (Fig. 13.14)—were identified using CIFER® from piloted frequency-sweep flight-test data. The initial model structure for this helicopter was developed earlier in this chapter in Sections 13.5.2 and 13.5.3, based on the analysis of the frequency-response tables. We now return to this example in order to present some of the advanced concepts that were used in completing the identification.

The results summarized herein for the hover flight condition were used in support of flight-control development and simulation modeling. This lightweight helicopter features an articulated rotor design and a small hinge offset, resulting in a small value of flap stiffness. The condition of Eq. (11.42) applies, and so the six-DOF quasi-steady model structure of Secs. 13.3 and Sec. 13.4 is well suited



**Fig. 13.14** Fire Scout P2 demonstrator — a variant of the Schweizer 333 (Northrop Grumman photo).

to this configuration and captures the important vehicle dynamics for frequencies up to about 12 rad/s. The example presented in this section is an excellent general template for system identification of six-DOF helicopter flight-dynamics models. The complexity of the identification problem for this fully coupled model structure is significantly greater than that of the three-DOF models for the XV-15 (Secs. 13.8 and 13.9) and STOVL (Sec. 13.10). A general template for system identification of higher-order models of helicopters (as is required for larger values of flap stiffness) is presented in Chapter 15.

Flight-test data for this helicopter were collected in the hover flight condition using piloted frequency sweeps and doublets in accordance with the guidelines of Chapter 5. The data were then filtered and processed to remove wild points and dropouts. Next, a complete kinematic consistency analysis was completed using the SMACK facility (Chapter 6). This analysis indicated that the data consistency as provided by the IMU was of excellent quality. Therefore there was little difference between the frequency responses obtained from the raw data and reconstructed data.

### 13.12.1 State-Space Model Structure

The basic six-DOF equations of motion are those of Sec. 13.3. The complete model structure has the eight states of Eq. (13.27), the four control inputs of Eq. (13.29), and the outputs of Eq. (13.30). There are a total of 64 aircraft parameters from Sec. 13.4.6, but we introduce the constraint that the lateral and longitudinal rotor delays are the same ( $\tau_{lat} = \tau_{lon}$ ) because physically they should be. This results in a model structure with a maximum of 63 identification parameters.

The frequency-response database was generated from the flight data using the MIMO methods of Chapters 7, 9, and 10. As presented in Sec. 13.5, the resulting

frequency ranges for acceptable coherence are shown in Table 13.1. Many of the responses are not important, indicated by “none,” and the associated derivatives that were dropped are shown in Table 13.2. Although the initial model structure had 63 identification parameters (60 stability and control derivatives and three time delays), this initial model reduction results in dropping 23 parameters for a total of 40 identification parameters in the initial model structure.

### 13.12.2 Effect of Dynamic Inflow

The vertical acceleration response to collective  $a_z/\delta_{\text{col}}$  in hover exhibits an increase in the magnitude and phase for frequencies greater than about 2.0 rad/s, as seen in Fig. 13.15. The same characteristic is also seen in the axial response to collective  $a_x/\delta_{\text{col}}$ . This lead or overshoot in the initial vertical acceleration response to collective inputs is associated with the vertical dynamic inflow  $v$ . Dynamic inflow accounts for the fact that the induced velocity change at the rotor does not occur instantaneously.<sup>196</sup> Without this effect, the magnitude and phase would remain constant at the higher frequencies (i.e., beyond about 2.0 rad/s). A complete physical model for coupled fuselage/coning/inflow is presented in Sec. 15.2.3. A simple model that captures this effect is a lead/lag dipole that can be appended to the collective input<sup>182</sup>:

$$\frac{\delta_{\text{col}}'}{\delta_{\text{col}}}(s) = \frac{T_1 s + 1}{T_2 s + 1} \quad (13.75)$$

where the augmented collective input  $\delta_{\text{col}}'$  is then used in place of the actual control input  $\delta_{\text{col}}$  in the equations of motion. In the present case, the six-DOF model structure was retained, and the frequency-response range for  $a_z/\delta_{\text{col}}$  was trimmed to exclude the data beyond 2 rad/s. The frequency-response range for the  $a_x/\delta_{\text{col}}$  was trimmed to exclude the data beyond 8 rad/s.

### 13.12.3 Effect of Engine/Governor/RPM Dynamics

The engine/governor/rotor rpm dynamics for helicopters have a typical time constant of about 0.25–1 s (depending on size of the aircraft). The main influence of these dynamics is seen in a larger phase roll-off in angular-rate responses to collective inputs ( $p/\delta_{\text{col}}$ ,  $q/\delta_{\text{col}}$ ,  $r/\delta_{\text{col}}$ ) than would be expected for a six-DOF response (i.e., in excess of  $-90$  deg). Additional state equations can be included to represent explicitly the engine/torque response and coupling to the aircraft dynamics, as demonstrated by Harding and Moody.<sup>197</sup> A simpler approach is to include the engine time constant as a Padé transfer function on the collective inputs to the angular response equations, as explained in Sec. 15.2.4. In the context of the six-DOF model structure, an adequate representation is to include an equivalent time delay  $\tau_{\text{col}}$  on the angular responses to collective ( $p/\delta_{\text{col}}$ ,  $q/\delta_{\text{col}}$ ,  $r/\delta_{\text{col}}$ ).

### 13.12.4 Isolation of the Speed Derivatives

In many single-rotor helicopter identification studies, it is difficult to achieve a good identification (i.e., satisfactory coherence) of the angular-rate (or attitude) frequency response at frequencies much below 1 rad/s. This is often due to poor

low-frequency excitation and high cross-control correlation. The poor low-frequency coherence can compromise the accuracy in the identification of the speed-damping derivatives ( $X_u$ ,  $Y_v$ ) and speed-stability derivatives ( $M_u$ ,  $L_v$ ). Further, there is significant coupling in the flapping response to longitudinal and lateral speed perturbations and therefore strong correlation among the speed derivatives ( $X_u$ ,  $X_v$ ,  $M_u$ ,  $M_v$ ,  $L_u$ ,  $L_v$ , etc.), which makes the accurate identification of these derivatives very difficult to achieve from dynamic response data. These problems are most significant for hovering flight. This section presents approaches to isolate the speed damping and speed-stability derivatives.

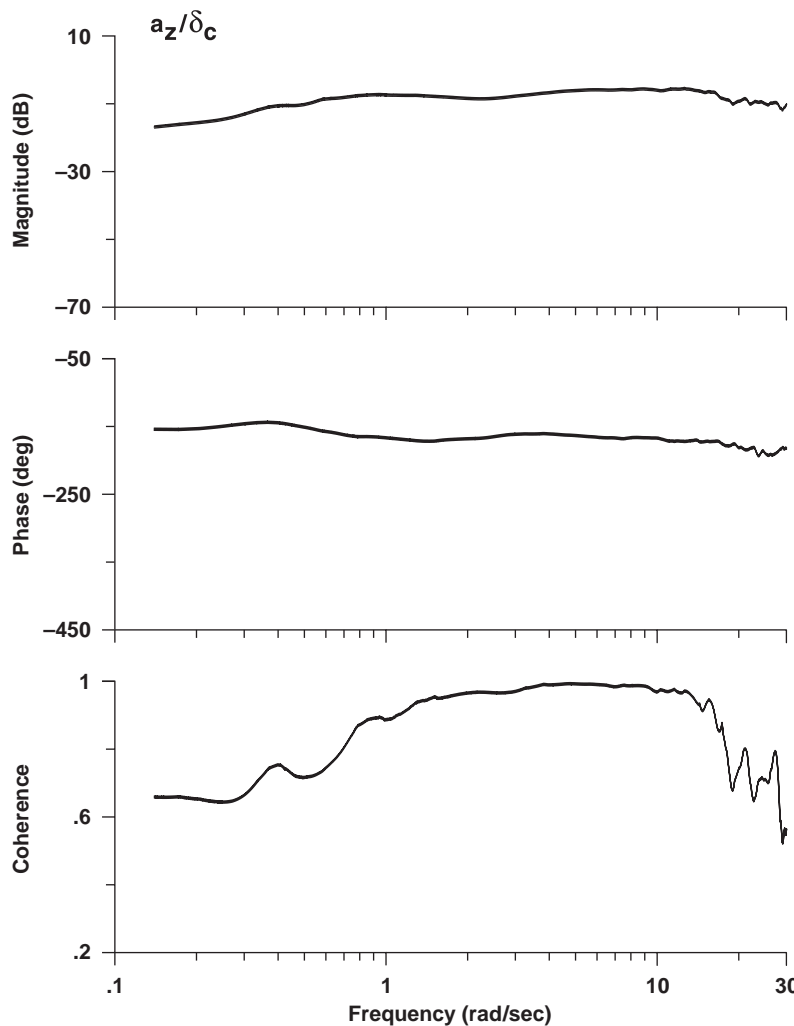


Fig. 13.15 Vertical acceleration response to collective in hover (Fire Scout P2).

**Speed-damping derivatives.** The initial identification studies of the Fire Scout P2 demonstrator for hover indicated that the on-axis speed-damping derivatives ( $X_u$ ,  $Y_v$ ) could not be accurately determined, showing high insensitivities, caused by the lack of coherence for low-frequency data (below 1 rad/s) in the key on-axis responses ( $a_x/\delta_{\text{lon}}$ ,  $\dot{u}/\delta_{\text{lon}}$ ,  $a_y/\delta_{\text{lat}}$ , and  $\dot{v}/\delta_{\text{lat}}$ ), as seen in Table 13.1. Further analysis showed that although the frequency responses to control inputs was inadequate at low frequency because of poor coherence there was good energy content in the signals  $\dot{u}$ ,  $\dot{v}$ ,  $\theta$ , and  $\phi$  and good kinematic consistency between the signals. This allows for the use of an alternate method for isolating these derivatives based on the frequency responses  $\dot{v}/\phi$  and  $\dot{u}/\theta$ .

The simplified model of the lateral force response for a hover trim condition

$$\dot{v} = Y_v v + g\phi \quad (13.76)$$

ignores all off-axis contributions and the influence of roll rate and lateral control inputs. However, this model is quite accurate at low frequencies. The transfer-function result

$$\frac{\dot{v}}{\phi}(s) = \frac{sg}{s - Y_v} \quad (13.77)$$

allows the direct identification of  $Y_v$  from the roll-sweep data, using the SISO analysis method of Sec. 10.4. As shown in Fig. 13.16, the frequency-response data  $\dot{v}/\phi$  have excellent coherence, including at low frequencies. The simple model of Eq. (13.77) is implemented using the transfer-function structure of Sec. 12.2.2 with the single identification parameter  $Y_v$ . The model is seen in Fig. 13.16 to be quite accurate ( $J = 21.9$ ) for a wide range of frequencies, and the parameter value  $Y_v = -0.0929$  is identified to excellent accuracy (CR = 15.3%). The same approach can be used to isolate the value for  $X_u$ . The isolated speed-damping derivatives can be fixed in the overall model structure, and the identification and model structure reduction proceed as usual.

A better approach, used herein, is to include the additional state equation of Eq. (13.76) (and an analogous equation for longitudinal speed) in the overall state-space identification model structure. Then the value of  $Y_v$  in Eq. (13.76) is constrained to the same parameter in the  $\dot{v}$  equation of motion (13.13). The resulting identified value will both match the simplified force equation and ensure a good overall model. In the present case, the insensitivity for  $X_u$  was excessive because of a lack of information content at the very low frequencies (i.e., 0.01 – 0.05 rad/s) needed to accurately determine this parameter. Instead, a constraint of  $X_u = 0.1 Y_v$  was implemented based on data for similar helicopters. This provided both an excellent fit of the available frequency-response data and excellent time-domain predictive agreement.

The technique of isolating the speed-damping derivatives in hover presented herein as discussed has been found by the leading author to be highly effective for many helicopter applications.

**Speed-stability derivatives.** Trim control data can be used to determine the relationships between the speed-stability derivatives and the remaining identified

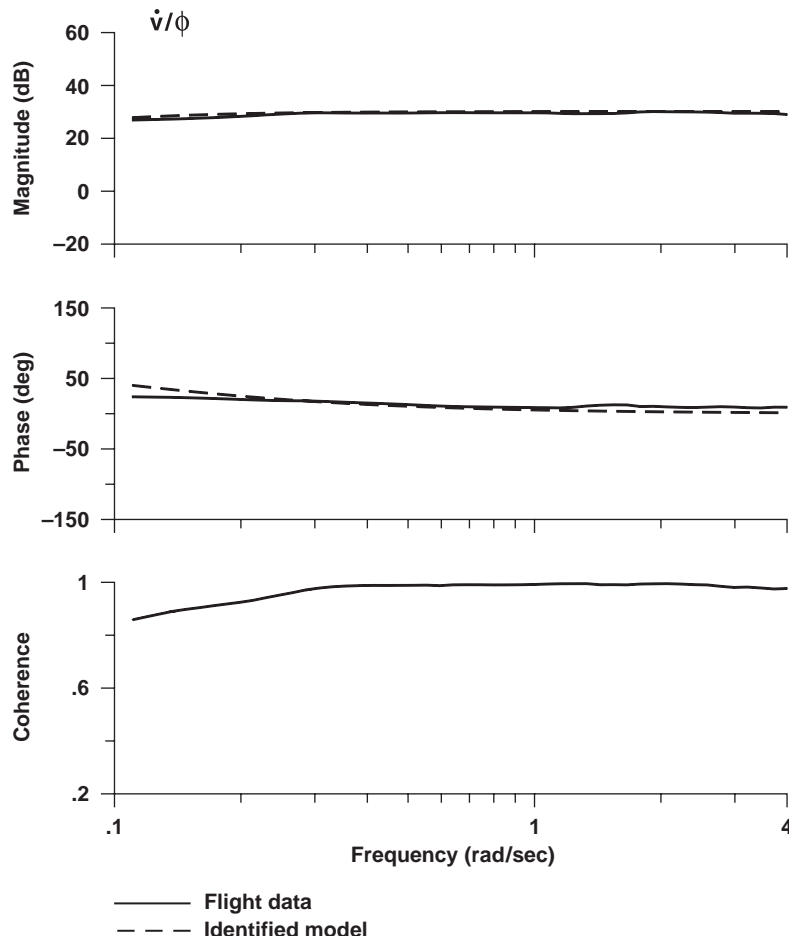


Fig. 13.16 Identification of lateral speed damping for hover (Fire Scout P2).

derivatives. This additional information content can be useful to achieve a dynamic model that has good predictive accuracy at very low frequency (where the frequency-response data are generally degraded) and that is compatible with the trim characteristics. For example, the pitching acceleration must be zero for all changes in trim condition (which we denote by  $\Delta$ ):

$$\dot{q} = 0 = M_u \Delta u + M_v \Delta v + M_w \Delta w + M_{\delta_{\text{lat}}} \Delta \delta_{\text{lat}} + M_{\delta_{\text{lon}}} \Delta \delta_{\text{lon}} + M_{\delta_{\text{ped}}} \Delta \delta_{\text{ped}} + M_{\delta_{\text{col}}} \Delta \delta_{\text{col}} \quad (13.78)$$

Solving for the speed derivative  $M_u$ , we have

$$M_u = - \left[ M_v \left( \frac{\Delta v}{\Delta u} \right) + M_w \left( \frac{\Delta w}{\Delta u} \right) + M_{\delta_{\text{lat}}} \left( \frac{\Delta \delta_{\text{lat}}}{\Delta u} \right) + M_{\delta_{\text{lon}}} \left( \frac{\Delta \delta_{\text{lon}}}{\Delta u} \right) + M_{\delta_{\text{ped}}} \left( \frac{\Delta \delta_{\text{ped}}}{\Delta u} \right) + M_{\delta_{\text{col}}} \left( \frac{\Delta \delta_{\text{col}}}{\Delta u} \right) \right] \quad (13.79)$$

where the terms in parentheses are the flight-test measurements of the trim state gradients and trim control gradients with respect to airspeed.

Standard practice for helicopter flight testing to determine static speed stability<sup>198</sup> requires that the off-axis controls remain fixed, so that the only remaining control gradient term is  $\Delta \delta_{\text{lon}} / \Delta u$ . If we ignore the coupling derivative  $M_v$  and the vertical force derivative  $Z_{\delta_{\text{lon}}}$  in the vertical equation of motion (13.14), a simplified expression is obtained (see also Refs. 198–200):

$$M_u = -M_{\delta_{\text{lon}}} \left( \frac{\Delta \delta_{\text{lon}}}{\Delta u} \right) + M_w \frac{Z_u}{Z_w} \quad (13.80)$$

where the first term dominates the expression. The relationship of Eq. (13.80) provides an independent estimate of the speed-stability derivative  $M_u$  to check that the identified model as based on the dynamic response is consistent with the static trim behavior.

The same approach provides an independent estimate of the lateral speed derivative  $L_v$ , based on the measured trim gradients for pure sideward flight. A simplified expression retaining the key terms is

$$L_v = - \left[ L_{\delta_{\text{lat}}} \left( \frac{\Delta \delta_{\text{lat}}}{\Delta v} \right) + L_{\delta_{\text{ped}}} \left( \frac{\Delta \delta_{\text{ped}}}{\Delta v} \right) \right] \quad (13.81)$$

In forward flight, the steady-heading sideslip test technique<sup>198</sup> is used to determine the required gradients in Eq. (13.81).

Finally, in hovering flight, the directional static-stability derivative  $N_v$  is small and can be difficult to determine. This derivative produces a yaw-moment (and resulting yaw-rate) response to lateral velocity. Therefore, in hover, the main source of information content to determine  $N_v$  is the  $r / \delta_{\text{lat}}$  (off-axis) response, which generally has poor coherence. This derivative can be estimated from the trim pedal gradient data using the simplified expression:

$$N_v = -N_{\delta_{\text{ped}}} \left( \frac{\Delta \delta_{\text{ped}}}{\Delta v} \right) \quad (13.82)$$

The relationships of Eqs. (13.80–13.82) can be implemented directly as constraint equations in the identification structure. An alternate approach is to obtain an initial identification model (prior to model structure reduction) with  $M_u$ ,  $L_v$ ,

and  $N_v$  as free parameters. This provides the values of the control derivatives needed to obtain independent estimates of the speed-stability derivatives from Eqs. (13.80–13.82). These trim-based estimates of the speed-stability derivatives are then fixed in the initial model, and model structure reduction proceeds as usual from this point. In either approach (i.e., constrained or fixed parameters), the inclusion of trim test data in the identification process can be important to make up for the lack of low-frequency coherence in the angular response data that is typical of helicopter flight tests in hover. Also, achieving consistency of the identified model with the trim data is important when identified models at several flight conditions are “stitched together” to form a full flight envelop model.<sup>201,202</sup>

We note that because of practical testing issues helicopter flight-test data for the trim control gradients  $\Delta\delta_{\text{lon}}/\Delta u$ ,  $\Delta\delta_{\text{lat}}/\Delta v$ ,  $\Delta\delta_{\text{ped}}/\Delta v$  are often not obtained with high precision or might not be well defined, especially for hover/low-speed flight. Using these gradients as just discussed might then mean that trim gradient errors are reflected directly in the constraint relationships between the key control derivatives and the speed-stability derivatives, and thus might degrade the match of the dynamic response. Further, some small-scale rotorcraft measurements using a dynamic response rig (discussed further in Sec. 15.3.2) show that inconsistencies between trim and dynamic values of the speed-stability derivatives (even a sign change) can reflect the presence of additional low-frequency dynamic states and nonlinear effects not correctly captured in the trim gradient relationships. The recommended approach, therefore, is to first identify the speed-stability derivatives as free parameters in the model structure, and then compare the results with the independent estimates based on the trim data, and assess the impact on the frequency- and time-response agreement of introducing the constraints (or fixed values) into the model structure. Generally, the identification of the speed-damping and speed-stability derivatives for forward-flight conditions is accomplished with good accuracy from the frequency-response data alone.

In the present case, a very limited amount of trim data was available, and the constraints were implemented only on  $M_u$  and  $L_v$ . The implementation of the speed derivative constraints [Eqs. (13.80) and (13.81)] resulted in a modest increase in the frequency-domain cost function as compared to allowing the derivatives to be free, while retaining good time-domain predictive characteristics (e.g., as shown later in Fig. 13.17). For this application, compatibility with the trim control gradients was desired to build a full flight-envelope simulation model of the Fire Scout P2 demonstrator from identification results at several flight conditions.

### 13.12.5 Final Identification Results

The final identification results are shown in Tables 13.19 and 13.20, and the associated cost functions in Table 13.21. The Cramér–Rao bounds have low values (most are less than 20%), indicating very good reliability of the identified model. These results are with the trim gradient constraints included in the model structure. An examination of these tables illustrates a number of points made in the preceding sections. For example, two time delays associated with main rotor flapping responses were constrained by the equation  $\tau_{\text{lat}} = \tau_{\text{lon}}$ , as discussed in

## STATE-SPACE MODEL IDENTIFICATION

421

**Table 13.19 Identification results for six-DOF helicopter model in hover (Fire Scout P2): F-matrix<sup>c</sup>**

Engineering symbols	Value	CR, %	Insens, %
$X_u$	-0.01277 <sup>a</sup>	_____	_____
$X_v$	0.000 <sup>b</sup>	_____	_____
$X_w$	0.000 <sup>b</sup>	_____	_____
$X_p$	0.000 <sup>b</sup>	_____	_____
$X_q$	0.6326	29.82	13.72
$X_r$	0.000 <sup>b</sup>	_____	_____
$Y_u$	-0.01022	17.29	6.56
$Y_v$	-0.1277	7.02	3.13
$Y_w$	0.000 <sup>b</sup>	_____	_____
$Y_p$	0.000 <sup>b</sup>	_____	_____
$Y_q$	0.000 <sup>b</sup>	_____	_____
$Y_r$	0.000 <sup>b</sup>	_____	_____
$Z_u$	0.000 <sup>b</sup>	_____	_____
$Z_v$	0.000 <sup>b</sup>	_____	_____
$Z_w$	-0.2656	10.90	4.65
$Z_p$	0.000 <sup>b</sup>	_____	_____
$Z_q$	0.000 <sup>b</sup>	_____	_____
$Z_r$	0.000 <sup>b</sup>	_____	_____
$L_u$	3.295E-03	8.39	1.73
$L_v$	-0.01671 <sup>a</sup>	_____	_____
$L_w$	-0.1592	12.97	3.84
$L_p$	-3.883	5.51	1.15
$L_q$	-0.2891	30.93	7.13
$L_r$	-0.4211	17.40	4.69
$M_u$	5.098E-03 <sup>a</sup>	_____	_____
$M_v$	0.000 <sup>b</sup>	_____	_____
$M_w$	0.000 <sup>b</sup>	_____	_____
$M_p$	0.000 <sup>b</sup>	_____	_____
$M_q$	-0.8167	7.43	2.76
$M_r$	0.000 <sup>b</sup>	_____	_____
$N_u$	0.000 <sup>b</sup>	_____	_____
$N_v$	-0.01747	18.14	3.69
$N_w$	-0.08342	15.65	5.09
$N_p$	-1.225	6.90	2.44
$N_q$	0.000 <sup>b</sup>	_____	_____
$N_r$	-0.3224	18.56	6.56

<sup>a</sup> Constrained parameter.

<sup>b</sup> Eliminated from model structure.

<sup>c</sup> All results in English units.

**Table 13.20 Identification results for six-DOF helicopter model in hover (Fire Scout P2)<sup>d</sup>**

Engineering symbols	Value	CR, %	Insens, %
<i>G-matrix</i>			
$X_{\delta_{\text{lat}}}$	0.000 <sup>a</sup>	—	—
$X_{\delta_{\text{lon}}}$	-0.1018	3.18	1.46
$X_{\delta_{\text{col}}}$	-0.02810	4.26	2.13
$X_{\delta_{\text{ped}}}$	0.000 <sup>a</sup>	—	—
$Y_{\delta_{\text{lat}}}$	0.05825	4.96	2.43
$Y_{\delta_{\text{lon}}}$	0.02227	8.31	4.12
$Y_{\delta_{\text{col}}}$	0.000 <sup>a</sup>	—	—
$Y_{\delta_{\text{ped}}}$	-0.04715	4.07	2.02
$Z_{\delta_{\text{lat}}}$	0.000 <sup>a</sup>	—	—
$Z_{\delta_{\text{lon}}}$	0.000 <sup>a</sup>	—	—
$Z_{\delta_{\text{col}}}$	-0.3697	4.95	1.82
$Z_{\delta_{\text{ped}}}$	0.000 <sup>a</sup>	—	—
$L_{\delta_{\text{lat}}}$	0.1333	4.33	0.76
$L_{\delta_{\text{lon}}}$	0.04050	5.10	1.46
$L_{\delta_{\text{col}}}$	0.01544	7.83	3.18
$L_{\delta_{\text{ped}}}$	0.03673	4.34	1.19
$M_{\delta_{\text{lat}}}$	0.000 <sup>a</sup>	—	—
$M_{\delta_{\text{lon}}}$	0.05106	3.19	1.32
$M_{\delta_{\text{col}}}$	0.000 <sup>a</sup>	—	—
$M_{\delta_{\text{ped}}}$	9.103E-03	5.69	2.81
$N_{\delta_{\text{lat}}}$	0.02565	7.01	2.74
$N_{\delta_{\text{lon}}}$	0.000 <sup>a</sup>	—	—
$N_{\delta_{\text{col}}}$	0.02861	5.60	2.49
$N_{\delta_{\text{ped}}}$	0.08727	4.14	1.85
$g \cos \Theta_0$	32.17 <sup>b</sup>	—	—
<i>Time delays</i>			
$\tau_{\text{lat}}$	0.04251	8.52	3.74
$\tau_{\text{lon}}$	0.04251 <sup>c</sup>	—	—
$\tau_{\text{col}}$	0.2523	4.91	1.67
$\tau_{\text{ped}}$	0.000 <sup>a</sup>	—	—

<sup>a</sup> Eliminated from model structure

<sup>b</sup> Fixed parameter

<sup>c</sup> Constrained parameter

<sup>d</sup> All results in English units

**Table 13.21 Cost functions for six-DOF helicopter model in hover (Fire Scout P2): Transfer-function costs**

Engineering symbols	Costs
$p/\delta_{\text{lat}}$	56.1
$r/\delta_{\text{lat}}$	68.2
$a_y/\delta_{\text{lat}}$	145.1
$v/\delta_{\text{lat}}$	90.5
$p/\delta_{\text{lon}}$	172.2
$q/\delta_{\text{lon}}$	96.5
$a_x/\delta_{\text{lon}}$	104.9
$a_y/\delta_{\text{lon}}$	126.1
$u/\delta_{\text{lon}}$	93.3
$p/\delta_{\text{col}}$	54.6
$r/\delta_{\text{col}}$	132.6
$a_x/\delta_{\text{col}}$	82.1
$a_z/\delta_{\text{col}}$	68.8
$p/\delta_{\text{ped}}$	31.0
$q/\delta_{\text{ped}}$	43.0
$r/\delta_{\text{ped}}$	134.9
$a_y/\delta_{\text{ped}}$	176.6
$v/\phi$	30.0
$u/\theta$	7.3
$J_{\text{ave}}$	90.2

Sec. 13.12.1. The equivalent time delay  $\tau_{\text{col}}$  was added to the model to account for the engine response, as discussed in Sec. 13.12.3. The speed-damping and speed-stability derivatives  $X_u$ ,  $L_v$ ,  $M_w$  were constrained, as discussed in Sec. 13.12.4. Finally, the accuracy analysis led to the eventual elimination of five stability derivatives (in addition to the nine control derivatives and the 14 stability derivatives that were eliminated in the initial model reduction, as discussed in Secs. 13.5.2 and 13.5.3).

The identified six-DOF quasi-steady state-space model generally provides a good characterization of the frequency-response flight data, as seen in the examples of Fig. 13.17 and is consistent with the overall cost function ( $J_{\text{ave}} = 90.2$ ), which is within the guideline of Eq. (12.23). We note that the dominant off-axis (angular coupling) response  $p/\delta_{\text{lon}}$  has a high cost function ( $J = 172.2$ ), though it is within the guidelines of Eq. (12.24). As seen in Fig. 13.17, the phase response cannot be adequately characterized by a six-DOF model structure.<sup>16</sup>

The on-axis damping parameters  $X_u$ ,  $Y_v$ ,  $Z_w$ ,  $L_p$ ,  $M_q$ , and  $N_r$  all have reasonable values (stable and of typical magnitude for helicopters with low hinge offset; Ref. 190), indicating that there is good translational and angular rate damping for the vehicle. The final value of the lateral speed-damping derivative ( $Y_v = -0.1277$ ) is close to the value obtained from the isolated identification. The

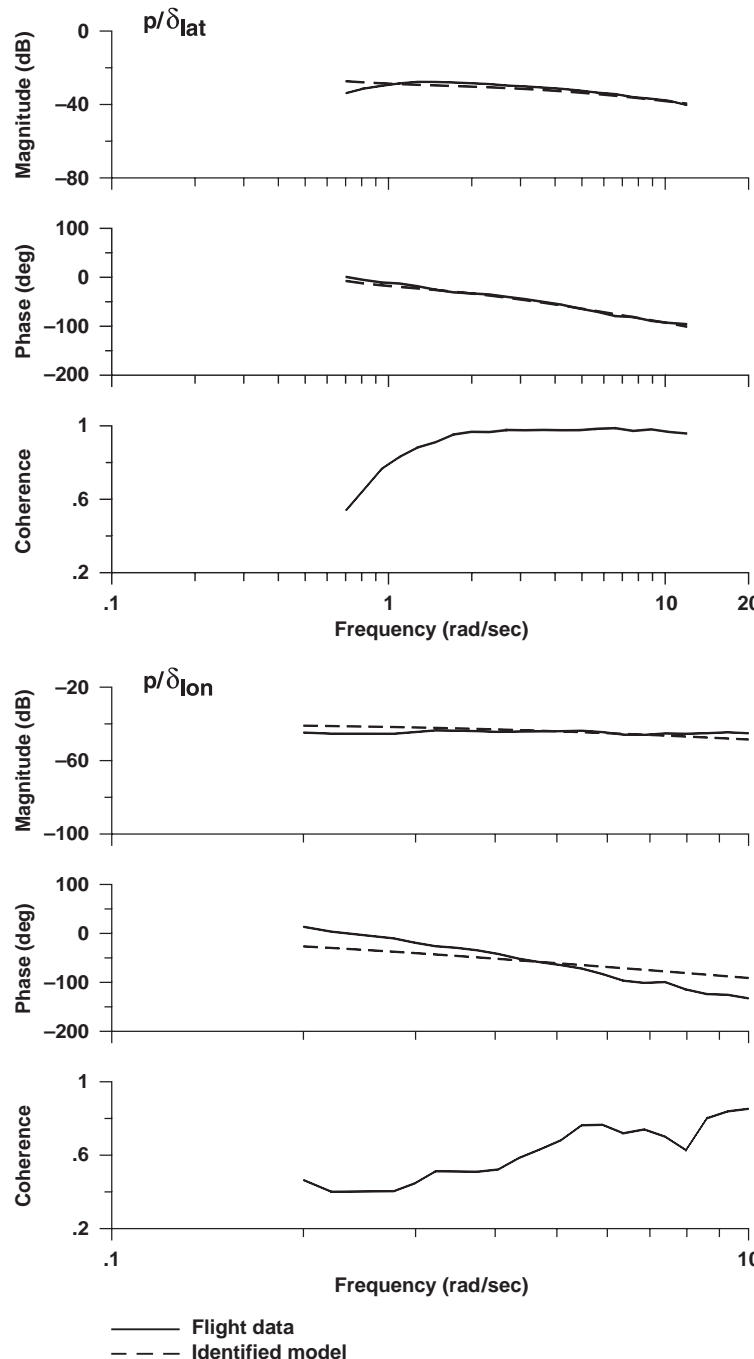


Fig. 13.17 Identification of six-DOF helicopter model in hover (Fire Scout P2) .

## STATE-SPACE MODEL IDENTIFICATION

425

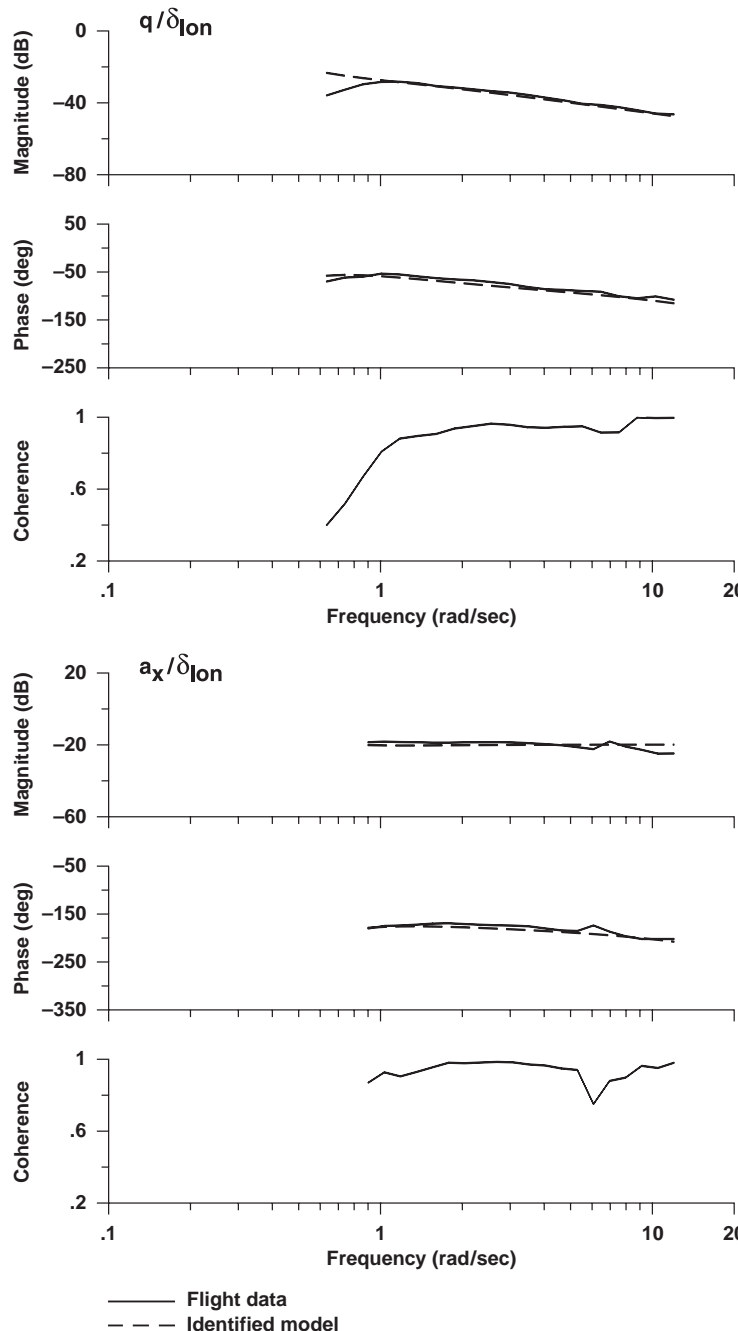
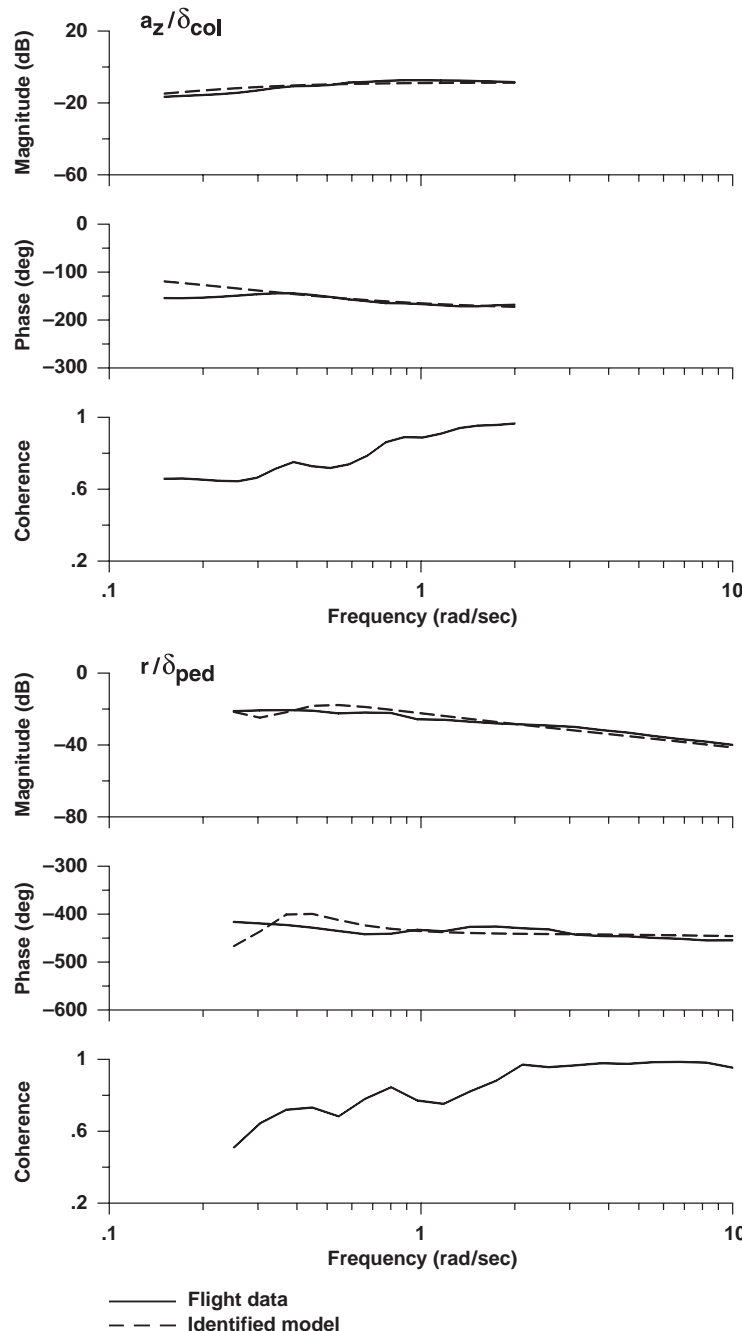


Fig. 13.17 Identification of six-DOF helicopter model in hover (Fire Scout P2) (continued).



**Fig. 13.17** Identification of six-DOF helicopter model in hover (Fire Scout P2) (continued).

speed-stability derivatives are obtained from the constraint equations (13.80) and (13.81) and are very small:  $M_u = 0.005098$  and  $L_v = -0.01671$ . The positive (stable) longitudinal speed derivative  $M_u$  reflects the positive longitudinal control derivative (stick aft results in a pitch-up moment,  $M_{\delta_{\text{lon}}} > 0$ ) and a negative trim gradient (stick forward with airspeed results in  $\Delta\delta_{\text{lon}}/\Delta u < 0$ ). The analogous situation for lateral flight produces the negative (stable) value of lateral speed derivative  $L_v$ . There is a very small but negative (i.e., unstable) static directional-stability derivative  $N_v$  for motions near hover and reflects the combined contributions from the tail rotor, vertical fin, engine, and fuselage. A small stable (positive) overall value would be expected from the trim data, but the introduction of the constraint [Eq. (13.82)] was found to degrade the identification in this case and was dropped; this indicates some inconsistency between the frequency-response data and the static behavior for this off-axis response pair (likely because of the coupled engine dynamics omitted from the model). The many other off-axis stability and control derivatives (e.g.,  $Y_u$ ,  $L_q$ ,  $Y_{\delta_{\text{lon}}}$ , etc.) are associated with the lateral/directional response coupling for a pitch control input, but not the reverse. This is caused by the large pitch inertia compared to the roll inertia.

The identified values for the rotor time constant ( $\tau_{\text{lat}} = \tau_{\text{lon}} = \tau_f = 0.04251\text{s}$ ) and roll-damping derivative  $L_p$  satisfy the requirement of Eq. (11.47) well, so that the quasi-steady approximation (six-DOF model) that was adopted is justified. The collective input time delay  $\tau_{\text{col}} = 0.2523\text{s}$  provides good phase tracking for the angular rate responses included in the identification ( $p/\delta_{\text{col}}$ ,  $r/\delta_{\text{col}}$ ). Both the rotor and engine response delays are very close to the identified values for the OH-58D helicopter,<sup>123</sup> which is of similar size.

The predictive capability of this model in the time domain is shown, for example, in the longitudinal stick doublet of Fig. 13.18. The prediction of the primary responses (pitch rate, longitudinal accelerator, and pitch angle) is excellent. The significant coupling into the roll rate and roll angle response is also predicted with reasonable fidelity—even though the cost function was higher than desirable for the associated frequency response  $p/\delta_{\text{lon}}$ , as seen in Table 13.21. Clearly a decoupled longitudinal state-space model would omit significant characteristics of the flight data response.

The identification results can be used to illustrate the contribution of each term in the equations of motion to an overall frequency-response pair. For example, consider the pitching equation for longitudinal control inputs [Eq. (13.18)]:

$$\dot{q} = M_u u + M_v v + \dots + M_w \dot{w} + M_q \dot{q} + \dots + M_{\delta_{\text{lon}}} \delta_{\text{lon}} \quad (13.83)$$

Taking the Laplace transform and dividing the equation by the control input  $\delta_{\text{lon}}(s)$ , we obtain

$$\begin{aligned} \frac{sq}{\delta_{\text{lon}}}(s) &= M_u \frac{u}{\delta_{\text{lon}}}(s) + M_v \frac{v}{\delta_{\text{lon}}}(s) \\ &+ \dots + s M_w \frac{w}{\delta_{\text{lon}}}(s) + M_q \frac{q}{\delta_{\text{lon}}}(s) + \dots + M_{\delta_{\text{lon}}} \end{aligned} \quad (13.84)$$

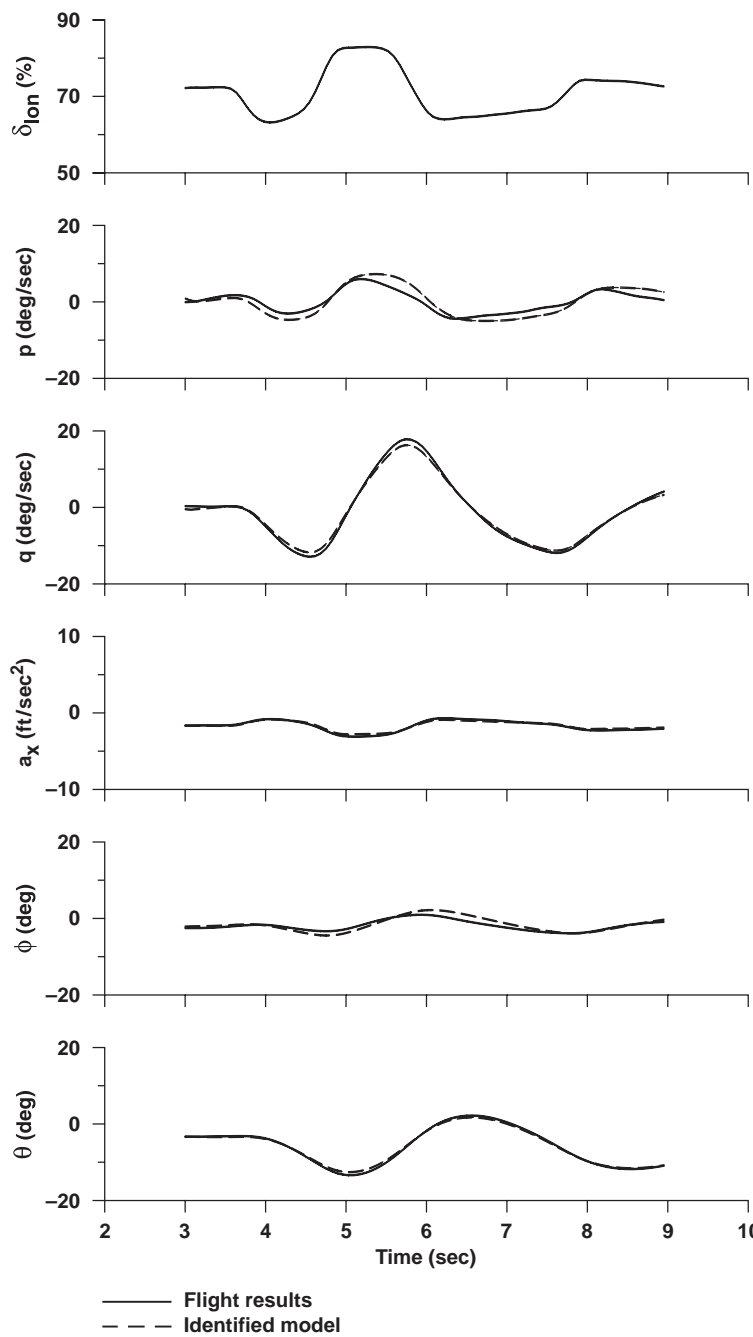


Fig. 13.18 Time-response verification for longitudinal stick doublet (Fire Scout P2, hover).

The individual terms (except for the last one) are composed of products of the identification parameters and the state-space model frequency-response functions. For example, the term  $M_q(q/\delta_{\text{lon}})$  is obtained from the identified derivative ( $M_q$  from Table 13.19) and the state-space frequency-response [ $q/\delta_{\text{lon}}$  from  $T(s)$  of Eq. (12.12)]. The total response on the left-hand side [ $s(q/\delta_{\text{lon}})$ ] and each contributing term are presented on the Bode plot of Fig. 13.19 (where the effect of the time delay  $\tau_{\text{lon}}$  has been excluded for illustrative purposes herein).

The figure shows that the contribution of  $M_u$  to the pitch-rate response is important only at low frequencies (i.e., below 0.5 rad/s). At very low frequency

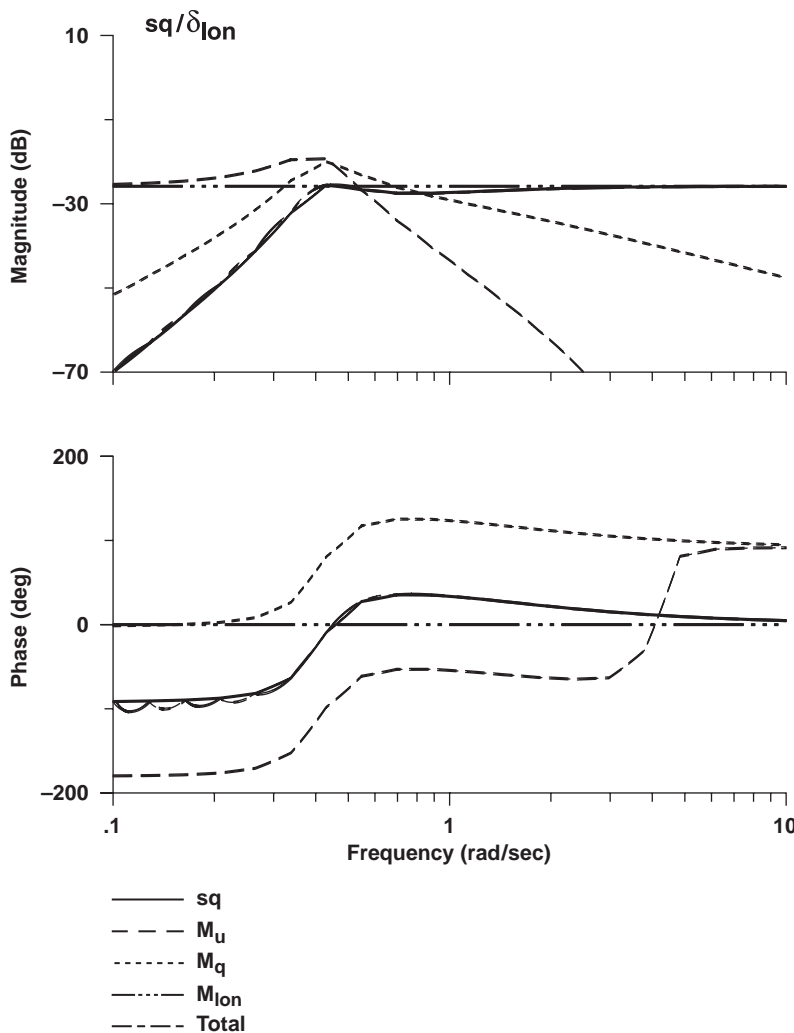


Fig. 13.19 Component contributions to overall pitch response.

(below 0.2 rad/s), this term is nearly cancelled by a nearly equal and opposite contribution from the control moment  $M_{\delta_{\text{lon}}}$ . This can be seen in nearly equal magnitudes, but phase contributions differing by about 180 deg. The speed stability is seen to dominate the overall pitch response only in the narrow frequency range of about 0.2–0.4 rad/s. Thus a reliable identification of the  $M_u$  derivative requires accurate flight-test data ( $q/\delta_{\text{lon}}$ ) in this critical frequency range. Yet, as can be seen from reference to Fig. 13.17, the coherence for  $q/\delta_{\text{lon}}$  is poor in this frequency range. This contributes to the need to introduce the trim control gradient constraint Eq. (13.80) as a supplemental source of dynamic information. The pitch damping  $M_q$  is seen to contribute an equal but opposite moment to  $M_u$  at the pitch response peak, dominating the pitch-rate response in the frequency range of 0.5–0.9 with continued influence up to about 2 rad/s. There are sufficient dynamic response data to ensure an accurate identification of this derivative (CR = 7.4%). Finally, the control derivative  $M_{\delta_{\text{lon}}}$  entirely dominates the pitch-rate response at frequencies greater than 1 rad/s, leading to an accurate identification of this derivative (CR = 3.2%). The calculation is checked by comparing the complex sum of the three separate components with the overall response [ $s(q/\delta_{\text{lon}})$ ] as shown in the figure (except for small round-off errors in the identification parameters).

The methods and quality of results obtained are typical of helicopter model identification using six-DOF model structures. Additional examples of helicopter state-space model identification with CIFER® using quasi-steady (six-DOF) model structures include the Bo-105,<sup>10</sup> AH-64,<sup>182</sup> and Kmax.<sup>173</sup>

## Problems

*State-space identification of stability and control derivative models with DERIVID*

**13.1** Complete a table of frequency-response ranges of acceptable coherence for state-space model identification of the XV-15 at cruise using your MIMO frequency-response database developed in **Problem 10.6**.

**13.2** Load the GTR simulation model  $F$  and  $G$  matrices “f\_gtrsimv170.dat” and “g\_gtrsimv170.dat” into the CIFER® database using utility 14. These matrices should be read using the “CIFER” format.

**13.3** Complete the stability and control derivative model identification for the cruise condition using your MIMO frequency-response database over the frequency ranges deemed acceptable in **Problem 13.1**. Use the GTR simulation values for the  $F$  and  $G$  matrices loaded into the database in **Problem 13.2** as your initial guess. Check that all cost and theoretical accuracy guidelines are met in the final converged model. Evaluate the influence of poor initial conditions on the identification results. Compare the state-space model results with your transfer-function results for cruise from **Problem 11.10**.

**13.4** Plot your state-space model identified in **Problem 13.3** against the flight data using utility 31. Then output your results in a table using utility 33.

**13.5** Complete a table of frequency-response ranges of acceptable coherence for state-space model identification of the XV-15 at hover using your MIMO frequency-response database developed in **Problem 10.6**. Perform a model structure reduction based on the frequency-response range table.

**13.6** Load the GTR simulation model  $F$  and  $G$  matrices “f\_gtrsimv0.dat” and “g\_gtrsimv0.dat” into the CIFER® database using utility 14. These matrices should be read using the “CIFER” format.

**13.7** Complete the stability and control derivative model identification for the hover condition using your MIMO frequency-response database over the frequency ranges deemed acceptable in **Problem 13.5**. To resolve data consistency issues discovered in **Problem 6.6**, use frequency responses for both  $\phi/\delta_a$  and  $p/\delta_a$  in the system identification. Fit  $\phi/\delta_a$  for the full frequency range of good coherence, but fit  $p/\delta_a$  only at frequencies of good coherence above 0.5 rad/s (where data consistency is acceptable). Use the GTR values for the  $F$  and  $G$  matrices loaded into the database in **Problem 13.6** as your initial guess. Check that all cost and theoretical accuracy guidelines are met in the final converged model. Evaluate the influence of poor initial conditions on the identification results. Compare the results of your state-space model with your transfer-function modeling results of **Problem 11.9**.

**13.8** Plot your state-space model identified in **Problem 13.7** against the flight data using utility 31. Then output your results in a table using utility 33.

**13.9** Calculate the eigenvalues and eigenvectors for your hover (**Problem 13.7**) or cruise (**Problem 13.3**) model, and analyze the various modes. Make sure to introduce proper scaling in the eigenvectors (Sec. 13.8.3).

**13.10** Use the method of Sec. 13.12.4 to isolate the speed-damping derivative  $Y_v$  in hover and compare the result with the complete identification (**Problem 13.7**).

#### *Theoretical accuracy metrics*

**13.11** Go back to the interim model results for cruise or hover (**Problem 13.3** or **Problem 13.7**). First consider the parameters with the larger insensitivities. Try changing these parameters, and watch to what extent the frequency-response errors change (look at the plots). Determine if the behavior is consistent with the values of the insensitivities.

**13.12** Look at the final model identification for either cruise or hover (**Problem 13.3** or **Problem 13.7**). Introduce variations in the final parameters for the response derivative  $L_p$  and the control derivative  $L_{\delta_a}$  based on the Cramér–Rao results ( $\pm 0.2\sigma$ ,  $\pm 0.5\sigma$ ,  $\pm 1.0\sigma$ ,  $\pm 2.0\sigma$ ). Compare the resulting frequency-response plots with the identification results (model and flight data). Are the results consistent with the estimates of parameter accuracy?

## 432 AIRCRAFT AND ROTORCRAFT SYSTEM IDENTIFICATION

**13.13** Now take one of your intermediate models for either cruise or hover (**Problem 13.3** or **Problem 13.7**) in which there are large Cramér–Rao bounds but low insensitivities. Examine the confidence ellipsoid, and see if you can use this to introduce variations in two parameters that should have an offsetting effect. Confirm your result by evaluating the frequency-response plots.

*Time vectors and component contributions for the XV-15*

**13.14** Determine the time vector of the identified roll mode ( $1/T_r$ ) for cruise or for the identified lateral “phugoid-type” mode in hover. (This can be performed within DERIVID or utility 38.) Then plot the roll-equation time vector (in MATLAB®, by hand, or another suitable tool).

**13.15** Plot the component contributions to the overall roll response [ $s(p/\delta_a)$ ] for the XV-15 in hover or cruise similarly to Fig. 13.19. Based on this plot, explain why it is difficult to accurately identify  $L_v$ .

*Model reduction based on frequency-response table*

**13.16** In most single rotor helicopters in hovering flight, the coupling response  $p/\delta_{\text{lon}}$  is important, but often the  $q/\delta_{\text{lat}}$  coupling response is small because of large pitch inertia that subdues gyroscopic coupling in the pitch response. In the case where  $q/\delta_{\text{lat}}$  has zero coherence, which stability derivatives would be eliminated?

*Isolation of speed-damping derivatives*

**13.17** How would you isolate the longitudinal speed-damping derivative  $X_u$  using relationships similar to Eqs. (13.76) and (13.77)?

## 14

# Time-Domain Verification of Identification Models

The frequency-response method for system identification, as illustrated in Fig. 2.1, starts with flight-test data collected in the time domain. From that point on, the identification method of Chapters 5 through 13 has been carried out entirely in the frequency domain, with the goal of identifying an accurate mathematical model of the system. The assessment of parametric identification results is based entirely on a comparison of the flight-data frequency responses with those of the model and the resulting frequency-domain cost function  $J_{ave}$ . An important assessment of model fidelity, robustness, and the limitations of the linear model is provided by evaluating its predictive capability in the time domain for test inputs, such as steps or doublets, that are dissimilar from those used in the identification.

Time-domain verification is accomplished by the direct integration of the equations of motion, using the flight-test measurements of the control inputs. The identification parameters are held fixed at this point. Only the flight-data biases and reference shifts are determined in the time domain because these cannot be found from the frequency domain analysis. The predicted response of the model is then compared with the flight data.

The key topics to be covered in this chapter include the following: motivation for time-domain verification, time-domain verification method, time-domain verification in CIFER® using VERIFY, and example results.

### 14.1 Motivation for Time-Domain Verification

Time-domain verification is an important method for assessing the predictive accuracy and reliability of the identified model. Confidence must be gained that the model is not “overly tuned” to the identification test data and the flight condition at which the data were collected. When the identification test data are largely based on frequency sweeps, as recommended herein, the verification uses dissimilar input forms, such as steps and doublets. Checking the fidelity of the model for a range of input amplitudes and off-nominal flight conditions allows an assessment of the limitations of the linearity assumption in the identification.

Time-domain verification is also useful in assessing the significance of model structure alternatives and the choices that were made during the model structure reduction process (Sec. 13.7). For example, we might consider increasing the model order or adding dynamic coupling to improve a particular frequency-response match. This often comes at the expense of considerable complexity, while offering only marginal overall improvement in the time-response predictive accuracy. On the other hand, we might consider dropping a particular frequency

## 434 AIRCRAFT AND ROTORCRAFT SYSTEM IDENTIFICATION

response showing low coherence. This results in reduced model complexity because the associated primary derivatives are dropped (Sec. 13.5.3). However, if the predictive accuracy in the time domain is degraded, then the flight tests or the frequency-response identification might need to be adjusted/repeated to obtain higher coherence for the offending response pair. Repeated flight testing might involve closer attention to achieving good signal-to-noise and reduced cross-control correlation. Improving the identification results might involve a closer scrutiny of individual sweep records to eliminate repeat maneuvers that were conducted in the presence of high levels of winds and turbulence.

### 14.2 Time-Domain Verification Method

In time-domain verification, direct numerical integration is conducted on the equations of motion of the identified model using the measured control inputs from flight data. The predicted outputs obtained from the model [Eq. (12.3)] are compared with the flight-data measurements. The time-domain verification method that follows also determines bias and reference-shift corrections to account for several sources of error: untrimmed reference conditions, disturbances, measurement noise, numerical integration errors, and unmeasured secondary controls.

The state equations of motion of the identified model are repeated from Eq. (12.2):

$$\dot{\mathbf{Mx}} = \mathbf{Fx} + \mathbf{Gu}(t - \tau) \quad (14.1)$$

These equations are augmented with canonical representations of the transfer-function structure (Sec. 12.2.2). The control input vector is the perturbation value from trim

$$\mathbf{u} = \mathbf{U}_{\text{data}} - \mathbf{U}_0 \quad (14.2)$$

where  $\mathbf{U}_{\text{data}}$  is the time history of the measured control vector and  $\mathbf{U}_0$  is the trim (steady-state) value of the control input vector.

An estimate of the trim control value  $\mathbf{U}_0$  is obtained from the initial condition or the average of the initial few seconds at the start of the test input. For actual test data, the start of the record is rarely a steady-state condition, and the pilot or SCAS is usually moving the control in a continuous manner to maintain a reference condition in the presence of turbulence and other disturbances. So this estimate is rarely accurate enough. Residual errors in the estimate of the reference control are included as an unknown acceleration bias vector  $\dot{\mathbf{x}}_b$  in the state equation:

$$\dot{\mathbf{Mx}} = \mathbf{Fx} + \mathbf{Gu}(t - \tau) + \dot{\mathbf{x}}_b \quad (14.3)$$

This constant bias term also provides a first-order correction for the effects of process noise in the estimate obtained from Eq. (14.1), such as turbulence, unmeasured secondary controls, and numerical integration errors. Because this correction is a constant vector, it does not change the dynamic characteristics of the predicted response.

The output equation form, repeated from Eq. (12.3), is

$$\dot{\mathbf{y}} = \mathbf{H}_0 \mathbf{x} + \mathbf{H}_1 \dot{\mathbf{x}} \quad (14.4)$$

but now it will include *only measured data channels*. The perturbation output vector for six-DOF model verification in a cruise condition will be

$$\mathbf{y} = \begin{bmatrix} \alpha_{nb} \\ \beta_{nb} \\ p \\ q \\ r \\ a_x \\ a_y \\ a_z \\ \phi \\ \theta \end{bmatrix} \quad (14.5)$$

which includes all of the measured signals, including the roll and pitch attitudes, and so is different from the output vector used in identification [Eq. (13.30)].

The perturbation time history of the flight data, needed for comparison with the identified model response of Eq. (14.5), is obtained by subtracting the trim (reference) output value  $\mathbf{Y}_0$  from the flight record:

$$\mathbf{y}_{\text{data}} = \mathbf{Y}_{\text{data}} - \mathbf{Y}_0 \quad (14.6)$$

As in the earlier case of the control input, an estimate of the reference output value  $\mathbf{Y}_0$  is obtained from the initial condition or the average of a few seconds of flight-test data just prior to the start of the test input. But this is generally not sufficiently accurate because the start of the record rarely corresponds to a steady-state condition. Additional contributions to the measured output can also be present because of sensor biases, misalignments of the instrumentation, and various other influences such as aerodynamic interference during the record.

Residual errors in the output estimate are included as a constant (unknown) reference-shift vector  $\mathbf{y}_{\text{ref}}$  in the perturbation model output equation of Eq. (14.4),

$$\mathbf{y} = \mathbf{H}_0 \mathbf{x} + \mathbf{H}_1 \dot{\mathbf{x}} + \mathbf{y}_{\text{ref}} \quad (14.7)$$

for comparison with the perturbation flight data  $\mathbf{y}_{\text{data}}$ . An accurate value of output reference shift  $\mathbf{y}_{\text{ref}}$  must be identified. As in the case of the bias correction of Eq. (14.3), the reference correction is a constant vector and does not change the dynamics of the identified model response.

The basic procedure for time-domain verification is to numerically integrate (fourth-order Runge–Kutta method herein) the equations of motion (14.3) and (14.7) using the measured (perturbation) control vector [ $\mathbf{u}$ , defined in Eq. (14.2)] and then compare the model response [ $\mathbf{y}$  of Eq. (14.7)] with the perturbation aircraft response  $\mathbf{y}_{\text{data}}$  of Eq. (14.6). The matrices  $\mathbf{M}$ ,  $\mathbf{F}$ ,  $\mathbf{G}$ , and  $\boldsymbol{\tau}$  have already been identified, and the matrices  $\mathbf{H}_0$  and  $\mathbf{H}_1$  are part of the model structure definition (Chapters 12 and 13). These matrices are all fixed in the time-domain verification process. However, the constant vectors  $\mathbf{x}_b$  and  $\mathbf{y}_{\text{ref}}$  are unknown, and they must be determined to achieve an accurate assessment of the identified model.

When the modes of the identified model are stable, all of the eigenvalues  $\lambda_i = \sigma_i + j\omega_i$ ,  $i = 1, 2, \dots, n$ , are in the left half-plane ( $\sigma_i < 0$ ). In this case, the influence of small errors in trim controls and measured outputs as obtained from the start of the record will die out at a rate of  $e^{\sigma_i t}$  and can be neglected. However, if the identified model contains unstable modes ( $\sigma_i > 0$ ), the effects of even small errors will increase at a rate  $e^{\sigma_i t}$ , eventually swamping the response prediction and making a valid assessment of model fidelity difficult to achieve. Even if the bias and reference-shift vectors associated with the flight condition at the beginning of the flight-data record are known with a high degree of accuracy, the buildup of errors from numerical integration alone would cause divergence for unstable models. This is a key reason that the unknown vectors  $\mathbf{x}_b$  and  $\mathbf{y}_{\text{ref}}$  must be identified with procedures that utilize all of the flight data, not just estimated based on the first 2 sec of flight data.

Sophisticated data reconstruction tools such as SMACK (Chapter 6) can be used to estimate the needed vectors  $\mathbf{x}_b$  and  $\mathbf{y}_{\text{ref}}$ . However, the simple output-error minimization method presented in the next section is noniterative (thus computationally very fast) and easily implemented, and it provides fully satisfactory results.

### 14.3 Estimating the Constant Bias and Reference Shift

The residual bias  $\mathbf{x}_b$  and reference-shift  $\mathbf{y}_{\text{ref}}$  vectors are collected into a single identification parameter vector  $\boldsymbol{\Theta}$ :

$$\boldsymbol{\Theta} = \begin{bmatrix} \dot{\mathbf{x}}_b \\ \mathbf{y}_{\text{ref}} \end{bmatrix} \quad (14.8)$$

There are  $n + n_o$  elements in the identification vector, corresponding to the sum of the number of states and outputs. The parameter value of  $\boldsymbol{\Theta}$  is sought, which minimizes the sum of the squares of the output errors. In other words, the cost function to be minimized is

$$J(\boldsymbol{\Theta}) = \sum_{i=1}^{n_t} [(\mathbf{y}_{\text{data}} - \mathbf{y})^T \mathbf{W} (\mathbf{y}_{\text{data}} - \mathbf{y})] \quad (14.9)$$

where

$\mathbf{y}_{\text{data}}$  = perturbation time-history vector from the verification flight data [Eq. (14.6)]  
 $\mathbf{y}$  = perturbation model time-history response vector [Eq. (14.7)] obtained from the integration of the model equations  
 $n_t$  = number of time-history points in the verification data record  
 $\mathbf{W}$  =  $n_o \times n_o$  diagonal matrix of weighting factors for each output, as in

$$\mathbf{W} = \text{diag} \left\{ \text{wt}_{y_1}^2, \text{wt}_{y_2}^2, \dots, \text{wt}_{y_{n_o}}^2 \right\} \quad (14.10)$$

These weighting factors balance the relative output amplitudes of the various signals in the cost function. A good rule of thumb is to select these based on the approximate amplitudes of the variables. For flight mechanics applications, a good choice is

$$1 \text{ deg-error} : 1 \text{ deg/s-error} : 1 \text{ ft/s-error} : 1 \text{ ft/s}^2\text{-error} \quad (14.11)$$

For a longitudinal model example, the weights will all be unity when the output errors are calculated as follows:  $\theta$  in deg,  $q$  in deg/s,  $u$  in ft/s, and  $a_x$  in ft/s<sup>2</sup>. When the output of the attitudes and attitude rates are in radians and radians/second, respectively, then the weights are  $\text{wt}_\theta = 57.3$ ,  $\text{wt}_q = 57.3$ .

Reference to Eqs. (14.3) and (14.7) shows that changes in the bias and reference shift parameter vector  $\Theta$  will have a linear influence on the cost function of Eq. (14.9). So, unlike the model identification problem of Eq. (12.20), the calculation for the parameter vector  $\Theta$  reduces to a simple linear least-squares solution. The solution is obtained in a single pass using the pseudo-inverse<sup>141</sup>:

$$\Theta = (\mathbf{D}^T \mathbf{W} \mathbf{D})^{-1} \mathbf{D}^T \mathbf{W} \mathbf{y}_e \quad (14.12)$$

where  $\mathbf{y}_e = \mathbf{y}_{\text{data}} - \mathbf{y}$  is the vector of perturbation output errors obtained with no corrections ( $\Theta = 0$ ) and  $\mathbf{D}$  is the matrix of gradients  $\partial \mathbf{y}_e / \partial \Theta$  calculated numerically. The values for the elements of the bias  $\mathbf{x}_b$  and the reference-shift  $\mathbf{y}_{\text{ref}}$  vectors determined by this calculation are substituted into Eqs. (14.3) and (14.7) to obtain the final perturbation model time histories  $\mathbf{y}$  for comparison with the perturbation flight data  $\mathbf{y}_{\text{data}}$ .

The solution of Eq. (14.12) minimizes the weighted least-squares error function of Eq. (14.9). The *rms fit error* is expressed as

$$J_{\text{rms}} = \sqrt{\left( \frac{1}{n_t \cdot n_o} \right) \sum_{i=1}^{n_t} [(\mathbf{y}_{\text{data}} - \mathbf{y})^T \mathbf{W} (\mathbf{y}_{\text{data}} - \mathbf{y})]} \quad (14.13)$$

which provides a useful overall measure of model time-domain accuracy. Experience shows that a value in the range of

*Guideline:*

$$J_{\text{rms}} \leq 1.0 \text{ to } 2.0 \quad (14.14)$$

generally reflects an acceptable level of accuracy for flight-dynamics modeling when the error function is calculated based on the units of Eq. (14.11). So, for example, a cost function of  $J_{\text{rms}} = 1.0$  reflects an overall rms error of 1 deg, 1 deg/s, 1 ft/s, and 1 ft/s<sup>2</sup>. A predictive cost value in the range of Eq. (14.14) is typical when the model identification meets the guidelines of Chapter 12:  $J_{\text{ave}} \leq 100$  [Eq. (12.23)] and  $\text{CR}_i \leq 20\%$  [Eq. (12.40)]. The recommended range is typical for verification of coupled models of helicopters, where the inputs and outputs of all degrees of freedom are included for a single maneuver. For example, the six-DOF model of the lightweight helicopter (Sec. 13.12) has an associated cost function for pitch inputs of ( $J_{\text{rms}} = 1.46$ ). This indicates good predictive accuracy, consistent with the plotted results of Fig. 13.18.

Fixed-wing studies usually involve a decoupled (three-DOF) model structure and often higher quality flight-test data. Lower cost functions are then achievable:

$$J_{\text{rms}} \leq 0.5 \text{ to } 1.0 \quad (14.15)$$

reflecting a higher degree of predictive accuracy, as for the identified models of the XV-15 (Secs. 14.7–14.9). The rms cost functions for the Shadow™ fixed-wing UAV results are  $J_{\text{rms}} = 0.53$  for the pitch input (Fig. 13.12) and  $J_{\text{rms}} = 0.57$  for the throttle input (Fig. 13.13), which are well within these guidelines, and consistent with the plotted time-domain results.

The Theil inequality coefficient (TIC), adopted by Jategaonkar et al.,<sup>185</sup> provides a normalized criterion ( $0 < \text{TIC} < 1$ ) for assessing model predictive accuracy. By including the relative weighting of [Eq. (14.10)], we have

$$\text{TIC} = \frac{\sqrt{[1/(n_t \cdot n_o)] \sum_{i=1}^{n_t} [(\mathbf{y}_{\text{data}} - \mathbf{y})^T \mathbf{W}(\mathbf{y}_{\text{data}} - \mathbf{y})]}}{\sqrt{[1/(n_t \cdot n_o)] \sum_{i=1}^{n_t} [\mathbf{y}^T \mathbf{W} \mathbf{y}]} + \sqrt{[1/(n_t \cdot n_o)] \sum_{i=1}^{n_t} [\mathbf{y}_{\text{data}}^T \mathbf{W} \mathbf{y}_{\text{data}}]}} \quad (14.16)$$

A value of  $\text{TIC} = 0$  corresponds to a model with perfect predictive capability, and a value close to  $\text{TIC} = 1$  corresponds to no predictive capability. Jategaonkar et al.<sup>185</sup> propose the following guideline:

*Guideline:*

$$\text{TIC} \leq 0.25 \text{ to } 0.30 \quad (14.17)$$

for good predictive agreement. The calculation of TIC in Eq. (14.16) normalizes the rms error by the perturbation response magnitudes ( $\mathbf{y}$  and  $\mathbf{y}_{\text{data}}$ ) and hence

reflects the errors as expressed in percentage terms. When the verification analysis includes many outputs [e.g.,  $n_o = 10$  in Eq. (14.5)], some of the off-axis response variables can exhibit small absolute variations. Thus a large percentage error in a response variable with a small absolute variation can result in a large overall value of TIC —even when the rms cost function  $J_{\text{rms}}$  is within an acceptable range.

In the case of the pitch-response verification for the lightweight helicopter example of Sec. 13.12, the result is  $\text{TIC} = 0.19$ , well within the guideline of Eq. (14.17), and again consistent with the good agreement of the plotted results of Fig. 13.18. The identified model for the Shadow™ produces  $\text{TIC} = 0.067$  and  $\text{TIC} = 0.35$  for the pitch and throttle inputs, respectively. The larger value for the throttle input verification reflects very small amplitudes for all of the responses except for longitudinal acceleration (Fig. 13.13), and so large relative percentage errors (and higher TIC).

A low time-domain cost function can sometimes be accompanied by large biases and reference shifts. This can be an indication of excessive error in the identified model or the presence of correlation effects in  $\Theta$  as discussed next.

#### 14.4 Correlation Problem

The solution for the correction vector  $\Theta$  becomes ill conditioned when varying two or more of the parameters has the same effect on the cost function. This is another example of the parameter correlation problem that was addressed in Sec. 12.3.3. Consider the following simple model of the longitudinal dynamics of a hovering helicopter:

$$\dot{q} = M_q q + M_u u + M_{\delta_e} \delta_e \quad (14.18)$$

$$\dot{u} = X_u u - g\theta + X_{\delta_e} \delta_e \quad (14.19)$$

$$\dot{\theta} = q \quad (14.20)$$

The measured signals included in the perturbation output vector are

$$\mathbf{y} = \begin{bmatrix} q \\ \theta \\ a_x \end{bmatrix} \quad (14.21)$$

The vector of bias corrections are included in the equations of motion (14.3), resulting in

$$\begin{bmatrix} \dot{q} \\ \dot{u} \\ \dot{\theta} \end{bmatrix} = \begin{bmatrix} M_q & M_u & 0 \\ 0 & X_u & -g \\ 1 & 0 & 0 \end{bmatrix} \begin{bmatrix} q \\ u \\ \theta \end{bmatrix} + \begin{bmatrix} M_{\delta_e} \\ X_{\delta_e} \\ 0 \end{bmatrix} \begin{bmatrix} \dot{\delta}_e \\ \delta_e \\ 0 \end{bmatrix} + \begin{bmatrix} \dot{q}_b \\ \dot{u}_b \\ \dot{\theta}_b \end{bmatrix} \quad (14.22)$$

## 440 AIRCRAFT AND ROTORCRAFT SYSTEM IDENTIFICATION

The vector of reference shifts is added to output equation as in Eq. (14.7) for comparison with the perturbation flight data measurements:

$$\begin{bmatrix} q \\ \dot{a}_x \\ \theta \end{bmatrix} = \begin{bmatrix} q \\ \dot{u} + g\theta \\ \theta \end{bmatrix} + \begin{bmatrix} q_{\text{ref}} \\ a_{x_{\text{ref}}} \\ \theta_{\text{ref}} \end{bmatrix} \quad (14.23)$$

The bias and reference-shift values make up the unknown parameter vector

$$\Theta = \begin{bmatrix} \dot{q}_b & \dot{u}_b & \dot{\theta}_b & q_{\text{ref}} & a_{x_{\text{ref}}} & \theta_{\text{ref}} \end{bmatrix} \quad (14.24)$$

We seek the value  $\Theta$  that minimizes the cost function of Eq. (14.9). For this model structure, the bias term  $\dot{\theta}_b$  in Eq. (14.22) and the reference shift  $q_{\text{ref}}$  in Eq. (14.23) produce the same change in the cost function and thus are fully correlated. This situation will cause the solution to be ill conditioned. As in the case of model identification, one parameter must be fixed (at zero or an a priori value), and the other can be retained in solution for  $\Theta$ . In practice, it has been found that a good approach is to include biases on all of the rigid-body state equations and include the reference shifts for all rigid-body measurements *except*  $p$ ,  $q$ , and  $r$ . This approach generally avoids all correlation problems in the solution. In the current example, we would fix  $q_{\text{ref}} = 0$  and include  $\dot{\theta}_b$  in the correction parameter vector  $\Theta$  of Eq. (14.24).

### 14.5 Data Conditioning for Time-Domain Verification

The test data included in the cost function should be based on an appropriate segment of the overall record. The verification record should start with about 2 s of the trim condition, to ensure that the reference-shift can be accurately determined, and finish with control recovery back to trim. Once the data segment is selected, the test data should be processed with a low-pass filter to eliminate signal content that is beyond the frequency range of applicability of the identified model. This step is important so that the comparison between the flight responses and model responses is for frequencies consistent with the identification process. For example, when validating a six-DOF quasi-steady flight-mechanics model, the flight input and output data should be processed with a low-pass filter having a bandwidth of about 12 rad/s.

### 14.6 Time-Domain Verification in CIFER® Using VERIFY

Time-domain model verification is carried out in CIFER® using the VERIFY module. As was the case with FRESPID (Sec. 7.11), the data source for VERIFY is time histories, and the same data conditioning options are available (e.g., filtering, scaling, decimation, start and end time). The user interface allows the individual

components of the bias  $\dot{x}_b$  and reference-shift  $y_{ref}$  terms to be included in the identification vector  $\Theta$ . Values for the weighting matrix [Eq. (14.10)] are also user definable, as appropriate to the units of the output variables [e.g., Eq. (14.11)]. The identification vector  $\Theta$  and resulting cost function are determined and displayed. Finally, all of the results are presented in plot and tabular form and then stored in the database. Results are presented as *total* (i.e., original) flight data  $U_{data}$  and  $Y_{data}$  vs total model prediction ( $y + Y_0$ ). Note that for notational convenience we retain the same notation on the time-history plots (e.g.,  $\delta_{lat}$ ,  $\delta_{lon}$ , ...,  $u$ ,  $v$ ,  $w$ ,  $p$ , ...), but are referring to *total* quantities in this case. The comparison of results between various cases stored in the database is useful in evaluating alternative model structures and in determining the sensitivity to input form, shape, and polarity (as an indication of the significance of nonlinearities).

#### 14.7 Closed-Loop Transfer-Function Model Verification for XV-15

This example demonstrates the verification of the XV-15 closed-loop roll-response model in hover as obtained in Sec. 12.8 (CLROLL2). Recall that this final (reduced) model is a second-order canonical structure representation of Eq. (12.71). The flight-test data were collected for a lateral step input  $\delta_{lat}$  with the roll and yaw SCAS-on. As shown in Fig. 14.1a, the record consists of about 2 s of trim, followed by a 2-s step, and then a recovery to trim.

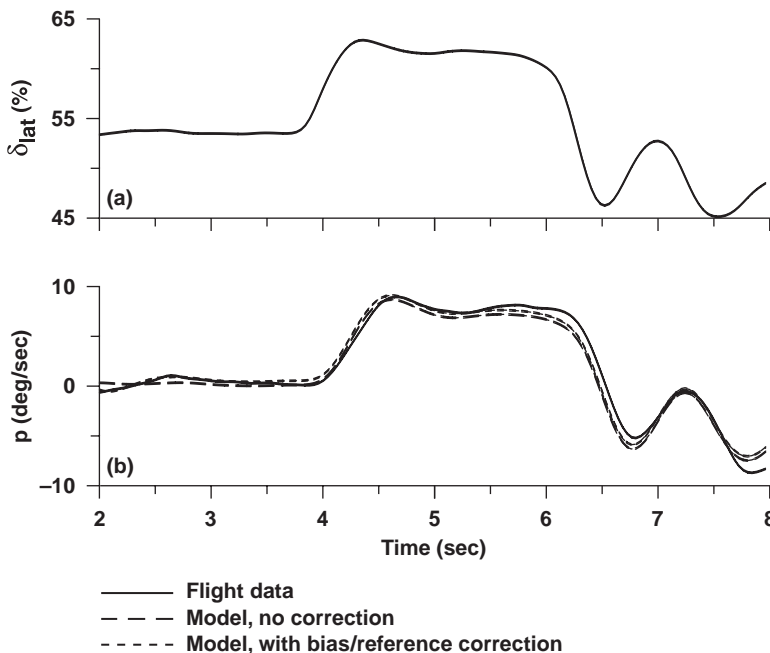


Fig. 14.1 Lateral step input for closed-loop model verification (XV-15, hover).

**Table 14.1 Roll-response verification results for closed-loop model (XV-15, hover)<sup>a</sup>**

Engineering symbols	CIFER® mnemonic	Identified bias and reference shift values
$\dot{x}_{1b}$	X1	0.881
$\dot{x}_{2b}$	X2	-0.081
$p_{ref}$	P	-0.707
Cost summary table		
$J_{rms}$	Cost	0.69
TIC	TIC	0.068

<sup>a</sup>Case name: CLROLL2#741.

The predicted model response and flight-test data for roll rate  $p$  are shown in Fig. 14.1b. The trim values were determined by examining the first 2-s of data. The dashed curve is the model response as obtained with *no bias or reference corrections*. The dotted line shows the model result including these corrections. The effect of the bias and reference-shift corrections is small because the closed-loop response is well damped. The correction values themselves are small, as shown in Table 14.1. The reference shift  $p_{ref}$  is less than 1 deg/s. The simple second-order (LOES) model is seen to provide a satisfactory prediction of the short-term closed-loop response, as also reflected in the good rms cost function value  $J_{rms} = 0.69$  and very low associated TIC = 0.068. Both cost functions are well within the guidelines.

#### 14.8 Bare-Airframe Model Verification for Cruise (XV-15)

This example shows the time-domain verification of the XV-15 bare-airframe model in cruise obtained in Sec. 13.8.3 (Table 13.7, V170M3).

The roll-step flight data were collected for the SCAS-off configuration (Fig. 13.1). The control input is dominated by the aileron surface deflection  $\delta_a$  for most of the record, as shown in Fig. 14.2. The deflection of the rudder  $\delta_r$  at about 10 s is associated with the piloted recovery when the roll input is removed. Both input time histories are included in the calculation of the model response for comparison with the flight data.

The aircraft response is shown in Fig. 14.3. Note that the model verification involves a large maneuver (40-deg roll angle), rather than small perturbations, to demonstrate fidelity for typical piloted flying tasks. The responses with no bias/reference-shift correction are shown again in dashes in Fig. 14.3, and they are already in good agreement with the flight data. Including the bias/reference-shift terms (dotted lines) corrects the small drift in roll rate  $p$ . The model now exhibits excellent overall predictive capability, even for this large transient maneuver. Clearly, the identified model is valid well beyond small perturbation motions. The results are consistent with the good time-domain cost functions

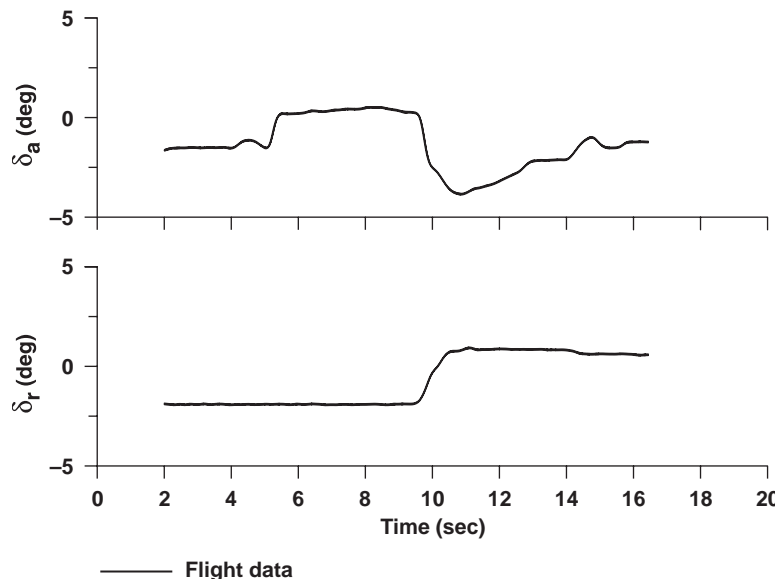


Fig. 14.2 Control inputs for roll-response verification (XV-15, cruise).

( $J_{\text{rms}} = 0.64$ , TIC = 0.038, of Table 14.2), frequency-response identification cost function ( $J_{\text{ave}} = 33.3$ ), and with the parameter accuracy metrics all being within the recommended guidelines.

The control inputs for a yaw-step input are shown in Fig. 14.4. While the dominant input is seen in the rudder surface  $\delta_r$ , both control channels are included in the calculation of the model response. The aircraft data and model predictions are shown in Fig. 14.5. Again, the transient motion is quite large, with a maximum roll angle of nearly 30 deg. The model responses with the bias/reference-shift correction included are shown in Fig. 14.5. There is excellent overall agreement of the model, as again reflected in the time-domain cost functions shown in Table 14.2. The coupled motions in roll, yaw, and sideslip associated with the Dutch-roll response (caused primarily by  $L_v$ ) are well predicted by the identified model, consistent with the good frequency-response fits.

Table 14.2 lists the identification biases and reference shifts for roll- and yaw-step response verifications. The  $\dot{v}$  bias term reflects small differences in the trim condition between the identification and verification flight conditions because this correction is correlated with the trim velocities in the Coriolis terms [ $U_0 r, W_0 p$  of Eq. (13.52)]. With the  $\dot{v}$  bias term excluded, there is only a minimal change in the cost functions ( $J_{\text{rms}} = 0.64$  and  $J_{\text{rms}} = 0.59$  for the aileron and rudder steps, respectively). This confirms that the  $\dot{v}$  bias correction term is of little importance for the model response with the stable dynamics of the cruise condition (Table 13.10).

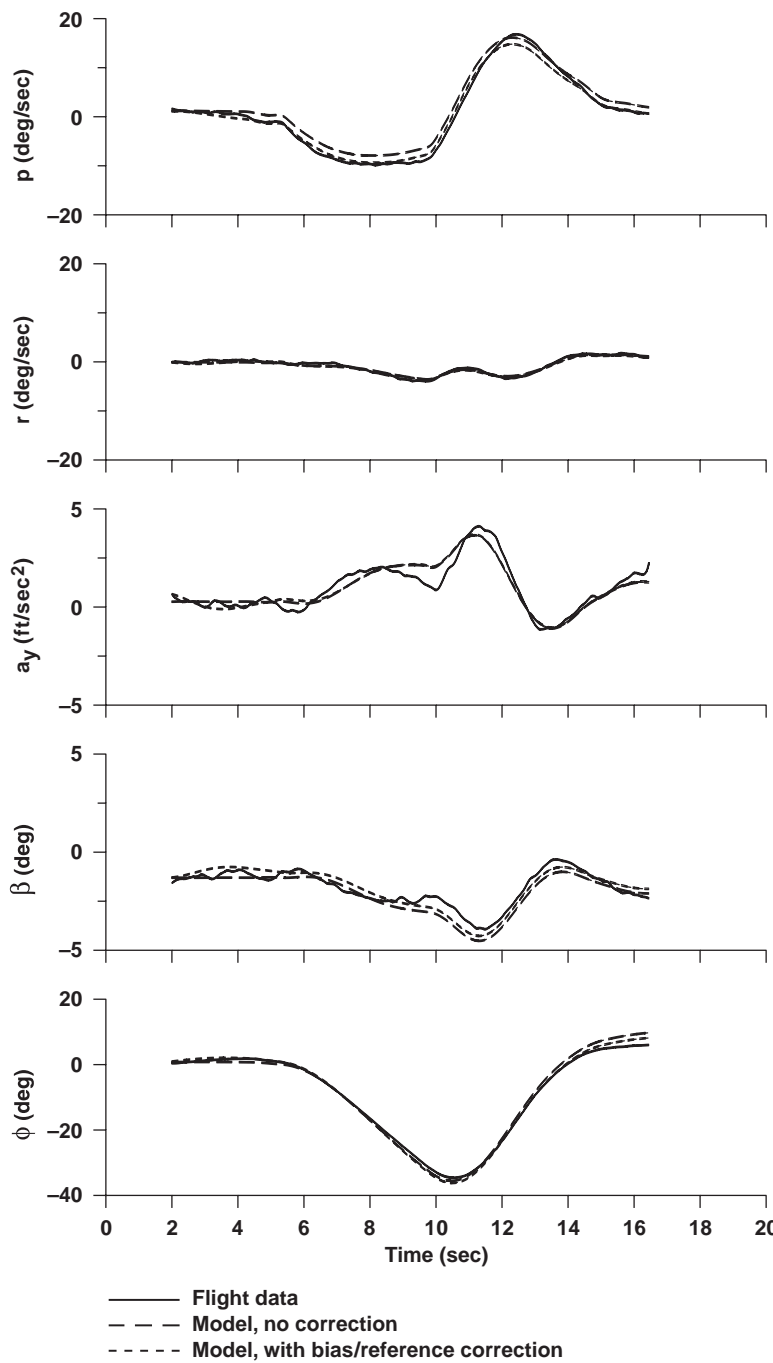


Fig. 14.3 Roll-response verification of bare-airframe model (XV-15, cruise).

Table 14.2 Verification results for bare-airframe model (XV-15 cruise)<sup>a</sup>

Engineering symbols	CIFER® mnemonic	Identified bias and reference-shift values	
		Roll step	Yaw step
$\dot{v}_b$	V	0.778	3.001
$\dot{p}_b$	P	-0.005	0.016
$\dot{r}_b$	R	-0.017	-0.006
$\dot{\phi}_b$	PHI	0.021	0.007
$P_{ref}$	P	0.000	0.000
$r_{ref}$	R	0.000	0.000
$a_{y_{ref}}$	AY	0.365	0.250
$\beta_{ref}$	BETA	0.013	-0.193
$\phi_{ref}$	PHI	0.158	-1.051
Cost summary table			
$J_{rms}$	Cost	0.64	0.55
TIC	TIC	0.038	0.049

<sup>a</sup>Case name: V170M3; Case ID: final cruise model.

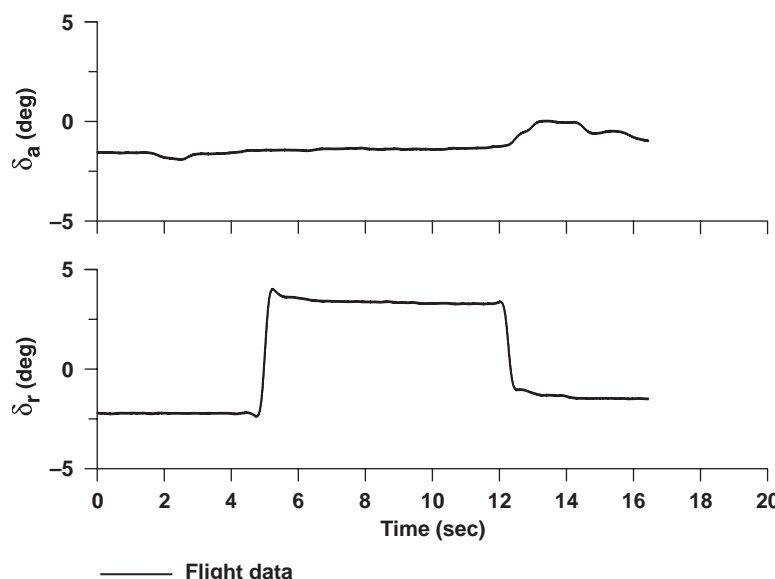


Fig. 14.4 Control inputs for yaw-response verification (XV-15, cruise).

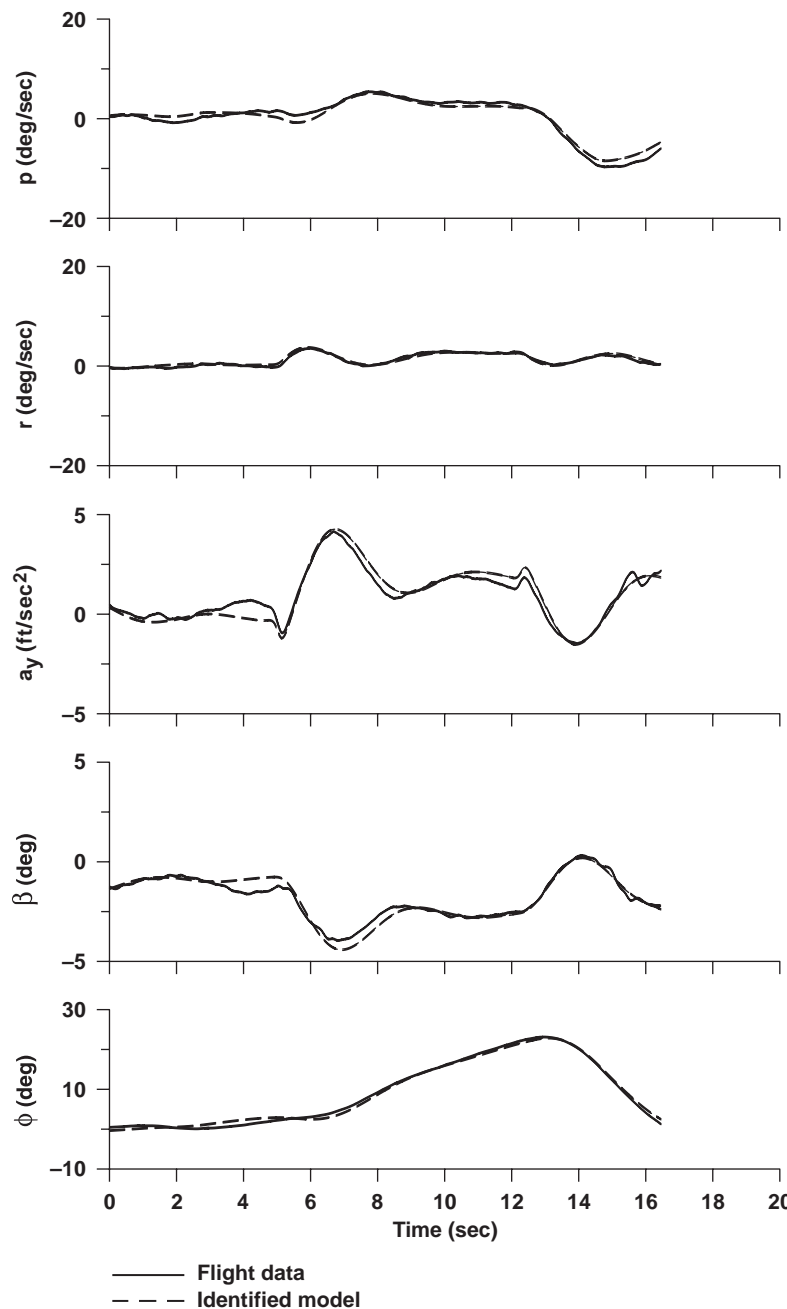


Fig. 14.5 Yaw-response verification of bare-airframe model (XV-15, cruise).

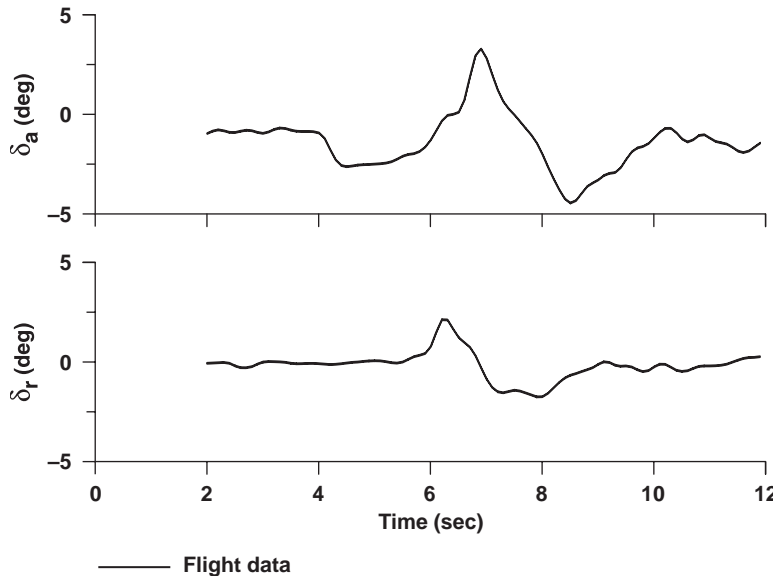


Fig. 14.6 Control inputs for roll-response verification (XV-15, hover).

#### 14.9 Bare-Airframe Model Verification for Hover (XV-15)

This example shows the verification of the bare-airframe hover model obtained in Sec. 13.9.3 (HVMODM3, Table 13.14) for a piloted roll input. The test data were taken with SCAS-off in the roll channel but SCAS-on in the yaw channel. The yaw channel responds during the roll step input, so that the verification must include both bare-airframe control surfaces ( $\delta_a$  and  $\delta_r$ ) as the inputs to the model (Fig. 14.6).

The measured responses ( $p$ ,  $r$ ,  $a_y$ ,  $\phi$ ) are shown in Fig. 14.7. As in the earlier examples, the solid line shows the flight-test data, the dashed line shows the results predicted without correcting for bias and reference shifts, and the dotted line shows the results with the corrections included.

Without the bias and reference-shift correction, the  $a_y$  response exhibits a clear offset. This reflects an inconsistency between the accelerometer alignment and the roll-angle measurement, as would be expected based on Eq. (6.34). Open-loop time integration of the unstable bare-airframe dynamics [ $t_{\text{double}} = 4.44$  s, Eq. (13.71)] causes the divergent behavior that is apparent in the angular responses. However, when the small bias and reference-shift corrections (Table 14.3) are included, the characteristics of the model response match the flight-test data very well, as also seen in the low values of the cost functions  $J_{\text{rms}} = 0.61$ , TIC = 0.065. The model demonstrates good predictive capability, even for the rather large transient roll angle (20 deg) of this maneuver. In addition, the yaw-response coupling is well captured. The ability to accurately identify an unstable bare-airframe state-space model from closed-loop test data using the frequency-response method (Chapter 8) is also verified in this example.

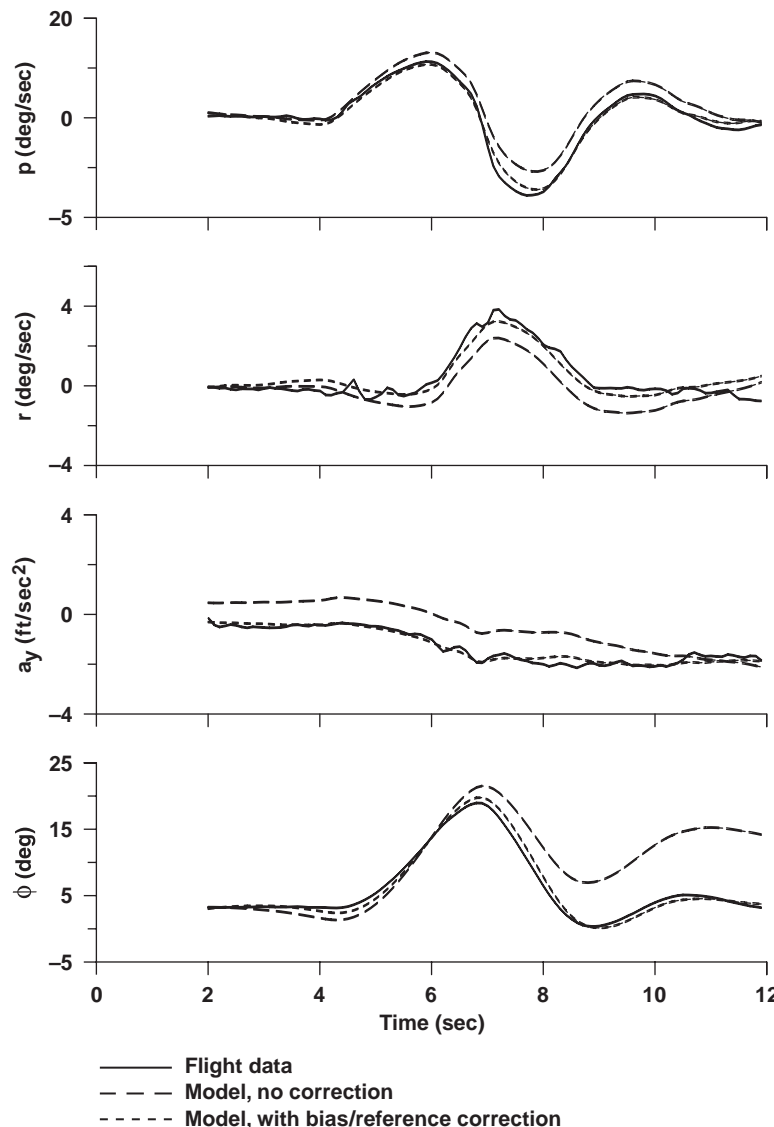


Fig. 14.7 Verification of bare-airframe model (XV-15, hover).

**Table 14.3 Roll-response verification results for closed-loop model (XV-15, hover)<sup>a</sup>**

Engineering symbols	CIFER® mnemonic	Identified bias and reference shift values
$\dot{v}_b$	V	0.875
$\dot{p}_b$	P	-0.004
$\dot{r}_b$	R	0.003
$\dot{\phi}_b$	PHI	0.018
$\dot{\phi}_{ref}$	PHI	-0.227
$p_{ref}$	P	0.000
$r_{ref}$	R	0.000
$a_{y_{ref}}$	AY	-0.772
Cost summary table		
$J_{rms}$	Cost	0.61
TIC	TIC	0.065

<sup>a</sup>Case name: HVMODM3#743; Case ID: final hover model.

## Problems

*Time-domain verification for the identified pendulum canonical model*

**14.1** Compare the nonlinear response of the stable pendulum to the prediction for the linearized (canonical) model (**Problem 12.2**) with VERIFY, using the simulated doublet response of the nonlinear pendulum saved in **Problem 5.9**. Introduce a small constant control input bias in the nonlinear simulation at the summing junction where process noise is added in Fig. P8.5. Compare the nonlinear response again to the identification model. Now repeat the verification and include the identification of the correction terms. How much does the cost  $J_{rms}$  change?

**14.2** Obtain hard copies of the results of **Problem 14.1** by utilizing CIFER® utilities 32 and 34.

**14.3** Compare the nonlinear response of the unstable pendulum to the prediction for the linearized (canonical) model (**Problem 12.4**) with VERIFY, using the simulated doublet response of the nonlinear pendulum saved in **Problem 5.9**. Introduce a small constant control input bias in the nonlinear simulation at the summing junction where process noise is added in Fig. P8.5. Compare the nonlinear response again to the identification model. Now repeat the verification, and include the identification of the correction terms. Do you see the need for the correction terms in unstable model verification? For best results use only the first 8–10 s of your doublet record.

**14.4** Obtain hard copies of the results of **Problem 14.3** by utilizing CIFER® utilities 32 and 34.

## 450 AIRCRAFT AND ROTORCRAFT SYSTEM IDENTIFICATION

**14.5a** Add process noise (as described in **Problem 7.14**) to the pendulum simulation of a verification doublet maneuver. How does the presence of the noise affect cost, bias, and offset for the stable pendulum time-domain verification as compared to **Problem 14.1**? Based on this analysis of noise vs cost, what can you say about the meaning of  $J_{\text{rms}} = 1$ ?

**14.5b** How does the presence of process noise in the verify maneuver affect cost, bias, and offset for the unstable pendulum time-domain verification as compared to **Problem 14.3**? For best results use only the first 8–10 s of your doublet record.

*Time-domain verification of the identified XV-15 state-space model*

**14.6** Complete the time-domain verification of your intermediate and final XV-15 models (hover or cruise) to demonstrate that the model structure reduction steps were correct and did not significantly degrade the predictive accuracy.

**14.7** Look at the final model identification of the XV-15 (hover or cruise). Introduce variations in the final identification parameters based on the Cramér-Rao results ( $\pm 0.2\sigma$ ,  $\pm 0.5\sigma$ ,  $\pm 1.0\sigma$ ,  $\pm 2.0\sigma$ ), and rerun the time-response verification for each case. Are the results consistent with the estimates of parameter accuracy?

**14.8** Compare the predictive capability of the identification model with the simulation (GTR) model at cruise or hover. Is the comparison of the time-response plots and the cost functions for identification vs simulation consistent with the frequency-response behavior?

## 15

## Higher-Order Modeling of Coupled Rotor/Fuselage Dynamics

Modern helicopters often feature rotor designs with larger equivalent hinge offsets and/or reduced moments of inertia to increase the effective flap stiffness for improved maneuverability and agility. The fuselage and rotor responses become fully coupled, and the quasi-steady assumption used in the model structures of Chapter 13 is no longer suitable. The accurate characterization of these configurations requires an extended model structure that includes explicitly the regressive flapping, coupled inflow/coning, and regressive lead-lag states of the rotor.

The *hybrid model structure* for coupled fuselage/rotor dynamics identification was proposed initially by Tischler and Cauffman<sup>15</sup> and is presented in its complete form in this chapter. The formulation is a general template for helicopter system identification, applicable to a wide range of design configurations and flight conditions. Flight-test identification results using this model structure are presented for the SH-2G helicopter (updated from Tischler and Tomashofski<sup>139</sup>). A series of models spanning the flight envelope was identified using a common model structure.

The key topics covered in this chapter include the following: background and literature on the identification of extended helicopter models, hybrid model structure for coupled rotor/fuselage identification, hybrid model identification of SH-2G helicopter dynamics, and lead-lag dynamics identification of S-92 helicopter.

### 15.1 Background and Literature on Identification of Extended Helicopter Models

The rotorcraft identification results of Chapters 13 and 14 were based on quasi-steady model structures, which characterize the aircraft forces and moments solely in terms of the fuselage states. For flight vehicles with symmetric configurations, such as fixed-wing, tilt-rotor, and V/STOL aircraft, the quasi-steady assumption results in three-DOF model structures for decoupled longitudinal and lateral/directional motion. The quasi-steady assumption is valid for helicopters with low flap stiffness rotors because in this case the dynamic system decouples into distinct fuselage and rotor model modes, as discussed in Sec. 11.7.1 and illustrated in Figs. 11.9 and 11.11. In state-space identification, the fuselage motions are embodied in a fully coupled six-DOF quasi-steady model structure, and the transient rotor response is included as equivalent time delays on the control inputs. For the light helicopter example of Sec. 13.12, which features a small hinge offset, the six-DOF model structure was seen to generally be satisfactory, except for the mismatch in the off-axis angular response  $p/\delta_{\text{lon}}$ .

## 452 AIRCRAFT AND ROTORCRAFT SYSTEM IDENTIFICATION

As the flap stiffness increases, the rotor and fuselage modes become coupled, as seen in the root-locus plot of Fig. 11.9, and the angular-rate response is now second-order [Eq. (11.40)] in the frequency range of interest. Transfer-function modeling results for the OH-58D helicopter (Sec. 11.7.2) clearly show the requirement for a coupled rotor/fuselage flap response. The transfer-function identification results for the Bo-105 helicopter (Sec. 11.8) show that the lead-lag air resonance dynamics must also be included for an accurate characterization of the coupled response to about 30 rad/s. The control system design study of Sec. 11.8 shows that the stability behavior of the lead-lag mode sets the limit on roll-rate feedback.

A general state-space model structure for helicopter flight mechanics that is applicable for a range of flap stiffness values and that can be applied across the flight envelope is needed. Such a model must include the explicit dynamics of rotor flapping, coning, dynamic inflow, lead-lag, and the engine torque response. The hybrid model structure<sup>139</sup> presented herein is well suited to this purpose. A detailed example for the SH-2G helicopter is given to illustrate the modeling methods and typical results.

Many excellent examples of helicopter identification results using coupled fuselage/rotor formulations are found in the literature, and they provide much additional background information for the material in this chapter. Kaletka and his colleagues from the DLR developed extended model structures and identification methods in a comprehensive effort involving the Bo-105 helicopter. This helicopter exhibits highly coupled dynamics of the fuselage and rotor systems, owing to the large equivalent hinge offset (12%). Some excellent examples of this work are Kaletka and von Gruenhagen,<sup>74</sup> Fu and Kaletka,<sup>36</sup> and Kaletka and Gimonet.<sup>37</sup> These references compare six-DOF (quasi-steady) vs higher-order model identification, showing the need for extended models to capture the high-frequency response characteristics that are critical for control system design applications. Houston and Black<sup>39</sup> examined aspects of identifying extended models of the vertical/coning/inflow degrees of freedom from flight-test data of the Puma helicopter.

The identification of higher-order helicopter models using CIFER<sup>®</sup> is reported widely in the literature, including application to the Bo-105,<sup>15</sup> B412HP,<sup>203</sup> AH-64,<sup>197,204</sup> OH-58D,<sup>123</sup> UH-60,<sup>103</sup> SBMR wind-tunnel test,<sup>92</sup> S-92,<sup>17</sup> SH-2G,<sup>139</sup> R50 UAV,<sup>205</sup> and RMAX UAV.<sup>206</sup>

This chapter presents the key rotor equations used in the hybrid model structure, without detailed derivation or discussion. Recommended reading covering helicopter flight mechanics is available in a number of excellent references: Chen,<sup>207,208</sup> Heffley et al.,<sup>21</sup> Curtiss,<sup>161</sup> Newman,<sup>209</sup> and Padfield.<sup>200</sup> A comprehensive treatment of helicopter analysis is that of Johnson.<sup>162</sup>

## 15.2 Hybrid Model Formulation

A general formulation for helicopter flight-dynamics identification, referred to as the *hybrid model structure*, that is applicable to a range of configurations (low to high flap stiffness) and is suitable for application across the entire flight envelope (hover to high forward-flight speeds) has been developed. The model

structure includes the key dynamic characteristics in the frequency range of about 0.2–30 rad/s and achieves good predictive accuracy for supporting the primary applications of flight mechanics, simulation, flight-control design/analysis, and handling qualities. Having a single model structure facilitates the interpolation of the identification parameters with airspeed, which is useful for flight-control design at intermediate conditions and for implementation in a continuous, full-envelope, piloted simulation (e.g., Aiken<sup>201</sup> and Tischler<sup>202</sup>).

The important dynamic characteristics in the frequency range of interest include (at least) the following 13 DOF: coupled fuselage/regressive-flap dynamics (eight DOF), coupled coning-inflow dynamics (two DOF), lead-lag dynamics (two DOF), and engine torque response (one DOF).

Kaletka and von Gruenhagen<sup>74</sup> included coupled fuselage/regressive-flapping dynamics in the identification of an eight-DOF dynamic model of the Bo-105 for high-bandwidth flight-control applications. Tischler and Cauffman<sup>15</sup> introduced the *hybrid model* concept for identifying coupled fuselage/regressive-flapping dynamics in a physically consistent model structure as an extension of the *primary analysis model* of Heffley et al.<sup>21</sup> This concept was further developed in CIFER® identification studies of the OH-58D<sup>123</sup> and UH-60<sup>153,210</sup> helicopters, and then formalized in a uniform identification model structure for the full flight envelope identification of the SH-2G helicopter.<sup>139</sup> Additional applications are mentioned in Sec. 15.1.

In the pitch and roll degrees of freedom, the hybrid model structure combines a physical model of coupled fuselage/regressive-flap dynamics and a canonical model of the regressive lead-lag dynamics for accuracy in the mid- to high-frequency range (1–30 rad/s), with a quasi-steady stability derivative (i.e., *lumped parameter*) model for accurate low-frequency dynamics modeling. The inclusion of explicit flapping dynamics takes the place of all of the conventional lumped quasi-steady rotor derivatives associated with angular motion and control inputs ( $L_p$ ,  $L_q$ ,  $L_{\delta_{lat}}$ ,  $X_q$ , etc.), which are dropped. This hybrid formulation is much more accurate than the standard six-DOF model formulation and is physically consistent by avoiding “double-booking” the rotor dynamics effects.

In an analogous hybrid modeling approach for the vertical response, a physical parametric model of coupled coning/inflow, providing an accurate response at higher frequencies, is combined with a stability derivative (quasi-steady) formulation that accurately characterizes the conventional heave damping  $Z_w$  and the other fuselage speed derivatives at lower frequencies. The responses to pedal inputs are well modeled by a conventional quasi-steady formulation. A simple model of the yaw response to collective inputs is included to account for the engine dynamics.

The present hybrid model structure 1) ensures that the coupled rotor and fuselage dynamics of the short-term response are correctly captured in the explicit rotor and inflow equations, 2) retains the response to translational motion and the many coupling effects in the quasi-steady speed derivatives, 3) improves model robustness by minimizing parameter correlation, and 4) achieves identification values that are physically meaningful. Note that the sign conventions adopted herein for flap and lead-lag motion are based on rotor rotation counter-clockwise as viewed from above, which is a U.S. standard.

### 15.2.1 Coupled Fuselage/Rotor Flapping Dynamics

In flight-dynamics applications, the flap dynamics of the rotor blades are best considered from the nonrotating frame of reference (e.g., from the fuselage). The motion of the rotor system can be represented as a disc or *tip-path plane*. Chen<sup>208</sup> provides a succinct derivation of the complete coupled tip-path plane dynamic equations for flight-dynamics applications. The three tip-path plane degrees of freedom of concern are defined relative to the shaft axis. These degrees of freedom are the longitudinal tilting or *longitudinal flap angle*  $\beta_{1c}$ , *lateral flap angle*  $\beta_{1s}$ , and vertical motion or *coning angle*  $\beta_0$ , as depicted in Fig. 15.1. Positive lateral flapping is for blade flap up over the right side (disc tilts to left), and positive longitudinal flapping is for blade flap up over rear (disc tilts forward). The primary rotor forces and moments transferred to the helicopter fuselage are associated with these three tip-path-plane angles.

The tip-path-plane dynamics are composed of three second-order flapping modes—excluding the *reactionless* mode for a four-bladed rotor, as it does not

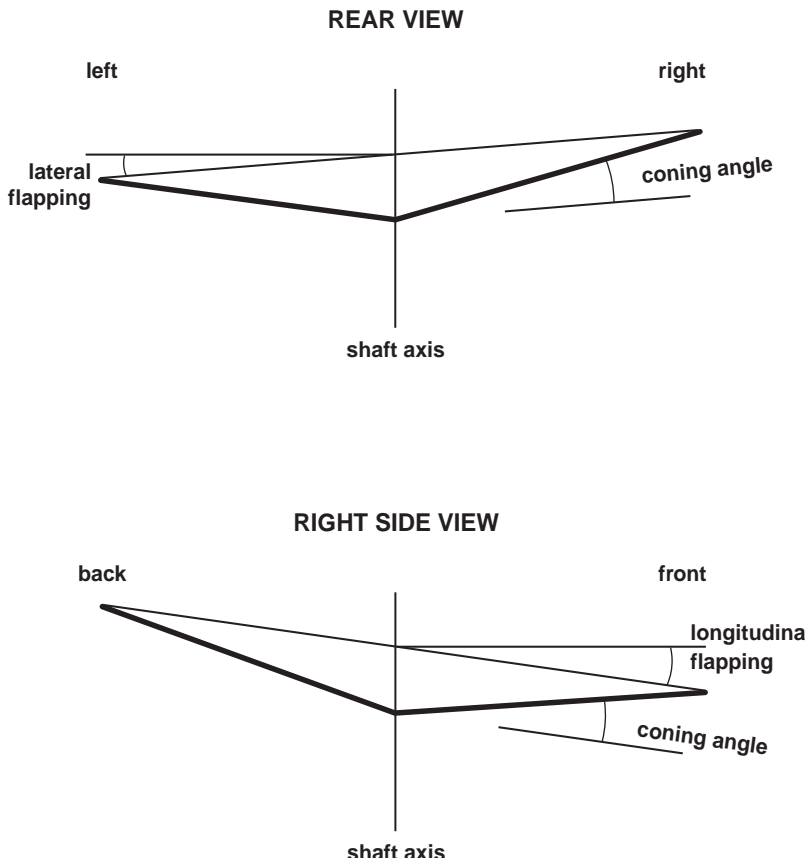


Fig. 15.1 Rotor tip-path-plane degrees of freedom.

affect the vehicle response.<sup>208</sup> Useful approximate expressions for the rotor mode characteristics are given by Heffley et al.<sup>21</sup> The lower frequency (regressing) flapping mode (involving  $\beta_{1c}$  and  $\beta_{1s}$ ) is well damped (typically  $\zeta_{f_r} \approx 1.0$ ); it has a natural frequency of about 1/2rev ( $\omega_{f_r} \approx 0.5\Omega$ ), or about 14 rad/s for a typical manned helicopter ( $\Omega \approx 27$  rad/s for the UH-60). This is the primary rotor mode of concern for helicopter flight dynamics and control. The higher-frequency (advancing) flap mode (again involving  $\beta_{1c}$  and  $\beta_{1s}$ ) is less well damped (typically  $\zeta_{f_a} \approx 0.25$ ); it has a frequency of about 2/rev ( $\omega_{f_a} \approx 2\Omega$ ), or about  $\omega_{f_a} = 54$  rad/s for a typical manned helicopter. This rotor mode is well above the frequency range of interest for most flight dynamics and control applications. Finally, the coning flap response (involving  $\beta_0$ ) is well damped (typically  $\zeta_{f_c} \approx 0.5$ ) and has a natural frequency of about 1/rev ( $\omega_{f_c} \approx \Omega$ ), or  $\omega_{f_c} = 27$  rad/s for a typical helicopter. This mode is important for dynamics and control considerations of the vertical degree of freedom.

As illustrated clearly by Heffley et al.,<sup>21</sup> there is a first-order *zero* in the on-axis cyclic flap response to cyclic control input that has nearly the same frequency as the well-damped second-order regressive flapping mode. Therefore, the regressive flap responses to cyclic inputs are accurately modeled as *two coupled first-order equations* for system-identification purposes. This is accomplished by dropping the terms involving flap acceleration and fuselage angular acceleration from Chen's equations. The rotor equations are further simplified for consideration of angular shaft motion by dropping the terms involving the translational degrees of freedom:

$$\tau_f \dot{\beta}_{1s} = -\beta_{1s} + Lf_{\beta_{1c}} \beta_{1c} + \tau_f p + Lf_{\delta_{lon}} \delta_{lon} + Lf_{\delta_{lat}} \delta_{lat} \quad (15.1)$$

$$\tau_f \dot{\beta}_{1c} = -\beta_{1c} + Mf_{\beta_{1s}} \beta_{1s} + \tau_f q + Mf_{\delta_{lon}} \delta_{lon} + Mf_{\delta_{lat}} \delta_{lat} \quad (15.2)$$

When the response and control coupling terms ( $Lf_{\beta_{1c}}$  and  $Lf_{\delta_{lon}}$ ) are neglected and the lateral control input  $\delta_{lat}$  is given in terms of radians of swashplate deflection (i.e.,  $Lf_{\delta_{lat}} = 1$ ;  $\delta_{lat} = \theta_{1c}$ ), the roll/flap equation of Eq. (15.1) reduces to that of Eq. (11.34). Note that the notation  $Lf$  is adopted to distinguish the flapping moments (on the rotor) from the fuselage moments  $L$ .

The rotor-flap time constant  $\tau_f$  can be estimated from the hinge offset and effective Lock number [Eqs. (11.35) and (11.37)]. The rotor-flap time constant is left as a free parameter in the identification, although it is constrained to a single common value in both the longitudinal and lateral flapping equations. Similarly, the rotor-dynamics cross-coupling terms  $Lf_{\beta_{1c}}$  and  $Mf_{\beta_{1s}}$  have analytic expressions and constraints in terms of the Lock number, but much recent experience has shown that these ideal expressions yield very poor off-axis prediction,<sup>16</sup> as is apparent for example from off-axis response correlation of the SH-2F analytical simulation model,<sup>211</sup> as shown in Section 15.3. Therefore these cross-coupling parameters are left as free and unconstrained in the identification. The on-axis control derivatives  $Lf_{\delta_{lat}}$  and  $Mf_{\delta_{lon}}$  are the principle longitudinal and lateral flap moments arising from swashplate deflection. These largely reflect the gearing between the cockpit control input and equivalent blade cyclic pitch angles  $\theta_{1c}$ .

and  $\theta_{1s}$ . For the (single-axis) roll response model of Sec. 11.7.1, the roll control derivative reduces to  $K_{\delta_{lat}}$  because the theoretical coefficient on  $\theta_{1c}$  in the flap equation (11.34) is unity.

The rotor is coupled to the fuselage through the key rotor moment and force stiffness terms ( $L_{\beta_{1s}}$  and  $Y_{\beta_{1s}}$  for the roll and lateral degrees of freedom,  $M_{\beta_{1c}}$  and  $X_{\beta_{1c}}$  for the pitch and longitudinal degrees of freedom). The force springs are constrained,

$$Y_{\beta_{1s}} = -X_{\beta_{1c}} \quad (15.3)$$

as would be expected from physical considerations, but the numerical value, theoretically equal to  $g$  ( $= 32.174$  ft/s $^2$ ), is left as an identification parameter because of the uncertainty in the exact location of the vertical center of gravity. Alternatively, these can be constrained to the gravity constant, and the center-of-gravity location can be determined in the identification.<sup>206</sup>

The state equations of Eqs. (13.12), (13.13), (13.17), and (13.18) become

$$\begin{aligned} \dot{u} = & -W_0q + V_0r - (g \cos \Theta_0)\theta + X_uu + X_vv + X_ww + X_rr \\ & + X_{\beta_{1c}}\beta_{1c} + X_{\delta_{ped}}\delta_{ped} + X_{\delta_{col}}\delta_{col} \end{aligned} \quad (15.4)$$

$$\begin{aligned} \dot{v} = & -U_0r + W_0p + (g \cos \Theta_0)\phi + Y_uu + Y_vv + Y_ww + Y_pp + Y_rr \\ & + Y_{\beta_{1s}}\beta_{1s} + Y_{\delta_{ped}}\delta_{ped} + Y_{\delta_{col}}\delta_{col} \end{aligned} \quad (15.5)$$

$$\dot{p} = L_uu + L_vv + L_ww + L_rr + L_{\beta_{1s}}\beta_{1s} + L_{\delta_{ped}}\delta_{ped} + L_{\delta_{col}}\delta_{col} \quad (15.6)$$

$$\dot{q} = M_uu + M_vv + M_ww + M_rr + M_{\beta_{1c}}\beta_{1c} + M_{\delta_{ped}}\delta_{ped} + M_{\delta_{col}}\delta_{col} \quad (15.7)$$

where again the primed notation ('') of Sec. 13.3.2 is implied (e.g.,  $L_v'$ ) but is dropped for notational convenience. Also, the  $Y_{\dot{v}}$  derivative of Eqn 13.13 is not generally included in helicopter applications.

There are two important aspects to note in this hybrid formulation. The first observation is the absence of the conventional quasi-steady rotor moment derivatives ( $L_p$ ,  $L_q$ ,  $M_p$ ,  $M_q$ ), quasi-steady rotor force derivatives ( $X_p$ ,  $X_q$ ,  $Y_q$ ), and quasi-steady rotor cyclic control derivatives ( $L_{\delta_{lon}}$ ,  $L_{\delta_{lat}}$ ,  $M_{\delta_{lon}}$ ,  $M_{\delta_{lat}}$ ,  $X_{\delta_{lon}}$ ,  $X_{\delta_{lat}}$ ,  $Y_{\delta_{lon}}$ ,  $Y_{\delta_{lat}}$ ). These *conventional* quasi-steady terms are a result of the six-DOF assumption that models the rotor as a simple time delay. With the current explicit representation of the rotor flapping response, these quasi-steady derivatives are omitted. Instead, the cyclic inputs ( $\delta_{lat}$ ,  $\delta_{lon}$ ) produce tip-path-plane flap responses ( $\beta_{1s}$ ,  $\beta_{1c}$ ) as modeled in eqns 15.1 and 15.2. These flap responses transmit forces and moments to the fuselage via the associated flap spring terms (e.g.,  $Y_{\beta_{1s}}\beta_{1s}$ ,  $M_{\beta_{1c}}\beta_{1c}$ , etc.) in eqns 15.4–15.7. *Effective values* for the quasi-steady derivatives can be obtained from the steady-state rotor response, such as

given in Eqs. (11.45) and (11.46). One quasi-steady force angular derivative  $Y_p$  is retained explicitly [Eq. (15.5)] to account for tail-rotor effects.

The second observation about the hybrid formulation is that the rotor equations consider the flapping response to angular shaft motions only (i.e.,  $p$  and  $q$ ). The flapping response to translation ( $u$ ,  $v$ ,  $w$ ) and the resulting rotor contributions to the forces and moments on the fuselage are contained in the quasi-steady speed derivatives (e.g.,  $X_u$ ,  $Y_u$ ,  $Y_v$ ,  $M_u$ ,  $L_v$ ). These speed derivatives are associated with low-frequency motions, and consequently the rotor time lag is not important here. This approach retains the many coupling terms that are needed to accurately match the low-frequency responses while maintaining a fairly simple (yet very accurate) formulation for the short-term flapping response.

### 15.2.2 Lead-Lag Dynamics

In addition to flapping motions, which are perpendicular to the tip-path plane, the rotor blades also experience in-plane or *lead-lag* motion about the lead-lag hinges. As in the case of flapping, these are best viewed in the nonrotating frame, and again there are three degrees of freedom of concern. (As in flapping, the reactionless mode for a four-bladed rotor is ignored, as it does not affect the vehicle response.) The lead-lag displacements, depicted in Fig. 15.2 with the appropriate sign conventions, reflect a lateral shift of the rotor blades  $\zeta_{1c}$ , a longitudinal shift of the rotor blades  $\zeta_{1s}$ , and a collective rotation  $\zeta_o$ . The lateral shift of the blades results in a lateral shift of the rotor c.g. from the rotor shaft axis of rotation, causing an associated sheer and rolling moment to be imparted to the fuselage. There is an analogous contribution in longitudinal shear and pitching moment for sine lag  $\zeta_{1s}$  displacement. Thus lead-lag motion can be visualized as a whirling of the rotor c.g. about the axis of rotation.<sup>169</sup> The collective lead-lag motion contributes a torque about the rotor shaft. The fundamental dynamic parameter  $v_\zeta$  is the lag natural frequency in the rotating frame normalized by the rotor rotational speed  $\Omega$ . This parameter has a value in the range of  $v_\zeta \approx 0.2$  to  $0.3$  for a typical articulated rotor helicopter.

When viewed in the nonrotating frame (i.e., from the fuselage), the lead-lag motion of the rotor system is composed of three lightly damped second-order modes (excluding the reactionless mode). The lower-frequency or *regressive lead-lag mode* (involving  $\zeta_{1c}$  and  $\zeta_{1s}$ ) is lightly damped (e.g.,  $\zeta_{1L} \approx 0.2$  for an articulated rotor system with mechanical lag dampers, and much lower damping for a hingeless rotor system, as seen in Sec. 11.8 for the Bo-105) with a natural frequency in the nonrotating frame of approximately  $(1 - v_\zeta)\Omega$ , or about  $0.75\Omega$ , to give  $\omega_{1L} = 20$  rad/s for a typical manned helicopter. The higher-frequency or *advancing lead-lag mode* (also involving  $\zeta_{1c}$  and  $\zeta_{1s}$ ) is more lightly damped with a natural frequency in the nonrotating frame of about  $(1 + v_\zeta)\Omega$ , or about  $1.25\Omega$ , to give  $\omega_{1A} = 34$  rad/s for a typical manned helicopter. Finally the *collective lag mode* (involving  $\zeta_o$ ) has the same natural frequency in the nonrotating and rotating frames of  $(v_\zeta\Omega)$ , or a value of  $0.25\Omega$ , to give  $\omega_{1c} = 7$  rad/s for a typical articulated helicopter. This mode couples into the shaft-torsion/engine/governor dynamics and is important in the design of engine/rotor-rpm controllers. The influence of the collective lag mode is absorbed in the effective time delay (Padé transfer function) for the engine response to collective input (Sec. 15.2.4).

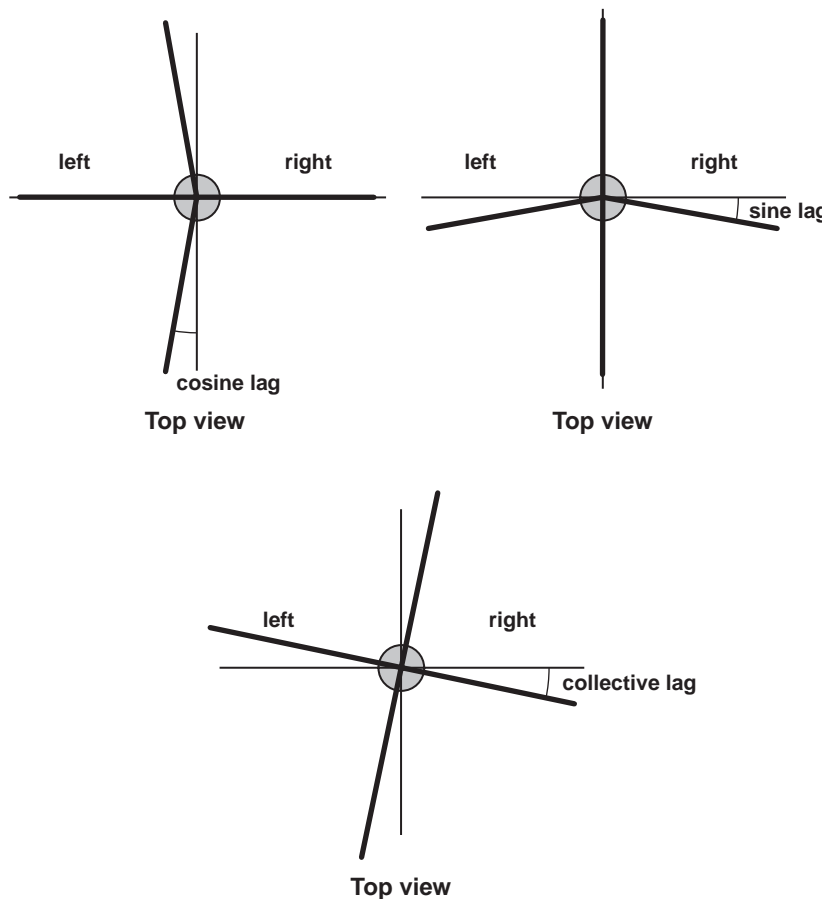


Fig. 15.2 Rotor lead-lag degrees of freedom.

The importance of coupled flap/lag/fuselage motion for helicopter flight mechanics and control analyses is addressed in depth by Curtiss.<sup>161</sup> The example application based on an articulated rotor configuration showed that the lead-lag dynamics add a closely spaced complex zero/pole pair (dipole) to the fuselage roll-rate responses. A limit on maximum roll-rate feedback gain arises from the destabilization of the cosine lead-lag dynamics. Tischler,<sup>18</sup> Tischler and Cauffman,<sup>15</sup> and the results summarized in Sec. 11.8 demonstrate this same characteristic using system-identification results for the Bo-105 (hingeless rotor) helicopter. The coupling of lead-lag and roll/flapping dynamics was a key aspect of the integrated rotor/control system development for the RAH-66 (Comanche) bearingless rotor helicopter.<sup>134</sup> In the excellent flight-mechanics analysis of coupled fuselage/flap/lag motion by Sahasrabudhe and Gold,<sup>169</sup> the lightly damped regressive lead-lag mode of the RAH-66 was successfully stabilized using feedbacks of the off-axis fuselage angular rates.

The complete coupled state-space equations for flap/lag motion are complex<sup>92,162</sup> and are not readily simplified for inclusion into the hybrid model structure. However, as already mentioned, the analysis by Curtiss<sup>161</sup> showed that the main flight-mechanics' influence on the regressive lead-lag dynamics is to contribute a closely spaced complex zero/pole (dipole) to the roll and pitch responses. Tischler (Ref. 18; summarized in Sec. 11.8) identified a transfer-function model of the Bo-105 roll response that included this dipole representation of the lead-lag influence. This extends the frequency range of applicability from about 12 rad/s (or about 0.6 regressive lag frequency) to about 30 rad/s, as is required for high-bandwidth flight-control applications. A complex dipole is appended to the roll-rate response that results from Eq. (15.6),

$$\frac{p'}{p} = \frac{K_{p'}[\zeta_{p'}, \omega_{p'}]}{[\zeta_{ll_r}, \omega_{ll_r}]} \quad (15.8)$$

and similarly to the pitch response that results from Eq. (15.7),

$$\frac{q'}{q} = \frac{K_{q'}[\zeta_{q'}, \omega_{q'}]}{[\zeta_{ll_r}, \omega_{ll_r}]} \quad (15.9)$$

with a common second-order denominator. This adds eight-identification parameters to the model structure. These dipoles are implemented in canonical form and contribute four additional canonical states to the overall hybrid model structure, as demonstrated by Fletcher<sup>153</sup> and denoted herein as  $\xi_{p1}$ ,  $\xi_{p2}$ ,  $\xi_{q1}$ ,  $\xi_{q2}$ .

As seen in the example of the Bo-105 (Fig. 11.14), the influence of these dipoles is restricted to a fairly narrowband near the regressive lead-lag frequency. For rotor systems with mechanical lead-lag dampers, the frequency range of influence is somewhat wider

$$0.6\omega_{ll_r} \leq \omega \leq 1.4\omega_{ll_r} \quad (15.10)$$

or about 12–28 rad/s for a typical articulated rotor helicopter. An effective approach is to first identify the hybrid model structure for frequencies up to  $\omega \leq 0.6\omega_{ll_r}$ , excluding the lead-lag dipoles. Then the hybrid model structure is fixed, and only the lead-lead dipoles are identified by fitting the on-axis roll-rate and pitch-rate responses  $p'/\delta_{lat}$  and  $q'/\delta_{lon}$  in the frequency range of Eq. (15.10).

This rather simple modeling approach has been found by the leading author to be quite accurate for many identification studies, including a flight-test study of the RAH-66 (Comanche), where the sensitivity of the regressive lead-lag response was tracked precisely for variations in flight condition and rotor system hardware. Examples of including lead-lag dynamics using the dipole modeling approach are well documented by Fletcher,<sup>153</sup> Tischler et al.,<sup>17</sup> and Harding and Moody<sup>197</sup> in identification studies of articulated-rotor helicopters, and by Dryfoos et al.<sup>134</sup> in a control system analysis of the RAH-66 bearingless rotor response. The identification of a complete state-space model of flap/lag/inflow dynamics of the Sikorsky bearingless main rotor (SBMR), using frequency-sweep data obtained from full-scale rotor tests in the NASA 40 × 80 ft wind tunnel, was presented by Tischler.<sup>92</sup>

### 15.2.3 Coupled Fuselage/Coning-Inflow Dynamics

The vertical response to collective  $w/\delta_{\text{col}}$  is dominated at low frequencies (below 1 rad/s) by the first-order heave damping characteristic,

$$\frac{w}{\delta_{\text{col}}} = \frac{Z_{\delta_{\text{col}}}}{s - Z_w} \quad (15.11)$$

with typical values of  $Z_w = -0.1$  to  $-0.3$  for hovering flight. At mid to high frequencies (in the range of about 1–12 rad/s), the influence of the heave damping mode is essentially negligible, and the vertical response is dominated by a lead term (a transfer-function zero) associated with the coupled dynamics of dynamic-inflow/coning. At higher frequencies, the vertical response is dominated by the second-order coning dynamics, which exhibit a natural frequency of about 1/rev, or  $\omega = 27$  for a typical manned helicopter. Chen and Hindson<sup>196</sup> have developed analytical models for the coupled inflow/coning/heave dynamics. By ignoring the aircraft heave motion, a simplified physical model of coupled inflow/coning response that is quite accurate at mid and high frequencies (above 1 rad/s) is obtained. The inflow dynamics equation can be written as

$$\dot{v} = \frac{-75\pi\Omega}{32} \left( \bar{v}_0 + \frac{a\sigma}{16} \right) C_0 v + v_{\dot{\beta}} \dot{\beta}_0 + \frac{25\pi\Omega^2 R}{32} \left( \frac{a\sigma}{8} \right) C_0 K_{\theta_0} \delta_{\text{col}} \quad (15.12)$$

and the trim inflow ratio is obtained from momentum theory for hovering flight as<sup>163</sup>

$$\bar{v}_0 = \sqrt{\frac{C_{T_0}}{2}} \quad (15.13)$$

where the trim thrust coefficient is defined as

$$C_{T_0} = \frac{T_0}{\rho\pi R^2(\Omega R)^2} \quad (15.14)$$

For hovering flight, an analytical expression is available for the  $v_{\dot{\beta}}$  coefficient:

$$v_{\dot{\beta}} = \frac{-25\pi\Omega R}{32} \left( \bar{v}_0 + \frac{a\sigma}{8} \right) C_0 \quad (15.15)$$

We adopt the Carpenter–Fridovich inflow constant ( $C_0 = 0.639$ ) based on the results of Tischler and Tomashofski.<sup>139</sup> The control gain  $K_{\theta_0}$  transforms the collective stick input to the collective component of the blade-root pitch angle  $\theta_0$ .

The coning dynamics, ignoring the influence of hinge offset, are expressed as a second-order differential equation:

$$\ddot{\beta}_0 = \frac{-\Omega\gamma}{8}\dot{\beta}_0 - \Omega^2\beta_0 - \frac{\Omega\gamma}{6R}v + \frac{\Omega^2\gamma}{8}K_{\theta_0}\delta_{\text{col}} \quad (15.16)$$

resulting in the two states of coning angle  $\beta_0$  and coning rate  $\dot{\beta}_0$ .

Finally the coning/inflow dynamics are coupled to the fuselage through the perturbation thrust coefficient  $C_T$  and the aircraft mass  $m$ . The hybrid model structure for the vertical dynamics is obtained from Eq. (13.14):

$$\begin{aligned} \dot{w} = & -V_0p + U_0q - (g \sin \Theta_0)\theta + Z_uu + Z_vv + Z_ww + Z_pp + Z_qq + Z_rr \\ & + \frac{-\rho\pi R^2(\Omega R)^2}{m}C_T + Z_{\delta_{\text{lon}}}\delta_{\text{lon}} + Z_{\delta_{\text{lat}}}\delta_{\text{lat}} + Z_{\delta_{\text{ped}}}\delta_{\text{ped}} \end{aligned} \quad (15.17)$$

where the perturbation thrust coefficient  $C_T$  is given by<sup>196</sup>

$$C_0C_T = \frac{0.543}{\Omega^2 R}\dot{v} + \frac{4\bar{v}_0}{\Omega R}C_0v + \frac{4\bar{v}_0}{3\Omega}C_0\dot{\beta}_0 \quad (15.18)$$

Note here again the absence of the quasi-steady collective control force derivative  $Z_{\delta_{\text{col}}}$  from the expression for the vertical acceleration [Eq. (15.17)]. Rather, control inputs cause an increase in blade angle of attack that increases coning [Eq. (15.16)] and inflow [Eq. (15.12)]. The associated dynamic variations in thrust [Eq. (15.18)] are transmitted to the fuselage [Eq. (15.17)], resulting in vertical acceleration.

We implement the algebraic equation for perturbation thrust coefficient [Eq. (15.18)] by introducing a fictitious state derivative ( $\dot{\eta}_{C_T} \equiv C_T$ ):

$$C_0\dot{\eta}_{C_T} = \frac{0.543}{\Omega^2 R}\dot{v} + \frac{4\bar{v}_0}{\Omega R}C_0v + \frac{4\bar{v}_0}{3\Omega}C_0\dot{\beta}_0 \quad (15.19)$$

This equation is rearranged as

$$C_0\dot{\eta}_{C_T} - \frac{0.543}{\Omega^2 R}\dot{v} - \frac{4\bar{v}_0}{3\Omega}C_0\dot{\beta}_0 = \frac{4\bar{v}_0}{\Omega R}C_0v \quad (15.20)$$

and implemented using the  $\mathbf{M}$  matrix. Finally, the vertical acceleration is written as

$$\begin{aligned} \dot{w} + \left[ \frac{\rho\pi R^2(\Omega R)^2}{m} \right] \dot{\eta}_{C_T} = & -V_0p + U_0q - (g \sin \Theta_0)\theta + Z_uu + Z_vv + Z_ww \\ & + Z_pp + Z_qq + Z_rr + Z_{\delta_{\text{lon}}}\delta_{\text{lon}} + Z_{\delta_{\text{lat}}}\delta_{\text{lat}} + Z_{\delta_{\text{ped}}}\delta_{\text{ped}} \end{aligned} \quad (15.21)$$

which again is implemented by making use of the  $\mathbf{M}$  matrix.

### 15.2.4 Yaw and Engine Dynamics

The yaw degree of freedom follows the standard quasi-steady form from Eq. (13.19):

$$\dot{r} = N_u u + N_v v + N_w w + N_p p + N_q q + N_r r + N_{\delta_{\text{lon}}} \delta_{\text{lon}} + N_{\delta_{\text{lat}}} \delta_{\text{lat}} + N_{\delta_{\text{ped}}} \delta_{\text{ped}} + N_{\delta_{\text{col}}} \delta_{\text{col}} \quad (15.22)$$

The effect of the engine dynamics on the fuselage response primarily manifests itself as a large additional phase lag in the  $p/\delta_{\text{col}}$ ,  $q/\delta_{\text{col}}$ ,  $r/\delta_{\text{col}}$  responses. In a comprehensive identification model study of the UH-60 helicopter, Fletcher<sup>153</sup> showed that an accurate prediction of the response coupling requires a complete representation of torque, rpm, and engine governor dynamics in the model structure. The complexity of an explicit engine/governor model is generally not warranted for a flight-dynamics identification model. However, identification studies on the SH-2G<sup>139</sup> and the Sikorsky S-92 helicopter<sup>17</sup> have shown that the influence of the engine dynamics on the yaw response to collective can be captured well as a Padé filter on the collective input ( $\delta_{\text{col}}$ ) in Eq. (15.22):

$$\frac{\delta'_{\text{col}}}{\delta_{\text{col}}}(s) = \frac{-s + 2/\tau_e}{s + 2/\tau_e} \quad (15.23)$$

where  $\tau_e$  is the engine time constant,  $\delta_{\text{col}}$  is the actual (pilot) collective control, and  $\delta'_{\text{col}}$  is the lagged or *effective* collective control included in pitch, roll, and yaw equations of motion to account for engine dynamics. [The six-DOF identification of the Fire Scout P2 demonstrator (Sec. 13.12.3) represented this Padé filter as an equivalent time delay on the collective input to angular rate responses  $\tau_{\text{col}}$ .]

The Padé filter can be written as

$$\frac{\delta'_{\text{col}}}{\delta_{\text{col}}}(s) = \left( \frac{4/\tau_e}{s + 2/\tau_e} \right) - 1 \quad (15.24)$$

or, equivalently, as

$$\delta'_{\text{col}} = \left[ \left( \frac{4/\tau_e}{s + 2/\tau_e} \right) \delta_{\text{col}} \right] - \delta_{\text{col}} \quad (15.25)$$

We need to express this last equation in state-space form. First, we define the quantity in the square bracket in terms of an *engine state*  $x_e$ , so that

$$\frac{x_e}{\delta_{\text{col}}}(s) = \frac{4/\tau_e}{s + 2/\tau_e} \quad (15.26)$$

which is expressed in the observable canonical form [from Eqs. (12.54) and (12.55)] as

$$\dot{x}_e = -\left(\frac{2}{\tau_e}\right)x_e + \left(\frac{4}{\tau_e}\right)\delta_{col} \quad (15.27)$$

or, more conveniently for identification, as

$$\tau_e \dot{x}_e = -2x_e + 4\delta_{col} \quad (15.28)$$

and  $\tau_e$  is implemented as an identification parameter in the  $M$  matrix. Finally, then,

$$\delta'_{col} = x_e - \delta_{col} \quad (15.29)$$

We again introduce a fictitious state and implement this algebraic equation for the lagged collective control in state-equation form:

$$\dot{\eta}_{\delta'_{col}} = x_e - \delta_{col} \quad (15.30)$$

Finally, the yaw acceleration equation from Eq. (15.22) becomes

$$\begin{aligned} -N_{\delta_{col}} \dot{\eta}_{\delta'_{col}} + \dot{r} = & N_u u + N_v v + N_w w + N_p p + N_q q + N_r r \\ & + N_{\delta_{lon}} \delta_{lon} + N_{\delta_{lat}} \delta_{lat} + N_{\delta_{ped}} \delta_{ped} \end{aligned} \quad (15.31)$$

and is implemented using the  $M$  matrix. The lagged collective is also introduced in place of the actual collective in the pitch and roll equations, just as in Eq. (15.31). The coning/inflow equations (15.12) and (15.16) use the *unlagged* collective as the input  $\delta_{col}$ .

Harding and Moody<sup>197</sup> implemented a simple second-order model of the rotor rpm/governor system in an identification of the AH-64 helicopter that accurately characterized the dynamic response and is an excellent alternative approach to the Padé filter of Eq. (15.23).

### 15.2.5 Complete State-Space Hybrid Model Structure

The complete hybrid model structure consists of 20 states:

$$\mathbf{x} = \begin{bmatrix} u & v & w & p & q & r & \phi & \theta & \beta_{1c} & \beta_{1s} & \xi_{p1} & \xi_{p2} & \xi_{q1} & \xi_{q2} & \dot{\beta}_0 & \beta_0 & \nu & \eta_{C_T} & x_e & \eta_{\delta'_{col}} \end{bmatrix}^T \quad (15.32)$$

Two of the states are algebraic ( $\eta_{C_T}$ ,  $\eta_{\delta'_{col}}$ ), so that there are actually 18 dynamic states and 18 eigenvalues in the hybrid model.

As before [Eqs. (13.29) and (13.30)], there are four bare-airframe controls,

$$\mathbf{u} = \begin{bmatrix} \delta_{\text{lat}} \\ \delta_{\text{lon}} \\ \delta_{\text{ped}} \\ \delta_{\text{col}} \end{bmatrix} \quad (15.33)$$

and nine measurements,

$$\mathbf{y} = \begin{bmatrix} u \\ v \\ w \\ p \\ q \\ r \\ a_x \\ a_y \\ a_z \end{bmatrix} \quad (15.34)$$

### 15.2.6 Hybrid Model Structure for Forward Flight

The hybrid model structure is unchanged for the forward-flight conditions. The fuselage aerodynamics contribute significantly, as does the rotor, to the quasi-steady speed derivatives in Eqs. (15.4–15.7), (15.17), and (15.22). The horizontal tail also contributes an aerodynamic damping moment derivative  $(M_q)_{\text{ht}}$  that is absorbed as an incremental increase in the effective rotor moment spring constants  $\Delta M_{\beta_{1c}} \approx (M_q)_{\text{ht}}/\tau_f$ . This term can only be independently identified when rotor state measurements are available.<sup>103</sup> There is an associated increment to the rotor force springs as a result of horizontal tail force contributions  $(X_q)_{\text{ht}}$ . For forward flight, the inflow constant  $[\nu_{\beta}$ , Eq. (15.12)] is included as a free identification parameter.

## 15.3 Hybrid Model Identification of SH-2G Helicopter

The H-2series helicopter (Fig. 15.3), manufactured by Kaman Aerospace Corporation, has been in the U.S. Navy fleet for over 30 years. Most notable among the H-2 series' features is the unique servoflap method of main rotor control. The flaps are separate airfoils riding aft of the blade trailing edge. They produce pitching-moment changes, which impel the main blade to free fly against the soft feathering spring to achieve aerodynamic equilibrium, thereby producing the desired collective and cyclic blade lift. This method provides a crisp and responsive control on a stable platform with very low vibration. The low control forces permit the helicopter to be flown easily with or without hydraulic boost.



**Fig. 15.3 U.S. Navy version of the SH-2G (Kaman Aerospace Corporation photo).**

An accurate flight-mechanics model over the entire speed range was needed to support the development of the AFCS and for use in piloted training simulators. Analytic models for the SH-2F configuration with the vertical/longitudinal dynamics uncoupled from the lateral/directional dynamics had previously been developed by Kaman. Two comprehensive, full-envelope, nonlinear simulation models of the SH-2F were also developed in support of the U.S. Navy NAVTO-LAND program and are referred to in this chapter as the STI model<sup>212</sup> and the NASA model.<sup>211</sup> The references provide tables of six-DOF perturbation derivatives for a range of speed conditions. There are significant differences between the latter two models for the key control and response derivatives. More importantly, there are significant discrepancies in the bare-airframe dynamic response comparisons between the simulation model and the flight-test data.<sup>211</sup>

A flight-test and system-identification program was conducted on the SH-2G helicopter to determine an accurate series of models in support of the development of a new digital flight-control system and piloted simulation. Higher-order state-space models, based on the hybrid model structure, were identified using CIFER® at three airspeeds that span the flight envelope (hover, 60 kn, and 100 kn). The results are summarized in the following sections. More detail on this project is available in Tischler and Tomashofski.<sup>139</sup>

### **15.3.1 SH-2G Flight Testing**

A complete battery of sweeps and doublets was performed using the flight-test methods of Chapter 5 at each of three trimmed airspeeds that spanned the flight envelope: hover, 60 kn, and 100 kn. The longitudinal and lateral sweeps were performed with the automatic stabilization equipment (ASE) engaged. This improved

the handling qualities for the conduct of the frequency-sweep tests and also provided information for ASE characterization. Pedal and collective sweeps were performed with the ASE off, as it was determined that isolation of bare-airframe characteristics in those axes was compromised if sweeps were done with the ASE engaged. The total inputs to the airframe (pilot + ASE) were recorded to allow the identification of the bare-airframe response characteristics. The control deflections were normalized to maximum deflection ( $\pm 1$  unit = full deflection). All sweeps were done with the optional hydraulic boost engaged. This provided a differential measurement to identify the second-order dynamics of the boost hydraulics.

### 15.3.2 Hover Flight Condition Identification

The frequency-response data were generated from the flight data using the MIMO methods of Chapters 7, 9, and 10. The resulting frequency ranges for acceptable coherence were determined. As with the results of Chapter 13, many of the responses were not important, and the associated derivatives were dropped, greatly simplifying the initial model structure.

The hybrid model structure of Sec. 15.2 was implemented with only minor modifications for application to the SH-2G configuration. In this study, the angular response modeling was limited to 12 rad/s, below the regressive lead-lag frequency, so that the lead-lag dynamics of Sec. 15.2.2 were ignored. Also, in the conventional rotor control method, the 1/rev blade-root pitch is fixed, as defined by the direct linkage inputs (i.e.,  $K_{\delta_{\text{lat}}}$  in Sec. 11.7.1). With servoflap control of the SH-2, the blade-root pitch angle is not a directly controlled parameter but rather is free to pitch so as to maintain aerodynamic equilibrium. Thus blade-root pitch is generated via the dynamic response of the soft blade-torsion spring to aerodynamic moments generated from the servoflaps. The steady-state change in blade pitch with change in servoflap deflection is thus accounted for in the identified parameters  $Lf_{\delta_{\text{lon}}}$  and  $Lf_{\delta_{\text{lat}}}$  of Eq. (15.1),  $Mf_{\delta_{\text{lon}}}$  and  $Mf_{\delta_{\text{lat}}}$  of Eq. (15.2), and  $K_{\theta_0}$  of Eqs. (15.12) and (15.16). The lagged collective  $\delta'_{\text{col}}$  was introduced only into the yaw-rate equation (Sec. 15.31) herein, though a small improvement was seen by introducing this into the pitch and roll equations as well.

The initial hover model structure was converged to a cost function of  $J_{\text{ave}} = 70.5$ , which is considered an excellent fit. The identification results clearly showed that the Carpenter–Fridovich value for the inflow constant ( $C_0 = 0.639$ ) of Eq. (15.12) provided the best fit of the flight-test data at hover (and forward flight), and so it was subsequently fixed at this value. This agrees with the findings of previous researchers.<sup>196</sup>

The model structure determination method of Sec. 12.3.4 was followed, resulting in a considerable reduction in the number of identified parameters, as seen in the final hover identification results of Table 15.1. The parameter insensitivities and Cramér–Rao bounds are nearly all within the suggested guidelines. The overall final cost function is low ( $J_{\text{ave}} = 71.3$ , Table 15.2) and reflects the excellent agreement of the identified model with the flight data, as shown in Fig. 15.4. The hybrid model structure thus very accurately captures the key dynamic characteristics of the SH-2G flapped-rotor configuration. Including the simple engine dynamics of Eq. (15.23) results in an excellent characterization of the yaw response to collective  $r/\delta_{\text{col}}$ , as seen in the low-cost function for this pair ( $J = 45.2$ ).

**Table 15.1 Hybrid model identification results (SH-2G, hover)<sup>a</sup>**

Engineering symbols	Value	CR, %	Insens, %
<b><i>M-matrix</i></b>			
$\tau_f$	0.2051	2.55	0.56
$\tau_e$	0.8886	9.07	3.41
<b><i>F-matrix</i></b>			
$X_u$	-0.06415	12.66	5.71
$X_v$	0.000 <sup>b</sup>	—	—
$X_w$	0.000 <sup>b</sup>	—	—
$X_r$	0.000 <sup>b</sup>	—	—
$g$	-32.20 <sup>c</sup>	—	—
$X_{\beta_{1c}}$	35.30	2.39	0.53
$Y_u$	-0.1592	11.86	1.37
$Y_v$	-0.3593	3.92	0.88
$Y_w$	0.000 <sup>b</sup>	—	—
$Y_p$	1.216	7.77	3.37
$Y_r$	0.000 <sup>b</sup>	—	—
$Y_{\beta_{1s}}$	-35.30 <sup>d</sup>	—	—
$Z_u$	0.000 <sup>b</sup>	—	—
$Z_v$	0.000 <sup>b</sup>	—	—
$Z_w$	-0.06857	12.94	6.39
$Z_p$	0.000 <sup>b</sup>	—	—
$Z_q$	0.000 <sup>b</sup>	—	—
$Z_r$	0.000 <sup>b</sup>	—	—
$L_u$	-0.04063	9.46	0.74
$L_v$	-0.08868	2.61	0.52
$L_w$	0.000 <sup>b</sup>	—	—
$L_r$	-0.3296	26.84	9.68
$L_{\beta_{1s}}$	-22.38	2.41	0.47
$M_u$	-4.484E-03	11.35	0.83
$M_v$	-8.806E-03	10.21	0.85
$M_w$	0.000 <sup>b</sup>	—	—
$M_r$	0.000 <sup>b</sup>	—	—
$M_{\beta_{1c}}$	-8.257	2.81	0.64
$N_u$	0.000 <sup>b</sup>	—	—
$N_v$	0.000 <sup>b</sup>	—	—
$N_w$	0.000 <sup>b</sup>	—	—
$N_p$	0.000 <sup>b</sup>	—	—
$N_q$	0.000 <sup>b</sup>	—	—
$N_r$	-0.6688	15.75	5.23
$Lf_{\beta_{1c}}$	-0.4171	7.05	1.21
$Mf_{\beta_{1s}}$	0.6807	6.30	1.59

(continued)

Table 15.1 Hybrid model identification results (SH-2G, hover)<sup>a</sup> (continued)

Engineering symbols	Value	CR, %	Insens, %
$v_{\dot{\beta}}$	-165.1 <sup>c</sup>	—	—
$K_{\theta_0}$	0.08268	2.92	1.44
$C_0$	0.6390 <sup>c</sup>	—	—
<i>G-matrix</i>			
$X_{\delta_{\text{ped}}}$	0.000 <sup>b</sup>	—	—
$X_{\delta_{\text{col}}}$	3.288	4.68	2.25
$Y_{\delta_{\text{ped}}}$	-5.369	3.57	1.71
$Y_{\delta_{\text{col}}}$	0.000 <sup>b</sup>	—	—
$Z_{\delta_{\text{lon}}}$	0.000 <sup>b</sup>	—	—
$Z_{\delta_{\text{lat}}}$	0.000 <sup>b</sup>	—	—
$Z_{\delta_{\text{ped}}}$	0.000 <sup>b</sup>	—	—
$L_{\delta_{\text{ped}}}$	-0.7305	5.77	2.58
$L_{\delta_{\text{col}}}$	0.000 <sup>b</sup>	—	—
$M_{\delta_{\text{ped}}}$	0.000 <sup>b</sup>	—	—
$M_{\delta_{\text{col}}}$	0.2251	11.11	2.40
$N_{\delta_{\text{lon}}}$	0.000 <sup>b</sup>	—	—
$N_{\delta_{\text{lat}}}$	0.000 <sup>b</sup>	—	—
$N_{\delta_{\text{ped}}}$	1.725	5.12	2.33
$N_{\delta_{\text{col}}}$	0.3577	6.04	2.72
$Lf_{\delta_{\text{lon}}}$	0.1769	4.31	0.77
$Lf_{\delta_{\text{lat}}}$	-0.09724	4.53	1.59
$Mf_{\delta_{\text{lon}}}$	0.2727	4.03	0.94
$Mf_{\delta_{\text{lat}}}$	0.1142	4.92	1.39
<i>Time delays</i>			
$\tau_{\text{lon}}$	0.000 <sup>b</sup>	—	—
$\tau_{\text{lat}}$	0.000 <sup>b</sup>	—	—
$\tau_{\text{ped}}$	0.03624	20.96	9.79
$\tau_{\text{col}}$	0.03409	12.61	6.24

<sup>a</sup>All results in English units.

<sup>b</sup>Eliminated from model structure.

<sup>c</sup>Fixed parameter in model structure.

<sup>d</sup>Constrained parameter in model structure.

 $\delta_{\text{ped}}$ , normalized units 0–2 (+ve right turn).

 $\delta_{\text{col}}$ , normalized units 0–2 (+ve up collective).

 $\delta_{\text{lon}}$ , normalized units 0–2 (+ve right stick).

 $\delta_{\text{lat}}$ , normalized units 0–2 (+ve forward stick).

**Table 15.2 Hybrid model identification cost functions (SH-2G, hover)**

Engineering symbols	Costs
$u/\delta_{\text{lon}}$	85.5
$v/\delta_{\text{lon}}$	147.8
$p/\delta_{\text{lon}}$	34.2
$q/\delta_{\text{lon}}$	43.3
$a_x/\delta_{\text{lon}}$	123.0
$a_y/\delta_{\text{lon}}$	43.5
$u/\delta_{\text{lat}}$	110.8
$v/\delta_{\text{lat}}$	168.2
$p/\delta_{\text{lat}}$	87.5
$q/\delta_{\text{lat}}$	107.2
$a_y/\delta_{\text{lat}}$	168.6
$v/\delta_{\text{ped}}$	3.3
$p/\delta_{\text{ped}}$	30.8
$r/\delta_{\text{ped}}$	55.0
$a_y/\delta_{\text{ped}}$	51.2
$u/\delta_{\text{col}}$	73.5
$w/\delta_{\text{col}}$	21.5
$q/\delta_{\text{col}}$	25.1
$r/\delta_{\text{col}}$	45.2
$a_x/\delta_{\text{col}}$	50.2
$a_z/\delta_{\text{col}}$	21.5
$J_{\text{ave}}$	71.3

The theoretical value for the rotor time constant is obtained from Eqs. (11.35) and (11.37), based on the SH-2G geometric characteristics:

$$(\tau_f)_{\text{theory}} = 0.206 \text{ s} \quad (15.35)$$

which agrees very closely with the identified value ( $\tau_f = 0.205 \text{ s}$ ). The theoretical value of flapping stiffness for the SH-2F configuration is given by Heffley et al.<sup>21</sup> based on an assumed inertia:

$$L_{\beta_{1s}} = -25.4 \text{ rad/s}^2/\text{rad} \quad (15.36)$$

which also agrees well with the CIFER® identification results ( $L_{\beta_{1s}} = -22.4 \text{ rad/s}^2/\text{rad}$ ). The ratio of the pitch and roll flapping stiffness terms

$$\left| \frac{L_{\beta_{1s}}}{M_{\beta_{1c}}} \right| = 2.7 \quad (15.37)$$

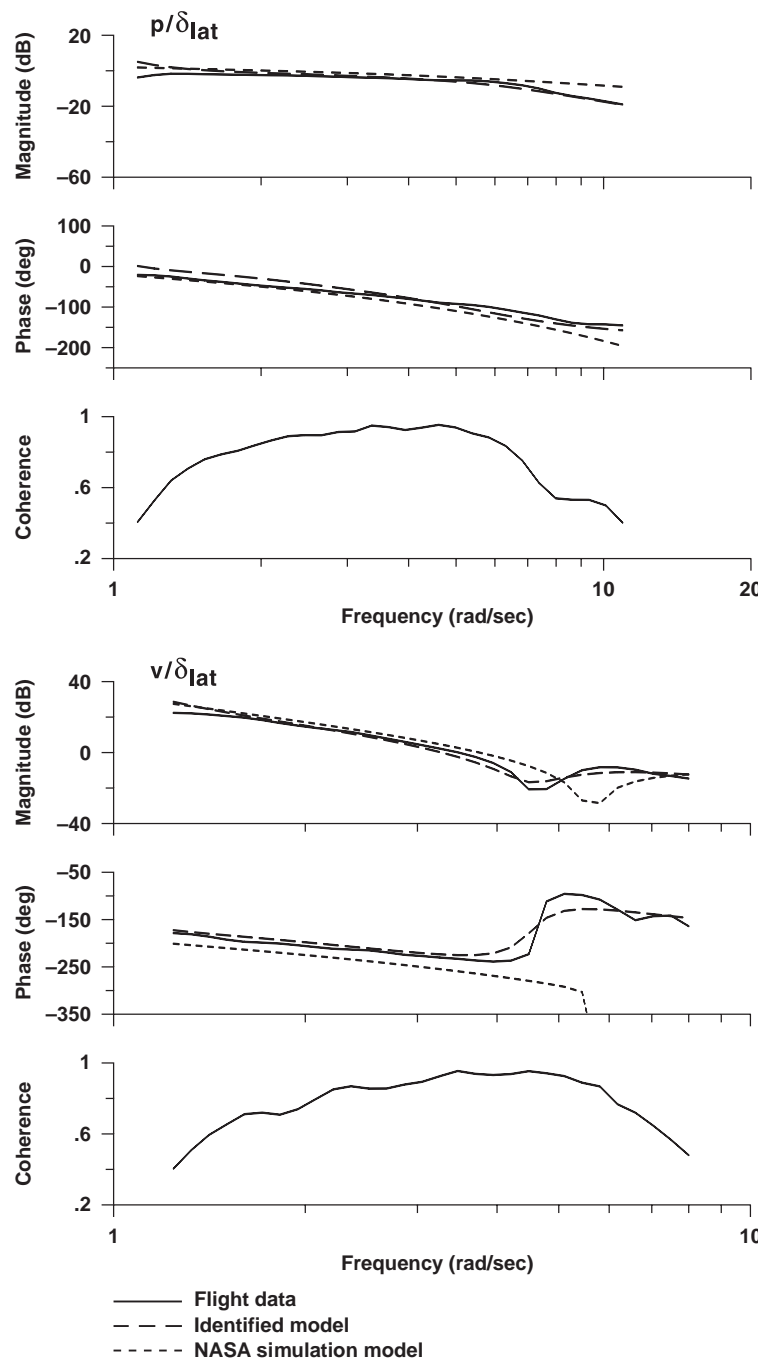


Fig. 15.4 Identification and simulation models for hover (SH-2G).

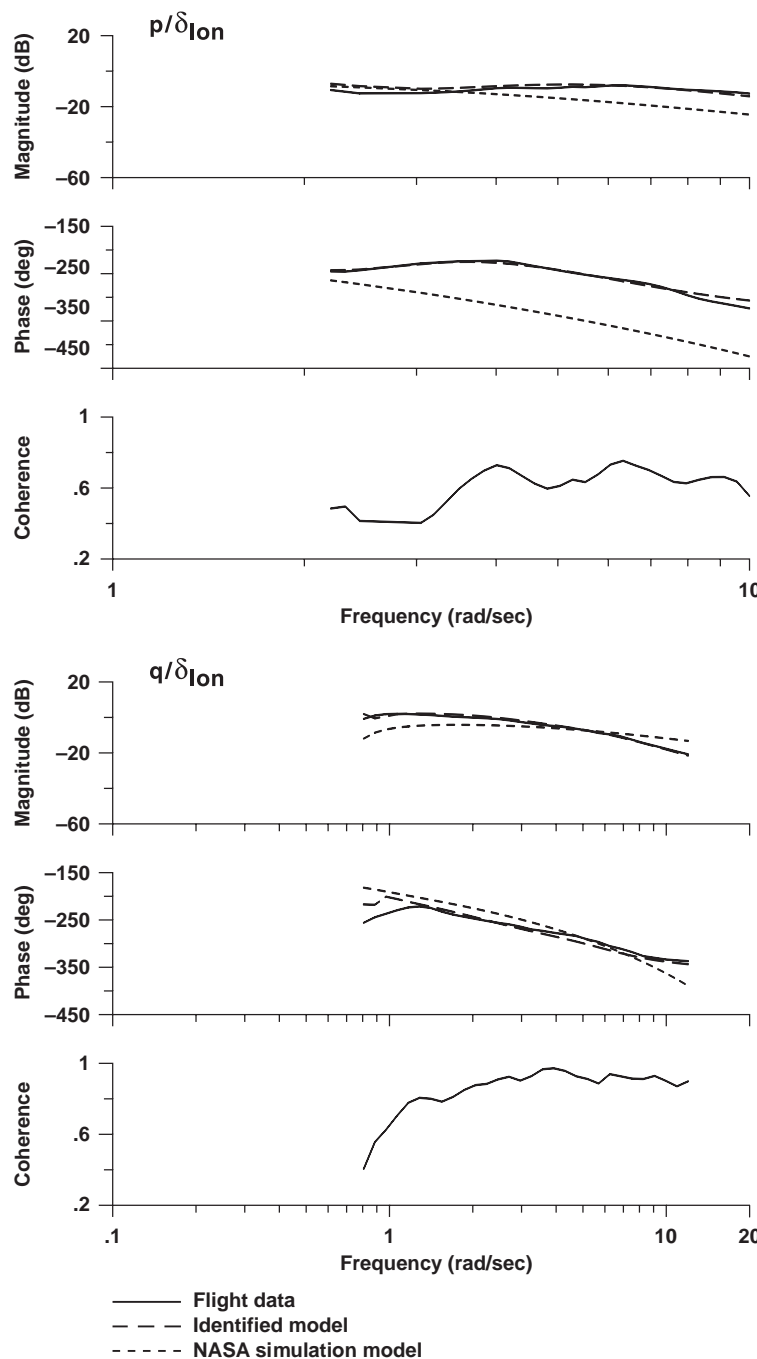


Fig. 15.4 Identification and simulation models for hover (SH-2G) (continued).

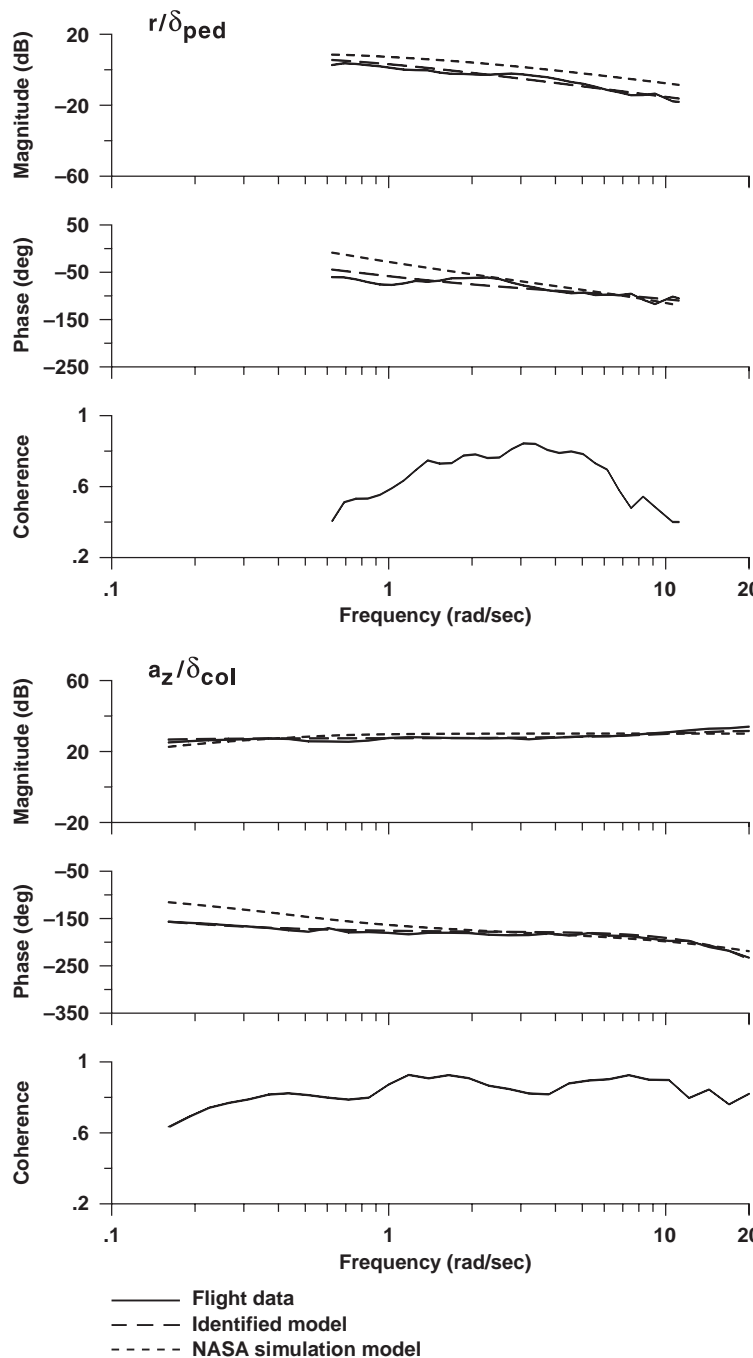


Fig. 15.4 Identification and simulation models for hover (SH-2G) (continued).

is the SH-2G ratio of pitch-to-roll moment of inertia and corresponds closely to the estimated value for the aircraft of 2.57. The flapping force stiffness derivatives  $X_{\beta_{1c}}$  and  $Y_{\beta_{1s}}$  are nearly equal to the gravity constant, which confirms that the data are kinematically consistent and that the placement of the accelerometers at the assumed c.g. is close to the actual c.g.

Finally, referring again to Table 15.1, the engine time constant is identified with a value of  $\tau_e = 0.89$  s. Adding the collective stick input delay ( $\tau_{col} = 0.034$  s) gives a total engine response delay to collective of 0.92 s. This result corresponds well with the approximately 1-s rise time seen in the rpm step response to collective for the UH-60 T700 engine,<sup>153</sup> which is the same engine as in the SH-2G.

Table 15.3 presents the 14 eigenvalues associated with the hover model (recall that the lead-lag canonical states are omitted in this example). The heave  $\lambda_2$  and yaw  $\lambda_4$  responses are first-order and are dominated by the damping derivatives  $Z_w$  and  $N_r$ , respectively. The engine rpm mode ( $\lambda_7 = -2/\tau_e$ ) again corresponds closely with the value given by Fletcher<sup>153</sup> for the UH-60 T700 engine.

The lateral dihedral stability has a small stable characteristic ( $L_v < 0$ ), which contributes to the stable lateral low frequency (phugoid) oscillation mode  $\lambda_5$  and  $\lambda_6$ . The identified  $L_v$  derivative value compares well with the NASA simulation, as shown later in Section 15.3.3. The analogous low-frequency longitudinal translational dynamics are characterized by two real (aperiodic) modes — one unstable and one stable ( $\lambda_1$  and  $\lambda_3$ , respectively). These dynamics reflect the identified very small, but unstable, longitudinal speed stability derivative ( $M_u < 0$ ). The low associated Cramér–Rao bound (about 11%) indicates that the estimated value is reliable. A *positive value* of the derivative  $M_u$  would be expected with a first principles analyses of the *steady-state response of an isolated rotor* to speed perturbations (i.e., caused by *blowback*; see Prouty<sup>163</sup> and Padfield<sup>200</sup>). This would be

**Table 15.3 Eigenvalues for identified hybrid model (SH-2G, hover): Eigenvalues ( $\lambda_i$ ) of  $[M_{\text{inverse}}][F]$**

	$(\lambda_i)_R$	$(\lambda_i)_I$	$\zeta_i$	$\omega_i$	Mode
$\lambda_1$	0.06595	0.0000	—	—	Pitch
$\lambda_2$	-0.06857	0.0000	—	—	Heave
$\lambda_3$	-0.1268	0.0000	—	—	Pitch
$\lambda_4$	-0.6688	0.0000	—	—	Yaw
$\lambda_5$	-0.07817	0.8950	0.08701	0.8984	Roll
$\lambda_6$	-0.07817	-0.8950	0.08701	0.8984	Roll
$\lambda_7$	-2.251	0.0000	—	—	Engine
$\lambda_8$	-1.729	-1.551	0.7445	2.323	Pitch/flap
$\lambda_9$	-1.729	1.551	0.7445	2.323	Pitch/flap
$\lambda_{10}$	-3.249	4.901	0.5525	5.880	Roll/flap
$\lambda_{11}$	-3.249	-4.901	0.5525	5.880	Roll/flap
$\lambda_{12}$	-19.31	0.0000	—	—	Inflow/coning
$\lambda_{13}$	-7.386	-27.24	0.2617	28.22	Coming
$\lambda_{14}$	-7.386	27.24	0.2617	28.22	Coming

consistent with a forward stick migration with airspeed in trim flight, as indicated in the first (dominant) term of Eq. (13.80). The simulation models do show a small but positive value of  $M_u$ , as shown later in Section 15.3.3.

Apparently there are other contributing factors that produce a slightly negative value of  $M_u$  as needed to match the longitudinal *dynamic responses* at low frequency ( $\omega \approx 0.5$  to 1.0) rad/s. Yet, the same value of  $M_u$  is inconsistent with an expected stable trim control gradient with velocity. The identified negative value of  $M_u$  could arise from the transient effects of the rotor wake and its impingement on the airframe and tail rotor, as well as the engine response to speed perturbations. Another possible contributor to this discrepancy is the assumption of a quasi-steady representation for the velocity derivatives. Dynamic measurements of rotorcraft in the Princeton longtrack (e.g., Curtiss et al.<sup>213</sup>) show a strong hysteresis effect in the pitching-moment response to velocity perturbations. The pitching moment is seen to change sign for accelerating vs decelerating flight. This characteristic also suggests the presence of unmodeled dynamics that could contribute to the inconsistencies between trim (static) and system-identification (dynamics) results for  $M_u$ .

The speed-stability constraint equations implemented for the six-DOF model [Eqs. (13.80) and (13.81)] can be extended to the hybrid model structure to *enforce consistency* with the measured trim control gradients. For example, using Eq. (11.45) and noting that  $K_{\delta_{\text{lat}}} = Lf_{\delta_{\text{lat}}}$  for the hybrid model

$$(L_{\delta_{\text{lat}}})_{\text{effective}} = Lf_{\delta_{\text{lat}}} L_{\beta_{1s}} \quad (15.38)$$

and from Eq. (13.81),

$$L_v = - \left[ Lf_{\delta_{\text{lat}}} L_{\beta_{1s}} \left( \frac{\Delta \delta_{\text{lat}}}{\Delta v} \right) + L_{\delta_{\text{ped}}} \left( \frac{\Delta \delta_{\text{ped}}}{\Delta v} \right) \right] \quad (15.39)$$

The analogous formulation can be adopted to constrain  $M_u$  using Eq. (13.80). A small improvement to the hover results presented herein was also noted by introducing the  $v/\phi(s)$  and  $u/\theta(s)$  responses and the associated constraints on  $Y_v$  and  $X_u$ , as discussed in Sec. 13.12.4. These speed-stability and speed-damping constraint techniques were implemented in the identification of the RMAX UAV small-scale helicopter by Cheng et al.<sup>206</sup> and resulted in an excellent hybrid model for the hover condition.

The dominant body-pitch/longitudinal flapping  $\lambda_8$  and  $\lambda_9$  and body-roll/lateral flapping dynamics  $\lambda_{10}$  and  $\lambda_{11}$  are characterized by well-damped second-order systems and thus cannot be modeled accurately in a classical six-DOF quasi-steady model structure. This same result was seen earlier for the OH-58D (Sec. 11.7.2) and the Bo-105 (Sec. 11.8). There are three modes associated with the coning/inflow dynamics ( $\lambda_{12}$ ,  $\lambda_{13}$ ,  $\lambda_{14}$ ). The lightly damped second-order coning mode has a natural frequency of 0.9/rev, which is reduced from the 1/rev frequency as a result of the influence of the inflow dynamics. This follows the analytical results of Chen and Hindson.<sup>196</sup>

Another noticeable aspect of the identification results is the pitch-roll response coupling of the SH-2G rotor. For a given pitch rate  $q$ , the resulting roll acceleration

exceeds the pitch acceleration, as seen from the effective roll-response coupling derivative ratios (determined from a quasi-steady reduction of the identified model; parameters listed in Section 15.3.3):

$$\left| \frac{L_q}{M_q} \right| = 1.1 \quad (15.40)$$

This indicates a large roll-response coupling to pitch inputs, as is typical for most helicopters. The analogous quasi-steady pitch-response coupling ratio for the SH-2G is

$$\left| \frac{M_p}{L_p} \right| = 0.25 \quad (15.41)$$

Finally, we can compare the pitch acceleration caused by roll rate (off-axis response) with the pitch acceleration caused by pitch rate (on-axis response) based on the quasi-steady ratio:

$$\left| \frac{M_p}{M_q} \right| = 0.68 \quad (15.42)$$

The pitch-response coupling ratios [Eqs. (15.41) and (15.42)] are larger than would be expected for the small hinge offset of the SH-2G ( $e/R = 3.1\%$ ), based on a comparison with other helicopters for which hover identification data are available (e.g., Refs. 10, 37, 153, and 182). The effective response coupling ratio  $|M_p/L_p|$  is nearly double the value for the large hinge-offset Bo-105 ( $e/R = 12\%$ ), and it would appear to be as a result of the unique characteristics of the servoflap control system. The shaft angular rates appear to change the torsional control moments of the SH-2G flap-controlled rotor with a phasing that increases the effective coupling ratio beyond that level expected based solely on the hinge offset.

These identification results are consistent with the work of Curtiss and Gao,<sup>214</sup> who developed a detailed flight-mechanics model of the SH-2 servoflap system. Their analysis demonstrated that a significant increase in angular response coupling arises from the soft torsional stiffness of this rotor. The amount of coupling is quite sensitive to the location of the blade aerodynamic center and center of gravity relative to the blade-pitch rotation axis. Padfield<sup>200</sup> also showed a significant increase in pitch-roll response coupling for soft torsional rotor configurations, in agreement with the SH-2G identification results.

### 15.3.3 Comparison of Identification and Simulation Models for Hover

Also shown in Fig. 15.4 is the comparison of the NASA simulation model<sup>211</sup> with the flight data and identified model for the hover flight condition. Equivalent time delays are included in the (six-DOF) NASA simulation models to approximate the identified rotor time constant and pedal and collective input

## 476 AIRCRAFT AND ROTORCRAFT SYSTEM IDENTIFICATION

delays and thereby provide a fairer comparison of results. The NASA simulation model exhibits considerable discrepancies, including the key on-axis responses ( $p/\delta_{\text{lat}}$ ,  $q/\delta_{\text{lon}}$ ,  $r/\delta_{\text{ped}}$ ,  $a_z/\delta_{\text{col}}$ ). The off-axis (coupling) response  $p/\delta_{\text{lon}}$  displays a large error in phase, as is common for helicopter simulation models.<sup>16</sup>

Tables 15.4 and 15.5 present a direct comparison of the identification parameters and cost functions of the identification model and the six-DOF simulation models from Ringland and Clement<sup>212</sup> and Pault et al.<sup>211</sup> The identification parameters listed in Table 15.4 are the *quasi-steady derivatives* obtained by numerically reducing the identified flapping and coning/inflow state-equations to quasi-steady form. There is reasonable agreement of the quasi-steady identification values with the simple expressions from Sec. 11.7.1. For example, the numerically reduced values for the key parameters of roll control effectiveness and roll damping are listed in Table 15.4 as  $L_{\delta_{\text{lat}}} = 2.526 \text{ rad/s}^2/\text{unit-control}$  and  $L_p = -3.577 \text{ rad/s}$ , respectively. Equation (11.45) gives an estimate of the effective control derivative of

$$(L_{\delta_{\text{lat}}})_{\text{effective}} = L f_{\delta_{\text{lat}}} L_{\beta_{1s}} = 2.176 \text{ rad/s}^2/\text{unit-control} \quad (15.43)$$

and Eq. (11.46) gives an estimate of the effective roll damping of

$$(L_p)_{\text{effective}} = \tau_f L_{\beta_{1s}} = -4.590 \text{ rad/s} \quad (15.44)$$

The differences are caused by the significant inter-axis coupling in the identified MIMO model as compared to the simple analysis, which is based on a two-DOF (roll-flap) dynamics model.

As expected from the plotted results, the frequency-response cost functions of Table 15.5 show that the identified model demonstrates substantially improved accuracy as compared to the simulation models of Ringland and Clement<sup>212</sup> and Pault et al.<sup>211</sup> Although in many cases there is fair agreement between one or the other of the simulations and the identified model in terms of parameter values or cost functions, there is no consistent trend as to which of the two simulation models gives the more accurate prediction. Clearly, the system-identification approach provides a much more accurate model for flight-control applications than had been available from the previous simulation models.

One noticeable aspect of the comparison in Table 15.4 is that the heave damping is significantly overestimated by both simulation models, as reflected in the low-frequency phase discrepancy in heave response  $a_z/\delta_{\text{col}}$  of the simulation models as compared to the flight data (Fig. 15.4). This is a failure in momentum theory that has been consistently reported in rotorcraft flight-mechanics studies (e.g., Refs. 54, 68, 196 and 215). Houston and Tarttelin<sup>215</sup> have conducted wind-tunnel measurements, flight tests, and system-identification modeling in a comprehensive study of this problem. Their study concluded that the conventional simulation theories do not capture the influence of unsteady wake aerodynamics and blade flexibility that are the source of the lower value for  $Z_w$  seen in the actual test data.

**Table 15.4 Simulation and (equivalent six-DOF) identification parameters (SH-2G, hover)<sup>a</sup>**

Engineering symbols	STI model	NASA model	Identification (reduced)
<i>F</i> -Matrix			
$X_u$	-0.02910	-0.03021	-0.06415
$X_v$	-8.500E-03	-0.4091	0.000
$X_w$	0.02630	0.06350	0.000
$X_p$	-2.323	-0.03290	3.839
$X_q$	4.352	4.988	5.640
$X_r$	-0.1616	-0.8409	0.000
$Y_u$	9.900E-03	7.800E-03	-0.1592
$Y_v$	-0.1032	-0.1981	-0.3593
$Y_w$	-0.02740	-0.01620	0.000
$Y_p$	-4.809	-4.139	-4.424
$Y_q$	-1.230	-2.059	2.352
$Y_r$	4.447	2.584	0.000
$Z_u$	-0.03840	-0.03344	0.000
$Z_v$	-0.02270	-0.02580	0.000
$Z_w$	-0.3299	-0.3209	-0.06857
$Z_p$	-0.9867	1.476	0.000
$Z_q$	1.631	-0.5120	0.000
$Z_r$	1.082	0.1905	0.000
$L_u$	3.000E-04	-1.860E-03	-0.04063
$L_v$	-0.03300	-0.07077	-0.08868
$L_w$	-0.01400	-5.696E-03	0.000
$L_p$	-6.068	-3.791	-3.577
$L_q$	2.580	2.347	1.492
$L_r$	1.814	0.4536	-0.3296
$M_u$	9.700E-03	0.01484	-4.484E-03
$M_v$	-1.000E-04	0.05106	-8.806E-03
$M_w$	8.000E-04	-1.997E-03	0.000
$M_p$	-0.9792	-0.2121	-0.8981
$M_q$	-1.822	-3.899	-1.319
$M_r$	0.1785	0.2577	0.000
$N_u$	-4.300E-03	-2.077E-03	0.000
$N_v$	0.02450	0.05242	0.000
$N_w$	8.700E-03	4.974E-03	0.000
$N_p$	6.000E-03	0.1757	0.000
$N_q$	-0.07240	0.03235	0.000

(continued)

**Table 15.4 Simulation and (equivalent six-DOF) identification parameters (SH-2G, hover)<sup>a</sup> (continued)**

Engineering symbols	STI model	NASA model	Identification (reduced)
$N_r$	-2.481	-1.796	-0.6688
<i>G-matrix</i>			
$X_{\delta_{\text{lon}}}$	4.937	4.968	10.81
$X_{\delta_{\text{lat}}}$	0.04980	0.05451	1.321
$X_{\delta_{\text{ped}}}$	0.000	0.000	0.000
$X_{\delta_{\text{col}}}$	2.806	3.461	3.288
$Y_{\delta_{\text{lon}}}$	-0.2292	-0.3980	-1.736
$Y_{\delta_{\text{lat}}}$	4.390	4.279	3.983
$Y_{\delta_{\text{ped}}}$	-6.988	-6.955	-5.369
$Y_{\delta_{\text{col}}}$	-1.977	-2.355	0.000
$Z_{\delta_{\text{lon}}}$	1.647	0.04438	0.000
$Z_{\delta_{\text{lat}}}$	0.04710	-2.917E-03	0.000
$Z_{\delta_{\text{ped}}}$	0.000	0.000	0.000
$Z_{\delta_{\text{col}}}$	-32.13	-32.00	-23.63
$L_{\delta_{\text{lon}}}$	-0.03280	-0.09352	-1.101
$L_{\delta_{\text{lat}}}$	3.974	4.078	2.526
$L_{\delta_{\text{ped}}}$	-2.452	-2.443	-0.7305
$L_{\delta_{\text{col}}}$	-0.5744	-0.8653	0.000
$M_{\delta_{\text{lon}}}$	-1.671	-2.736	-2.528
$M_{\delta_{\text{lat}}}$	8.000E-03	0.02671	-0.3090
$M_{\delta_{\text{ped}}}$	0.08620	0.09305	0.000
$M_{\delta_{\text{col}}}$	0.1449	0.09190	0.2251
$N_{\delta_{\text{lon}}}$	-0.07670	-6.419E-03	0.000
$N_{\delta_{\text{lat}}}$	-3.000E-03	0.06116	0.000
$N_{\delta_{\text{ped}}}$	4.368	4.256	1.725
$N_{\delta_{\text{col}}}$	2.076	2.006	-0.3577
<i>Times delays</i>			
$\tau_{\text{lon}}$	0.2000	0.2000	0.2000
$\tau_{\text{lat}}$	0.2000	0.2000	0.2000
$\tau_{\text{ped}}$	0.06265	0.06265	0.05000
$\tau_{\text{col}}$	0.03482	0.03482	0.05000

<sup>a</sup>All results in English units.

$\delta_{\text{lon}}$ , normalized units 0–2 (+ve right stick).

$\delta_{\text{lat}}$ , normalized units 0–2 (+ve forward stick).

$\delta_{\text{ped}}$ , normalized units 0–2 (+ve right turn).

$\delta_{\text{col}}$ , normalized units 0–2 (+ve up collective).

**Table 15.5 Simulation and identification model cost functions (SH-2G, hover)**

Engineering symbols	STI model	NASA model	Identification
$u/\delta_{\text{lon}}$	99.6	308.4	85.5
$v/\delta_{\text{lon}}$	5477	6228	147.8
$p/\delta_{\text{lon}}$	3048	2280	34.2
$q/\delta_{\text{lon}}$	341.2	513.5	43.2
$a_x/\delta_{\text{lon}}$	886.8	2035	123.0
$a_y/\delta_{\text{lon}}$	1668	977.6	43.5
$u/\delta_{\text{lat}}$	384.7	2001	110.8
$v/\delta_{\text{lat}}$	830.8	7342	168.2
$p/\delta_{\text{lat}}$	126.0	227.2	87.5
$q/\delta_{\text{lat}}$	656.4	2042	107.2
$a_y/\delta_{\text{lat}}$	1752	2036	168.6
$v/\delta_{\text{ped}}$	5.9	123.5	3.3
$p/\delta_{\text{ped}}$	920.2	314.0	30.8
$r/\delta_{\text{ped}}$	470.6	563.1	55.0
$a_y/\delta_{\text{ped}}$	377.3	109.3	51.2
$u/\delta_{\text{col}}$	1379	1338	73.5
$w/\delta_{\text{col}}$	198.9	188.9	21.5
$q/\delta_{\text{col}}$	8313	7095	25.1
$r/\delta_{\text{col}}$	2925	2968	45.2
$a_x/\delta_{\text{col}}$	104.6	92.3	50.2
$a_z/\delta_{\text{col}}$	198.9	188.9	21.5
$J_{\text{ave}}$	1436	1856	71.3

### 15.3.4 Identification Results for 60 and 100 kn

The identification process for 60 and 100 kn closely followed the hover approach just detailed. One aspect of the forward-flight identification is the high insensitivity of the speed-damping derivative  $X_u$  because of the lack of sufficient low-frequency longitudinal response data content. Therefore, the simulation values<sup>212</sup> were fixed in the identification for 60 and 100 kn. A second aspect for forward flight is that there is no significant  $r/\delta_{\text{col}}$  response, as indicated both in the time response to collective inputs and the lack of coherence for this pair. Therefore the engine dynamics were also dropped for forward flight.

Tables 15.6 and 15.7 compare the identification results for all three flight conditions. The average cost functions are  $J_{\text{ave}} = 100$  and  $J_{\text{ave}} = 93$  for 60 and 100 kn, respectively, again indicating excellent characterization of the flight data.

There are generally quite smooth trends of the identification parameters with airspeed. This is seen, for example, in the monotonic increase in the rotor spring parameters  $L_{\beta_{1s}}$  and  $M_{\beta_{1c}}$ , which reflect increasing rate damping with speed and include the influence of the horizontal tail, as discussed earlier. An interesting result is that the rotor time constant reduces at the highest flight speed (100 kn) to an identified value of  $\tau_f = 0.13$  s, which agrees very closely with the theoretical

Table 15.6 Identification results for three flight conditions (SH-2G)<sup>a</sup>

Engineering symbols	Hover	60 kn	100 kn
<b><i>M-matrix</i></b>			
$\tau_f$	0.2051	0.2090	0.1279
$\tau_e$	0.8886	—	—
<b><i>F-matrix</i></b>			
$X_u$	-0.06415	-0.06036	-0.03760 <sup>b</sup>
$X_v$	0.000 <sup>c</sup>	0.000 <sup>c</sup>	0.000 <sup>c</sup>
$X_w$	0.000 <sup>c</sup>	0.000 <sup>c</sup>	0.000 <sup>c</sup>
$X_r$	0.000 <sup>c</sup>	0.000 <sup>c</sup>	0.000 <sup>c</sup>
$X_{\beta_{1c}}$	35.30	35.08	48.28
$Y_u$	-0.1592	-0.2202	0.2160
$Y_v$	-0.3593	-0.1153	-0.07071
$Y_w$	0.000 <sup>c</sup>	0.000 <sup>c</sup>	0.000 <sup>c</sup>
$Y_p$	1.216	1.730	-2.605
$Y_r$	0.000 <sup>c</sup>	3.297	0.000 <sup>c</sup>
$Y_{\beta_{1s}}$	-35.30 <sup>d</sup>	-35.08 <sup>d</sup>	-48.28 <sup>d</sup>
$Z_u$	0.000 <sup>c</sup>	0.2954	0.2064
$Z_v$	0.000 <sup>c</sup>	0.000 <sup>c</sup>	0.000 <sup>c</sup>
$Z_w$	-0.06857	-0.3532	-0.3130
$Z_p$	0.000 <sup>c</sup>	0.000 <sup>c</sup>	0.000 <sup>c</sup>
$Z_q$	0.000 <sup>c</sup>	0.000 <sup>c</sup>	-11.74
$Z_r$	0.000 <sup>c</sup>	-11.43	0.000 <sup>c</sup>
$L_u$	-0.04063	-8.644E-03	0.02068
$L_v$	-0.08868	-0.02272	-5.527E-03
$L_w$	0.000 <sup>c</sup>	0.000 <sup>c</sup>	6.633E-03
$L_r$	-0.3296	0.000 <sup>c</sup>	0.000 <sup>c</sup>
$L_{\beta_{1s}}$	-22.38	-25.48	-27.36
$M_u$	-4.484E-03	-6.052E-03	-8.669E-03
$M_v$	-8.806E-03	2.726E-03	2.939E-03
$M_w$	0.000 <sup>c</sup>	3.922E-03	2.230E-03
$M_r$	0.000 <sup>c</sup>	0.000 <sup>c</sup>	0.5622
$M_{\beta_{1c}}$	-8.257	-10.09	-10.15
$N_u$	0.000 <sup>c</sup>	0.01966	-0.01581
$N_v$	0.000 <sup>c</sup>	0.01836	4.872E-03
$N_w$	0.000 <sup>c</sup>	0.000 <sup>c</sup>	0.000 <sup>c</sup>
$N_p$	0.000 <sup>c</sup>	-0.1380	0.000 <sup>c</sup>

Table 15.6 (continued)

Engineering symbols	Hover	60 kn	100 kn
$N_q$	0.000 <sup>c</sup>	0.000 <sup>c</sup>	0.000 <sup>c</sup>
$N_r$	-0.6688	-1.352	-1.609
$Lf_{\beta_{1c}}$	-0.4171	-0.2656	0.000 <sup>c</sup>
$Mf_{\beta_{1s}}$	0.6807	0.5145	0.000 <sup>c</sup>
$v_{\dot{\beta}}$	-165.1 <sup>b</sup>	1.054E+03	788.6
$K_{\theta_0}$	0.08268	0.06116 <sup>b</sup>	0.06076
<i>G-matrix</i>			
$X_{\delta_{\text{ped}}}$	0.000 <sup>c</sup>	0.000 <sup>c</sup>	0.000 <sup>c</sup>
$X_{\delta_{\text{col}}}$	3.288	0.000 <sup>c</sup>	0.000 <sup>c</sup>
$Y_{\delta_{\text{ped}}}$	-5.369	-5.330	-6.515
$Y_{\delta_{\text{col}}}$	0.000 <sup>c</sup>	0.000 <sup>c</sup>	0.000 <sup>c</sup>
$Z_{\delta_{\text{lon}}}$	0.000 <sup>c</sup>	17.17	21.54
$Z_{\delta_{\text{lat}}}$	0.000 <sup>c</sup>	5.991	0.000 <sup>c</sup>
$Z_{\delta_{\text{ped}}}$	0.000 <sup>c</sup>	0.000 <sup>c</sup>	0.000 <sup>c</sup>
$L_{\delta_{\text{ped}}}$	-0.7305	-1.126	-1.497
$L_{\delta_{\text{col}}}$	0.000 <sup>c</sup>	0.000 <sup>c</sup>	1.460
$M_{\delta_{\text{ped}}}$	0.000 <sup>c</sup>	0.1191	0.000 <sup>c</sup>
$M_{\delta_{\text{col}}}$	0.2251	0.6818	0.9268
$N_{\delta_{\text{col}}}$	0.000 <sup>c</sup>	0.000 <sup>c</sup>	0.000 <sup>c</sup>
$N_{\delta_{\text{lon}}}$	0.000 <sup>c</sup>	0.3669	0.000 <sup>c</sup>
$N_{\delta_{\text{lat}}}$	1.725	1.802	2.053
$N_{\delta_{\text{ped}}}$	0.3577	0.000 <sup>c</sup>	0.000 <sup>c</sup>
$N_{\delta_{\text{col}}}$	0.1769	0.1360	0.07245
$Lf_{\delta_{\text{lon}}}$	-0.09724	-0.1087	-0.09909
$Lf_{\delta_{\text{lat}}}$	0.2727	0.2751	0.2605
$Mf_{\delta_{\text{lon}}}$	0.1142	0.06323	0.03182
<i>Time Delays</i>			
$\tau_{\text{lon}}$	0.000 <sup>c</sup>	0.000 <sup>c</sup>	0.000 <sup>c</sup>
$\tau_{\text{lat}}$	0.000 <sup>c</sup>	0.000 <sup>c</sup>	0.000 <sup>c</sup>
$\tau_{\text{ped}}$	0.03624	0.05201	0.05542
$\tau_{\text{col}}$	0.03409	0.09272	0.08263

<sup>a</sup> All results in English units.

<sup>b</sup> Fixed parameter in model structure.

<sup>c</sup> Eliminated from model structure.

<sup>d</sup> Constrained parameter in model structure.

$\delta_{\text{ped}}$ , normalized units 0–2 (+ve right turn).

$\delta_{\text{col}}$ , normalized units 0–2 (+ve up collective).

$\delta_{\text{lon}}$ , normalized units 0–2 (+ve right stick).

$\delta_{\text{lat}}$ , normalized units 0–2 (+ve forward stick).

Table 15.7 Identification cost functions (SH-2G)

Engineering symbols	Hover	60 kn	100 kn
$u/\delta_{\text{lon}}$	85.5	72.7	194.1
$v/\delta_{\text{lon}}$	147.8	352.4	_____ <sup>a</sup>
$w/\delta_{\text{lon}}$	_____ <sup>a</sup>	48.0	135.6
$p/\delta_{\text{lon}}$	34.2	147.3	106.9
$q/\delta_{\text{lon}}$	43.2	23.6	53.1
$a_x/\delta_{\text{lon}}$	123.0	66.2	43.4
$a_y/\delta_{\text{lon}}$	43.5	_____ <sup>a</sup>	_____ <sup>a</sup>
$a_z/\delta_{\text{lon}}$	_____ <sup>a</sup>	129.9	42.6
$v_z/\delta_{\text{lon}}$	_____ <sup>a</sup>	22.7	_____ <sup>a</sup>
$u/\delta_{\text{lat}}$	110.8	166.6	_____ <sup>a</sup>
$v/\delta_{\text{lat}}$	168.2	_____ <sup>a</sup>	_____ <sup>a</sup>
$w/\delta_{\text{lat}}$	_____ <sup>a</sup>	107.6	98.1
$p/\delta_{\text{lat}}$	87.5	43.0	88.2
$q/\delta_{\text{lat}}$	107.2	112.3	194.5
$r/\delta_{\text{lat}}$	_____ <sup>a</sup>	141.9	_____ <sup>a</sup>
$a_y/\delta_{\text{lat}}$	168.6	104.8	60.3
$a_z/\delta_{\text{lat}}$	_____ <sup>a</sup>	67.5	92.7
$u/\delta_{\text{ped}}$	_____ <sup>a</sup>	84.7	109.8
$v/\delta_{\text{ped}}$	3.3	114.6	110.1
$w/\delta_{\text{ped}}$	_____ <sup>a</sup>	63.5	15.9
$p/\delta_{\text{ped}}$	30.8	64.6	36.4
$q/\delta_{\text{ped}}$	_____ <sup>a</sup>	71.6	17.7
$r/\delta_{\text{ped}}$	55.0	174.3	166.2
$a_y/\delta_{\text{ped}}$	51.2	33.1	54.6
$a_z/\delta_{\text{ped}}$	_____ <sup>a</sup>	46.7	_____ <sup>a</sup>
$u/\delta_{\text{col}}$	73.5	_____ <sup>a</sup>	_____ <sup>a</sup>
$w/\delta_{\text{col}}$	21.5	_____ <sup>a</sup>	128.2
$p/\delta_{\text{col}}$	_____ <sup>a</sup>	_____ <sup>a</sup>	46.6
$q/\delta_{\text{col}}$	25.1	273.2	208.2
$r/\delta_{\text{col}}$	45.2	_____ <sup>a</sup>	_____ <sup>a</sup>
$a_x/\delta_{\text{col}}$	50.2	_____ <sup>a</sup>	_____ <sup>a</sup>
$a_z/\delta_{\text{col}}$	21.5	25.1	35.6
$J_{\text{ave}}$	71.3	100.0	92.7

<sup>a</sup> Excluded from identification.

value ( $\tau_f = 0.12$  s) based on the geometric Lock number  $\gamma$ . This should be expected at this flight condition ( $\mu = V_{\text{tot}}/\Omega R = 0.25$ ), where dynamic inflow effects on the rotor time constant are not significant [ $\gamma^* = \gamma$ , Eq. (11.37)].

A key feature is the monotonic reduction with airspeed of SH-2G pitch-roll coupling, as evidenced by the reduction in the control coupling derivatives  $Lf_{\delta_{\text{lon}}}$

and  $Mf_{\delta_{\text{lat}}}$  and the reduction to zero at 100 kn of the flap response coupling parameters  $Lf_{\beta_{1c}}$  and  $Mf_{\beta_{1c}}$ . The flap response coupling derivatives result in an equivalent reduction to zero in the six-DOF pitch-response coupling ratios  $|M_p/L_p|$  and  $|M_p/M_q|$ . This trend was also verified by a direct comparison of the off/on-axis frequency-response ratios (e.g.,  $[q/\delta_{\text{lat}}]/[p/\delta_{\text{lat}}]$ ) for the three airspeeds. Neither simulation model predicts this significant level of coupling reduction with airspeed.

There is a monotonic decrease in the primary lateral speed-damping derivative  $Y_v$ ; this decrease is correctly captured by the STI simulation model,<sup>212</sup> but the NASA model predicted the reverse trend.<sup>211</sup> Finally, for forward flight the simulation values for heave damping more closely track the flight-test results (the average identified value for 60 and 100 kn is  $Z_w = -0.33 \text{ rad/s}$ ), as has previously been reported, for example, in Houston and Tarttelin.<sup>215</sup>

### 15.3.5 Time-Response Verification

The predictive capability of the identified models is assessed by driving each model with doublet data not used in the identification process. As explained in Chapter 14, the identified stability and control derivative parameters are held fixed, and only the bias and reference-shift corrections are determined. The doublet response comparisons for all flight conditions are shown in Figs. 15.5–15.7 for each of the four inputs. The results show that the identified model generally has excellent predictive accuracy ( $J_{\text{rms}} \approx 1$  to 2), even for the rather large responses in the verification records (up to 30 deg/s). Notice again that these verification plots reflect the total response variables as can be seen for example in the starting value of vertical acceleration ( $a_z = -32.174 \text{ ft/s}^2$ ).

The large roll-response coupling is apparent, as expected for a longitudinal input in hover ( $|p_{\text{max}}|/|q_{\text{max}}| \approx 1.0$ ), and is well captured by the equivalent six-DOF cross-coupling ratio ( $|L_q/M_q| = 1.1$ ). The pitch-response coupling is about 30%, which is also well predicted by the identified model and is consistent with the reduced six-DOF coupling ratio  $|M_p/L_p| = 0.25$ .

### 15.3.6 Summary of SH-2G Identification Project

The frequency-domain system-identification methods commonly used on conventional helicopters are seen to be well suited to the SH-2G flap-controlled rotor configuration. Although key SH-2G response characteristics are not adequately modeled by existing analytical simulations, the flight-identified models for the SH-2G closely match the frequency-response flight-test database and accurately predict the time-domain response to control doublet inputs. The identified models are characterized by highly coupled fuselage-rotor dynamics, a high degree of pitch-roll interaxis control coupling, and important effects of engine dynamics. The identified derivatives are shown to vary smoothly with airspeed and are consistent with theoretical predictions for standard hinge-offset rotors.

The hybrid model structure provides a consistent and accurate characterization of the coupled fuselage/rotor/inflow/engine dynamics across the entire flight envelope. This model structure is well suited to system identification of all helicopters, but is required for configurations that feature larger values of rotor flap stiffness.

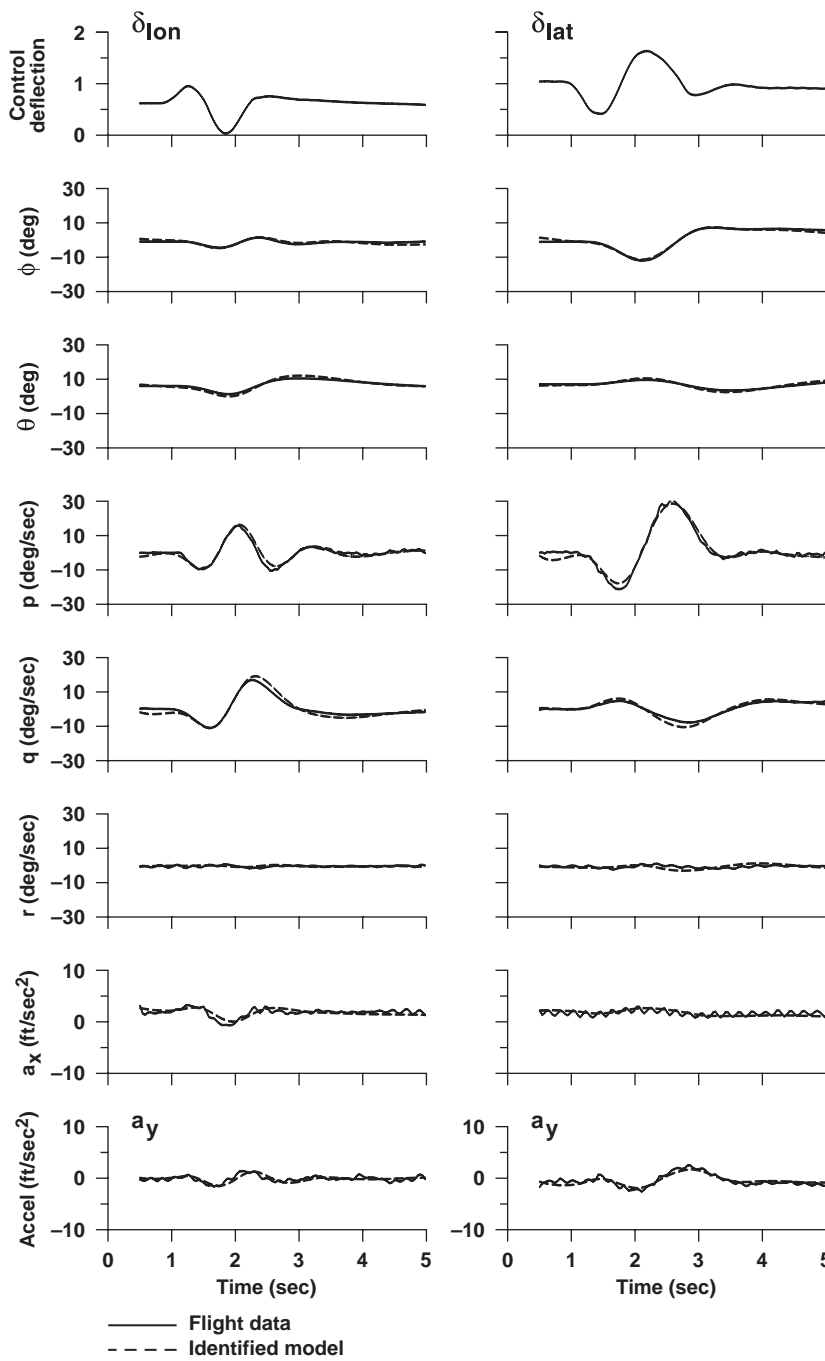


Fig. 15.5 Time-response verification of identified model for hover (SH-2G).

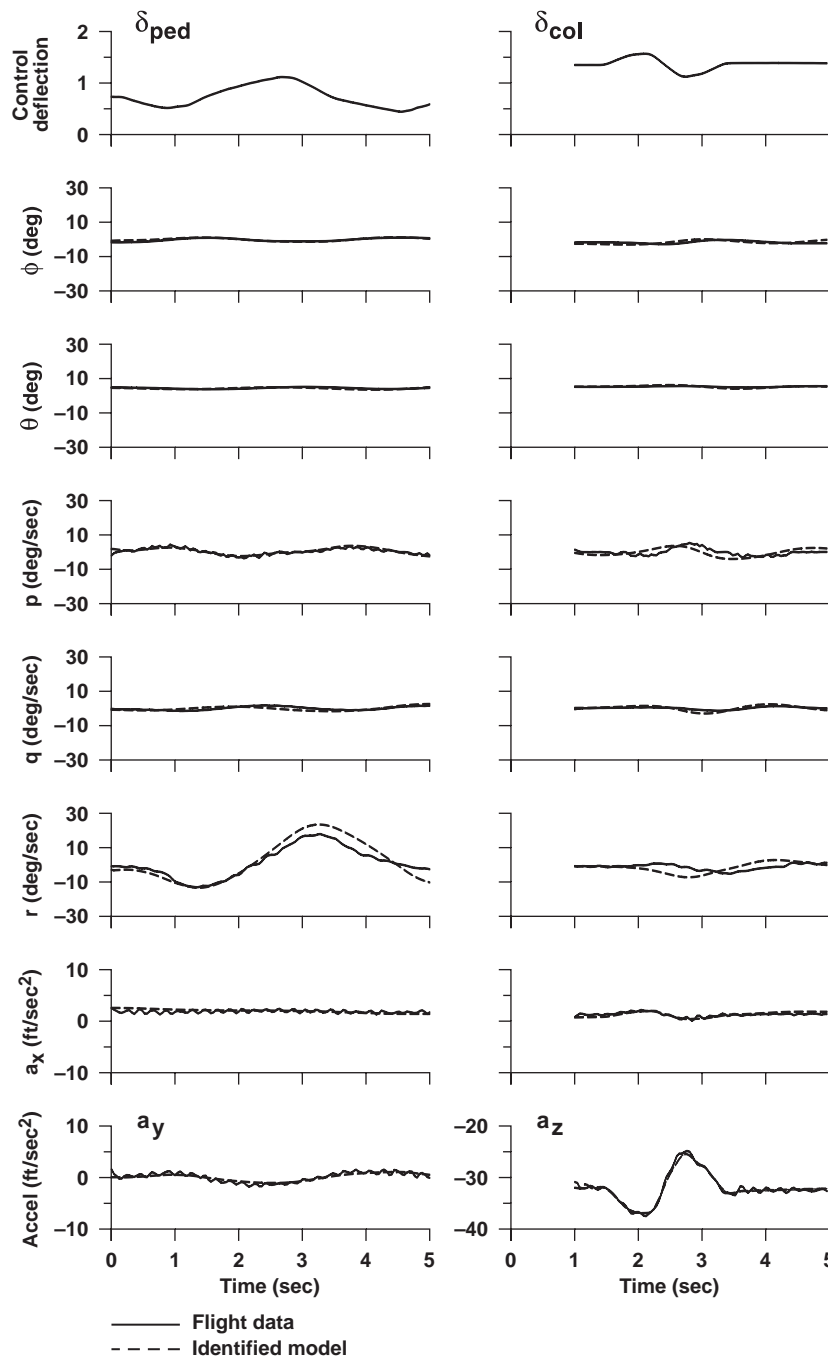


Fig. 15.5 Time-response verification of identified model for hover (SH-2G) (continued).

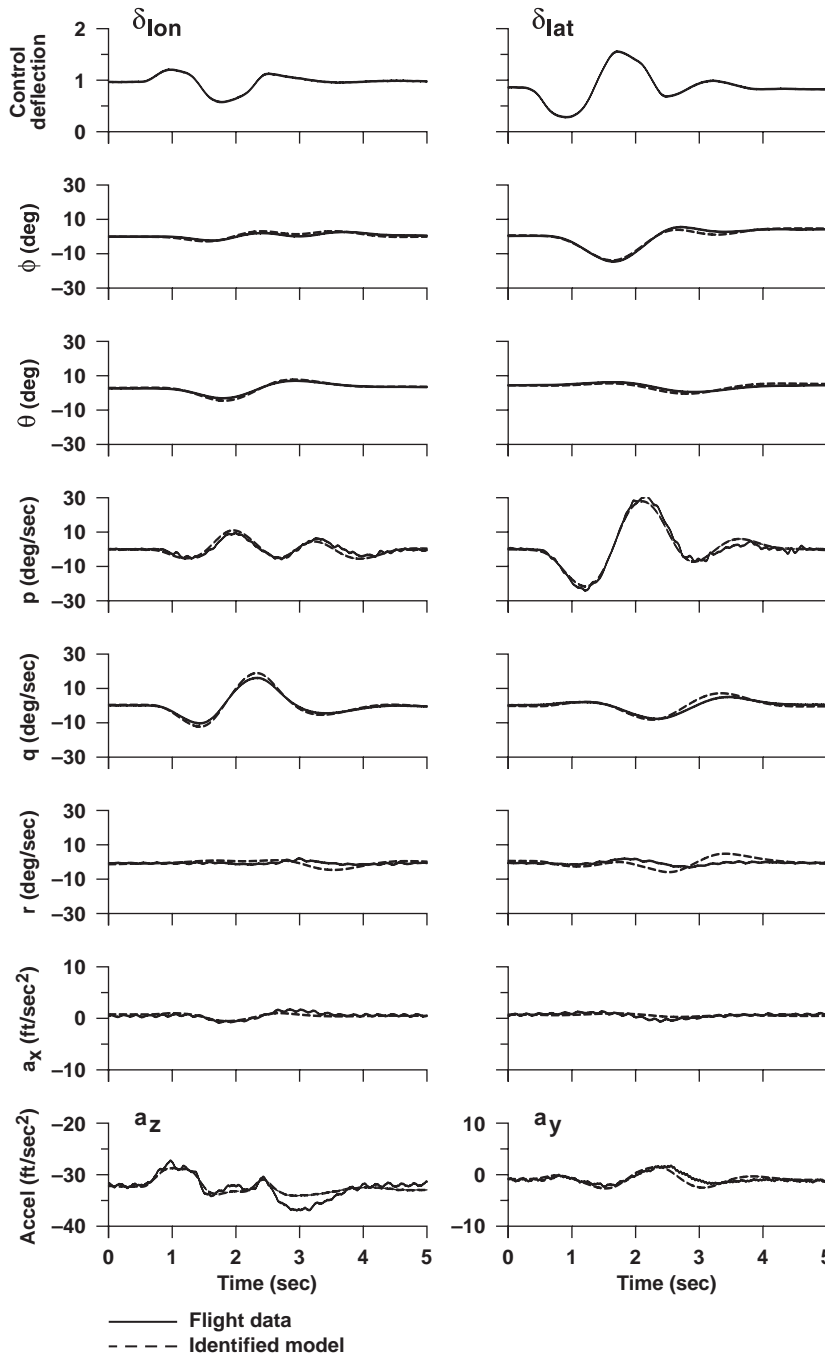


Fig. 15.6 Time-response verification of identified model for 60 kn (SH-2G).

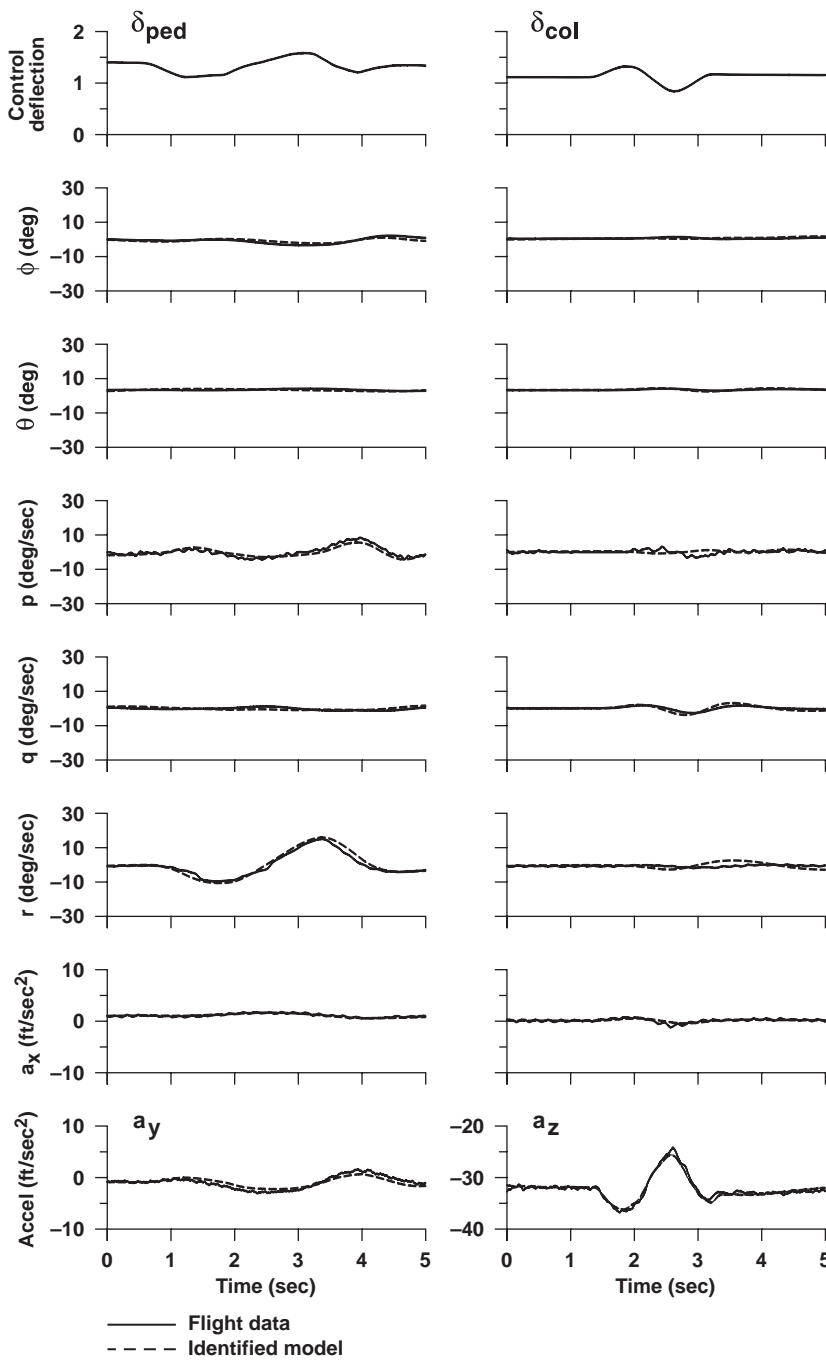


Fig. 15.6 Time-response verification of identified model for 60 kn (SH-2G) (continued).

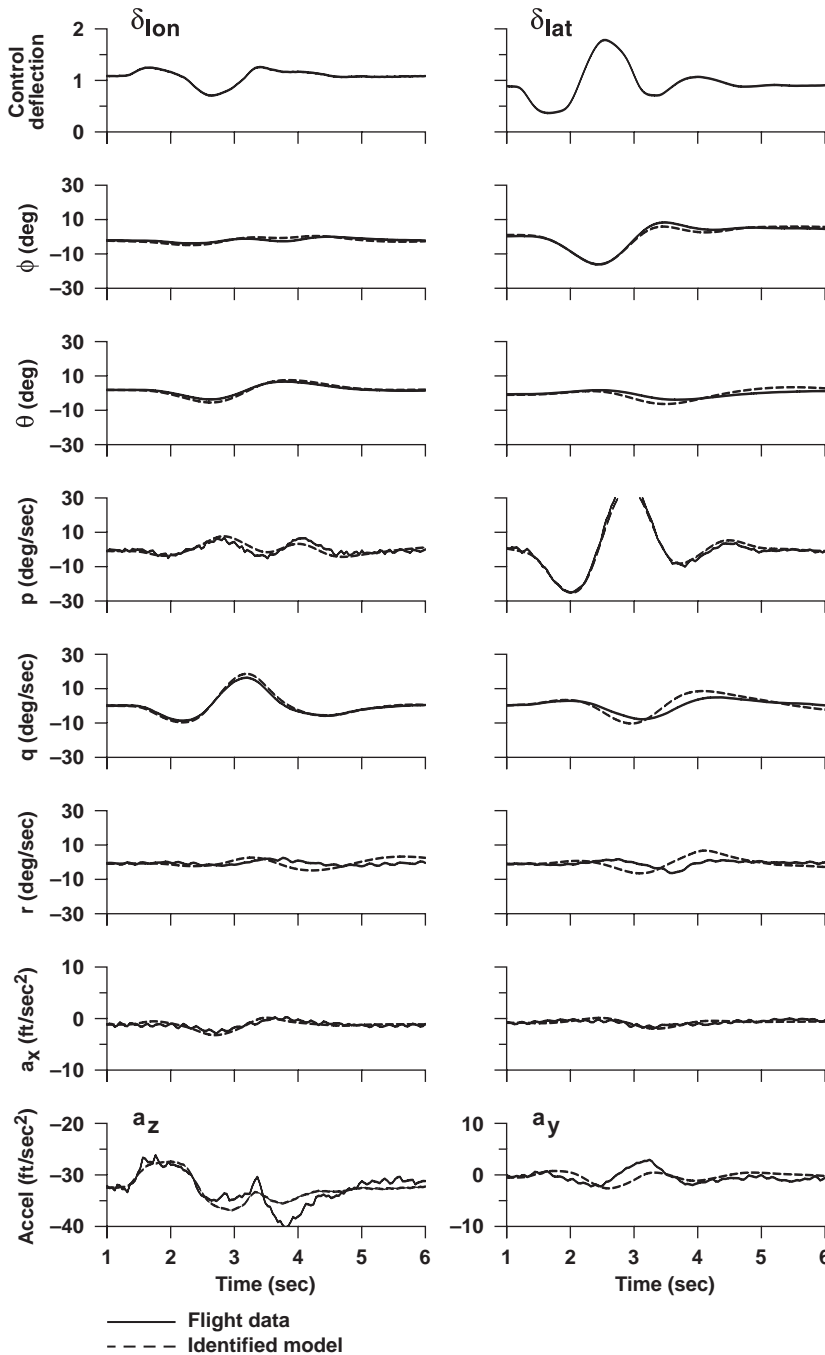


Fig. 15.7 Time-response verification of identified model for 100 kn (SH-2G).

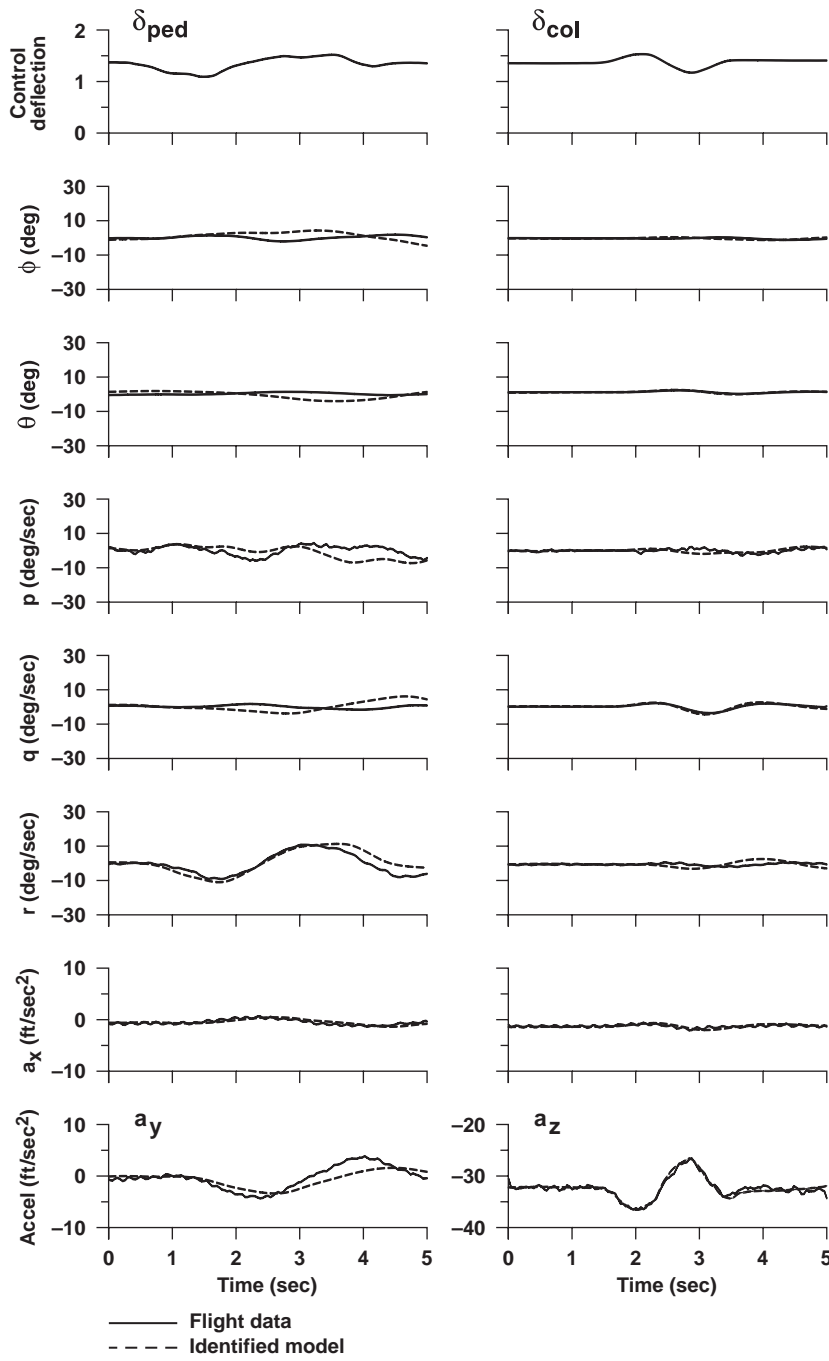


Fig. 15.7 Time-response verification of identified model for 100 kn (SH-2G) (continued).

### 15.4 Lead-Lag Dynamics Identification for S-92 Helicopter

The coupled rotor/fuselage/engine dynamics of the S-92 helicopter in hover were identified by Tischler et al.<sup>17</sup> using the hybrid model structure. The regressive lead-lag dynamics were included in the model, using the dipole characterization of Eqs. (15.8) and (15.9). The influence of these dynamics can be seen in the *notch* characteristic at a frequency of about 20 rad/s in the roll and pitch responses (Fig. 15.8). The coherence drops at this frequency because of the

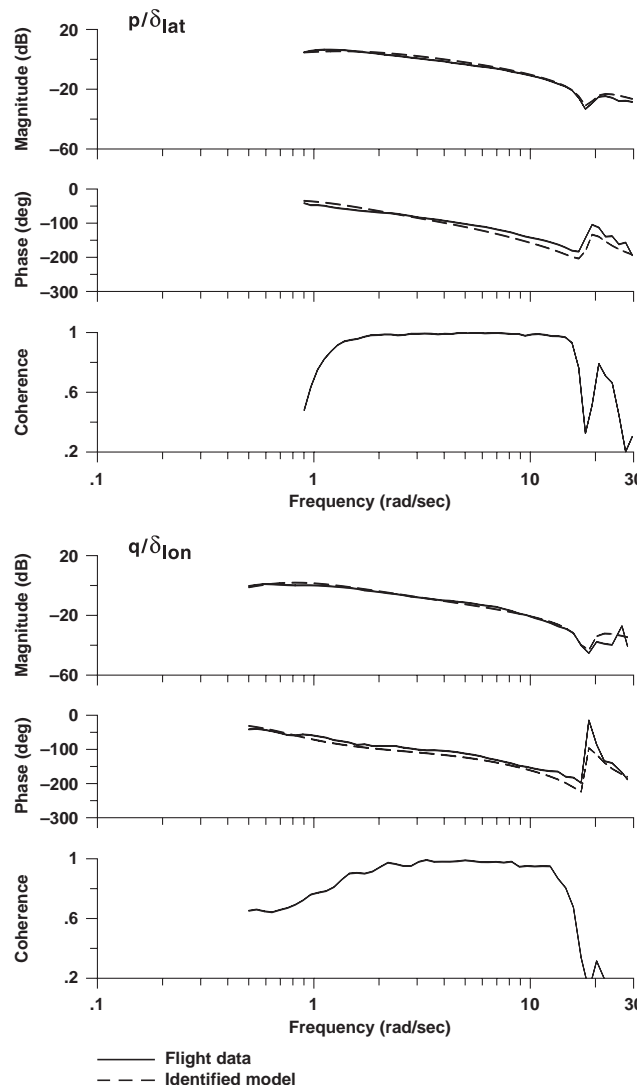


Fig. 15.8 Hybrid model identification including lead-lag dynamics (S-92, hover).

reduction in signal to noise associated with the drop in the magnitude response at the notch center. The identified hybrid model, shown in the dashed line, agrees well with the frequency-response data. The regressive lead-lag mode is identified as [ $\zeta_{ll_r} = 0.183$ ,  $\omega_{ll_r} = 19.0$  rad/s]. The UH-60A helicopter has a similar rotor system to the S-92. Fletcher<sup>210</sup> identified the regressive lead-lag mode for the UH-60A as [ $\zeta_{ll_r} = 0.175$ ,  $\omega_{ll_r} = 18.9$  rad/s], which is in close agreement with the results herein.

## Problems

### *Analytical calculations of Bo-105 lateral flapping dynamics*

**15.1** The Bo-105 helicopter has the following characteristics<sup>21</sup>:  $a = 5.73$  1/rad,  $\sigma = 0.070$ ,  $R = 16.11$  ft,  $c = 0.89$  ft,  $\Omega = 44.4$  rad/s,  $W = 4620$  lb,  $I_b = 142$  slug-ft<sup>2</sup>,  $\rho = 0.00237$  slug/ft<sup>3</sup>, and  $1/\tau_f = 10.8$  s<sup>-1</sup>. Calculate the geometric Lock number [Eq. (11.36)]. Compare the geometric Lock number with that of the SH-2G ( $\gamma = 5$ ). What does this indicate about the SH-2G rotor as compared to the Bo-105? Then determine the effective (reduced) Lock number of the Bo-105 with Eq. (11.37) and correct the rotor-flap time constant with the corrected Lock number.

**15.2** Determine the theoretical value of  $L_{\beta_{1s}}$  [Eq. (11.33)] for the Bo-105 if  $W = 4620$  lb,  $h_r = 5.0$  ft,  $I_x = 1330$  slug-ft<sup>2</sup>,  $n_b = 4$ ,  $M_\beta = 10.3$  slug-ft,  $\Omega = 44.4$  rad/s,  $e = 1.92$  ft, and  $K_\beta = 8900$  ft-lb/rad (Ref. 21). What is the largest contribution to flapping stiffness  $L_{\beta_{1s}}$ : the height of the rotor-hub, the hinge offset, or the rotor-blade flap spring?

### *Identification of Bo-105 lateral coupled fuselage/rotor dynamics with measurements of fuselage states*

**15.3** You are an engineer, and you are given flight data for Bo-105 lateral sweeps for the purpose of system identification. These “flight” data are simulated from a simple simulation model and provided on the AIAA website with a readme file containing flight numbers and signal names/units. Perform a SISO identification of  $p/\delta_{lat}$ ,  $\dot{v}/\delta_{lat}$  with FRESPID, and then combine the windows using COMPOSITE windowing. Note that the simulation data contain process noise to simulate real flight data that an engineer might be given for identification.

**15.4** Identify a three-DOF coupled fuselage/rotor model using DERIVID with states  $p$ ,  $v$ ,  $\phi$ , and  $\beta_{1s}$ . Select outputs  $p$  and  $v$ , and use the frequency responses of the fuselage states  $p/\delta_{lat}$  and  $\dot{v}/\delta_{lat}$  determined in **Problem 15.3**. Use the theoretical parameters for  $\tau_f$  and  $L_{\beta_{1s}}$  calculated in **Problems 15.1** and **15.2** as initial guesses, and use the identified SH-2G parameters of Chapter 15 as initial guesses for all other derivatives. Do the theoretical accuracy parameters fall within the guidelines given in Chapter 12? How well do  $\tau_f$  and  $L_{\beta_{1s}}$  match the theoretical values calculated in **Problems 15.1** and **15.2**? Hint: Try fixing  $Y_{\beta_{1s}}$  to the theoretical value ( $-g$ ).

**15.5** Identify the frequency-response  $v/p$ . Then build on **Problem 15.4**, and include this frequency response in the identification by adding the constraint on the speed-damping derivative  $Y_v$  as detailed in Sec. 13.12.4. How does the constraint affect the theoretical accuracy parameters? Now how well do  $\tau_f$  and  $L_{\beta_{1s}}$  match the theoretical values calculated in **Problems 15.1** and **15.2**?

**15.6** As in Sec. 13.12.4, use the trim data shown in Table P15.6 to estimate the lateral speed derivative  $L_v$  from the identified values as obtained from **Problem 15.5**. Use a curve-fitting technique to determine  $\Delta\delta_{\text{lat}}/\Delta v$ . Fix  $L_v$  to its calculated value in your identified model, and reconverge the solution. How does the constraint affect the theoretical accuracy parameters? How well do  $\tau_f$  and  $L_{\beta_{1s}}$  match the theoretical values calculated in **Problems 15.1** and **15.2**? What is a possible explanation as to why this constraint causes the identified model to move further away from the theoretical values of  $\tau_f$  and  $L_{\beta_{1s}}$ ?

**Table P15.6 Trim data**

Velocity, ft/s	$\delta_{\text{lat}}, \%$
-10	-2.0313
-5	-0.1065
0	0.09
5	0.9151
10	3.103

*Identification of Bo-105 lateral coupled fuselage/rotor dynamics with measurements of fuselage and rotor states*

**15.7** Now, suppose that the Bo-105 has been instrumented with a rotor flap-angle measurement sensor. Using the simulated flight data for  $\beta_{1s}$  for the same Bo-105 lateral sweep “flight test,” perform a SISO identification of  $\beta_{1s}/\delta_{\text{lat}}$  with FRESPID, and then combine the windows using COMPOSITE windowing.

**15.8** Repeat the system identification of **Problem 15.4** including rotor flap-angle  $\beta_{1s}$  as an additional output in your DERIVID identification. Incorporate the frequency response  $\beta_{1s}/\delta_{\text{lat}}$  into the identification. How does this affect the theoretical accuracy parameters? How well do  $\tau_f$  and  $L_{\beta_{1s}}$  match the theoretical values calculated in **Problems 15.1** and **15.2**?

**15.9** Determine the eigenvalues and eigenvectors of the system identified in **Problem 15.7**, and analyze the identified helicopter modes.

*Quasi-steady lateral model identification for Bo-105*

**15.10** Use DERIVID to identify a quasi-steady model for the Bo-105 lateral hover dynamics (with states  $p$ ,  $v$ ,  $\phi$ ) from frequency responses identified in **Problem 15.3**. The delay  $\tau_{\text{lat}}$  is used to represent effectively the rotor delays

associated with flapping. How does the average cost compare to the coupled rotor-fuselage model (**Problem 15.8**)? What does this say about the level of rotor-body coupling? How does the identified value of  $L_p$  compare to the theoretical effective value  $(L_p)_{\text{effective}}$  [Eq. (11.46)] as obtained from the identification results of **Problem 15.8**? How does the identified value of  $L_{\delta_{\text{lat}}}$  compare to the theoretical effective value  $(L_{\delta_{\text{lat}}})_{\text{effective}}$  [Eq. (11.45)] as obtained from the identification results of **Problem 15.8**?

**15.11** Do you think that the quasi-steady (two-DOF) model identified in **Problem 15.10** is an adequate model structure? Is the condition for lightly coupled fuselage and rotor responses given in Eq. (11.42) met?

**15.12** Determine the eigenvalues and eigenvectors of the quasi-steady model identified in **Problem 15.10**, and analyze the identified helicopter modes. How does this compare to the coupled fuselage/rotor model from **Problem 15.9**?

**15.13** Determine the sensitivity of the identified value of  $L_p$  to the frequency range of fit for the system identification of **Problem 15.10**.

*Time-domain verification of coupled fuselage/rotor model and quasi-steady model for Bo-105*

**15.14** Complete the time-domain verification of your coupled fuselage/rotor model identified in **Problem 15.8**. Use the doublet “flight” data that are provided on the AIAA website for your verification. Use the appropriate utilities to obtain hard copies of your results.

**15.15** Complete the time-domain verification of your quasi-steady model identified in **Problem 15.10**. Use the doublet “flight” data that are provided on the AIAA website for your verification. Use the appropriate utilities to obtain hard copies of your results. Then compare the predictive capability of the quasi-steady model to that of the coupled fuselage/rotor model (**Problem 15.14**). Can you attribute the discrepancies in the time-domain response of the quasi-steady model to any specific characteristics of its frequency-domain fit (**Problem 15.10**)?

This page intentionally left blank

## Appendix A

### Summary of Suggested Guidelines

**Table A.1 Suggested guidelines**

Guideline	Topic	Chap.	Page	Eq.
$\omega_f \geq 5 \cdot \omega_{\max}$	Select the filter cutoff frequency $\omega_f$ , also referred to as the filter bandwidth, to be at least five times the maximum frequency of interest of model applicability $\omega_{\max}$	5	89	5.1
$\omega_s \geq 5 \cdot \omega_f$	Choose a sample rate $\omega_s$ , the same for all of the signals, with a value of at least a factor of 5 above the filter frequency $\omega_f$	5	90	5.2
$T_{\text{rec}} \geq (4 \text{ to } 5)T_{\max}$	For frequency sweeps, the minimum total record length $T_{\text{rec}}$ relative to the length of the longest period $T_{\max}$ in a record	5	93	5.11
$\gamma_{xy}^2 \geq 0.6$	Lower limit of the coherence function $\gamma_{xy}^2$ to achieve acceptable accuracy in a frequency-response identification (In addition, the coherence function should not be oscillating.)	7	166	7.54
$n_d \geq 5$	Minimum number of independent time-history averages $n_d$ in a concatenated record	7	169	7.57
$T_{\text{win}} = 2T_{\max}$	Nominal window size $T_{\text{win}}$ relative to the length of the longest period of interest $T_{\max}$	7	170	7.60
$T_{\text{win}} \leq 0.5T_{\text{rec}}$	Maximum window size $T_{\text{win}}$ relative to the length of the record $T_{\text{rec}}$	7	171	7.61
$T_{\text{win}} \leq (1/5)T_F$	Maximum window size $T_{\text{win}}$ relative to the concatenated record length $T_F$	7	171	7.64
$T_{\text{win}} \geq 20(2\pi/\omega_{\max})$	Minimum window size $T_{\text{win}}$ relative to the maximum frequency of interest	7	172	7.65

(continued)

## 496 AIRCRAFT AND ROTORCRAFT SYSTEM IDENTIFICATION

Table A.1 Suggested guidelines (continued)

Guideline	Topic	Chap.	Page	Eq.
$T_{\text{win}} \geq 11/(\zeta\omega_n)$	For structural system identification, the minimum window size $T_{\text{win}}$ relative to the structural damping ratio $\zeta$ and the undamped natural frequency $\omega_n$	7	174	7.72
$T_{\text{rec}} \geq 22/(\zeta\omega_n)$	For structural system identification, the minimum record length $T_{\text{rec}}$ relative to the structural damping ratio $\zeta$ and the undamped natural frequency $\omega_n$	7	174	7.73
$T_F \geq 55/(\zeta\omega_n)$	For structural system identification, the concatenated record length $T_F$ relative to the structural damping ratio $\zeta$ and the undamped natural frequency $\omega_n$	7	175	7.74
$S(\omega) > 3$	Minimum signal-to-noise ratio [ $S(\omega)$ ] needed to achieve a satisfactory frequency-response bias error ( $\epsilon_b < 0.1$ )	8	214	8.18
$\bar{\sigma}_n(\omega) < 0.33$	Maximum noise-to-signal rms ratio [ $\bar{\sigma}_n(\omega)$ ] needed to achieve a satisfactory frequency-response bias error ( $\epsilon_b < 0.1$ )	8	215	8.20
$(\gamma_{\delta_1\delta_2}^2)_{\text{ave}} < 0.5$	Maximum average value of the cross-control coherence $(\gamma_{\delta_1\delta_2}^2)_{\text{ave}}$ to achieve a satisfactory MIMO solution	9	236	9.18
$J \leq 100$	Maximum value of cost function $J$ to achieve satisfactory accuracy for SISO transfer-function model	11	280	11.8
$(\gamma_{xy}^2)_{\text{cut}} = 0.4$	Suggested value for the coherence cutoff parameter $(\gamma_{xy}^2)_{\text{cut}}$ , used to avoid data that exhibit local drops in coherence below this threshold	12	328	12.22
$J_{\text{ave}} \leq 100$	Maximum value of overall average cost function $J_{\text{ave}}$ for MIMO state-space model to achieve an acceptable level of accuracy	12	329	12.23
$J_l \leq 150 \text{ to } 200$	Upper limit of individual cost functions $J_l$ to achieve satisfactory overall predictive accuracy (applies mostly to off-axis responses)	12	329	12.24

(continued)

## APPENDIX A: SUMMARY OF SUGGESTED GUIDELINES 497

Table A.1 Suggested guidelines (continued)

Guideline	Topic	Chap.	Page	Eq.
$\overline{CR}_i \leq 20\%$	Upper limit of the Cramér–Rao bounds $CR_i$ that (together with $J_{ave} \leq 100$ ) reflects a highly reliable state-space model identification with good predictive accuracy. (Several of the largest Cramér–Rao bounds can be in the range of 20–40% without loss of reliability or cause for concern.)	12	334	12.40
$\bar{I}_i < 10\%$	A reasonable goal for insensitivities $\bar{I}_i$ for the frequency-response method. (Several of the largest insensitivities can be in the range of 10–20% without loss of reliability or cause for concern.)	12	336	12.45
$\Delta J_{ave} \approx 1$ to 2	Magnitude of jump increase $\Delta J_{ave}$ in the average cost function that indicates that the process of reconverging the cost function should be terminated; the previous result should be used	12	339	12.52
$\Delta J_l \approx 10$ to 20	Magnitude of jump increase $\Delta J_l$ in the cost function of an individual frequency-response pair $l$ that indicates that the process of reconverging the cost function should be terminated; the previous result should be used	12	339	12.53
$(\gamma_{xy}^2)_{\text{threshold}} = 0.6$	A frequency-response pair $T_l$ should be excluded if the coherence function $\gamma_{xy}^2$ for that pair never rises above the threshold <i>within the frequency range of interest</i> . (The data for that pair should also be excluded if the magnitude or phase plots indicate other serious problems with the data.)	13	373	13.42
$(\gamma_{xy}^2)_{\text{fitting range}} \geq 0.5$	Coherence function threshold used to select the fitting range ( $\omega_1, \omega_{n_0}$ of Sec. 12.2.3) for a frequency-response pair that has acceptable coherence [i.e., the pair satisfies the threshold specified in the guideline of Eq. (13.42)]	13	373	13.43

(continued)

## 498 AIRCRAFT AND ROTORCRAFT SYSTEM IDENTIFICATION

Table A.1 Suggested guidelines (continued)

Guideline	Topic	Chap.	Page	Eq.
$\text{dec\_span} \geq 0.3$	Frequency-response pair should be excluded from the analysis if $\text{dec\_span} < 0.3$ , where $\text{dec\_span} = \log(\omega_{\max}/\omega_{\min})$	13	374	13.45
$J_{\text{rms}} \approx 1.0$ to $2.0$	Range of values for the rms fit error that generally reflects an acceptable level of accuracy in the time domain for flight-dynamics modeling	14	438	14.14
$\text{TIC} \leq 0.25$ to $0.3$	Range of values for the Theil inequality coefficient that generally reflects an acceptable level of accuracy in the time domain for flight-dynamics modeling	14	438	14.17

## References

<sup>1</sup>Soderstrom, T., and Stoica, P., *System Identification*, Prentice-Hall International, Upper Saddle River, NJ, 1989.

<sup>2</sup>Pintelon, R., and Schoukens, J., *System Identification: A Frequency-Domain Approach*, IEEE Press, New York, 2001.

<sup>3</sup>Williams, J. E., and Vukelich, S. R., “*The USAF Stability and Control Digital Datcom. Volume 1: User's Manual [Final Report, Aug. 1977 – Nov. 1978]*,” Air Force Flight Dynamics Lab., Wright-Patterson Air Force Base, Ohio, AFFDL-TR-79-3032-VOL-1, 1979.

<sup>4</sup>“*Aeronautical Design Standard, Handling Qualities Requirements for Military Rotorcraft*,” USAAMCOM ADS-33E-PRF, U.S. Army Aviation and Missile Command, Huntsville, Alabama, March, 2000.

<sup>5</sup>Dept. of Defense Interface Standard, “*Flying Qualities of Piloted Aircraft*,” USAF MIL-STD-1797, 1997.

<sup>6</sup>Klein, V., and Morelli, E. A., *Aircraft System Identification: Theory and Practice*, AIAA, 2006.

<sup>7</sup>Taylor, L. W., Jr., “*Application of a New Criterion for Modeling Systems*,” AGARD, CP-172, Nov. 1974.

<sup>8</sup>Kashyap, R. L., “A Bayesian Comparison of Different Classes of Dynamic Models Using Empirical Data,” *IEEE Transactions on Automatic Control*, Vol. AC-22, No. 5, 1977, pp. 715–727.

<sup>9</sup>Tischler, M. B., “System Identification Methods for Aircraft Flight Control Development and Validation,” *Advances in Aircraft Flight Control*, Taylor and Francis, London, 1996, pp. 35–59.

<sup>10</sup>Hamel, P. G. (ed.), *Rotorcraft System Identification*, AGARD-AR-280, 1991.

<sup>11</sup>Tischler, M. B. (organizing ed.), *Advances in Aircraft Flight Control*, Taylor and Francis, London, 1996.

<sup>12</sup>Theodore, C. R., Tischler, M. B., and Colbourne, J. D., “Rapid Frequency-Domain Modeling Methods for Unmanned Air Vehicle Flight Control Applications,” *Journal of Aircraft*, Vol. 41, No. 4, 2004, pp. 735–743.

<sup>13</sup>Tischler, M. B., and Kaletka, J., “Modeling XV-15 Tilt-Rotor Aircraft Dynamics by Frequency and Time Domain Identification Techniques,” *AGARD FMP Symposium on Rotorcraft Design and Operations*, AGARD, Paper no. 9, June 1987.

<sup>14</sup>Kaletka, J., Tischler, M. B., von Gruenhagen, W., and Fletcher, J. W., “Time and Frequency-Domain Identification and Verification of BO 105 Dynamic Models,” *Journal of the American Helicopter Society*, Vol. 35, No. 4, 1991, pp. 25–38.

<sup>15</sup>Tischler, M. B., and Cauffman, M. G., “Frequency-Response Method for Rotorcraft System Identification: Flight Applications to BO-105 Coupled Rotor/

## 500 AIRCRAFT AND ROTORCRAFT SYSTEM IDENTIFICATION

Fuselage Dynamics," *Journal of the American Helicopter Society*, Vol. 37, No. 3, 1992, pp. 3-17.

<sup>16</sup>Mansur, M. H., and Tischler, M. B., "An Empirical Correction Method for Improving Off-Axis Response in Flight Mechanics Helicopter Models," *Journal of the American Helicopter Society*, Vol. 43, No. 2, 1998, pp. 94-102.

<sup>17</sup>Tischler, M. B., Colbourne, J. D., Jenkins, J. L., Cicolani, L. S., Cheung, K. K., Wright, S. C., Acunzo, A. C., Yakzan, N. S., and Sahasrabudhe, V., "Integrated System Identification and Flight Control Optimization in S-92 Handling-Qualities Development," *American Helicopter Society Annual Forum*, May 2001.

<sup>18</sup>Tischler, M. B., "System Identification Requirements for High-Bandwidth Rotorcraft Flight Control System Design," *Journal of Guidance, Control, and Dynamics*, Vol. 13, No. 5, 1990, pp. 835-841.

<sup>19</sup>Colbourne, J. D., Tischler, M. B., and Rodgers, K., "Flight Control Design for an Unmanned Rotorcraft Program with a Rapid Development Schedule" *American Helicopter Society Annual Forum*, May 2001.

<sup>20</sup>Tischler, M. B., Blanken, C. L., Cheung, K. K., Swei, S. S. M., Sahasrabudhe, V., and Faynberg, A., "Modernized Control Laws for UH-60 BLACK HAWK: Optimization and Flight Test Results," *Journal of Guidance, Control, and Dynamics*, Vol. 28, No. 5, 2005, pp. 964-978.

<sup>21</sup>Heffley, R. K., Bourne, S. M., Curtiss, H. C., Jr., Hindson, W. S., and Hess, R. A., "Study of Helicopter Roll Control Effectiveness Criteria," NASA CR 177404, April 1986.

<sup>22</sup>Monnich, W., and Jategaonkar, R. V., "Data Base Development for Level D Simulation—Lessons Learned," NATO RTO-MP11, Paper no. 14, March 1999.

<sup>23</sup>Hamel, P. G., and Jategaonkar, R. V., "The Role of System Identification for Flight Vehicle Application — Revisited," NATO RTO-MP-11, Paper no. 2, March 1999.

<sup>24</sup>Hamel, P. G., and Jategaonkar, R. V., "The Evolution of Flight Vehicle System Identification," *AGARD Structures and Materials Panel Specialists' Meeting on Advanced Aeroservoelastic Testing and Data Analysis*, Paper no. 19, May 1995.

<sup>25</sup>Milliken, W. F., "Progress in Dynamic Stability and Control Research," *Journal of the Aeronautical Sciences*, Vol. 14, No. 9, 1947, pp. 493-499.

<sup>26</sup>Greenberg, H., "A Survey of Methods for Determining Stability Parameters of an Airplane from Dynamics Flight Measurements," NACA TN-2340, April 1951.

<sup>27</sup>Schofield, B. L., Twisdale, T. R., Kitto, W. G., and Ashurst, T. A., "Development of Handling Qualities Testing in the 70's: A New Direction," *AGARD Proceedings on Criteria for Military Handling Qualities of Military Aircraft*, AGARD CP 333 Paper no. 23, FT Worth, Texas, April 1982.

<sup>28</sup>Eggleston, J. M., and Mathews, C. W., "Application of Several Methods for Determining Transfer Functions and Frequency Response of Aircraft from Flight Data," NACA Rep. 1204, 1954.

## REFERENCES

## 501

<sup>29</sup>Donegan, J. J., Robinson, S. W., Jr., and Gates, O. B., Jr., "Determination of Lateral-Stability Derivatives and Transfer-Function Coefficients from Frequency-Response Data for Lateral Motions," NACA Rep. 1225, 1955.

<sup>30</sup>Kaufman, L., and Peress, K., "A Review of Methods for Predicting the Helicopter Longitudinal Response," *Journal of Aeronautical Science*, Vol. 23, No. 3, 1956, pp. 259-263.

<sup>31</sup>Schultz, E. R., "The Determination of Helicopter Longitudinal Stability Derivatives from Flight Test Data," WADC, Technical Report 55-438, U.S. Air Force, Wright Patterson Air Force Base, Ohio, March 1959.

<sup>32</sup>Marchand, M., and Koehler, R., "Determination of Aircraft Derivatives by Automatic Parameter Adjustment and Frequency Response Methods," AGARD, CP 172, Paper no. 17, Nov. 1974.

<sup>33</sup>Klein, V., "Maximum Likelihood Method for Estimating Airplane Stability and Control Parameters from Flight Data in the Frequency Domain," NASA Technical Paper 1637, May 1980.

<sup>34</sup>Marchand, M., and Fu, F. H., "Frequency-Domain Parameter Estimation of Aeronautical Systems Without and With Time Delay," *7<sup>th</sup> IFAC Symposium*, York, UK, July 1985.

<sup>35</sup>Kaletka, J., and Fu, K-H., "Frequency-Domain Identification of Unstable Systems Using X-31 Aircraft Flight Test Data," AIAA Paper 93-3635-CP, Aug. 1993.

<sup>36</sup>Fu, K-H., and Kaletka, J., "Frequency-Domain Identification of B0-105 Derivative Models with Rotor Degrees of Freedom," *Journal of the American Helicopter Society*, Vol. 38, No. 1, 1993, pp. 73-83.

<sup>37</sup>Kaletka, J., and Gimonet, B., "Identification of Extended Models from BO 105 Flight Test Data for Hover Flight Condition," *21<sup>st</sup> European Rotorcraft Forum*, Saint-Petersburg, Russia, Paper VII-7, Aug.-Sept. 1995.

<sup>38</sup>Black, C. G., Murray-Smith, D. J., and Padfield, G. D., "Experience with Frequency-Domain Methods in Helicopter System Identification," *12<sup>th</sup> European Rotorcraft Forum*, Paper 76, Sept. 1986.

<sup>39</sup>Houston, S. S., and Black, C. G., "On the Identifiability of Helicopter Models Incorporating Higher-Order Dynamics," *Journal of Guidance, Control, and Dynamics*, Vol. 14, No. 4, 1991, pp. 840-847.

<sup>40</sup>Houston, S. S., "Identification of a Autogyro Longitudinal Stability and Control Characteristics," *Journal of Guidance, Control, and Dynamics*, Vol. 21, No. 3, 1998, pp. 391-399.

<sup>41</sup>Morelli, E. A., "Low Order Equivalent System Identification for the Tu-144LL Supersonic Transport Aircraft," *Journal of Guidance, Control, and Dynamics*, Vol. 26, No. 2, 2003, pp. 354-362.

<sup>42</sup>Twisdale, T. R., and Ashurst, T. A., Jr., "System Identification from Tracking (SIFT), A New Technique for Handling-Qualities Test and Evaluation," AFFTC-TR-77-27, U.S. Air Force Flight Test Center, Nov. 1977.

## 502 AIRCRAFT AND ROTORCRAFT SYSTEM IDENTIFICATION

<sup>43</sup>Hoh, R. H., Myers, T. T., Ashkenas, I. L., Ringland, R. R., and Craig, S., "Development of Handling Quality Criteria for Aircraft with Independent Control of Six Degrees of Freedom," Air Force Wright Aero Lab., AFWAL-TR-81-3027, Wright Patterson Air Force Base, Ohio, April 1981.

<sup>44</sup>Jex, H. R., and Mitchell, D. G., "Stability and Control of the Gossamer Human-Powered Aircraft by Analysis and Flight Test," NASA CR 3627, Oct. 1982.

<sup>45</sup>Hogue, J. R., Jex, H. R., and Magdaleno, R. E., "Engineering Performance Tests of UH-1 and UH-60 Training Simulator Motion Bases and Visual Systems," Systems Technology, Inc., WP 1183-3, Hawthorne, California, Sept. 1982.

<sup>46</sup>Hall, I. A. M., "Frequency Response Method for Measuring Aircraft Dynamic Characteristics," British Aircraft Corp., Ae. 217, July 1964.

<sup>47</sup>Magdaleno, R. E., "The STI Frequency Domain Analysis Routine (FREDA)," Systems Technology, Inc., WP-407-2, June 1978.

<sup>48</sup>DiMarco, R. J., and Magdaleno, R. E., "User's Manual for Multi-Output Frequency Response Parameter Identification Program," Systems Technology, Inc., WP 0407-07, Hawthorne, California, Oct. 1987.

<sup>49</sup>Hodgkinson, J., LaManna, W. J., and Heyde, J. L., "Handling Qualities of Aircraft with Stability and Control Augmentation Systems—A Fundamental Approach," *Aeronautical Journal*, Vol. 80, No. 782, 1976, pp. 75-81.

<sup>50</sup>Bischoff, D. E., and Palmer, R. E., "Investigation of Low Order Lateral Directional Transfer Function Models for Augmented Aircraft," AIAA Guidance and Control Conference, Paper 82-1610, Aug. 1982, pp. 579-586.

<sup>51</sup>Mitchell, D. G., and Hoh, R. H., "Low-Order Approaches to High-Order Systems: Problems and Promises," *Journal of Guidance, Control, and Dynamics*, Vol. 5, No. 5, 1982, pp. 482-489.

<sup>52</sup>Hoh, R. H., Mitchell, D. G., Ashkenas, I. L., Klein, R. H., Heffley, R. K., and Hodgkinson, J., "Proposed MIL Standard and Handbook—Flying Qualities of Air Vehicles, Vol. II: Proposed MIL Handbook," AFWAL-TR-82-3081, U.S. Air Force Wright Aeronautical Lab, Wright-Patterson Air Force Base, Ohio, Nov. 1982.

<sup>53</sup>Tischler, M. B., Leung, J. G. M., and Dugan, D. C., "Frequency-Domain Identification of XV-15 Tilt-Rotor Aircraft Dynamics in Hovering Flight," AIAA 2<sup>nd</sup> Flight Testing Conference Paper 83-2695, Las Vegas, Nevada, Nov. 1983.

<sup>54</sup>Tischler, M. B., Fletcher, J. W., Diekmann, V. L., Williams, R. A., and Cason, R. W., "Demonstration of Frequency-Sweep Test Technique Using a Bell-214-ST Helicopter," NASA TM 89422, ARMY TM 87-A-1, April 1987.

<sup>55</sup>Graham, D., and McRuer, D. T., *Analysis of Nonlinear Control Systems*, Dover, New York, 1971.

<sup>56</sup>McRuer, D. T., Ashkenas, I. L., and Graham, D., *Aircraft Dynamics and Automatic Control*, Princeton Univ. Press, NJ, 1973.

<sup>57</sup>Raisinghani, S. C., and Goel, A. K., "Frequency-Domain Application of Gauss-Newton Method to Extract Aircraft Longitudinal Parameters," *Aeronautical Journal*, Vol. 90, No. 891, 1986, pp. 27-34.

## REFERENCES

## 503

<sup>58</sup>Lebacqz, J. V., and Govindaraj, K. S., "Implicit Model Following and Parameter Identification of Unstable Aircraft," *Journal of Guidance and Control*, Vol. 3, No. 2, 1980, pp. 119-123.

<sup>59</sup>Hodgkinson, J., *Aircraft Handling Qualities*, AIAA Educational Series, AIAA, Reston, VA, 1998.

<sup>60</sup>Dugan, D. C., "The XV-15 Tilt-Rotor Flight-Test Program," NASA TM 86846, Oct. 1985.

<sup>61</sup>Tischler, M. B., "Frequency-Response Identification of XV-15 Tilt-Rotor Aircraft Dynamics," NASA TM 89428, ARMY TM 87-A-2, Ph.D. Dissertation, Stanford Univ., CA, May 1987.

<sup>62</sup>Maisel, M. D. (coordinator), "NASA/Army XV-15 Tilt Rotor Research Aircraft Familiarization Document," NASA TM X-62407, 1975.

<sup>63</sup>Cauffman, M. G., and Tischler, M. B., *CIFER ver. 2.2—Comprehensive Identification from Frequency Responses*, Vol. 1—Class Notes, Army TR-94-A-017, NASA CP 3226; Vol. 2—User's Manual, Army TR-94-A-018, NASA CP 3226, Sept. 1994.

<sup>64</sup>Tischler, M. B., Colbourne, J. D., Morel, M. R., and Biezad, D. J., "A Multi-disciplinary Flight Control Development Environment and Its Application to a Helicopter," *IEEE Control Systems Magazine*, Vol. 19, No. 4, 1999, pp. 22-33.

<sup>65</sup>Rupnik, B., "CIFER®-MATLAB Interfaces: Development and Application," M. S. Thesis, Dept. of Aerospace Engineering, California Polytechnic State Univ., San Luis Obispo, CA, April 2005.

<sup>66</sup>Hamel, P. G., and Aiken, W., Jr. (eds.), *Methods for Aircraft State and Parameter Identification*, AGARD-CP-172, May 1975.

<sup>67</sup>Williams, J. N., Ham, J. A., and Tischler, M. B., "Flight Test Manual: Rotorcraft Frequency Domain Flight Testing," U.S. Army Aviation Technical Test Center, Airworthiness Qualification Test Directorate, AQTD Project No. 93-14, Edwards AFB, California, Sept. 1995.

<sup>68</sup>Chen, R. T. N., and Tischler, M. B., "The Role of Modeling and Flight Testing in Rotorcraft Parameter Identification," *Vertica*, Vol. 11, No. 4, 1987, pp. 619-647.

<sup>69</sup>Chen, R. T. N., "Input Design for Aircraft Parameter Identification: Using Time-Optimal Control Formulation," AGARD –CP-172, Paper 13, May 1975.

<sup>70</sup>Mehra, R. K., and Gupta, N. K., "Status of Input Design for Aircraft Parameter Identification," AGARD, CP-172, May 1975.

<sup>71</sup>Morelli, E. A., "Practical Input Optimization for Aircraft Parameter Estimation," NASA CR 191462, May 1993.

<sup>72</sup>Morelli, E. A., "Flight Test Validation of Optimal Input Design and Comparison to Conventional Inputs," AIAA Atmospheric Flight Mechanics Conference Paper 97-3711, Aug. 1997, pp. 573-583.

<sup>73</sup>Plaetschke, E., and Schulz, G., "Practical Input Signal Design," AGARD LS 104, Paper 3, 1979.

## 504 AIRCRAFT AND ROTORCRAFT SYSTEM IDENTIFICATION

<sup>74</sup>Kaletka, J., and von Gruenhagen, W., "Identification of Mathematical Derivative Models for the Design of a Model Following Control System," *American Helicopter Society Annual Forum*, May 1989.

<sup>75</sup>Jategaonkar, R. V., and Monnich, W., "Identification of Do-328 Aerodynamic Database for a Level D Flight Simulator," AIAA, Paper 97-3729-CP, AIAA Modeling and Simulation Technologies Conference Aug. 1997, pp. 248-258.

<sup>76</sup>Young, P., "An Assessment of Techniques for Frequency-Domain Identification of Helicopter Dynamics," Ph.D. Dissertation, Dept. of Electronics, Univ. of York, UK, June 1989.

<sup>77</sup>Young, P., and Patton, R. J., "Comparison of Test Signals for Aircraft Frequency Domain Identification," *Journal of Guidance, Control, and Dynamics*, Vol. 13, No. 3, 1990, pp. 430-438.

<sup>78</sup>Morelli, E. A., "Multiple Input Design for Real-Time Parameter Estimation in the Frequency Domain," *13th IFAC Conference on System Identification*, Aug. 2003.

<sup>79</sup>Franklin, G. F., and Powell, J. D., *Digital Control of Dynamic Systems*, Addison Wesley Longman, Reading, NA, 1981.

<sup>80</sup>Tischler, M. B., Williams, J. N., and Ham, J. A., "Comments on the New ADS-33 Process: Cautions for Implementation," *Journal of the American Helicopter Society*, Vol. 41, No. 3, 1996, pp. 194-195.

<sup>81</sup>McLean, D., *Automatic Flight Control Systems*, Prentice-Hall International, Hertfordshire, UK 1990.

<sup>82</sup>Weiss, S., Friemelt, H., Plaetschke, E., and Rohlf, D., "X-31A System Identification Using Single-Surface Excitation at High Angles of Attack, *Journal of Aircraft*, Vol. 33, No. 3, 1996, pp. 485-490.

<sup>83</sup>Hoh, R. H., Mitchell, D. G., Aponso, B. L., Key, D. L., and Blanken, C. L., "Proposed Specification for Handling Qualities of Military Rotorcraft: Vol. 1—Requirements," *U.S. Army Aviation Systems Command*, TR 87-A-4, St. Louis, MO 1988.

<sup>84</sup>Tischler, M. B., Fletcher, J. W., Morris, P. M., and Tucker, G. E., "Flying Quality Analysis and Flight Evaluation of a Highly Augmented Combat Rotorcraft," *Journal of Guidance, Control, and Dynamics*, Vol. 14, No. 5, 1991, pp. 954-964.

<sup>85</sup>Ballin, M. G., and Dalang-Secretan, M. A., "Validation of the Dynamic Response of a Blade-Element UH-60A Simulation Model in Hovering Flight," *Journal of the American Helicopter Society*, Vol. 36, No. 4, 1991, pp. 77-88.

<sup>86</sup>Tischler, M. B., Driscoll, J. T., Cauffman, M. G., and Freedman, C. J., "Study of Bearingless Main Rotor Dynamics from Frequency-Response Wind Tunnel Test Data," *American Helicopter Society, Aeromechanics Specialists Conference on Aerodynamics, Acoustics and Dynamics*, San Francisco, CA Jan 1994, pp. 6.3-1-6.3-25.

<sup>87</sup>Acree, C. W., Jr., and Tischler, M. B., "Determining XV-15 Aeroelastic Modes from Flight Data with Frequency-Domain Methods," NASA TP 3330, USAATCOM TR-93-A-004, May 1993.

## REFERENCES

## 505

<sup>88</sup>Caldwell, B. D., "The FCS-Structural Coupling Problem and Its Solution," AGARD-CP-560, Paper 16, Jan. 1995.

<sup>89</sup>Caldwell, B., and Felton, R., "Validation of FCS Structural Coupling Stability Characteristics Through In-flight Excitation," AGARD Research and Technology Organization, NATO RTO-MP-11, Paper 9, March 1999.

<sup>90</sup>Kothmann, B. D., and Armburst, J., "RAH-66 Comanche Core AFCS Control Law Development: DEMVAL to EMD," *American Helicopter Society Annual Forum*, June 2002.

<sup>91</sup>Brenner, M. J., Lind, R. C., and Voracek, D. F., "Overview of Recent Flight Flutter Testing Research at NASA Dryden," NASA TM 4792, April 1997.

<sup>92</sup>Tischler, M. B., "Identification of Bearingless Main Rotor Dynamic Characteristics from Frequency-Response Wind-Tunnel Test Data," *Journal of the American Helicopter Society*, Vol. 44, No. 1, 1999, pp. 63-76.

<sup>93</sup>Lisoski, D., and Tischler, M. B., "Solar Powered Stratospheric Research Aircraft Flight Test and System Identification," NATO RTO-MP-11, Paper no. 27, March 1999.

<sup>94</sup>Keller, J. F., Hart, D. C., Shubert, M. W., and Feingold, A., "Handling Qualities Specification Development for Cargo Helicopters," *American Helicopter Society Annual Forum*, May 1995.

<sup>95</sup>Gerlach, O. H., "Determination of Performance and Stability Parameters from Non-Steady-Flight Test Maneuvers," Society of Automotive Engineers, Paper 700236, New York, March 1970.

<sup>96</sup>Wingrove, R. C., "Applications of a Technique for Estimating Aircraft States from Recorded Flight Test Data," AIAA, Paper 72-965, Sept. 1972.

<sup>97</sup>Klein, V., and Schiess, J. R., "Compatibility Check of Measured Aircraft Responses Using Kinematic Equations and Extended Kalman Filter," NASA TN D-8514, Aug. 1977.

<sup>98</sup>Breeman, J. H., and Simons, J. L., "Evaluation of a Method to Extract Performance Data from Dynamic Maneuvers for a Jet Transport Aircraft," International Council of the Aeronautical Sciences, Jan. 1978.

<sup>99</sup>Bach, R. E., Jr., "State Estimation Applications in Aircraft Flight-Data Analysis: A User's Manual for SMACK," NASA RP 1252, March 1991.

<sup>100</sup>Fletcher, J. W., "Obtaining Consistent Model of Helicopter Flight-Data Measurement Errors Using Kinematic-Compatibility and State-Reconstruction Methods," *American Helicopter Society Annual Forum*, May 1990.

<sup>101</sup>Friehmelt, H., "Quality Effects on Parameter Identification — An X31A Study Case," *Atmospheric Flight Mechanics Conference*, AIAA, Reston, VA, 1997, pp. 784-790.

<sup>102</sup>Kayton, M., and Fried, W. R., *Avionics Navigation Systems*, Wiley, New York, 1997, pp. 317-324.

<sup>103</sup>Fletcher, J. W., and Tischler, M. B., "Improving Helicopter Flight Mechanics Models with Laser Measurements of Flapping," *American Helicopter Society Annual Forum*, April-May 1997.

## 506 AIRCRAFT AND ROTORCRAFT SYSTEM IDENTIFICATION

<sup>104</sup>Franklin, G. F., Powell, J. D., and Emami-Naeini, A., *Feedback Control of Dynamic Systems*, 3rd ed., Addison Wesley Longman, Reading, NA, 1994.

<sup>105</sup>Ramirez, R. W., *The FFT: Fundamentals and Concepts*, Prentice-Hall, Upper Saddle River, NJ, 1985.

<sup>106</sup>Bendat, J. S., and Piersol, A. G., *Random Data: Analysis and Measurement Procedures*, 2nd ed., Wiley, New York, 1986.

<sup>107</sup>Bendat, J. S., and Piersol, A. G., *Engineering Applications of Correlation and Spectral Analysis*, 2nd ed., Wiley, New York, 1993.

<sup>108</sup>Otnes, R. K., and Enochson, L., *Basic Techniques, Applied Time Series Analysis*, Vol. 1, Wiley, New York, 1978.

<sup>109</sup>Nuttall, A. H., "Spectral Estimation by Means of Overlapped Fast Fourier Transform Processing of Window Data," Naval Underwater Systems Center, NUSC Rep. 4169, Newport, Rhode Island, Oct. 1971.

<sup>110</sup>Nuttall, A. H., "Estimation of Cross-Spectra via Overlapped Fast Fourier Transform Processing," Naval Underwater System Center, AD-A013 026, New London, Connecticut, July 1975.

<sup>111</sup>Carter, C., Knapp, C. H., and Nuttall, A. H., "Estimation of the Magnitude-Squared Coherence Function via Overlapped Fast Fourier Transform Processing," *IEEE Transaction on Audio and Electroacoustics*, Vol. 21, No. 4, 1973, pp. 337-344.

<sup>112</sup>Rabiner, L. R., and Gold, B., *Theory and Application of Digital Signal Processing*, Prentice-Hall, Upper Saddle River, NJ, 1975.

<sup>113</sup>Biernson, G., *Feedback System Design, Principles of Feedback Control*, Vol. 1, Wiley, New York, 1988.

<sup>114</sup>Rabiner, L. R., Schafer, R., and Rader, C. M., "The Chirp Z-Transform Algorithm," *IEEE Transactions on Audio and Electroacoustics*, Vol AU-17., pp. 86-92, June 1969.

<sup>115</sup>Sahai, R., Cicolani, L. S., Tischler, M. B., Blanken, C. L., Sullivan, C. C., Wei, M. Y., Ng, Y-S., and Pierce, L. E., "Flight-Time Identification of Helicopter-Slung Load Frequency Response Characteristics Using CIFER®," *AIAA Paper*, Aug. 1999.

<sup>116</sup>Fabunmi, J. A., "Developments in Helicopter Ground Vibration Testing," *Journal of the American Helicopter Society*, Vol. 31, No. 3, 1986, pp. 54-59.

<sup>117</sup>Rocklin, G. T., Crowley, J., and Vold, H., "A Comparison of  $H_1$ ,  $H_2$ , and  $H_v$  Frequency Response Functions," *Proceedings of the Third International Modal Analysis Conference*, Vol. 1, 1985, Orlando, Florida, pp. 272-278.

<sup>118</sup>McRuer, D. T., and Krendel E. S., "Mathematical Models of Human Pilot Behavior," AGARDograph No. 188, Nov. 1974.

<sup>119</sup>Anderson, F., and Klyde, D. H., "A Limited Evaluation of the Pilot Cutoff Frequency Parameter," Systems Technology, Inc., Working Paper 1310-13, Hawthorne, California, Sept. 1997.

## REFERENCES

## 507

<sup>120</sup>Atencio, A., Jr., "Fidelity Assessment of a UH-60A Simulation on the NASA Ames Vertical Motion Simulator," NASA TM 104016, USAATCOM TR 93-A-005, Sept. 1993.

<sup>121</sup>Blanken, C. L., and Pausder, H. J., "Investigation of the Effects of Bandwidth and Time Delay on Helicopter Roll-Axis Handling Qualities," *Journal of the American Helicopter Society*, Vol. 39, No. 3, 1994, pp. 24-33.

<sup>122</sup>Lusardi, J., Blanken, C., and Tischler, M. B., "Piloted Evaluation of a UH-60 Mixer Equivalent Turbulence Simulation Model," *American Helicopter Society Annual Forum*, May 2003.

<sup>123</sup>Ham, J. A., Gardner, C. K., and Tischler, M. B., "Flight Testing and Frequency Domain Analysis for Rotorcraft Handling Qualities Characteristic," *Journal of the American Helicopter Society*, Vol. 40, No. 2, 1995, pp. 28-38.

<sup>124</sup>Capone, P., "Linearization of Aircraft Models: A Flight Control System and Flying Qualities Perspective," NATO RTO Symposium on Challenges in Dynamics, System Identification, Control and Handling Qualities for Land, Air, Sea and Space Vehicles, Berlin, Germany, May 2002.

<sup>125</sup>Tischler, M. B., "Digital Control of Highly Augmented Combat Rotorcraft," NASA TM 88346, ARMY TR 87-A-5, May 1987.

<sup>126</sup>Kim, F. D., Celi, R. C., and Tischler, M. B., "Higher-Order State-Space Simulation Models of Helicopter Flight Mechanics," *Journal of the American Helicopter Society*, Vol. 38, No. 4, 1993, pp. 16-27.

<sup>127</sup>Smith, R. E., Hodgkinson, J., and Snyder, R. C., "Equivalent System Verification and Evaluation of Augmentation Effects on Fighter Approach and Landing Flying Qualities," U. S. Air Force Wright Aeronautical Lab., AFWAL-TR-81-3116, Vol. 2, Wright-Patterson Air Force Base, Ohio, 1981.

<sup>128</sup>Tischler, M. B., "System Identification Methods for Aircraft Flight Control Development and Validation," NASA TM 110369, Army TR-95-A-007, Oct. 1995.

<sup>129</sup>Buchholz, J. J., Bauschat, J. M., Hahn, K. U., and Pausder, H. J., "ATTAS & ATTHeS In-Flight Simulators: Recent Application Experiences and Future Programs," AGARD CP577, Paper no. 31, April 1996.

<sup>130</sup>Churchill, G. B., and Dugan, D. C., "Simulation of the XV-15 Tilt Rotor Research Aircraft," NASA TM-84222, March 1982.

<sup>131</sup>Cicolani, L. S., McCoy, A. H., Sahai, R., Tyson, P. H., Tischler, M. B., Rosen, A., and Tucker, G. E., "Flight Test Identification and Simulation of a UH-60A Helicopter and Slung Load," *Journal of the American Helicopter Society*, Vol. 46, No. 2, April 2001, pp. 140-160.

<sup>132</sup>Strope, K., Borden, C., and Harding, J., "Verification and Validation of a UH-60 FLIGHTLAB® Model in Support of the UH-60M Limited User Test," *American Helicopter Society Annual Forum*, June 2004.

<sup>133</sup>„Military Specification, Flight Control Systems-General Specification for Design, Installation, and Test of Piloted Aircraft," USAF MIL-F-9490D, U.S. Air Force, June 1975.

## 508 AIRCRAFT AND ROTORCRAFT SYSTEM IDENTIFICATION

<sup>134</sup>Dryfoos, J. B., Kothmann, B. D., and Mayo, J., "An Approach to Reducing Rotor-Body Coupled Roll Oscillations on the RAH-66 Comanche Using Modified Roll Rate Feedback," *American Helicopter Society Annual Forum*, May 1999.

<sup>135</sup>McCoy, A. H., "Flight Testing and Real-Time System Identification Analysis of a UH-60A Black Hawk Helicopter with an Instrumented External Sling Load," M.S. Thesis, Naval Post Graduate School, Dept. of Aeronautical Engineering, Monterey, CA, Dec. 1997.

<sup>136</sup>Clarke, R., Burken, J. J., Bosworth, J. T., and Bauer, J. E., "X-29 Flight Control System: Lessons Learned," *Advances in Aircraft Flight Control*, edited by M. B. Tischler, Taylor and Francis, Washington, DC, 1996, pp 345–368.

<sup>137</sup>Spaulding, C. M., Mansur, M. H., Tischler, M. B., Franklin, J. A., and Hess, R. A., "Nonlinear Inversion Control for a Ducted Fan UAV," *AIAA Atmospheric Flight Mechanics Conference* Paper no. 2005-6231, Aug. 2005.

<sup>138</sup>Wingrove, R. C., and Edwards, F. G., "A Technique for Identifying Pilot Describing Functions from Routine Flight-Test Records," NASA TN D-5127, May 1969.

<sup>139</sup>Tischler, M. B., and Tomashofski, C., "Flight Test Identification of SH-2G Flapped-Rotor Helicopter Flight Mechanics Models," *Journal of the American Helicopter Society*, Vol. 47 No. 1, 2002, pp. 18–32.

<sup>140</sup>Clarke, R., Allen, M. J., Dibley, R. P., Gera, J., and Hodgkinson, J., "Flight Test of the F/A-18 Active Aeroelastic Wing Airplane," *AIAA Atmospheric Flight Mechanics Conference* AIAA Paper 2005-6316, Aug. 2005.

<sup>141</sup>Strang, G., *Linear Algebra and its Applications*, Academic Press, New York, 1980.

<sup>142</sup>Gill, P. E., Murray, W., and Pitfield, R. A., "The Implementation of Two Revised Quasi-Newton Algorithms for Unconstrained Optimization," National Physical Lab., Div. of Numerical Analysis and Computing, NPL-NAC-11, Middlesex, UK, Aug. 1972.

<sup>143</sup>Bischoff, D. E., "The Definition of Short-Period Flying Qualities Characteristics via Equivalent Systems," *Journal of Aircraft*, Vol. 20, No. 6, 1983, pp. 494–499.

<sup>144</sup>Field, E. J., Rossitto, K. F., and Hodgkinson, J., "Flying Qualities Applications of Frequency Responses Identified from Flight Data," *Journal of Aircraft*, Vol. 41, No. 4, 2004, pp. 711–720.

<sup>145</sup>Kailath, T., *Linear Systems*, Prentice-Hall, Upper Saddle River, NJ, 1980.

<sup>146</sup>Blakelock, J. H., *Automatic Control of Aircraft and Missiles*, 2nd ed., Wiley, New York, 1991.

<sup>147</sup>Hodgkinson, J., and Buckley, J., "NAVFIT User's Guide," McDonnell Aircraft Co., St Louis, MO, Oct. 1978.

<sup>148</sup>Himmelblau, D. M., *Applied Nonlinear Programming*, McGraw-Hill, New York, 1972.

## REFERENCES

## 509

<sup>149</sup>Tilly, D. M., "Three Algorithms for Parametric Frequency Domain System Identification," Lawrence Livermore National Lab., Rep. UCID-20255, Livermore, California, Nov. 1984.

<sup>150</sup>Franklin, J. A., *Dynamics, Control, and Flying Qualities of V/STOL Aircraft*, AIAA Education Series, AIAA, Reston, VA, 2002.

<sup>151</sup>Glusman, S. I., Dabundo, C., and Landis, K. H., "Evaluation of ADOCS Demonstrator Handling Qualities," *American Helicopter Society Annual Forum*, Washington, DC, 1987, pp. 705–716.

<sup>152</sup>Landis, K. H., Davis, J. M., Dabundo, C., and Keller, J. F., "Advanced Flight Control Research and Development at Boeing Helicopters," *Advances in Aircraft Flight Control*, Taylor and Francis, London, 1996, pp. 103–142.

<sup>153</sup>Fletcher, J. W., "Identification of UH-60 Stability Derivative Models in Hover from Flight Test Data," *Journal of the American Helicopter Society*, Vol. 40, No. 1, 1995, pp. 32–46.

<sup>154</sup>Hoh, R. H., and Ashkenas, I. L., "Development of VTOL Flying Qualities Criteria for Low Speed and Hover," Systems Technology, Inc., TR-1116-1, Hawthorne, CA, Dec. 1979.

<sup>155</sup>Smith, R. E., and Sarrafan, S. K., "Effect of Time Delay on Flying Qualities: An Update," *Journal of Guidance, Control, and Dynamics*, Vol. 9, No. 5, 1986, pp. 578–584.

<sup>156</sup>Givan, M. E., LaManna, W. J., and Hodgkinson, J., "LONFIT User's Guide," McDonnell Aircraft, St. Louis, MO, 1978.

<sup>157</sup>Hodgkinson, J., "A History of Low Order Equivalent Systems for Aircraft Handling Qualities Analysis and Design," *AIAA Atmospheric Flight Mechanics Conference*, Paper 2003-5466, Aug. 2003.

<sup>158</sup>Field, E. J., van Paassen, M. M., Stroosma, O., and Salchak, P. W., "Validation of Simulation Models for Piloted Handling Qualities Evaluations," *AIAA Modelling and Simulation Technologies Conference Paper* 2004-5268, Aug. 2004.

<sup>159</sup>Chen, C. T., *Linear System Theory and Design*, CBS College Publishing, New York, 1984.

<sup>160</sup>Houston, S. S., "Identification of a Coupled Body/Coning/Inflow Model of the Puma Vertical Response in the Hover," *Vertica*, Vol. 13, No. 3, 1989, pp. 229–250.

<sup>161</sup>Curtiss, H. C., Jr., "Stability and Control Modeling," *Vertica*, Vol. 12, No. 4, 1988, pp. 381–394.

<sup>162</sup>Johnson, W., *Helicopter Theory*, Princeton Univ. Press, NJ, 1980.

<sup>163</sup>Prouty, R. W., *Helicopter Performance Stability and Control*, Krieger, Malabar, FL, 1995.

<sup>164</sup>Landis, K. H., and Glusman, S. I., "Development of ADOCS Controller and Control Laws: Vol. 1—Executive Summary; Vol. 2—Literature Review and Preliminary Analysis; Vol. 3—Simulation Results and Recommendations," NASA CR-177339, March 1985.

## 510 AIRCRAFT AND ROTORCRAFT SYSTEM IDENTIFICATION

<sup>165</sup>Heffley, R. K., and Jewell, W. F., "Aircraft Handling Qualities Data," NASA-CR-2144, Dec. 1972.

<sup>166</sup>Mettler, B., Tischler, M. B., and Kanade, T., "System Identification of Small-Sized Unmanned Helicopter Dynamics," *American Helicopter Society Annual Forum*, May 1999.

<sup>167</sup>Mettler, B., *Identification Modeling and Characteristics of Miniature Rotorcraft*, Kluwer Academic, Norwell, MA, 2002.

<sup>168</sup>Warmbrodt, W., and Peterson, R. L., "Hover Test of a Full-Scale Hingeless Rotor," NASA TM-85990, Aug. 1984.

<sup>169</sup>Sahasrabudhe, V., and Gold, P. J., "Reduced Rotor Body Coupling Using Active Control," *American Helicopter Society Annual Forum*, June 2004.

<sup>170</sup>Iliif, K. W., "Aircraft Identification Experience," AGARD LS 104, Paper 6, Nov. 1979.

<sup>171</sup>Tischler, M. B., "Advancements in Frequency-Domain Methods for Rotorcraft System Identification," *Vertica*, Vol. 13, No. 3, 1989, pp. 327-343.

<sup>172</sup>Maine, R. E., and Iliif, K. W., "Theory and Practice of Estimating the Accuracy of Dynamic Flight-Determined Coefficients," NASA RP 1077, 1981.

<sup>173</sup>Colbourne, J. D., Cicolani, L., Frost, C. R., Tischler, M. B., Tomashofski, C., and LaMontagne, T., "System Identification and Control System Design for the BURRO Autonomous UAV," *American Helicopter Society Annual Forum*, May 2000.

<sup>174</sup>Whalley, M., Takahashi, M., Schulein, G., Freed, M., Christian, D., Patterson-Hine, A., and Harris, R. "The Army/NASA Autonomous Rotorcraft Project," *American Helicopter Society Annual Forum*, May 2003.

<sup>175</sup>Lewis, W., and Catterall, R. C., "Determination of Navion Stability and Control Derivatives Using Frequency-Domain Techniques," AIAA Modeling and Simulation Technologies Conference, Paper 99-4036, Aug. 1999.

<sup>176</sup>Kaletka, J., and Langer, J. J., "Correlation Aspects of Analytical, Wind Tunnel and Flight Test Results for a Hingeless Rotor Helicopter," AGARD-CP-339, Feb 1983, pp. 16-1-16-16.

<sup>177</sup>Burrows, R. R., and McDaniel, G. A., "A Method of Trajectory Analysis with Multi-Mission Capability and Guidance Application," AIAA Guidance, Control and Flight Dynamics Conference, Paper 68-844, Aug. 1968.

<sup>178</sup>Tischler, M. B., Ringland, R. F., Jex, H. R., Emmen, R. D., and Ashkenas, I. L., "Flight Dynamics Analysis and Simulation of Heavy Lift Airships: Vol. II—Technical Manual," NASA CR 166471, Dec. 1982.

<sup>179</sup>Morelli, E. A., and Klein, V., "Accuracy of Aerodynamic Model Parameters Estimated from Flight Test Data," *Journal of Guidance, Control, and Dynamics*, Vol. 20, No. 1, 1997, pp. 74-80.

<sup>180</sup>Milne, G. W., "Identification of a Dynamics Model of a Helicopter from Flight Tests," Ph.D. Dissertation, Stanford Univ., Dept. of Aeronautics and Astronautics CA, Dec. 1986.

## REFERENCES

## 511

<sup>181</sup>Brogan, W. L., *Modern Control Theory*, 2nd ed., Prentice-Hall, Upper Saddle River, NJ, 1985, pp. 324–327.

<sup>182</sup>Schroeder, J. A., Tischler, M. B., Watson, D. C., and Eshow, M. E., “Identification and Simulation Evaluation of a Combat Helicopter in Hover,” *Journal of Guidance, Control, and Dynamics*, Vol. 18, No. 1, 1995, pp. 31–38.

<sup>183</sup>Foster, J. D., Moralez, E., III, Franklin, J. A., and Schroeder, J. A., *Integrated Control and Display Research for Transition and Vertical Flight on the NASA V/STOL Research Aircraft (VSRA)*, NASA TM-100029, Oct. 1987.

<sup>184</sup>Bryson, A. E., *Control of Spacecraft and Aircraft*, Princeton Univ. Press, NJ, 1994, pp. 132–133.

<sup>185</sup>Jategaonkar, R., Fischenberg, D., and von Gruenhagen, W., “Aerodynamic Modeling and System Identification from Flight Data—Recent Applications at DLR,” *Journal of Aircraft*, Vol. 41, No. 4, 2004, pp. 681–691.

<sup>186</sup>“Special Section: Flight Vehicle System Identification—Part 1,” *Journal of Aircraft*, Vol. 41, No. 4, 2004, pp. 681–752.

<sup>187</sup>“Special Section: Flight Vehicle System Identification—Part 2,” *Journal of Aircraft*, Vol. 42, No. 1, 2005, pp. 1–288.

<sup>188</sup>Arnold, U. T. P., Keller, J. D., Curtiss, H. C., Jr., and Reichert, G., “The Effect of Inflow Models on the Predicted Response of Helicopters,” *Journal of the American Helicopter Society*, Vol. 43, No. 1, 1998, pp. 25–36.

<sup>189</sup>Schulein, G. J., Tischler, M. B., Mansur, M. H., and Rosen, A., “Validation of Cross-Coupling Modeling Improvements for UH-60 Flight Mechanics Simulations,” *Journal of the American Helicopter Society*, Vol. 47, No. 3, 2002, pp. 209–213.

<sup>190</sup>Heffley, R. K., Jewell, W. F., Lehman, J. M., and Van Winkle, R. A., “A Compilation and Analysis of Helicopter Handling Qualities Data,” NASA CR 3144, Aug. 1979.

<sup>191</sup>Hui, K., “Advanced Modeling of the Engine Torque Characteristics of a Bell 412HP Helicopter,” AIAA Atmospheric Flight Mechanics Conference, Paper no. AIAA 1999-4110, Aug. 1999.

<sup>192</sup>Harendra, P. B., Joglekar, M. J., Gaffey, T. M., and Marr, R. L., “A Mathematical Model for Real-Time Flight Simulation of the Bell Model 301 Tilt Rotor Research Aircraft,” NASA CR-114614, April 1982.

<sup>193</sup>Churchill, G. B., and Gerdes, R. M., “Advanced AFCS Development on the XV-15 Tilt Rotor Research Aircraft,” *American Helicopter Society Annual Forum*, May 1984.

<sup>194</sup>Engelland, S. A., Franklin, J. A., and McNeill, W. E., “Simulation Model of a Mixed-Flow Remote-Lift STOVL Aircraft,” NASA TM-102262, Feb 1990.

<sup>195</sup>Lucas, J., Martin, B., Dynetics, Ericsson, L., Catterall, C., Cole, M., “Combining Static Analyses and Frequency Domain System Identification to Enhance the Accuracy of a Fixed-Wing UAV Simulation,” AIAA Aerospace Sciences Meeting, AIAA 2006-640, Jan. 2006.

<sup>196</sup>Chen, R. T. N., and Hindson, W. S., “Influence of Dynamic Inflow on the Helicopter Vertical Response,” NASA TM 88327, June 1986.

## 512 AIRCRAFT AND ROTORCRAFT SYSTEM IDENTIFICATION

<sup>197</sup>Harding, J. W., and Moody, S., "Identification of AH-64D Dynamics to Support Flight Control System Evaluations," *American Helicopter Society Annual Forum*, June 2005.

<sup>198</sup>Cooke, A. K., and Fitzpatrick, E. W. H., *Helicopter Test and Evaluation*, AIAA Educational Series, AIAA, Reston, VA, 2002, pp.185–194.

<sup>199</sup>Curtiss, H. C., Jr., "Dynamic Stability of V/STOL Aircraft at Low Speeds," *Journal of Aircraft*, Vol. 7, No. 1, 1970, pp. 72–78.

<sup>200</sup>Padfield, G. D., *Helicopter Flight Dynamics: The Theory and Application of Flying Qualities and Simulation Modeling*, AIAA, Reston, VA, 1996, p. 137.

<sup>201</sup>Aiken, E. W., "A Mathematical Representation of an Advanced Helicopter for Piloted Simulator Investigations of Control-System and Display Variations," NASA TM 81203, AVRADCOM TM 80-A-2, July 1980.

<sup>202</sup>Tischler, M. B., "Aerodynamic Model for Piloted V/STOL Simulation," Systems Technology, Inc., WP 1171-2, Hawthorne, California, May 1982.

<sup>203</sup>Hui, K., and Srinivasan, R., "Inclusion of High-Order Rotor Dynamics to Improve the Dynamic Model of a Single Rotor Helicopter in Hover," NATO RTO-MP-11, March 1999.

<sup>204</sup>Harding, J. W., "Frequency-Domain Identification of Coupled Rotor/Body Models of an Advanced Attack Helicopter," *American Helicopter Society Annual Forum*, Washington, DC, 1992, pp. 751–779.

<sup>205</sup>Mettler, B., Tischler, M. B., and Kanade, T., "System Identification Modeling of a Small-Scale Unmanned Rotorcraft for Flight Control Design," *Journal of the American Helicopter Society*, Vol. 47, No. 1, 2002, pp. 50–63.

<sup>206</sup>Cheng, R. P., Tischler, M. B., and Schulein, G. J., "RMAX State-Space Helicopter Model Identification for Hover and Forward Flight," *Journal of the American Helicopter Society* April, Vol 51, No. 2, pp. 202–210.

<sup>207</sup>Chen, R. T., "A Simplified Rotor System Mathematical Model for Piloted Simulation," NASA TM 78575, May 1979.

<sup>208</sup>Chen, R. T., "Effects of Primary Rotor Parameters on Flapping Dynamics," NASA TP 1431, 1980.

<sup>209</sup>Newman, S., *The Foundations of Helicopter Flight*, Halsted Press 1994.

<sup>210</sup>Fletcher, J. W., "A Model Structure for Identification of Linear Models of the UH-60 in Hover and Forward Flight," NASA TM-110362, Aug. 1995.

<sup>211</sup>Paulk, C. H., Astill, D. L., and Donley, S. T., "Simulation and Evaluation of the SH-2F Helicopter in a Shipboard Environment Using the Interchangeable Cab System," NASA TM 84387, Aug. 1983.

<sup>212</sup>Ringland, R. F., and Clement, W. F., "Systems Definition Phase NAVTO LAND Rotary Wing Program, SH-2F Control Laws Development, Volume I, Analytical Development," Systems Technology, Inc., TR-1177-1-I, Hawthorne, CA, April 1982.

<sup>213</sup>Curtiss, H. C., Jr., Putman, W. F., and Lebacqz, J. V., "An Experimental Investigation of the Longitudinal Dynamics Stability Characteristics of a Four-Propeller Tilt-Wing VTOL Model," Princeton Univ., Rep. 774, NJ, Feb. 1968.

## REFERENCES

## 513

<sup>214</sup>Curtiss, H. C., Jr., and Gao, Z., "Modeling the Effects of Blade Torsional Flexibility in Helicopter Stability and Control," *Journal of the American Helicopter Society*, Vol. 30, No. 1, 1985, pp. 35-42.

<sup>215</sup>Houston, S. S., and Tarttelin, P. C., "Theoretical and Experimental Correlation of Helicopter Aeromechanics in Hover," *American Helicopter Society Annual Forum*, May 1989, pp 617-639.

This page intentionally left blank

# Index

*Page numbers for definitions are in boldface.*

- accelerometer measurements, 369
- accuracy analysis
  - DERIVID, 347
  - state-space models, 330–340
  - validation, 334–335
- actuators, 315
- aerodynamic angle measurements, 368
- aeroelastic models, 310–312
- aircraft dynamics, fixed wing, *see* decoupled lateral directional; decoupled longitudinal
- aircraft dynamics, rotary wing, *see* hybrid fully coupled; quasi-steady; quasi-steady longitudinal; quasi-steady lateral directional
- automated sweeps, *see* frequency sweeps, automated
- autospectrum, input and output, **153**
  - see also* conditioned: autospectrum
- bare-airframe identification, 226
  - bias error, 211–215, 221, 226
  - closed-loop testing, 35, 61, 95, 97, 209
  - no noise, 216–219
  - open-loop, 65, 95–97
  - with noise, 220–222
- see also* XV-15 identification in hover; closed-loop flight testing
- bias error
  - bare-airframe identification, 211–215, 221, 226
  - bias, 15, 25, 32
  - normalized bias error, **172, 213**
    - parametric identification, 223–224
    - parametric identification, 223–224
    - signal-to-noise ratio, 213–215
    - spectral function identification, 154
    - window size, 173, 260
- bias vector, 32, 436–439
- binning, 157
- Bode plot, 3
  - interpretation, 149–152
- body-axis coordinate systems, 363
- broken-loop response, 197, 256–257
- canonical models
  - observable canonical structure, 344
- pendulum, 348–350
- regressive lead-lag dynamics, 453
- structural response identification, 353–357
- structure, **343**–345
  - XV-15 in hover, 350–353
- case studies, *see* pendulum; XV-15
  - identification in cruise; XV-15
  - identification in hover
- chirp z-transform (CZT), **27**, 157–158
- CIFER
  - applications, 51
  - database, 69
  - dataflow, 71–72
  - description, 16–17
  - interface to other tools, 79–81
  - naming convention, 77
  - programs, 69–73
  - utilities, 73–75, 78–79
- see also* COMPOSITE; DERIVID; FRESPID; MISOSA; NAVFIT; VERIFY
- CIFER, using
  - menu, 73
  - navigation, 74
  - user interface, 70–71, 73–78
- closed-loop flight testing, 9, 60
  - bare-airframe identification, 95–97, 209
  - XV-15 in hover, 60–61
- coherence function, 30, **165**–167
  - cutoff parameter, **328**
  - guidelines, 373
  - threshold, **373**
- collective rotation, 457
- COMPOSITE, 263
  - FRESPID and MISOSA, workflow in SISO and MIMO analyses, 266–268
  - composite frequency-response estimate, 260, **262**
- composite spectral estimates, 262
- composite windowing, 27
  - closed-loop SISO identification of XV-15 in hover, 268–271
- COMPOSITE, 263
  - MIMO identification of Bo-105 helicopter, 271–272
  - pendulum, 263–266
  - structural system identification, 273–274
- concatenated record length, 171

conditioned  
  autospectrum, 237  
  cross spectrum, 237  
  frequency response, 237  
  spectral quantities, 237–239

CONDUIT, 196, 298

confidence ellipsoid  
  used in structure determination, 339  
  vector, 338

coning (rotor), 452, 460–461  
  angle, 454, 461  
  dynamics, 461  
  flap response, 455  
  flapping mode, 455  
  rate, 461

consistency, *see* data consistency

constrained parameters, 370

control correlation, high, 248

control derivatives, 11, 32, 42, 324, 361  
  nonlinear simulation, 403

control input correlation, 231

control rigging calibration, 141

control system design, 452  
  rotorcraft, models for, 307–310

control system model, validation, 196–200

control system, MIMO, broken-loop  
  response, 256–257

coordinate systems  
  body-axis, 363  
  stability-axis, 363

correlated inputs, 232

correlation coefficient, 337

cost function  
  average, for state-space models, 327  
  composite, 262  
  guidelines for state-space models, 329, 339  
  matrix form for state-space model, 332

rms fit error, 437  
  state-space models, 327–329

structure determination, 339  
  transfer-function models, 280

coupled dynamics  
  coning-inflow, 453  
  fuselage/regressive-flap, 453  
  fuselage/rotor, 452  
  inflow/coning/heave, 460–461  
  rotor/fuselage/engine, 490–491

coupling  
  dynamic, 85  
  one-way, 294, 303  
  rotor-body, 299

Cramér–Rao bounds, 42, 331  
  correlation, 335  
  estimated, 333  
  guideline, 334  
  insensitivity, 335  
  interpretation, 335–338  
  structure determination, 339

validation, 334–335

Cramér–Rao inequality, 331

cross spectrum, 153

cross talk, 248

cross-control coherence, 234

cross-over frequency, 182

cutoff frequency, 182–183

data collection, 89

data conditioning  
  verification, 440

data consistency, 25, 119  
  angular, 130–133  
  control rigging calibration, 141  
  faulty data, 139  
  simple methods, 129–141  
  translational, 135–139

database  
  CIFER, 69  
  database #1 (XV-15 in hover), 58, 62  
  database #2 (XV-15 in cruise), 58, 65–67  
  frequency response, 371–377

dataflow, CIFER, 71–72

decade span, 373

decoupled lateral directional model, 6

decoupled longitudinal model, 6

DERIVID, 347–348  
  accuracy analysis, 347  
  model structure reduction, 347

describing functions, 18, 27, 149, 152, 164

deterministic errors (systematic), 25, 119  
  frequency domain, 154  
  time domain, 121

digitized measurements, 133

Dirichlet condition, 148

discrete Fourier transform (DFT), 152, 157

doublets, 2, 16, 88

dynamic coupling, 85, 230

dynamic inflow, 415, 452

dynamic inflow/coning, 460–461

dynamics, *see* models

eigenvalues, 349, 386–391

eigenvectors, 386–391

engine  
  dynamics, 415, 462–463  
  Padé filter representation, 462  
  torque, 452  
    response, 453

equation-error method, 30

equations of motion, 16, 345  
  coordinate systems, 363  
  differential equations, 323  
  Euler angles, 365  
  force equations, 363–364  
  matrix form, 32, 324  
  moment equations, 364–365  
  physical model structure, 362–365

state and control matrices, 367  
state and control variables, 366  
state-space form, 366, 371  
error model, 130  
error parameters, 123  
errors  
deterministic (systematic), 25, 119  
measurement, 119  
nondeterministic (random), 26, 119  
Euler angles  
measurements, 367  
relationships, 365  
excitation, *see* input signals for identification

fast Fourier transform (FFT), 157–158  
filter cut-off frequency, 89  
filters, 89  
Kalman, 124  
fixed parameters, 279, 346, 370

Hessian matrix, **331**, 336  
approximation, 332  
correlation coefficient, 337  
hinge offset, 451, 455, 461  
hybrid fully coupled model, 7  
hybrid model identification, S-92  
helicopter, 490–491  
hybrid model identification, SH-2G  
helicopter, 464–483  
compared to simulation, 475–476  
cruise, 479  
flight testing, 465–466  
hover, 466–483  
summary, 483  
verification, 483  
hybrid model structure, 346, 361, 451  
complete, 463–464  
engine dynamics, 462–463  
formulation, 452–464  
forward flight, 464  
state equations, 456  
vertical dynamics, 461  
yaw dynamics, 462–463

identification vector  
model identification, **328**  
model verification, **436**

inflow, 460–461  
constant, 460  
dynamics equation, 460  
ratio, **460**

input signals for identification  
3-2-1-1 inputs, 16, 85, 112  
doublets, 2, 16, 88, 112  
frequency range of applicability, 83–85  
multi-input maneuver, 254–256  
multistep inputs, 16, 85, 112  
optimal input design, 85, 112  
overview, 83–85  
piloted inputs, 84  
Schroeder-phased input, 86  
*see also* frequency sweeps, automated  
(computer generated); frequency  
sweeps, piloted; pilot inputs

input vector, 32, 325

input-output pairs  
faulty data, 139  
transfer-function models, 282

input-output system, 1

inputs  
fixed-wing, 1–2  
helicopter, 1–2  
instrumentation of, 89  
*see also* excitation

insensitivity, **336**  
correlation, 337  
Cramér–Rao bounds, relationship with, 336  
guideline, 336

implications, 336  
interpretation, 336  
unnecessary parameters, 336

instrumentation  
bias, 123  
errors, 133–135  
requirements, 88–90

interaxis dynamic coupling, 230–231

interfaces, CIFER, 79–81

Kalman filter, 124

kinematic consistency  
maneuver, 129  
methods, 120–124

Laplace transform, 33, 149, 325, 393

lateral-directional dynamics, fixed wing, 293–298

LATFIT, 298

lead-lag (rotor), 452  
displacements, 457  
dynamics, 453, 457–459, 490–491  
natural frequency, 457  
Padé transfer function representation, 457  
regressive mode, 457  
sine lag displacement, 457

linear models  
describing functions, 18, 27, 149  
frequency response, 27  
frequency sweep, 91  
methods for, 15  
numerical extraction from nonlinear, 48, 187–406  
system identification, 27, 48

Lock number, 300, 455

LONFIT, 298

lower-order equivalent system (LOES), 277–278, 287, 342

maneuvers  
kinematic consistency, 129  
multiple inputs for MIMO solution, 247, 254–256  
*see also* piloted inputs

mass (*M*) matrix, 42, 324, 461, 463

maximum likelihood (ML) method, 86, 321

maximum unnoticeable added dynamics  
(MUAD)  
boundaries, 190

MCLAWS, 196

measurement matrices, 369

measurement vector, 32, 324, 367  
accelerometer, 369  
aerodynamic angles, 368  
Euler angles, 367  
miscellaneous measurements, 369  
velocity, 368

measurements  
closed-loop hover flight test, 60–61  
digitized, 133  
errors, 119–120  
open-loop cruise flight test, 64–65  
menu, CIFER, 73  
MIMO frequency-response data matrix, 362  
MIMO frequency-response database, 28, 34, 71, 277, 342  
MIMO state-space model identification  
basic concepts, 323–329  
fixed-wing UAV (Shadow™ 200 Block IB), 406–407  
lightweight manned helicopter (Fire Scout P2 demonstrator), 413–430  
nonlinear simulation, 402–406  
physical models, 359  
S-92 helicopter, 490–491  
SH-2G helicopter, 464–483  
XV-15 in cruise, 379–394  
XV-15 in hover, 394–402  
MISOSA, 249–250  
model structure  
decoupled stability and control, 345  
examples, 360  
fully coupled 6-DOF quasi-steady, 451  
hybrid (high-order helicopter model), 346, 361, 451–452  
quasi-steady, 346, 361, 451  
model structure determination, 28  
confidence ellipsoids, 339  
Cramér–Rao bounds, 339  
overparameterized, 340  
state-space models, 338–340  
model structure reduction, 338–340, 347, 378–379  
based on frequency-response table, 374–377  
XV-15 in cruise, 382–386  
XV-15 in hover, 395, 398  
model structures  
canonical, 342  
key points, 346–347  
lower-order equivalent system (LOES), 342  
physical, 343  
types of, 342  
model verification, *see* verification, 88  
models, *see* aeroelastic; control system;  
decoupled lateral directional; decoupled longitudinal; fixed-wing dynamics; flight-mechanics; frequency-response; hybrid fully coupled; linear; nonlinear; nonparametric; parametric; physical; quasi-steady; quasi-steady: longitudinal; quasi-steady: lateral directional; rotary-wing dynamics; simulation; state-space; subsystem; transfer-function  
moment equations, 364–365  
multi-input / multi-output, *see* MIMO  
multi-input / single-output, *see* MISO  
multi-input frequency response  
identification, 229  
from MISO analyses, 247–248  
general solution, 245–248  
hovering helicopter, 250–254  
MISOSA, 249–250  
two inputs, 234–237, 239–244  
XV-15 in cruise, 239–244  
multiple coherence, 239  
multiple inputs  
bias error, 233  
correlated inputs, 231–232  
SISO solution, limiting conditions, 230, 233  
two-input example, 231–237, 239–244  
*see also* MIMO; MISO  
naming convention, CIFER, 77  
NAVFIT, 284–285  
navigation, CIFER, 74  
noise, 15  
in closed-loop identification, 210–222  
effect on bare-airframe identification in  
closed-loop testing, 210–222  
effect on bias error, 148  
effect on bias error in spectral function  
identification, 154  
effect on coherence function, 165  
effect on frequency-response accuracy, 162–163, 168, 177, 210  
effect on random error in spectral function  
identification, 154  
effect on spectral analysis of time-history  
signals, 178  
feedback through SCAS, 210  
flight testing, implications for, 224  
at input, 154, 160, 162–164, 166, 210  
at output, 154, 160–161, 164–165, 193, 210–211  
process noise, 15, 30, 55, 160–161, 163, 166, 170, 192, 210–211, 213, 341, 434  
noise to signal ratio, 163  
nondeterministic errors (random), 26, 119  
frequency domain, 154  
time domain, 122  
nonlinear models, 152, 187–190, 402–406  
methods for, 15  
system identification, 27  
*see also* describing functions  
nonlinear simulation, 402  
nonparametric models, 9–12, 152  
*see also* frequency-response models  
off-axis response, definition of, 230  
on-axis response, definition of, 230  
one-way coupling, 294, 303  
open-loop flight testing

- bare-airframe identification, 65, 95, 97
- measurements, 64–65
  - see also* XV-15 in cruise
- optimal input design, 85
- organization of book, 20–22
- output error method, 30, 342
- output vector, 324
- outputs
  - fixed-wing, 1–2
  - helicopter, 1–2
  - instrumentation of, 89
- overlapped windowing, 154
- overparameterized, 12, 283, 340
- parameters
  - dropped, 338–340
  - fixed and free, 346
  - physical constraints, 347
- parametric models, 5, 9–12, 25, 28, 277
  - see also* state-space models; transfer-function models
- partial coherence, 238
- pendulum
  - canonical state-space model, 348–350
  - composite windowing, 263–266
  - frequency-response identification, 177–178
  - problem description, 55–58
  - transfer-function model, 285–286
  - unstable dynamics, 225
- periodograms, 154
- perturbation methods, classical, 402
- physical model structure, 11, 149, 343, 345–346, 359, 362
  - 3-DOF lateral/directional, 379–402
  - 3-DOF longitudinal, 406–407
  - 6-DOF MIMO, 413–430
  - background, 360–361
  - complex multibody systems, 371
  - coupled fuselage/regressive-flap dynamics, 453
  - equations of motion, 362–365
  - fixed, free, and constrained parameters, 370–371
  - fixed-wing UAV (Shadow™ 200 Block IB), 406–407
- initial setup, 377–378
- lightweight manned helicopter (Fire Scout P2 demonstrator), 413–430
  - dynamic inflow, 415
  - engine/governor/rpm dynamics, 415
  - final results, 420–430
  - speed derivatives, 415, 417–420
- measurement matrices, 369
- measurement vector, 367
- state and control matrices, 367
- state and control variables, 366
- time delay matrix, 370
- pilot cross-over frequency, 182
- pilot cutoff frequency, 182–183
- pilot inputs
  - non-sweep maneuvers, 112–117
  - recommended, 86–88
  - see also* frequency sweeps, piloted; excitation
- poles, 279
- power decibels, 154
- primary control, 230
- quasi-steady derivatives, 461, 476
  - speed, 453
  - stability, 453
- quasi-steady model, 7, 188, 303, 346, 361, 451
  - lateral directional, 7
  - longitudinal, 7
- random error, 26, 119, 175, 221
  - window size, 260
- reactionless mode, 4-bladed rotor, 454, 457
- real-time telemetry, 94, 99
- record length, 84, 93, 154, 171
  - concatenated, 171
- reduction, model structure, 378–379
- reference shift, 15, 32
- reference-shift vector, 32, 436–439
- rms fit error, 437
- roadmap, frequency-response method, 25–29
- rotary-wing dynamics model, 7
- rotor equations, 455
- rotor flapping,
  - see* flapping (rotor)
- rotor modes, 452
- rotor-body coupling, 299
- rotorcraft dynamics
  - flap stiffness, 305–306
  - quasi-steady approximation, 304
  - simple roll-response model, 303
  - transfer-function models, 299–310
- rotorcraft system identification, 8–9
- rotor-flap time constant, 455
- sample rate, 89
- scale factor, 123
- SCAS, 95–97
  - bare-airframe identification, 209
  - noise feedback, 210
- Schur product, 326
- secondary control, 230
- sensitivity analysis, 28
- sensor dynamics, 326
- servoelastic modes, 193
- sign conventions, 453–454, 457
- signal-to-noise ratio
  - effect on bias error, 213–215
- simulation
  - closed-loop, 61

compared to system identification, 6–8  
simulation models, 188  
error bounds (fidelity criteria), 190  
error response function, **190**  
GENHEL, 183, 188  
GTR, 382, 386, 395, 398  
off-line testing, 105–106  
SH-2G helicopter, 475–476  
stability and control derivatives, 403  
validation, 37–39, 190–191  
SIMULINK, 196  
single-input / single-output, *see* SISO  
SMACK, 124–129  
spectral analysis, 26–27  
applications and examples, 178–200  
frequency content, 158  
of time histories, 178–182  
spectral estimates  
calculating, 152  
composite, 260, 262  
conditioned, 237–239  
rough, 153, 260  
smooth, **155**, 260  
weighted average, 261  
stability derivatives, 11, 32, 324, 361  
nonlinear simulation, 403–406  
stability margin  
direct estimate, 192  
indirect estimate, 192  
specification, 192–193  
testing, 191–196  
stability-axis coordinate systems, 363  
state equations, 32, 42  
engine/governor/rotor rpm dynamics, 415  
hybrid model, 456  
state vector, 32  
state-space model identification, 5, 321  
accuracy, 327  
accuracy analysis, 330–340  
advantages, 322–323  
canonical models, 343–345  
cost function, 327–329  
matrix form, 332  
DERIVID, 347–348  
frequency range, 329  
frequency-response database, 371–377  
frequency-response method,  
advantages, 340–342  
frequency-response table, 372–377, 380,  
394  
identification algorithm, 328  
initial setup, 377–379, 382, 394–395  
key features, 340–342  
matrices, 324  
model definition, 342–347  
model structure, 324, 359  
model structure reduction, 374–379,  
382–386, 395, 398  
parameters, 324  
physical models, 345–346, 359  
speed-stability derivatives, 417–420  
structure determination, 338–340  
transfer-function model included, 326–327  
*see also* canonical models; MIMO state-space model identification; physical model structure  
state-space model identification, examples  
3-DOF lateral/directional, 379–402  
closed-loop response, 350–353  
fixed-wing UAV (Shadow™ 200 Block IB), 406–407  
lightweight manned helicopter (Fire Scout P2 demonstrator), 413–430  
nonlinear simulation, 403  
pendulum, 348–350  
S-92 helicopter, 490–491  
SH-2G helicopter, 464–483  
structural response, 353–357  
XV-15 in cruise, 379–394  
XV-15 in hover, 350–353, 394–402  
state-space models  
*see also* model structures  
structural response identification, 353–357  
automated frequency sweeps, 106–108  
composite windowing, 273–274  
window size, 172–175  
subsystem models, 314–315  
swashplate deflection, 455  
system identification  
basic concepts, 1–6  
compared to simulation, 6–8  
special challenges for rotorcraft, 8–9  
system identification methods, *see* frequency domain; frequency response; output error; time-domain  
systematic errors, 119  
telemetry, real-time, 94, 99  
Theil inequality coefficient (TIC), **438**  
thrust coefficient, **460**–461  
tilt-rotor, *see* XV-15 characteristics; XV-15 configurations; XV-15 identification in cruise; XV-15 identification in hover  
time delay, 15, 31  
equivalent, 32, 279  
matrix, **325**, 370  
time histories  
spectral analysis, 178–182  
time shift, 123  
time vector diagram, 393  
time-domain methods, 33–34  
time-domain verification, *see* verification  
time-response methods, 15  
tip-path plane, 454  
deflection, 299  
transfer-function models, 5

cost function, 280  
equivalent time delay, 279  
factored form, 279  
free and fixed parameters, 279, 284  
frequency range of fit, 282  
generalized form, 278  
identification method, 39–40, 277–281  
identification with NAVFIT, 284–285  
input–output pairs, 282  
magnitude and phase weights, 280  
order of numerator and denominator, 282–283  
overparameterized, 283  
parameters, 41, 279  
poles and zeros, 41–42, 279  
state-space model, included in, 326–327  
structure, 281–284  
time delay, equivalent, 283–284  
transfer-function models, examples  
    1-DOF aircraft model, 149–152  
    aeroelastic, 310–312  
    control system design, 307–310  
    flight mechanics, 298–306  
    handling qualities, 286–298  
    handling qualities evaluation of ADOCS demonstrator, 287–293  
    lower-order equivalent system (LOES), 287  
    OH-58D with high flap stiffness, 305–306  
    pendulum, 285–286  
    rotorcraft dynamics, 299–310  
    simultaneous identification, 298  
    subsystems, 314–315  
    XV-15 in cruise, 293–298  
turbulence, 224

unbiased estimate, 161  
    *see also* maximum unnoticeable added dynamics (MUAD)  
unnoticeable dynamics, 294  
unstable system, 16, 148, 152  
    dynamics, 9, 34  
    identification, 225–226  
user interface, CIFER, 70–71, 73–78  
utilities, CIFER, 73–75, 78–79

validation  
    control system model, 196–200  
    criteria, 190  
    simulation model, 190–191  
velocity measurements, 368  
verification, 29, 88, 433  
    bias vector, 436–439  
    correlation problem, 439–440  
    data conditioning, 440  
    identification vector, **436**  
    method, 434–436  
    motivation, 433–434

reference-shift vector, 436–439  
rms fit error, **437**  
Theil inequality coefficient (TIC), **438**  
VERIFY, 440–441  
verification, examples  
    fixed-wing UAV (Shadow™ 200 Block IB), 407  
    SH-2G helicopter, 483  
    XV-15 in cruise, 45–48  
    XV-15 in cruise, physical model, 442–443  
    XV-15 in hover, 48–51  
    XV-15 in hover, canonical model, 441–442  
    XV-15 in hover, physical model, 447  
VERIFY, 440–441  
vibration analysis, 178–182

weights  
    composite windowing, 261  
    state-space models, 328  
transfer-function models, 280  
verification, 437  
    window shaping function, 155  
white noise, 104–105  
wind, 224  
window overlap, 168  
window shaping function, 155  
window size, 154  
    bias error, 173  
    maximum, 170–172, 263  
    minimum, 172, 263  
    nominal, 170  
    range for composite windowing, 260  
    selecting, 263  
    structural response identification, 172–175  
    tradeoffs, 169, 175, 259–260  
    weighted average, **262**

windowing, 154–157  
    composite, 259–262  
    number of windows, 154–156

wing bending, 311

XV-15 characteristics  
    cruise, 64  
    hover, 58–61

XV-15 configurations, 35–36, 58

XV-15 identification in cruise  
    3-DOF lateral/directional model, 379–394  
    database #2, 58  
    dynamic characteristics, 64  
    final identification results, 386–394  
    flight-test conditions, 58  
    frequency sweeps, 36–37  
    frequency-response table, 380  
    initial model structure, 379, 382  
    measurements, 64–65  
    MISO solution, two inputs, 239–244  
    model structure reduction, 382–386  
    roll and yaw controls, 64

## INDEX

523

stability and control derivative model  
identification, 41–42

transfer-function model, 39–40, 293–298

verification, 45–48

verification of physical model, 442–443

XV-15 identification in hover

- 3-DOF lateral/directional model, 394–402
- bare-airframe identification, 215–222
- canonical model, 350–353
- composite windowing for closed-loop SISO  
identification, 268–271
- database #1, 58
- dynamic characteristics, 58–60
- final identification results, 398–402
- flight-test conditions, 58

frequency-response table, 394

initial model structure, 394–395

model structure reduction, 395, 398

roll and yaw controls, 58–60

stability and control derivative model  
identification, 48–51

verification, 48–51

verification of canonical model, 441–442

verification of physical model, 447

yaw dynamics, 462–463

zeros, 279

zoom transform,  
*see* chirp z-transform (CZT)

This page intentionally left blank

## Supporting Materials

To download your software and any software updates, please go to <http://www.aiaa.org/publications/supportmaterials>. Follow the instructions provided and enter the following password: **velocity**.

A complete list of titles in the AIAA Education Series and other AIAA publications is available at <http://www.aiaa.org>.